

Volume II



**SYSTEMS CONTROL TECHNOLOGY, INC.**

1801 PAGE MILL RD. □ P.O. BOX 10180 □ PALO ALTO, CALIFORNIA 94303 □ (415) 494-2233

ANTHOLOGY OF RAIL DYNAMICS RESEARCH

References Suggested for Inclusion in  
Final Report

Assembled for:

Analysis and Evaluation Division  
Office of Rail Safety Research  
Federal Railroad Administration  
Washington, D.C. 20590

April, 1982

## REFERENCE 17

### AN IMPROVED NUMERICAL METHOD AND COMPUTER PROGRAM FOR COUNTERFORMAL CONTACT STRESS PROBLEMS

B. Paul,  
Professor of Mechanical Engineering

and

J. Hashemi  
Research Fellow  
University of Pennsylvania  
Philadelphia, Pennsylvania

#### ABSTRACT

A numerical method is given for the solution of frictionless counterformal contact stress problems. By modifying the previously described simply-discretized method, and by introducing an automatic mesh generating procedure for the changing contact region, it has been possible to make major improvements in the generality, stability, accuracy and efficiency of the numerical procedures. The method has been verified by comparison with known solutions for the Hertzian case. Numerical examples for non-Hertzian cases include the first known solution for non-Hertzian contact of a railroad wheel and rail. The mesh generation and boundary iteration procedure introduced is applicable to a wider class of problems with changing boundaries, such as: determination of wheel-rail adhesion-slip boundary, determination of elastic-plastic interfaces for residual stress problems, etc.

#### 1. INTRODUCTION

Many situations arise in engineering practice where contacting surfaces cannot be modelled as second-degree polynomials over the contact region, and therefore cannot be analyzed by the classical method of Hertz (1). Until recently, there existed no general way of analyzing non-Hertzian problems. However, Singh and Paul (2) have introduced a numerical approach to the problem which broadens considerably the range of contact stress problems that can be solved. For the historical background of the problem and references to recent related work by Kalker and Randen (3), Conry and Seirig (4), and others, see the discussion in (2).

Contact stress problems with load-dependent contact regions are classified as counterformal problems or conformal problems accordingly as the dimensions of the contact region are small or large, compared to the local radii of curvature of the contacting surfaces. Counterformal contact problems in turn are subdivided into Hertzian problems, where the contacting surfaces are locally quadratic, and non-Hertzian otherwise; all conformal problems are non-Hertzian. In this paper, we develop a general purpose procedure for solving counterformal contact problems, and illustrate the procedure by several examples, including the first known solution for non-Hertzian contact stresses at the interface of a steel wheel on a steel rail (Figs. 8-10).

The present work represents an extension of the simply-discretized method

introduced by Singh and Paul (2) who found that the original method was severely limited in its range of application because of numerical instabilities. Although these numerical difficulties could be overcome by a method of functional regularization, as explained in Singh and Paul (5), the efficiency and accuracy suffered in the process. The modification of the simply discretized method used here improves its efficiency and accuracy, but more importantly, it eliminates the need to specify arbitrary "regularization parameters," and paves the way for the solution to the more complex problems of conformal contact.

The second major theme of the current work is the development of a systematic and automatic procedure for identifying the continuously changing, load-dependent "contact boundary curve", which encloses the contact region. An effective iteration procedure is devised which allows us to automatically overlay any given candidate contact region (i.e., trial region) with a rectangular mesh that suitably reflects the changes in size and shape of the contact region as the solution proceeds. This mesh generation scheme, which is applicable to conformal problems as well, is essential to the success of the method. Nor is it a trivial extension of existing procedures, since current finite difference and finite element methods operate with an initially defined system geometry that remains essentially fixed throughout the course of solution. The mesh generation procedures developed herein will be applicable to a wider class of problems with changing boundaries, e.g.: the changing region of locked versus slipped areas in railroad "wheel creep" problems, changing elastic-plastic boundaries for problems of plastic flow and residual stresses, melt interfaces in two-phase heat transfer problems, etc.

In the next section, we formulate the basic integral equation governing all counterformal contact stress problems. In Sec. 3 we show how the integral equation is to be discretized, and the problem is converted into one of numerical analysis. In Sec. 4 we show that when the initial trial contact boundary is defined by a suitably chosen "interpenetration curve", the true contact region is entirely enclosed by this interpenetration curve. This important result enables us to simplify considerably and improve the rate of convergence of the procedure. In Sec. 5 we use the result of Sec. 4 to devise a mesh generation and boundary refinement scheme for the continually changing candidate boundaries that ultimately converge to the true contact boundary. The computer program used to generate the numerical results is briefly described in Sec. 6, and several numerical examples are given in Sec. 7. Conclusions are summarized in Sec. 8.

## 2. FORMULATION OF THE GOVERNING INTEGRAL EQUATION

Let the two bodies be denoted as body 1 and body 2. Cartesian coordinate axes are set up for each body with the initial contact point as common origin. Axes  $(x,y)$  lie in the tangent plane of the two surfaces at the initial contact point, with  $z_1$  and  $z_2$  pointing into bodies 1 and 2, respectively. Both surfaces are frictionless. Due to the applied force, material points in the two bodies undergo rigid-body translation and elastic deformation.

The initial separation of points on the two bodies with common  $(x,y)$  coordinates is given by the known surface function

$$f(x,y) \equiv z_1(x,y) + z_2(x,y) \quad (1)$$

If the bodies are pressed together, points that are well removed from the contact region will undergo a rigid body displacement, whereas points near the contact region will undergo a rigid body motion plus superposed elastic deformations. In general, the rigid-body motion of body 1 relative to body 2 is defined by six parameters. For simplicity, we assume, at this point, that the rigid body motion of body 1 relative to body 2 consists of a translation through the distance  $\delta$  in the direction of axis  $z_2$ . The quantity  $\delta$  is called the rigid body approach. The methods of this paper may be extended to cover the more general case where several or all of the six possible degrees of (rigid-body) freedom are permitted.

If  $w_1$  and  $w_2$  represent the elastic displacements of bodies 1 and 2 in the directions of  $z_1$  and  $z_2$ , the separation of points having common  $(x,y)$



coordinates becomes in the deformed state (6, p. 320).

$$s = w_1 + w_2 + z_1 + z_2 - \delta \quad (2)$$

The region of the  $(x,y)$  plane within which contact occurs will be designated by  $\Omega$ ; its boundary will be called the contact boundary. It is necessary that

$$s = w_1 + w_2 + z_1 + z_2 - \delta = 0 \text{ (within } \Omega \text{)} \quad (3)$$

$$s = w_1 + w_2 + z_1 + z_2 - \delta > 0 \text{ (outside } \Omega \text{)} \quad (4)$$

Equation (3) follows from the definition of contact, and Inequality (4) follows from the impenetrability of matter. For the class of problems under consideration (counterformal contact), the dimensions of the contact region are assumed to be small compared to local radii of curvature of the indenting surfaces. Hence, it is permissible to consider the two bodies as elastic half spaces in order to correlate the displacement field  $w$  with the pressure field  $p$  inside the contact region  $\Omega$ . For points on the frictionless surfaces of the bodies,  $w$  and  $p$  are related by integrating the Boussinesq solution for a normal point load, which leads to the following equation ((7), p. 365).

$$w_i(x,y) = \frac{(1-\nu_i^2)}{\pi E_i} \int_{\Omega} \frac{p(x',y') dx' dy'}{[(x-x')^2 + (y-y')^2]^{1/2}}; \quad (i = 1,2) \quad (5)$$

where  $\nu_i$  and  $E_i$  are Poisson's ratio and Young's moduli of the two bodies, and  $\Omega$  is the projection of the contact region on the tangent plane  $(x,y)$ . Because the two bodies cannot exert tension upon one another, a physically meaningful solution requires that

$$p(x,y) \geq 0 \text{ inside } \Omega \quad (6)$$

Conditions (3)-(6) define the contact problem which must be solved to obtain the pressure field  $p$ , and contact region  $\Omega$  for a given approach  $\delta$ .

After finding  $p$  and  $\Omega$ , one may evaluate the forces and moments needed to produce the given approach, i.e.

$$F_z = \int_{\Omega} p \, dx \, dy, \quad M_x = - \int_{\Omega} y p \, dx \, dy, \quad M_y = \int_{\Omega} x p \, dx \, dy \quad (7-a,b,c)$$

By combining Eqs. (1), (2), and (5) we see that the following integral equation must be satisfied for all values of  $(x,y)$

$$k \int_{\Omega} \frac{p dA}{r} = k \int_{\Omega} \frac{p(x',y') dx' dy'}{[(x-x')^2 + (y-y')^2]^{1/2}} = \delta - f(x,y) \quad (8)$$

where

$$k = (1-\nu_1^2)/\pi E_1 + (1-\nu_2^2)/\pi E_2 \quad (9)$$

Finally, we note that since the pressure  $p$  vanishes outside of  $\Omega$  and is positive inside  $\Omega$ , it must vanish on the boundary of  $\Omega$  if  $p$  is to be continuous. This will be the case when the surface function  $f(x,y)$  is continuous (e.g. with well-rounded indentors). However, when the profile function is discontinuous (e.g. when sharp corners occur on the indentors) the pressure need not vanish along the contact boundary, and indeed it will become infinite for perfectly sharp edged indentors.

#### 4. ENCLOSURE OF CONTACT REGION BY INTERPENETRATION CURVE FOR COUNTERFORMAL PROBLEMS

We will assume that the actual relative motions of the two bodies are completely known at points well removed from the contact region, and that the corresponding curve of intersection (interpenetration curve) is well defined. In short, we assume that the rigid body approach is specified and seek to find both the contact region, and the contact pressure distribution. For an initial (candidate) contact region we utilize the region inside the interpenetration curve.

When restricting our attention to problems of counterformal (but not necessarily Hertzian) contact, we will show that the actual contact region lies inside the interpenetration curve associated with a fixed approach. Consider Fig. 1 which shows a cross-section through the  $z$  axis of two bodies, (1) and (2), which initially touch at a common point  $C_1$  (in body 1) or  $C_2$  (in body 2). The  $z$  axis passes through  $C_1$  and points along the common normal into body 1. The cross-section of body 1 is initially a curve  $M_1C_1N_1$  and that of body 2 is a curve  $M_2C_2N_2$ .

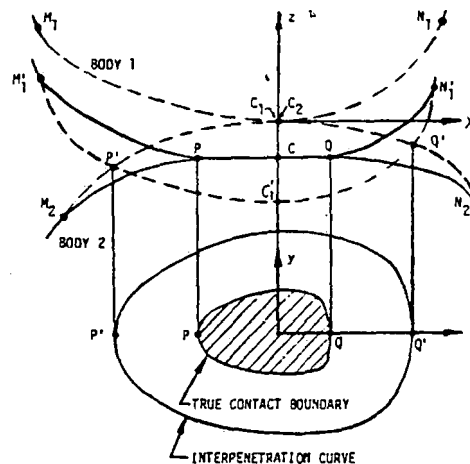


Fig. 1 Interpenetration curve surrounds true contact boundary for counterformal contact.

Due to the rigid body approach, body 1 moves towards body 2 and becomes the curve  $M_1'C_1'N_1'$ , which intersects body 2 at points  $P'$  and  $Q'$  on the (spatial) interpenetration curve. However, physical interpenetration is impossible, and mutual pressures will be exerted on the bodies so that curve  $M_1'C_1'N_1'$  is pushed upward (deforms elastically), and becomes the curve  $M_1CN_1$ . Similarly, curve  $M_2C_2N_2$  is pushed downward (deforms elastically) into the curve  $M_2CN_2$ . All points in the neighborhood of  $C$  lie on the common "contact region" of the deformed surfaces, and points  $P$  and  $Q$  mark the extremities of the contact region, in the view shown.

Because we are considering counterformal contact, the elastic deformation is governed by Boussinesq's displacement function. This requires that any pressure exerted on body 1 in the neighborhood of  $C$  must cause the curve  $M_1CN_1$  to lie above the curve  $M_1'C_1'N_1'$ . Similarly, the pressures on body 2 must cause curve  $M_2CN_2$  to lie below curve  $M_2C_2N_2$ . Therefore,  $Q$  and  $P$  must both lie inside the lune-shaped region  $P'C_1'Q'C_1'P'$ . In other words, the true contact boundary points  $P$  and  $Q$  must lie between points  $P'$  and  $Q'$  on the interpenetration curve.

Precisely the same reasoning can be applied to conditions in the  $yz$  plane or

indeed in any cross-section through the  $z$  axis. Thus we may conclude that for counterformal contact, the true contact region lies entirely inside the interpenetration curve associated with the true rigid body approach.

This result may appear to contradict the results found by Singh and Paul (2), who showed examples of contact boundaries which crossed "interpenetration curves" for Hertzian ellipses. However, it should be noted that Singh and Paul defined their "interpenetration" differently from us. They replaced  $\delta$  in Eq. (10) by an arbitrarily chosen length  $d$ . Then they treated  $\delta$  as an unknown which had to be solved for along with the unknown pressures  $p_i$ . By permitting  $\delta$  to "float" in this fashion, and accepting whatever value of  $\delta$  was associated with the final boundary (when convergence did occur) they injected the possibility of indeterminacy into the formulation of the problem--which contributed to the ill-posed character of their formulation. The present authors arrived at this conclusion independently, but should like to acknowledge a suggestion to the same effect by J. R. Barber (9), in a comment on the paper by Singh, Paul and Woodward (10).

Thus the starting curves used by Singh and Paul were quite different from those being used in this work. The improved accuracy and efficiency, stemming from the current method of defining interpenetration curves, represents a significant improvement.

Quantitative results on the size and shape of the contact boundary, relative to the interpenetration curve as now defined, are given in (8), for the case of Hertzian contact; these results confirm (for Hertzian problems) the conclusions reached in this section.

It should also be noted that the conclusions drawn in this section are valid under conditions of counterformal contact. For conformal contact we cannot conclude that the interpenetration curve encloses the true contact curve in every case.

## 5. MESH GENERATION AND BOUNDARY DETERMINATION

It is essential that we devise efficient methods for modifying the candidate contact boundary curves and for automatically overlaying them with appropriately defined networks of cell boundaries. The procedure described below, which utilizes rectangular cells, with sides parallel to the  $x$  and  $y$  axes, has been found to be versatile and efficient. We will, for simplicity, assume that the contact region is symmetric about the  $x$  axis (as it would be for a wheel axis parallel to the  $x$  axis, and a rail axis parallel to the  $y$  axis).

The first candidate contact boundary is the interpenetration curve corresponding to the assumed state of rigid body motion. For example, Fig. 2 shows such a curve together with coordinate axes ( $x, y$ ). The  $x$ -diameter will be divided uniformly into  $m_x$  segments of width  $h_x$ ; in Fig. 1,  $m_x = 9$ . Nonuniform cell divisions can be used if desired.<sup>1</sup>

Field points are defined to be those points in the center of each cell. Let  $x_i$  ( $i = 1, 2, \dots, m_x$ ) be the abscissa of the midpoint of cell  $i$ . The boundary curve, at abscissa  $x_i$ , will have an upper ordinate  $y_i^U$  and a lower ordinate  $y_i^L$ . The vertical chord through  $x_i$ , of length  $(y_i^U - y_i^L)$ , should be divided into  $m_y$  segments of height  $h_y$ . In general, the  $m_y$  segments need not be uniformly distributed, and may depend upon  $x_i$ . When the contact region is symmetric about the  $x$  axis,  $y_i^L = -y_i^U$ , and we will choose  $m_y$  to be an odd number; then the middle cell of the column will be centered exactly on the  $x$  axis, as shown in Fig. 2, where  $m_y = 9$ . Only that region above the axis of symmetry is shown in the Figure.

When symmetry exists about the  $y$  axis a similar procedure may be followed for the subdivisions along the abscissa.

Each cell is given an identification number  $i$ , and the pressure within cell domain  $\Omega_i$  is assumed to have the constant value  $p_i$ . The unknowns  $p_i$  are found by solving linear equations (14). If any of the calculated pressures  $p_i$  are negative, the implication is that the corresponding field point  $(x_i, y_i)$  actually lies outside the true contact region.

<sup>1</sup>In numerical work, it has been found useful to use at least two different values of  $h_x$  on each side of the origin so that a finer mesh can be generated near the edges of  $\Omega$ .

value  
the  $x$   
column  
Assum  
at  $y$   
until  
Fig.  
 $y = y$   
ordin

(as i  
calcu  
where

be re

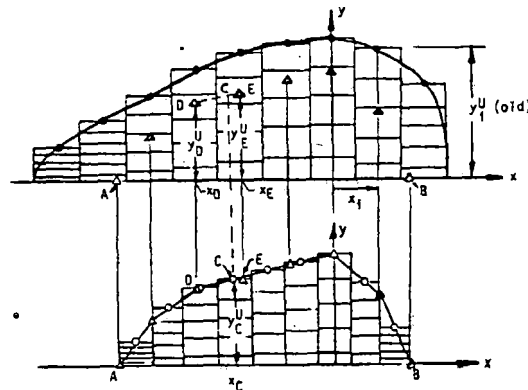


Fig.2 (a) • Initial candidate contact curve.  
(b) Δ Subsequent candidate contact curve.  
○ Interpolated points on latest contact curve.

To redefine the contact boundary we start at the leftmost end and scan the values of  $p$  along the column of cells for which  $x = x_j = \text{constant}$ , starting at the  $x$  axis and working outwards towards the boundary. If no cells in this column have positive pressure we go on to scan the next column on the right. Assuming that the contact region includes the cell on the abscissa<sup>2</sup>, the pressure at  $y = 0$  will be positive. Incrementing  $y$  by  $h_y$ , we scan parallel to the  $y$  axis until we find a pressure  $p^N$ , which is negative at the ordinate  $y = y^N$ . Then (see Fig. 3) we interpolate linearly between  $p^N$  and the last positive pressure  $p^P$  (at  $y = y^P$ ) to find  $y^0$ , the point where  $p = 0$ . We now replace the old upper boundary ordinate  $y_j^U$  by  $y^0$ .

If all pressures are positive in all the cells of the column for which  $x = x_j$  (as in Fig. 4), the new boundary ordinate is found by fitting a parabola to the calculated pressure profile, near the old boundary, and finding the ordinate  $y^0$  where the extrapolated pressure vanishes. Methods of fitting the parabola

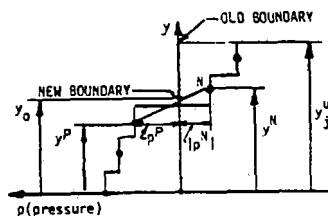


Fig.3 Pressure distribution, at  $x = x_1 = \text{constant}$ , when pressure changes from positive to negative.

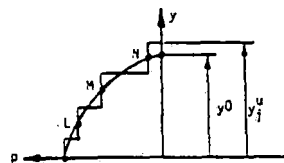


Fig.4 Pressure distribution, at  $x = x_j = \text{constant}$ , when pressures are all positive.

<sup>2</sup>For nonsymmetric or nonconvex contact regions this assumption will have to be relaxed and the procedure modified slightly.



through the three points L,M,N (or, in special cases, through the two points M and N) in such a way that  $p$  is a one-valued function of  $y$  are described in Ref. (8).

If the pressure is positive in the neighboring column of cells, where  $x = x_j + h_x$ , the process is repeated to find the new ordinate  $y_{j+1}^U$  corresponding to zero pressure on the upper boundary. The process is continued for all  $x_j$  until one reaches a cell on the abscissa with negative pressures--or until all  $m_x$  columns on the abscissa have been considered.

At this point, the upper boundary of the new contact region has been defined by an array of values  $y_j^U$  associated with the old field points  $x_j$ . These points on the new boundary are denoted by the small open triangles in Fig. 2.

For counterformal contact problems, the new candidate contact boundary will be inside the old one, and we must rearrange the mesh layout to preserve accuracy. Towards that end, we find the new major diameter (AB in Fig. 2) by interpolation (or extrapolation) exactly as in Figs. 3 and 4, except that  $y$  is replaced by  $x$  in the process.

The new major diameter is now subdivided into  $m_x$  cells in the same manner as the old diameter was. This defines a whole new array of field points with abscissas  $x_1, x_2, \dots, x_{m_x}$ . To find the corresponding values  $y_1^U, y_2^U$ , we interpolate between the points on the upper boundary just found. Thus to find  $y_C^U$  corresponding to abscissa value  $x_C$ , in Fig. 2(b), we interpolate linearly between the known points D and E shown in Fig. 2(a); i.e.

$$y_C^U = \frac{y_D^U (x_E - x_C) + x_E^U (x_C - x_D)}{x_E - x_D} \quad (17)$$

The interpolated point C is marked by a small open circle in Fig. 2(b). Similar circles mark all other updated values of  $y_j^U$  in Fig. 2(b).

At this point, we have completely defined a new candidate contact boundary with known ordinate values along the midline of each column of cells. These updated midline ordinates  $y_j^U$  may now be subdivided into  $m_y$  segments, thereby defining the new meshwork of cells corresponding to the new contact region  $\Omega$ . We may now recalculate the pressures for the new region  $\Omega$  by use of Eqs. (14).

The newly calculated pressures may be used to refine the candidate boundary by repeating the procedure used for the old boundary, and the process may be repeated as often as necessary, or until the boundary stabilizes within specified tolerances.

## 6. ORGANIZATION OF COMPUTER PROGRAMS

### Main Program--COUNTACT<sup>3</sup>

A computer program called COUNTACT--which stands for "COUNterformal CONTACT"--has been based on the analysis just described. It has two principal versions, COUNTACT-1 and COUNTACT-2, which deal respectively with contact areas having one or two axes of symmetry. In rail-wheel problems there will always be at least one axis of symmetry (across the rail axis) for wheelsets at zero yaw angle. For certain positions of the wheel along the rail (where wheel curvature, and rail curvature are each uniform throughout the contact region) two axes of symmetry will exist. A version of the program for problems which are axisymmetric about an axis normal to the contacting surfaces has been called COUNTAXI.<sup>4</sup>

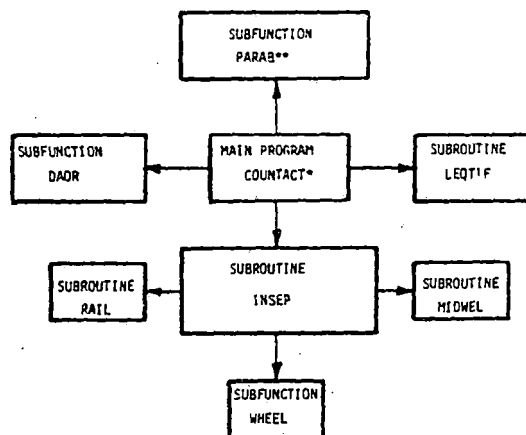
The purpose of the main program is to manage input and output, to call appropriate subprograms as needed, and to interlink the various components needed for the overall program logic. Figure 5 shows the relationship of the main program to the subprograms. In Fig. 5, the arrows point from the calling program to the called program. The following subprograms are used:

<sup>3</sup>The program is described in greater depth in the User's Manual (11).

<sup>4</sup>Mathematical considerations peculiar to axisymmetric problems are described in (8).

SL  
cribed  
point p  
SL  
cients  
SL  
routine  
SL  
functio  
SL  
railroad  
appropri  
(see Fi  
Suc  
for any  
SL  
railhead  
No  
MIDWEL  
appropri  
for cou  
M  
of COUNT  
SL  
SL  
tic inte  
the rec.

The  
position  
throughs  
and we c  
known an  
In



Notes: \* COUNTACT-1 for one axis of symmetry  
 \* COUNTACT-2 for two axes of symmetry  
 \*\* PARAB2 or PARAB3 for two or three point parabolas

Fig.5. Organization of Program COUNTACT. Arrows point from calling program to called program.

Subfunction PARAB: does the parabolic interpolation (or extrapolation) described in Sec. 5. PARAB2 and PARAB3 are versions which use two-point or three-point parabolas respectively.

Subfunction DAOR: calculates the integral  $\int dA/r$  required for the coefficients  $b_{ij}$  (see Eq. (15)).

Subroutine LEQTIF: solves the linear algebraic equations (14). This routine comes from the library of IMSL (12).

Subroutine INSEP: furnishes the initial separation; i.e. the surface function, Eq. (1).

Subroutine MIDWEL: provides the coordinates of an axial cross-section of a railroad wheel (body 1); i.e. it computes the term  $z_1(x,0)$  of Eq. (1) in an appropriate set of coordinates  $(\xi, \zeta)$  localized at the initial point of contact (see Figs. and ).

Subfunction WHEEL: computes the profile function  $z_1(x,y)$  for body 1 (wheel) for any  $(x,y)$  in the contact region.

Subroutine RAIL: computes the profile function  $z_2(x,y)$  for body 2 (the railhead).

Note: For counterformal problems, the functions computed by subprograms MIDWEL, WHEEL, and RAIL may be approximated as piecewise quadratic functions in appropriately transformed coordinates. A detailed discussion of these functions for counterformal and conformal cases is given in Ref. (13).

MAIN Program COUNTAXI: The logic for axisymmetric problems varies from that of COUNTACT in the following ways:

Subroutine PROFIL: replaces the routine INSEP.

Subroutines: MMDELK and MMDELE: (which are IMSL programs for complete elliptic integrals of the first and second kind) are used in place of DAOR to compute the required integrals.

## 7. EXAMPLES

The first example is that of rail and wheel contact where the wheel is so positioned that the principal curvatures of wheel and rail are each uniform throughout the contact patch. In this case, the solution is essentially Hertzian, and we can compare the accuracy and convergence of the numerical method against known analytical solutions.

In the second example we solve another case of rail and wheel contact, where

the solution cannot be obtained analytically because the rail curvature has a jump discontinuity in the region of contact.

The third example is that of parallel rollers with crowned edges, where the solution cannot be obtained analytically.

The fourth example deals with an axisymmetric problem, and shows the great resolving power (capability of predicting extremely steep stress gradients) of the methods introduced in this work.

In all of these examples the bodies are made of steel with the following elastic properties:

$$E = 30 \times 10^6 \text{ psi} \quad \text{Modulus of Elasticity (207,000 MPa)}$$

$$\nu = .3 \quad \text{Poisson's ratio}$$

**Example 1. Hertzian Case of Rail and Wheel Contact Stresses:** Let the initial point of contact of rail and wheel be point O shown in Fig. 6, and the applied load be such that the contact patch is small and within a region of uniform curvature.

The numerical solution to the problem is obtained by using the computer program "CONTACT-2" (counterformal contact stresses between bodies with two axes of symmetry).

The program requires as input the rigid body approach  $\delta$ , and the candidate contact region plus the desired initial mesh arrangement.

For  $\delta = .0004 \text{ in. (10.16 } \mu\text{m)}$ , the complete computer output is given in (8), for: pressure distribution, load (force F), and boundary of contact region. Both the contact patch and the pressure distribution have the well-known ellipsoidal distribution associated with Hertzian contact problems.

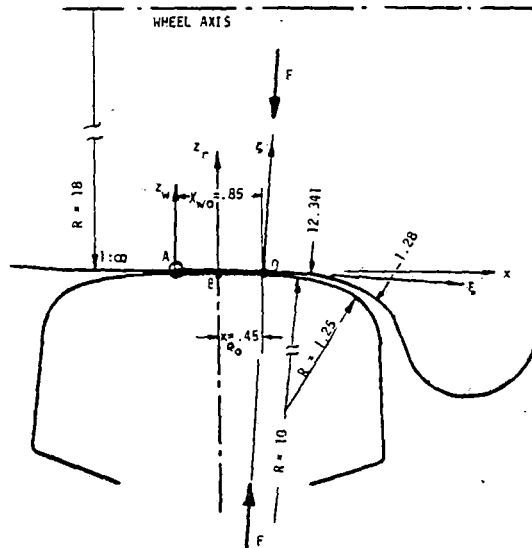


Fig. 6 Example 1  
Rail and wheel in Hertzian contact.

Figure 7 shows the process of mesh generation starting with the interpenetration contact area; note the rapid convergence of the solution.

To check the accuracy of the numerical procedure, we computed the Hertzian solution.

Table 2 shows a comparison of the theoretical results (Hertz) and those obtained with the computer program (CONTACT-2) where F is applied force (lb),  $p_0$  is peak contact pressure (psi), a and b (in.) are semidiameters of the contact patch.

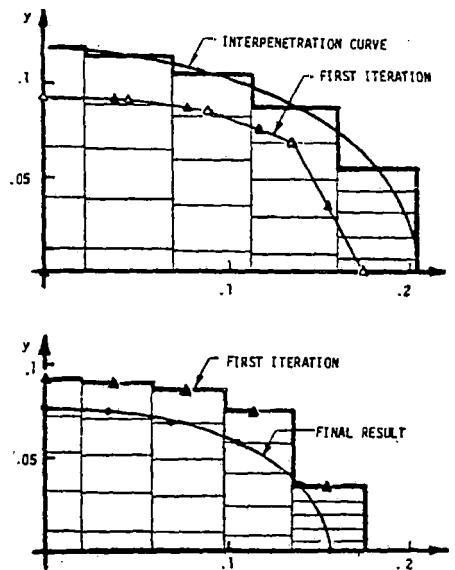


Fig. 7. Showing mesh development and convergence of contact boundary.

Table 2

Quantity	Hertz	COUNTACT-2	% Error
F	1006.6	1006.6	0
$p_0$	$.3924 \times 10^5$	$.3941 \times 10^5$	0.43
a	.15935	.1562	2
b	.07678	.0767	0.1

The total CPU time for solving this problem on an IBM 370/168 computer was 5.7 sec., at a cost of \$2.83, including compilation.

Example 2. Non Hertzian Rail-Wheel Contact: Let the initial point of contact of rail and wheel be point O, shown in Fig. 8. In this case, the minimum radius of curvature of the rail changes from 10 in. (.254 m) to 1.25 in.(0.0318 m) at point O.

The numerical solution to the problem is obtained by using the computer program COUNTACT-1, with detailed results reported in (8) for  $\delta = .005$  in. (127  $\mu$ m). A plot of pressure distribution along the x-axis is given in Fig. 9. The contact patch is shown in Fig. 10. These are the first published results for non-Hertzian rail-wheel contact stresses that the authors are aware of.



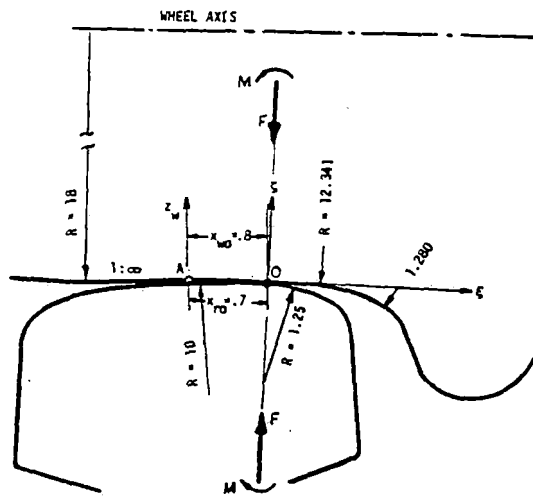


Fig. 8 Example 2  
Contact is non Hertzian. Note jump in rail  
curvature at point O.

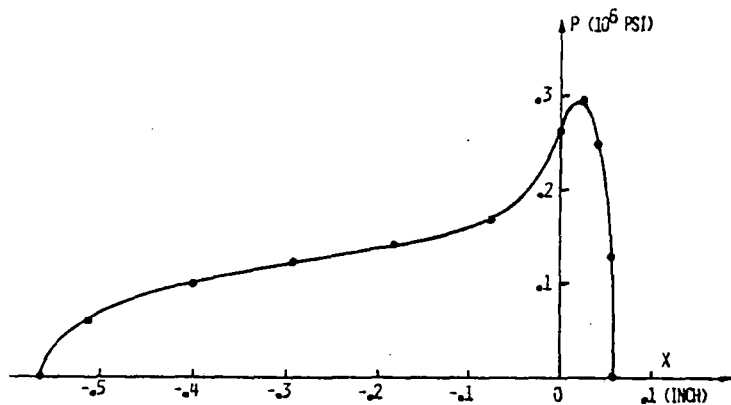


Fig. 9 Pressure Distribution, Force = 34 072 lb (151 560 N),  
Moment = -5 365 in.lb (606.2 N.m), Approach = 0.005 in. (127  $\mu$ m)

**Example 3. Crowned-Roller Contact Problem:** This is a case where a long cylinder contacts a cylinder with parallel axis and crowned edges. The purpose of this example is to show that the method can handle problems with extremely large radii of curvature that may be desired to keep stress concentration low. With the dimensions (in inches) shown in Fig. 11, and an approach of  $\delta = 0.00065$  in. (16.5  $\mu$ m), a plot of pressure distribution along the x-axis is as shown in Fig. 12.

Figure 13 shows the calculated contact patch, with the final mesh layout. In the absence of the crown radius the sharp edges of the lower cylinder would produce infinite contact pressure. Note that a crown radius of 85 in. (2.159 m) results in a negligible stress concentration. Only by use of this (or a comparable) numerical analysis is it possible (at present) to determine the effectiveness of a specified crown radius.

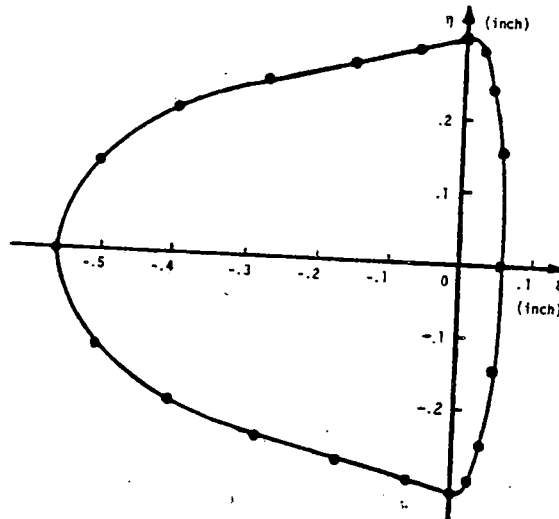


Fig. 10 Contact patch,  $F = 34.072 \text{ lb. (151.560 N)}$ ,  
 $\delta = 0.005''$  corresponding to  $(127 \mu\text{m})$

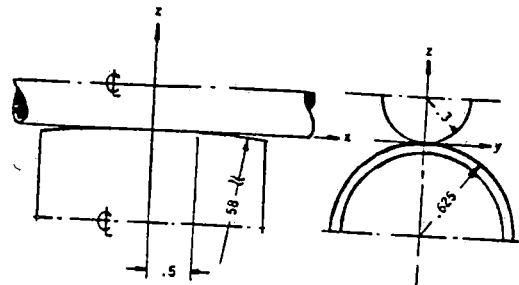


Fig. 11 Example 3  
 Crowned cylinder on parallel cylinder

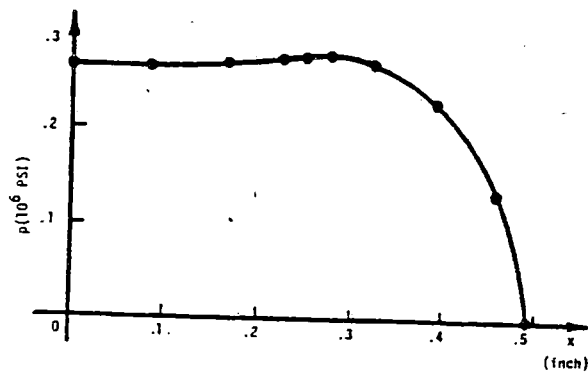


Fig. 12 Pressure distribution along  
 the longitudinal axis.

### 3. DISCRETIZATION OF THE INTEGRAL EQUATION

For a given rigid body approach  $\delta$ , Eq. (8) must be solved for the pressure field  $p(x,y)$  and for the contact region  $\Omega$ . We will begin by assuming a candidate contact region  $\Omega$ , which is bounded by the curve of intersection which would arise if surface 1 were displaced relative to surface 2, along the  $z_2$  axis by distance  $\delta$ . The projection of this curve on the  $x,y$  plane is called the interpenetration curve, and is given by

$$f(x,y) = \delta \quad (10)$$

With  $\Omega$  specified, Eq. (8) is an integral equation of the first kind, which we will solve by a modification of the Simply Discretized Method (SDM) of Singh and Paul (2).

We first discretize the domain  $\Omega$  of the integral equation into  $n$  subdomains  $\Omega_1, \Omega_2, \dots, \Omega_n$ , where each subdomain  $\Omega_j$  is called cell "j". Now Eq. (8) reduces to

$$\int_{\Omega_1} \frac{pdA}{r} + \int_{\Omega_2} \frac{pdA}{r} + \dots + \int_{\Omega_n} \frac{pdA}{r} + \dots = \frac{\delta - f(x,y)}{k} \quad (11)$$

where

$$dA = dx' dy'; \quad r = [(x' - x)^2 + (y' - y)^2]^{1/2} \quad (12)$$

If cell  $j$  is small enough so that the pressure  $p(x,y)$  over that cell can be considered a constant  $p_j$ , then Eq. (11) reduces to:

$$\int_{\Omega} \frac{pdA}{r} = \sum_{j=1}^N p_j \int_{\Omega_j} \frac{dA}{r} = \frac{\delta - f(x,y)}{k} \quad (13)$$

Therefore, there is an unknown  $p_j$  associated with each subregion  $\Omega_j$ .

To find the  $n$  unknown values of  $p_j$  we select  $n$  field points  $(x_i, y_i)$  within each cell and write Eq. (13), for each of these points, in the form:

$$\sum_{j=1}^n b_{ij} p_j = d_i, \quad (i = 1, n) \quad (14)$$

where,

$$b_{ij} = \int_{\Omega} \frac{dA}{r} = \int_{\Omega} \frac{dx' dy'}{[(x_i - x')^2 + (y_i - y')^2]^{1/2}} \quad (15)$$

$$d_i = \frac{\delta - f(x_i, y_i)}{k} \quad (16)$$

Although the required quadrature can be done in closed form, certain approximations prove to be convenient. Full details on the evaluation of the coefficients  $b_{ij}$  are given in Ref. (8).

If matrix  $[b_{ij}]$  is nonsingular, Eq. (14) may be solved for the candidate pressures  $p_j$ . If these values of  $p_j$  do not satisfy conditions (6) and (4), we must modify the assumed contact region  $\Omega$ , as described in the following sections.

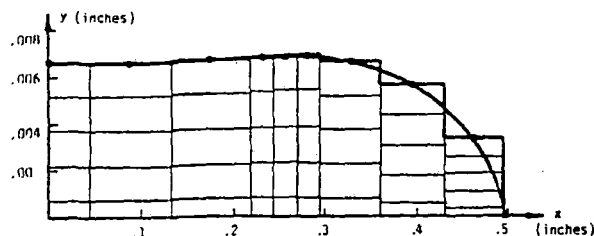


Fig. 13. Mesh layout

**Example 4. Non-Hertzian Axisymmetric Problem (Crowned Circular Stamp).**  
For the crowned circular stamp shown in Fig. 14, the pressure distribution is plotted in Fig. 14, for  $\delta = .001$  in. ( $25.4 \mu\text{m}$ ).

Note the extremely steep pressure gradient near the crowned edge. This example shows that the present numerical method is capable of dealing with such intense stress concentrations.

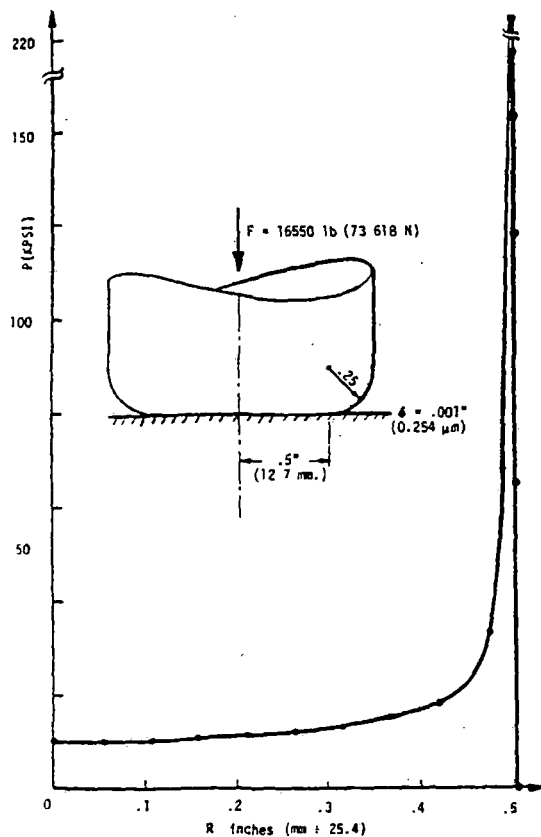


Fig. 14. Flat axisymmetric punch with rounded edges.

way as  
has be  
ary of  
with a  
1  
the tr  
suitab  
(  
are pr  
I  
Hertzi  
compar  
T  
a rail  
T  
to kee  
T  
i.e. c  
T  
proble  
determ

Ti  
with ti  
tion.

1  
G. A.)  
elastic  
pp. 156  
Verhang  
2  
Contact  
3  
Elastic  
Journal  
4  
Design  
Trans.  
5  
Equatio  
Enginee  
6  
Intersc  
7  
McGraw-  
8  
formal  
26, Con  
Departm  
delphia  
9  
communi  
10  
Connect  
Between  
Ed. by



## 8. CONCLUSIONS

The simply discretized method of Singh and Paul has been modified in such a way as to improve its stability accuracy and efficiency. In addition a technique has been developed to automatically refine successive iterations for the boundary of the contact region and to overlay each successive trial contact region with a suitable meshwork for discretizing the governing integral equations.

It is shown that the newly defined interpenetration curve, always surrounds the true contact region for counterformal contact problems, and serves as a suitable initial trial boundary curve.

Computer programs based on these ideas are described and numerical results are presented.

The first numerical example demonstrates the accuracy of the method for a Hertzian contact problem, where the exact theoretical solution is available for comparison.

The second example is the first known solution for non Hertzian contact of a rail-wheel contact stress problem.

The third example illustrates how the analysis can be used as a design tool to keep stress concentrations low.

The fourth example shows that the numerical method has great resolving power; i.e. can predict extremely steep pressure gradients.

The method used shows great promise for the solution of nonconformal contact problems and for many other important problems with changing boundaries; e.g. determination of elastic-plastic boundaries in problems of residual stress, etc.

## 9. ACKNOWLEDGMENT

The research described in this paper was supported by Contract DOT-OS-60144 with the Federal Railroad Administration of the U. S. Department of Transportation.

## 10. REFERENCES

- 1 Hertz, H., Miscellaneous papers (Translated by Jones, D. E. and Schott, G. A.) Macmillan and Company; London, 1896. Translated from: "On the contact of elastic bodies," Journal für die Reine und Angewandte Mathematik, Vol. 92, 1881, pp. 156-171; also "On the contact of rigid elastic solids and on hardness," Verhandlungen des vereins zur Beförderung des Gewerbefleißes, Nov. 1882.
- 2 Singh, K. P. and Paul, B., "Numerical Solution of Non-Hertzian Elastic Contact Problems," Journal of Applied Mechanics, Trans. of ASME, 1974, pp. 29-35.
- 3 Kalker, J. J and Van Randen, Y., "A Minimum Principle for Frictionless Elastic Contact with Application to Non-Hertzian Half-Space Contact Problems," Journal of Engineering Mathematics, Vol. 6, 1972, pp. 193-206.
- 4 Conry, T. F., and Seirig, A., "A Mathematical Programming Method for Design of Elastic Bodies in Contact," Journal of Applied Mechanics, Vol. 38, No. 1, Trans. ASME, Vol. 93, Series E, 1971, pp. 388-392.
- 5 Singh, K. P. and Paul, B., "A Method for Solving Ill-Posed Integral Equations of the First Kind," Computer Methods in Applied Mechanics and Engineering, Vol. 2, 1973, pp. 339-348.
- 6 Lur'e, A. I., Three Dimensional Problems of the Theory of Elasticity, Interscience, New York, 1964.
- 7 Timoshenko, S. P., and Goodier, J. N., Theory of Elasticity, 3rd edition, McGraw-Hill, New York, 1970.
- 8 Paul, B. and Hashemi, J., "An Improved Numerical Method for Counterformal Contact Stress Problems," Technical Report No. 3, July 1977, FRA-ORD-78-26, Contract DOT-OS-60144, Federal Rail Administration. Also MEAM Report 77-1, Department of Mech. Engr. and Applied Mechanics, Univ. of Pennsylvania, Philadelphia, PA.
- 9 Barber, J. L., University of Newcastle-upon-Tyne, Great Britain, Private communication (1976).
- 10 Singh, K. P., Paul, B., and Woodward, W. S., "Contact Stress for Multiply-Connected Regions -- the Case of Pitted Spheres," in the Mechanics of Contact Between Deformable Bodies, Proc. IUTAM Symposium, at Enschede, Netherlands (1974), Ed. by A. D. dePater and J. J. Kalker, Delft University Press, 1975.

11 Paul, B. and Hashemi, J., "User's Manual for Program COUNTACT, Technical Report No. 4, September 1977, FRA-ORD-78-27, Contract DOT-OD-60144, Federal Rail Administration. Also MEAM Report 77-2, Department of Mech. Engr. and Applied Mechanics, Univ. of Pennsylvania, Phila., PA.

12 IMSL, Library 1, Reference Manual, Ed.5. IMSL, 7500 Bellaire Blvd., Houston, Texas (1975).

13 Paul, B., and Hashemi, J., "Wheel-Rail Geometry Associated with Contact Stress Analysis," Technical Report No. 6, Contract DOT-OS-60144, Federal Rail Administration. Also MEAM Report 77-3, Department of Mech. Engr. and Applied Mechanics, Univ. of Pennsylvania, Phila., PA.

Isolati  
Editor

1973 E  
Editor:

Rock M  
Editor:

Mechar  
Editor:

Survey:  
Editors

Numeri  
Editor:

Structu  
Editor:

Applied  
Editor:

Reliabili  
Editors:

1975 Bi  
Editors:

Boundar  
AMD  
Editors:

Vibration  
Editors:

Inelastic  
Editor: C

Finite El  
Vol. 1  
Editors:

Mechanic  
Editor: B

The Effect  
Editors: S

Propagati  
Editor: E

**R. Hull**  
Graduate Research Assistant.

**N. K. Cooperrider**  
Assoc. Professor.  
Mem. ASME

Department of Mechanical Engineering,  
Arizona State University,  
Tempe, Ariz.

# Influence of Nonlinear Wheel/Rail Contact Geometry on Stability of Rail Vehicles

*Nonlinear behavior caused by wheel flanges, worn wheel treads, and dry friction can have an important effect on rail-vehicle stability. In this paper the influence of such nonlinearities on the stability of rail freight vehicles is investigated using quasi-linearization techniques. Nonlinear equations of motion are presented that describe the lateral behavior of a 9-degree-of-freedom representation of a complete freight car with three-piece trucks. The nonlinear wheel/rail geometric constraint functions for the rolling radii, angle of wheel/rail contact, and wheelset roll angle are found by a numerical technique. The suspension description includes dry friction where appropriate. The hunting stability of the freight car is studied by employing describing-function techniques. Results are presented for a typical freight car with three different wheel profiles. The stability results illustrate the dependence of behavior on the amplitudes of vehicle motions. Application of the results in realistic situations and suggestions for future quasi-linear studies are discussed.*

## Introduction

Research into the problem of rail-vehicle hunting has been conducted around the world during the past few decades to develop a qualitative understanding of the hunting phenomenon. Most analytic studies of rail-vehicle hunting have employed linearized equations of vehicle motion or quite simplified vehicle models. Both the linearizing assumptions and the modeling simplifications used in these studies limit the fidelity of the analytic results. For some vehicles, such as the North American freight car with its three-piece trucks, the linear theory appears to have limited utility because of the numerous nonlinear characteristics governing the behavior of such vehicles. The study reported in this paper has attempted to alleviate some of the shortcomings of previous analytic approaches by employing quasi-linearization techniques to deal with the nonlinear characteristics of the North American freight car.

Linear analyses of rail-vehicle dynamics have provided approximations for the critical speeds of hunting and estimates of the frequency and mode shape of the vehicle response at speeds below the

critical speed. This work has provided an invaluable understanding of the nature of the influences of the various vehicle parameters on the hunting stability of rail vehicles. Much of the literature in this field is discussed by Law and Cooperrider [1].<sup>1</sup> An application of linear theory to the dynamics of the North American freight car was conducted by Blader [2] and Blader and Kurtz [3].

Relatively few investigators have considered the nonlinear effects that act to sustain the hunting oscillations and that may in certain cases influence the critical speed that marks the onset of hunting. Nonlinear characteristics that are frequently present in rail vehicles include dry friction, suspension clearances, nonlinear creep forces, and effects of curved wheel and rail profiles. With few exceptions, most nonlinear studies have utilized analog or digital computers to integrate the equations of motion.

Although very complete simulations of complex systems are possible with this approach, the practicality of such simulations is severely limited by the expense of computer time and the need to simulate the response to a wide variety of initial conditions to thoroughly understand the system behavior. Discussion of these studies may be found in the references [1].

Quasi-linearization techniques such as the method of Krylov and Bogoliubov (K and B) and the describing-function method have been employed to study the effect of isolated nonlinearities on simple ve-

Contributed by the Rail Transportation Division and presented at the Winter Annual Meeting, New York, December 5-10, 1976, of THE AMERICAN SOCIETY OF MECHANICAL ENGINEERS. Manuscript received at ASME Headquarters July 28, 1976. Paper No. 76-WA/RT-2.

<sup>1</sup> Numbers in brackets designate References at end of paper.

hicle models. DePater [4] and his students van Bommel [5] and Stassen [6] used the K and B technique and statistical linearization to investigate the limit-cycle behavior of a rigid dual-axle truck model with several nonlinearities. Law [7] and Law and Brand [8] used the K and B method to study the limit-cycle behavior of a single wheelset with curved wheel profiles and flange contact. Garg [9] employed the describing-function techniques to examine the effects of nonlinear wheel profiles on wheelset stability. The nonlinear representations of the wheel/rail geometry employed in all these studies were simplifications of the actual wheel/rail geometry.

It has long been known that nonlinear wheel/rail geometry strongly influences rail-vehicle dynamics. The character of the wheel/rail geometry determines variables such as the rolling radii of the wheels, the contact angles between wheel and rail, and the roll angle of the wheelset. These variables, in turn, enter the equations of motion through the contact forces exerted between the wheels and rails. Nearly all previous studies have approximated the actual geometry to obtain simplified expressions for these terms. Recently several studies have been undertaken to rectify this state of affairs. The extensive analyses completed in Europe have been reported by the Office for Research and Experiments [10]. That report describes work by the British, French, and German railways to develop devices for recording wheel and rail profiles and subsequently to analyze the data to determine the wheel/rail geometric-constraint relationships that are needed for dynamic analysis. A project to develop this capability in the United States has been reported [11, 12]. As a result of this work the actual nonlinear functions describing the variations of the rolling radii, contact angles, and wheelset roll with wheelset lateral position can be computed for arbitrary wheel and rail profiles.

This paper reports results of a project to employ describing-function techniques to study the limit-cycle behavior of a North American freight car with nonlinear wheel/rail geometry and suspension characteristics. The wheel/rail geometry was determined by an approach

previously described [11, 12]. The results of the preliminary efforts on this project have also been described [13]. A companion paper [14] describes the portion of this study devoted to applying a similar technique to analyze the limit-cycle behavior of a single wheelset.

## Vehicle Model

The North American freight truck studied in the project reported here has the following major components: two wheelsets, two sideframes, and one bolster. The arrangement of these components is shown schematically in Fig. 1. The sideframes rest directly on bearing adapters that sit on the bearings. The bolster is connected to the sideframes by a suspension system that allows relative vertical movement, relative lateral movement within limits, and relative angular motion about all axes. Very little relative longitudinal motion is possible between bolster and sideframe.

The freight-car body rests directly on the truck-bolster centerplate. Rotation about a vertical axis of the truck bolster relative to the car body is resisted by friction at the centerplate.

In this study we have assumed that the sideframe is connected to the wheelsets by the equivalent of a ball joint that allows relative angular rotation but precludes any relative translational motion. In addition, we have assumed that there is no relative longitudinal motion between the bolster and sideframe. The lateral truck motion, then, can be described by the following three degrees of freedom: truck lateral displacement ( $X_{TF}$ , front truck,  $X_{TR}$ , rear truck), truck yaw displacement ( $\theta_{TF}$ , front truck,  $\theta_{TR}$ , rear truck), and truck warp displacement ( $\theta_{WF}$ , front truck,  $\theta_{WR}$ , rear truck). These variables are illustrated in Fig. 1.

The freight-car body was represented by a rigid body. The three degrees of freedom of this rigid body that couple to the lateral vehicle motion are the car-body lateral displacement ( $X_C$ ), the car-body yaw displacement ( $\theta_C$ ), and the car-body roll displacement ( $\phi_C$ ).

In this model we have neglected roll motions of the sideframes. We

## Nomenclature

$\alpha$ = one-half rail gauge	$I_{BY}$ = bolster yaw moment of inertia	$W_F, W_R$ = axle load (including axle weight)
$A$ = amplitude of sinusoidal input	$I_{BZ}$ = bolster roll moment of inertia	$\bar{x}$ = vector of variables of some system
$A_1$ = amplitude of ( $\dot{x}_{TF} - \dot{x}_c - h_2\dot{\phi}_c - L_c\dot{\theta}_c$ )	$I_{CY}$ = car-body yaw moment of inertia	$X_{TF}, X_{TR}$ = truck c.g. lateral displacement
$A_2$ = amplitude of ( $\dot{x}_{TR} - \dot{x}_c - h_2\dot{\phi}_c + L_c\dot{\theta}_c$ )	$I_{CZ}$ = car-body roll moment of inertia	$X_{T/C}$ = lateral truck bolster-to-sideframe displacement
$A_3$ = amplitude of ( $d\dot{\phi}_c$ )	$I_{FY}$ = sideframe yaw moment of inertia	$X_C$ = car-body c.g. lateral displacement
$A_4$ = amplitude of ( $\dot{\theta}_{WF}$ )	$I_{WY}$ = wheelset yaw moment of inertia	$X_W$ = wheelset lateral displacement
$A_5$ = amplitude of ( $\dot{\theta}_{WR}$ )	$K_X$ = lateral-suspension stiffness per sideframe	$\bar{y}$ = vector of nonlinear functions
$A_6$ = amplitude of ( $\dot{\theta}_{WF} + \dot{\theta}_{TR} - \dot{\theta}_c$ )	$K_Y$ = vertical-suspension stiffness per sideframe	$\bar{y}_q$ = quasi linearization of $\bar{y}$
$A_7$ = amplitude of ( $\dot{\theta}_{WR} + \dot{\theta}_{TR} - \dot{\theta}_c$ )	$K_{\theta W}$ = warp stiffness per truck	$\alpha$ = vector that depends on the properties of $\bar{x}$
$d$ = semispacing of sideframes	$L_C$ = semi-truck center spacing	$\delta_{L1}, \delta_{L2}, \delta_{L3}, \delta_{L4}$ = left-wheel/rail contact angles
$F$ = total force	$L_T$ = semi-truck wheelbase	$\delta_{R1}, \delta_{R2}, \delta_{R3}, \delta_{R4}$ = right-wheel/rail contact angles
$F_0$ = friction force	$m_B$ = bolster mass	$\epsilon$ = mean square error
$\bar{f}$ = vector of nonlinear functions	$m_C$ = car-body mass	$\theta_C$ = car-body yaw angle
$f_{11}$ = lateral creep coefficient	$m_F$ = sideframe mass	$\theta_{TF}, \theta_{TR}$ = truck yaw angle
$f_{12}$ = lateral/spin creep coefficient	$m_W$ = wheelset mass	$\theta_{WF}, \theta_{WR}$ = truck warp angle
$f_{22}$ = spin creep coefficient	$N$ = describing-function matrix	$\xi_{XR}, \xi_{XL}$ = lateral creepage
$f_{33}$ = longitudinal creep coefficient	$N_{XR}, N_{XL}$ = normal force at wheel/rail contact	$\xi_{ZR}, \xi_{ZL}$ = longitudinal creepage
$F_{XSF}, F_{XSR}$ = lateral-suspension force, per sideframe	$r_{L1}, r_{L2}, r_{L3}, r_{L4}$ = left-wheel rolling radii	$\xi_{\theta R}, \xi_{\theta L}$ = spin creepage
$F_{YSF}, F_{YSR}$ = vertical-suspension force, per sideframe	$r_{R1}, r_{R2}, r_{R3}, r_{R4}$ = right-wheel rolling radii	$\phi_C$ = car-body roll angle
$F_{OX}$ = lateral friction force, per sideframe	$r_0$ = centered-wheel rolling radius	$\phi_W$ = wheelset roll angle
$F_{OY}$ = vertical friction force, per sideframe	$T_{BF}, T_{BR}$ = torque at centerplate, per truck	$\psi$ = dummy variable
$h_1$ = vertical distance, truck c.g. to body c.g.	$T_{OB}$ = friction torque at centerplate, per truck	$\omega$ = frequency
$h_2$ = vertical distance, car-bolster to car-body c.g.	$T_{OW}$ = warp friction torque, per truck	( $\bar{\phantom{x}}$ ) = vector
	$T_{\theta WF}, T_{\theta WR}$ = warp torque, per truck	( $\underline{\phantom{x}}$ ) = matrix
	$V$ = vehicle speed	

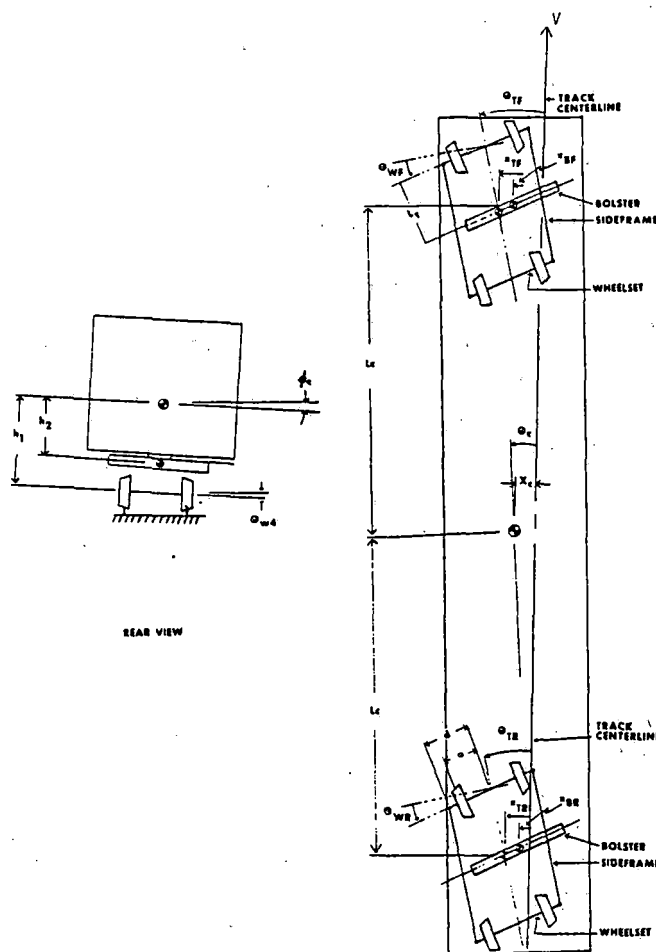


Fig. 1 Vehicle model

have also assumed that the bolster remains parallel to the wheelsets and translates laterally and vertically with the car body. The range of validity of this three-degree-of-freedom truck and rigid car-body model is discussed in a companion paper [15].

The effects of track irregularities were not introduced into the model. We also neglected the flexibility of the rail and track system and assumed that the car body c.g. traveled along the track at a constant velocity  $V$ .

For this rail vehicle traveling on tangent track under the conditions described above, the only forces exerted on the vehicle components are the contact forces between the wheel and rail and the suspension forces acting between the vehicle components. In many cases these forces are caused by nonlinear mechanisms.

**Wheel/Rail Geometry.** The nature of the forces exerted between the wheel and rail, both in the plane of contact and normal to it, is determined by the geometry of the wheel and rail. Railway wheelsets, as they roll along the track, are constrained to move laterally and vertically in a prescribed space determined by the geometry of the wheels, rails, and track structure. The wheelset position may be described by two independent variables: the lateral position of its geometric center relative to the track centerline,  $X_W$ , and the angular rotation of the wheelset about a vertical axis,  $\theta_W$ . The remaining motions of the wheelset such as roll or vertical movement are determined by geometric constraints.

In studying the lateral dynamics of a rail vehicle, the following information must be known as a function of the independent variable  $X_W$ :<sup>2</sup>

$r_L$  = rolling radius of left wheel

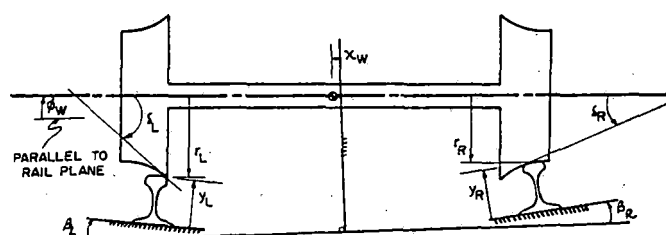


Fig. 2 Wheel/rail contact geometry

$r_R$  = rolling radius of right wheel

$\delta_L$  = angle between the contact plane on the left wheel and the axle centerline

$\delta_R$  = angle between the contact plane on the right wheel and the axle centerline

$\phi_W$  = wheelset roll angle.

These constrained variables and corresponding coordinate systems are illustrated in Fig. 2.

Solutions for the wheel/rail geometric constraint functions were obtained numerically with a technique previously described [12]. Three configurations of wheel and rail profiles that cover a wide range of possible combinations were used in this study. The first of these was a new-wheel profile on a worn-rail profile at a nominal rail gauge of 56.5 in. (1.435 m). The geometric constraint functions for this situation are shown in Fig. 3. Because half the difference in contact angles  $\frac{1}{2}(\delta_L - \delta_R)$  and the normalized difference in rolling radii  $[(r_L - r_R)/2a]$  appear as isolated terms in the equations of motion, these functions are also shown in this figure. Note that the rail head and wheel profile are plotted below the graphs for the contact-point functions. As expected, all the constraint relationships for the new wheel are nearly linear until the wheelset is displaced laterally far enough for the flange to contact the rail.

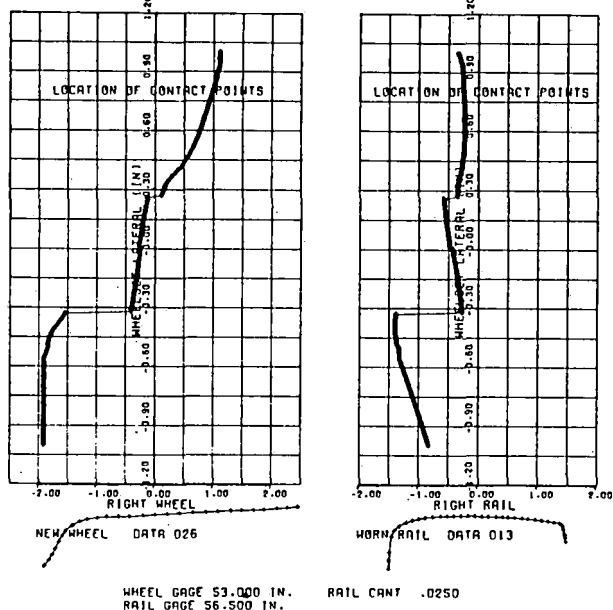
The second combination studied here was a standardized worn-wheel profile developed by the Canadian National Railroad on a new rail. This wheel profile, labeled Profile A by the CN, closely matches the shape of a new rail head. Consequently, it should not change its shape as it wears. The profiles, contact positions, and geometric constraint functions for this wheel/rail combination are shown in Fig. 4. The constraint functions for this situation are nearly linear until flange contact is reached, but the slopes of the functions are about three times larger than the corresponding slopes of functions for new wheels.

The third wheel/rail combination used here was a modified Heumann wheel profile on the same worn-rail profile used for the new-wheel study. The original Heumann profile was designed with the expressed intention of obtaining single-point contact between wheel and rail at all wheelset lateral positions. The profile used here is a modification of the original profile developed by Eck and Berg [16]. We see in Fig. 5 that the contact of this modified Heumann profile on a worn rail closely approximates single-point contact. The geometric constraint functions are nearly continuous functions that are approximately linear for small wheelset lateral displacements. The slope about the origin is quite steep, much steeper than those of either of the previous wheel/rail combinations.

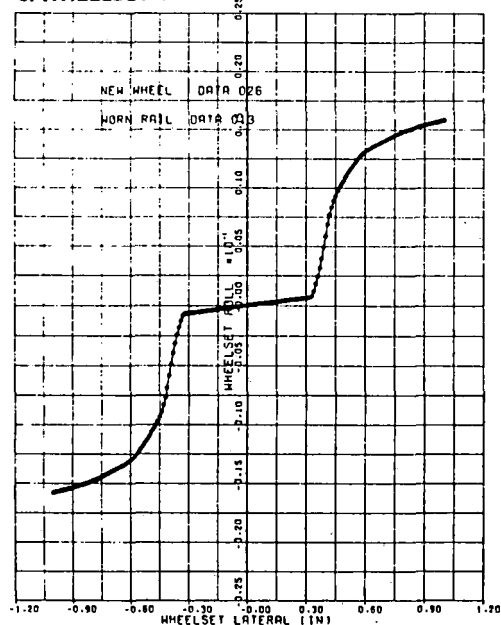
**Creep Forces and Moments.** The creep forces and moments are exerted between wheel and rail in the plane of contact because of a difference in the strain rates, or creepages, of the two bodies in the contact region. In general, two elastic bodies in rolling contact may have both a relative translational creepage and a relative spin creepage. For the wheel/rail contact problem, the translational creepage is the relative sliding velocity of the wheel over the rail di-

<sup>2</sup> The dependence of these functions on wheelset yaw is a second-order effect that has been ignored here.

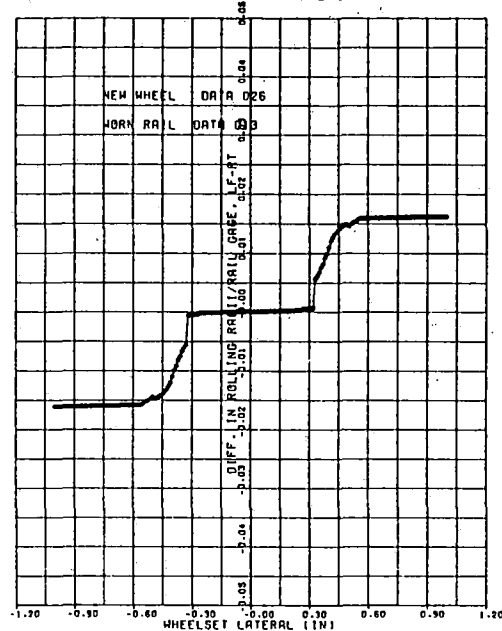
**a. WHEEL CONTACT POSITION**      **b. RAIL CONTACT POSITION**



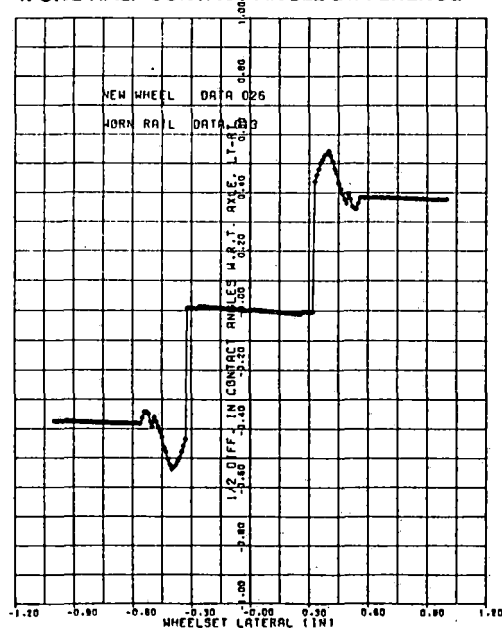
**c. WHEELSET ROLL**



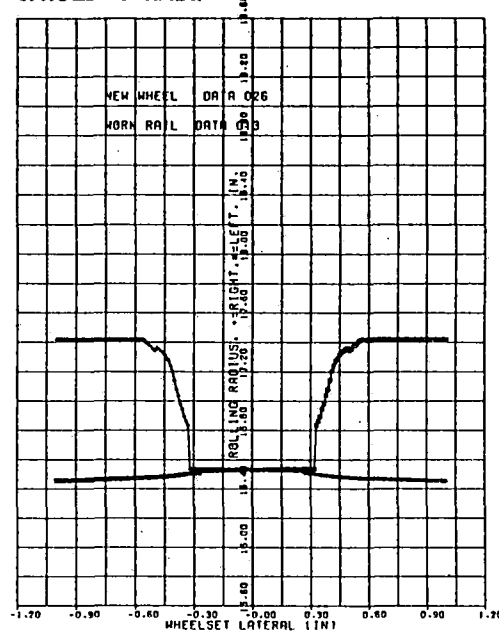
**d. NORMALIZED ROLLING RADIUS DIFFERENCE**



**f. ONE HALF CONTACT ANGLE DIFFERENCE**



**e. ROLLING RADI**



**g. CONTACT ANGLES**

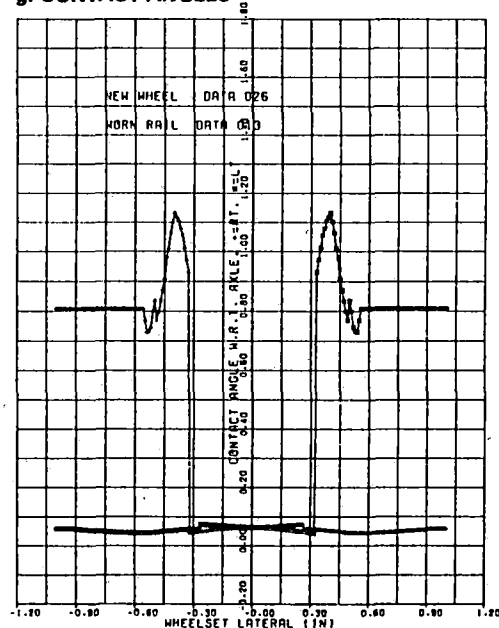


Fig. 3 New-wheel geometric characteristics



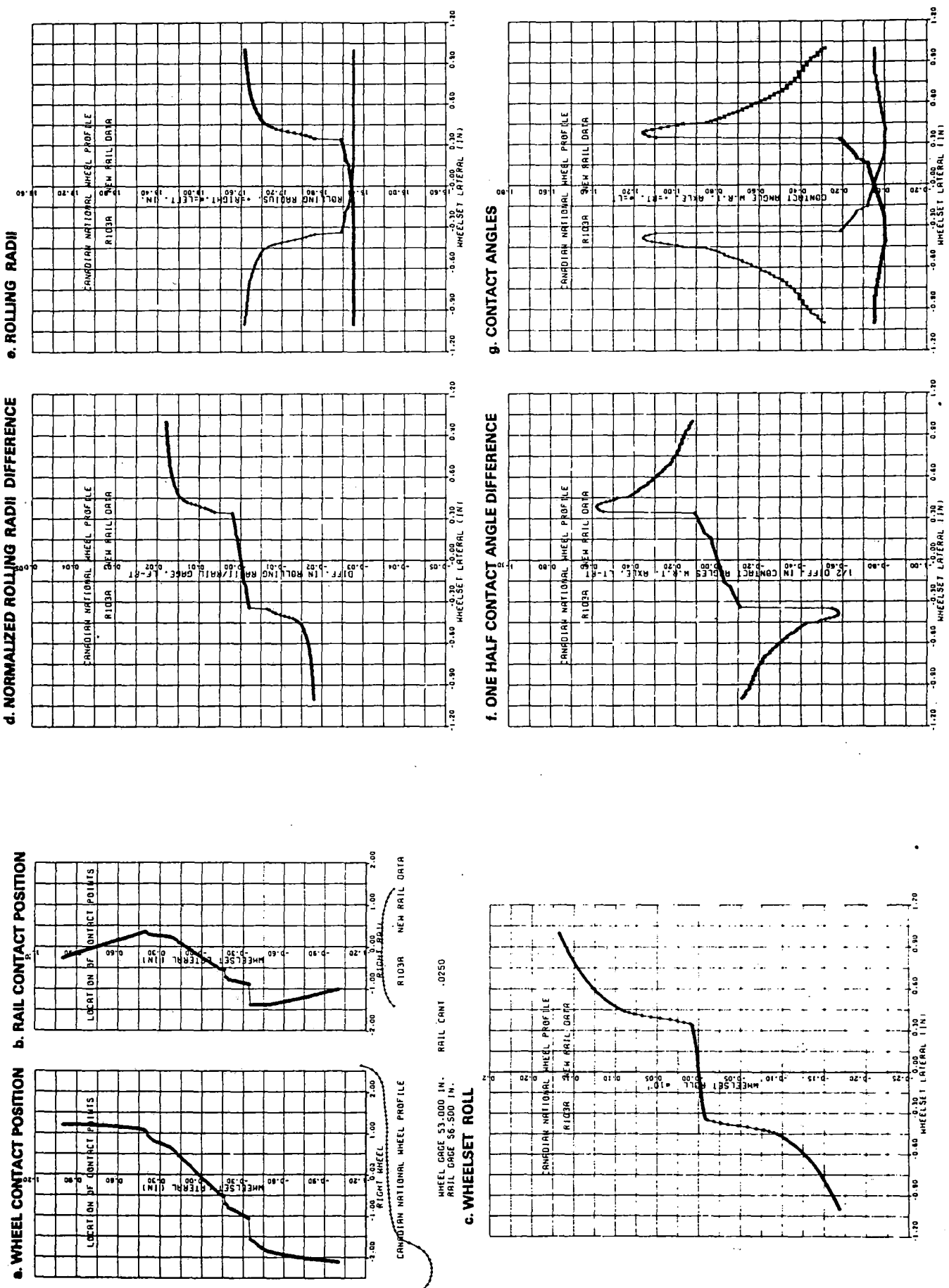
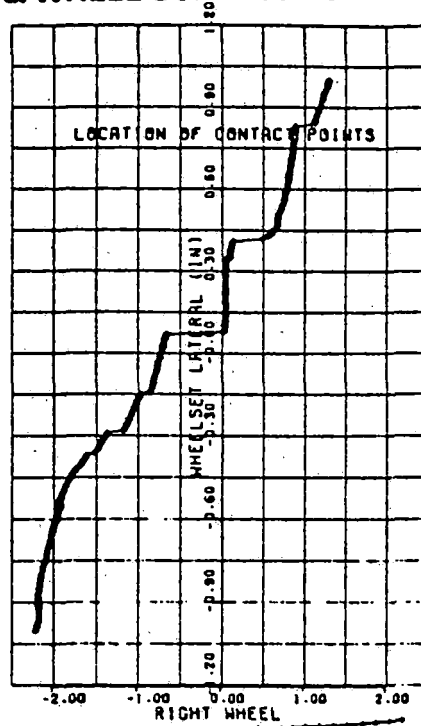
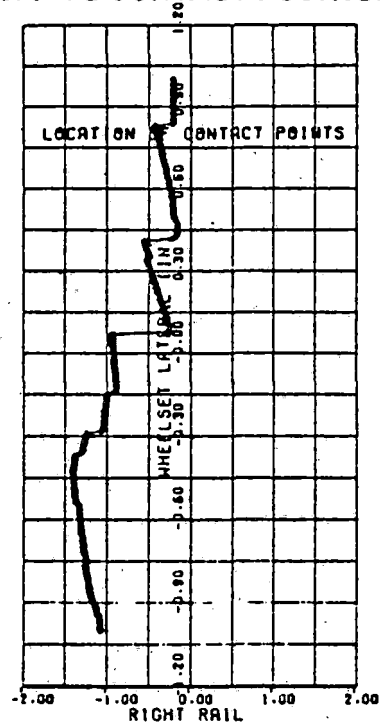


Fig. 4 Canadian National wheel geometric characteristics

### a. WHEEL CONTACT POSITION



### b. RAIL CONTACT POSITION



HEUMANN PROFILE DATA 008

WORN RAIL DATA 013

WHEEL GAGE 53.000 IN.  
RAIL GAGE 56.500 IN.

RAIL CANT .0250

### c. WHEELSET ROLL

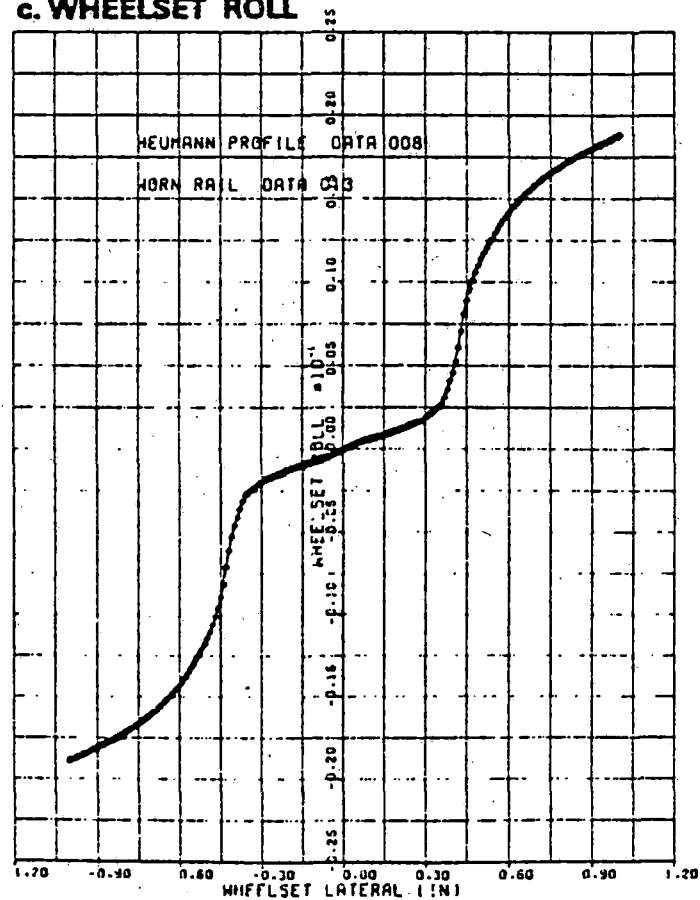
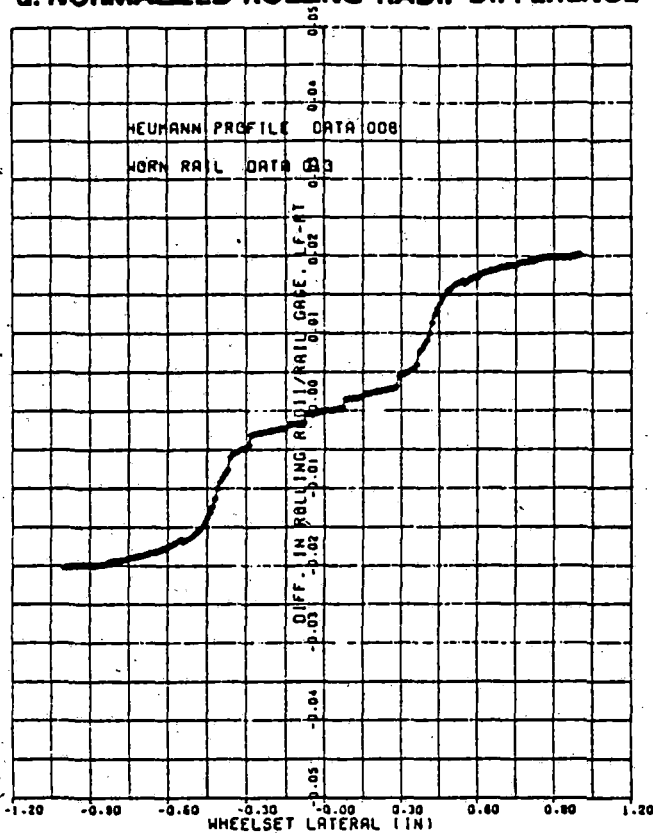
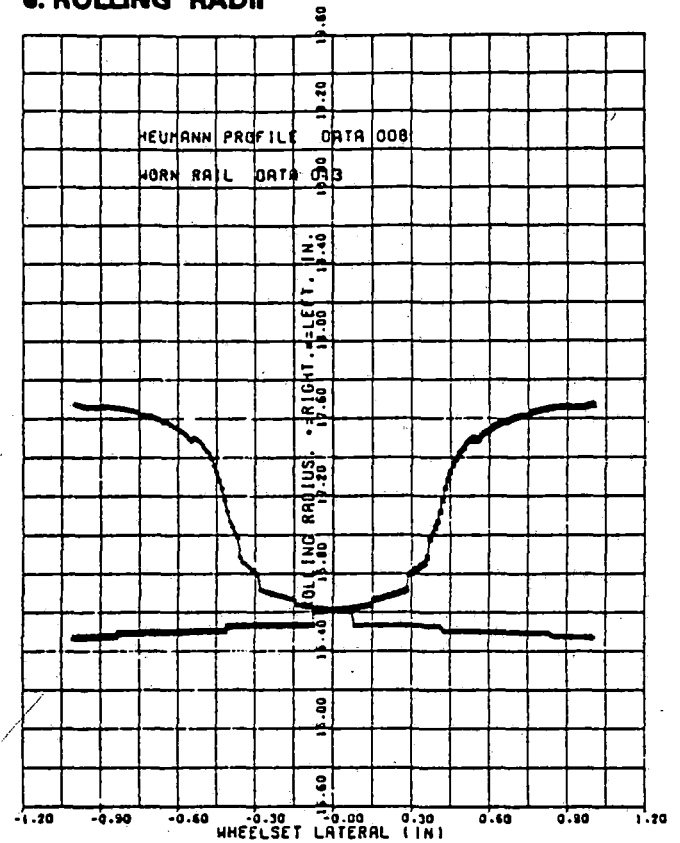


Fig. 5 Heumann wheel geometric characteristics

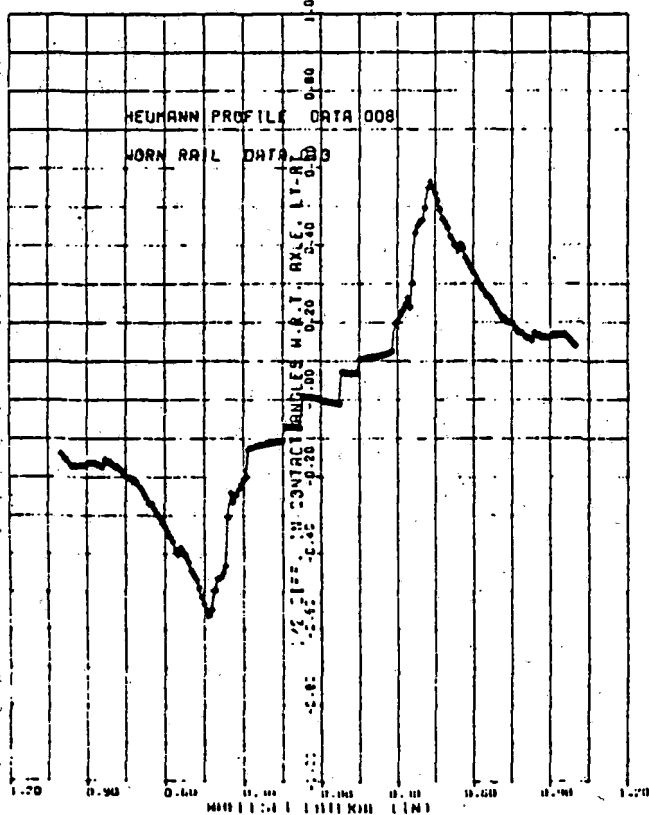
**d. NORMALIZED ROLLING RADII DIFFERENCE**



**e. ROLLING RADII**



**f. ONE HALF CONTACT ANGLE DIFFERENCE**



**g. CONTACT ANGLES**

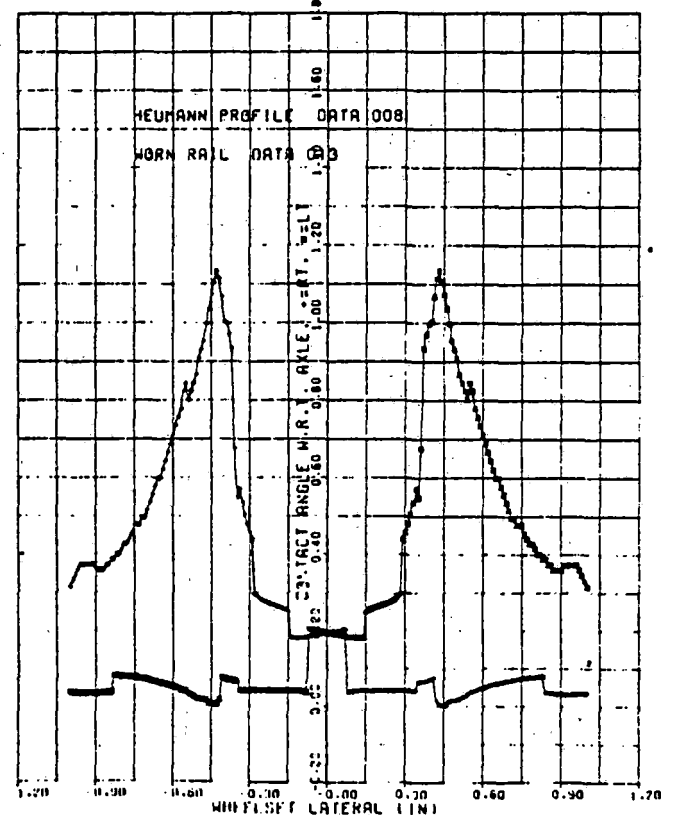


Fig. 5 (Cont'd.)

vided by the forward velocity of the wheel. The spin creepage is the component of the wheelset angular velocity normal to the wheel/rail contact plane divided by the wheel forward velocity. The lateral, longitudinal, and spin creepages for the leading wheelset of the front truck are given by the following expressions:

$$\xi_{XR} = \xi_{XL} = \frac{1}{V} (\dot{x}\theta_{TF} + L_T\dot{\theta}_{TF}) - (\theta_{WF} + \theta_{TF}) \quad (1)$$

$$\xi_{ZR} = 1 + \frac{a}{V} (\dot{\theta}_{TF} + \dot{\theta}_{WF}) - \frac{r_R(x_{w1})}{r_0} \quad (2)$$

$$\xi_{ZL} = 1 - \frac{a}{V} (\dot{\theta}_{TF} + \dot{\theta}_{WF}) - \frac{r_L(x_{w1})}{r_0} \quad (3)$$

$$\xi_{\theta R} = \frac{\delta_R}{r_0} + \frac{\dot{\theta}_{TF} + \dot{\theta}_{WF}}{V} \quad (4)$$

$$\xi_{\theta L} = -\frac{\delta_L}{r_0} + \frac{\dot{\theta}_{TF} + \dot{\theta}_{WF}}{V} \quad (5)$$

where

$\xi_{XR}, \xi_{XL}$  = lateral creepages

$\xi_{ZR}, \xi_{ZL}$  = longitudinal creepages

$\xi_{\theta R}, \xi_{\theta L}$  = spin creepages

$a$  = one-half the rail gauge

$L_T$  = one-half the truck wheelbase

$r_0$  = centered rolling radius of the wheels

$V$  = vehicle forward velocity

$x_{w1} = X_{TF} + L_T\theta_{TF}$

Similar expressions can be written for the other wheelsets. Note that the nonlinear geometric constraint functions for the wheel rolling radii,  $r_L(x_{w1})$  and  $r_R(x_{w1})$ , enter the equations of motion through the longitudinal creepage terms. The contact-angle functions enter through the spin creepage. For small creepages the relationship between the creep forces and moments and the creepages may be represented by linear relationships where the constants of proportionality are called the creep coefficients. These creep coefficients depend on the wheel and rail geometry, the wheel and rail materials, and the normal force between the two bodies. The theory of Kalker [17] was used to compute these coefficients for this study.

**Gravitational Stiffness Forces.** The remaining contact forces between the wheel and the rail are the normal forces exerted in a direction perpendicular to the plane of contact. When a symmetric wheelset is centered on a symmetric track, the normal forces on the left and right wheels will be equal in magnitude and slightly inclined inward from the vertical. The sum of the vertical components of the two normal forces will equal the axle load, and the lateral components will be opposite in sign, with a zero resultant lateral force on the wheelset. The angle of the contact plane is determined by the wheel and rail profiles.

In general, the contact angle of the contact plane with respect to the axle centerline will vary as the wheelset moves laterally and will differ from left to right wheels, as seen in Figs. 3-5. The magnitude of the lateral component of the normal force is determined by the magnitude of the vertical force and by the angle of the contact plane. In the model used here we assumed that the vertical forces at all wheels were equal to the proportionate share of the vehicle weight. Then, for small contact angles, the lateral resultant of the normal contact forces on the leading wheelset of the front truck is given by the following expression:

$$N_{XR} + N_{XL} = -W_F \left( \frac{\delta_L - \delta_R}{2} + \phi_w \right) \quad (6)$$

where

$N_{XR}, N_{XL}$  = lateral components of the normal force at left and right wheels

$W_F$  = axle load on the front wheelset

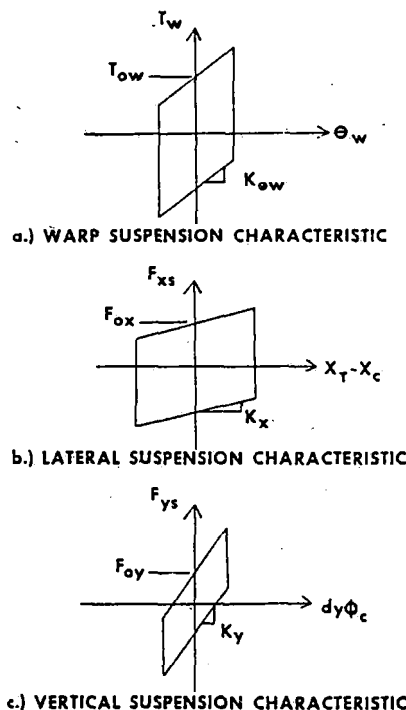


Fig. 6 Suspension characteristics

The nonlinear geometric constraint functions for the wheel/rail contact angles and the wheelset roll enter the equations of motion through these gravitational stiffness terms.

**Suspension Forces.** The most important nonlinearity found in freight-car suspensions is coulomb, or dry, friction. Nonlinear springs due to stops and deadband regions or slope are also present, but in our judgment they are less important in determining stability.

All of the suspension connections in the freight car include dry friction. Within the truck itself, warp motion of the truck is resisted at the six connections between the sideframes and the wheelsets and bolster by friction and stiffness that can be modeled by a linear spring with stiffness  $K_{\theta W}$  in parallel with a coulomb friction of magnitude  $T_{\theta W}$ . This composite torque is represented by the function  $T_{\theta W}$ . This characteristic is illustrated in Fig. 6(a).

The suspension between the bolster and the sideframes was modeled in both the vertical and lateral directions by a linear spring in parallel with dry friction. The spring rates and friction-force levels in the two directions may be different, as seen in Figs. 6(b) and 6(c).

Rotation of the truck bolster relative to the car body is resisted by friction at the centerplate. This resistance is represented by dry friction with a breakout torque of  $T_{\theta B}$ .

**Equations of Motion.** Equations of motion for the freight vehicle subject to the forces described above are given in Table 1. Details of the derivation of these equations may be found in references [15, 18, 19].

Typical values for the parameters appearing in these equations are given in Table 2. These parameters are for an 80-ton hopper car on 70-ton Ride Control trucks. Most of these values were obtained by tests conducted as part of the Association of American Railroads track-train dynamics program, as reported in references [20, 21].

### Quasi-Linearization

Quasi-linearization is the approximation of a nonlinear operation by a linear one that depends on some properties of the input to the nonlinearity. It is similar to linearization in that it results in a linear description of the system, but it is not true linearization, because the

Table 1 Freight-car equations of motion

FRONT TRUCK LATERAL

$$2(m_F + m_W)\ddot{x}_{TF} + 4\frac{f_{11}}{V}\dot{x}_{TF} + 4\frac{f_{12}}{V}\dot{\theta}_{TF} - 4f_{11}\theta_{TF} + 4\frac{f_{12}}{V}\dot{\theta}_{WF} - 4f_{11}\theta_{WF} + (W_F - \frac{2f_{12}}{r_o})(\frac{\delta_{L1} - \delta_{R1}}{2} + \frac{\delta_{L2} - \delta_{R2}}{2}) + W_F(\phi_{W1} + \phi_{W2}) + 2\frac{f_{11}r_o}{V}(\dot{\phi}_{W1} + \dot{\phi}_{W2}) = -2F_{XSF}$$

FRONT TRUCK YAW

$$\begin{aligned} -4\frac{f_{12}}{V}\dot{x}_{TF} + (2I_{WY} + 2I_{FY} + 2L_{TW}^2 + 2d^2m_F + I_{BY})\ddot{\theta}_{TF} + (4\frac{f_{22}}{V} + 4a^2\frac{f_{33}}{V} + 4\frac{L_{TF}^2}{V})\dot{\theta}_{TF} + (4f_{12} - 2aW_F\delta_o)\theta_{TF} + (2I_{WY} + 2d^2m_F + I_{BY})\ddot{\theta}_{WF} + (4\frac{f_{22}}{V} + 4\frac{a^2f_{33}}{V})\dot{\theta}_{WF} \\ + (4f_{12} - 2aW_F)\theta_{WF} + (L_{TW} - \frac{2L_{TF}f_{12}}{r_o})(\frac{\delta_{L1} - \delta_{R1}}{2} - \frac{\delta_{L2} - \delta_{R2}}{2}) + W_{FT}(\phi_{W1} - \phi_{W2}) + 2\frac{r_o L_{TF} f_{11}}{V}(\dot{\phi}_{W1} - \dot{\phi}_{W2}) - \frac{2r_o f_{12}}{V}(\dot{\phi}_{W1} + \dot{\phi}_{W2}) \\ - 2\frac{f_{22}}{r_o}(\frac{\delta_{L1} - \delta_{R1}}{2} + \frac{\delta_{L2} - \delta_{R2}}{2}) + 2a f_{33}(\frac{r_{L1} - r_{R1}}{2r_o} + \frac{r_{L2} - r_{R2}}{2r_o}) = -T_{BF} \end{aligned}$$

FRONT TRUCK WARP

$$\begin{aligned} -4\frac{f_{12}}{V}\dot{x}_{TF} + (2I_{WY} + 2d^2m_F + I_{BY})\ddot{\theta}_{TF} + (4\frac{f_{22}}{V} + 4a^2\frac{f_{33}}{V})\dot{\theta}_{TF} + (4f_{12} - 2aW_F\delta_o)\theta_{TF} + (2I_{WY} + 2d^2m_F + I_{BY})\ddot{\theta}_{WF} + (4\frac{f_{22}}{V} + 4\frac{a^2f_{33}}{V})\dot{\theta}_{WF} + (4f_{12} - 2aW_F\delta_o)\theta_{WF} \\ - \frac{2f_{22}}{r_o}(\frac{\delta_{L1} - \delta_{R1}}{2} + \frac{\delta_{L2} - \delta_{R2}}{2}) - 2\frac{r_o f_{12}}{V}(\dot{\phi}_{W1} + \dot{\phi}_{W2}) + 2a f_{33}(\frac{r_{L1} - r_{R1}}{2r_o} + \frac{r_{L2} - r_{R2}}{2r_o}) = -T_{\theta WF} - T_{BF} \end{aligned}$$

REAR TRUCK LATERAL

$$2(m_F + m_W)\ddot{x}_{TR} + 4\frac{f_{11}}{V}\dot{x}_{TR} + 4\frac{f_{12}}{V}\dot{\theta}_{TR} - 4f_{11}\theta_{TR} + 4\frac{f_{12}}{V}\dot{\theta}_{WR} - 4f_{11}\theta_{WR} + (W_R - \frac{2f_{12}}{r_o})(\frac{\delta_{L3} - \delta_{R3}}{2} + \frac{\delta_{L4} - \delta_{R4}}{2}) + W_R(\phi_{W3} + \phi_{W4}) + 2\frac{f_{11}r_o}{V}(\dot{\phi}_{W3} + \dot{\phi}_{W4}) = -2F_{XSR}$$

REAR TRUCK YAW

$$\begin{aligned} -4\frac{f_{12}}{V}\dot{x}_{TR} + (2I_{WY} + 2I_{FY} + 2L_{TW}^2 + 2d^2m_F + I_{BY})\ddot{\theta}_{TR} + (4\frac{f_{22}}{V} + 4a^2\frac{f_{33}}{V} + 4\frac{L_{TF}^2}{V})\dot{\theta}_{TR} + (4f_{12} - 2aW_R\delta_o)\theta_{TR} + (2I_{WY} + 2d^2m_F + I_{BY})\ddot{\theta}_{WR} + (4\frac{f_{22}}{V} + 4\frac{a^2f_{33}}{V})\dot{\theta}_{WR} \\ + (4f_{12} - 2aW_F)\theta_{WR} + (L_{TW} - \frac{2L_{TF}f_{12}}{r_o})(\frac{\delta_{L3} - \delta_{R3}}{2} + \frac{\delta_{L4} - \delta_{R4}}{2}) + W_{RT}(\phi_{W3} - \phi_{W4}) + 2\frac{r_o L_{TF} f_{11}}{V}(\dot{\phi}_{W3} - \dot{\phi}_{W4}) - \frac{2r_o f_{12}}{V}(\dot{\phi}_{W3} + \dot{\phi}_{W4}) \\ - 2\frac{f_{22}}{r_o}(\frac{\delta_{L3} - \delta_{R3}}{2} + \frac{\delta_{L4} - \delta_{R4}}{2}) + 2a f_{33}(\frac{r_{L3} - r_{R3}}{2r_o} + \frac{r_{L4} - r_{R4}}{2r_o}) = -T_{BR} \end{aligned}$$

REAR TRUCK WARP

$$\begin{aligned} -4\frac{f_{12}}{V}\dot{x}_{TR} + (2I_{WY} + 2d^2m_F + I_{BY})\ddot{\theta}_{TR} + (4\frac{f_{22}}{V} + 4a^2\frac{f_{33}}{V})\dot{\theta}_{TR} + (4f_{12} - 2aW_R\delta_o)\theta_{TR} + (2I_{WY} + 2d^2m_F + I_{BY})\ddot{\theta}_{WR} + (4\frac{f_{22}}{V} + 4\frac{a^2f_{33}}{V})\dot{\theta}_{WR} + (4f_{12} - 2aW_R\delta_o)\theta_{WR} \\ - 2\frac{f_{22}}{r_o}(\frac{\delta_{L3} - \delta_{R3}}{2} + \frac{\delta_{L4} - \delta_{R4}}{2}) - 2\frac{r_o f_{12}}{V}(\dot{\phi}_{W3} + \dot{\phi}_{W4}) + 2a f_{33}(\frac{r_{L3} - r_{R3}}{2r_o} + \frac{r_{L4} - r_{R4}}{2r_o}) = -T_{\theta WR} - T_{BR} \end{aligned}$$

CAR BODY LATERAL

$$(m_C + 2m_B)\ddot{x}_C - 2h_2m_B\ddot{\phi}_C = 2F_{XSF} + 2F_{XSR}$$

CAR BODY YAW

$$(I_{CY} + 2L_C^2m_B)\ddot{\theta}_C = 2L_C F_{XSF} - 2L_C F_{XSR} + T_{BF} + T_{BR}$$

CAR BODY ROLL

$$2h_2m_B\ddot{x}_C + (I_{CZ} + 2I_{BZ} + 2h_2^2m_B)\ddot{\phi}_C - h_2(m_C + 2m_B)g\phi_C = 2h_2F_{XSF} + 2h_2F_{XSR} - 2dF_{YSF} - 2dF_{YSR}$$

characteristics of the linear approximation change with certain properties of the signals circulating through the system. The major advantage of using quasi-linear analysis is that, while the resulting quasi-linearized system is effectively linear, the system response depends on signal amplitude, a basic characteristic of nonlinear behavior.

The describing-function approach [22, 23] to quasi-linearization is particularly convenient for investigating the occurrence and stability of sustained nonlinear oscillations, or limit cycles. Quasi-linearization of a nonlinear system involves replacing the nonlinear functions  $\bar{y} = \bar{f}(\bar{x})$  with linear functions of the form  $\bar{y}_q = N(\bar{\alpha})\bar{x}$ , where  $\bar{\alpha}$  is a vector that depends on the properties of  $\bar{f}$ . The describing-function approach selects the terms of the matrix  $N(\bar{\alpha})$  to minimize the mean square error  $\epsilon$  between the nonlinear and the quasi-linear

responses to a given input  $\bar{x}$ , i.e., [23]

$$\min_N |\epsilon|^2 = \min_N \overline{(\bar{f} - N\bar{x})^T(\bar{f} - N\bar{x})} \quad (7)$$

given  $\bar{f}$  and  $\bar{x}$ .

To carry out the minimization suggested in equation (7), the input signal  $\bar{x}(t)$  must be specified. In general [23],  $\bar{x}(t)$  can be composed of sinusoidal, constant-bias, and gaussian random-input signals. Because this discussion concerns only the prediction of self-excited limit cycles, only sinusoidal inputs are considered.

For the case of a sinusoidal input, the parameter vector  $\bar{\alpha}$  consists of the amplitude  $A$  and frequency  $\omega$ . For an odd memoryless static nonlinearity  $y = f(x)$  and a sinusoidal input signal  $x = A \sin \omega t$ , the minimizing linearization, or describing function, is given [23] by

Table 2 Vehicle characteristics for empty 80-ton hopper car

Mass Properties			
$I_{BY}$	(Bolster yaw moment of inertia)	= 178.6	slug-ft <sup>2</sup>
$I_{BZ}$	(Bolster roll moment of inertia)	= 178.6	slug-ft <sup>2</sup>
$I_{CY}$	(Car body yaw moment of inertia)	= 234,000.	slug-ft <sup>2</sup>
$I_{CZ}$	(Car body roll moment of inertia)	= 13,000.	slug-ft <sup>2</sup>
$I_{FY}$	(Sideframe yaw moment of inertia)	= 77.6	slug-ft <sup>2</sup>
$I_{WY}$	(Wheelset yaw moment of inertia)	= 448.5	slug-ft <sup>2</sup>
$m_B$	(Bolster mass)	= 36.1	slugs
$m_C$	(Car body mass)	= 1102.	slugs
$m_F$	(Side frame mass)	= 24.0	slugs
$m_W$	(Wheelset mass)	= 76.6	slugs
Suspension Properties			
$K_X$	(Lateral suspension stiffness)	= 24,000.	lb/ft
$K_Y$	(Vertical suspension stiffness)	= 265,800.	lb/ft
$K_{\theta W}$	(Warp stiffness)	= $3.81 \times 10^6$	ft-lb/radian
$F_{OX}$	(Lateral suspension friction force)	= 5200.	lb
$F_{OY}$	(Vertical suspension friction force)	= 3120.	lb
$T_{OB}$	(Bolster friction torque)	= 606.	ft-lb
$T_{OW}$	(Warp friction torque)	= 4271.	ft-lb
Creep Coefficients (Full Kalker values)			
$f_{11}$	(Lateral creep coefficient)	= $1.15 \times 10^6$	lb
$f_{12}$	(Lateral/spin creep coefficient)	= 6750.	ft-lb
$f_{22}$	(Spin creep coefficient)	= 42.1	ft <sup>2</sup> -lb
$f_{33}$	(Longitudinal creep coefficient)	= $1.262 \times 10^6$	lb

$$N(A) = \frac{4}{\pi A} \int_0^{\pi/2} y(A \sin \psi) \sin \psi d\psi \quad (8)$$

where  $y = f(x) \approx N(A)x$ . Tables of sinusoidal-input describing functions for various nonlinear functions are available in several references [22, 23].

**Limit-Cycle Investigation.** If the dynamic equations for the nonlinear system are placed in state-variable form

$$\dot{\bar{x}} = \bar{f}(\bar{x}) \quad (9)$$

where the vector  $\bar{f}(\bar{x})$  includes the nonlinear elements of the system model, then a describing function matrix  $N(\bar{a})$  can be computed employing the definition of equation (7). For the case of sinusoidal inputs, the parameter vector  $\bar{a}$  consists of the amplitudes of the state vector  $\bar{A}$  and the frequency  $\omega$  of the system oscillation. The matrix  $N$  will also contain the original linear descriptions of system components as well as the appropriate describing functions for the nonlinear components. Our quasi-linearized model becomes

$$\dot{\bar{x}} = N(\bar{A}, \omega) \bar{x} \quad (10)$$

The system described by equation (10) can be investigated to determine the existence, amplitude, and frequency of possible limit cycles. The limit cycles, sustained self-excited nonlinear oscillations, are assumed approximately sinusoidal in this approach.

The existence of a limit cycle in equation (10) requires that  $N(\bar{A}, \omega)$  have a pair of purely imaginary eigenvalues, since limit cycles are purely oscillatory. Additionally, the amplitude and frequency of the limit cycle must satisfy the relationships of the eigenvector and frequency associated with the purely imaginary eigenvalue as well as the condition that  $N(\bar{A}, \omega)$  have such a pair of purely imaginary eigenvalues.

Many numerical approaches are available for finding limit cycles that meet these conditions. One approach is to use numerical opti-

Table 2 (Cont'd)

Dimensions			
$a$	(One half the rail gauge)	= 2.48	ft
$d$	(One half sideframe spacing)	= 3.25	ft
$h_1$	(Truck c.g. to car body c.g. vertical distance)	= 2.99	ft
$h_2$	(Car body c.g. to bolster vertical distance)	= 2.99	ft
$L_C$	(One half truck center distance)	= 16.9	ft
$L_T$	(One half truck wheelbase)	= 2.833	ft
$r_o$	(Nominal wheel radius)	= 1.375	ft

mization techniques to solve the nonlinear algebraic equations that define the limit-cycle conditions. This approach for the rail-vehicle problem is discussed in a companion paper [14]. An alternate approach, which is used here, solves for limit cycles by investigating in an iterative fashion the eigenvalues of the linear problem that corresponds to a motion at a given amplitude. Limit cycles are found by employing information in one of the least-damped eigenvalues of the describing-function matrix  $N(\bar{A}, \omega)$  to lead iteratively to the values of amplitude and frequency that correspond to purely imaginary eigenvalues.

In the iterative technique the amplitude of one state  $A_k$  is chosen, and the remaining amplitudes and the system frequency are found from the eigenvalue with the smallest real part<sup>3</sup> and its associated eigenvector. At each step, initial values for evaluating the describing-function matrix are found by employing the frequency and eigenvector of the preceding step. The eigenvalue/eigenvector computation is repeated to improve the correspondence between the amplitudes and frequency used in computing the describing functions and those that result from the eigenvalue/eigenvector computation. New values for one of the system parameters, such as the vehicle speed, are chosen to move in a direction that drives the real part of the eigenvalue with the smallest real part toward zero.

Information about the stability of the limit cycles is a side product of this technique. The limit-cycle stability is found by varying the amplitude of the limit cycle a small amount. If the limit cycle is stable, slightly smaller amplitudes should result in the corresponding eigenvalue having a positive real part, and larger amplitudes should produce a negative real part. The opposite situation should prevail for an unstable limit cycle [23].

## Analysis

The numerical approach described in the preceding section was employed to obtain the results discussed below. The approach was programmed in FORTRAN for computation on a digital computer. Only the basic analytic procedure will be presented here. A more complete discussion of the algorithm and analytic procedure is available elsewhere [24].

**Describing Functions.** Describing functions for the nonlinear terms in the equations of motion were obtained by the technique discussed above. Analytic expressions were obtained for the suspension force describing functions, while the wheel/rail constraint-function describing functions required numerical computation.

As discussed earlier, the suspension forces consist of the dry friction and stiffness in the connections between the members. This composite force was modeled by a linear spring in parallel with dry friction. The forces (or torques) due to dry friction and linear springing can be handled separately when they occur in parallel. The total force (or

<sup>3</sup> In a few cases, the eigenvector shape of the least-damped eigenvalue is distinctly different from the state vector assumed in computing the eigenvector and is not reproducible when its shape is assumed for the eigenvector. In this case, the eigenvalue with the next smallest real part is used.



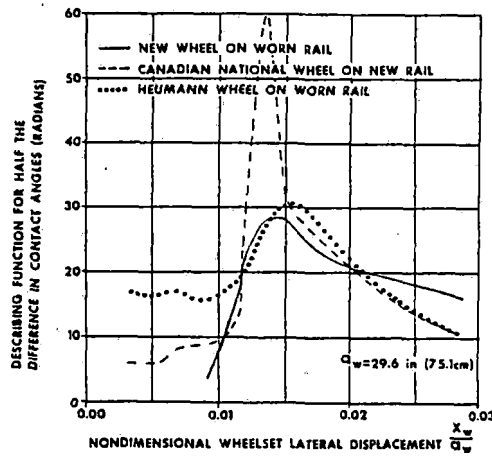


Fig. 7 Rolling-rail describing functions

torque) is simply the sum of the forces (or torques) due to the two mechanisms. The spring force is already linear and is defined by the spring constant  $k$ ; times the spring deflection. The force (or torque) due to dry friction is a nonlinear function of the velocity difference between the two contacting members.

When the state-variable approach is applied, the velocity is one of the states. Thus the dry-friction force can be considered as an odd memoryless static (i.e., not a function of derivatives of the state) nonlinearity, and equation (8) can be used to calculate its describing function. The friction force is given by a function of the form

$$F = F_0 \text{sign}(\dot{X}) \quad (11)$$

Substitution of this function into equation (8) yields the describing function:

$$N(A) = \frac{4F_0}{\pi A} \quad A = \text{amplitude of } \dot{X} \quad (12)$$

In the four different situations in which dry friction occurs in the equations of motion, the describing functions for the nonlinearities have this form. The resulting quasi-linearizations for these four cases are

Lateral Suspension:

$$F_{XSF} = K_X(X_{TF} - X_C - h_2\phi_C - L_C\theta_C) + \frac{4F_{OX}}{\pi A_1}(\dot{X}_{TF} - \dot{X}_C - h_2\dot{\phi}_C - L_C\dot{\theta}_C) \quad (13)$$

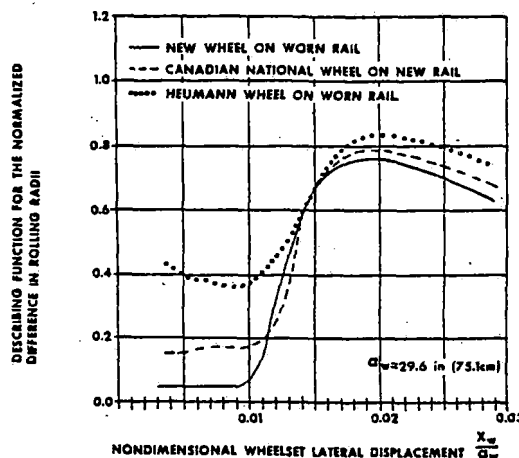


Fig. 8 Contact-angle describing functions

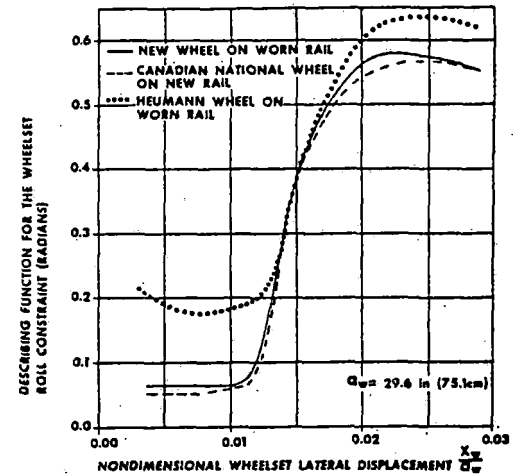


Fig. 9 Wheelset-roll describing functions

$$F_{XSR} = K_X(X_{TR} - X_C - h_2\phi_C + L_C\theta_C) + \frac{4F_{OX}}{\pi A_2}(\dot{X}_{TR} - \dot{X}_C - h_2\dot{\phi}_C + L_C\dot{\theta}_C) \quad (14)$$

where  $A_1$  is the amplitude of  $(\dot{X}_{TF} - \dot{X}_C - h_2\dot{\phi}_C - L_C\dot{\theta}_C)$  and  $A_2$  is the amplitude of  $(\dot{X}_{TR} - \dot{X}_C - h_2\dot{\phi}_C + L_C\dot{\theta}_C)$ .

Vertical Suspension:

$$F_{YSR} = F_{YSF} = K_Y(d\phi_C) + \frac{4F_{OY}}{\pi A_3}(d\dot{\phi}_C) \quad (15)$$

where  $A_3$  is the amplitude of  $(d\phi_C)$ .

Warp Suspension:

$$T_{\theta WF} = K_{\theta W}(\theta_{WF}) + \frac{4T_{OW}}{\pi A_4}(\dot{\theta}_{WF}) \quad (16)$$

$$T_{\theta WR} = K_{\theta W}(\theta_{WR}) + \frac{4T_{OW}}{\pi A_5}(\dot{\theta}_{WR}) \quad (17)$$

where  $A_4$  is the amplitude of  $(\dot{\theta}_{WF})$  and  $A_5$  is the amplitude of  $(\dot{\theta}_{WR})$ .

Yaw Suspension:

$$T_{BF} = \frac{4T_{OB}}{\pi A_6}(\dot{\theta}_{WF} + \dot{\theta}_{TF} - \dot{\theta}_C) \quad (18)$$

$$T_{BR} = \frac{4T_{OB}}{\pi A_7}(\dot{\theta}_{WR} + \dot{\theta}_{TR} - \dot{\theta}_C) \quad (19)$$

where  $A_6$  is the amplitude of  $(\dot{\theta}_{WF} + \dot{\theta}_{TF} - \dot{\theta}_C)$  and  $A_7$  is the amplitude of  $(\dot{\theta}_{WR} + \dot{\theta}_{TR} - \dot{\theta}_C)$ .

As explained earlier, the constraints on the motion of the wheelset due to the geometry of wheel/rail contact describe the nature of the contact forces between wheel and rail. The geometric constraint functions are illustrated in Figs. 3-5. These constraints are odd memoryless static nonlinearities, and thus equation (8) can be used to calculate their describing-function quasi-linearizations. Because the constraint functions were obtained numerically, the describing functions were also computed numerically. The resulting describing functions for the constraints are plotted in Figs. 7-9.

The constraint functions were defined as functions of nondimensional wheelset lateral motions (wheelset lateral motions divided by half the rail gauge). The quasi-linearizations, then, are given by the describing functions times the nondimensional wheelset lateral motions.

As expected, the describing functions are approximately constant for small wheelset lateral motions, but they increase rapidly once the contact moves to the wheel flange. The maximum values are reached

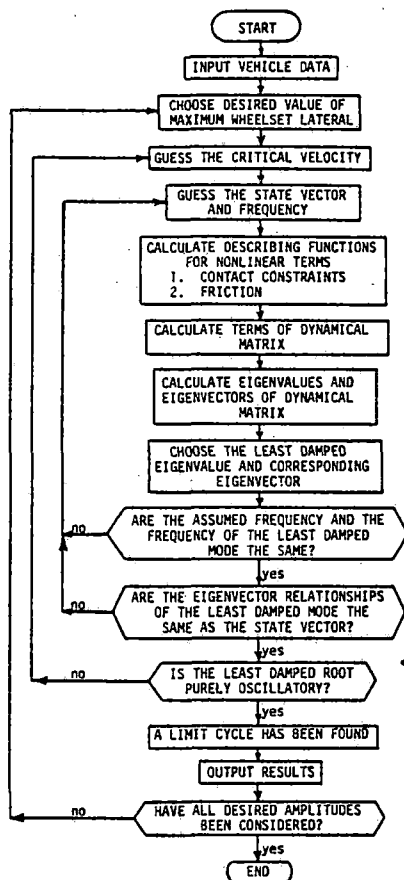


Fig. 10 Computational algorithm

when the contact position is near the steepest portion of the flange. As the contact position moves on beyond this point, the describing functions decrease.

The major differences between the different wheel profiles in this study show up at small wheelset lateral amplitudes. The new wheel describing functions for all three constraint functions have small values in this range, while the Heumann wheel values are several times larger in the same range. The describing functions for the Canadian National Profile A fall between these two extremes in the rolling-radii and contact-angle cases, while the roll-angle describing function is slightly smaller than the new-wheel values.

**Stability Analysis.** A flow chart of the computer algorithm used to find the limit cycles is shown in Fig. 10. The algorithm implements the iterative procedure described previously for describing-function quasi-linearization and eigenvalue/eigenvector analysis to find limit cycles.

In the procedure the first value of the maximum<sup>4</sup> wheelset lateral displacement is specified, and estimates of the critical velocity, state vector, and frequency are made. In an inner loop, describing functions are obtained using these estimates, and eigenvalues and eigenvectors are calculated. Estimation of the frequency and the state vector is repeated until the estimates are consistent with the least-damped eigenvalue and eigenvector computed. An outer loop iteratively estimates velocity to find the critical velocity at which the limit cycle occurs. This process is repeated for the next value of maximum wheelset lateral displacement.

New estimates for the frequency and state vector in the inner loop are made by choosing, as improved guesses, the frequency and the eigenvector relationship of one of the least-damped modes. Generally the iteration procedure will then converge to a frequency and state

vector that are consistent with the least-damped mode frequency and eigenvector.

A linear extrapolation on the estimated velocity based on the damping in the least-damped mode is used in the outer loop to move toward the critical velocity, where there is a mode with zero damping. This process provides the amplitudes, mode shapes, frequency, and critical speed of all possible limit cycles of the system, stable and unstable.

## Results

Initial results for the freight car were calculated considering the wheel/rail contact constraints as the only nonlinearities. Linear descriptions formulated by assuming constant amplitudes and frequency were used for the damping terms. In addition, results for the freight vehicle with Canadian National wheel profiles were computed with both the nonlinear wheel/rail functions and dry friction.

Stable and unstable limit-cycle wheelset lateral amplitudes as a function of speed for the three vehicle configurations are shown in Fig. 11. The wheelset lateral amplitude referred to in this figure is the maximum lateral amplitude of any of the four wheelsets. All four wheelsets do not generally have the same amplitude. Stable limit cycles are indicated by solid lines, and unstable limit cycles by dashed lines. In general, the space to the left of each curve may be described as stable, in the sense that motions beginning at any amplitude in this region will decrease in amplitude. In the opposite sense, motions beginning with amplitudes in the region to the right of the stable and unstable limit-cycle curves will grow in amplitude, reaching either a stable limit cycle or becoming unbounded. Amplitudes slightly larger or smaller than an unstable limit cycle will grow or decay in amplitude to move away from that limit cycle. Amplitudes slightly larger or smaller than a stable limit cycle will tend to decay or grow in amplitude to move back to that stable limit cycle.

The results for the vehicle with the contact nonlinearities alone indicate that the critical velocity is almost independent of amplitude until flange contact is reached. For the new conical wheel the unstable limit-cycle curve is vertical until the flange contacts.

For the Canadian National and modified Heumann profiles, which are more representative of worn wheels, there is slightly more variation because the tread area is not strictly conical, but hollowed. This results in a greater (but still small) variation in the contact constraints with displacement. The small variation indicates that linear theory is good until flange contact is reached.

The first occurrence of flange contact is characterized by a stable limit cycle that extends to a high velocity. The velocity is quite large for the new-wheel case. The hunting phenomenon that has been observed for actual rail vehicles is described by such stable limit cycles. As shown in Fig. 11, the freight car running on new wheels will hunt at speeds above 145 fps (44.2 m/s). The freight vehicle with Canadian National wheels, which are representative of slightly worn wheels, and the same vehicle with modified Heumann wheels also will hunt, but the initial speeds at which this occurs are much lower.

The effect of flange contact appears to be very stabilizing, as would be expected. This is why, once the flange comes into contact, the critical speed extends far to the right, especially for the new-wheel case. At high speeds, small amplitudes of wheelset lateral displacement are unstable, and they grow until flange contact limits them. The speed range for stable limit cycles with the Canadian National and modified Heumann wheel profiles is smaller.

Stable limit cycles occur at two distinct regions of flange contact for the Canadian National wheel profile. The indication is that two distinct modes of hunting are possible here. In the lower mode only a wheelset of the rear truck contacts the flange. In the higher mode a wheelset of each truck experiences flange contact.

The modified Heumann profile configuration experiences hunting over a limited range of speeds at low amplitudes that do not include flange contact. This is probably due to the fact that the concavity or describing function for the difference in wheel radii decreases with amplitude in this range, as seen in Fig. 7. This is caused by the extreme nonlinearity of the contact geometry.

<sup>4</sup> "Maximum" means the maximum value for any of the four wheelsets. Each wheelset generally has a different amplitude.

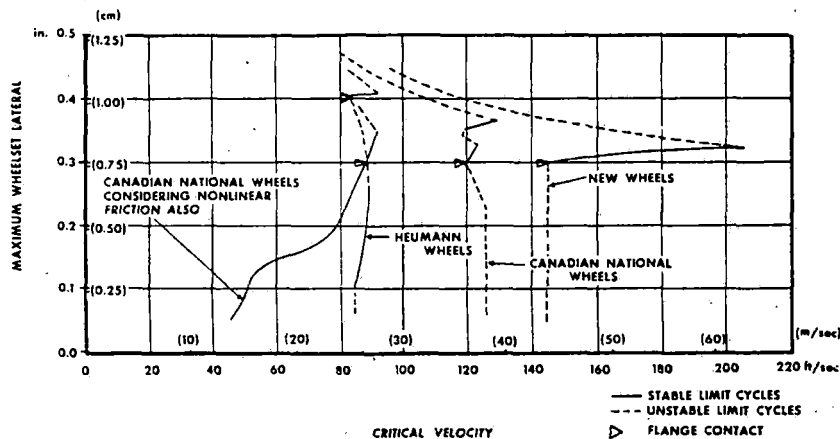


Fig. 11 Limit-cycle amplitudes versus velocity

The effects of nonlinear friction on the critical velocity are shown in Fig. 11 for the Canadian National wheel profile. Note that at low amplitudes the stability is drastically reduced. Although stable limit cycles are predicted at low speeds, these have very low amplitudes. Stable limit cycles are also found at large amplitudes. The stable limit cycles, or hunting, in which flange contact is present occur at higher speeds, closer to (but still below) the speed that has been found in linear analyses.

The low critical speeds found for nonlinear damping at low amplitudes are caused by the vehicle acting more as a rigid body, because the forces due to dry friction are relatively large. At larger amplitudes the initial breakaway force of the dry friction is easily overcome, and the vehicle acts more as a system of separate elements between which a large amount of relative motion is possible.

The effects of dither (random vibrations or motions between system elements due to track irregularities, etc.) may come into play here to overcome the breakaway force and thus raise the critical speeds at low wheelset lateral amplitudes. Consequently, it is doubtful that the low-amplitude limit cycles are of practical interest. The dry-friction results shown here are contrary to those found with the single-wheelset model. In that case [14] dry friction was found to be very stabilizing at lower amplitudes. However, this difference can be explained by the fact that the single-wheelset model was assumed sprung to a reference body, representing the vehicle body, moving at a constant speed down the track. The large force provided by the friction elements at small amplitudes stabilized the wheelset against the reference. For the complete vehicle the friction elements at low amplitudes force it to behave as a large rigid body that will have a low critical hunting speed. Scheffel [25] notes that suspending the wheelset to the vehicle rather than to ground reduces the effectiveness of the constraints (the suspension) in stabilizing the hunting behavior.

It should also be noted that the limit cycles shown plotted in Fig. 11 were not the only limit cycles found. Limit cycles for speeds higher than the critical speeds could be found in some situations. These secondary limit cycles generally had a different mode shape than the primary limit cycles occurring at lower speeds. It would be expected that the limit cycles occurring in practice would depend on the initial conditions and inputs to the vehicle. In the study of rail-vehicle dynamics the greatest interest is in the lowest speeds at which the rail vehicle might become unstable. Consequently, only the primary limit cycles need to be found.

Eigenvector relationships, or mode shapes, for the limit cycles found for the new-wheel case are shown in Fig. 12. The abrupt change in mode shape upon flange contact is quite apparent here. Before flange contact the mode shape is constant for the new wheel. This is to be expected, because the new-wheel tread surface is conical until the flange contacts the rail. When the tread region is curved, as in the Canadian National and modified Heumann wheel profiles, the mode shape is not constant when the wheelset lateral amplitudes keep the

contact in the tread region. Generally, the frequency and the amplitudes of the truck yaw and truck warp of the limit cycle follow the conicity shown in Fig. 7.

The truck yaw and warp for the new wheel, which has a small conicity, are small, as shown in Fig. 12; they are correspondingly larger for the worn-wheel representations. The frequency of the limit cycles before flange contact is also found to be quite a bit smaller for the new wheel, as compared to the worn-wheel representations (12 rad/s for the new, 21 rad/s for the Canadian National, and 26 rad/s for the modified Heumann profile). Both these effects can be attributed to the larger conicity of the Canadian National and Heumann wheel profiles.

The ratio of car-body lateral displacement to rear-truck lateral displacement, as shown in Fig. 12, is quite large for the vehicle with new wheels. This may be because the frequency of the limit cycle is below the resonant frequency for car-body lateral motion. The results for the worn-wheel cases show relatively insignificant car-body lateral motion, as would be expected at high frequencies.

The limit cycles without flange contact for all three cases are characterized by the front and rear trucks having approximately equal lateral amplitudes. Once the flange begins coming into contact, the mode shapes are quite different. For the new wheel the limiting mode with flange contact is a fishtailing mode. As shown in Fig. 12, this mode is characterized by large lateral motions of the rear truck, small lateral motions of the front truck, and small disturbance of the vehicle body. For all three wheel profiles, frequencies for limit cycles with

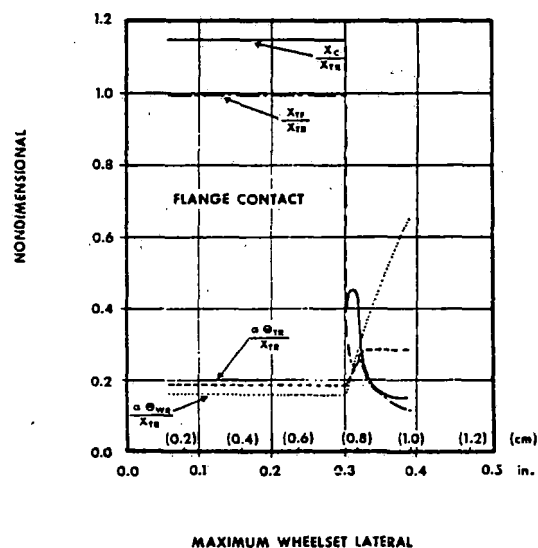


Fig. 12 Limit-cycle mode shapes for new wheel on new rail

flange contact approach a single high value in the neighborhood of 30.5 rad/s.

For the new wheel there were actually two mode shapes found for the limit cycles with flange contact, but since the two were symmetric, only the fishtailing mode was plotted in Fig. 12. The other mode that was found occurred at the same velocities and frequencies, but with large motions of the front truck instead of the rear truck. Car-body motions were the same.

## Conclusions

The results of this study indicate that nonlinear wheel/rail contact geometry and dry friction should be considered in rail-vehicle analysis because they significantly influence the hunting behavior of such vehicles. Although the critical hunting speed for small-amplitude motions varies widely with different wheel/rail geometry, it appears that linear descriptions of wheel/rail contact geometry may be sufficient for studying these small motions. Nonlinear contact geometry must be considered to study the limit-cycle motion that can occur when the wheelset lateral motion exceeds the flange contact boundary.

Stable limit cycles, representing vehicle hunting behavior, were found to exist over certain speed ranges that were determined in part by the wheel/rail contact geometry. The mode shapes of the large-amplitude limit cycles were asymmetric, generally with larger rear-truck motions than front-truck motions.

Our results indicate that dry friction in the vehicle suspension will lower the critical speeds. For small motions, friction causes the vehicle to tend to perform as one rigid body, which results in low-amplitude limit cycles at low speeds. However, the low-amplitude limit cycles may not be of practical importance because effects such as dither may reduce the effective friction. At large amplitudes dry friction also causes the limit cycles to occur at speeds lower than predicted with equivalent linear damping. This indicates that the amplitudes and frequencies used to obtain the equivalent linear values were too large and points out the importance of the quasi-linear techniques for handling such nonlinearities.

A better model for the suspension structure is worth consideration. One model that has been suggested represents the suspension by two elements in parallel. One element would be a stiffness that represents the suspension springs. The other element would consist of a stiffness in series with a dry friction. The series stiffness would represent the elasticity of vehicle components, and the friction term would represent the joint friction. Thus, even when the friction element remains locked, there could be relative motion between vehicle components due to the series stiffness element. These would probably increase the speed at which low-amplitude limit cycles occur.

The effects of dry friction at low amplitudes found in this study are directly opposite the effects of dry friction found in a single-wheelset analysis. This suggests that the stabilizing effects of friction found in the single-wheelset analysis may not be of practical importance.

The quasi-linear approach used here appears to be a very practical method for the investigation of rail-vehicle stability. However, the algorithms used to implement the technique need development to improve their convergence to the correct mode and frequency. Comparison of this numerical approach with other alternatives such as optimization techniques should also be made to determine the most efficient computational scheme.

Future effort on this problem should include validation of the quasi-linear results by comparison with numerical integration results, comparison of the quasi-linear results with experimental vehicle results, and further refinement of the computational algorithms to permit general use of this approach. Other nonlinear effects such as wheel slip should be investigated with this technique.

## Acknowledgment

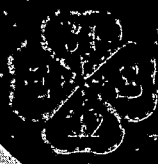
The effort described in this paper was supported in part by contract DOT-OS-40018 with the Federal Railroad Administration and contract DOT-TSC-902 with the U. S. Department of Transportation,

Transportation Systems Center. The latter contract was issued by the Transportation Systems Center in support of the Federal Railroad Administration. The cooperation of the Association of American Railroads in this project is also gratefully acknowledged.

Professor E. Harry Law of Clemson University, and Professor J. Karl Hedrick of M.I.T., co-principal investigators in these two projects, made significant contributions to the work reported in this paper.

## References

- 1 Law, E. H., and Cooperrider, N. K., "Literature Survey of Railway Vehicle Dynamics Research," *Journal of Dynamic Systems, Measurement, and Control*, TRANS. ASME, Series G, Vol. 96, No. 2, June 1974, pp. 132-164.
- 2 Blader, F. B., "Free Lateral Oscillations in Long Freight Trains," PhD thesis, Queen's University, Kingston, Ontario, 1972.
- 3 Blader, F. B., and Kurtz, E. F., Jr., "Dynamic Stability of Cars in Long Freight Trains," *JOURNAL OF ENGINEERING FOR INDUSTRY*, TRANS. ASME, Series B, Vol. 96, No. 4, Nov. 1974, pp. 1159-1167.
- 4 DePater, A. D., "The Approximate Determination of the Hunting Movement of a Railway Vehicle by Aid of the Method of Krylov and Bogoliubov," *Applied Scientific Research*, Section A, Vol. 10, 1961, pp. 205-228.
- 5 van Bommel, P., "Application de la Theorie des Vibrations Nonlineaires sur le Probleme du Mouvement de Lacet d'un Vehicule de Chemin de Fer," doctoral thesis, Technical University of Delft, The Netherlands, 1964.
- 6 Stassen, H. G., "Random Lateral Motions of Railway Vehicles," doctoral dissertation, Technische Hogeschool, Delft, The Netherlands, 1967.
- 7 Law, E. H., "Analysis of the Nonlinear Dynamics of a Railway Vehicle Wheelset," PhD thesis, Department of Mechanical Engineering, University of Connecticut, Storrs, Conn., 1971.
- 8 Law, E. H., and Brand, R. S., "Analysis of the Nonlinear Dynamics of a Railway Vehicle Wheelset," *Journal of Dynamic Systems, Measurement, and Control*, TRANS. ASME, Series G, Vol. 95, No. 1, Mar. 1973, pp. 28-35.
- 9 Garg, D. P., "Describing Function Techniques for the Nonlinear Analysis of the Dynamics of a Rail Vehicle Wheelset," Final Report, U. S. DOT(TSC), July 1975.
- 10 "Geometry of the Contact Between Wheelset and Track, Part I: Methods of Measurement and Analysis," Question C116, Interaction between Vehicle and Track, Report No. 3, Office for Research and Experiments (ORE), International Union of Railways, Utrecht, The Netherlands, Oct. 1973.
- 11 Cooperrider, N. K., Law, E. H., Hull, R., Kadala, P. S., and Tuten, J. M., "Analytical and Experimental Determination of Nonlinear Wheel/Rail Geometry," *Proceedings of a Symposium on Railroad Equipment Dynamics*, ASME, 1976, pp. 41-70.
- 12 Cooperrider, N. K., Law, E. H., Hull, R., Kadala, P. S., and Tuten, J. M., "Analytical and Experimental Determination of Nonlinear Wheel/Rail Geometric Constraints," Report No. FRA-OR and D-76-244 (PB 25290), Dec. 1975.
- 13 Cooperrider, N. K., Hedrick, J. K., and Law, E. H., "The Application of Quasi-Linearization Techniques to the Prediction of Nonlinear Railway Vehicle Response," presented before IUTAM Symposium on the Dynamics of Vehicles on Roads and Railway Tracks, Delft, The Netherlands, Aug. 1975.
- 14 Hannebrink, D. N., Lee, H. S. F., Weinstock, H., and Hedrick, J. K., "Influence of Axle Load, Track Gauge, and Wheel Profile on Rail-Vehicle Hunting," ASME Paper No. 76-WA/RT-3.
- 15 Hadden, J. A., and Law, E. H., "Effects of Truck Design on Hunting Stability of Railway Vehicles," ASME Paper No. 76-WA/RT-1.
- 16 Eck, B. J., and Berg, N. W., "Looking for Tomorrow's Wheel Profile," ASME Winter Annual Meeting, Detroit, November 1973.
- 17 Kalker, J. J., "On the Rolling Contact of Two Elastic Bodies in the Presence of Dry Friction," doctoral dissertation, Technische Hogeschool, Delft, The Netherlands, 1967.
- 18 Hedrick, J. K., Cooperrider, N. K., and Law, E. H., "Computational Methods for Predicting the Nonlinear Response of Rail Vehicles Using Quasi-Linearization," report in preparation for the U. S. DOT Transportation Systems Center.
- 19 Law, E. H., and Cooperrider, N. K., "Linear Analyses of Railway Car Dynamics," report in preparation for the Federal Railroad Administration.
- 20 Abbott, P. W., Morosow, G., and Macpherson, J., "Track-Train Dynamics," SAE Paper 751058, Nov. 1975.
- 21 "70 Ton Truck Component Data, Physical Restraints, Mechanical Properties, Damping Characteristics," *Track-Train Dynamics Harmonic Roll Series*, Vol. 2, 1974.
- 22 Siljak, D., *Nonlinear Systems: The Parameter Analysis and Design*, Wiley, New York, 1969.
- 23 Gelb, A., and Vander Velde, W., *Multiple-Input Describing Functions and Nonlinear Design*, McGraw-Hill, New York, 1968.
- 24 Hull, R., "An Investigation into Nonlinear Railway Vehicle Response," MSE thesis, Department of Mechanical Engineering, Arizona State University, Tempe, Ariz., 1976.
- 25 Scheffel, H., "Wheelset Suspensions Designed to Eliminate the Detrimental Effects of Wheel Wear on the Hunting Stability of Railroad Vehicles," *Proceedings of a Symposium on Railroad Equipment Dynamics*, ASME, 1976, pp. 1-40.



an ASME  
publication

\$3.00 PER COPY \$1.50 TO ASME MEMBERS

The Society shall not be responsible for statements or opinions advanced in papers or in discussion at meetings of the Society or of its Divisions or Sections, or printed in its publications. Discussion is printed only if the paper is published in an ASME journal or Proceedings. Released for general publication upon presentation. Full credit should be given to ASME, the Technical Division, and the author(s).

C. A. Sciammarella

Professor

L. Năilescu

Research Assoc.

S. Kumar

Professor and Chairman

B. B. Seth

Research Assoc.

Illinois Institute of Technology  
Chicago, Ill.

## Similitude Law for the Creep-Adhesion Function in Dry Contact

*This paper describes an experimental study on the dry friction-creep phenomenon. The study has been carried out on a test-rig. The simulated wheel has an elliptical area of contact similar to the actual locomotive wheel and is made of a 1070 plain carbon steel. The testing was conducted with variable contact stresses up to approximately 200,000 psi and equivalent speeds of approximately 5 miles per hour. The results of the test show that all the different creep-adhesion curves obtained by changing the normal loads can be reduced to one single dimensionless curve. This can be achieved if the actual nominal area of contact experimentally measured, is introduced in the corresponding expressions. A law of constancy of the product of the creep times the area of contact for dry, clean contact surfaces and a constant value of adhesion and normal load is presented.*

### Introduction

The steel wheel and rail friction is a problem that has created a great deal of interest both in the past and in the current technical literature. Its importance is increasing in the measure that more effective locomotive design requires increasing load transfer between wheel and rail.

The stresses and relative displacements at the wheel-rail interface are of primordial importance in most of the basic technical problems facing railway technology. The wheel and rail wear, braking, acceleration, headway limits, draw bar pull, hunting and other oscillation and stability problems depend on the interaction phenomena taking place at the wheel-rail interface. In spite of the intensive efforts, both theoretical and experimental, a complete understanding is still lacking.

To experimentally investigate the phenomena of adhesion, creep and wear, simulating closely the conditions of railroad wheel and rail interaction, a facility has been developed at the Department of Mechanics, Mechanical and Aerospace Engineering of the Illinois Institute of Technology with the cooperation and assistance of the General Motors Electro-Motive Division. Some of the significant findings of the current research are reported in this paper.

### Review of Related Literature

There has been an extensive amount of work done both in the theoretical and the experimental aspects of the rail-wheel contact problem. This work covers a period starting around 1867 to the present. Numerous survey papers on the subject have been written.

Cable, Jr. [1] has written a good descriptive account of the various factors involved in understanding adhesion. A total of 57 references is given in his paper, going as far back as 1873.

A survey of the work on adhesion done in Germany and other European countries, along with extensive technical discussion including reference to the various available theories, has been given by Verbeck [2]. Law and Cooperrider [3] have also discussed the wheel/rail interaction forces, creep and provided an extensive list of references.

Collins and Pritchards [4] have a good coverage of the aspects of contamination effects on adhesion. Marta and Mels [5] and Marta, Mels, Itami [6] have written a good scientific account of the wheel-rail adhesion problem and reviewed briefly the factors that affect adhesion, including considerations and tests of full locomotives. Meier [7] has reviewed many of the tests conducted to establish the coefficient of friction.

Closely connected to the problem of wheel-rail interaction is the problem of contact stresses and displacements. A great deal of references exist on this area. Fortunately there are some very good surveys; some of the recent ones are written by Kalker [8], Johnson [9] and Brémond [10].

Surveys of the contact problem with emphasis on adhesion and creep phenomena have been given by Ollerton [11], Johnson [12], and Kalker [13]. More recently B. Paul [14] has made a survey of rail-wheel stress problems and has included some of the most recent work in this area.

### Brief Description of the Test Facility

The test facility on which this study has been carried out was originally designed and manufactured by the Electro-Motive Division of the General Motors Company. The facility has been described in detail elsewhere [15, 16]. In May 1974 the facility was moved to the Illinois Institute of Technology. At IIT changes were made on the mechanical, electrical and recording of data to improve performance and accuracy. A detailed description of the improved facility is given

Contributed by the Rail Transportation Division for presentation at the Winter Annual Meeting, San Francisco, Calif., December 10-15, 1978 of THE AMERICAN SOCIETY OF MECHANICAL ENGINEERS. Manuscript received at ASME headquarters July 1, 1978. Paper No. 78-WA/RT-6.

Copies will be available until Sept. 1979.

in [16], and is planned to be published in another paper. Fig. 1 shows a schematic of the test facility. The facility essentially consists of a small wheel riding on a large wheel, Fig. 1, under a normal force which is maintained constant during the tests. The large wheel has a diameter of approximately 36 in. and represents the rail. The large wheel is manufactured with a steel typical of rail material. The small wheel of diameter 8 in. simulates the locomotive wheel. The periphery of the small wheel has a profile radius so as to make the contact stresses between the small and the large wheel similar to those of the locomotive and rail. A ratio of the major axis of the ellipse of contact to the minor axis equal to 1.568, typical of the U.S.A. locomotives was selected. Besides the two wheels and corresponding motors the facility consists of:

- (1) Electrical Controls
  - a) Speed
  - b) Power
- (2) Mechanical Controls
  - a) Alignment of the axis of rotation of the wheels
  - b) Angle of attack
- (3) Output Devices
  - a) Measurement of speeds
  - b) Measurement of forces

The small wheel is connected through a flexible coupling to a small D. C. motor. During the tests one of the motors acts as generator, providing the necessary braking torque. The energy generated by the braking torque is dissipated as heat through a bank of resistors. The big wheel is powered by a locomotive traction motor, and during the tests, drives the small wheel.

The reliability and the accuracy of the experimental data depends on the alignment of the test facility. If the two wheels of the rig are misaligned in any of the  $x$ ,  $y$ , and  $z$  axis directions, Fig. 2, forces will be introduced at the contact areas. The angle of attack, angle between the axis  $z$  and  $z'$  of Fig. 2 can be controlled by a positioning screw.

The two outputs provided by the facility are forces and speeds. To measure speeds of rotation magnetic pick-ups are utilized. Each axle holds a 144 tooth gear and each tooth produces a count. The counts are displayed by two electronic counters.

The second wheel is supported by a frame connected to a 3-D dynamometer that measures forces in the  $y$  axis (axial direction), the  $z$  axis (longitudinal direction) and  $x$  axis (transversal direction). The dynamometer has three strain gage bridges connected through a switching and balancing unit to a digital strain gage meter. A calibration of the dynamometer was performed by applying known forces in the axial, longitudinal and transversal directions. The calibration was performed *in situ*, and under the same conditions of operation that are present when the tests are performed.

### First Series of Tests Performed

The first series of tests performed with the rig had the purpose to investigate the coefficient of friction versus creep function under changing normal loads, in dry contact.

The independent variables in the tests were the vertical load and the longitudinal load and the dependent variable the creep values.

The creep values during the experiment were calculated by means of the equation:

$$\xi = 1 - \frac{\omega_S R_S}{\omega_B R_B} = 1 - \frac{N_S R_S}{N_B R_B} \quad (1)$$

where:

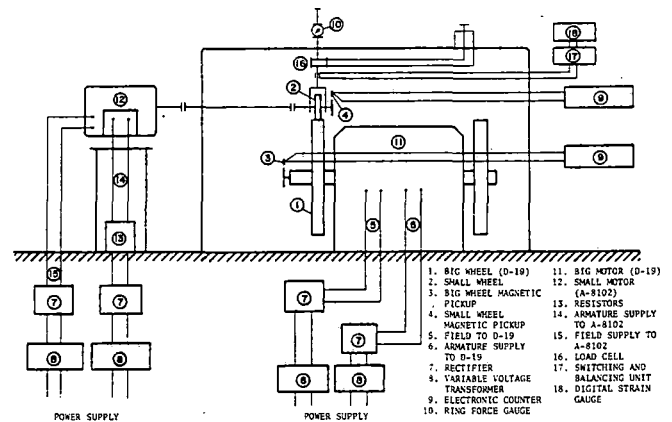


Fig. 1 Schematic arrangement of the DOT-GM-IT Wheel-Rail Test Facility

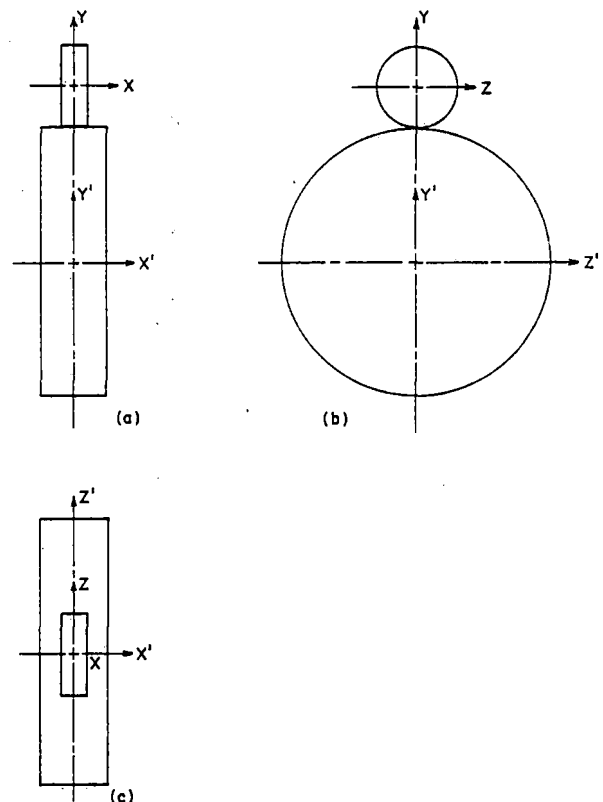


Fig. 2 Axes of Alignment

$N_S$  = Speed of the small wheel in rpm  
 $N_B$  = Speed of the big wheel in rpm  
 $R_S$  = Radius of the small wheel in inches  
 $R_B$  = Radius of the big wheel in inches

### Nomenclature

$a_R, b_R$  = major and minor axes of the replica ellipse  
 $a_T, b_T$  = major and minor axes of the true contact ellipse  
 $A_R$  = apparent area of contact from the replica  
 $A_T$  = true area of contact  
 $G$  = shear modulus of steel

$N$  = normal force  
 $N_B$  = speed of the big wheel in rpm  
 $N_S$  = speed of the small wheel in rpm  
 $R_B$  = radius of the big wheel  
 $R_S$  = radius of the small wheel  
 $T$  = tangential force  
 $\xi$  = creep (slip)  
 $\mu$  = coefficient of friction

$\mu_C$  = maximum coefficient of friction

### Subscripts

$R$  = concerning replica  
 $T$  = true value  
 $B$  = concerning big wheel  
 $S$  = concerning small wheel



The radius of the big wheel was measured to 0.0254 mm with a Pi-tape. A Pi-tape is a tape that by measuring the wheel perimeter provides directly the value of the wheel's diameter with a precision of 0.0254 mm. The radius of the small wheel was also measured to 0.0254 mm. An upper bound for the error in the measurement of the creep is computed in Appendix A. According to these computations the values of creep can be considered accurate to 0.0005. As the test takes place the large and the small wheels show wear. The radii  $R_S$  and  $R_B$  are reduced by small amounts. The percentage in  $R_S$  is however, more. It can be shown that if the change of radius of the small wheel is 0.0076 mm, the creep will be affected by 0.00005 (see Appendix B).

The coefficient of friction at both values of creep was obtained by dividing the tangential force  $T$  by the normal force  $N$

$$\mu = \frac{T}{N} \quad (2)$$

The error in measuring the tangential force  $T$  obtained from the calibration tests is 22.249 N.

During the tests, the speed of the big wheel was kept near 50 rpm. This rotational speed is equivalent to a speed of 8.224 Kms per hour.

Another quantity measured during the test was the area of contact. It was observed that as the wheels roll appreciable wear takes place. This wear changes the area of contact since the transversal radius of the small wheel is changed by the wear. The tests were carried out using several wheels and the wheels were changed when the contact ellipse showed a departure from the elliptic shape characterized by the ratio of the major to the minor axis.

To obtain the contact area the following procedure was developed. A piece of replicating tape of the type utilized in electron microscopy was inserted between the two wheels and the wheels were pressed against each other. An impression of the contact area is left on the tape. The area is magnified through a shadograph and the area is determined.

A basic assumption of this technique is the similitude between the contact area and the impression left in the tape. This assumption has been checked by measuring the ratio of the major to the minor axis of the contact ellipse. It was verified that this ratio agrees with the theoretical value 1.568 within the experimental error. For smooth surfaces the replica's area is larger than the actual contact area. As a double checking of this technique, tapes of decreasing thicknesses were utilized to make replicas. A plot of area of the replica versus thickness was made and the value of the area was extrapolated to zero thickness. The extrapolated area agreed well with the theoretically computed value. In the case of rough surfaces, the presence of the tape produces an additional effect, the effect of the roughness in the contact area is eliminated. This effect is opposite to the effect of the thickness of the tape.

However none of these effects needs to be considered to compute the actual contact area. If we call  $A_R$  of the replica and  $A_T$  the true area,

$$A_R = \frac{\pi}{4} a_R b_R \quad (3)$$

where  $a_R$  is the major axis of the replica ellipse and  $b_R$  the minor axis. Likewise

$$A_T = \frac{\pi}{4} a_T b_T \quad (4)$$

where  $a_T$  and  $b_T$  are the major and minor axes of the contact ellipse.

Dividing (3) by (4) one obtains

$$\frac{A_T}{A_R} = \frac{a_T b_T}{a_R b_R} \quad (5)$$

Using the similitude between the contact area and its replica,

$$\frac{a_T}{a_R} = \frac{b_T}{b_R} = C \quad (6)$$

and

$$A_T = C^2 A_R \quad (7)$$

The value of  $C$  can be easily determined by measuring the contact track that is left in the small wheel by rolling. Microscopic observation shows a well-defined track that can be measured accurately. Rather than measuring directly on the track width on the rig, the following procedure was followed. By means of an acrylic material, replicas were made of portions of the track of the small wheel. This replica was utilized to measure the width of the track. The quantity  $C$  was computed by means of equation (6).

## Test Procedure

Before starting each experiment, the big and the small wheels were cleaned with trichlorethylene in order to eliminate surface impurities. The small wheel was lifted and the strain-gage bridges of the dynamometers were balanced. Contact was then established between the two wheels, the desired normal load was applied and the big wheel motor was started. The big wheel was then driving the small wheel and certain longitudinal force was measured by the strain indicator. This reading was brought to zero by supplying power to the small motor. Creep was gradually introduced by braking the small wheel. The tangential force developed between the wheels was measured by means of the strain indicator. The values of the revolutions of the small and big wheels were recorded from the values displayed by the counters. The creep values were increased until gross slip was observed.

After every test, a track was formed on the big wheel and so a new surface was used for each experiment by moving the big wheel in the lateral direction. When the entire surface of the big wheel was covered with tracks, a light cut was taken across the wheel. A high speed tool was placed in a tool holder which is connected to the base of the rig and traverses the wheel width. The wheel then was grounded with a tool grinder and finally polished with 320 and 400 grit emery papers to obtain a 20  $\mu$ m finish. The wheel finish is 15  $\mu$ m.

## The Results

Figs. 3-6 show the average curves of longitudinal coefficient of friction vs. longitudinal creep for the different utilized loads. Actual measured points are indicated in the graphs. The dispersion of values is very large and shows the intrinsic randomness of the observed phenomena. Fig. 7 shows all the curves plotted together. One can see that the average curves fit a well-defined pattern. This pattern is evidenced in Fig. 8 where values of the coefficient of friction versus normal load have been plotted for constant values of creep. All the curves of Fig. 8 are almost parallel, indicating a common decreasing trend for the longitudinal coefficient of friction with the normal load, practically independent of the values of the creep.

The areas of contact were measured according to the previously described procedure. Fig. 9 shows the area of contact versus the normal load for smooth new surfaces. Measured values of the contact area for the four different carried-out tests are given in Fig. 10. The values correspond to the different wheels utilized during the test. In the same graph, the Hertz's theory area values are plotted. One can see considerable difference between the theoretical and the experimental values.

## Data Analysis

It is a well-known fact that for perfectly smooth surfaces the coefficient of friction curves versus creep can be represented in a dimensionless form. The dimensionless variables are  $\mu/\mu_C$  and  $Gab\xi/\mu_CN$ , where  $\mu_C$  is the maximum coefficient of friction,  $G$  the shear modulus of the steel and all other variables have been previously defined. We have reduced all our data to dimensionless form. It was observed that in order to obtain a single curve it is necessary to utilize the actual nominal area of contact rather than the theoretical area of contact. The dimensionless curve is plotted in Fig. 11. This curve coincides with the theoretical values predicted by Kalker [13]. It can be concluded that the law of similitude holds good for dry contact not only for perfectly smooth surfaces, but also for surfaces that become rough due to the wear phenomenon.

The observed fact that all the different plots of coefficient of friction versus creep can be reduced to a single dimensionless form by utilizing

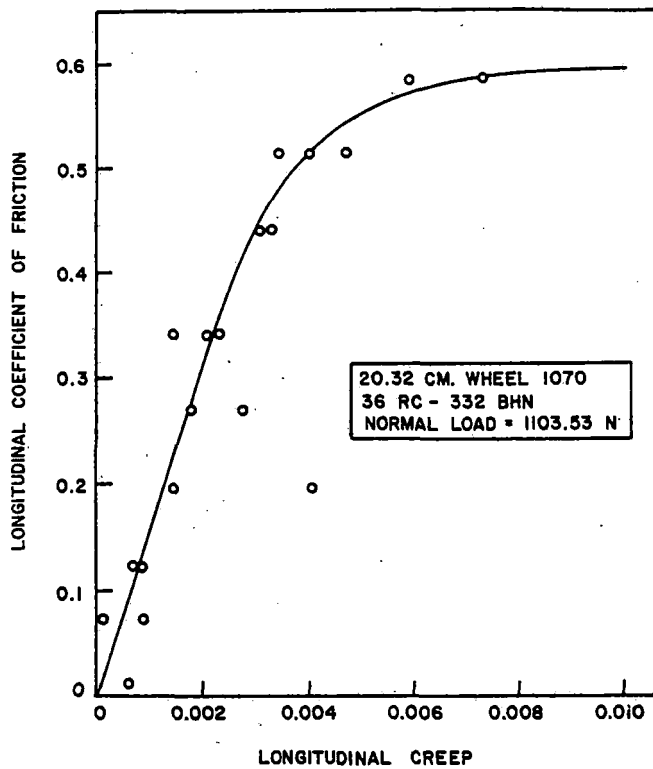


Fig. 3 Longitudinal Coefficient of Friction versus Longitudinal Creep

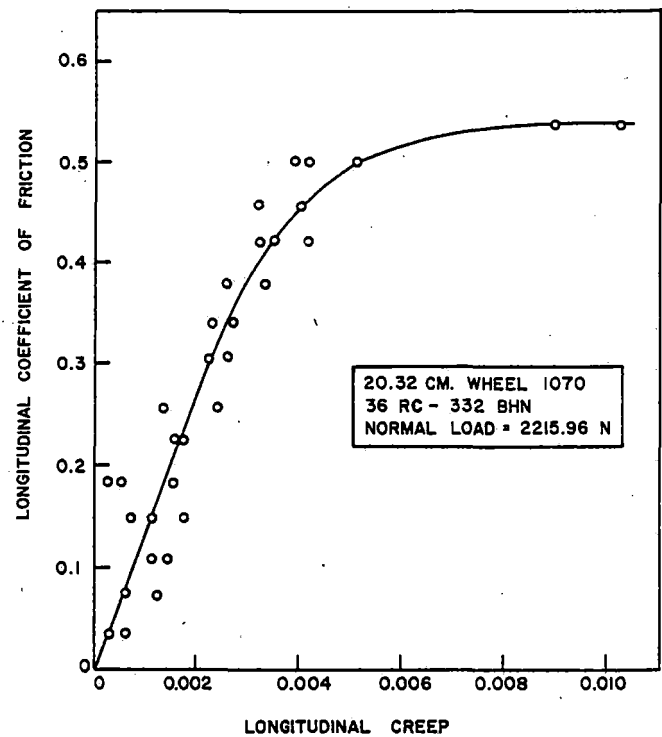


Fig. 4 Longitudinal Coefficient of Friction versus Longitudinal Creep

the actual area of contact (rather than the theoretical), has very important implications. As the plastic deformations and the wear progress with the rolling time, the area of contact increases, Fig. 10. If we look at the dimensionless factor  $Gab\xi/\mu_c N$ , to obtain the same

values of this factor for the same values of  $\mu_c N$  and for increasing values of the product  $a b$  (proportional to the contact area), requires a reduction of the value of the creep  $\xi$ . In other words, the product of the creep and the area of contact must be a constant. This law has

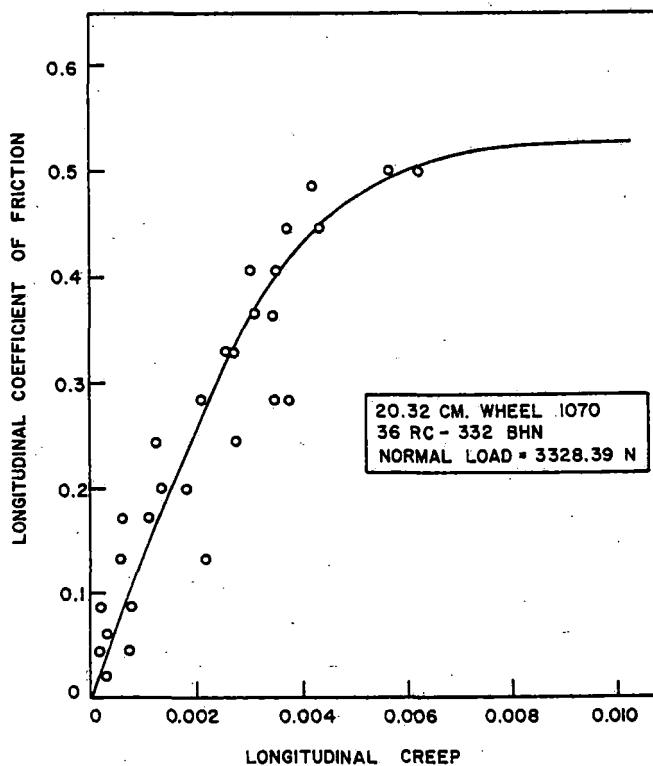


Fig. 5 Longitudinal Coefficient of Friction versus Longitudinal Creep

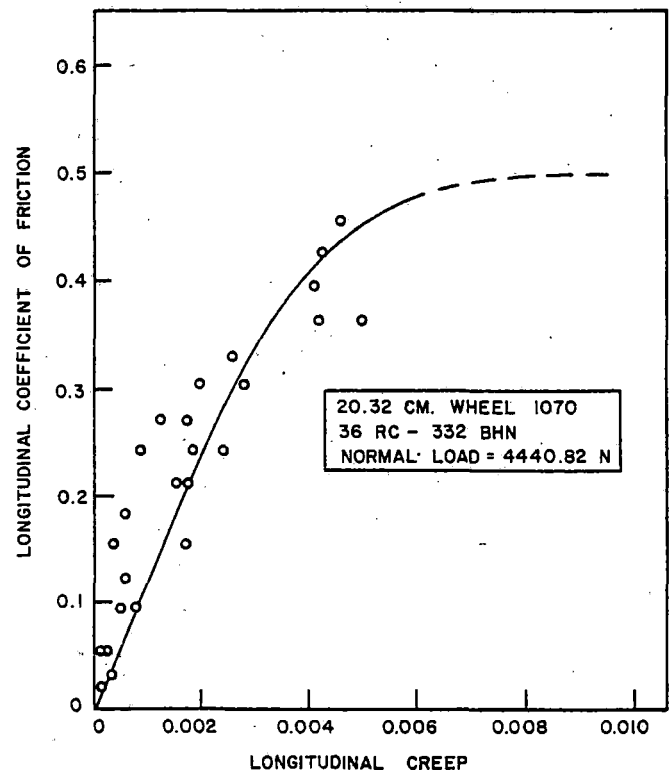


Fig. 6 Longitudinal Coefficient of Friction versus Longitudinal Creep

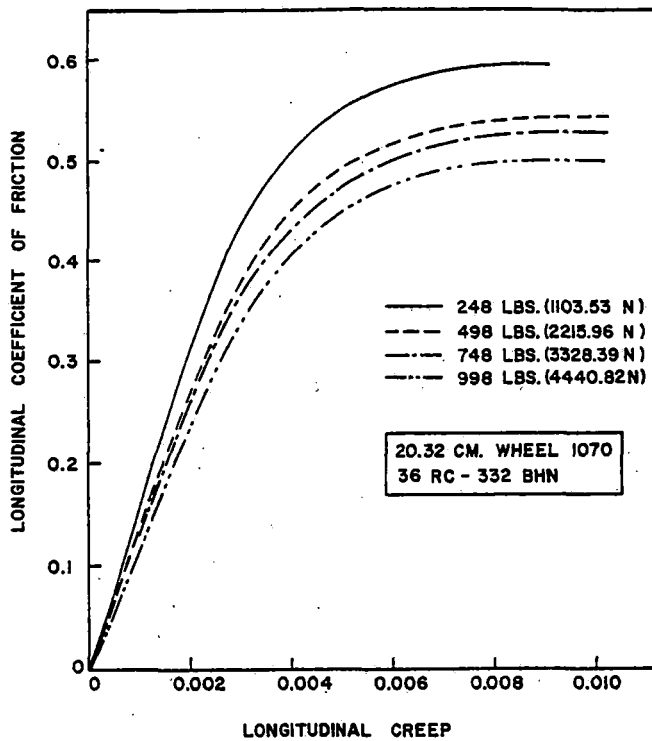


Fig. 7 Longitudinal Coefficient of Friction versus Longitudinal Creep

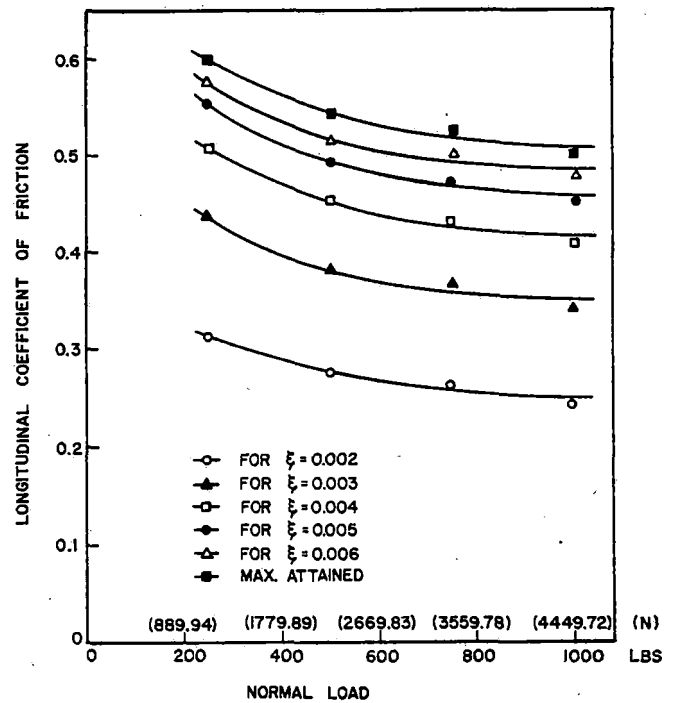


Fig. 8 Longitudinal Coefficient of Friction versus Normal Load

been checked in a series of tests reported in [17] and seems to be of general validity for dry contact for smooth as well as moderately rough contacting surfaces, as found in laboratory wheel-rail simulation.

### Conclusions and Discussion

Tests to obtain the coefficient of friction versus creep for different normal loads in dry contact were conducted. These tests were short

duration tests and the magnitude of the wear of the interacting surfaces was kept to a level preserving the elliptical contact with a preestablished ratio of the major to the minor axis. All these tests show a large dispersion of the friction creep data. However, average values follow clearly discernible trends. All these data can be reduced to one single dimensionless curve that also fits the values computed by Kalker. The observed behavior of the contacting surfaces has important implications. Master curves for the coefficient of friction

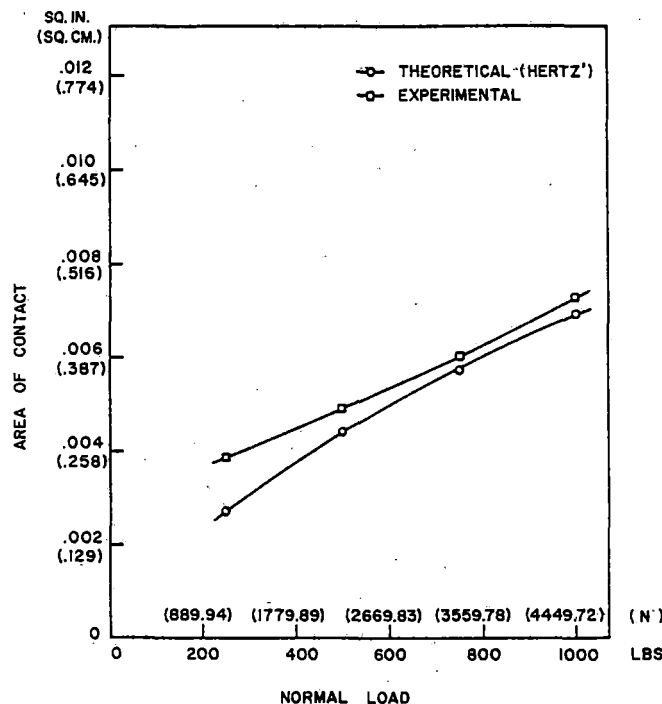


Fig. 9 Area of Contact versus Normal Load for Smooth New Surface

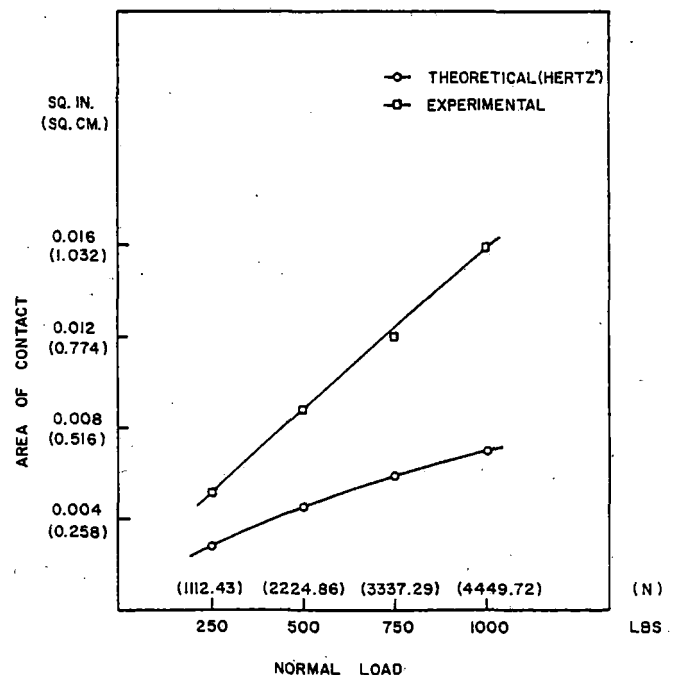


Fig. 10 Area of Contact versus Normal Load

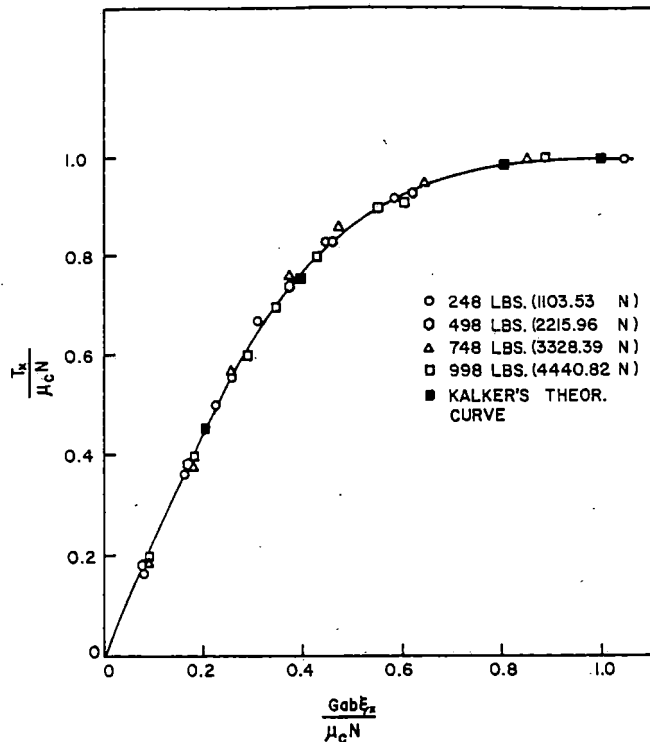


Fig. 11 Nondimensional Creep Curve

versus creep can be obtained from experiments such as those reported in this paper. This master curve can be utilized in practical applications if the area of contact can be computed or measured and the maximum coefficient of friction is known. This coefficient can be measured and is a function of the normal load. Fig. 8 shows that the longitudinal coefficient of friction is a function of the normal load for constant creep and all the coefficients of friction versus normal load show the same trend. This trend is predicted by the theoretical analysis of Vermeulen and Johnson [18] and Kalker [13]. Another important conclusion that also has considerable practical importance is the law of constancy of the product of creep times the contact area. It also can be shown [17] that this law is implied in the Carter [19] and Poritsky [20] elastic analysis of rolling with friction. However this law seems also valid beyond the limitations of the elastic analysis since our observations have been made under conditions that include plastic deformations, wear and rough surfaces.

Care was taken to conduct all the tests with the same standard procedures. The reliability and repeatability of these tests depends on several factors. If we look to the dimensionless curve we see that a very important quantity is  $\mu_c$ . The values of  $\mu_c$  are determined by the mechanical properties of the materials of the wheels utilized in the tests, and of the possible contaminants that appear in the interface. Contaminants were minimized by keeping the surface thoroughly clean. However there is an important uncontrolled contaminant (Ferric Oxide) that cannot be easily controlled unless the test rig is operated under humidity-controlled conditions. The reported tests were carried out during the winter months under mostly dry atmosphere conditions. The wear of the wheels was also periodically observed through the acrylic replicas and tape impressions of the contact areas. The total validity and consistency of the obtained results can be best judged through the fact that the averages of the measured values can be reduced to a unique dimensionless expression.

### Acknowledgments

This research work was sponsored by the U. S. Department of Transportation, the General Motors Electro-Motive Division, the Association of American Railroads and the Illinois Institute of Technology under Contract No. DOT-OS-40103. Their support of this study is thankfully acknowledged.

We are very thankful to the Engineering staff of the Electro-Motive Division of General Motors and especially to Messrs. Henry Marta, Ken Mels, Lauren Johnson, and Gordon Itami for providing technical assistance toward this study. Sincere thanks are extended to Mr. R. Gandhi for providing enormous assistance during experimentation. Our gratitude is due to Mr. Gene Ginani and Jerry Busiel for their technical assistance.

### References

- 1 Cabbie, G. M., Jr., "Understanding Wheel-Rail Adhesion," ASME Paper No. 60-RR-3, 1960.
- 2 Verbeek, H., "Present Knowledge of Adhesion and Its Utilization," *Rail International*, June, 1973.
- 3 Law, E. H., and Cooperrider, N. K., "A Survey of Rail Vehicle Dynamics Research," ASME (Special Issue on Ground Transportation), June, 1974.
- 4 Collings, A. H., and Pritchard, C., "Recent Research in Adhesion," *Railway Engineering Journal*, Sept., 1972.
- 5 Marta, H. A., and Mels, K. D., "Wheel-Rail Adhesion," ASME JOURNAL OF ENGINEERING FOR INDUSTRY, Aug., 1969.
- 6 Marta, H. A., and Mels, K. D., Itami, G. A., "Friction Creep Phenomenon of Adhesion Between Steel Wheels and Rails," 1971 ASME/IEEE Spring Conference.
- 7 Meier, D. R., "Is Rail Adhesion a Limitation on the Grow of Internally Powered Locomotives," ASME Paper No. 62-WA294.
- 8 Kalker, J. J., "Aspects of Contact Mechanics," *Proceedings of IUTAM Symposium on "Contact Between the Deformable Bodies"*, Sept. 1975.
- 9 Johnson, K. L., "Non-Hertzian Contact of Elastic Spheres," *Proceedings of the IUTAM Symposium on Contact Between Deformable Bodies*, Delft Holland, 1975.
- 10 Bremond, B. H., "Resolution du Probleme de Contact Elastique plan avec Frottement a partir de donnees Experimentales," Doctoral Thesis of the University Claude Bernard Lyon, France, 1976.
- 11 Ollerton, E., "Stress in the Contact Zone," paper 10, *Proceedures of the Institution of Mechanical Engineers*, Vol. 178, Part 3E, 1963-1964.
- 12 Johnson, K. G., "A Review of the Theory of Rolling Contact Stresses," *Wear*, 9, 1966.
- 13 Kalker, T. J., "On the Rolling of Two Elastic Bodies in the Presence of Dry Contact," Doctoral Thesis Delft Technological University, 1967.
- 14 Paul, B., "A Review of Rail-Wheel Contact Stress Problems," MEAM Report 75-1, U. S. Department of Transportation Contract DOT-OS-40093, University of Pennsylvania, 1975.
- 15 Itami, G. A., "The Study of Friction-Creep Phenomenon of Adhesion Between Steel Wheels and Rails," Thesis, General Motors Institute, 1968.
- 16 Karamchandani, K. C., Kumar, S., Sciammarella, C. A., Seth, B., Nailescu, L., Kalpakjian, S., "Friction-Creep and Wear Studies for Steel Wheel and Rail," U. S. Department of Transportation Contract DOT-OS-40103, Report No. IIT, Trans. 75-1.
- 17 Sciammarella, C. A., Kumar, S., Press, M., Seth, D. B., "Generalized Relations for Creep-Adhesion Function in Dry Contact," to be presented at the 6th International Wheel Set Congress, Colorado Springs, October, 1978.
- 18 Vermeulen, P. J., and Johnson, K. L., "Contact of Non-Spherical Elastic Bodies Transmitting Tangential Forces," *ASME Journal of Applied Mechanics*, 1964, pp. 338-340.
- 19 Carter, F. W., "On the Action of a Locomotive Driving Wheel," *Proc. Royal Soc. A*, Vol. 112, pp. 151-157, 1926.
- 20 Poritsky, H., "Stresses and Deflections of Cylindrical Bodies in Contact with Application to Contact Gears and Locomotive Wheels," *ASME Journal of Applied Mechanics*, 72, 1930, pp. 191-201.

## APPENDIX A

Longitudinal creep may be defined as the longitudinal slip velocity divided by the actual rolling velocity.

$$\text{Longitudinal creep} = \frac{\text{longitudinal slip velocity}}{\text{actual rolling velocity}}$$

or

$$\xi_x = \frac{R_B N_B - R_S N_S}{R_B N_B}$$

where  $\xi_x$  = longitudinal creep

$N_B$  = speed of the big wheel

$N_S$  = speed of the small wheel

$R_S$  = radius of the small wheel

$R_B$  = radius of the big wheel

$$\xi_x = 1 - \frac{R_S N_S}{R_B N_B}$$

Now let  $\frac{R_S}{R_B} = \nu$

$$\xi_x = 1 - \nu \frac{N_S}{N_B}$$

$$d\xi_x = -d\nu \frac{N_S}{N_B} + \nu \frac{N_S}{N_B^2} dN_B - \frac{\nu}{N_B} dN_S$$

Since,  $\nu = \frac{R_S}{R_B}$

$$\text{and } d\nu = -\frac{R_S}{R_B^2} dR_B + \frac{dR_S}{R_B}$$

It is desired to find the uncertainty in the creep measurement when uncertainty in radius is 0.00254 mm and frequency is 1/144 = 0.009.

For the testing purpose the rig is operated at  $N_S = 518$  and  $N_B = 116$

$$\nu = \frac{R_S}{R_B} = \frac{10.16}{45.03} = 0.2256$$

$$\begin{aligned} d\nu &= \frac{R_S}{R_B^2} dR_B + \frac{dR_S}{R_B} \\ &= -\frac{4.00}{(17.73)^2} - \frac{10.16}{(45.03)^2} \times 0.00254 + \frac{0.00254}{(45.03)} \\ &= -0.0000127 + 0.0000564 \\ &= 0.0000437 \end{aligned}$$

Substituting in equation (i)

$$\begin{aligned} d\xi_x &= -d\nu \frac{N_S}{N_B} + \nu \frac{N_S}{N_B^2} dN_B - \frac{\nu}{N_B} dN_S \\ &= -0.0000437 \times \frac{518}{116} + 0.2256 \frac{518}{(116)^2} \\ &\quad \times 0.0069 - \frac{0.2238}{116} \times 0.2 \\ &= -0.0001951 + 0.000060 - 0.0003858 \end{aligned}$$

$$= -0.000520$$

## APPENDIX B

Calculation of error due to reduction in diameters of the two wheels with wear.

The change in diameter of the small wheel when the rig was operating at 4449.72N and .3 coefficient of friction for 5 hours was observed to be 0.00152cm.

$$\nu = \frac{R_S}{R_B}$$

$$d\nu = \frac{R_S}{R_B^2} dR_B + \frac{dR_S}{R_B}$$

$$\text{Now, } R_S = \frac{20.1097}{2} = 10.0548 \text{ cm}$$

$$R_B = \frac{89.8957}{2} = 44.9478 \text{ cm}$$

$$dR_S = 0.00076 \text{ cm}$$

$$dR_B = 0.00076 \text{ cm (Assumed to be approximately same)}$$

$$\text{Hence } d\nu = \frac{10.0548}{(44.9478)^2} \times 0.0076 + \frac{0.00076}{44.9478}$$

$$\text{or } d\nu = -0.0000037 + 0.0000169$$

$$d\nu = 0.0000132$$

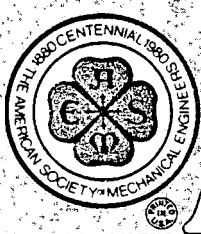
The change in longitudinal creep  $d\xi_x$  is written as

$$d\xi_x = -\frac{N_S}{N_B} + \nu \frac{N_S}{N_B^2} dN_B - \frac{\nu}{N_B} dN_S$$

$$d\xi_x = -0.0000132 \times \frac{442.6}{99.2} + 0 + 0$$

$$d\xi_x = 0.0000588$$

Hence the maximum error introduced in the creep readings by not taking the change in diameter into account is 0.0000588 which is very small. The value of  $N_S$  and  $N_B$  are taken when the rig is operating at 4449.72N normal load and 0.3 coefficient of friction for 5 hours.



AN ASME PUBLICATION  
\$4.00 per copy \$2.00 for ASME Members

# ASME

THE AMERICAN SOCIETY OF MECHANICAL ENGINEERS  
345 E 47 St., New York, N.Y. 10017

The Society shall not be responsible for statements or opinions advanced in papers or in discussion at meetings of the Society or of its Divisions or Sections, or printed in its publications. Discussion is printed only if the paper is published in an ASME Journal or Proceedings. Released for general publication upon presentation. Full credit should be given to ASME, the Technical Division, and the author(s).

REFERENCE 49

T.-L. Yang

E. D. Howerter

R. L. Inman

Ensco, Inc.,  
Springfield, VA

## Inertial and Inductive Measurement Techniques for Track Geometry

*Under the Federal Railroad Administration's Automatic Track Inspection Program, there are three track geometry measuring vehicles current conducting routine track inspections. A fourth one is being constructed and is scheduled to join the inspection fleet in 1981. ENSCO developed the instrumentation and data processing systems used in these inspection vehicles and has been operating them for the FRA. This paper gives an overview of the inertial and inductive measurement techniques and the associated data processing algorithms used in these track geometry measuring vehicles. A brief history is also provided on the evolutionary development of each of the measurement techniques.*

### INTRODUCTION

The Federal Railroad Administration (FRA) of the Department of Transportation (DOT) has sponsored the development of automated track geometry measuring cars since 1966 for supporting track inspection and rail research activities. Several generations of measurement instrumentation and data processing capabilities have evolved in the development process. Currently under the Automated Track Inspection Program (ATIP), the FRA Office of Safety operates three track geometry survey vehicles; these are T-2 (with T-4 as its support vehicle), T-3 (with T-1 as its support vehicle) and T-6 (operated without a support vehicle). These survey vehicles are operated routinely on a prescheduled basis to cover approximately 70,000 miles of track annually. Electronic sensing devices and data processing equipment installed in these vehicles measure track geometry at speeds up to 120 miles per hour, record the data on magnetic tape, display the measurements on oscillographs and produce an exception report in accordance with the Federal Track Safety Standards.

A fourth track geometry survey vehicle, T-10 (see Figure 1), has just been completed and is scheduled to join the FRA ATIP fleet in 1981. T-10 is based on a self-propelled coach, the Budd SPV2000, and incorporates the latest generation of inertial and inductive measurement techniques as well as the associated real-time digital processing algorithms.

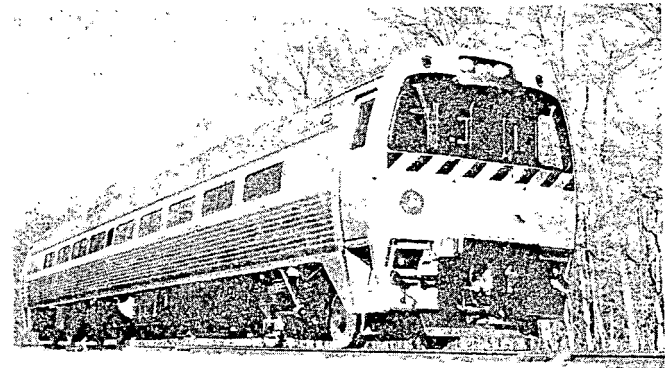


Figure 1. Track Survey Vehicle T-10.

ENSCO supported the FRA in the development and the operation of the current ATIP track inspection fleet and is also responsible for the design and the fabrication of the latest instrumentation used in T-10. This paper presents a brief description of the inertial and inductive measuring concepts and data processing techniques employed in the FRA track survey vehicles.

### BACKGROUND

Initial layout and construction of railroad tracks rely on conventional survey techniques to establish earth-based references. Subsequent surveys of track geometry are generally for the purposes of identifying critical geometrical defects that are safety hazards, providing data to calculate and prescribe the proper repair, evaluating the service performance of the track and planning long-range maintenance activities. The instrumentation and data processing equipment used in the FRA track geometry survey vehicles are designed to acquire the data at normal track speed from a moving vehicle to meet the general purposes described above. Specifically, the identification of track geometry defects must be done in accordance with



the format and the allowable thresholds provided in the Federal Track Safety Standards.

Gage measurement is made in terms of the absolute distance between the inner faces of the two rails. No additional external reference is needed to establish the measurement. The inductive technique to measure truck-to-rail distances was chosen for several reasons. A non-contact transducer is preferred because of the high test speed involved. Among the various non-contact proximity sensing techniques, a high-frequency magnetic approach requires a relatively small transducer and is reasonably insensitive to harsh environmental conditions. The small size of the sensor allows it to be servo-controlled to maintain its distance from the rail so that the measurement is always within the linear range of the transducer, and, to focus on the FRA-specified measuring point of 5/8" below the surface of the rail.

The truck-to-rail measurements made with the inductive transducers are also used as a part of the alignment system which determines the smoothness of each rail in the lateral direction. The general interest in alignment is in its spatial frequency content which could induce vehicle lateral dynamics. Because of typical rail vehicle construction, alignment deviations from a wavelength of a few inches to several hundred feet are of interest. The significance of the long wavelength components generally begins to diminish at 150 feet for speeds up to 90 mph and at 200 feet up to 120 mph. The Federal Track Safety Standards define maximum allowable alignment irregularities in terms of deviations from uniformity measured in a 62-foot midordinate-to-chord offset (MCO). The use of a pseudo-inertial measurement reference provides both the broad range of wavelength coverage needed for track-train dynamic research and the 62' MCO (as well as MCO's of other chord lengths) required for checking compliance. An accelerometer, after appropriate processing, measures the oscillatory movements of the truck lateral to the track centerline. The processed output of the accelerometer is sometimes referred to as the pseudo-space curve for the truck path. A pseudo-space curve can be interpreted as the inertial trajectory of the truck with its long wavelength components and the d.c. component removed. The left and right side truck-to-rail distances and the servo-positions are combined with the pseudo-space curve of the truck to form the pseudo-space curve representing the alignment of each rail.

The general interest in rail surface profile is over a broad range of wavelength pertinent to vehicle dynamics, similar to the case of rail alignment. Since the running wheels in a measuring vehicle provide natural loaded contact measuring points, the vertical movements of a wheel combined with a pseudo-vertical inertial reference would meet the profile measurement requirements. Two vertically mounted accelerometers are used over the measurement axle to establish the pseudo-inertial references for the left and the right rails.

Superelevation (often referred to interchangeably as crosslevel), is measured with respect to the local horizontal plane, therefore, a local vertical reference must be established on the moving vehicle. A true inertial attitude reference, such as a stabilized platform used in spacecrafts, does not meet the requirement because the local gravitational vector is

not fixed inertially. For this reason, an inclinometer mounted on the floor of the car across the measuring axle is used as the basic transducer to sense the tilt angle of the floor relative to the gravitational vector. Complex filtering and compensations using outputs from two rate-of-turn gyros and truck-to-carbody displacement transducers are needed to eliminate errors in the measurement due to vehicle dynamics. Tilt angle of the track, which converts directly to superelevation, is then obtained by measuring the axle-to-carbody roll angle.

Vehicle speed, distance, track curvature and track location measurements are also made by the survey vehicles to provide location reference and to furnish necessary inputs to the processing algorithm. With the nominal sample rate of one foot, the magnetic Automatic Location Detector (ALD) system can provide correlation within  $\pm 6$  inches between track location and geometry data. Curvature and curvature rate data are analyzed by onboard software to detect transition points between tangents, spirals and curves so that appropriate standards can be applied.

## MEASUREMENT SYSTEM DESCRIPTION

### System Overview

The Track Geometry Measurement System (TGMS) has the capability to measure gage, curvature, crosslevel, warp, profile and alignment of the track. The conversion of the transducer signals to the measurement of the track parameters is performed primarily in the onboard computer by digital algorithms. The general approach for all of the basic parameters is to condition the raw transducer signals with an appropriate filter whose frequency response characteristics are designed to mate with the digital computations performed in the onboard computer. The conditioned transducer signals are then digitized at a constant distance interval of one foot.

Each of the conditioned transducer inputs is then examined by a specially designed digital algorithm to detect signal fault conditions. The conditioned transducer signals are stored on a digital magnetic tape which serves as a permanent record.

The digitized sensor signals are then processed through digital filters whose frequency response characteristics are matched with their analog counterparts. The hybrid filter formed by combining the effects of both the analog and the first stage of digital filtering yields sensor signals whose phase characteristics are invariant with regard to distortion normally introduced by variations in vehicle speed and direction of travel.

These processed sensor signals are then used to calculate the necessary track geometry parameters required for exception detection and display. Track geometry parameters are scaled and displayed on strip chart recorders for the track inspectors and the system operator. These track geometry measurements are distance synchronized to a common location reference even though the transducers are mounted on different locations within the vehicle. The strip charts are distance based so that one mile of data is displayed on approximately 18 inches of paper regardless of speed. Exception report is printed on a line printer in which each detected exception to the Federal Track Safety Standard is reported with respect to its location on the track. The measurement of traversed

distance is accomplished by an axle-driven tachometer (optical encoder) which also controls the computer for distance-based data acquisition. Vehicle speed is calculated from time elapsed between two consecutive distance interrupts through the use of a highly accurate, crystal controlled oscillator as a time base.

A simplified system schematic is shown in Figure 2. The dependency between measured parameters and input transducers is shown in Figure 3. It can be seen that several measurements are generally required to obtain each of the track geometry parameters and that each transducer serves as inputs to many geometry parameters.

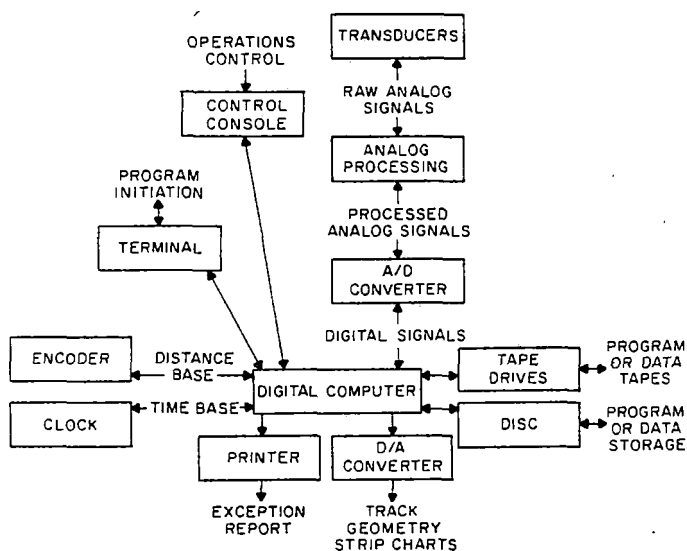


Figure 2. Track Geometry System Schematic.

#### GAGE

The earliest gage measurement system used capacitive, non-contact proximity sensors. These sensors were mounted parallel to each rail, facing the inside of the railhead in the shadow of the wheel flanges. The lateral positions of the sensors were fixed relative to the wheels so that the range of each sensor must cover 0.2" to 2.0" in order to accommodate typical lateral excursions of the wheels. These sensors were retractable vertically by a remote signal to clear switches and road crossings.

Adding the two conditioned sensor signals to the distance between them produced a measurement of track gage.

The main weaknesses of the capacitive system are that at a range of two inches, the response is quite nonlinear and that the electro-static field is subject to fringing and distortion due to grass, debris, water and snow.

A servo-magnetic gage system was developed to overcome the problems inherent in the capacitive system. This system also measured the relative position between the truck and each rail, but utilized an inductive transducer, servo-controlled to maintain a nominal distance from the rail to keep the sensor

TRACK GEOMETRY PARAMETER		ALIGNMENT	PROFILE	CROSSLEVEL	CURVATURE	GAGE	SPEED	ALIGNMENT
TRANSDUCERS	TACHOMETER	X	X	X	X	X	X	X
	TIME BASE	X	X	X	X		X	
	GAGE LEFT	X				X		
	GAGE RIGHT	X				X		
	LATERAL CAR-TO-TRUCK DISPLACEMENT LEAD TRUCK				X			
	LATERAL CAR-TO-TRUCK DISPLACEMENT TRAIL TRUCK FRONT		X		X			
	LATERAL CAR-TO-TRUCK DISPLACEMENT TRAIL TRUCK BACK		X		X			
	CARBODY YAW RATE	X	X	X	X			
	CARBODY ROLL RATE	X	X	X				
	CARBODY INCLINOMETER	X	X	X				
	VERTICAL AXLE-TO-CAR DISPLACEMENT LEFT	X	X	X				
	VERTICAL AXLE-TO-CAR DISPLACEMENT RIGHT	X	X	X				
	PROFILE ACCELEROMETER LEFT		X					
	PROFILE ACCELEROMETER RIGHT		X					
	ALIGNOMETER ACCELEROMETER	X						

Figure 3. Track Geometry Parameter Transducer Dependency.

well within its linear range. The magnetic sensing technique is relatively immune to all but the most severe weather conditions. The sensor is retractable vertically, and is also equipped with a relatively inexpensive breakaway support to protect the measurement coil. Most recent sensor arm design employs a spring-loaded resilient arm holder which allows sensor to deflect and return when hit by a track obstruction.

Figure 4 shows the basic measurement concept and Figure 5 is the beam used to house the gage transducers. An error signal from each magnetic sensor is fed into a servo-control loop to maintain a nominal distance of approximately 1/2 inch from the gage side of the railhead. The relative position of each sensor is measured by a linear displacement transducer, summed with the error signal, conditioned and digitized by an onboard data collection system.

The digitized sensor inputs are then examined by a specially designed digital algorithm to detect out-of-range and lack-of-activity fault conditions. After being stored in cyclic arrays to synchronize the measurements of track gage with the remaining track geometry parameters, the input voltages are summed and added to an offset number to yield the final measurement of track gage. The resultant measurement of

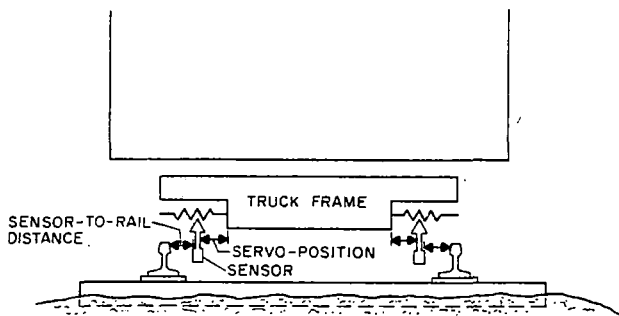


Figure 4. Gage System Sensor Configuration.

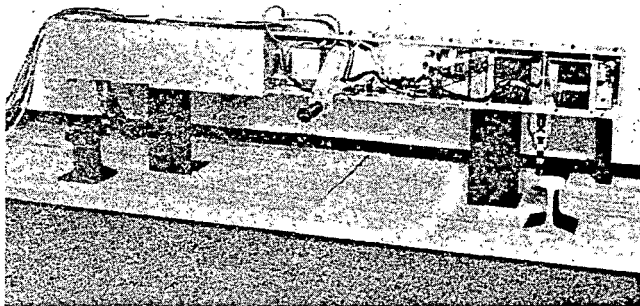


Figure 5. Instrumentation Crossbeam.

track gage is then used for exception detection. Finally, the measurement of track gage is scaled for output display.

#### CURVATURE

The curvature system utilizes five transducers which consist of a yaw-rate gyro mounted in the carbody, two displacement transducers measuring the relative lateral distance between the leading truck and the carbody, a displacement transducer measuring the relative lateral distance between the trailing truck and the carbody, and an optical encoder. Figure 6 shows the gyro and inclinometer package used in T-10.

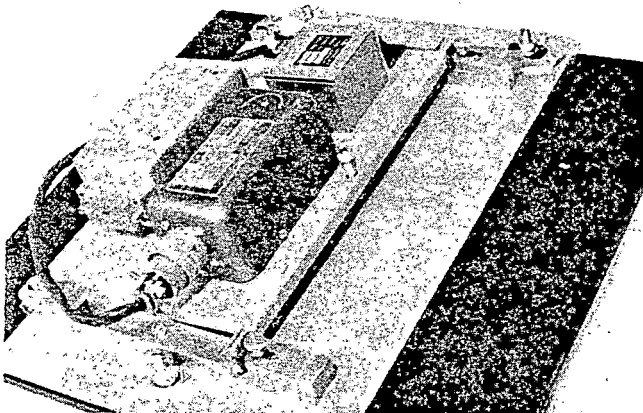


Figure 6. Gyro and Inclinometer Package for T-10.

The yaw-rate gyro is used to supply a voltage proportional to the yaw rate of the carbody. This voltage is conditioned by an analog low-pass filter  $B(s)$  with a gain and zero offset. The magnitude response of this analog filter is shown in Figure 7 for  $v = 9$  mph and 80 mph. It is significant to note that the fixed time frequency corner implies a variable spatial frequency corner which is dependent on the speed of the vehicle. The filtered signal is digitized at a sample interval of one foot. A debias command can be enabled by the operator when the vehicle is stationary, this effectively eliminates any residual bias in the output of the yaw rate gyro.

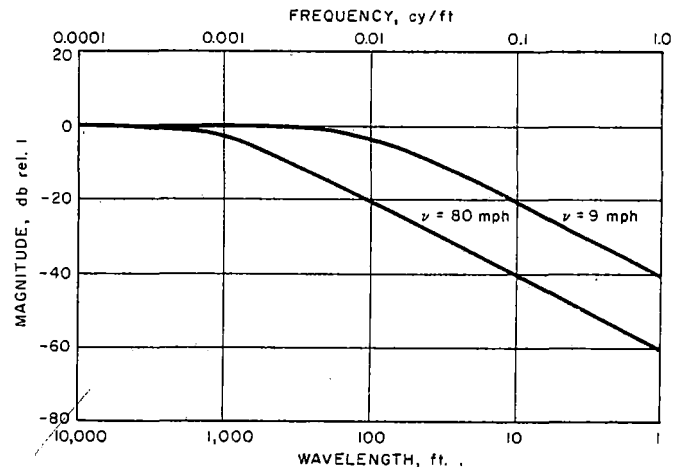


Figure 7. Magnitude Response of First Order Analog Filter,  $B(s)$ .

The debiased signal is then processed by a digital filter. This bandpass filter has variable spatial frequency characteristics, as shown in Figure 8, similar to those of the first order analog filter,  $B(s)$ . The magnitude response characteristics of the first order hybrid filter formed by the analog filter,  $B(s)$ , and the digital filter,  $C(z)$ , is shown in Figure 9. The first order hybrid filter has a spatial frequency characteristic which is independent of the vehicle speed and direction. An extremely close approximation is used in the actual implementation of  $C(z)$  to facilitate efficient numerical calculations in the computer.

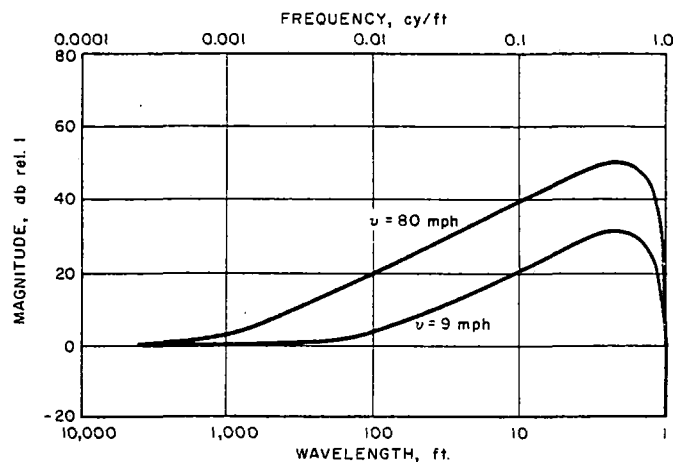


Figure 8. Magnitude Response of First Order Digital Filter,  $C(z)$ .

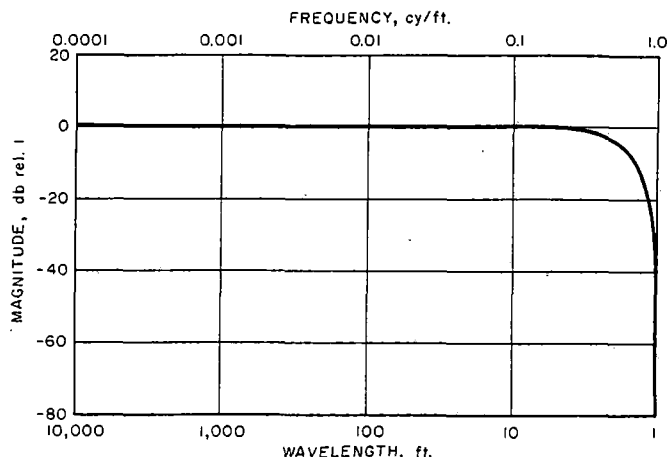


Figure 9. Magnitude Response of First Order Hybrid Filter.

The yaw-rate gyro output, after the hybrid filter, represents the temporal rate-of-change of vehicle heading  $d\phi/dt$  with a high-frequency cutoff which is constant in spatial frequency. In order to convert this measurement to track curvature, we note that:

$$\frac{\Delta\phi_c}{\Delta x} = \frac{\frac{\Delta\phi}{\Delta t}}{\frac{\Delta x}{\Delta t}}$$

where  $\frac{\Delta\phi_c}{\Delta x}$  = the change in the heading of the carbody over the distance interval,  $\Delta x$ ,

$\frac{\Delta\phi}{\Delta t}$  = the change in the heading of the carbody over the time interval,  $\Delta t = T_z$

and  $\frac{\Delta x}{\Delta t}$  = the average speed of the vehicle over the distance interval,  $\Delta t$

This implies that  $C(z)$  must be divided by velocity, or equivalently, multiplied by the time interval  $T_z$ , to obtain the change in the heading of the carbody over the unit sample distance interval. Since the carbody yaw rate as seen by the gyro contains oscillatory yaw motions of the carbody relative to the truck which are not directly representative of track geometry, corrections must be introduced.

Three displacement transducers are used to supply voltages proportional to the lateral translation of the trucks relative to the carbody. These voltages are conditioned by an amplifier and are digitized in conjunction with the other transducers each foot of vehicle travel. The signals from the two displacement transducers located on leading truck,

are combined to yield the front carbody-to-truck lateral translation. The third displacement transducer located on the trailing truck, yields the trailing carbody-to-truck lateral translation.

The two measurements of lateral translations of the trucks relative to the carbody provide the measurement of the oscillatory motions of the carbody and are subtracted from the measured yaw rate per unit distance.

This corrected yaw rate  $\Delta\phi_c/\Delta x$  is then low-pass filtered to yield a measure of track curvature.

The rate of change of track curvature is also calculated by a digital filter. Track curvature and rate of change of track curvature are used in a curve analysis algorithm to detect curve transitions and type, i.e., tangent, spiral and curve, for use in determining which thresholds to apply to the track parameters in exception reporting.

#### CROSSLEVEL

The Compensated Accelerometer System (CAS) for measuring crosslevel was developed in the 1974 - 75 period. In the CAS, an accelerometer used as an inclinometer, paired with a roll rate gyroscope, became the primary roll angle measurement. Compensations for yaw rate and lateral accelerations were included. The original CAS and a subsequent improvement employed a complex multiple-pole analog computer to perform the processing. The complex processing scheme has now been implemented in T-10 with digital algorithms which eliminates most of the remaining errors inherent in analog computers. The T-10 crosslevel system utilizes four transducers in addition to the debiased yaw rate gyro signal and time-between-samples (TBS) datum used in the track curvature algorithm. These additional transducers consist of a carbody mounted inclinometer, a roll rate gyro, and two displacement transducers. The transducer mounting configuration for the crosslevel system is shown schematically in Figure 10. The carbody mounted inclinometer (see Figure 6) is used to calculate the low frequency components of the carbody roll angle with respect to gravity. Compensation factors are included to counteract the accelerations sensed by the inclinometer due to: centrifugal acceleration of the vehicle, motion of the inclinometer about the yaw center of the vehicle, roll accelerations of the carbody about the track and about its own roll center, and lateral translations of the vehicle. The carbody mounted roll rate gyro is used to calculate the high frequency components of the carbody roll angle with respect to gravity. The two displacement transducers are used to measure the relative roll angle between the carbody and measuring axle.

The voltage produced by the inclinometer is conditioned by an analog low-pass filter with a gain and zero offset. The magnitude response of this analog filter has a fixed time frequency corner and therefore a variable spatial frequency corner which is dependent on the speed of the vehicle. After being processed by this analog filter the signal is digitized at a sample interval of one foot.

For the purpose of profile and alignment calculations, the digitized signal is processed by a digital filter which mates with the analog filter given above to form the second order hybrid processing filter.

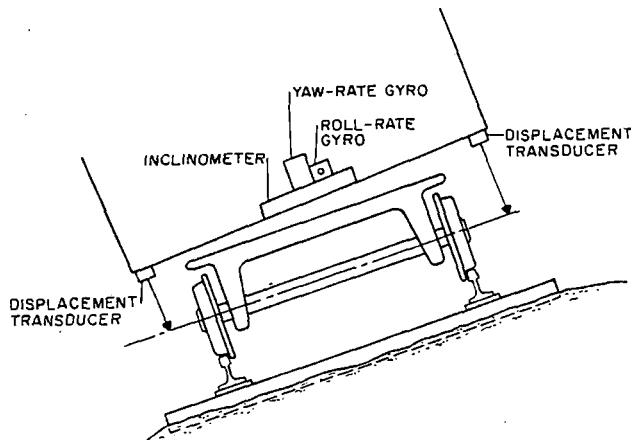


Figure 10. Crosslevel System Sensor Configuration.

The magnitude response characteristics of the second order hybrid filter has spatial frequency characteristics which are independent of vehicle speed and direction.

The digital portion of the second order hybrid filter is rescaled to yield a short mid-chord offset (MCO) of the acceleration signal. This signal is used later in profile and alignment calculations to compensate for errors introduced by carbody roll motions.

For the purpose of obtaining the low-frequency roll angle of the carbody, the digitized inclinometer signal is processed by a first order low-pass filter. This low-pass filter is designed to match the effects of the first order filter applied to the roll rate gyro signal which provides the high-frequency portion of the roll angle.

Two types of errors are contained in the inclinometer signal due to yaw motions of the car, these are the centrifugal acceleration and the acceleration sensed by the inclinometer due to movement about the yaw center of the vehicle. Correction terms are obtained using the yaw rate gyro input. The correction terms are combined and processed by a second order low-pass filter. This low-pass filter is designed to match the effects of the second order filter applied to the inclinometer signal.

These filtered correction terms are applied to the filtered inclinometer signal which is then low-pass filtered to remove the remaining error introduced by the pure lateral translation of the carbody.

The composite filter has a constant time corner approximately two octaves below the lateral rigid carbody natural frequency (typically around 1.25 Hz).

To obtain the high frequency components of the carbody roll angle the roll rate gyro signal is processed by filter whose frequency response is complementary to that applied to the inclinometer signal.

The filter data from the inclinometer and roll-rate-gyro are then combined to yield the carbody roll angle,  $\theta_c$ , over the pass band of interest. The two displacement transducers are then used to calculate

the roll angle between the carbody and the track,  $\theta_{ct}$ . The track roll angle  $\theta_t = \theta_c + \theta_{ct}$ , is then scaled to a reference baselength to yield track crosslevel.

## PROFILE

The first inertial profilometer used on the FRA inspection cars was based on a sensor developed by the Electromotive Division of General Motors. The sensor consists of a classic spring-mass system mounted on the truck with acceleration and displacement measurements of the mass. The original sensor was rather bulky and weighed approximately 90 pounds. Subsequent improvements resulted in an order of magnitude reduction in weight and a significant size reduction. The latest profilometer system, used in T-10 eliminated the truck-mounted spring-mass sensor altogether; an inertial reference is established in the carbody instead.

The T-10 profile system utilizes two inertial transducers in addition to the transducers used in the crosslevel and curvature systems. These transducers consist of two vertically oriented carbody mounted accelerometers located over the two carbody-to-axle displacement transducers. The profile system transducer arrangement is shown schematically in Figure 11. The profile transducer assembly used in T-10 is shown in Figure 12.

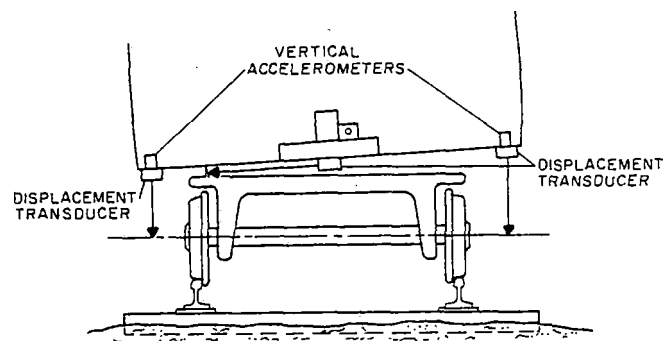


Figure 11. Profile System Sensor Configuration.

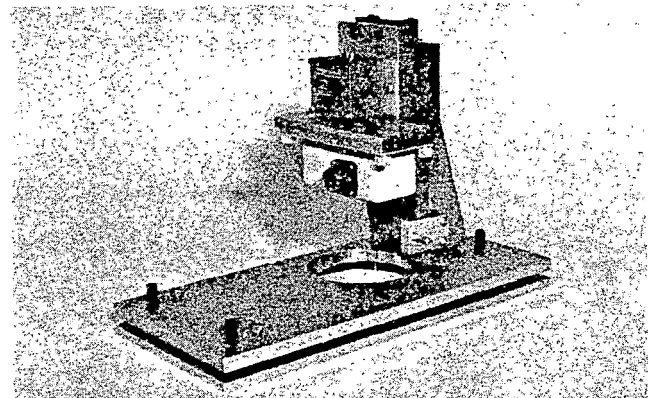


Figure 12. Profile Transducer Assembly.

The carbody mounted accelerometers are used to provide an inertial reference and the displacement transducers are used to yield a measurement from the inertial reference to the rail to obtain the measurements of individual rail profile. The voltages produced by the accelerometers are conditioned by an analog low-pass filter with a gain and zero offset. The frequency response of this analog filter is the same as  $F(s)$  discussed in Section 3.4.

Following the digitization of the conditioned accelerometer signals they are processed by a digital filter whose frequency response is the same as  $G(z)$  discussed in Section 3.4. These operations produce a basic datum whose spatial frequency characteristics are nearly independent of vehicle speed and direction. Recall that the acceleration signal becomes a short mid-chord offset (MCO) representative of the input parameter after it has been processed by the filter characterized by  $G(z)$ . These basic data are then compensated for the relative roll angle between the carbody and the track to reference the measurement of profile perpendicular to the plane formed by the tops of the railheads. The basic datum from the accelerometers is also adjusted with a gravity and centrifugal acceleration correction. These basic data are then combined with the corresponding short MCO's of the inertial references from the carbody to the track calculated from the displacement transducers. The calculations discussed above are completed for both sides of the vehicle and then a compensation is performed to correct for the fact that the transducers are not mounted directly over the rail.

The next step in the processing is to convert the short MCO's to a MCO with a longer baselength or to a pseudo-space curve. This is accomplished by processing the short MCO data through a digital filter with the appropriate frequency response.

Since the processed signals still contain undesirable long wavelength information, a composite filter is then formed to perform the conversion and long-wavelength removal simultaneously. If we separate the total effect of the composite filter into a conversion operation and a high pass operation, then, the high-pass portion of the operation can be characterized by the frequency response shown in Figure 13.

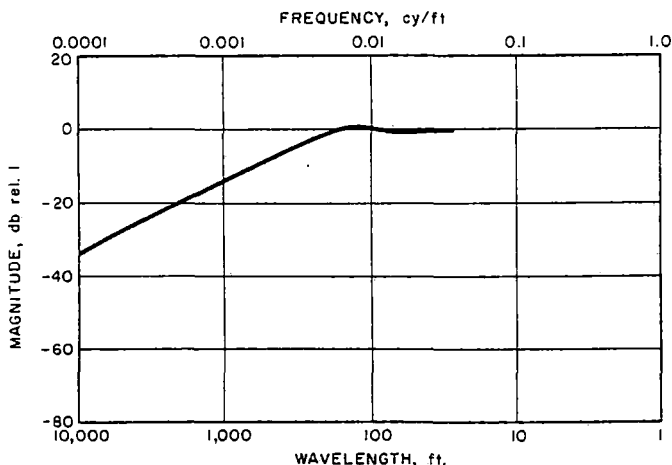


Figure 13. Magnitude Response of the High-Pass Portion of the Profile Digital Filter.

The composite digital filter used in T-10 is one which performs the high pass filtering and conversion from the short MCO to a 62' MCO. The profile output of the analog and digital filters represent deviations from average profile measured in the form of a 62' MCO. Different digital filters can be used to obtain MCO's of other chord lengths or a pseudo-space curve, in which case, the response shown in Figure 13 becomes the true response of the measured profile.

#### ALIGNMENT

The first successful inertial alignment system was installed in T-6 which utilized a foam-isolation technique for mounting accelerometers. The T-10 alignment system design is identical in concept to the T-6 system.

The T-10 alignment system basically consists of an accelerometer mounted on the instrumented beam assembly to provide an inertial reference and the gage sensors to yield measurements from the inertial reference to the individual rails. The alignment system configuration is shown schematically in Figure 14. The track roll angle calculated from the crosslevel system is used to compensate for the variations of the alignment accelerometer orientation with respect to gravity and for the accelerations induced due to the fact that the alignment accelerometer is not in the plane of measurement.

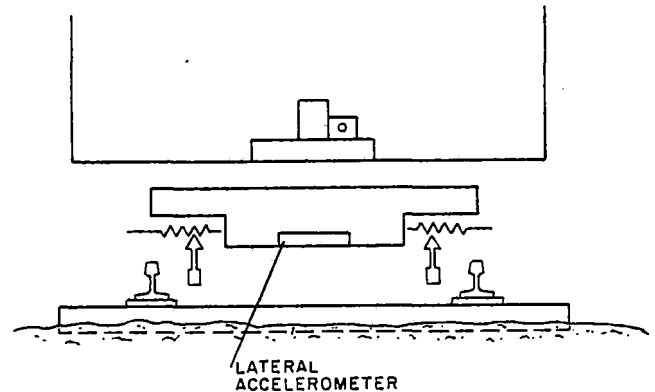


Figure 14. Alignment System Sensor Configuration.

The voltage produced by the accelerometer is conditioned by an analog low-pass filter with a gain and zero offset. Following the digitization of the conditioned accelerometer signals it is debiased by a digital filter.

Following the digitization and debiasing of the conditioned accelerometer signal it is processed by a digital filter. These operations produce a basic datum whose spatial frequency characteristics are nearly independent of vehicle speed and direction. The form of this basic datum is a short mid-chord offset (MCO) representative of the input parameter. This basic datum is then adjusted to compensate for the fact that the inclinometer is sensitive to lateral accelerations induced by gravity component due to roll angle and by roll acceleration because the accelerometer is not mounted in the plane connecting the individual railheads. The signals from the gage sensors

are then used to calculate a short MCO of the distance between the inertial reference and the gage side of the railhead. The short MCO calculated from the individual gage sensors are combined with the inertial reference provided by the corrected alignment accelerometer to yield a short MCO of the alignment of each rail.

The next step in the processing is to convert the short MCO of the individual rail alignments to a MCO with a longer baselength or a pseudo-space curve. Long wavelength information is removed by filtering the short-to-long MCO conversion. The response of the high-pass portion of the digital filter is same to the one used in profile processing shown previously in Figure 13.

#### ADVANTAGES AND DISADVANTAGES OF THE SYSTEM

The use of pseudo-inertial references for profile, alignment and crosslevel measurement provides the uniform accuracy needed for the full range of spatial frequencies pertinent to vehicle dynamics. Mid-chord offset measurements of any chord length, including the 62-foot chord, can be obtained easily from the inertial-based measurements.

The use of hybrid analog/digital processing schemes allows the reproduction of accurate track geometry measurements independent of vehicle speed or direction of travel. The use of digital data processing techniques also allows the synchronization of all measured parameters to a common track location reference even though the transducers are mounted at different locations of the vehicle and various distance delays are introduced by processing algorithms.

The non-contact magnetic sensing technique permits the measurement of gage and alignment from the 5/8" point below the rail head. This system is not affected except for the very extreme weather conditions.

The use of load carrying wheels for rail surface measurements (profile and crosslevel) and non-contact transducers near a wheel-rail contact point for line measurements (alignment and gage) makes it possible to measure track geometry under the load of the measuring vehicle and at the highest speed permitted by the track.

The major disadvantage of an inertial-based system is the inability to measure at low speeds. The profile and alignment systems will have degraded measurement accuracies below 15 mph, the measurement accuracies are not to be relied upon below 5 mph. The curvature measurement is accurate down to approximately 2 mph; gage and crosslevel measurements are the only two that remain accurate to 0 mph.

## REFERENCE 51

### CLASSIFYING TRACK BY POWER SPECTRAL DENSITY

John C. Corbin

and

William M. Kaufman

ENSCO, Inc.

Springfield, Virginia

### ABSTRACT

Historically, the Power Spectral Density (PSD) has been used as a diagnostic tool and as a classifier in many disciplines. This paper illustrates how this valuable tool can be applied to railway track geometry data to assist in the understanding and management of the permanent way.

The PSD can be used to diagnose random and periodic behavior in the track surface (profile). Three parameters are developed that are capable of describing this behavior. Furthermore, the PSD can be used to classify the track. Two of these parameters have a strong impact on the deviations of a 19-m (62-ft) midchord offset. Within prescribed confidence limits, these can be tied to the Federal Railroad Administration's track safety standards. This permits the assignment of the speed class at which the track may be economically maintained without major overhauling.

### INTRODUCTION

Many engineering disciplines benefited from the use of the Power Spectral Density (PSD) as a diagnostic tool and as a classifier. In the former capacity, it can be used with vibration and acoustic data to detect the imminent failure of bearings, gear trains, and other mechanical parts [1]. In the realm of classification, it can be used with a variety of time and space series data to recognize spoken words, to read and recognize optical patterns, and to identify the operational modes of equipments [2].

### Background

The nucleus of the PSD evaluation is the Discrete Fourier Transform (DFT). It prescribes the complex operations required to convert a series of time or distance sampled data into a sampled frequency spectrum. Individual operations in the DFT are both numerous and difficult. Therefore, routine evaluations of PSD's require a digital processing capability. For this reason, extensive applications of the PSD did not develop until the late 1950's.



Almost immediately, the PSD was applied to the study of vehicle guideway roughness. The first investigation using DFT methods was performed by Houbolt and his associates on airport runways [3,4]. A consistent pattern was observed to characterize these early PSD's. Later investigations would reveal that this pattern applies to guideways and surfaces generally [5].

Shortly thereafter, PSD's were used to study the irregularities of railway track. The earliest investigations were performed by Gilchrist of British Rail [6] in support of Wickens' vehicle dynamic research [7]. Unfortunately, automated digital data collection systems for track geometry measurement did not exist at that time. Manual survey methods were used which limited measurements to track segments of relatively short duration and which resulted in the investigation of only four different types of track.

Recent years have witnessed the advent of fully instrumented track geometry test cars such as those operated by the Federal Railroad Administration (FRA) [8]. These cars contain digital data collection equipment and magnetic tape storage capability which make possible the collection, storage, and cataloging of data from a variety of track types.

#### Precautions

The use and interpretation of PSD data deserve some comment. Some points that are quite important are:

- The PSD suppresses phase information. Therefore, it never can be useful for pinpointing specific track defects of an event nature. Nor is it alone a reliable indicator of when a track is in need of repairs [9].
- When the input process is random, the PSD is an estimator of the process statistics. The PSD itself is a distributed random variable, even when the input is stationary. The standard error of a single PSD ordinate can be of the order of the ordinate itself [10].
- To reduce the variance of the PSD estimators, the averaging of several such PSD's from consecutive track geometry records is done [11]. This requires that the track statistics be stationary over all intervals so averaged.
- To further reduce the variance of the PSD estimators, several adjacent frequency bands are averaged together [11]. This has the effect of reducing the frequency resolution. This is not a serious problem since higher resolution produces a jagged spectrum whose salient features are obscured [10].
- Proper handling of the data requires that long-term biases and trends in the data be removed. A number of signal-processing techniques are available to do this [5,12]. Failure to remove these biases and trends can result in spectral noise components that mask the track geometry variations.

#### THE PSD AS A TRACK DIAGNOSTIC

There are three basic processes associated with the irregularity of a homogeneous segment of railway track [13]. These are:

- A periodic deterministic process
- A stationary random process
- A modulated periodic deterministic process

The first and third of these derive from the periodic nature of the rail which is made up of 11.9-m (39-ft) segments.

Each of the above processes contributes in a unique way to the vehicle dynamics and to the degradation of railway track. Therefore, the usefulness of the PSD as a diagnostic tool is greatly enhanced by its ability to separate and quantify the three processes. To do this, it is first necessary to understand how the individual processes contribute to the PSD, and how they combine to produce a composite PSD.

This is indeed a reasonable objective if there are common properties peculiar to all PSD's. In the course of this investigation as well as those of others, the PSD patterns from divergent types of railway track have been studied. These have included smooth high-speed and rough branchline track, joint-bar connected and continuous welded rail (CWR), new construction, well maintained older construction, and poorly maintained older construction. Despite this wide range of conditions, a consistent pattern emerges in PSD's of track geometry.

#### Basic Processes

##### Periodic Deterministic

The first of the processes was identified as a periodic deterministic one. The principal source of this irregularity in railway track is the segmented nature of rail. In profile, the distortion that has been historically associated with the periodic process is known as a rectified sine wave (RSW) [14], whose shape is shown in Figure 1. The amplitude is defined as  $B$ , and values as large as 7.6 cm (3 in.) have been reported. Evidence of this shape is found even on CWR.

The deterministic process shows up in the PSD as a series of very narrow lines. For a true periodic deterministic process, these lines are arbitrarily narrow and infinitely high, but they contain an area that is proportional to their line strength (or power). In practice, the PSD has limited frequency resolution. This results in a broadening of the spectral lines and a reduction in the amplitudes. This happens in such a way that the area enveloped by the line is a constant.

The phenomenon of line broadening is illustrated by the three drawings of Figure 2. Figure 2(a) shows the line spectrum associated with an ideal periodic deterministic process. The frequency resolution of the PSD is shown in Figure 2(b). This resolution interacts with the line spectrum to yield the resultant in Figure

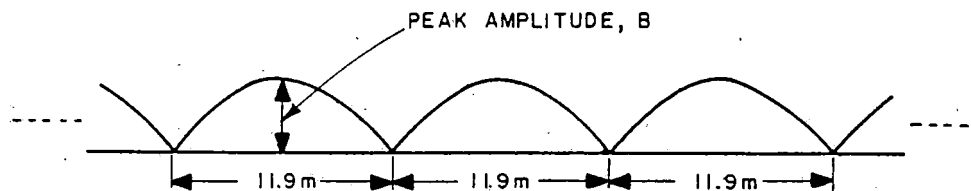
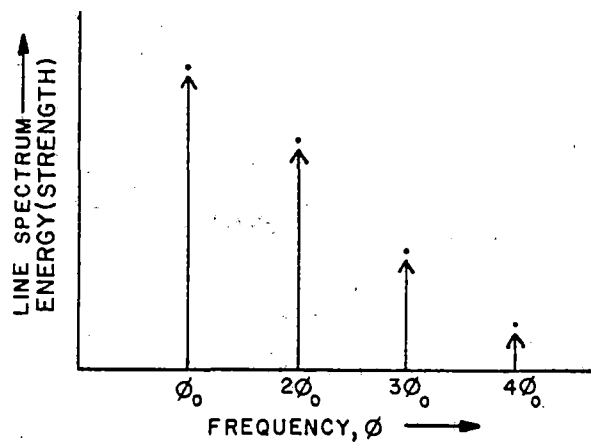
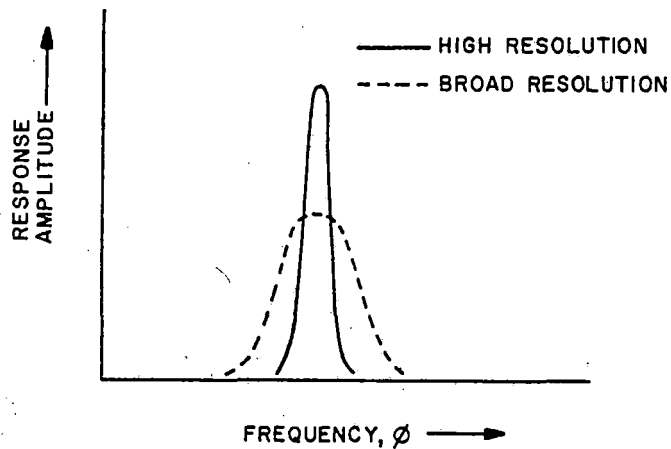


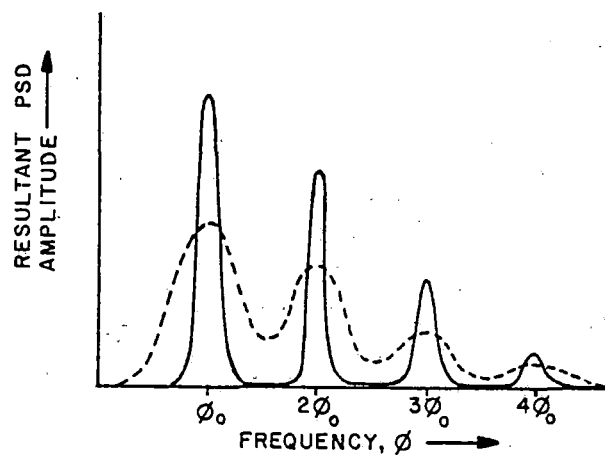
Fig. 1. Salient features of rectified sine wave periodic deterministic process



(a) Line energy process associated with harmonic process



(b) Broadening effect due to data truncation and processing



(c) Resultant PSD of harmonic process after broadening--note loss of distinct lines with excessive broadening

Fig. 2. Periodic deterministic process of line energy spectrum and sequence showing effects of limited resolution on this spectrum

2(c). Note that a broad resolution results in considerable smearing and overlapping of the spectral lines. This is illustrated by the dotted curves in both Figures 2(b) and 2(c).

The RSW is a harmonic process (that is, the line elements occur at frequencies,  $\phi_0$ ,  $2\phi_0$ ,  $3\phi_0$ , etc.).  $\phi_0$  is the fundamental frequency in cycles/meter. It defines the basic repetition rate of the periodic geometry. The amplitude of each component is given as follows:

$$B_n \equiv \text{strength of the component at frequency } n\phi_0$$

$$B_n = \frac{2B}{(4n^2 - 1)\pi} ; n = 1, 2, 3... \quad (1)$$

The PSD processes such discrete frequency components in a mean square sense. In other words, the area under the spread-out spectral line is the mean square level of the equivalent sinusoid. Thus the spectral strength  $Q_n$  is given by

$$Q_n = \frac{1}{2} B_n^2 = 2 \left[ \frac{B}{(4n^2 - 1)\pi} \right]^2 \quad (2)$$

Values for the first two components are

$$Q_1 = 2.25 \times 10^{-2} B^2 \text{ (11.9-m wavelength)}$$

$$Q_2 = 9.00 \times 10^{-4} B^2 \text{ (5.95-m wavelength)}$$

#### Stationary Random

Independent of the periodic processes that occur in railway track is an underlying random irregularity in the rail which derives from a variety of sources. Initially, when the track is laid, the causes of surface roughness are imperfections in the rolling process and irregularities introduced in the rail during laying. Later on, these undulations combine with vertical and lateral train dynamics and with variability in the track support medium to cause additional development in the random behavior.

The PSD associated with the random behavior of railway track can be expected to be a smooth function of frequency, devoid of any substantial peaks or dips. Such a spectrum (shown in Figure 3) is known as a continuum. Kendall and Stuart [10] point out that estimates of such a spectrum can be very jagged unless some form of smoothing or averaging is performed to reduce the variability of the spectral ordinate. An averaging process involving several miles of data accomplishes this smoothing. Several adjacent frequency lines are also combined to achieve further reduction in ordinate variance [11].

Early researchers quickly realized that the PSD for the random behavior of man-made surfaces could be represented by [4,9]:

$$S_z(\phi) = \frac{A}{\phi^2} \quad (3)$$

where:

$S_z(\phi)$  is the PSD for vertical profile having units of  $(m^2/\text{cycle}/m)$

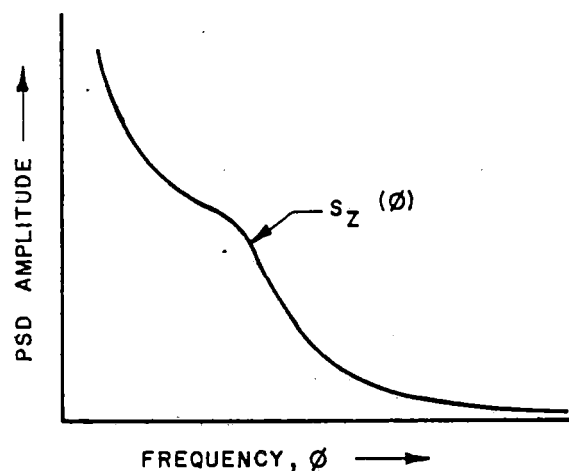


Fig. 3. PSD of random process

$\phi$  is frequency in (cycle/m)

A is a constant that describes the surface roughness  
( $\text{m}^2/\text{cycle}/\text{m}$ )

This form is found to describe the random behavior in a wide range of guideways including railway track, highways, and airport runways. It is generally valid over the wavelengths that are of dynamic importance to the respective system and speed ranges. Typical values of A for rail surface are:

- $10^{-8} \text{ m}^2/\text{cycle}/\text{m}$  for very smooth surfaces
- $10^{-6} \text{ m}^2/\text{cycle}/\text{m}$  for very rough surfaces

In dealing with railway PSD's, we have found that the above form is quite satisfactory for wavelengths longer than 6 m. Somewhere in this range, there is a transition to a faster rate of roll-off for shorter wavelengths. If  $\phi_c$  is designated as the transition frequency, then the PSD format that best represents random railway track behavior in both profile and alignment is given by

$$S_z(\phi) = \begin{cases} \frac{A}{\phi^2} & , 0 < \phi \leq \phi_c \\ \frac{A\phi_c^2}{\phi^4} & , \phi_c \leq \phi < \infty \end{cases} \quad (4)$$

The physical explanation of this change in behavior is as follows. For low frequencies, track wandering is limited by survey accuracy. This accuracy decreases with increasing wavelength, which accounts for the  $A/\phi^2$  relationship.  $\phi_c$ , the stiffness of the rail, limits the amount of irregularity in line and surface for these shorter wavelengths. The rail is free to do a limited random walk. It is restricted by the long wavelength adherence to the survey baseline and by the short wavelength memory of direction.

For very long wavelengths (100 m or more), the design characteristics of the track become important. Since these are either compatible with or unimportant to vehicle dynamics and ride comfort

requirements, it is not necessary to consider them in a statistical sense. For convenience, and without prejudice to the model, the  $A/\phi^2$  behavior is retained for these very low frequencies.

#### Modulated Periodic

Modulation of a periodic process results in a reshaping of the narrow spectral lines associated with the periodic deterministic process. Experience with railway track PSD's indicates that several different types of modulation signatures are possible. These are:

- Simple broadening
- Development of a single sideband
- Development of symmetrical sidebands

An example of simple broadening of the spectral line is shown in Figure 4(a). The figure depicts spreading above and beyond the degree expected from the PSD resolution previously discussed. This spreading may result from a random uncorrelated distribution of the depressions at rail joints. An example is shown in Figure 5(a). Alternatively, it can derive from the more correlated onset and cessation of the rectified sine wave pattern as shown in Figure 5(b), where the permanent way includes alternate cut and fill, bridges, or a subgrade with widely varying geology.

Unfortunately, the PSD cannot distinguish between these two extreme cases, but railway vehicles can. In the correlated example, five cycles of a large amplitude-rectified sine wave are grouped together. This is more serious than the same distribution of dips uniformly spread out over, say, 20 joints, where intervening joint deviations are much smaller. The former is capable of setting up rock and roll in a consist running at the resonant speed, which can result in wheel-lift derailment.

The other two modulation signatures prevalent in PSD's are shown in Figures 4(b) and 4(c). Both have an interesting origin. Prior to 1939, the standard rail length in the United States was 10 m (33 ft). When the rail is replaced with the current 11.9-m (39-ft) standard, the 10-m wavelength appears in the PSD's of this track. The theory is that the 10-m rail experienced the same problem of rail joint weakness and that the attendant rectified sine wave works its way into the ballast and subgrades. Hence, the term "ballast memory" was attached to this phenomenon.

To illustrate the implications of ballast memory, consider the illustrations of Figure 6. Figure 6(a) shows the fundamental component of the 10-m rectified sine wave that is left behind, even after reworking of the ballast and the subgrade. Figure 6(b) displays the rectified sine wave shape that is assumed by the new rail. The latter combines linearly or nonlinearly to produce the patterns in Figures 6(c) and 6(d).

For the linear combination, no new frequencies are produced. The spectrum will show lines corresponding to the 10-m wavelength, and to the 11.9-m wavelength and its harmonics. Based on limited experience with this type of PSD signature, the linear combination appears to result when CWR is the replacement.

The nonlinear interaction process is set up as follows. The severity of the low joints on the 11.9-m rail is greatest where the joint falls at a 10-m low spot. This is a true modulation process, where the carrier frequency is  $\phi_0$ , corresponding to the 11.9-m wavelength. The modulation frequency  $\epsilon$  corresponds to the difference between the two fundamental frequencies:

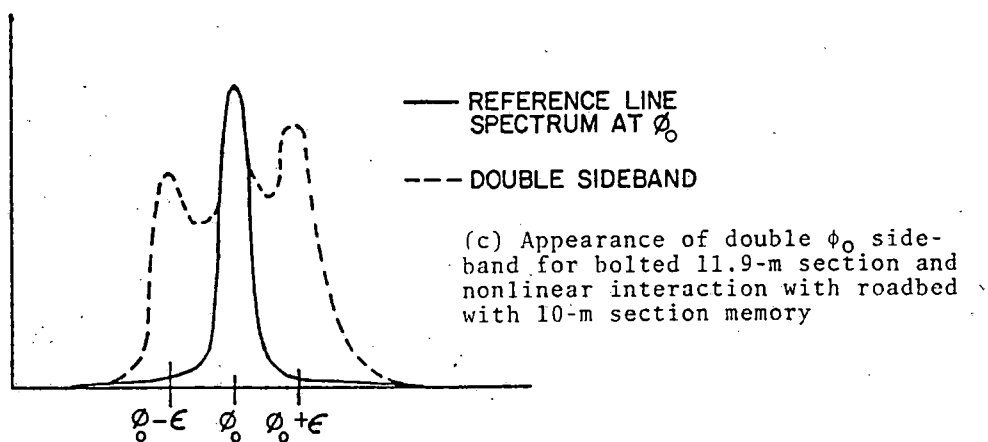
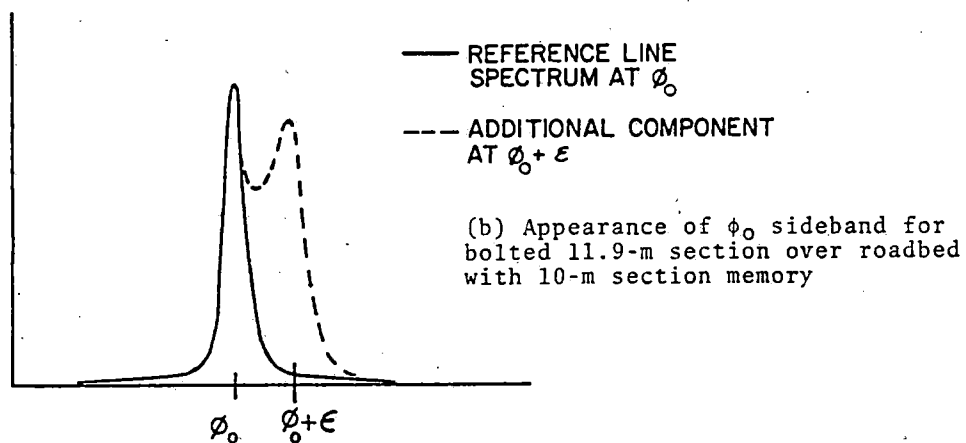
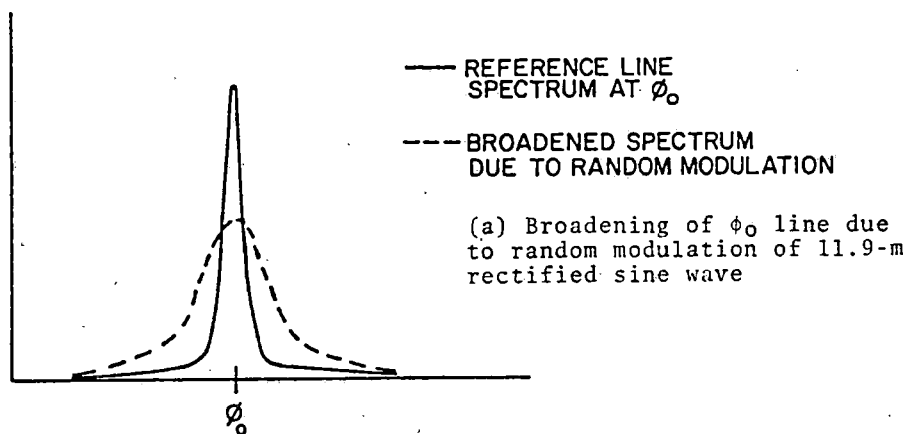


Fig. 4. Effects of modulations on periodic deterministic process

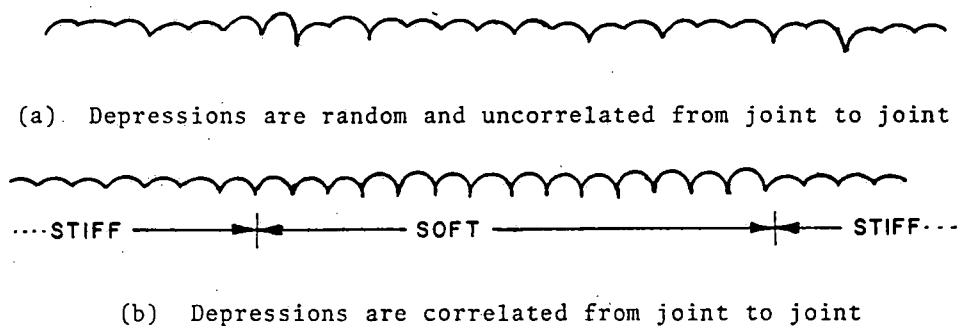


Fig. 5. Extreme examples of modulation resulting in spectral broadening

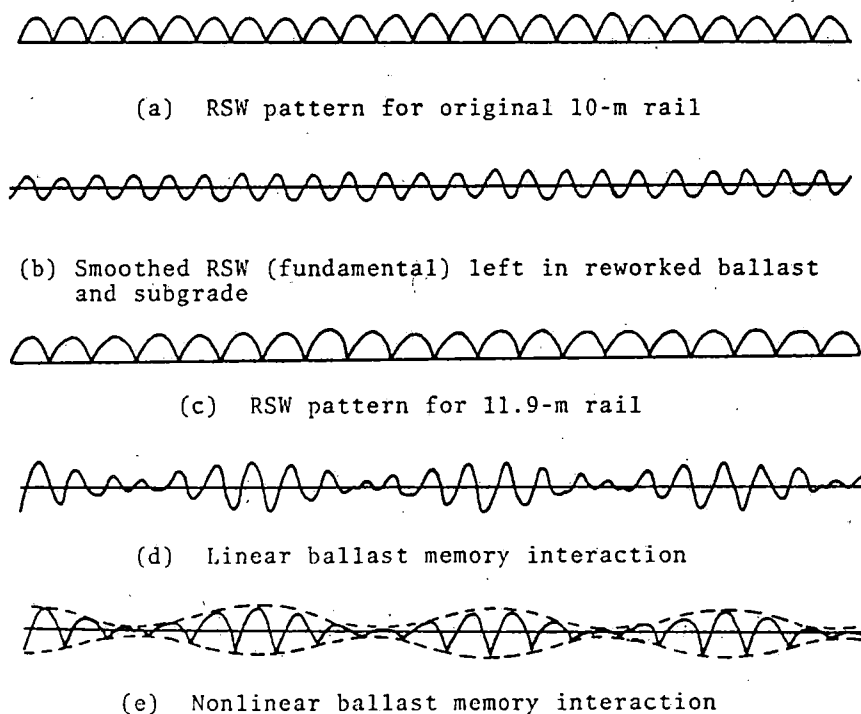


Fig. 6. Mechanisms for producing linear and nonlinear interactions



$$\epsilon = \frac{1}{10.0} - \frac{1}{11.9} = \frac{1}{65.5} \text{ (cycles/m)} \quad (5)$$

$\epsilon$  is illustrated in Figure 6(e) by the dotted line envelope. Two symmetrical sidebands are produced at frequencies  $\phi_0 + \epsilon$  and  $\phi_0 - \epsilon$ , as shown by the PSD in Figure 4(c). This modulation appears to result when joint bars in new rail have had an opportunity to loosen.

Both Figures 5 and 6 reveal that broadening due to modulation processes imply higher peak levels of quasi-periodic behavior than the simple interpretation of line energy indicates. Caution is required in evaluating these broadened PSD's. For example, Equation (2) may not be valid as the estimator of the effective value of B for a selection of track.

#### Method for Analyzing Composite PSD's

The PSD that is actually encountered does not resemble the simplified illustrations shown in Figures 3 and 4. Instead, it is a composite that includes contributions from all three basic processes. To use the PSD as a diagnostic tool, it is necessary to extract each of the basic processes from the combination.

One way of doing this analysis is to assume that all periodic processes are independent of the random process. When this assumption is involved, the PSD's of the independent processes become additive. The relationship between the periodic, the random, and the composite PSD's is illustrated by Figure 7(a).

Most PSD's generated from the data of the FRA track geometry cars are in log-log format as shown in Figure 7(b). In this representation, the logarithm of the amplitude is plotted against the logarithm of the frequency. This has the advantage that power-law relationships show up as straight-line segments. However, the separation of independent processes is more difficult.

The cases of the modulated periodic and periodic deterministic processes are obviously correlated. The procedure followed is to group them together and then treat both as being independent of the random stationary process. Then the specific nature of the modulation is extracted from composite spectra by examination of the line shape at frequency  $\phi_0$ .

#### Examples Using Real Data

Figure 8 shows six examples of PSD's generated from actual profile data. Four were chosen because they represent the full range of characteristics described previously. The fifth is included because it shows a section of very rough track constructed from 10-m rail. The sixth is illustrative of new construction. They will be used to demonstrate how the values of A, B, and  $\phi_c$  are extracted.

The first step in each case is to determine the stationary random PSD. This is done by a pair of straight-line fits to the data which are represented by a series of solid dots. During this procedure, it is necessary to avoid data in the neighborhood of known peaks at  $\phi_0$ ,  $2\phi_0$ ,  $3\phi_0$ , etc. Since  $\phi_c$  usually lies between  $\phi_0$  and  $2\phi_0$ , lower frequency data points are used to establish the best fit for a line of slope -2. This corresponds to the  $A/\phi^2$  part of the PSD. A similar procedure is used on the higher frequency part of the data using a line of slope -4. Their point of intersection defines frequency  $\phi_c$ . The value of A can be determined graphically by extending the slope -2 line and noticing its ordinate at a frequency of 1 cycle/m. Alternatively, it can be computed using Equation (3) by substituting the ordinate and the abscissa of any point lying on the slope -2 line.

By virtue of the assumed independence of the periodic and random behavior, the PSD's add linearly. This fact is used to generate the data points indicated by the symbol x. The peak shape is shown by connecting the points with a dotted line. To keep the analysis simple, only the peak at  $\phi_0$  is analyzed. Further analysis of the peak makes use of some helpful rules from electrical engineering as illustrated in Figure 9. First, the maximum ordinate of the peak is defined, and its value is  $C_1$ . The bandwidth of the peak  $\beta$  is defined at the level  $\frac{1}{2}C_1$ . Then the power in the peak is given by

$$Q_1 = \beta C_1$$

(6)

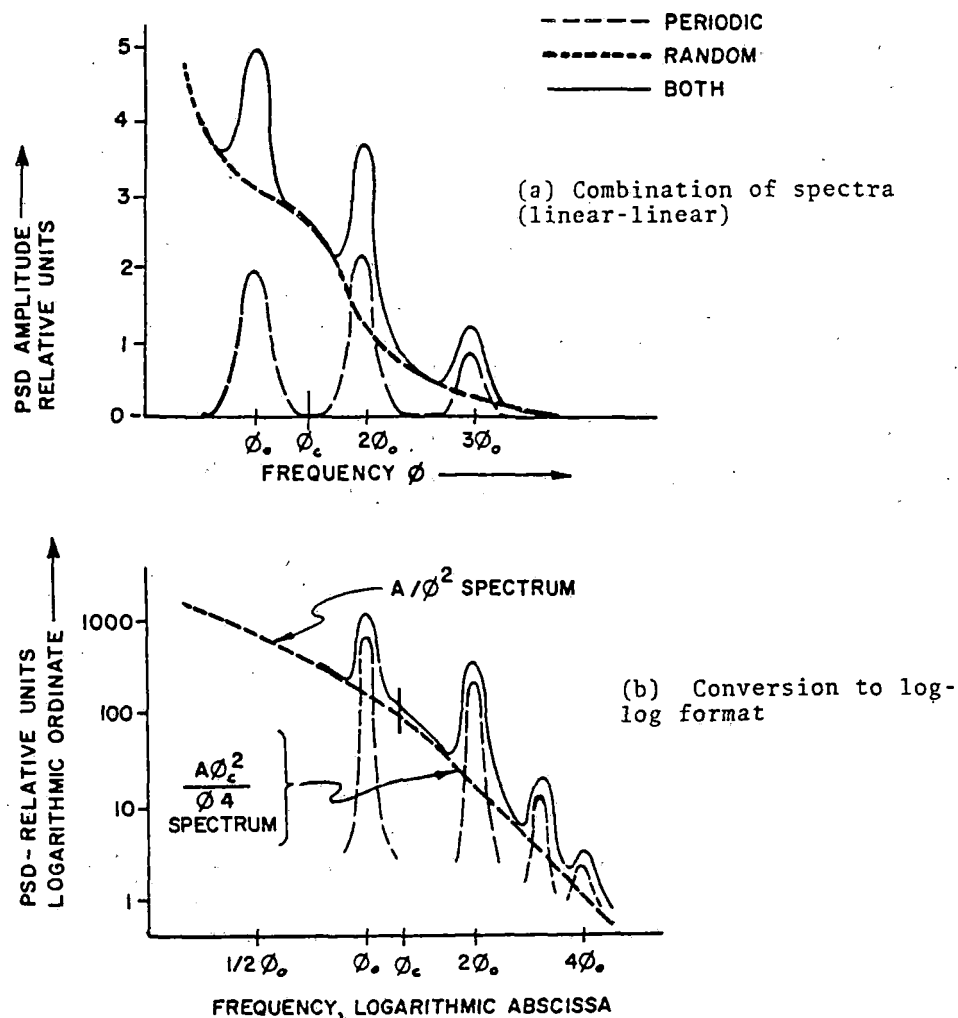
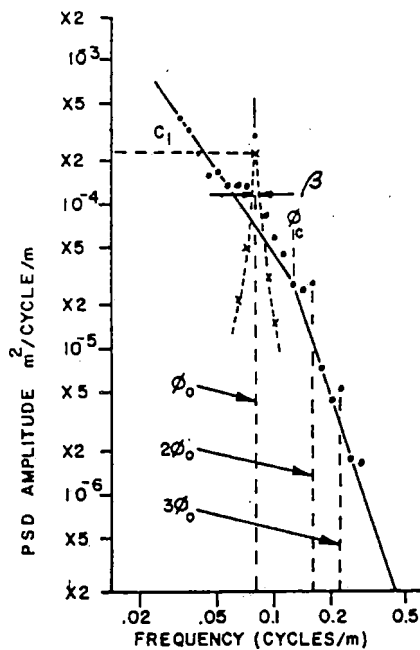
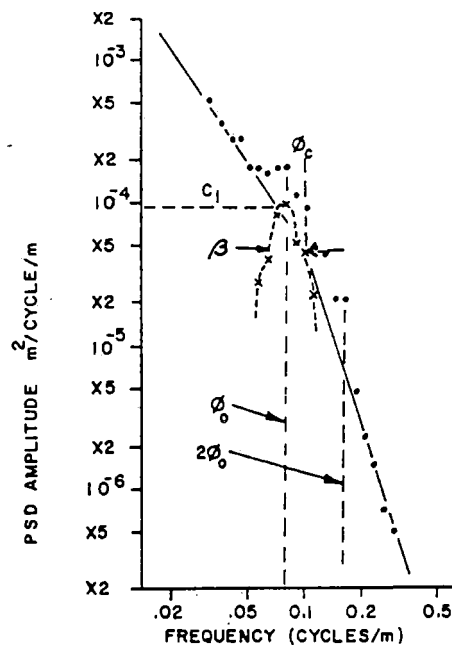


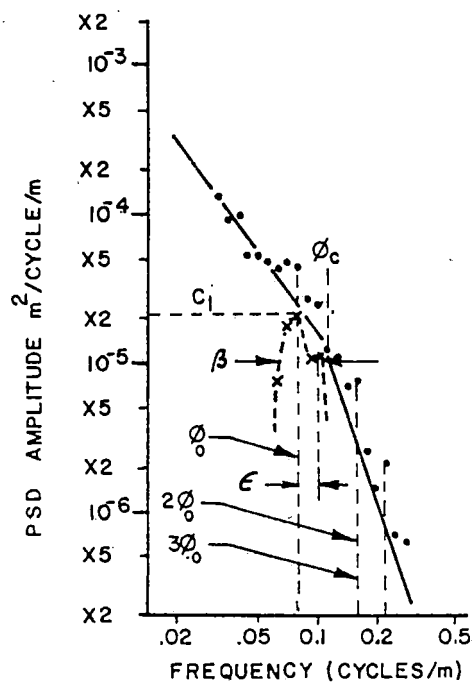
Fig. 7. Combination of periodic deterministic and random process PSD's in linear and logarithmic formats



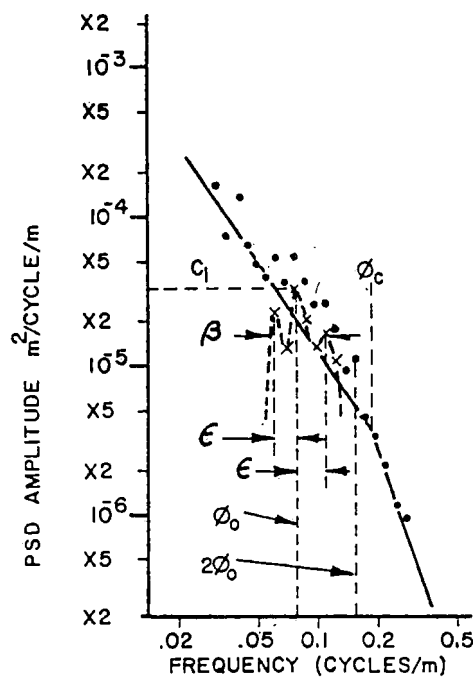
(a) Narrow-band periodic deterministic



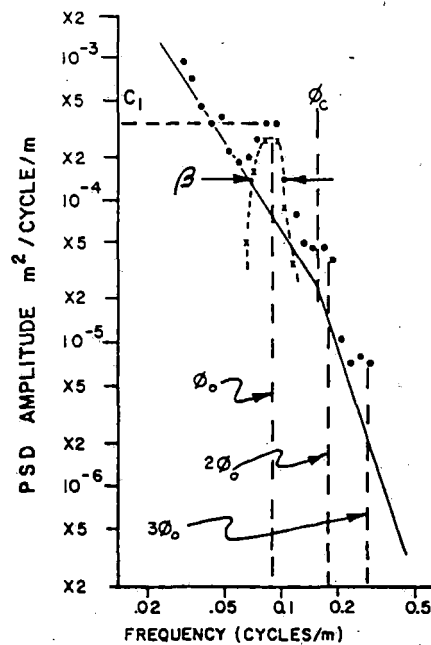
(b) Broadened narrow-band spectrum due to modulation



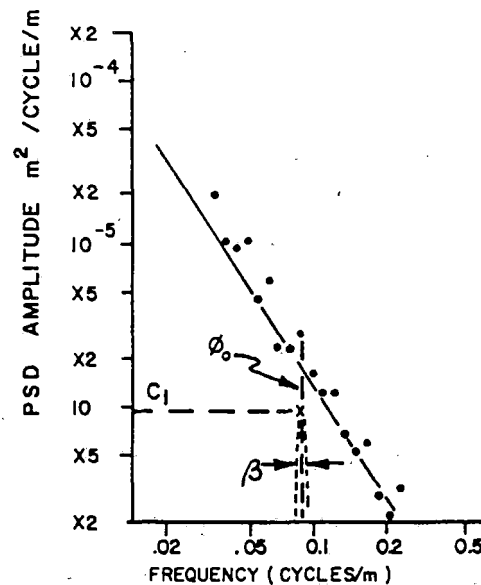
(c) Development of single sideband-linear ballast memory interaction



(d) Development of double sideband-nonlinear ballast memory interaction



(e) Rough branch line conditions for 9.1-m rail



(f) Very good surface characteristics

Fig. 8. Examples showing extraction of salient features from PSD's of single rail profile

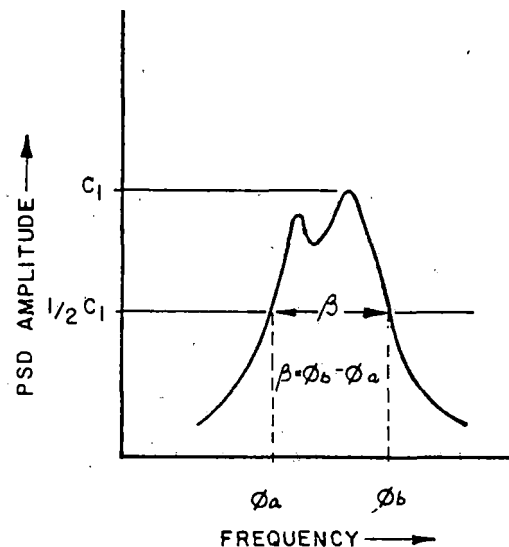


Fig. 9. Method for extracting peak features

Finally, Equation (2) is inverted to evaluate B using  $Q_1$  above. This gives

$$B = 3\pi\sqrt{\frac{1}{2}BC_1} \quad (7)$$

The scheme described above was used to extract the values of A,  $\phi_c$ , and B from a number of PSD's including those shown in Figure 8. These results are summarized in Table 1. Other salient features of these track sections, such as the value of  $\phi_0$  and appropriate comments, are also noted. Intermediate parameters  $C_1$  and  $\beta$  are also listed.

#### USING THE PSD AS A TRACK CLASSIFIER

In a previous paper [15], the use of the PSD as a classifier was examined. It combined a knowledge of vehicle speed, vehicle responses at that speed, and a ride quality specification. The result was an indication of the acceptability or nonacceptability of the track, the speed, and/or the vehicle dynamics. When one or all of these are found to be unacceptable, the result is a cost-effective decision by management to alter one of these three factors; that is:

- Fix the track
- Reduce the speed
- Modify the vehicle

This previous effort required a considerable amount of information that is not generally available to the track manager. First, the response of many vehicles operating at all speeds was needed. A PSD specification for vehicle performance was also required. The question of analysis and interpretation must be handled.

The present approach to classifying track by PSD bypasses these obstacles. It is based on the FRA track safety standards [16] which use the 19-m midchord offset (MCO) as a classifier. However, this classification scheme is a PSD technique. It does not give the number of exceptions to the FRA standards nor does it indicate their location. Rather, its utilization by the track engineer is to indicate a speed class. This might be the target level at which the railroad can economically maintain a homogeneous section of permanent way.

#### Chord Sensitivity to Surface Processes

Parameters A and B bear a direct relationship to the output of a MCO. For chords on the order of 10-m and longer, the range of maximum sensitivity falls below  $\phi_c$ . For this reason the effect of  $\phi_c$  on chord output is small and its influence can be ignored. Then, the effective PSD for the random process is given by Equation (3).

The standard deviation  $\sigma$  of a chord that is constructed on the  $A/\phi^2$  spectrum is given as [4]

$$\sigma(L) = \pi\sqrt{\frac{1}{2}AL} \quad (8)$$

where L is the chord length in meters.

TABLE 1  
SUMMARY OF RESULTS FROM GRAPHICAL ANALYSIS OF PSD'S

Zone No.	Figure No.	$A$ ( $m^2/cy/m$ )	$\phi_o$ ( $cy/m$ )	$\phi_c$ ( $cy/m$ )	$C_1$ ( $m^2/cy/m$ )	$\beta$ ( $cy/m$ )	B (mm)	Symbol Fig. 11	Comments
1	N/A	$1.7 \times 10^{-7}$	0.084	0.13	$6.6 \times 10^{-5}$	0.012	6.4	O	Examples of good high-speed main line, CWR 3 is example of ballast memory, CWR
2	8(c)	$1.7 \times 10^{-7}$	0.084	0.11	$2.0 \times 10^{-5}$	0.040	6.0	O	
3	N/A	$1.5 \times 10^{-7}$	0.084	0.11	$3.5 \times 10^{-5}$	0.025	6.6	O	
4	N/A	$2.0 \times 10^{-7}$	0.084	0.12	$9.5 \times 10^{-5}$	0.010	6.6	$\Delta$	Examples of fair high-speed main line, CWR
5	N/A	$2.0 \times 10^{-7}$	0.084	0.13	$4.5 \times 10^{-5}$	0.010	4.5	$\Delta$	
6	N/A	$1.5 \times 10^{-7}$	0.084	0.12	$2.8 \times 10^{-5}$	0.016	4.8	$\Delta$	
7	8(a)	$5.0 \times 10^{-7}$	0.084	0.13	$2.5 \times 10^{-4}$	0.010	11.0	$\square$	Examples of fair high-speed main line, joint bar connected 7 is example of very narrow peak, 11.9-m wavelength
8	N/A	$3.0 \times 10^{-7}$	0.084	0.14	$1.5 \times 10^{-4}$	0.016	11.0	$\square$	
9	N/A	$2.5 \times 10^{-7}$	0.084	0.11	$8.0 \times 10^{-5}$	0.010	6.0	$\square$	
10	8(b)	$5.0 \times 10^{-7}$	0.084	0.10	$1.0 \times 10^{-4}$	0.040	13.5	X	Example of simple broadening, joint bar connected
11	8(d)	$1.4 \times 10^{-7}$	0.084	0.18	$3.2 \times 10^{-5}$	0.060	9.5	X	Example of ballast memory, joint bar connected
12	8(e)	$8.0 \times 10^{-7}$	0.109	0.18	$2.9 \times 10^{-4}$	0.050	25.0	X	Example of very rough branch line, joint bar connected
13	8(f)	$1.2 \times 10^{-8}$	0.084	>0.25	$9.5 \times 10^{-6}$	0.010	0.8	$\emptyset$	Example of new CWR construction

The MCO of a random process is itself a distributed random variable. Hence, it is possible to establish a threshold  $\alpha\sigma$ . Depending on the specific nature of the distribution, there exists a certain confidence that the threshold will not be exceeded. For  $\alpha = 3$ , the probability that the MCO is within the  $3\sigma$  bounds is:

- 0.99 for a normally distributed random variable
- 0.8 for the worst case distribution (Tchebychev inequality).

The sensitivity of the chord to the periodic components is more complicated. To visualize why this is so, Figure 10 is provided. It illustrates the sensitivity of the peak offset of 19- and 9.5-m MCO's, given an 11.9-m RSW. In addition, the sensitivities of both chords to other RSW lengths commonly encountered in practice were also computed. The results of combinations of chord length and rail length are presented in Table 2.

These results indicate that the 9.5-m MCO has good response characteristics to the RSW of frequently encountered rail lengths. By contrast, the 19-m MCO has a highly variable response, being partially sensitive to 11.9- and 11-m RSW's and exhibiting considerable attenuation on 10- and 9.1-m RSW's.

The seriousness of this problem is difficult to assess. Most joint bar-connected rail is in a staggered configuration. Thus, a low joint in one rail is accompanied by a high spot on the other. While a series of low joints may not generate a profile exception for the 19-m MCO, it will generate crosslevel exceptions.

Current methods in laying rail are changing this picture. Panel track that is joint-bar connected and that has no stagger at all is becoming popular. In conventional track laying, stagger is avoided or reduced in order to control the rock and roll problem. In this scenario, crosslevel is not a reliable tool for detecting low joints that are missed by the 19-m MCO.

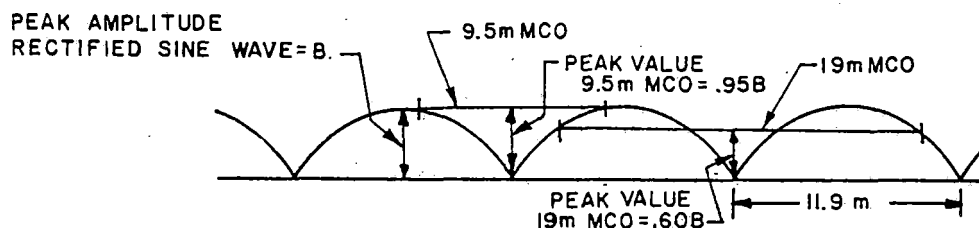


Fig. 10. Peak sensitivities of 19-m and 9.5-m MCO's to rectified sine wave

TABLE 2  
CHORD SENSITIVITY TO RECTIFIED SINE WAVE (RSW):  
CHORD LENGTH VERSUS RAIL LENGTH

MCO	11.9-m RSW	11-m RSW	10-m RSW	9.1-m RSW
9.5 m	0.95	0.98	1.00	1.00
10.4 m	0.99	1.00	1.00	0.99
19 m	0.60	0.42	0.19	0.10

Because of modulation effects, severity of low joints is a statistically distributed variable. The effective peak value of a RSW on the 19-m MCO will be given by  $\gamma B$ .  $\gamma$  is a constant that gives a certain confidence that the 19-m MCO will not exceed  $\gamma B$ . It includes the effect of chord sensitivity. In this discussion a value of  $\gamma = 2$  is chosen.

#### Classification Method

Since the two processes are independent, their variances add, and the classification scheme is given by

$$\sqrt{(\alpha \sigma L)^2 + (\gamma B)^2} \leq D_m^{(L)} \quad (9)$$

$D_m^{(L)}$  is the exception level for the chord of length  $L$  and a track of class  $m$ . Using  $L = 19$  m, and the values of  $\alpha$  and  $\gamma$  assigned above,

$$2754A + 4B^2 \leq D_m^{(19 \text{ m})} \quad (10)$$

Introducing values of  $D_m^{(19)}$  from the FRA track safety standards can be used to classify the track.

On a graph of  $A$  versus  $B$ , Equation (10) produces a family of six curves that define the boundaries for the six classes of track. These are shown in Figure 11. A straight line intersects these curves. Points falling to the left of this line have a preponderance of random behavior. Points falling to the right have a greater amount of periodic behavior.

#### RESULTS AND CONCLUSIONS

Using the graphical method of Figure 11, the track sections were classified. These results are summarized in Table 3 along with the railroad's assignment of track class. Observations and conclusions drawn from this table include:

- Where correct data is available, there is good agreement between the railroad classifications and the classifications assigned by Figure 11.
- Between the time of survey and the railroad assignment of Class 6, Zones 3 and 4 had extensive ballast, tie, and resurfacing work. Reliable estimates of previous speed limit or classification could not be found.
- Zones 7 and 8 were classified in the lower range of Class 5, while their actual classification by the railroad is Class 4. Following the philosophy developed in this paper, these sections could be upgraded to Class 5 with only minor work on ballast, ties, and surfaces.
- All points tended to cluster near the line of equal  $A$  and  $B$  behavior. Thus, degradation in the random component is accompanied by a deterioration in the periodic process.
- On the average, joint bar-connected rail sections exhibited higher  $B$  behavior than  $A$  behavior. The converse was true of CWR.



LEGEND: O, Δ, ∅ : CWR  
X, □ : BOLTED

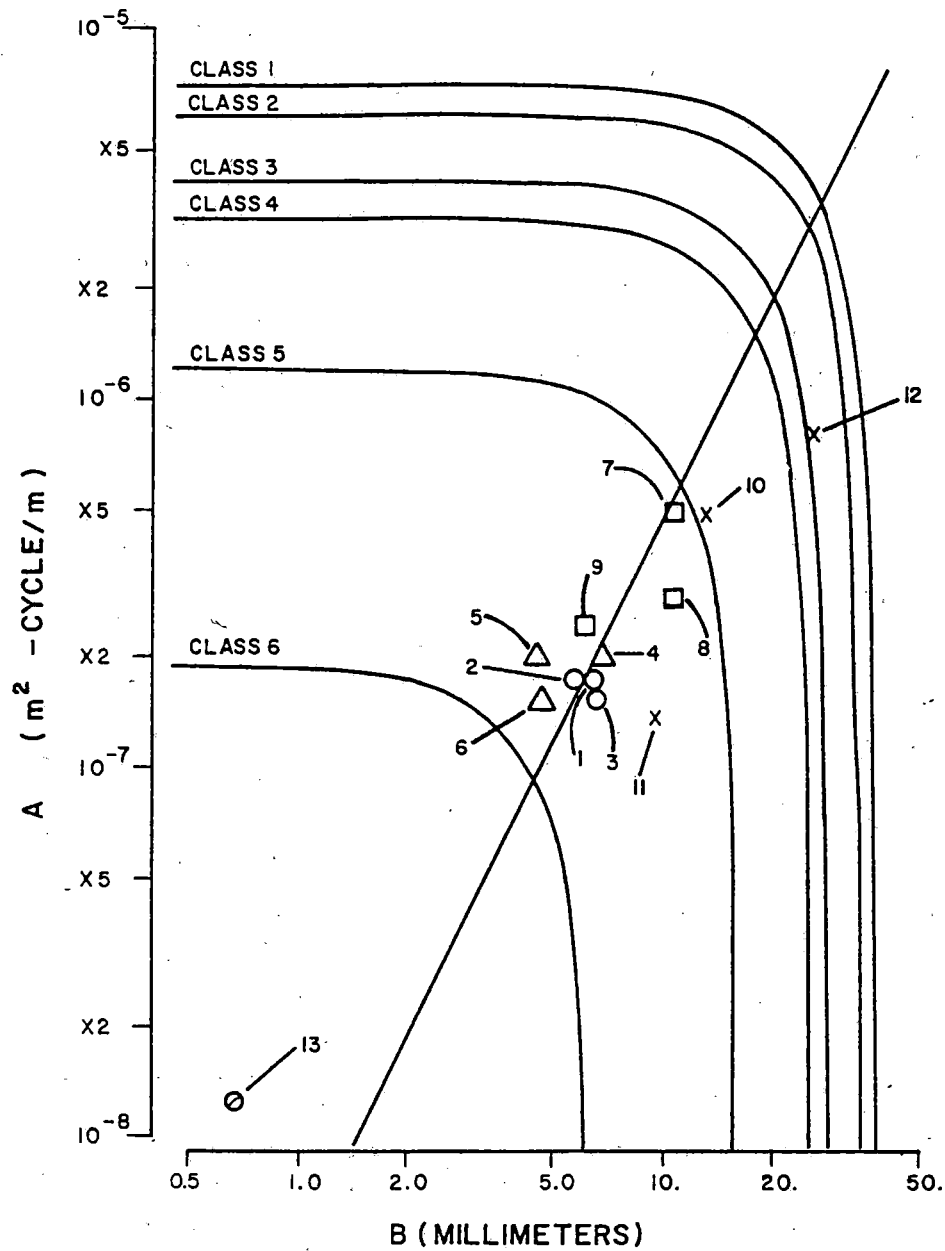


Fig. 11. Classification of track sections listed in Table 1

TABLE 3  
SUMMARY OF CLASSIFICATION SCHEME OF FIGURE 11  
VERSUS RAILROAD ASSIGNED CLASS

Zone No.	Railroad Classification	Classification by Figure 11	Comments
1	Class 5 (145 kmh)	Class 5	Railroad classification does not apply at time of survey. Earlier figures are not available.
2	Class 5 (145 kmh)	Class 5	
3	Class 6 (177 kmh)	Class 5	
4	Class 5 (145 kmh)	Class 5	Railroad classification does not apply at time of survey. Earlier figures are not available.
5	Class 6 (177 kmh)	Class 5	
6	Class 5 (145 kmh)	Class 5+	Speed limited by curves. Has been used in special tests to 200 kmh.
7	Class 4 (129 kmh)	Class 5-	
8	Class 4 (129 kmh)	Class 5-	
9	Class 5 (145 kmh)	Class 5	
10	Class 4 (129 kmh)	Class 4	
11	Class 5 (145 kmh)	Class 5	
12	Class 2 (48 kmh)	Class 2	
13	Class 4 (129 kmh)	Class 6+	

The PSD's analyzed in this paper were drawn from some of the earlier catalogs of track geometry data. While some effort was exerted to get a broad coverage of track types and classes, most of the zones studied ended up as Class 5. We are continuing an investigation of this technique using more recent track geometry data. This data, in turn, can be cross-checked against more reliable railroad estimates of track class.

#### ACKNOWLEDGMENTS

The PSD's and other corroborating information presented in this paper were processed at an earlier date under an FRA track geometry data collection program. The authors thank the FRA for the use of this data.

#### REFERENCES

- Frarey, J. L., "Development of Gear Failure Detection Methods," Technical Report, Contract No. N00014-68-C-0455, December 1970. (AD-720-735).
- Fukunaga, K., Introduction to Statistical Pattern Recognition, Academic Press, 1972.
- Walls, J. H., Houbolt, J. C., and Press, H., "Some Measurement and Power Spectra of Runway Roughness," Technical Note 3305, National Advisory Committee for Aeronautics (NACA), Langley Field, Va, November 1954.
- Houbolt, J. C., "Runway Roughness Studies in the Aeronautical Field," Proc. Am. Soc. Civil Engr., J. Air Transport Division, Vol. 87, No. AT 1, March 1961, pp. 11-31.

5. Van Deusen, B. D., "A Statistical Technique for the Dynamic Analysis of Vehicles Traversing Rough Yielding and Non-yielding Surfaces," NASA-CR-659, Contract NASW-1287, April 1967. (N67-19898)
6. Gilchrist, A. O., "A Report on Some Power-Spectral Measurements of Vertical Rail Irregularities," British Rail Research Department, Report No. DYN/8, August 1965.
7. Wickens, A. H., "General Aspects of the Lateral Dynamics of Railway Vehicles," Am. Soc. Mech Engr., Paper No. 68-WA/RR-3, Railroads Division, Winter Annual Meeting, December 1968.
8. Gerhardt, C. L. and May, J. T., "DOT Test Train Program System Instrumentation Manual," Report No. DOT-FR-72-1, January 1972.
9. Coleman, T. L. and Hall, A. W., "Implications of Recent Investigations on Runway Roughness Criteria," NATO Advisory Group for Aeronautical Research and Development, Report No. 416, Flight Mechanics Panel, Paris, January 1963.
10. Kendall, M. G. and Stuart, J., The Advanced Theory of Statistics, Vol III, Ch. 49, Spectrum Theory, Charles Griffin & Co., London, 1968.
11. Burnes, R. D., "Power Spectral Density Program Manual," Report No. DOT-FR-72-4, May 1972.
12. Bendat J. S. and Piersol, A. G., Random Data: Analysis and Measurement Procedures, J. Wiley and Sons, 1971.
13. Corbin, J. C., "Statistical Characterization of Railway Track Behavior," ASME/IEEE, Joint Railroad Conference, Pittsburgh, IEEE Paper No. C74902-3IA, April 1974.
14. Ahlbeck, P. R., Day, J. B., Prause, R. H., and Meachum, H. C., "Comparative Analysis of Freight and Passenger Rail Vehicles," Final Report, DOT-FR-20077, March 1974.
15. Yang, T-L and Corbin, J. C., "Application of Guideway Roughness Power Spectral Density as a Management Tool," Am. Soc. Mech. Engr, Second Intersociety Conference on Transportation, Denver, Paper No. 73-ICT-114, September 1973.
16. The Federal Register, Vol. 36, No. 203, October 20, 1971, pp. 20339, amended October 6, 1972.

# Performance-Based Track-Quality Measures and Their Application to Maintenance-of-Way Planning

J.C. CORBIN AND A.E. FAZIO

A methodology for obtaining quantitative measures of track quality based on rail-vehicle performance is described. Loaded-track geometry is treated as the driving impetus for vehicle dynamic response. It is interpreted in terms of system failure, which in turn is linked to basic maintenance requirements. In this treatment, the failure mode is restricted to high probability of derailment. This is felt to be an appropriate criterion since it drives the track-maintenance programs of most eastern freight railroads; however, this methodology could be used to evaluate track quality according to some other criterion, e.g., rider comfort. Given this framework, the benefits associated with various types of track maintenance can be analytically evaluated according to their respective costs. In addition, the relative contributions of various track degraders (e.g., heavy cars) can be measured and the appropriate charges made to shippers who use these vehicles.

To date, there exist no widely accepted numerical estimators of railroad track quality (1,2). This is quite surprising, since it has been believed for some time that a quantitative measure of track quality would permit railroad managements to allocate scarce maintenance-of-way resources and funds (3,4). More recently, new developments have added impetus to the effort to find measures that will be accepted by the railroad community. Mergers and acquisitions are making it difficult for management to be familiar with the condition and maintenance needs of the enlarged systems. The deregulation of the railroads makes it mandatory that realistic estimates of users' costs be developed. This is particularly true of that cost component associated with track maintenance and degradation.

Numerical estimators of track quality exist and can be classified according to the method by which they are derived (5). They include

1. Observations of track's structural parameters, such as defective ties, drainage condition, rail size, and rail condition;
2. Measurements of track deflection, such as those obtained by the Decarotor (6), which are used to make inferences regarding track strength; and
3. Measurements of loaded-track geometry as obtained by using an automated track survey vehicle (7).

Such raw data as those generated by the above methods may be quite numerous--as many as 10 000 data values per kilometer per parameter. Hence, they are often converted into more-tractable compact summaries that represent track condition over, say, a 1-km interval. Examples would be defective ties per kilometer, average track strength over a 1-km interval, or standard deviations of track gage over a 1-km interval. Expressed in this form, the summaries are called track-quality indices (TQIs).

A number of planning models have been developed and proposed for implementation by the railroads. The input consists of a specific set of TQIs, and the output is an allocation schedule for maintenance resources. Such models have been derived by using empirical formulations (8), regression analyses (9), and the calculus of variations. All the planning models assume that the TQIs are valid, that the indices are objective summaries of track condition, and that they are minimally affected by noise, statistical sampling uncertainty, and other extraneous influences.

## DEFINITION OF TRACK QUALITY

The design of a parametric measure of track condition has as its point of departure a general definition of what is meant by track quality. Good track shall be considered to be that which can support desired train movement for at least some time after the quality has been determined. Implicit in this statement are two important concepts:

1. The classification of the track (good or poor) cannot be made independently of the type of service to be provided by that track. Thus, development of a measure of track quality requires analysis of the entire system, which includes vehicle configuration and speed as well as track characteristics. One might expect that the measure of track that applies to track that supports movement of mixed freight at 60 km/h would be quite different from that which applies to passenger operations at 120 km/h.

2. A careful distinction must be made between instantaneous measurement of track quality, which relates to the present ability of the track to support the desired train movement, and the rate of change of track quality, which relates to the future ability of the track to support the desired train movement. Parameters that are good measures of track quality may provide little or no indication of the rate of change in track quality. However, many factors that are now used to estimate track quality provide excellent indicators of this rate of change.

The vehicle can be modeled as a predetermined mathematical operator whose input is displacement. If the velocity of the vehicle is known, this displacement can be expressed as a function of time and is shown as  $z(t)$  in Figure 1. The displacement of the wheel set (assuming that there is no wheel lift) is the loaded-track geometry. The vehicle model, i.e., the mathematical operator or filter, operates on  $z(t)$  to determine displacement  $x(t)$  and force  $g(t)$  at various points in the vehicle. The equation of motion, to solve for  $x(t)$  and  $y(t)$  in terms of input  $z(t)$  is as follows:

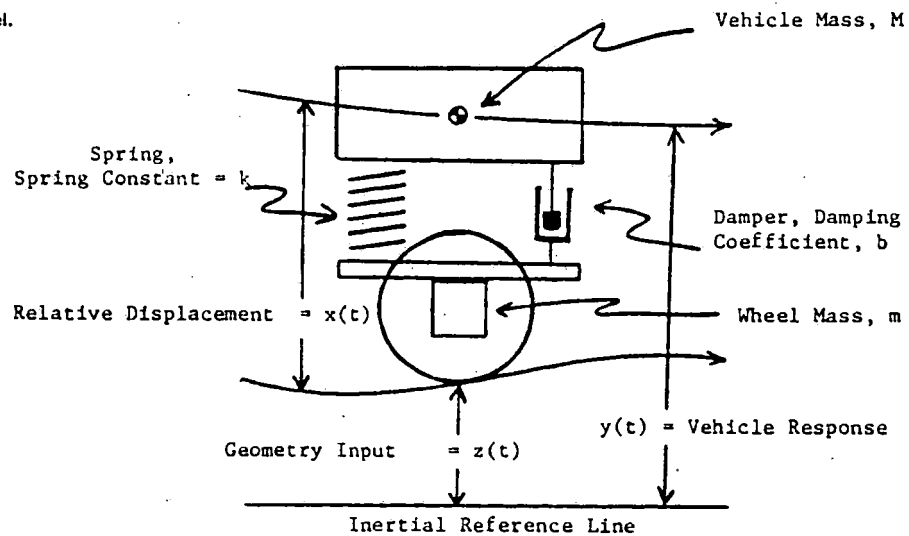
$$M(d^2y/dt^2) + b(dx/dt) + kx = 0 \quad (1)$$

where  $y(t) = x(t) + z(t)$  and the other terms are defined in Figure 1. Use Equation 1 together with the following equation to solve for force  $g(t)$  into the wheel set:

$$g(t) = m(d^2z/dt^2) - b(dx/dt) - kx \quad (2)$$

For a specific model and vehicle, the validity of predicted responses can be ascertained by tests. Varying degrees of sophistication are possible; however, for the purposes of this illustrative exercise, the simple linear model of Figure 1 is used. The methodology described in this paper is being pursued under a Federal Railroad Administration (FRA) contract by using a more-appropriate model.

Figure 1. Simplified vehicle dynamic model.



#### DEFINITION OF PERFORMANCE-BASED TRACK-GEOMETRY DESCRIPTOR

Immediate or instantaneous performance is determined on the basis of observed accelerations, relative displacements in the vehicle components, and force levels transmitted through vehicle and track members. These can be related to derailment potential, fatigue of track and vehicle components, lading damage, and ride comfort. This is not a new concept—it has served as the basis of numerous previous dynamic investigations the goal of which was to relate geometry variations to vehicle behavior (10). This study differs from others in the following key aspects:

1. No a priori assumptions are made as to the nature of the track-geometry input.
2. Simple linear models are used to obtain the salient response modes of a given vehicle to track-geometry perturbations.
3. These response modes are converted to the frequency domain. There the response signature is inverted to ascertain what maximum magnitude of track-geometry perturbation may be permitted in order to keep the vehicle response within acceptable limits. Since the conversion from spatial to temporal frequency depends on vehicle speed, the vehicle response and inversion must be performed for all speeds up to and including posted track speed. Since the track must be maintained to permit trains to operate at all speeds up to track speed, the worst-permissible geometry perturbation (i.e., that which just causes the limiting vehicle response) must be found for each wavelength. These worst-permissible perturbations for each wavelength define an envelope that identifies the maximum amplitude of the geometry perturbations for each wavelength. Track must be maintained within this envelope in order to restrict vehicle behavior to the limiting response levels.
4. The final envelope so obtained for a given track speed is used to define the filter that processes track geometry to relate excessive variations in geometry to excessive responses in vehicles. For bidirectional traffic, this filter has either a symmetric or antisymmetric impulse response, depending on the response mode examined.
5. The filter defined by the enveloping procedure has a finite number of free parameters (at least three, at the most four) that can be adjusted to

account for more-detailed and more-accurate models of vehicles. Alternatively, these free parameters can be adjusted on the basis of full-scale vehicle tests on special track sections or on shakers.

Alternatively, performance-based track-geometry descriptors (PBTGDs) can be extended to include high-speed passenger service in which passenger comfort is an added criterion. The undesired vehicle response would be that which results in excessive levels of acceleration experienced by a rider in the vehicle.

As cited in the introduction, the vehicle model that will be used to illustrate this approach to formulating a PBTGD of track quality will be extremely simple. The vehicle's configuration is that of point mass  $M$  suspended by a linear spring-damper combination that has spring constant  $k$  and damping coefficient  $b$ . It is driven by geometry perturbations  $z(t)$  that act on a wheel that has mass  $m$ . This model is that schematized in Figure 1.

#### DEVELOPMENT OF PBTGDs BY USING SIMPLE VEHICLE MODEL

##### Long-Wavelength Control

Typical rail vehicles have bump stops and other nonlinear constraining elements. When the relative displacement between  $M$  and  $m$  reaches critical levels, this implies that certain undesirable responses are occurring in the vehicle-track system. For example, large upward displacements in the suspension may indicate that the vertical forces vanish so that wheel lift may result. In the horizontal direction, large displacements may indicate that bump stops are engaged and direct coupling occurs between  $M$  and  $m$ , which results in large lateral forces at the contact zone between the wheel and the rail. Therefore, one measure of derailment tendency for this simple model is the relative displacement between  $M$  and  $m$ . The equations of motion for the relative displacement between  $M$  and  $m$  are as follows:

$$M(d^2x/dt^2) + b(dx/dt) + kx = M(d^2z/dt^2) \quad (3)$$

where

$z = z(t)$  = inertial track-geometry input as a function of time  $t$ ,

$y = y(t)$  = inertial response of mass  $m$  as a function of  $t$ , and.

$x = x(t)$  = relative displacement between  $M$  and  $m$  as a function of  $t = y(t) - z(t)$ .

$$|X(\phi)/Z(\phi)|^2 = v^4 \phi^4 / [v^4 \phi^4 + 2(2p^2 - 1)v^2(f')^2 \phi^2 + (f')^4] \quad (4)$$

where

- $f$  = temporal frequency (Hz),
- $v$  = forward speed,
- $\phi$  = spatial frequency (cycles/km) =  $f/v$ ,
- $Z(\phi)$  = Fourier transform of track-geometry input (time to spatial frequency),
- $X(\phi)$  = Fourier transform of relative displacement,
- $f'$  = resonant frequency:  $(f')^2 = k/[(2\pi)^2 \times M]$ , and
- $p$  = damping factor:  $p^2 = b^2/(4kM)$ .

For a resonance of 0.5 Hz, a damping factor of 0.2, and a speed of 100 km/h, the response characteristic shown by the line in Figure 2 is produced. It is characterized by a concentrated peak at a wavelength of 55 m, which tapers off at unit gain (1 cm input = 1 cm relative displacement output) for wavelengths shorter than resonance and which rolls off dramatically at wavelengths longer than resonance.

The transmissibility can be inverted to prescribe the peak value of geometry input that produces a fixed acceptable level of relative displacement. The track geometry that causes 2.54 cm of relative displacement in the same vehicle that travels 100 km/h is shown by the curve in Figure 3. Reducing the vehicle's forward speed produces additional curves, indicated by appropriately labeled broken lines in Figure 4, and these serve to illustrate the enveloping procedure for 100-km/h track. The en-

Figure 2. Vehicle relative displacement response to geometry input as function of spatial frequency.

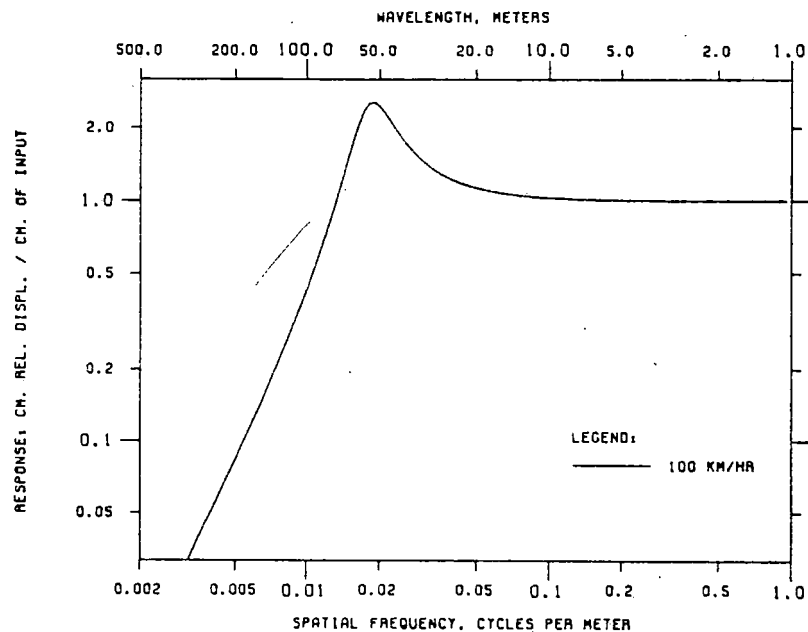


Figure 3. Geometry control required as function of spatial frequency.

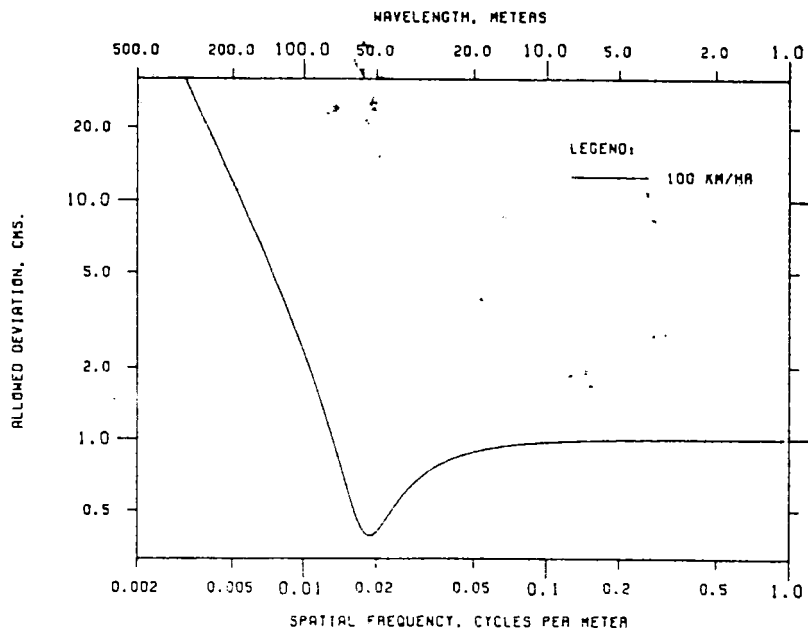


Figure 4. Enveloping for track speeds up to 100 km/h.

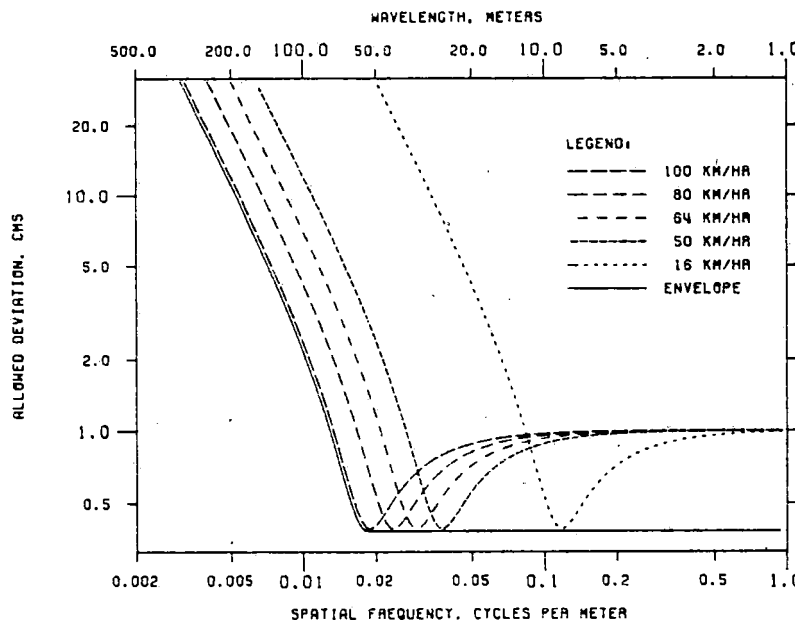
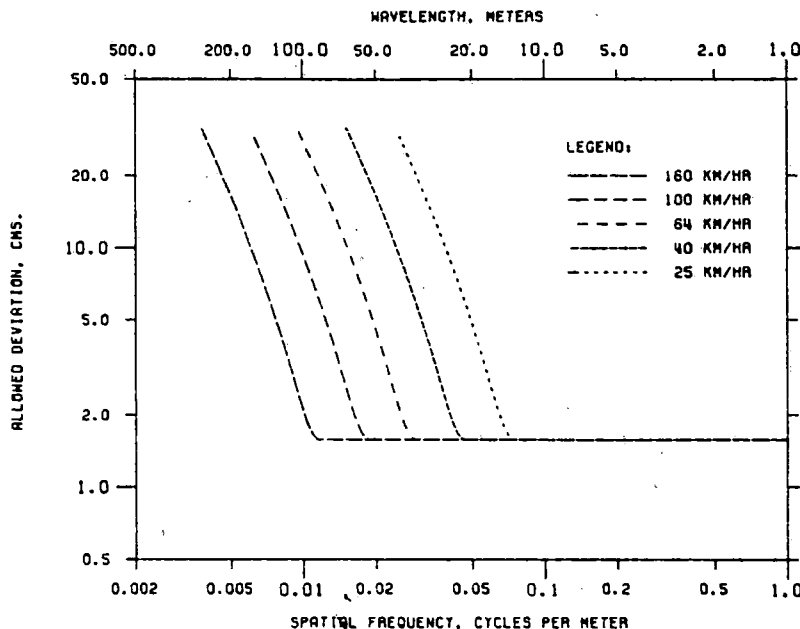


Figure 5. Cross-level requirement for 16-m boxcar that has high center of gravity for several track speeds.



velope that results from varying the speed over all speeds through 100 km/h is shown by a solid line.

The enveloping procedure is repeated to get the PBTGD for other track speeds. The result is the family of curves shown in Figure 5. [Note that the ordinate of Figure 5 has been shifted in anticipation of some numerical results from a study by the Transportation Systems Center (TSC) to be discussed later.] Aside from the issue of scale, these curves exhibit the following salient features:

1. They are characterized by the need to maintain the track-geometry perturbations at a constant level of amplitude that extends from the wavelength of resonance at maximum permissible speed to arbitrarily short wavelengths  $\lambda$ ;
2. At longer wavelengths, the need to control geometry amplitude tails off dramatically and, ultimately, the relaxation of amplitude grows at

$\lambda^2$  in the long-wavelength limit; and

3. The initial rapidity with which control of wavelengths longer than top-speed resonance may be relaxed is controlled by damping factor  $b$ .

The wavelength response characteristics of measurement tools and machines used to support track maintenance are such that the first feature listed above will have the greatest impact on maintenance costs (11,12).

#### Short-Wavelength Control

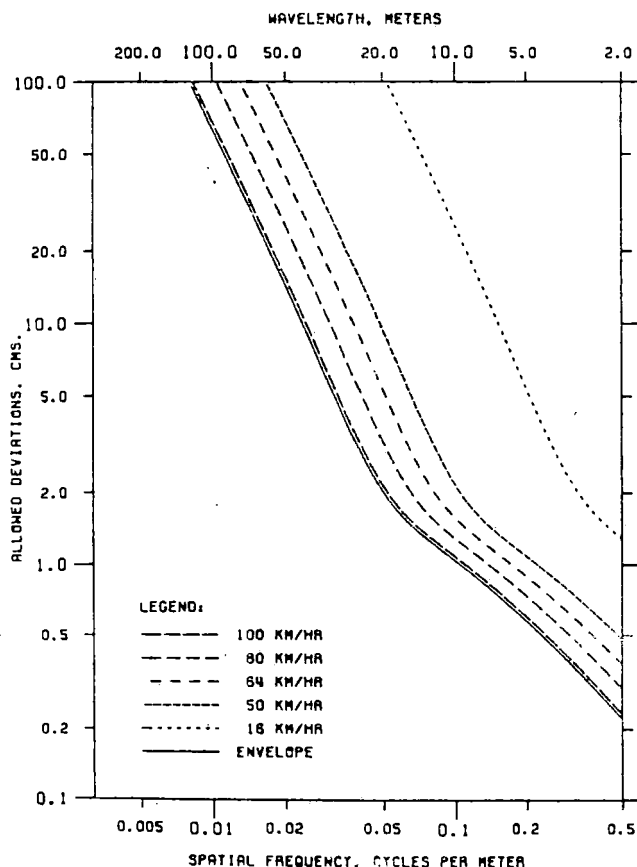
The descriptor derived in the preceding section has a mathematical form that is defined for both long and short wavelengths. As stated in item 1 above, the descriptor developed by limiting relative displacement  $x(t)$  in the vehicle permits a geometry perturbation that has a 1.6-cm amplitude for arbi-

trarily short wavelengths. Thus, according to this formulation, a geometry deviation that has this amplitude and a wavelength of 0.5 m is permissible. A short-wavelength deviation of this magnitude is clearly not acceptable to a real vehicle; it is therefore concluded that a response mode other than relative displacement controls the short-wavelength input. Hence, the high-frequency dynamic force augment at the contact zone between the wheel and the rail is examined. Dynamic augment is defined as the added force above static loading needed to make all the vehicle masses follow the geometric irregularities in the track. Because of the isolation between mass components provided by spring in the suspension system, the effective mass loading at the contact zone between the wheel and the rail can vary significantly as a function of frequency, speed, and suspension parameters. This component of vehicle performance contributes to high derailment tendency through accelerated wear, fatigue, and flaw growth in both the rail and the vehicle components.

The vehicle model used for illustrative purposes is still that shown in Figure 1, but now spring and damping constants appropriate for vehicle response to profile and alignment geometry perturbations are used. For typical mixed freight that responds to profile, the unsprung mass becomes that part of a wheel set and side frame seen at one wheel, and the sprung mass becomes that share of bolster, car body, and lading load applied to one wheel. The pertinent parameters and equation of motion are given below:

$$M(d^2g/dt^2) + b(dg/dt) + kg = Mm(d^4z/dt^4) + (M + m)b(d^3z/dt^3) + (M + m)k(d^2z/dt^2) \quad (5)$$

Figure 6. Allowed profile deviations based on static plus dynamic wheel load < 143 kN enveloped for 100-km/h operation.



where  $g = g(t)$  = force transmitted across wheel-rail contact zone and other terms were defined earlier.

$$|G(\phi)/Z(\phi)|^2 = (2\pi)^4 m^2 v^4 \phi^4 [v^4 \phi^4 + 2(\lambda_q^2 - 1)v^2 (f'')^2 \phi^2 + (f'')^4] \div [v^4 \phi^4 + 2(\lambda_p^2 - 1)v^2 (f')^2 \phi^2 + (f')^4] \quad (6)$$

where

- $G(\phi)$  = Fourier transform of wheel-rail force,
- $q^2 = (1 + r)p^2$  = effective damping factor for numerator transition,
- $(f'')^2 = (1 + r)(f')^2$  = effective resonant frequency for numerator transition, and
- $r = M/m$  = ratio of sprung to unsprung mass.

The associated performance-based envelope for this response mode is again developed by inverting the transmissibility. This envelope prescribes the extent to which geometry variations must be controlled in order to keep the dynamic augment plus static wheel load less than 143 kN—a value chosen for illustrative purposes only. The results of using this performance criterion for a variety of operating speeds are shown in Figure 6. Note that the curves do not interpenetrate each other as speed is changed (as they did in Figure 4), so the envelope for a given track speed is the vehicle requirement when it is running at that speed.

#### Control of Combination of Short and Long Wavelengths

The total performance requirements of the vehicle are now obtained by combining the results of Figures 5 and 6. The principle used is that the resultant envelope for a given track speed is the envelope of the envelopes obtained for all the different failure modes for that speed.

On this basis, the family of curves shown in Figure 7 is obtained. For the speed regime displayed in Figure 7, the following observations are made:

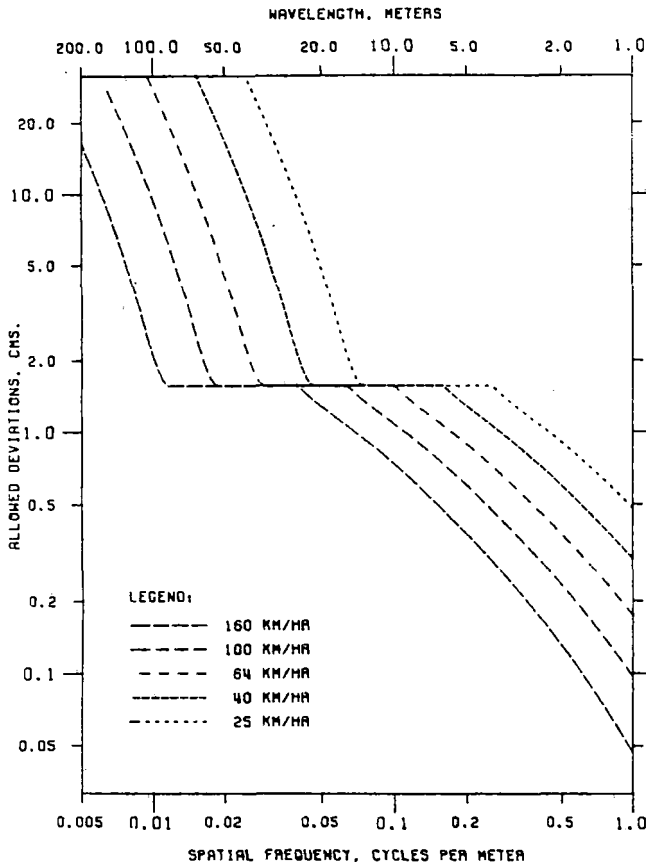
1. For long wavelengths (>100 m) the amplitudes can increase dramatically and ultimately approach a  $\lambda^2$ -characteristic;
2. For intermediate wavelengths, the level of control is constant; and
3. For short wavelengths (<7 m) progressively greater levels of control are needed; this increasing control also approaches a  $\lambda^2$ -characteristic.

The Figure 7 control characteristics can be squared so that they can be interpreted as power levels of allowed geometry deviations. In this form, they can be compared with empirical and analytical representations of the power spectral density (PSD) of rail profile as is done for 64-km/h track and shown in Figure 8 [based on a study conducted for TSC (13)]. When this is done, it is observed that the control properties of the PBTGD produce geometry variations in profile the power content of which resembles that of existing track. This is a key result since (a) no a priori assumptions were made with respect to the track input; yet (b) safe vehicle performance does not require a track the PSD of which is materially different from that found for existing track. Stated another way, existing track structure has geometry variations the form of which is suited to vehicle performance.

TSC has investigated freight-car roll response to cross-level input (14). Based on preliminary findings, the lowest (worst-case) roll resonance is of the order of 0.5 Hz, and wavelengths shorter than resonance must be held to 1.6 cm. This is the rationale for the scaling on the ordinate of Figure 5.



Figure 7. Allowed profile deviations for several track speeds when harmonic-roll and wheel-load requirements are combined.



It should be noted that this descriptor differs from those currently used in two key aspects:

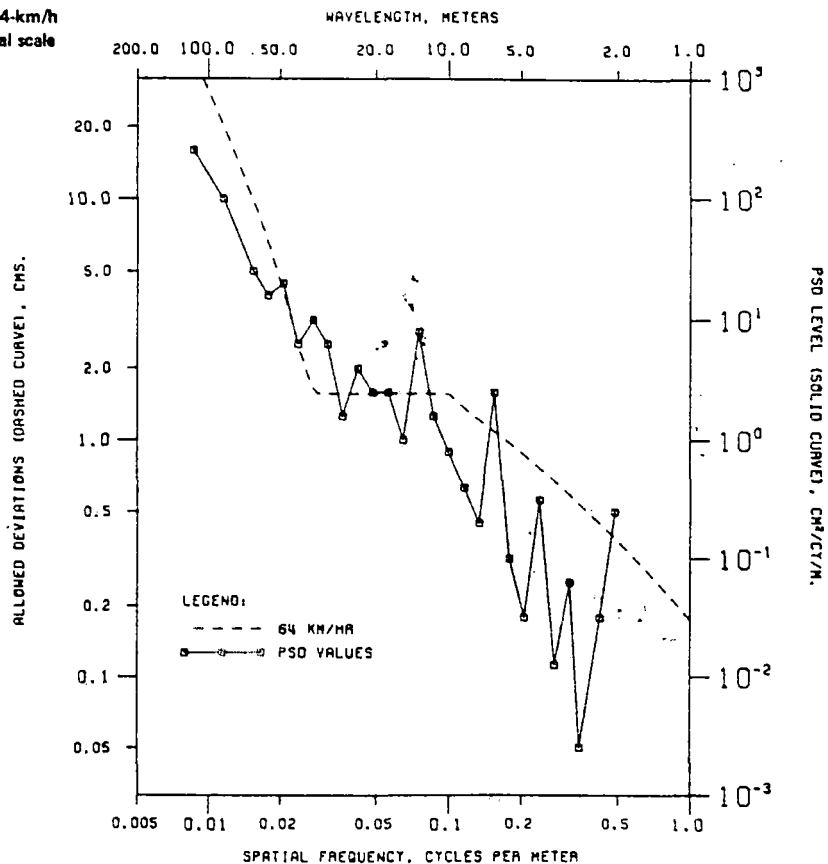
1. The wavelength response of the new descriptor varies with track speed, whereas the wavelength response of current descriptors (warp of a given length) is constant with respect to track speed; and
2. The comparison threshold of current descriptors varies with respect to track speed, whereas the comparison threshold of this descriptor remains fixed.

#### EXTENSION TO REAL VEHICLES AND MORE-ELABORATE MODELS

It is hypothesized here that these salient characteristics outlined above are ascribable to all vehicle models regardless of how complex or nonlinear they may be. In other words, long-wavelength performance is such that the amplitudes of geometry deviations must be maintained constant. The longest wavelength for which this must be done is determined by track speed. The nature of maintenance machines and practices is such that roll-off or relaxation of control over longer wavelengths is not critical. This hypothesis states that the curves in Figure 4 are not restricted to a simple linear model and that they can be applied to more-elaborate and representative nonlinear vehicle models. This hypothesis is being tested as part of a research project sponsored by FRA and Consolidated Rail Corporation (Conrail) in which this methodology will be applied to more-accurate vehicle models to determine effective threshold and resonances for four specific freight vehicles. The validation will be conducted as follows.

First, a single sine-wave track-geometry input will be tested. The amplitude will be adjusted so that it complies with descriptor requirements.

Figure 8. Overlay of allowed profile deviations for 64-km/h track with a PSD generated by 64-km/h track (vertical scale adjusted for best fit).



Emphasis will be on frequencies near key vehicle body resonances and for various phase relationships that are input at each end of the vehicle.

Following this, the vehicle model will be subjected to pairs of sine waves of different frequencies the combined magnitude of which does not exceed the descriptor requirement. The two frequencies,  $f_1$  and  $f_2$ , are chosen on the basis that they are related as a rational harmonic, i.e.,

$$|n_1 f_1 - n_2 f_2| < p f' \quad (7)$$

where  $n_1$  and  $n_2$  are integers,  $p$  is the damping factor, and  $f'$  is the resonant frequency.

#### PERFORMANCE-BASED TRACK-QUALITY INDICES

##### TQIs as Summaries of PBTGDs

The PBTGD provides a mapping between the track geometry at a point and vehicle performance. The PBTGD generates as many data values as are recorded by the geometry car. For FRA's T-6 vehicle, this means that there will be more than 5000 values for the PBTGD per kilometer of track. This is clearly far too much data to be of use in long-range track maintenance planning. Although a section-gang foreman, who is responsible for the daily upkeep of, say, 81 km of track, would be interested in each value of the PBTGD, an engineer or planner who has a wider responsibility requires some type of statistical summary that is representative of track quality over large track segments. Such summary statistics, as mentioned earlier, are defined as TQIs. Deriving the TQIs from PBTGDs allows the former to be interpreted as indicative of vehicle performance.

##### Types of Summaries

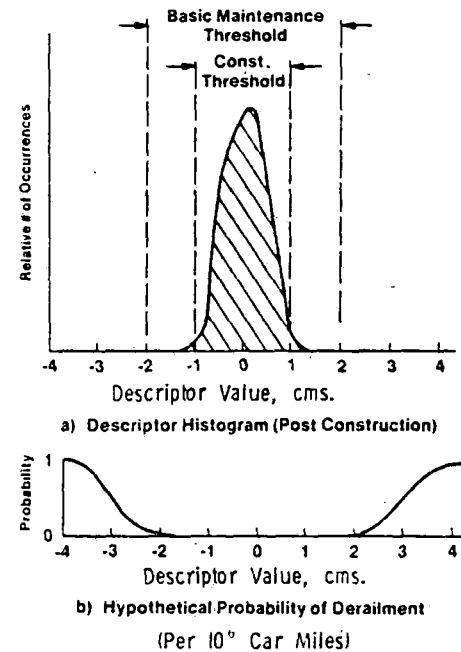
Both root-mean-square (RMS) and exception-type statistics have been used as TQIs; however, by 1980, only Southern Railway had formulated a TQI that could be called performance-based (8). The most significant drawback of RMS-type TQIs (mean, standard deviation, etc.) is that information regarding discrete geometry deviations is totally suppressed, but when these deviations are not directly linked to poor vehicle performance, their retention is not critical. Concurrently, the use of a rank-order TQI requires the definition of one or more thresholds of acceptability for the magnitude of the geometry deviations. With the exception of track gauge (and Southern's thresholds for track warp), these levels have been set arbitrarily (1); i.e., they have not had vehicle performance as their basis. Hence, in the case of TQIs that are derivatives of PBTGDs, it appears favorable to use RMS statistics.

However, the situation changes when a PBTGD, which directly relates the amplitude and wavelength of a geometry perturbation to probability of vehicle failure, is used as the basis for a TQI. In this case it is desirable for the TQI to retain some information regarding particularly poor values, i.e., high probability of derailment, of the PBTGD. Likewise, there now exists a rationale for assigning thresholds to be used in formulating TQIs from rank-order statistics.

##### Use of Histogram to Develop TQI

Figure 9 shows a hypothetical histogram of values that might be developed for some PBTGD as a result of a track-geometry survey. Each recorded value of the PBTGD is on the histogram. Since a particular track-geometry input evokes a definite response in the vehicle model, failure in the model (Figure 1)

Figure 9. Histogram of PBTGD versus derailment probability.



was deterministic. The transition from model behavior to real vehicle behavior introduces uncertainties that arise in two ways:

1. For a given vehicle type, the dynamical characteristics, e.g., spring constants, will vary from the nominal according to some probability distribution; and
2. For a given vehicle response, the probability of vehicle derailment is not binomial (for example, for this study, the level of acceptable wheel-rail force was defined as 143 kN; obviously, this does not imply that track will always sustain a loading of 142.9 kN and will certainly fail at a force of 143.1 kN).

In Figure 9 a hypothetical density function for probability of vehicle derailment has been mapped onto values of the PBTGD. In practice, this function must be estimated by using empirical techniques. This figure also indicates that there are two hypothetical thresholds:  $T_1$ , which is the acceptance standard for new or rebuilt track; and  $T_2$ , which represents the threshold for immediate spot maintenance. The latter threshold is set by management personnel, who determine these thresholds based on what is considered to be the acceptable risk of derailment.

Figure 9 clarifies the problems associated with selecting a TQI. A section-gang foreman is interested in every incident in which the PBTGD is equal to or exceeds  $T_2$ . A TQI that suppresses these individual locations is of no particular use. However, a chief engineer who is planning next season's production maintenance program would be more interested in the general shape of the histogram (sample moments) and in the rate of migration of points to the extremes. The engineer would not, however, be totally uninterested in the number of points that lie outside  $T_2$ . This dual interest seems to lead to a hybrid TQI, one that combines the characteristics of RMS and exception-level statistics. For example, the critical threshold  $T_2$  could be expressed as  $T_2 = \bar{x} + ns$ , where  $\bar{x}$  is the sample mean,  $s$  is the sample

Figure 10. Viscous-blob model of track degradation by using PBTGDs.

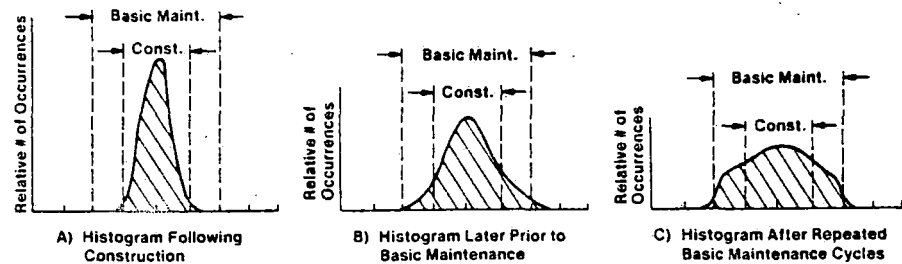
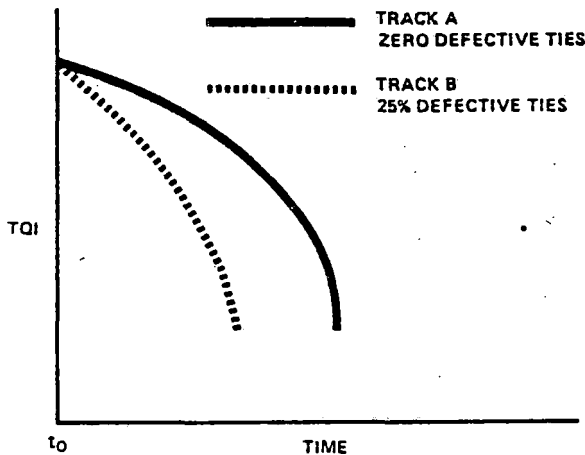


Figure 11. Hypothetical change in track quality with time.



standard deviation, and  $n$  is a pure number. The value of  $n$  would indicate when the maintenance program for a track segment changed from basic to production ( $n$  will decrease as the track deteriorates).

#### TRACK DETERIORATION

Figure 10 depicts three successive PBTGD histograms, each separated by a time interval, for a segment of track that is deteriorating with accumulating time or tonnage. The histogram tends to flatten, as would a viscous blob resting on a horizontal surface. The PBTGD histogram or its derivative TQIs say little (except for the hypothesis that poor track degrades faster than good track) about the rate at which this flattening process occurs. In order to determine the rate of track deterioration for a given level of track use, structural characteristics must be incorporated. Consider, for example, two contiguous track segments A and B that hypothetically receive identical use (annual tonnage, wheel-load distribution, train speed, etc.) and that both have 25 percent of the ties defective. Segment A is tied and surfaced so that no defective ties remain in the track. Simultaneously track segment B is surfaced but none of the defective ties are replaced. The behavior of a geometric TQI is qualitatively illustrated in Figure 11. Shortly after the track has been surfaced, the PBTGD histogram will indicate that the tracks are of approximately the same quality. (This would not be true if segment B was excessively deteriorated. If, for example, 60 percent of the ties were defective, it would be difficult to surface the track properly.) Due to the defective ties in segment B, its geometry will deteriorate more quickly than that of segment A. The differing rates of deterioration are

qualitatively indicated in Figure 11.

Although it is a common and expeditious assumption to assume that track structure is elastic, it is the deviation from elastic behavior that results in deterioration of the track surface. Nonelastic behavior occurs primarily in the tie fastenings (spikes) and in the ballast and subgrade. Efforts are under way to develop constitutive relations for track surface (6,15) that could provide the basis for an analytical model of track-surface deterioration. Another approach, which is being pursued as a part of the joint FRA-Conrail maintenance-of-way planning research program, involves the empirical observation of the deterioration of selected revenue trackage (9).

Many parameters have heretofore been used to estimate track condition even though they lack a direct relation to vehicle performance, e.g., defective-tie counts. Some of these will prove to be excellent indicators of the rate of change of the quality of the track surface. We are thus led to the following scenario:

1. A purely geometric TQI, which provides a macroscopic measure of track quality and which is a derivative of PBTGDs, and
2. A function that describes track deterioration as the change in this TQI,  $\Delta TQI = f(S, U, P, M)$ , where  $S$  is significant structural parameters (e.g., rail weight, track stiffness, and tie condition);  $U$  is use factors, which include annual tonnage and its wheel-load spectrum;  $P$  is present track quality; and  $M$  is any miscellaneous parameter, e.g., unusual rainfall.

#### CONCLUSION

At the risk of oversimplifying the developmental problems, a framework for formulating measures of track quality has been described. The method advocated requires a clear distinction between measures of present track quality and indicators of the rate of change of track quality. It is the thesis of this paper that the former be made up only of data that represent loaded-track geometry since this is what determines the behavior of a given vehicle traversing the track.

The actual development of PBTGDs is quite a bit more complicated than presented here. It requires detailed analysis of combinatorial geometry inputs, i.e., multiple frequencies of a given geometry and simultaneous excitation of two geometry inputs or combinations of geometry deviations (16).

#### ACKNOWLEDGMENT

This research is being supported by the Office of Freight Systems of FRA. It forms part of the maintenance-of-way planning research program in which Conrail and FRA are cooperating.

## REFERENCES

1. H. Baluch and others. Methodology for Quantification and Means of Improvement of Track Structure Condition with a Particular Interest to Its Heterogeneity. Polish People's Republic, Institute of Railway Research, Warsaw, 1977.
2. S.D. Tayabji and M. Thompson. Considerations in the Analysis of Conventional Railway Track Support System. Transportation Engineering Journal of ASCE, Vol. 103, No. TE2, March 1977, pp. 280-291.
3. J. Juillerat and R. Rivier. L'Etat géométrique quantifié (Quantified Geometric State of Railroad Track Geometry). Bull. Tech. de la Suisse Romande, Vol. 97, March 1971, pp. 55-63.
4. K. Bradley and others. Acquisition and Use of Track Geometry Data in Maintenance-of-Way Planning. Tech. Rept. FRA-ORDED-75-27, March 1975. NTIS: PB-241196/AS.
5. A.E. Fazio and P. Olekszyk. Formulation of a Parametric Measure of Track Quality. Transportation Engineering Journal of ASCE (to be published).
6. A.M. Zarembski, D.P. McConnell, and W.S. Lovelace. New Car for Measurement and Evaluation of Gage-Widening Resistance of Track. Proc., American Railway Engineering Association, Vol. 82, Nov.-Dec., 1980, p. 175.
7. R. Rousse. Les moyens modernes de mesure et d'analyse des données relatives au contrôle de l'état géométrique des voies ferrées (Modern Methods for the Measurement and Analysis of Track Geometry Data). Imprimerie Bron SA, Lausanne, June 1974.
8. R. Tuve. An Application of Track Geometry Data to Track Maintenance Planning on the Southern Railway. Presented at 59th Annual Meeting, TRB, Transportation Research Board, Jan. 1980.
9. A. Hamid and others. A Prototype Maintenance-of-Way Planning System. Federal Railroad Administration, U.S. Department of Transportation, Rept. FRA/ORD-80/55, March 1980.
10. E.H. Law and N.K. Cooperider. Literature Survey of Railway Vehicle Dynamics Research. In Surveys of Research in Transportation Technology, ASME, Applied Mechanics Division, Vol. AMD-5, Nov. 1973, pp. 49-78.
11. C. Esveld. Spectral Analysis of Track Geometry for Assessing the Performance of Maintenance Machines. International Union of Railways, Utrecht, Netherlands, Rept. DT77/D117, March 1978.
12. C. Esveld and F. Groenhuysen. Planning of Mechanized Track Maintenance by the Netherlands Railways, Based on Track Recording Car Data. Rail International, May 1980, pp. 282-294.
13. J.C. Corbin. Statistical Representation of Track Geometry. Federal Railroad Administration, U.S. Department of Transportation, Rept. FRA/ORD-80/22-1, March 1980.
14. H. Weinstock. Railcar Harmonic Roll Response to Periodic Track Crosslevel Variations. Transportation Systems Center, Cambridge, MA, Limited Distribution Working Paper, WP-743-C-15-075, Dec. 1979.
15. E.T. Seelig and others. A Theory for Track Maintenance Life Prediction. U.S. Department of Transportation, Rept. DPB-50/79/22, Aug. 1979.
16. F. Dimasi and H. Weinstock. A Parametric Study to Relate Railcar Speed to Permissible Combinations of Track Geometry Deviations. Dynamic Systems, Measurement and Control Journal of ASME, Vol. 100, Dec. 1978, pp. 252-259.

*Publication of this paper sponsored by Committee on Track Structure System Design.*

## THE DEVELOPMENT OF ANALYTICAL MODELS FOR RAILROAD TRACK DYNAMICS

D. R. Ahlbeck, Researcher, H. C. Meacham, Section Manager  
R. H. Prause, Associate Section Manager

Applied Dynamics and Acoustics Section, Battelle-Columbus  
Laboratories, Columbus, Ohio

### ABSTRACT

A renewed interest during the past decade in high-speed rail transportation has underlined a need for better understanding of the dynamic interaction between vehicle and track. Speeds in excess of 100 miles per hour tax the presently-used rail-tie-ballast track structure in terms of long-term stability and required track accuracy. Hence the investigation of improved structures with better dynamic response characteristics and greater stability has followed in the wake of improved high-speed railcar design.

This paper presents some recent developments in analytical modeling of railroad track structures for the study of vehicle-track dynamic interaction by computer simulation. A technique for describing the track structure, which is a complex distributed-parameter system, as a lumped-parameter model of one or more degrees of freedom is developed; and the use of this model to generate both the "on-car" and "trackside" response is examined. Field measurements taken on mainline track of several North American railroads are used to evaluate the accuracy and define the necessary modifications of the computer model.

Predictions of better overall system response and long-term stability from this computer model have aided in the preliminary design of several new track structures which are currently undergoing field evaluation.

### INTRODUCTION

A renewed interest during the past decade in high-speed rail transportation has underlined a need for better understanding of the dynamic interaction between vehicle and track. Freight train speeds of 80 mph and passenger train speeds up to 160 mph will undoubtedly become commonplace in the near future, taxing the presently-used rail-tie-ballast track structure to the extreme in terms of long-term stability and required track accuracy. In addition to speed, car size and load ratings have increased dramatically, adding further stress to an overburdened structure. The investigation of improved track structures with better dynamic response characteristics and greater stability has followed in the wake of improved equipment design as an effort to strengthen the weak link in the total system.

We have all become aware, during the past several years, of the

problem facing the railroads: a series of spectacular derailments involving the movement of flammable or noxious substances had made front-page news. Some of these accidents are directly related to the condition of the track: since 1962 there has been a nearly exponential rise in the number of train accidents attributed to track, or "maintenance of way" [1]. Part of the problem lies in the current economic situation in which most railroads find themselves; and as a consequence the track suffers from "deferred maintenance". However, another part of the problem is the inability of the structure, basically unchanged in concept since the early days of steam railroading, to handle the high speeds and loads of modern equipment.

In order to predict the dynamic response of new track structures, as well as to provide design guidance, a study of several new concepts by computer modeling techniques was conducted [2]. Basic to this study was the development and validation of a model of the existing track structure of rails, ties, ballast and subgrade. A computer model of the track was combined with a simplified model of a Department of Transportation research car to generate data for comparison with field measurements. The present paper describes the development of this track model and the results of subsequent validating experiments.

#### DEVELOPMENT OF A MODEL

The complexity of a model representing the track structure depends, of course, on the purpose of the simulation and the data to be generated. If the gross behavior of the vehicle sprung mass in response to long wavelength disturbances is the sole concern, a model of as few as two degrees of freedom can suffice, and the track can be represented by a simple spring-damper. If, however, the detailed behavior of track structure and unsprung masses in response to short wavelength disturbances is of importance, eighteen or more degrees of freedom may be required, and the track model becomes correspondingly complex. To begin we will focus our attention on the track as a simple spring.

##### *Stiffness of a Continuous Rail*

The accepted theory for the vertical deflections of rails is based on considering the rail as a continuous elastic beam continuously supported by an elastic foundation [3,4]. Although the rail-tie-ballast system represents a discrete series of springs rather than a continuous foundation, the results of theory are more or less in good agreement with experimental data for commonly-used rail sizes and tie spacings. According to theory, the static deflection  $y$  of a point  $X$  on a beam due to a fixed point load  $P$ , can be calculated by:

$$y = \frac{PB}{2K} \alpha(X) \quad \text{in.} \quad (1)$$

where

$$\begin{aligned} \alpha(X) &= e^{-\beta X} (\cos \beta X + \sin \beta X) \\ \beta &= (K/4EI)^{1/4} \quad \text{in.}^{-1} \end{aligned}$$

$K$  = foundation stiffness, lb/in. per in.

$EI$  = flexural rigidity of the rail, lb-in.<sup>2</sup>

$X$  = horizontal distance from the point load,  $P$ , in.

A plot of the normalized beam deflection curve,  $a(X)$  versus the parameter  $\beta X$ , is shown in Fig. 1. For an "average" mainline track the distance from the point load to the point of zero deflection is roughly ten feet.

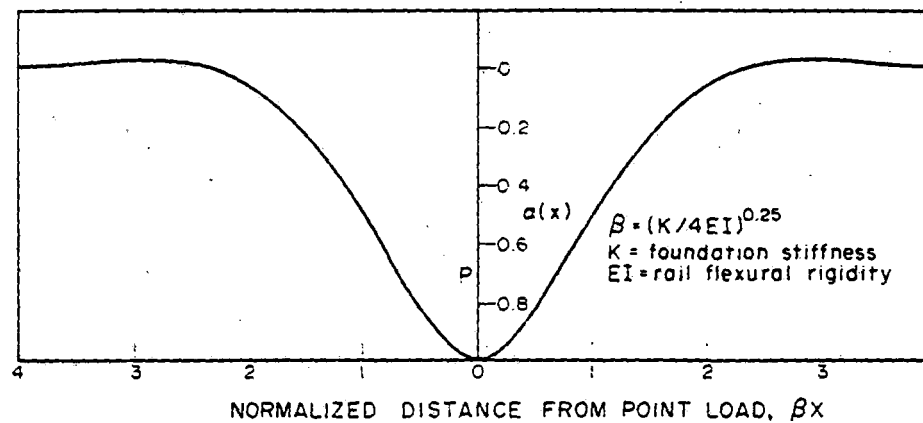


Fig. 1 Ideal Rail Deflection Shape Due to Point Load,  $P$ , as a Function of Normalized Distance,  $\beta X$

Since the wheelbase of a railway truck can vary from nearly nine feet to less than six feet, the point load beneath one wheel can produce additional deflection beneath an adjacent wheel, and vice versa:

$$y_1 = \frac{P_1 \beta}{2K} + \frac{P_2 \beta}{2K} a(L)$$

$$y_2 = \frac{P_1 \beta}{2K} a(L) + \frac{P_2 \beta}{2K}$$

where  $L$  = truck wheelbase.

Since this is a linear theory, superposition of the deflections due to multiple wheel loads may be assumed. For the moment, however, we will ignore the adjacent wheel and consider the track stiffness under a single point load. Knowing the rail flexural rigidity and foundation stiffness, the track stiffness per rail becomes:

$$K_T = \frac{2K}{\beta} = 2 \sqrt[4]{4EI K^3} \text{ lb/in.} \quad (2)$$

While rail flexural rigidity can be readily found in engineering handbooks, foundation stiffness is less easily obtained. For a detailed

analysis of conventional track, one must be able to calculate this stiffness from particular track parameters, such as tie size and spacing, ballast depth and modulus, and soil properties [5]. Therefore, the rail supports are considered as vertical springs of stiffness  $k$  at each tie, so that foundation stiffness can be related to tie spacing,  $l_t$ :

$$K = k/l_t \quad \text{lb/in./in.} \quad (3)$$

In Fig. 2,  $k$  is the series equivalent of the spring rate of a rail pad (if any), tie, and one-half the ballast-subgrade stiffness beneath the tie:

$$\frac{1}{k} = \frac{1}{k_{\text{pad}}} + \frac{1}{k_{\text{tie}}} + \frac{2}{k_{\text{bs}}} \quad (4)$$

The reason for halving the ballast-subgrade spring rate is that there is actually a continuity of the deflection of ballast and subgrade between adjacent loaded ties. This continuity is not accounted for in the fundamental assumption of an elastic foundation, and experiments indicate that each tie supporting a loaded rail is approximately twice as compliant as when loaded individually [5]. The ballast-subgrade stiffness, in turn, is a series equivalent of the ballast and subgrade individual spring rates:

$$\frac{1}{k_{\text{bs}}} = \frac{1}{k_b} + \frac{1}{k_s} \quad (5)$$

From the theory of elasticity, the effective stiffness of the ballast depends upon the area and shape of the loading area of the tie, the distribution of the loading pressure, and the elastic properties of the ballast. Good results can be obtained with a simplified model that assumes uniform loading and uniform pressure distribution at every depth in an imaginary pyramid spreading downward through the ballast. Basically, the material outside the "pyramid" is assumed not stressed at all, while the material within is only under vertical compression. Consequently, Poisson's ratio effects are replaced by the "angle of internal friction," a familiar property in soil mechanics that indicates the inclination of the sides of the pyramid to the vertical and thus determines the degree to which the load is distributed as it is transferred downward. Based on this model, the ballast stiffness is calculated to be:

$$k_b = \frac{C(l - w)E_b}{l_n \frac{l}{w} \frac{(w + Ch)}{(l + Ch)}} \quad \text{lb/in.} \quad (6)$$

where

$E_b$  = Young's modulus for ballast, lb/in.<sup>2</sup>

$l$  = length of loading area, in.

$w$  = width of loading area, in.

$h$  = ballast depth

$C$  =  $2 \tan \alpha$

$\alpha$  = angle of internal friction (20° assumed for ballast).

The subgrade portion of the pyramids from adjacent ties are assumed to spread out and overlap, and this overlapping is accounted for in the



factor of one-half in calculating the combined ballast-subgrade stiffness. The subgrade stiffness is calculated by multiplying the base area of the pyramid at the ballast-subgrade interface times the soil modulus:

$$k_s = K_o (l + Ch)(w + Ch) \quad \text{lb/in.} \quad (7)$$

where  $K_o$  = soil modulus, lb/in.<sup>2</sup>/in.

#### Stiffness of a Jointed Rail

One of the more important sources of rail vertical (and lateral) irregularity is the rail joint, that necessary incongruity even in this new age of welded rail. The loss in effective rail bending stiffness at a joint can reduce overall stiffness to as little as 25 percent of the nominal "infinite rail" stiffness, depending on the condition of the joint. The exaggerated deflections at the joint eventually result (after sufficient traffic) in permanent deformation of the rail and ballast. In jointed track this produces the rectified sine-wave profile typical of older track.

In Fig. 3 the ratio of jointed-rail stiffness to infinite-beam stiffness in the vicinity of the joint is shown for two types of connection: a pinned joint supporting shear, but no bending; and a free joint. Again, the distance from the joint is normalized by the rigidity factor,  $\beta$ . Effects of the joint disappear beyond  $\beta X = 2$ , or roughly 10 feet for average track. Both of these cases in Fig. 3 are somewhat severe: a joint in good condition might allow perhaps 25 to 30 percent loss in stiffness.

To adapt the joint effect to a computer model, the curves of Fig. 3 can be used to modify the rail stiffness beneath each wheel. A good approximation of the curve can be generated directly:

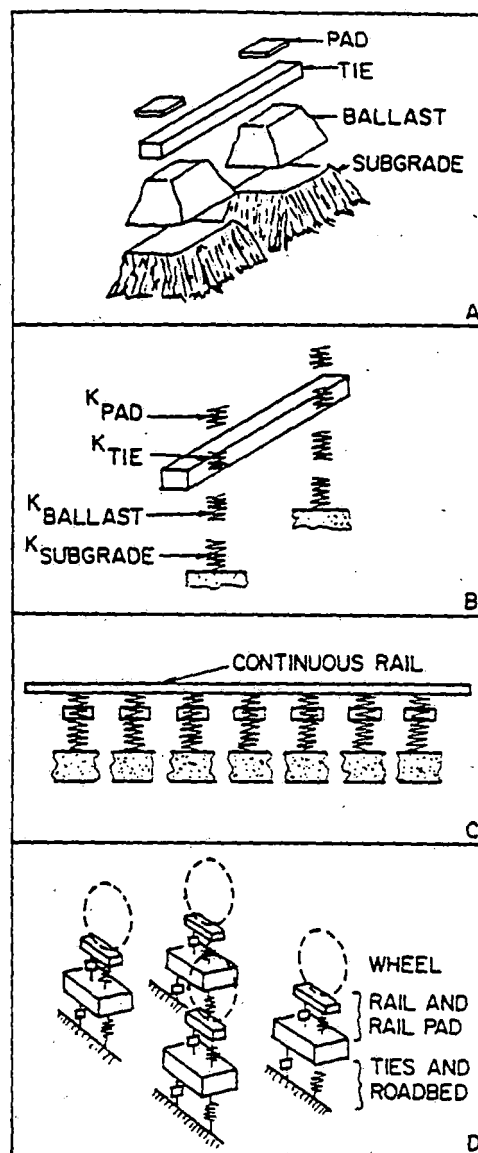


Fig. 2 Steps in the Development of a Dynamic Model of a Conventional Track Structure

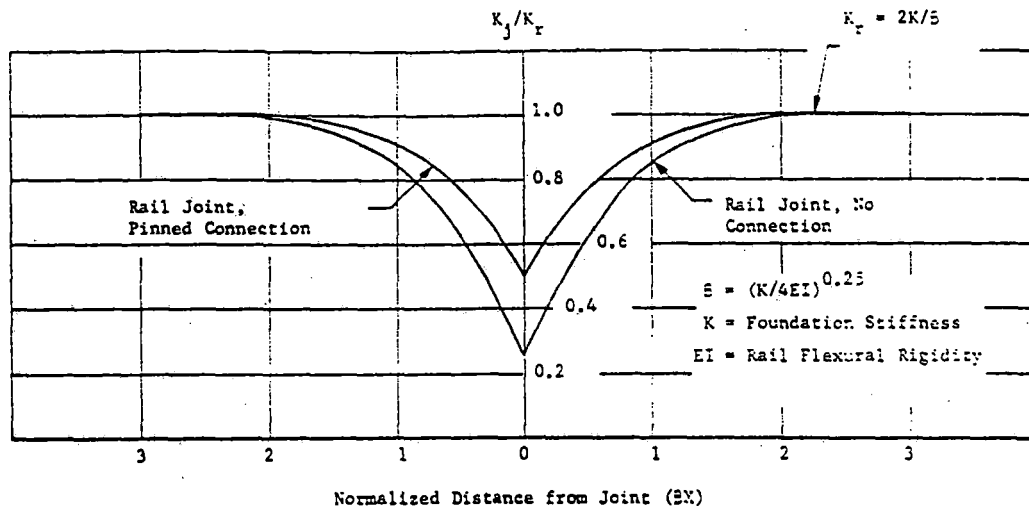


Fig. 3 Ratio of Rail Stiffness Near a Joint ( $K_j$ ) to Nominal Rail Stiffness Near Midspan of the Rail ( $K_r$ )

$$K_j/K_r = 1 - (1 - \xi)(1 - \sin \theta)^2 \quad (8)$$

where  $\xi = K_j/K_r$  minimum,  $\theta = 0.65 BX$  for  $0 \leq \theta \leq \pi/2$ , and  $K_j$  = stiffness at joint, lb/in.

#### A Dynamic Model

One problem of interest in developing the dynamic model of the track structure is the response due to a time varying force with point of application moving along the track at some velocity,  $V$ . The limiting cases for this coupled problem are (a) a stationary harmonic force ( $V = 0$ ), and (b) a constant force moving at train speed,  $V$ .

The solution of the response due to a constant force moving along the rail at velocity  $V$  depends on the ratio of the train speed to the critical velocity of the track structure. This critical velocity is the lowest velocity at which a free wave will propagate and is given [6,7] as:

$$V_c = (4EI/\rho)^{1/4} \quad \text{in./sec} \quad (9)$$

where  $\rho$  = track mass per unit length, lb sec<sup>2</sup>/in<sup>2</sup>.

Using parameters for the rail-tie-ballast type structure, this critical velocity is calculated to be about 1100 miles per hour, producing dynamic errors of less than 3 percent at speeds of 250 mph if the traveling-wave phenomenon is completely ignored. We are therefore justified in representing the track structure as a lumped-parameter, spring-mass-damper model "moving" beneath each wheel at train speed,  $V$ , for present-day vehicle speeds of 150 mph or less.

A schematic diagram is shown in Fig. 4 representing a lumped-parameter model of one rail and one-half of the unsprung mass of a 4-wheel truck.

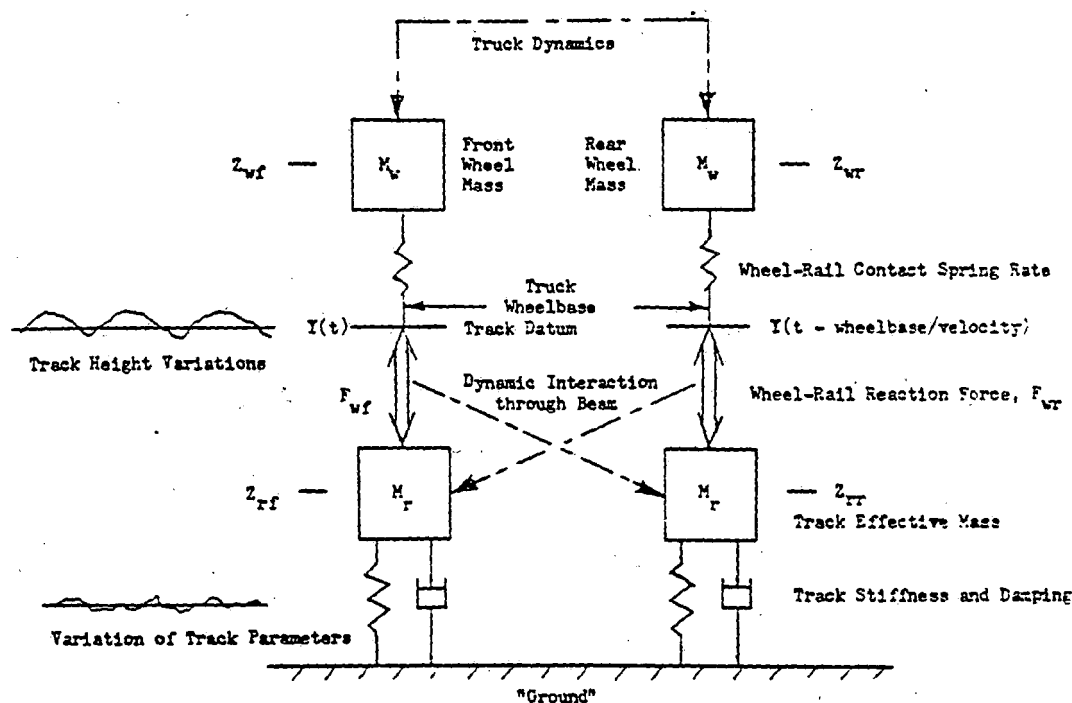


Fig. 4 Simplified Vehicle-Track Dynamic System Boundary

A contact stiffness between wheel and rail, calculated from Hertzian contact strain formulae based on wheel and rail crown radii, is used to generate a wheel-rail reaction force. Spatial variations in rail nominal position (rail surface under static load) provide the primary input to this model; although spatial variations in track parameters (rail stiffness near a joint, for example) provide an additional disturbance. Deflections of the rail under each wheel are influenced by loads at the adjacent wheels acting through the continuous beam. Implicit in this concept is the influence on deflections of loads on the opposite rail, acting through the ties (as beams) and the ballast section.

Another problem of interest is the *dynamic response of a fixed point in the track structure ("trackside"), acted on by a sequence of approaching and receding wheels*. To examine the "trackside" dynamics, a lumped-parameter model is used, in all respects identical with the model beneath each wheel, but with time-invariant parameters. Wheel-rail reaction forces are then imposed on the rail mass of this model, modulated by the theoretical beam deflection function according to the distance from the fixed point, as shown by Fig. 5:

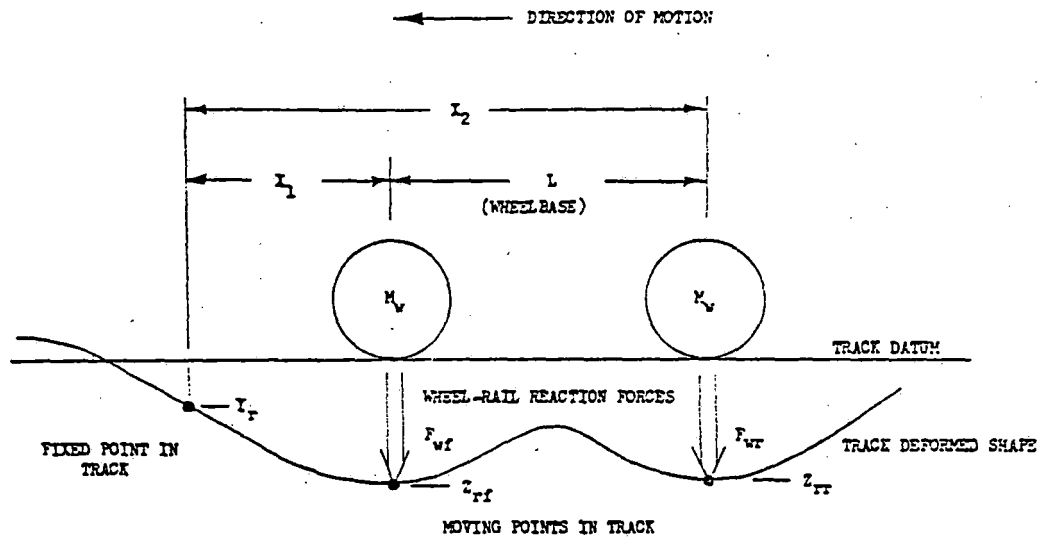


Fig. 5 Schematic of Spatially Fixed and Moving Points in the Dynamic Solution of Track Structure Response

$$Y_r(s) = 1/(K_r + C_r s + M_r s^2) \quad (10)$$

$$\alpha(X) = e^{-\beta X} (\cos \beta X + \sin \beta X) \quad (11)$$

$$y_r = Y_r(s) [F_{wf} \alpha(X_1) + F_{wr} \alpha(X_2)] \quad (12)$$

$$z_{rf} = Y_r(s) [F_{wf} + F_{wr} \alpha(L)] \quad (13)$$

$$z_{rr} = Y_r(s) [F_{wf} \alpha(L) + F_{wr}] \quad (14)$$

#### Mass and Damping

The effective lumped-parameter mass of the track has in the past been derived from the first natural frequency of a beam on an elastic foundation:

$$M_r = 3\rho/28 \quad \text{overall mass of track} \quad (15)$$

where  $\rho$  = effective mass per unit length of tie, ballast and rail.

While this may be adequate for the low-frequency phenomena associated with the vehicle sprung and unsprung masses and suspensions (even the "wheel-hop" phenomenon), this single-mass model is not sufficient to simulate wheel/rail impact. To provide better high-frequency resolution, the rail mass must be considered separate from the tie/ballast or slab/subgrade mass. In the case of a slab track with resilient pads, the resulting structure consists of two continuous beams on elastic foundations of different moduli, as analyzed by Hetenyi [4]. With the standard track structure, the tie/ballast "beam" has relatively little bending rigidity.

The effective mass of the rail alone can be calculated from eq. (15), based on the "foundation modulus" of the discrete tie or pad stiffnesses:

$$m_r = 3\rho_r/2\beta_r^* \quad \text{rail effective mass} \quad (16)$$

$$\beta_r = \left[ k_{\text{pad}} k_{\text{tie}} / (L_t) (k_{\text{pad}} + k_{\text{tie}}) (4EI) \right]^{1/4} \quad (17)$$

Calculating the tie and ballast effective mass is a less well-defined exercise, and one must resort to the empirical approximations of soil mechanics. One such approximation [8] assumes an effective pyramid of ballast beneath each tie, with sides the width of the tie and the effective depth based again on the "friction angle",  $\alpha$ :

$$\rho_b = \frac{d_b w A_t C_m}{g(2 \tan \alpha) L_t} \quad \text{mass per unit length} \quad (18)$$

where  $d_b$  = ballast specific weight,  $w$  = tie width,  $L_t$  = tie spacing,  $g$  = gravity constant, and  $C_m$  = an empirical coefficient (Ref. [8])

The empirical coefficient,  $C_m$ , is dependent on several factors, including the cohesive properties of the ballast, and can be assumed equal to (or slightly greater than) one. A second empirical method for estimating the ballast mass, based on the seismic shear wave propagation, can also be used [9]:

$$\rho_b = 0.28 k_b A_t / \pi v_{\text{seis}}^2 \quad \text{mass per unit length} \quad (18)$$

where  $A_t$  = tamped area of half-tie,  $k_b$  = effective ballast/subgrade stiffness under half-tie, and  $v_{\text{seis}}$  = seismic shear wave velocity.

With either approximation, the effective mass of ties and ballast are then found from the natural frequency of a continuous beam on an elastic foundation [10], based on the overall track characteristics. This is predicated on the ties/ballast transmitting little moment as a "beam":

$$m_b = 3.0 (W_{\text{tie}} / 2g L_t + \rho_b) / 2\beta \quad (19)$$

Damping is perhaps even more difficult to define quantitatively. We may assume the rail, probably the tie, contribute negligible damping to the structure, so that energy dissipation occurs solely in the ballast. Qualitatively, the damping is hysteretic in nature [11] and depends upon many factors: type and condition of the ballast, degree of compaction, amount of "fines" and moisture present, etc. Tests performed by the AAR on clean ballast of good quality have indicated equivalent viscous damping factors of 15 to 25 percent of "critical damping", based on the apparent natural frequency of the test sample. Kurzweil [12] has calculated the theoretical damping due to radiation of energy into a "halfspace" and has concluded that this form of energy loss is significantly greater than the damping due to the ballast/soil loss factor. By this method, the effective damping (in the vertical mode) may

\*) British investigators have used 0.4 times rail-plus-half-tie effective mass for their impact model (see Ref. [18])

range from 40 to 100 percent of critical damping, based on the effective mass and stiffness of the track without additional unsprung mass.

#### Track Lateral Model

So far we have considered only the vertical track model. A lateral model of the track may also be derived in a similar manner, as a continuous beam on an elastic foundation. Because of the more complex load paths and inherent nonlinearities in the lateral support, the model can be considerably more complicated, however. The rail, eccentrically loaded, transmits the load in torsion and shear through the fasteners and tie plates to the ties, where the load is distributed to the ballast section (with some maximum friction-limited force per tie). Lateral deflections of the rail head relative to "ground" for an applied lateral load (the effective lateral compliance) are highly dependent on the vertical loads simultaneously applied. Track lateral stiffness, then, is to some extent directly proportional to the vertical load, and consequently is a nonlinear term.

Up to the point of flange contact, the rail lateral effective stiffness (and damping) acts in series with the wheel-rail effective stiffness and damping. These terms are dependent upon the wheel-rail creep forces and gravitational stiffness (functions of wheel and rail geometry, wheel load and forward velocity), and are adhesion-limited, which introduces still another nonlinearity into the model formulation.

Static lateral track models used by Battelle have included the rail as a continuous beam supported at discrete points by torsional and shear stiffnesses (the fasteners). These models have been used primarily to determine gage spread under lateral and vertical combined loads [2,5]. To date, Battelle's dynamic models have used a lateral stiffness and damping based on the creep coefficients described by Wickens [13], limited by some adhesion level; and following flange contact, the rail-head-to-ground lateral stiffness (based on representative measured values) has been used as a simple, linear spring model with damping.

#### Track Geometry

One of the most important aspects of a track structure model is the spatially-varying geometry that is the "forcing function" of both prototype vehicle and model [14]. Three basic track geometries have been used to represent spatial variations of track surface, cross level, and alignment (gage, to date, has not been varied in Battelle's programs):

- (1) *Shaped random spectra* (power spectral density of geometry) - used to describe the expected random variation of track geometry as a function of distance, or wavelength, along the track. Linear, frequency-domain model.
- (2) *Discrete spectra* - used to describe particular track geometry variations from repetitive constructional effects, such as half-staggered rail joints, as a function of distance, or wavelength, along the track. Linear, frequency-domain or nonlinear, time-domain models.

- (3) *Discrete transient geometry* - a spatial variation versus distance along the track representing a "one-shot" disturbance such as a grade crossing, turnout, or low rail joint. Nonlinear, time-domain model.

An example of the shaped random spectrum for track cross level used in a recent study [15] is shown in Fig. 6, compared with the range of measured data from both North American and British railroad tracks. It is interesting to note the effect of staggered (North American) and coincident (British) rail joints on the cross level spectra. An example of a measured rail surface profile is shown in Fig. 7. This type of profile has been modeled quite adequately by the rectified sinewave. With half-staggered joints, the discrete spectral components of the rectified sinewave provide odd-harmonic excitation in roll, even harmonic excitation in bounce, based on the rail length.

In addition to the three track geometry inputs, the effects of curving must also be considered in the vehicle-track model. Curving may be transient (the dynamic effects on the spiral into a curve) or steady-state (the quasi-static effects in the body of the curve). Transient and steady-state curve effects are considered in three areas: track geometry (superelevation, for example), wheel-rail geometry (rail curvature, angle of attack), and the horizontal acceleration field acting through the centers of mass.

#### VALIDATION OF THE MODEL

Validation of a mathematical model consists of a direct comparison of computed problem variables (forces, deflections, etc.) with real-world measurements of the system modeled. Response amplitudes and natural frequencies, when matched to the desired degree of accuracy over the frequency range of interest, provide confidence in the ability of the mathematical model to simulate the prototype system. A validated model can then be used as a tool for the study of parameter variations, for a system design evaluation, or to study the system under different excitation and load environments.

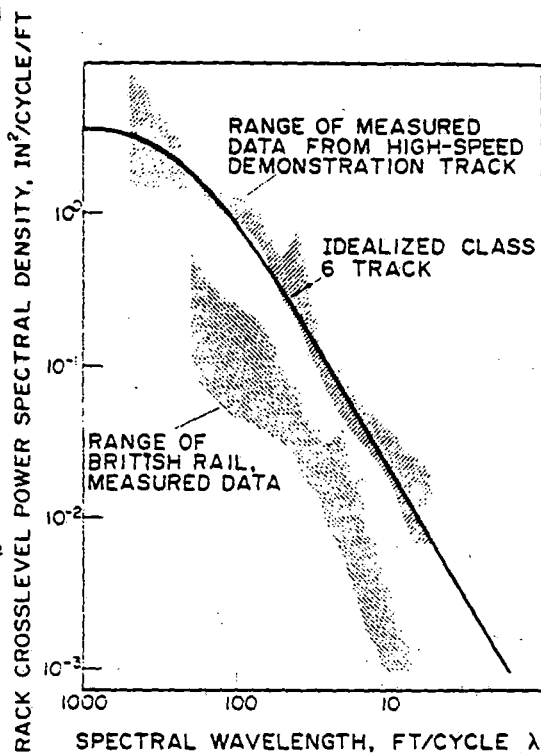


Fig. 6 Example of Approximate Random Input (Track Cross Level Geometry) Used with Vehicle-Track Model, Compared with Range of Measured Data

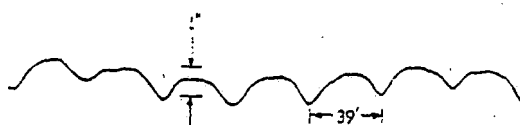


Fig. 7 Measured Rail Surface Profile, Bolted-Joint Track in Poor Condition

As so often happens, the "cart" goes before the "horse"; the mathematical modeling can progress far more rapidly than the validating measurements can be gathered. In the following sections, we examine very briefly some dynamic models used in the recent past, and evaluate these models with respect to measurements of dynamic response of typical railroad track.

#### *Transient Response Model*

One of the earliest vehicle-track models used by Battelle is the "half-car" model shown in Fig. 8. Programmed on an EAI Model 680 analog computer, the model was used for an evaluation of the dynamic interaction of a typical vehicle (in this example the DOT Test Car) with various track structures [2,5]. Although linear parameters were used to simulate the track structure, a Biot model [16] with hysteretic damping was used to represent one variation, the asphalt-slab track. Zero wheel-rail force at wheel lift and (in some cases) friction damping in the suspension were also programmed in the model.

A track joint was chosen as the primary "disturbance function" for computer simulation to provide a response with a reasonably high signal-to-noise ratio. Each track joint was simulated as having both a reduced stiffness and a profile error (a low spot or "slack") due to deformation from traffic. For validation work, computer runs were simulated at speeds up to 150 miles per hour for joints of 75 percent and 50 percent of nominal stiffness, profile errors up to 0.3 inch. A nominal track structure, based on the work of Birmann [17] and preliminary field experiments, with an overall stiffness of 221,000 lb/in. per rail (under a point load) was programmed: this represented a track with 140 lb/yd rail, 7 x 9 x 102-in. wooden ties on 21-in. centers, 18 inches of ballast with an elastic modulus of 30,000 lb/in.<sup>2</sup>, and a subgrade modulus of 100 lb/in.<sup>3</sup>. In addition, runs were made with a stiffer track (389,000 lb/in. per rail) representing 24 inches of ballast with a 40,000 lb/in.<sup>2</sup> modulus, and a subgrade of 150 lb/in.<sup>3</sup> modulus.

A typical computer output as seen "trackside" is shown in Fig. 9: this represents the lead truck of the test car passing a fixed point in the track. Although the resolution in time is poor, the "P1" and "P2" forces on the rail [18] can be readily seen. In this example the P1 half-cycle time-duration is less than one (scale) millisecond, and the P2 half-cycle time duration is roughly 25 milli-seconds. The accuracy of the P1 impact force depends, of course, on the rail mass and contact stiffness chosen to respond to this localized and short-duration pulse. The relatively low value of calculated P1 force, as well as low rail acceleration peaks (measured values at a rail joint typically exceed 300 g), is indicative that a smaller, more localized, rail mass actually responds to a joint impact than the mass calculated from the continuous beam equations. The method of computing the "equivalent force" at the joint from deflection and pad stiffness also means that the rail inertial force is not seen trackside, similar to the actual measurement situation.

#### *Experimental Measurements*

Several series of experimental measurements of track dynamic response have been conducted by Battelle, the first in early 1969, and the most



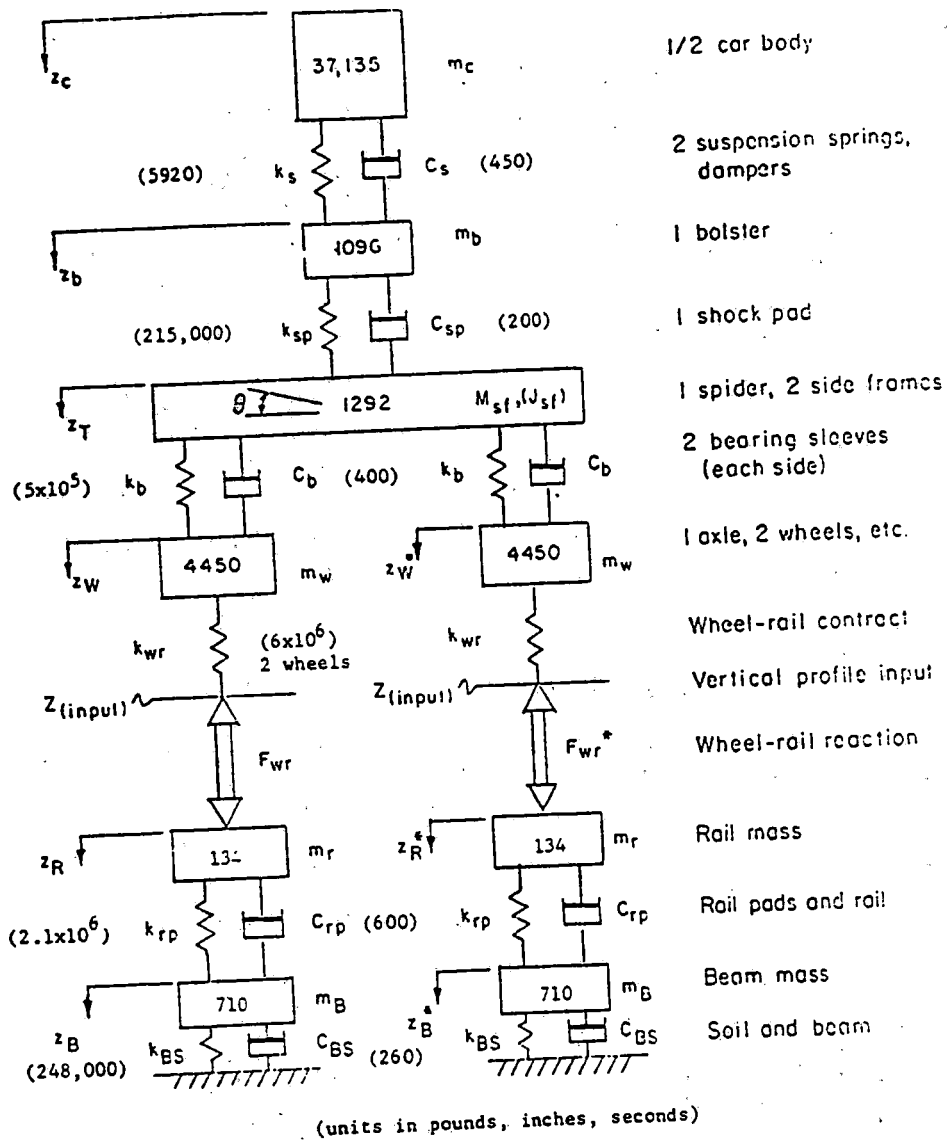


Fig. 8 Time-Domain Model Representing Portion of Rail Vehicle (DOT Test Car) and Track Structure Associated with One Truck

recent in January 1975. Specialized instrumentation was designed and built to measure the following track response variables:

- (a) Rail-tie vertical, lateral and angular displacements
- (b) Rail-"ground" vertical and lateral absolute displacements
- (c) Tie plate vertical load and transverse moment
- (d) Rail lateral (shear) load
- (e) Rail vertical accelerations
- (f) Ballast and subgrade pressures

Measurements were made on the Penn Central high-speed track near Bowie, Maryland, to provide a comparison and (hopefully) validation of the transient response model of Fig. 8. Bolted-joint track at an impedance bond in the otherwise continuous-welded track afforded the coincident rail joints for comparison with the simulated results. A typical oscillographic trace recorded during this experimental setup is shown in Fig. 10. One interesting deviation from the typical computer response shown in Fig. 9 was immediately apparent: due to a joint gap of roughly 5/8-in. (plus some chamfer, or batter), the tie plate load was instantaneously relieved before the dynamic "spike" load, unlike the sudden increase in load produced by the "gapless" computer model. The P1 and P2 forces (though attenuated through the rail effective mass) can be seen clearly in the tie plate load, and because of the gap the P1 force is relatively high.

Tests provided a wide range of useable data, in terms of speeds and types of traffic; test train runs as high as 126 mph were recorded. From this data the vertical stiffness of the test track was obtained as shown by Fig. 11. The track stiffness away from the joint was found to be very nearly linear: a 500 to 700 lb preload was recorded on the tie plate, and an average 46 percent of

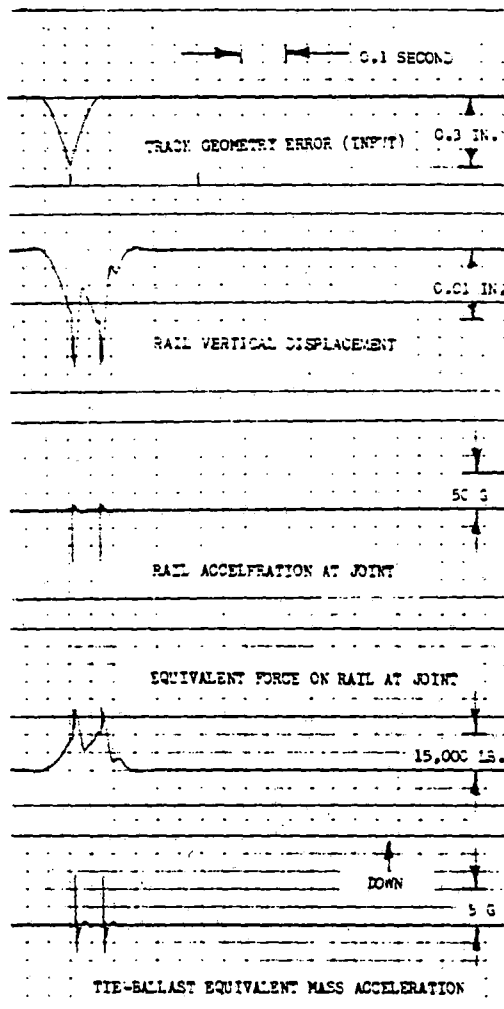


Fig. 9 Simulated Trackside Response at Low Joint, Time-Domain Computer Model, Rail Vehicle at 90 mph over Standard Tie-Ballast Track with 75% of Nominal Stiffness at Joint 0.3 inch Low

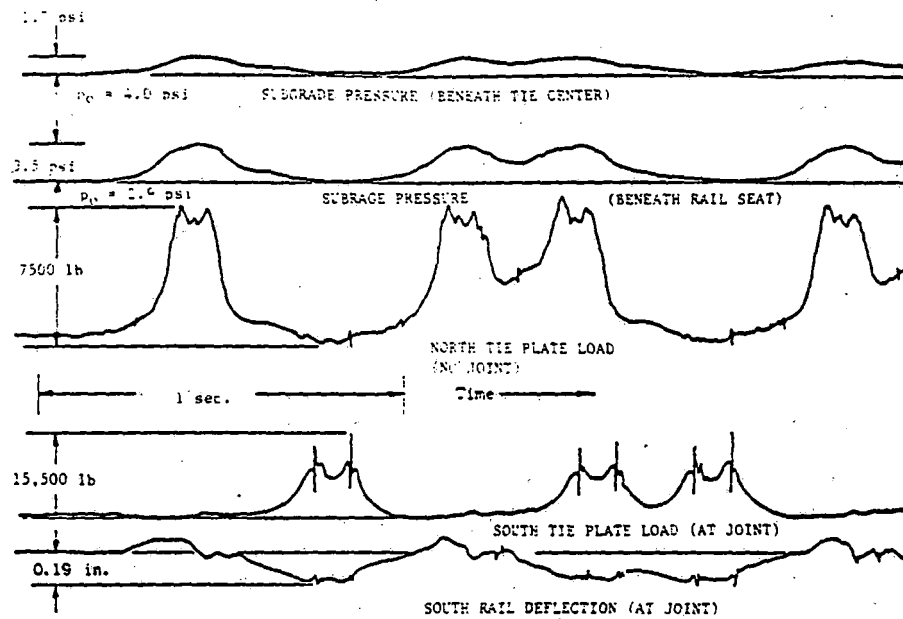


Fig. 10 Track Dynamic Response to DOT Test Train  
at 55 mph, Penn Central High Speed Track  
at Bowie, Maryland, December 10, 1969

the static wheel load was supported by the instrumented tie plate. The overall stiffness of 351,000 to 492,000 lb/in. (calculated by dividing a single wheel load by maximum rail deflection) was significantly higher than the 221,000 lb/in. used in the computer runs.

At the joint a decidedly non-linear characteristic was found, with an average stiffness under higher loads (the steeper slope) of 140,000 lb/in., about one-third of the stiffness away from the joint. The use of a 75 percent joint stiffness (166,000 lb/in.) and a "geometric error" of 0.1 to 0.3 inch in the previous computer program was, then, coincidentally quite close to the test conditions measured nearly a year later.

Rail vertical acceleration data using a high frequency-response recording system were obtained, as

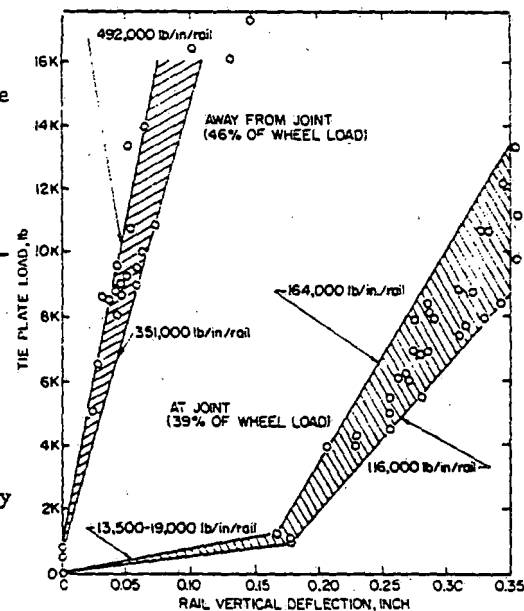


Fig. 11 Measured Track Spring Rate At a Joint and Away From a Joint

well as tie plate load and pressure cell data. For one day's runs both tie plate load cells were located away from the joint, opposite one another on the same tie. The tie plate located under the west rail was found to carry roughly 40-42 percent of the wheel load, slightly less than the 46 percent carried under the east rail. Of particular note were rail accelerations at the joint, reaching well over 300 g with the 115 mph Metroliner.

A comparison of computed and measured response is shown in Table 1.

	Speed	Tie Plate Load		Wheel Load*		Displacement In. Max Nom "Spike"	Rail Acceleration, G	
		Lb Peak	Lb P-P	Lb Peak	Lb P-P		+	-
Computer	30			16,800	2,700	0.278		
Test	26.4	7,670	3,410	16,700	7,410	0.280	0.315	
Computer	60			20,400	4,850	0.289		
Test	55.6	7,850	4,260	17,100	9,270	0.290	0.330	
Computer	90			22,700	7,800	0.299		
Test	88.0	10,250	7,000	22,300	15,200	0.274	0.370	
Computer	120			24,300	11,800	0.310		
Test	115	13,300	8,860	28,900	18,900	0.286	0.357	
Computer	30						3.7	17
Test	25.1						24	65
Computer	60						12	34
Test	55.2						98	206
Computer	90						12	49
Test	86.2						130	239
Computer	120						13	67
Test	120.1						290	335

\* Assuming tie plate supports 46 percent of wheel load.

Table 1 Comparison of Computed and Measured Track Response Data

In this table the computer data for the runs with a "geometric error" of 0.2 inch are compared with the field data. A good comparison between peak wheel loads is found, but the measured "spikes" or impulse loads are much higher, in spite of the fact that both "computer rails" had joints side-by-side. As mentioned before, the comparison of data traces showed that the gap in the actual rail due to cold weather at the time of measurements changed the response qualitatively as well as quantitatively.

The computer traces (see Fig. 9) of the simulated "standard" track at a fixed point during passage of one truck of the model DOT test car showed two distinct frequencies: a higher-frequency response seen in the force and acceleration traces (160-170 Hertz) and a lower-frequency response (26 Hz). The higher frequency results from the rail effective mass oscillating on the tie stiffness, while the lower frequency represents the sum of the unsprung masses (test car truck, rail, and ballast effective masses) oscillating on the overall track spring rate. An even higher frequency (roughly 800 Hz) was present, but not evident due to the slow chart speed: this represents the

"contact resonance" of the rail mass on the wheel-rail contact stiffness.

In examining the test traces, the 26 Hz was found to be quite distinct in subgrade pressures and occasionally in rail absolute displacement. A potpourri of higher frequencies was generated by the test train, varying in distinctness from run to run. The more prominent frequency bands noted were: 25-30 Hz, 50-70 Hz, 100-130 Hz, 150-170 Hz, 250-260 Hz, 450-500 Hz, and (with the high chart speed) 800 Hz. The actual track structure appears to be nonlinear enough to generate harmonics and subharmonics, depending on the type of excitation.

#### Recent Track Measurements

Track dynamic response measurements were made on high-speed tangent track under both summer and winter ambient conditions during a recent AAR Track Train Dynamics Program task. Although the task was aimed primarily at the measurement of dynamic track gauge, tie plate loads and rail vertical and lateral absolute deflections were also measured. This provided an additional opportunity to compare actual measurements with computed values from the analytical track models.

The track at the measurement site consisted of 133 lb/yd (66 kg/m) continuous welded rail on 8 x 14-in. 1:40-cant tie plates, a processed phosphate-ore ballast with at least a 24-in. depth, and a subgrade of uniform fill material (probably crushed lava rock and sand). Estimated track parameters used to calculate the track stiffness (eqs. 2 through 7) are given in Table 2. From these parameters, the individual and overall stiffnesses of the track structure are calculated from linear theory, and are listed in Table 3.

Parameter	Numerical Values	
Rail weight	133 lb/yd	66 kg/m
Flexural rigidity, EI	24.9(10) <sup>8</sup> lb-in. <sup>2</sup>	7.15(10) <sup>8</sup> MN-m <sup>2</sup>
Tie spacing, $l_t$	23 in.	58.4 cm
Tie tamped area, $A_t$	360 in. <sup>2</sup>	2323 cm <sup>2</sup>
Tie width, w	9 in.	22.9 cm
Ballast depth, h	24 in.	61.0 cm
Ballast modulus, $E_b$	30,000 lb/in. <sup>2</sup>	207 MN/m <sup>2</sup>
to	40,000 lb/in. <sup>2</sup>	276 MN/m <sup>2</sup>
Subgrade modulus, $K_o$	150 lb/in. <sup>2</sup>	1.03 MN/m <sup>2</sup>
to	500 lb/in. <sup>2</sup>	3.45 MN/m <sup>2</sup>
Ballast density, $\rho_b$	2200 lb/ft <sup>3</sup>	35,200 kg/m <sup>3</sup>
Subgrade density, $\rho_s$	2500 lb/ft <sup>3</sup>	40,000 kg/m <sup>3</sup>

Table 2 Estimated Values of Track Parameters

Calculated Parameter	Numerical Values	
$k_b$ (ballast stiffness)	944,000 lb/in	165 MN/m
	to 1,260,000 lb/in	220 MN/m
$k_s$ (subgrade stiffness)	229,000 lb/in	40 MN/m
	to 762,000 lb/in	133 MN/m
$k_{bs}$ (combined stiffness)	184,000 lb/in	32 MN/m
	to 475,000 lb/in	83 MN/m
$k_t$ (assumed tie stiffness)	$1(10)^6$ lb/in	175 MN/m
$K$ (track modulus, per rail)	3,650 lb/in	25 MN/m/m
	to 8,350 lb/in	58 MN/m/m
$\beta$ (inverse characteristic length)	.0246 in <sup>-1</sup>	.97 m <sup>-1</sup>
	to .0303 in <sup>-1</sup>	1.2 m <sup>-1</sup>
$K_r$ (track stiffness to point load, per rail)	297,000 lb/in	52 MN/m
	to 551,000 lb/in	97 MN/m
$\lambda$ (influence coefficient)*	0.13	
	to -0.01 (uplift)	
$y$ (total vertical deflection)*	.125 in	3.2 mm
	to .059 in	1.5 mm

(\*) Based on a 33,000-pound wheel load and a 72-inch axle spacing (100T car)

Table 3 Calculation of Track Stiffness and Deflections Under Load

Typical force and deflection traces are shown in Fig. 12 for heavy 100-ton (LC3) and 125-ton (LC4) covered hopper cars, and 6-axle radio-controlled diesel units, at a train speed near 50 miles per hour. In Fig. 13 a group of empty 100-ton covered hopper cars are shown near 60 miles per hour. Both of these recordings were made under winter ambient (frozen ballast) conditions. To check the comparison between the measured and computed deflection shapes, the idealized deflection curves were plotted, based on two identical cars coupled together: two loaded 125-ton cars ( $P = 39,200$  lb), and two empty 100-ton cars ( $P = 8,000$  lb). Points from typical measured deflection curves were then plotted over these linear, idealized curves (in reality, a time-variation compared with an ideal spatial variation). Results of these plots are shown in Fig. 14. It is immediately apparent from this plot that

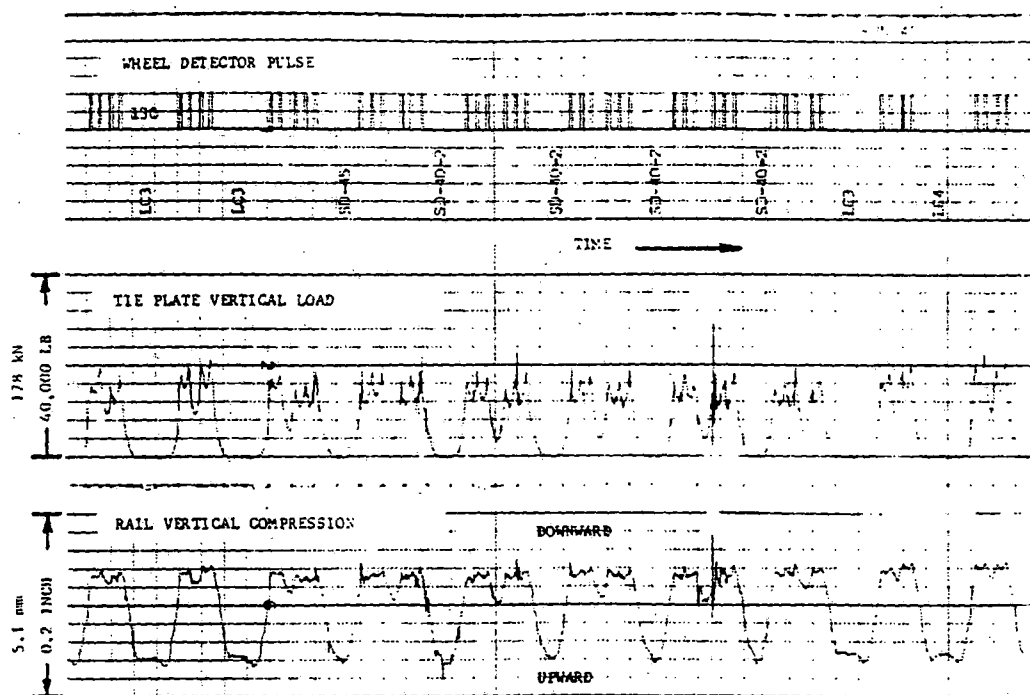


Fig. 12 Tie Plate Vertical Load and Rail Vertical Deflection  
Under Heavy Freight Cars and Locomotives of Unit Train  
(Train Speed 50 mph, 80 kph)

track modulus ( $K$ ) exhibits a nonlinear, "hardening" spring rate quite similar to an elastomeric pad in compression. While the deflection under maximum wheel load (purposely matched by choice of a track modulus of 5500 lb/in/in, or 38 MN/m/m) agrees well in magnitude and shape, the deflection under light wheel load is actually three times greater than calculated. The slight increase in deflection from a 39,000-lb. wheel load (LC4 car) over the 33,000-lb. wheel load (LC3 car) is indicative of the very high tangent stiffness under load.

To pursue this further, representative data points were plotted for a range of wheel loads under both summer and winter conditions. Ranges of tie plate vertical loads and corresponding vertical absolute rail deflections are shown in Fig. 15. From an average value of locomotive-induced tie plate loads (assumed to be 33,000-pound vertical wheel loads, and limited to lower-speed recordings), the instrumented tie plate was found to support about 33 percent of the wheel load in summer, about 48 percent in winter. Tangent stiffness values under maximum static wheel loads (per rail) were calculated from these tie plate-to-wheel load ratios, assuming (for the locomotives) a negligible influence from adjacent wheels. Choosing nominal, linear stiffness values from these curves (rail deflection under heavy wheel load), "secant" values of 290,000 lb/in (51 MN/m) for summer, and 425,000 lb/in (74 MN/m) for winter are calculated, which fall reasonably close to the

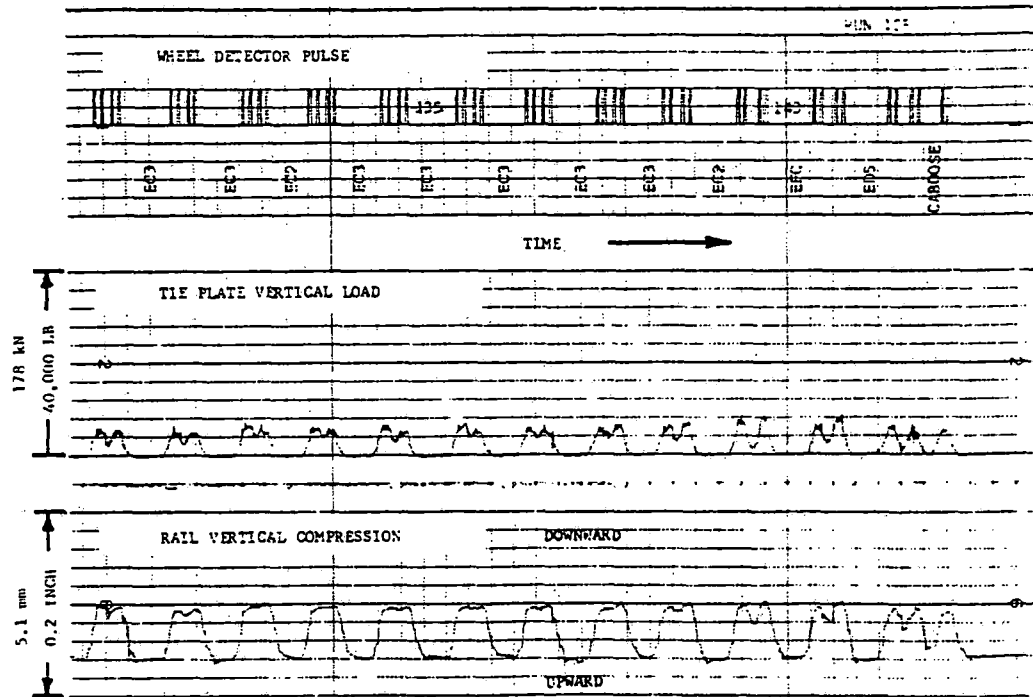
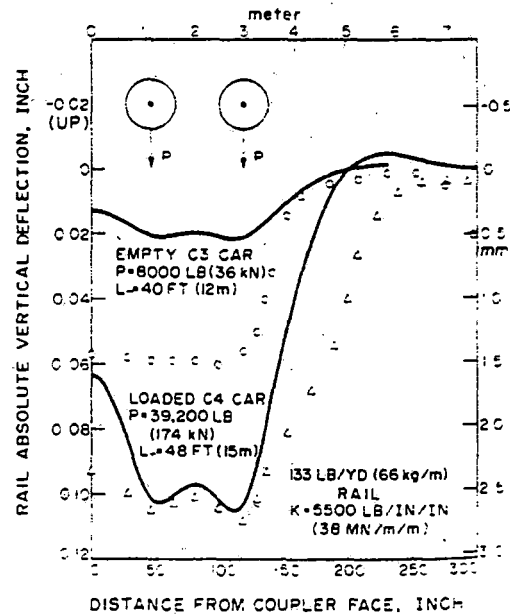


Fig. 13 Tie Plate Vertical Load and Rail Vertical Deflection Under Empty and Lightly-Loaded Freight Cars (Train Speed 60 mph, 97 kph)

calculated values of Table 3. The tangent stiffness, however, for small oscillations about the static load, is seen to be roughly twice the calculated stiffness.

It is apparent from the deflection traces of Figs. 12 and 13 that the track structure is highly damped under vertical load. Even the high impact load of a flat wheel on one diesel unit (Fig. 12) is very quickly damped. Oscillation frequencies of 20 to 25 Hz were observed, as well as higher-frequency oscillations of 88 to 100 Hz under impact loads, with higher static wheel loads. Under light cars (6000 to 9000-pound wheel loads),

Fig. 14 Comparison of Idealized (Linear Beam on Elastic Foundation) and Measured Rail Deflection Shapes Under Wheel Loads of Coupled Cars





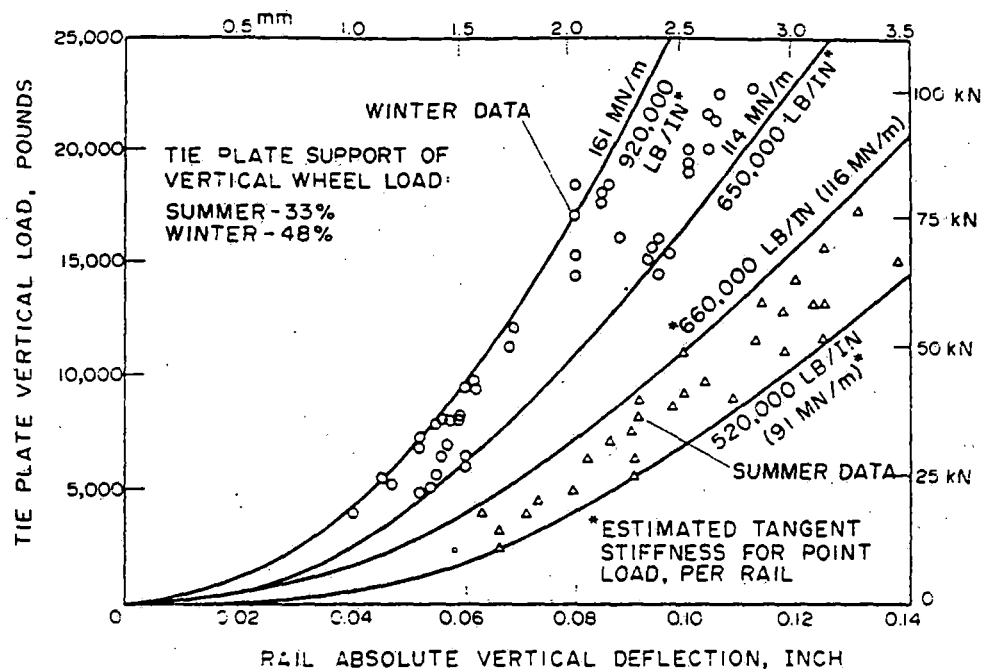


Fig. 15 Tie Plate Load Versus Rail Vertical Deflection Downward From Rest Position, 133 lb/yd Rail

impact oscillations of 50 to 70 Hz were observed.

Experimental measurements of rail lateral stiffness were also conducted by applying a lateral force to the rail in increments of 1000 pounds up to 10,000 pounds maximum, simultaneously with a 33,000-pound vertical wheel load. A patch of Teflon tape and a witch's brew of Molykote and EP grease were applied under the wheel to reduce lateral frictional hysteresis. Under these conditions, a lateral stiffness of 330,000 lb/in (58 MN/m) was measured at the rail head, reasonably linear up to this load level. Lateral oscillations in dynamic gauge were noted in recordings, particularly at rail temperatures near or above the "laying" temperature, ranging from 20 Hz under heavy wheel loads (particularly locomotives), down to 15 Hz under the light wheel load of a caboose. Absolute lateral oscillations near 10 Hz were occasionally seen under impact loading.

#### CONCLUSIONS

Analytical models of track structures have been developed based on linear theory, and in the recent past these models have been used in comparative analyses of vehicle-track interaction resulting from structural parameter variations. Measurements of track dynamic response have shown some areas of good agreement between the model and the actual structure, and also some areas in the models in need of modification and refinement. Specifically:

- (1) Linear theory can provide a reasonably good estimate of overall track stiffness (maximum deflection under the static wheel load of a heavy rail vehicle), but the tangent spring rate may vary from 0.3 to 2.0 times the calculated stiffness over the expected range of wheel loads. The simulated stiffness can best be handled by the nonlinear function  $K_r = C_K \sqrt{P}$ , where  $C_K$  is a curve-fitting term.
- (2) Track damping in the vertical mode appears to be relatively high, probably 50 to 100 percent of critical damping based on the track natural frequency. In modeling track damping, a linear hysteretic function, with a high loss factor calculated for the track natural frequency, will probably best match the actual track impedance.
- (3) To provide an accurate "impact" model necessary for calculating the higher-frequency wheel-rail forces at joints and other surface anomalies, a frequency-dependent mass model must be used to simulate highly localized effects in the rail itself. Lower-frequency phenomena can be simulated adequately by the effective mass of the continuous beam on elastic foundation.

#### ACKNOWLEDGEMENTS

The authors wish to acknowledge the support and sponsorship of the Federal Railroad Administration, U. S. Department of Transportation, and the AAR-FRA-RPI-TDA Track Train Dynamics Program in the areas of track modeling and field measurements, and the Union Pacific Railroad for their active support in the most recent track measurement studies.

#### REFERENCES

- [1] Myers, E. T., "Are Track and Roadway Adequate?," Modern Railroads, March, 1968.
- [2] Meacham, H. C. et al, "Studies for Rail Vehicle Track Structures," Department of Transportation (FRA) Report No. FRA-RT-71-45, April 30, 1970.
- [3] Seely, F. B., and Smith, J. O., "Advanced Mechanics of Materials," John Wiley and Sons, 2nd Edition.
- [4] Hetényi, M., "Beams on Elastic Foundation," The University of Michigan Press, 1946.
- [5] Meacham, H. C., et al, "Study of New Track Structure Designs Phase II," Summary Report to United States Department of Transportation from Battelle Memorial Institute, February 28, 1969.
- [6] Timoshenko, S. P., "Method of Analysis of Statical and Dynamic Stresses in Rail," The Collected Papers of Stephen P. Timoshenko, McGraw-Hill, 1953.
- [7] Kennedy, J. T., Jr., "Steady-State Vibrations of Beams on Elastic Foundation for Moving Load," Journal of Applied Mechanics, December, 1954.

- [8] Leonards, G. A., "Foundation Engineering," McGraw-Hill, 1962.
- [9] Poppitz, J. V., "Simplified Dynamics of Hardened Buried Buildings," The Shock and Vibration Bulletin, August, 1968, pp. 187-204.
- [10] Meirovitch, L., "Analytical Methods in Vibrations," McMillan, 1967, pp. 437-440.
- [11] Barkan, D. D., "Dynamics of Bases and Foundations," McGraw-Hill, 1962.
- [12] Kurzweil, L., "Dynamic Track Compliance," DOT Transportation Systems Center, Report No. GSP-067, May 22, 1972.
- [13] Wickens, A. H., "The Dynamics of Railway Vehicles on Straight Track: Fundamental Considerations of Lateral Stability," Interaction Between Vehicle and Track, The Inst. of Mech. Engrs. Proc. 1965-66, Vol. 180, Part 3F.
- [14] Ahlbeck, D. R., Prause, R. H., and Meacham, H. C., "An Application of Computer Modeling Techniques to Predict the Effects of Railroad Track Geometry," The Intersociety Conference on Transportation, Denver, Colo., September 24-27, 1973.
- [15] Ahlbeck, D. R., Prause, R. H., et al, "Comparative Analysis of Dynamics of Freight and Passenger Rail Vehicles," Report No. FRA-ORD&D-74-39, Department of Transportation, March 1974.
- [16] Caughey, T. K., "Vibration of Dynamic Systems with Linear Hysteretic Damping (Linear Theory)," Proc. 4th U. S. National Congress on Applied Mechanics (ASME), 1962.
- [17] Birmann, F., "Track Parameters, Static and Dynamic," Interaction Between Vehicle and Track, The Institute of Mechanical Engineers, Proc. 1965-66, Vol. 180, Part 3F.
- [18] Jenkins, H. H., et al, "The Effect of Track and Vehicle Parameters on Wheel/Rail Vertical Dynamic Forces," Railway Engineering Journal, January 1974, pp. 2-26.

#### DISCUSSION

- L. Steinbeisser (T. U. Munich):* Did you preload the ballast in your measurements of track dynamic compliance?
- R. H. Prause:* Yes, there was a static preload applied. The impact load was superimposed on the static preload.
- L. Steinbeisser (T. U. Munich):* But then you disregard the effect of the vehicle unsprung weight.

*R. H. Prause:* Yes, that's correct. This is intentional. We are trying to characterize the track dynamics by themselves. We can measure the effective mass and stiffness of the track, and then we combine it with the vehicle unsprung mass in the models. We have uncoupled the dynamics of the measurement car from the actual track measurement by measuring the force and the response at the rail.

Only the deflections of the car wheels will feed back in through the track. If the measurement point is not far enough away from the car wheels, then that will influence our response measurements. We were 20 feet away and the measurements showed that there was very little influence from the wheels. Also, this would only be important in the low frequency range. The car body is essentially isolated by the secondary suspension system above 2 Hz. We were operating basically in the 5 to 50 or 60 Hz range where the car body is well isolated from the feedback path through the wheels.

*J. Eisenmann (T. U. Munich):* You showed some graphs of rail track measurements. Were they taken only at one place or at several places?

*D. R. Ahlbeck:* We've made track deflection measurements only at one place on tangent track in Idaho. We've looked at about five different sites on the different track structures, but the description here referred only to the Idaho site. Now there is naturally some variation in construction within any track structure. There is some random variation of rail seat clearance, plate seating, etc.

*J. Eisenmann (T. U. Munich):* In your measurements, the maximum value is about twice the mean value. The measurement on only one place can give no answer about the mean value and the standard deviation. Therefore it's very important for measurements on outside track to do these at ten to twelve points. Both mean value and standard deviation are important for classifying the quality of track.

*D. R. Ahlbeck:* That's very true. We've found, for instance, on the Penn Central Track at Bowie that there is a substantial difference from one rail to the other rail even though you would think there would be uniformity in that particular spot.

*C. O. Frederick (BR):* Did you check the deformations of the cross-ties? You said that most of your measurements were on the rail. Did you get any lateral measurements, in particular of cross-tie displacements and any other displacements measured laterally?

*D. R. Ahlbeck:* We looked at the lateral absolute displacement of the rail to absolute ground and we found that this displacement was a rather random affair. During the summertime we felt that there might have been some minor movement of the cross-tie itself, although we did not have a measurement between the rail base and the cross-tie. We felt that there was some minor movement of the tie in the ballast under high lateral load primarily due to truck hunting. Now, in the wintertime, the tie is pretty well frozen into the ballast and there we saw permanent deformation of the spike and we found deformation on the order of 0.070 inches.

*G. C. Martin (AAR):* The Fourier transform of the force impulse had minima at

50 and 100 Hz and the track compliance graphs also showed several minima at 50 Hz. How do you know that the response wasn't really caused by the fact that you had no force input at that frequency?

*R. H. Prause:* We always look at a coherence function for the transfer function. The coherence function at those frequencies showed that the data weren't valid. In the vicinity of 50 and 100 Hz you have essentially zero input energy in the excitation, and therefore what you're measuring for a response is probably extraneous system noise. It doesn't correlate at all with the input. So that's the reason the coherence function gives a value 1, and shows that the data were invalid.

*R. Vlamincik (Boeing):* In your presentation you showed models which respond primarily in the vertical direction. I was wondering if you made any attempts to model any lateral phenomena; for example, misaligned rails.

*D. R. Ahlbeck:* We've handled the lateral model as a geometry and as a spring-damper only. We have not tried to model the mass effects in the lateral direction. By spring-damper I mean a lateral spring rate and damping that are based on the wheel geometry, forward speed of the train, and the vertical load. This is the creep coefficient described by Wickens up to the point of flange contact, and then after flange contact we model it simply as a spring damper of the overturn of the rail. So it's essentially a bilinear spring rate and, of course, we have the alignment geometry; but we have not attempted at this point to go down through the track structure to model the effect of lateral stability, the movement of the track structure on the ballast, or the effect of ballast mass in the lateral direction.

**J. A. Hadden<sup>1</sup>**

Research Assistant,  
Assoc. Mem. ASME

**E. H. Law**

Assoc. Professor,  
Mechanics and Mechanical Engineering,  
Mem. ASME

Department of Mechanical Engineering,  
Clemson University,  
Clemson, S.C.

# Effects of Truck Design on Hunting Stability of Railway Vehicles

*A general model of a dual-axle railway vehicle truck is derived. By suitable choices of primary suspension elements, this general model may be specialized to become (1) a roller-bearing freight truck, (2) a plain-bearing freight truck, (3) a roller-bearing truck with primary suspension elements, (4) a passenger truck, (5) a generic model of a freight truck with interconnected wheelsets, or (6) a rigid truck. The truck model is combined with a car body capable of lateral and roll displacements. The effects of the various design parameters on the critical speed for hunting are examined for each configuration.*

## Introduction

As part of a study of freight-car dynamics under contract DOT-OS-40018, a generalized 9-degree-of-freedom analytical model of a freight truck was derived. This model is sufficiently general to allow specialization to the following configurations: roller-bearing truck, plain-bearing truck, rigid-frame truck with primary suspension, flexible-frame truck with primary suspension, truck with interconnected wheelsets, and completely rigid truck. The truck model was used in conjunction with either of two car-body models: a pseudo-car body having lateral and roll degrees of freedom (equipped with only one truck) and a 5-degree-of-freedom car body that, in addition to the usual rigid-body motions of yaw, lateral displacement, and roll, has an approximate representation of the first lateral bending mode and first torsional mode.

Parametric studies were conducted with both car models to investigate the effects on hunting stability of various vehicle designs.

The simpler car model (equipped with one truck) was used to investigate the stability of various truck designs. As the more complex car equipped with two trucks used substantially more computer time, it was used with only one truck design (conventional roller-bearing trucks) to investigate the effects on stability of car-body flexibility, car-body type, and car-body center-of-gravity height. The results of the study on truck design are discussed in this paper, and the results

of the study of the complete car with two trucks are reported in [1].<sup>2</sup>

The objectives of the study discussed in this paper were (1) to develop a general freight-truck model that can be used for design studies and diagnostic studies, (2) to use the model to investigate the validity of a simpler freight-car model with roller-bearing trucks developed by Cooperrider and Law [2], (3) to use the model to investigate the hunting stability of a limited number of possible truck designs and the effects of various design parameters for each design.

## Description of Models

The study was conducted using two linearized freight-car models. One is an 11-degree-of-freedom (11-DOF) model of a single truck and pseudo-car body. The other is a more sophisticated 23-degree-of-freedom (23-DOF) model of a complete freight car consisting of two trucks and a car body that is flexible in the first yaw and roll bending modes. Schematics of the first model are shown in Fig. 1.

The trucks for both the 11-DOF and 23-DOF models are identical. Each truck consists of two wheelsets connected to the truck frame by lateral and longitudinal suspension elements. The truck frame consists of two sideframes and a bolster connected by lateral and vertical suspension elements. Each wheelset has lateral, yaw, and torsional degrees of freedom. The two sideframes are assumed to move together laterally and in yaw. Sideframe roll motions have been neglected. In addition, the sideframes can warp, or rotate about the truck centerline, to form a parallelogram in the horizontal plane. The bolster can move laterally with respect to the sideframes and can yaw about its center of gravity such that it remains parallel to the lines through the ends of the sideframes. Thus each truck has 9 degrees of freedom; these are

<sup>1</sup> Currently, Researcher, Battelle's Columbus Laboratories, Columbus, Ohio.

Contributed by the Rail Transportation Division and presented at the Winter Annual Meeting, New York, December 5-10, 1976, of THE AMERICAN SOCIETY OF MECHANICAL ENGINEERS. Manuscript received at ASME Headquarters July 28, 1976. Paper No. 76-WA/RT-1.

<sup>2</sup> Numbers in brackets designate References at end of paper.

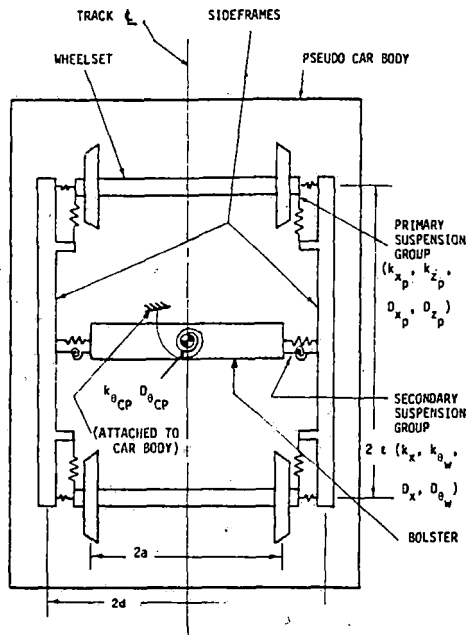


Fig. 1(a) Schematic of 11-DOF model, equilibrium configuration (plan view)

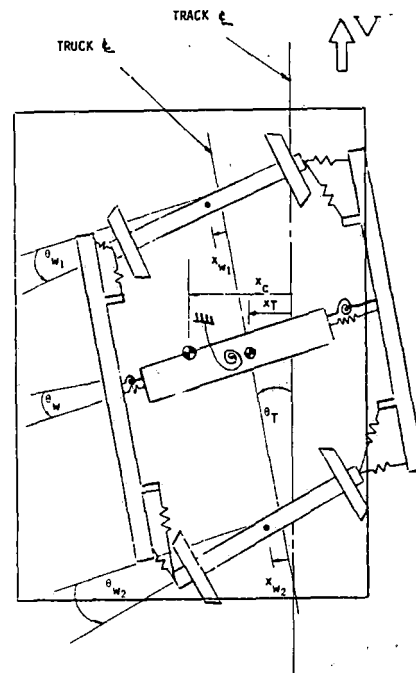


Fig. 1(b) Schematic of 11-DOF model, disturbed configuration (plan view)

wheelset lateral, yaw, and torsional displacements for each of two wheelsets, plus lateral, yaw, and warp displacements of the truck frame.

For the 11-DOF model the pseudo-car body or half-car body has lateral and roll degrees of freedom, but it cannot yaw. The 23-DOF

model includes a two-mass car-body model with 5 degrees of freedom. These are lateral and yaw displacements in the rigid-body mode, yaw displacement in the first lateral bending mode, and roll displacements of each mass, or half-car body.

The nominal truck configuration is a 70-ton ASF Ride Control truck

## Nomenclature

$a$  = one-half track gauge, ft  
 $a_1$  = coefficient of first-order term of series expansion of wheelset roll angle  
 $D_{AX}$  = axle torsional damping coefficient, ft-lb-s/rad  
 $D_x$  = secondary-suspension lateral damping coefficient, lb-s/ft  
 $D_{x_p}$  = primary-suspension lateral damping coefficient, lb-s/ft  
 $D_y$  = secondary-suspension vertical damping coefficient, lb-s/ft  
 $D_{z_p}$  = primary-suspension longitudinal damping coefficient, lb-s/ft  
 $D_{\theta_{CP}}$  = yaw damping coefficient for centerplate connection, ft-lb-s/rad  
 $D_{\theta_w}$  = secondary-suspension warp damping coefficient, ft-lb-s/rad  
 $d$  = one-half distance between sideframes, ft  
 $f_c$  = frequency of least-damped mode at critical speed, Hz  
 $f_{11}, f_{33}$  = lateral and longitudinal creep coefficients, lb/wheel  
 $f_{12}, f_{22}$  = lateral spin and spin-creep coefficients, ft-lb/wheel and ft<sup>2</sup>-lb/wheel, respectively  
 $h$  = height of car body centroid above bolster, ft  
 $I_{B_y}, I_{B_z}$  = centroidal mass moments of inertia of bolster in yaw and roll, respectively, slug-ft<sup>2</sup>

$I_{c_3}$  = centroidal mass moment of inertia of car body in roll, slug-ft<sup>2</sup>  
 $I_{s_2}$  = centroidal mass moment of inertia of sideframe in yaw, slug-ft<sup>2</sup>  
 $I_{w_1}, I_{w_2}$  = mass moments of inertia of wheelset about centroidal axes parallel to and normal to axle centerline, respectively, slug-ft<sup>2</sup>  
 $k_{AX}$  = axle torsional stiffness coefficient, ft-lb/rad  
 $k_x$  = secondary-suspension lateral spring constant, lb/ft  
 $k_{x_L}$  = lateral spring constant for wheelset interconnection, lb/ft  
 $k_{x_p}$  = primary-suspension lateral spring constant, lb/ft  
 $k_y$  = secondary-suspension vertical spring constant, lb/ft  
 $k_{z_p}$  = primary-suspension longitudinal spring constant, lb/ft  
 $k_{\theta_{CP}}$  = yaw spring constant for centerplate connection, ft-lb/rad  
 $k_{\theta_L}$  = yaw spring constant for wheelset interconnection, ft-lb/rad  
 $k_{\theta_w}$  = secondary-suspension warp spring constant, ft-lb/rad  
 $l$  = semiwheelbase, ft  
 $m_B$  = bolster mass, slugs  
 $m_c$  = car body mass, slugs

$m_s$  = mass of one sideframe, slugs  
 $m_w$  = wheelset mass, slugs  
 $r_o$  = wheel rolling radius at equilibrium, ft  
 $V$  = forward speed at equilibrium, fps or mph  
 $V_c$  = critical speed, fps or mph  
 $W_{APP}$  = axle load, lb  
 $x_c$  = lateral displacement of pseudo-car-body centroid, ft  
 $x_T$  = lateral displacement of truck centroid, ft  
 $x_{w_1}, x_{w_2}$  = lateral displacement of front and rear wheelset centroids on front truck relative to truck centerline, ft  
 $\Delta_1$  = coefficient of first-order term of series expansion of contact-angle difference function  
 $\delta_0$  = average contact angle at equilibrium, rad  
 $\theta_T$  = yaw displacement of truck frame, rad  
 $\theta_w$  = warp displacement of truck frame, rad  
 $\theta_{w_1}, \theta_{w_2}$  = yaw displacements of front and rear wheelsets relative to lines through ends of sideframes, rad  
 $\lambda_1$  = effective wheel conicity, rad  
 $\phi_c$  = roll displacement of pseudo-car body, rad

## Subscripts

$o$  = nominal value

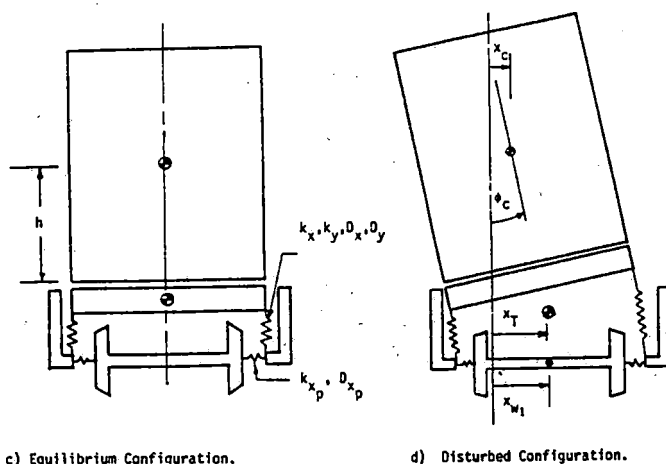


Fig. 1(c)(d) Schematic of 11-DOF model (front view).

modified by the addition of primary-suspension springs with stiffnesses corresponding approximately to those on the LIMRV vehicle [3]. The nominal car-body model is an empty 80-ton open-hopper car. The nominal model parameters for the 11-DOF model are listed in Table 1.

Most of this study was conducted using the simpler 11-DOF model, because one major objective was to identify trends in stability due to truck configuration rather than to identify the behavior of a specific vehicle. In addition, the 23-DOF model was more than 10 times as expensive to run on the computer as the 11-DOF model. However, certain results for the 11-DOF model were compared with those obtained using the 23-DOF model.

Table 1 Nominal design parameters for 11-degree-of-freedom model

Masses and Inertias			
$m_w = 76.6$ slugs (1117.9 kg)	$m_b = 36.1$ slugs (526.8 kg)	$I_{w1} = 53.1$ slug ft <sup>2</sup> (72.0 kg m <sup>2</sup> )	$I_{b2} = 178.6$ slug ft <sup>2</sup> (242.1 kg m <sup>2</sup> )
$I_{w2} = 448.5$ slug ft <sup>2</sup> (608.1 kg m <sup>2</sup> )	$I_{b1} = 178.6$ slug ft <sup>2</sup> (242.1 kg m <sup>2</sup> )	$m_s = 24.0$ slugs (350.2 kg)	$m_c = 551.0$ slugs (8041.2 kg)
$I_{s2} = 77.6$ slug ft <sup>2</sup> (105.2 kg m <sup>2</sup> )	$I_{c1} = 6500.0$ slug ft <sup>2</sup> (8812.8 kg m <sup>2</sup> )	Geometry	
$z = 2.8$ ft	$d = 3.25$ ft (0.991 m)	$r_o = 1.375$ ft (0.419 m)	$a = 2.46$ ft (0.750 m)
$h = 2.994$ ft (0.913 m)		Wheel/Rail Contact Parameters*	
$f_{11} = 994,670$ lb/wheel (4,426 x 10 <sup>5</sup> N/wheel)	$\delta_1 = 0.0$	$f_{12} = 4607$ lb ft/wheel (6245.3 N-m/wheel)	$\delta_o = 0.05$
$f_{22} = 77.5$ lb ft <sup>2</sup> /wheel (32.02 N-m <sup>2</sup> /wheel)	$\alpha_1 = 0.05$	$f_{33} = 1.153 \times 10^6$ lb/wheel (5.129 x 10 <sup>6</sup> N/wheel)	$\lambda_1 = 0.05$

\*Creep coefficients are obtained from Walker's linear theory.

Table 1 (Cont'd)

Suspension Parameters			
$k_{x_p} = 2.9 \times 10^5$ lb/ft (4.23 x 10 <sup>6</sup> N/m)	$k_{\theta_L} = 0.0$ lb-ft/rad (0.0 N-m/rad)	$D_{x_p} = 0.0$ lb sec/ft (0.0 N-sec/m)	
$k_{z_p} = 3.8 \times 10^5$ lb/ft (5.55 x 10 <sup>6</sup> N/m)	$D_{x_p} = 0.0$ lb sec/ft (0.0 N-sec/m)	$D_{z_p} = 0.0$ lb sec/ft (0.0 N-sec/m)	
$k_{AX} = 2.26 \times 10^6$ lb ft/rad (3.06 x 10 <sup>6</sup> N-m/rad)	$D_{AX} = 0.0$ ft-lb-sec/rad (0.0 N-m-sec/rad)	$D_x = 1.2645 \times 10^4$ lb sec/ft (1.8441 x 10 <sup>5</sup> N-sec/m)	
$k_x = 24,000$ lb/ft (350,000 N/m)	$D_y = 7587$ lb sec/ft (110,600 N-sec/m)	$D_{\theta_{CP}} = 2409$ ft-lb-sec/rad (3268 N-m-sec/rad)	
$k_y = 2.658 \times 10^5$ lb/ft (3.879 x 10 <sup>6</sup> N/m)	$D_{\theta_{CP}} = 2409$ ft-lb-sec/rad (3268 N-m-sec/rad)	$D_{\theta_W} = 9318$ ft-lb-sec/rad (12,640 N-m-sec/rad)	
$k_{\theta_{CP}} = 50.0$ lb ft/rad (67.6 N-m/rad)			
$k_{\theta_W} = 4.011 \times 10^6$ lb ft/rad (5.42 x 10 <sup>6</sup> N-m/rad)			
$k_{x_L} = 0.0$ lb/ft (0.0 N/m)			

$$W_{APP} = 12,695 \text{ lb} \\ (56,467.4 \text{ N})$$

$$V_c = 136.7 \text{ fps} \\ (41.5 \text{ m/sec})$$

## Analysis

The equations of motion describing the lateral dynamics of both the 11- and 23-DOF vehicles comprise a system of the form

$$[m]\{\ddot{x}\} + [c]\{\dot{x}\} + [k]\{x\} = \{0\}$$

For the 11-DOF vehicle the mass, damping, and stiffness matrices are 11 x 11, while in the case of the 23-DOF vehicle they are 23 x 23. As neither rail irregularities nor traversal of curves are considered, the right-hand side is identically zero. These equations are derived and presented in [1]. For the sake of brevity they are not reproduced here.

After Laplace-transforming the system of equations, a QR algorithm was used in a digital computer program, and the eigenvalues and eigenvectors were obtained.

## Results

The 11-DOF and 23-DOF models were validated by checking the behavior in limiting cases to existing models. For example, the primary-suspension stiffness of the 11-DOF model was made very large in an attempt to converge to a 5-degree-of-freedom (5-DOF) model that included a single truck with ball-joint approximations to the wheelset/sideframe connections that exist on a roller-bearing truck. The results of this validation process are shown in Fig. 2, where critical speed is plotted against nondimensional primary lateral stiffness for a constant ratio  $k_{x_p}/k_{z_p}$ . In all cases nondimensional values of parameters are obtained by normalization with the nominal parameter values. For primary lateral and longitudinal stiffnesses that are 100 times the nominal LIMRV values, the critical speed of the 11-DOF model is within 1 percent of that of the 5-DOF model. These high values of stiffnesses are of the order of those measured in tests conducted by Brenco [4] for roller-bearing connections. The frequency, damping, and mode shape of the least-damped or truck-hunting modes for the 5-DOF and stiff 11-DOF models are very similar. These results indicate that modeling the wheelset/sideframe connections as ball joints is adequate for stability analysis of roller-bearing trucks.

**Modified Freight Truck.** The freight-truck model with the primary suspension was called the modified freight truck. Variations in the primary-suspension stiffnesses were made with this configuration to determine the sensitivity of critical speed to these changes.

The critical speed of the model for the nominal primary-suspension stiffness is 93 mph (150 km/hr), about 10 mph (16 km/hr) higher than the critical speed for the roller-bearing truck (RBT) configuration with high primary-suspension stiffness. At one-half the nominal



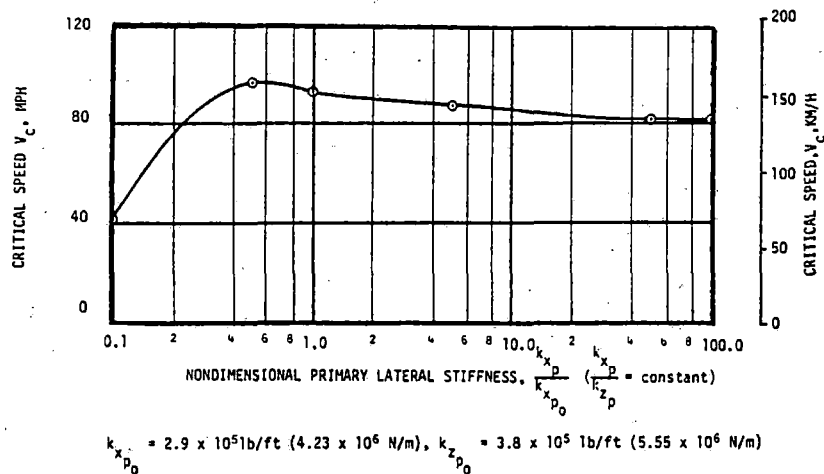


Fig. 2 Effect of primary-suspension stiffness on critical speed of 11-DOF model (nominal warp stiffness)

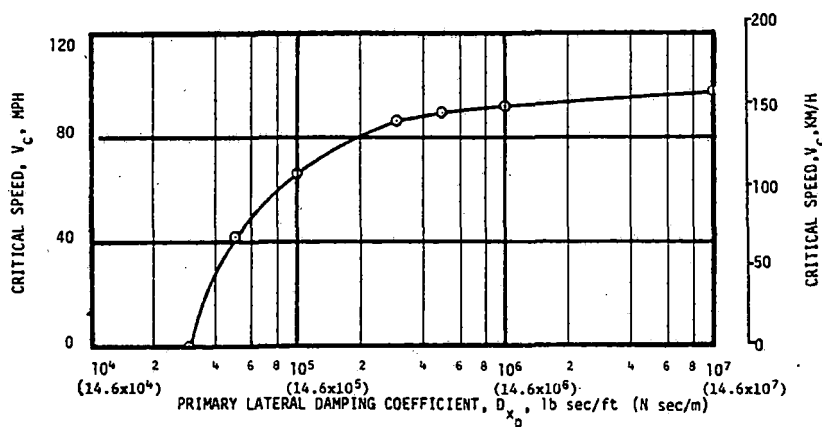


Fig. 3 Effect of primary lateral damping on critical speed of 11-DOF model ( $k_{xp}/k_{x_{p0}} = 0, k_{zp}/k_{z_{p0}} = 100$ , nominal warp stiffness)

values of primary-suspension stiffness the critical speed is about 15.5 percent higher than that of the RBT. The nominal value of warp stiffness was used for the model.

**Plain-Bearing Truck.** In an attempt to model a plain-bearing truck, the longitudinal primary-suspension stiffness was made stiff by increasing it to 100 times the nominal value. The lateral primary-suspension stiffness was set equal to zero, and the lateral primary damping coefficient was varied. The effect of lateral primary damping on critical speed for this configuration is shown in Fig. 3.

The critical speeds of freight cars with plain-bearing trucks have been observed to be about 10 mph (16 km/hr) lower than for similar freight cars with roller-bearing trucks [5]. To achieve this 10-mph (16-km/hr) decrease in critical speed for the plain-bearing truck with a zero lateral primary stiffness, a value of damping for the lateral primary suspension (per side) of  $4.5 \times 10^4 \text{ lb-s/ft } (6.57 \times 10^5 \text{ N-s/m})$  was necessary. This value of primary lateral damping seems rather high. Assumptions that seem reasonable for calculating an equivalent viscous damping for friction in the plain bearings are as follows: (1) the amplitude of wheelset lateral displacement relative to the journal box (zero to peak) is 0.5 in. (1.3 cm); (2) the frequency of oscillation near the critical speed is 1.5 Hz; (3) the coefficient of friction between the axle and journal box is 0.16 (corresponding to steel sliding on lubricated steel); (4) the normal load at each journal box is equal to one-half of the axle load. The calculated equivalent viscous damping using these assumptions is about  $3.3 \times 10^3 \text{ lb-s/ft } (4.81 \times 10^4 \text{ N-s/m})$ , which is about 90 percent less than the value that gives a critical speed thought to be representative of a plain-bearing truck.

The low value of lateral primary damping coefficient obtained from the equivalent viscous damping approximation using the four abovementioned "reasonable" assumptions was used, and lateral primary stiffness was added to check the effect on the critical speed of the model. Since the only lateral restoring force existing for a plain-bearing configuration is provided at large lateral wheelset displacements by stops, the effective lateral primary stiffness provided by the plain bearing is at best very small for small displacements. A critical speed thought to be representative of a plain-bearing truck was reached for a value of lateral primary stiffness equal to 20 percent of the nominal LIMRV value. This value is in all likelihood too large for small amplitudes of wheelset lateral motion where contact with stops does not occur.

If the vehicle is in sustained hunting or limit-cycle motion, it is reasonable to use describing functions [6] to obtain equivalent linear values for nonlinear suspension characteristics [7]. As previously mentioned, the critical speeds of typical freight cars equipped with plain-bearing trucks have been observed to be about 10 mph (16 km/hr) less than when equipped with roller-bearing trucks. However, critical speed in this context refers to the speed at which sustained hunting oscillations (i.e., limit cycles) occur. This is to be contrasted with the use of the term critical speed to refer to the speed at which a linearized set of equations representing these types of systems exhibits instability. Law [8] has used the term linear critical speed to distinguish this latter case from the former.

A value of lateral primary stiffness of 20 percent of the nominal LIMRV value is obtained via use of the describing function when a

ratio of lateral wheelset amplitude (relative to the journal boxes) to available clearance of 1.015 is used. The actual value of lateral stiffness obtained via this approach is about 0.2 percent of the stiffness of the stops, which is assumed to be approximately that of a roller-bearing connection [4, 9]. These figures do not seem to be unrealistic, and in the absence of actual test data they seem to lend credence to the plain-bearing truck model and assumed suspension values.

A stability analysis addresses the question of stability of motion following a small disturbance from equilibrium. The model of the wheelset/sideframe connection (i.e., zero stiffness) used for the plain-bearing truck is therefore reasonable for a stability analysis, as small motions would not result in contact of the axle with the stops. Thus the high value of damping would be appropriate for use. For this study the latter model is chosen as the plain-bearing truck model (i.e.,  $k_{xp} = 0$ ,  $D_{xp} = 4.5 \times 10^4$  lb-s/ft or  $6.57 \times 10^5$  N-s/m). This high value of damping then implies very small wheelset displacements relative to the journal box.

A linear iterative technique, together with describing function descriptions of the suspension nonlinearities, has been used by Cooperrider et al. [7] to find the amplitude and frequency of limit cycles and the speeds at which they occur. This technique could be employed to predict the limit-cycle oscillations for plain-bearing configurations where contact of the wheelset with the bearing stops occurs.

The effect of warp stiffness on the critical speed of the plain-bearing

truck model is shown in Fig. 4. The critical speed decreases rapidly as the warp stiffness is decreased or increased from the nominal value. Thus the critical speed for this model cannot be increased by modifying the warp stiffness. Similar results were obtained by Cooperrider and Law [2] for a 9-degree-of-freedom (9-DOF) model of a freight car with a roller-bearing truck.

The effect of lateral primary stiffness on critical speed for a stiff longitudinal primary suspension and nominal warp stiffness is shown in Fig. 5. The critical speed is zero for lateral primary stiffness below about 1000 times less than the nominal stiffness. The critical speed increases with increasing lateral stiffness until the nominal LIMRV stiffness is reached. Then as the lateral primary stiffness is increased above the nominal value, the critical speed decreases slightly and approaches the critical speed for the roller-bearing truck configuration.

**Rigid-Truck Frame.** The effects of lateral and longitudinal primary-suspension stiffness on critical speed are shown in Fig. 6 for a value of warp stiffness that is  $10^4$  times higher than the nominal freight-truck value. This value of warp stiffness makes the truck frame effectively rigid. For the nominal primary suspension the critical speed for the rigid-frame truck is about 87 mph (140 km/hr), 6.5 percent lower than for the modified freight-truck model with nominal warp stiffness. For values of primary suspension from 10 percent of nominal values to full nominal values, the truck has characteristics typical of

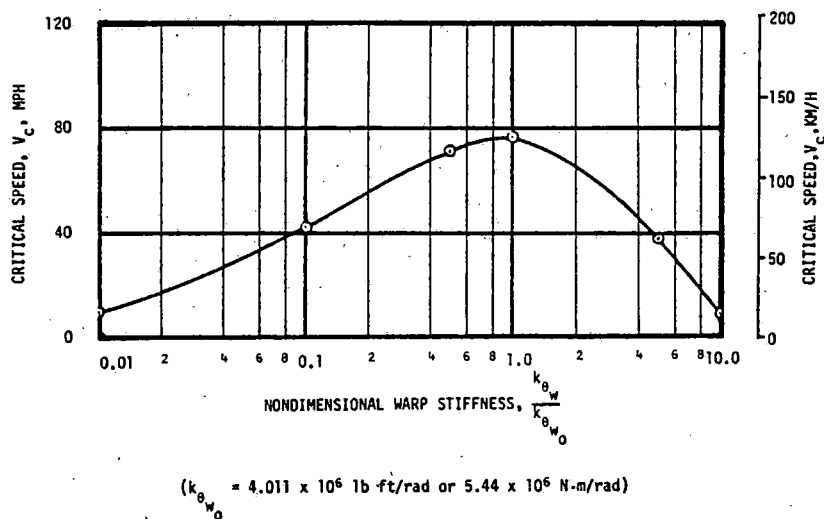


Fig. 4 Effect of warp stiffness on critical speed of 11-DOF model for plain-bearing truck configuration

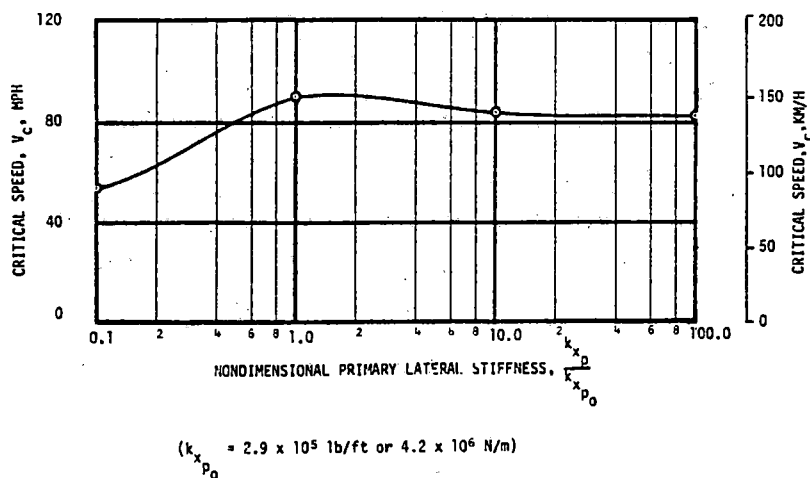


Fig. 5 Effect of primary lateral stiffness on critical speed of 11-DOF model ( $k_w/k_{w0} = 100$ , nominal warp stiffness)

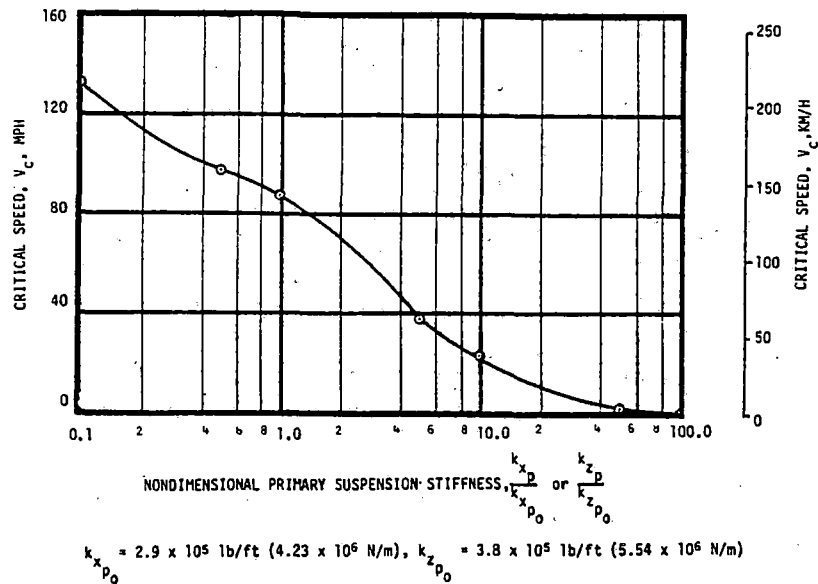


Fig. 6 Effect of primary-suspension stiffness on critical speed of 11-DOF model ( $k_{\theta}/k_{\theta_0} = 10^4$ )

passenger trucks, i.e., a rigid-truck frame and soft primary suspension.

The critical speed decreases with increasing primary stiffness. For a stiff primary suspension and a stiff truck frame, the truck is effectively rigid. The critical speed is very low due to the low secondary yaw stiffness used for the model (50 lb-ft/rad or 68 N-m/rad). As shown by Clark and Law [10], the secondary yaw stiffness is a stabilizing effect for a vehicle with rigid trucks. When the secondary yaw stiffness was increased ( $k_{\theta_{CP}} = 2.66 \times 10^5 \text{ lb-ft/rad}$  or  $3.61 \times 10^5 \text{ N-m/rad}$ ) the critical speed for the rigid-truck model increased to about 30 mph (48 km/hr).

There is very little yaw-restoring torque provided at the centerplate for conventional freight cars. Thus a rigid truck design with a conventional centerplate connection is not desirable from the point of view of low, and even zero, critical speed. It would also exhibit poor curving performance due to the constraint placed on motions of the wheelsets relative to the truck frame.

**Comparison of Truck Designs.** Thus roller-bearing truck, plain-bearing truck, passenger truck, rigid truck configurations and a model of a freight truck with primary-suspension elements have been obtained with the 11-DOF model by adjusting the primary-suspension parameters and the warp stiffness. The roller-bearing truck (RBT) model consists of a stiff primary suspension with stiffnesses that are 100 times the nominal values, as well as nominal warp stiffness. The plain-bearing truck (PBT) model consists of stiff longitudinal primary suspension (100 times the nominal value), zero lateral primary stiffness, a lateral primary damping coefficient of  $4.5 \times 10^4 \text{ lb-s/ft } (6.57 \times 10^5 \text{ N-s/m})$ , and nominal warp stiffness. The passenger-truck (PT) model consists of the nominal primary suspension and a high warp stiffness ( $10^4$  times the nominal value), which corresponds to a truck frame that is effectively rigid. The nominal model consists of a 70-ton ASF Ride Control truck frame, but a primary suspension typical of the LIMRV vehicle. This may be thought of as a modified freight-truck (MFT) model. The stabilities of these four models are now compared.

The frequency and the damping ratio of the least-damped or hunting mode for the four models are shown in Fig. 7. The frequency is almost linear with speed for each model. At a given speed the frequency for the MFT model is slightly higher than the frequencies for other models. The frequency of the RBT model is the lowest of the four cases. The frequencies of the PBT and PT models are about the same. The damping ratios for the nominal, RBT, and PT models decrease with speed. The damping ratio for the PBT model increases

with speed for speeds up to about 35 mph (56 km/hr), and then decreases with speed.

The critical speed for each model is the speed at which the damping ratio changes sign from positive to negative. As indicated by the damping-ratio-versus-speed curves in Fig. 7, the MFT model has the highest critical speed (93.2 mph or 150 km/hr), followed by the PT model (87.0 mph or 140 km/hr), the RBT model (83.2 mph or 134 km/hr), and the PBT model (76.4 mph or 123 km/hr). For a 50 percent decrease in the primary-suspension stiffnesses of the PT model the critical speed of the PT model is about 37 percent higher than the

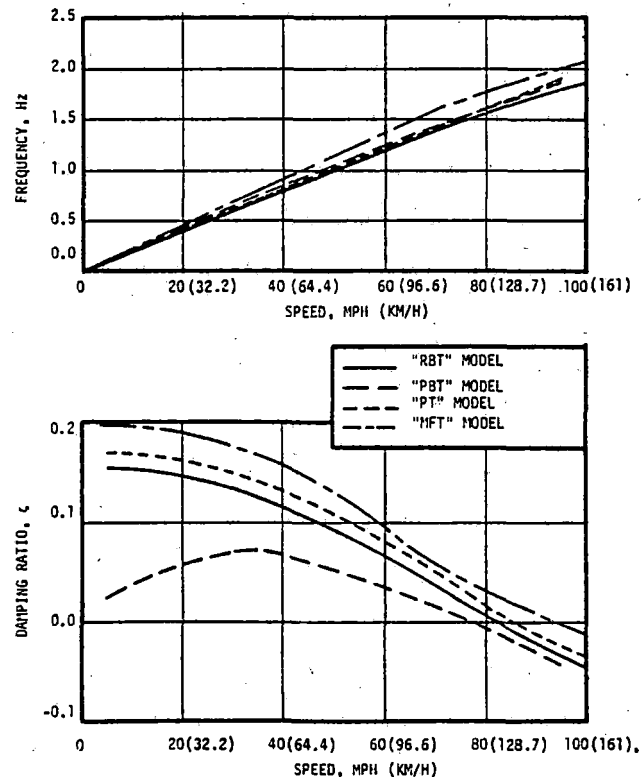


Fig. 7 Frequency and damping ratio versus speed for different truck configurations of 11-DOF model

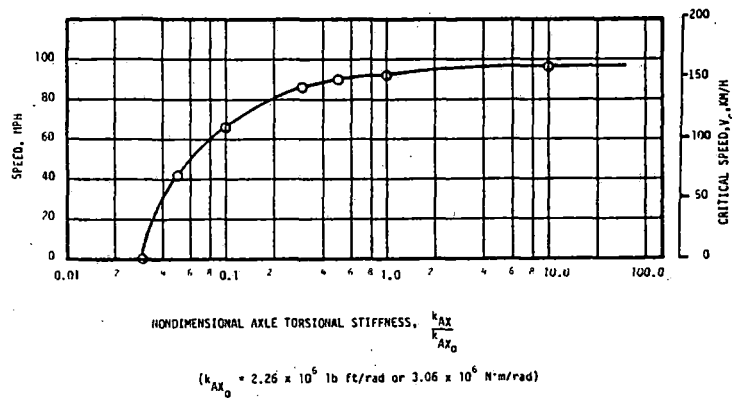


Fig. 8 Effect of axle torsional stiffness on critical speed of nominal 11-DOF model

highest critical speed of the MFT model.

**Effect of Axle Torsional Stiffness.** The effect of axle torsional stiffness on the critical speed of the nominal model is shown in Fig. 8. The results are quite similar to the results obtained by Doyle and Prause [11] for their vehicle model. The critical speed decreases with decreasing axle torsional stiffness and is zero below an axle torsional stiffness that corresponds to an axle diameter of about 2.5 in. (6.4 cm) (typical wheelset axles are about 6 in. or 15.2 cm in diameter). The unstable mode is similar to the hunting mode for the MFT model, but the amplitudes of the axle torsional displacements vary with the stiffness.

For the case of independently rotating wheels, or zero torsional stiffness, the solution indicates a zero eigenvalue. This implies that there is no preferred equilibrium point and that the wheelsets may wander randomly from side to side in response to track irregularities. While there is no longer a possibility of severe hunting with independently rotating wheels, there does exist the possibility of greater flange wear. This should be investigated carefully before utilizing independently rotating wheels to avoid hunting. The same type of behavior was predicted when cylindrical wheels were used, and the same precautions discussed above should be observed.

**Wheelset Interconnection Study.** The idea of interconnecting the wheelsets of a freight truck has been suggested recently by List [12] and Scheffel [13, 14] with the objective of increasing the critical speed for hunting and improving curving performance. Wickens [15] has discussed the stability and curving performance of generalized multi-axle vehicles having interconnected wheelsets and has indicated that aspects of the idea were utilized as early as 1877. Weinstock [16] has also analyzed the effects on the kinematic modes of shear and bending spring interconnections between wheelsets of a two-axle vehicle.

The 11-DOF model was modified to study the stability with interconnected wheelsets. A schematic of the wheelsets without the rest of the vehicle is shown in Fig. 9.

The wheelsets are assumed to be connected to each other by a yoke or frame. The mass and inertia of the frame are lumped into the two wheelsets. For simplicity, the effect of the frame on the radius of gyration of the wheelset is neglected, and only the added mass affects the yaw moment of inertia of the wheelsets. As a result, the mass-and-yaw moment of inertia of each wheelset is increased by 20 percent. A primary suspension is assumed at the wheelset/sideframe connections. The lateral stiffness of the primary suspension elements was kept the same as listed in Table 1. However, the value of the longitudinal stiffness was decreased to  $k_{zp} = 72,000 \text{ lb/ft}$  ( $1.05 \times 10^6 \text{ N/m}$ ), and the axle torsional stiffness was increased by a factor of  $10^3$ .

The model is intended to be generic and does not represent any specific design. Some of the nominal design parameters are "ballpark" estimates of the Prototype I truck discussed by List, et al. [12].

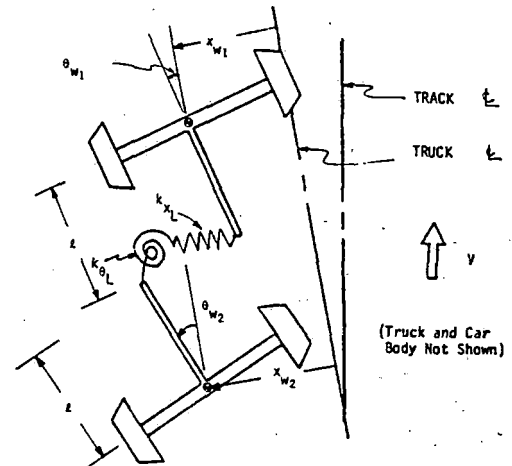


Fig. 9 Schematic of interconnected-wheelset model (plan view)

The study performed with this model examined the effect on critical speed of variations in the bending and shear stiffnesses  $k_{\theta L}$  and  $k_{xL}$ , respectively, between the wheelsets. As shown in Fig. 9, the interconnection stiffnesses  $k_{\theta L}$  and  $k_{xL}$  are in addition to the other primary and secondary suspension elements in the truck. The effects of shear stiffness on critical speed for three values of bending stiffness are shown in Fig. 10.

The critical speed of the vehicle with increased wheelset mass-and-yaw moment of inertia (due to the interconnection yoke or frame), but with zero values for  $k_{xL}$  and  $k_{\theta L}$  and reduced  $k_{zp}$ , was found to be 70 mph (113 km/hr). At a value of interconnection bending stiffness of  $1.67 \times 10^6 \text{ ft-lb/rad}$  ( $2.26 \times 10^6 \text{ N-m/rad}$ ), critical speed exceeded 70 mph (113 km/hr) for all values of shear stiffness explored. At a higher value of bending stiffness ( $3.34 \times 10^6 \text{ ft-lb/rad}$  or  $4.54 \times 10^6 \text{ N-m/rad}$ ), critical speed exceeded 70 mph (113 km/hr) up to a value of shear stiffness of about  $7 \times 10^5 \text{ lb/ft}$  ( $1.02 \times 10^7 \text{ N/m}$ ). Above this value of shear stiffness, critical speed decreased to about 60 mph (97 km/hr). For values of bending stiffness of  $1.67 \times 10^6 \text{ ft-lb/rad}$  ( $2.26 \times 10^6 \text{ N-m/rad}$ ) and  $3.34 \times 10^6 \text{ ft-lb/rad}$  ( $4.53 \times 10^6 \text{ N-m/rad}$ ), the curves of critical speed versus shear stiffness exhibited maximum values of 98 and 92 mph (158 and 148 km/hr), respectively, near a shear stiffness value of  $10^5 \text{ lb/ft}$  ( $1.46 \times 10^6 \text{ N/m}$ ). The most important result, however, is that for zero bending stiffness, critical speed increased from about 76 to 198 mph (122 to 319 km/hr), as shear stiffness increased from about  $10^4$  to  $10^6 \text{ lb/ft}$  ( $1.46 \times 10^5$  to  $1.46 \times 10^7 \text{ N/m}$ ).

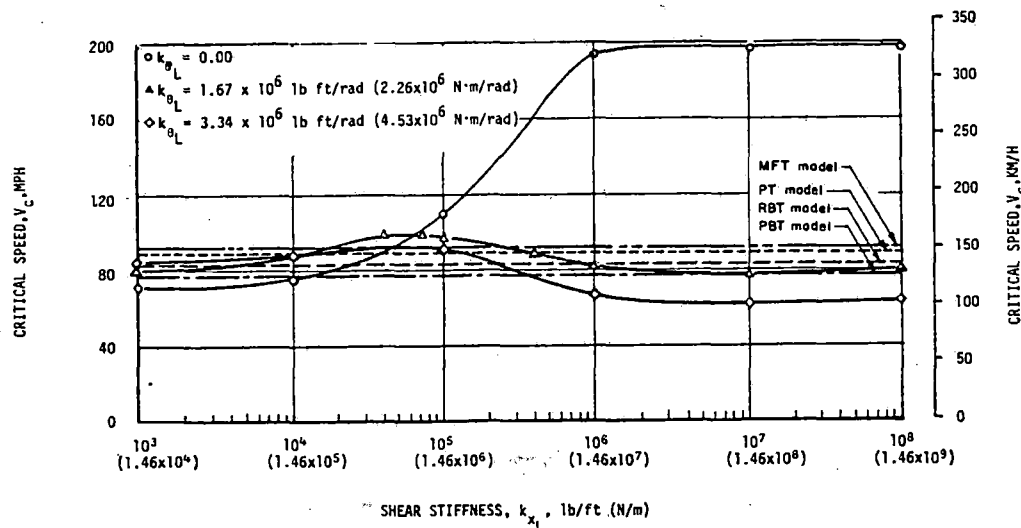


Fig. 10 Effect of shear stiffness on critical speed of 11-DOF model with interconnected wheelsets for different values of bending stiffness

However, as Weinstock [16] noted in his study, a change of creep coefficient can dramatically affect the truck behavior. At a value of  $k_{xL} = 10^8$  lb/ft ( $1.459 \times 10^9$  N/m),  $k_{\theta L} = 0$ , and nominal values for other parameters, we found a critical speed of about 198 mph (319 km/hr) for the values of creep coefficients as listed in Table 1. When the values of creep coefficients were decreased by 50 percent for this configuration the critical speed dropped from 198 mph to about 70 mph (319 to 113 km/hr). As actual values of the creep coefficients from about 50 to 100 percent of the full Kalker values are expected in practice, vehicle designers should consider a large range for values of creep coefficients. This large sensitivity to creep coefficient has also been found for freight cars equipped with conventional roller-bearing trucks [2].

Two additional cases for  $k_{\theta L} = 0$  were examined. For each of these the longitudinal primary stiffness was set equal to zero. Thus the total bending stiffness between axles was zero. In the first of these additional cases  $k_{xL} = 0$ , and in the second  $k_{xL} = 10^8$  lb/ft ( $1.459 \times 10^9$  N/m). In the first case two unstable oscillatory modes were present at all speeds investigated from 5 to 105 mph (8–170 km/hr), with one mode more lightly damped than the other. Each mode has a frequency very close to the kinematic frequency of a single isolated wheelset. In the second case where  $k_{xL} = 10^8$  lb/ft ( $1.459 \times 10^9$  N/m), only one unstable oscillatory mode occurred, again at all speeds examined from 5 to 105 mph (8–170 km/hr) and at a frequency very close to the kinematic frequency of a single isolated wheelset.

To realize the benefits of wheelset interconnection with this configuration, it appears necessary to have a shear interconnection that is effectively rigid, as well as some optimum value of total interaxle bending stiffness as determined by the interconnection bending stiffness and the longitudinal primary stiffnesses.

We calculated the critical speed for the vehicle with all three values of bending stiffness at a shear stiffness of  $1 \times 10^{10}$  lb/ft ( $1.46 \times 10^{11}$  N/m). The computed values of critical speed for bending stiffnesses of 0,  $1.67 \times 10^6$ , and  $3.34 \times 10^6$  lb-ft/rad (0,  $2.26 \times 10^6$ , and  $4.53 \times 10^6$  N-m/rad) are 199, 80, and 61 mph (320, 129, and 98 km/hr), respectively. Thus even at this high level of shear stiffness the critical speed for zero bending stiffness shows no signs of decreasing.

As expected, the shape of the least-damped mode for the vehicle with interconnected wheelsets changes with increasing shear stiffness. At zero bending stiffness with shear stiffness above about  $1 \times 10^6$  lb/ft ( $1.46 \times 10^7$  N/m) there are large truck and car-body lateral motions, with the car body lagging the truck by about 60 deg. The wheelset lateral motions relative to the truck are each about 20 percent of the magnitude of truck lateral motions; they are in phase with one another, and they lead the truck lateral motions by about 130 deg. Truck yaw and car roll are about the same magnitude, and they lead truck

lateral motions by about 120 and 60 deg, respectively. Truck warp is very small and is about 7 percent of truck yaw. Front-wheelset yaw and rear-wheelset yaw relative to the ends of the sideframes are about one-third of the magnitude of truck yaw and are out of phase with each other. Front-wheelset yaw lags truck lateral motion by about 90 deg. A sketch of this mode shape is shown in Fig. 11.

At a value of shear stiffness of  $1 \times 10^4$  lb/ft ( $1.46 \times 10^5$  N/m) and zero bending stiffness, the shape of the least-damped mode is very similar to that of a vehicle with no wheelset interconnection but with all other parameters identical.

Both Wickens [15] and Weinstock [16] have developed general 4-degree-of-freedom models of two wheelsets interconnected by shear- and bending-stiffness elements. Weinstock examined the kinematic motions of the system (i.e., inertia and mass terms neglected) and

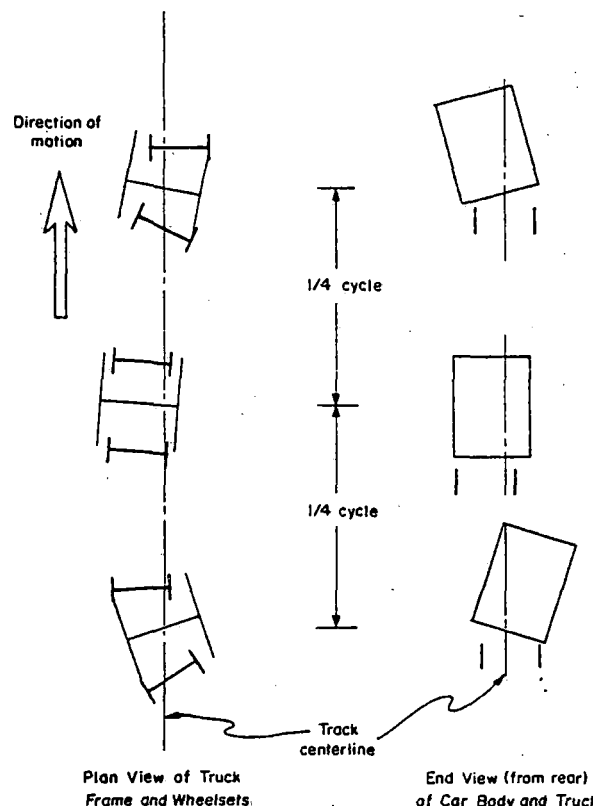


Fig. 11 Mode shape of least-damped mode for model with interconnected wheelsets

found that the damping ratio of one mode, when plotted against the nondimensional interconnection lateral stiffness for various constant ratios of nondimensional yaw to lateral interconnection stiffness, exhibited a distinct maximum value. He also noted that for small values of either the lateral or the yaw interconnection stiffness the solution was the kinematic oscillation of a single wheelset. Wickens, in an approximate solution to the full set of dynamic equations, found two oscillatory modes, the frequency of each being the kinematic frequency of a single wheelset. He found that in general the damping of both oscillations is positive at low speeds. As speed increases, the damping increases and then decreases until one mode becomes unstable. In the case where the total bending stiffness between axles is zero, Wickens found the critical speed to be zero, with the vehicle undergoing a neutrally damped steering oscillation at the kinematic frequency. The value of interconnection shear stiffness did not affect this result. Wickens also examined the limiting case of zero bending stiffness and infinite shear stiffness and found the solution to contain a zero eigenvalue, which would imply neutral stability and no preferred equilibrium position.

Our results, as described above for the full dynamic case of the vehicle having a truck with interconnected wheelsets (as well as a truck frame), show many similarities to those obtained by Weinstock and Wickens for simpler, generalized models. Our cases with zero values for interconnection bending stiffness and longitudinal primary stiffness, in having a slightly unstable oscillation at wheelset kinematic frequency, are similar to both Weinstock's and Wickens' results. We found that at  $k_{xL} = 10^8 \text{ lb/ft}$  ( $1.459 \times 10^9 \text{ N/m}$ ), critical speed increases from zero at a value of total bending stiffness (interconnection bending plus longitudinal primary stiffnesses) of zero, reaches a value of about 198 mph (319 km/hr) at an intermediate value of total bending stiffness, and then decreases to lower values as total bending stiffness increases further. This is very similar to Weinstock's results for the damping of one of the kinematic modes.

Scheffel [13] has analyzed both a 4-degree-of-freedom two-axle vehicle with interconnected wheelsets and a 5-degree-of-freedom two-axle vehicle identical to the former vehicle except for an added body mass capable of lateral motions. For both Scheffel's vehicles the wheelsets were interconnected directly by a shear connection and indirectly through massless sideframes by longitudinal primary-stiffness elements. Scheffel found, as did Wickens, that the solution exhibited a zero eigenvalue or neutral stability for infinite interconnection shear stiffness and zero longitudinal primary stiffness. (Wickens' analogous case is that for zero bending stiffness.)

**Complete Freight Car.** A limited number of cases were investigated for the 23-DOF model of the complete car with two trucks. As mentioned previously, each truck had 9 degrees of freedom, and the car body had 5 degrees of freedom, permitting an approximate consideration of the effects of car-body lateral bending and torsion.

The computer time required for investigation of the stability of the 23-DOF model was significantly more than that required for the 11-DOF model. Consequently, only roller-bearing truck configurations were used, while investigations concentrated on the effects of car-body flexibility, car-body type, and car-body center-of-gravity location.

These results have been reported [1]; since they are not germane to the main topic of this paper, they will not be discussed here. However, a complete freight-car model and an accompanying computer program have been developed that may be used for truck design studies as were described above for the 11-DOF model.

It should not be inferred that the actual values of critical speed obtained for the 11-DOF model would match those for a complete car of the "same" design. The 11-DOF model is used for the sake of economy to investigate stability trends. After possible design choices are identified with the simpler model, the complete car model should always be used to check conclusions.

## Conclusions

1 The 11-DOF model has been checked in a limiting case against an existing 5-DOF model with ball-joint wheelset/sideframe connections. The behaviors of the two models were essentially identical.

Thus it appears that the assumption of ball-joint wheelset/sideframe connections is adequate for stability analyses of roller-bearing freight trucks.

2 The versatility of the 11-DOF model has been demonstrated. By adjusting primary-suspension parameters and warp stiffness, several different truck configurations may be obtained. These include a roller-bearing truck, a plain-bearing truck, a passenger truck, and a freight truck with primary suspension. A configuration with interconnected wheelsets may also be obtained.

3 The addition of primary suspension to a freight truck can improve or degrade the stability. For values of primary-suspension stiffness below 30 percent of the nominal LIMRV values the critical speed is lower than that for the RBT model. Near the nominal values the critical speed is as much as 15.5 percent higher than that for the RBT model. Thus it appears that the addition of primary suspension can significantly improve the stability of a freight truck.

4 With the exception of the interconnected-wheelset configuration, the passenger-truck (PT) model offers the greatest improvement in stability over the roller-bearing (RBT) model. For decreases of more than 50 percent in the lateral and longitudinal primary stiffnesses of the PT model from the nominal LIMRV values, the PT model has the highest critical speed of the four models considered without wheelset interconnection, followed by the MFT, RBT, and PBT models.

5 The effect of the nominal axle torsional stiffness on stability for all configurations of the 11-DOF model is practically negligible. The critical speed of the nominal model decreases with decreasing axle torsional stiffness and is zero for a stiffness corresponding to an axle diameter of about 2.5 in. (6.4 cm).

6 The use of interconnected wheelsets can improve freight-car stability. From the limited parameter study reported here, it appears that the best choice of interconnection from the point of view of stability (curving was not examined) is that of zero bending stiffness and very high shear stiffness. Although no attempt was made to find an optimum combination of interconnection bending stiffness and longitudinal primary stiffness (to yield a total interaxle bending stiffness), an optimum value probably does exist, as indicated by the trends of our results. The critical speed for this configuration is quite sensitive to the values of the creep coefficients.

## Acknowledgments

The work described in this paper was supported by the U.S. Department of Transportation under Contract DOT-OS-40018. The Association of American Railroads (AAR) Research Center is a co-operating industry on this project. The AAR supplied many of the values of the parameters used. They have also given assistance in many other ways too numerous to mention.

Dr. Neil Cooperrider of Arizona State University is co-principal investigator on the project. He has contributed significantly to the work on which this paper is based.

Opinions expressed in this paper are those of the authors and do not necessarily represent the position of the Department of Transportation or the AAR, while conducting the work described in this paper, both authors were affiliated with Clemson University.

## References

- 1 Hadden, J. A., "The Effects of Truck Design and Component Flexibility on the Lateral Stability of Railway Freight Vehicles," MS thesis, Department of Mechanical Engineering, Clemson University, Clemson, S.C., 1976.
- 2 Cooperrider, N. K., Law, E. H., "Parametric Study of Freight Car Stability—Preliminary Results," informal report, Contract DOT-OS-40018, Department of Mechanical Engineering, Arizona State University, Tempe, Ariz., Sept. 9, 1975.
- 3 Pearce, T. G., and May, B. J., "A Study of the Stability and Dynamic Response of the Linear Induction Motor Test Vehicle," FRA-RT-70-25, Sept. 1969, Office of High Speed Ground Transportation, Washington, D.C. (PB-192718).
- 4 Moyar, G. J., "Summary of Freight Car Journal Roller Bearing Characterization," presented at the Second Conference on Track/Train Dynamics Interaction, Chicago, Ill., Dec. 4-6, 1974.
- 5 Private telephone conversation between Howard Dwyer and E. H. Law, Nov. 26, 1975.
- 6 Gelb, A., and Vander Velde, W. E., *Multiple-Input Describing Functions and Nonlinear System Design*. McGraw-Hill, New York, 1968.

- 7 Cooperrider, N. K., Hedrick, J. K., Law, E. H., and Malstrom, C. W., "The Application of Quasi-Linearization to the Prediction of Nonlinear Railway Vehicle Response," presented at the IUTAM Symposium on Vehicle Mechanics, Delft, The Netherlands, Aug. 1975.
- 8 Law, E. H., "Analysis of the Nonlinear Dynamics of a Railway Vehicle Wheelset," PhD thesis, Department of Mechanical Engineering, University of Connecticut, Storrs, Conn., 1971.
- 9 Raven, F. H., *Automatic Control Engineering*, McGraw-Hill, New York, 1968.
- 10 Clark, J. W., and Law, E. H., "Investigation of the Truck Hunting Instability Problem of High-Speed Trains," report D110294-2, United Aircraft Research Laboratories, East Hartford, Conn., Aug. 1966.
- 11 Doyle, G. R., and Prause, R. H., "Hunting Stability of Rail Vehicles With

Torsionally Flexible Wheelsets," ASME Paper No. 75-WA/RT-2.

12 List, H. A., Caldwell, W. N., and Marcotte, P., "Proposed Solutions to the Freight Car Truck Problems of Flange Wear and Truck Hunting," ASME Paper No. 75-WA/RT-8.

13 Scheffel, H., "The Hunting Stability and Curving Ability of Railway Vehicles," *Rail International*, Feb. 1974, pp. 154-176.

14 Scheffel, H., "A New Design Approach for Railway Vehicle Suspension," *Rail International*, Oct. 1974, pp. 638-651.

15 Wickens, A. H., "Steering and Dynamic Stability of Railway Vehicles," *Vehicle System Dynamics*, Vol. 5, No. 1-2, Aug. 1975, pp. 15-46.

16 Weinstock, H., "Analyses of Rail Vehicle Dynamics in Support of Development of the Wheel Rail Dynamics Research Facility," U.S. Department of Transportation Report UMTA-MA-06-0025-73-2, June 1973 (PB222654).

## CONTENTS (CONTINUED)

- 151 Torsional Amplitude Growth With Resonant Forcing (76-WA/DE-20)  
S. Doughty
- 153 The Use of a Random Algorithm for Dynamic Optimization of Mechanisms (76-WA/DE-22)  
B. Z. Sandler
- 157 A Computer Simulation Model for Determining Fleet Size and Composition (76-WA/Mgt-1)  
G. C. Schultz and E. E. Enscoe, Jr.
- 162 Effects of Truck Design on Hunting Stability of Railway Vehicles (76-WA/RT-1)  
J. A. Hadden and E. H. Law
- 172 Influence of Nonlinear Wheel/Rail Contact Geometry on Stability of Rail Vehicles (76-WA/RT-2)  
R. Hull and N. K. Cooperrider
- 186 Influence of Axle Load, Track Gauge, and Wheel Profile on Rail-Vehicle Hunting (76-WA/RT-3)  
D. N. Hannebrink, H. S. H. Lee, H. Weinstock, and J. K. Hedrick
- 196 Performance Characteristics of Freight-Car Trucks Determined Through Road Testing (76-WA/RT-4)  
R. Byrne and J. A. Andresen
- 206 Numerical Solution of a Deep-Drawing Problem (76-WA/Prod-3)  
E. I. Odell and W. E. Clausen
- 210 Optimization of Cutting Conditions for Multi-Pass Operations Considering Probabilistic Nature in Machining Processes (76-WA/Prod-4)  
K. Iwata, Y. Murotsu, and F. Oba
- 218 Stochastic Geometry of Anisotropic Random Surfaces With Application to Coated Abrasives (76-WA/Prod-9)  
S. M. Pandit, F. Nassirpour, and S. M. Wu
- 225 Cut-Forming: A New Method of Producing Wire (76-WA/Prod-12)  
T. Hoshi and M. C. Shaw
- 229 Assessment of Deep-Drawability and Stretchability by Bulge Test of Concentrically Grooved Metal Disks (76-WA/Prod-14)  
N. Kawai and Y. Kurosaki
- 237 On the Doubly Regenerative Stability of a Grinder: The Combined Effect of Wheel and Workpiece Speed (76-WA/Prod-19)  
R. A. Thompson
- 242 The Frictional Mechanism on the Surface of Metal Being Plastically Deformed by Drawing (76-WA/Prod-22)  
N. Kawai, T. Nakamura, and M. Iwata
- 250 Stiffness of Machine Tool Joints: A Random-Process Approach (76-WA/Prod-23)  
T. R. Thomas and R. S. Sayles
- 257 On the Mechanics of Tapping by Cutting (76-WA/Prod-25)  
W. E. Henderer
- 263 High-Speed Films of the Incipient Cutting Process in Machining at Conventional Speeds (76-WA/Prod-26)  
J. H. L. Thé
- 269 Rigidity Analysis and Optimization of Warren Beams in Torsion (76-WA/Prod-32)  
R. C. Bahl, S. Chandra, and P. C. Pandey
- 274 Design of a Fiber Optic Pressure Transducer (75-WA/DE-8)  
R. H. Pahler, Jr. and A. S. Roberts, Jr.
- 281 Fracture and Wear as Factors Affecting Stochastic Tool-Life Models and Machining Economics (75-WA/Prod-8)  
S. Rossetto and R. Levi
- 287 Discussion and Closures on Previously Published Papers

**D. N. Hannebrink**

Research Assistant,  
Mechanical Engineering,  
Massachusetts Institute of Technology,  
Cambridge, Mass.

**H. S. H. Lee**

Mechanical Engineer,  
Transportation Systems Center,  
U. S. Department of Transportation,  
Cambridge, Mass.

**H. Weinstock**

Mechanical Engineer,  
Transportation Systems Center,  
U. S. Department of Transportation,  
Cambridge, Mass.

**J. K. Hedrick**

Assoc. Professor,  
Mechanical Engineering,  
Massachusetts Institute of Technology,  
Cambridge, Mass.  
Assoc. Mem. ASME

# Influence of Axle Load, Track Gage, and Wheel Profile on Rail-Vehicle Hunting

*Analyses have been conducted on the influence of axle load, track gage, and wheel contour on the hunting behavior of simplified models of wheelsets for typical freight- and passenger-car suspensions. The capability of the wheel flange to limit hunting oscillations is found to increase with wheel axle load. The use of worn wheel contours or excessively tight gage is found to increase the susceptibility of the wheelset to excessive and unstable hunting oscillations. For freight-car applications, coulomb friction in the suspension (e.g., constant-contact side bearings) may act to increase the range of speeds over which hunting will not occur and may permit operation at higher speeds for extremely straight track. However, if track irregularities are sufficient to cause a breakout of the friction, drastic hunting oscillations leading to derailment can occur. Regions of stable limit-cycle hunting and unstable operating conditions are defined. Computational algorithms and computer programs for predicting the boundaries of stable, unstable, and limit-cycle behavior for the wheelset and more complex rail-car analytic models, using the describing-function type of analysis, are presented and reviewed.*

## Introduction

The hunting behavior of rail cars limits the speed of safe operation of trains. Wheel/rail forces that result from hunting oscillations act to deteriorate truck and track components at an accelerated rate, resulting in increased maintenance costs to assure safe operations. The hunting phenomenon is a self-excited lateral oscillation that is produced by the forward speed of the rail car and the wheel/rail guidance forces that result from the conicity associated with the wheel/rail contours [1].<sup>1</sup> These wheel/rail interaction forces act to effectively change the damping and dynamic behavior of the rail-car system as a function of speed. There are usually two critical speeds associated with the hunting phenomenon. At a relatively low characteristic speed (possibly 25–50 mph) in cars with lightly damped suspensions the phenomenon is observed as a large (possibly violent) lateral (including yaw and roll) oscillation of the car body [1]. At speeds above and below this speed the oscillations are reduced. This low-speed oscillation normally does not result in a catastrophic sit-

uation and can be controlled by adding damping to the suspension system. At higher speeds the hunting phenomenon appears as violent oscillations of the wheel axles and truck assemblies that are limited only by flange action and possible derailment. This self-excited oscillation begins at a critical vehicle speed and becomes more violent at all speeds above the critical speed.

The analyses that were initially used to explain and predict the hunting behavior of rail cars assumed the existence of perfectly conical wheels and made use of linear systems analysis procedures [1]. This type of analysis was effective in explaining hunting behavior and in predicting the onset of hunting on perfectly straight track with new wheels. However, these analyses were not capable of predicting behavior with worn wheel profiles or with forces that might be associated with a car in a hunting condition; nor were they capable of explaining the influence of wheel axle loadings on hunting behavior. The introduction of the concept of gravitational stiffness to account for the centering forces generated by the curvature and the contact forces between wheel and rail provided a mechanism for taking into account the influence of axle loading on hunting behavior [1]. The calculation of the gravitational stiffness was based on the curvatures of the wheel and the rail at the effective contact point. This resulted in a good small-amplitude approximation. The analyses generally considered flange contact as a condition to be avoided, a condition at the limit of the analyses. Analyses of large-amplitude oscillations were performed by numerical integration of the differential equations of motion, where the action of the flange was considered as a special case in which the effective gravitational stiffness was infinite and motion

<sup>1</sup> Numbers in brackets designate References at end of paper.

Contributed by the Rail Transportation Division and presented at the Winter Annual Meeting, New York, December 5–10, 1976, of THE AMERICAN SOCIETY OF MECHANICAL ENGINEERS. Manuscript received at ASME Headquarters August 2, 1976. Paper No. 76-WA/RT-3.



was controlled by the rail stiffnesses [3]. These analyses permitted an assessment of the relative magnitudes of forces associated with hunting behavior and permitted some investigation of the effects of track gage on hunting-induced forces and the effect of rail stiffness on limiting the amplitude of motion. The computation costs associated with direct numerical integration required that analyses be restricted to highly simplified analytic models. However, the assumption of infinite gravitational stiffness at flange contact provides no mechanism for wheel climb or for derailment without track failure.

There have been relatively few analytic investigations (as opposed to digital integration of the differential equations) of rail vehicles including nonlinear effects. DePater [4] used the method of Krylov and Bogoliubov to analyze a 2-degree-of-freedom model. Law and Brand [5] utilized this method to analyze a single wheelset that modeled flange contact as a very stiff spring with a deadband.

In the summer of 1974 a pilot study was conducted by Garg [6] at the DOT Transportation Systems Center to evaluate the feasibility of applying the describing-function approach to the analysis of limit-cycle behavior of rail cars during hunting oscillations, including large-amplitude oscillations and a continuous representation of wheel profile that included flange action. As discussed in the following paragraphs, the describing-function approach provides a systematic means of establishing quasi linearization of the key nonlinearities as a function of amplitude. The analyses of reference [6] were based on a simplified representation of the rail as a knife-edge support. In September of 1974 contract DOT-TSC-902 was issued by Transportation Systems Center to Clemson University to provide more realistic describing functions of the wheel/rail contact interaction forces and to develop algorithms for determining these describing functions, as well as means of applying them to complex vehicle representations to predict the occurrence and stability of limit cycles and the forced response of a rail vehicle to sinusoidal and statistical track irregularities. Reference [7] describes the early work under this contract. This present study will describe the application of the describing-function approach to investigate the influence of track gage, axle load, and wheel profile on the hunting behavior of simple wheelsets.

The results of the analyses presented here demonstrate that the practice of using a 1/4-in. tight gage on tangent track, as adopted by some transit properties and some railroads, is effective in reducing the amplitude of limit-cycle oscillations and the accompanying wheel/rail forces during hunting conditions. However, the use of tight gage increases the susceptibility to hunting as a result of track geometry irregularities. Equipment using flanges with reduced effective flange clearances will be more susceptible to track-irregularity-induced hunting than it would be on standard-gage track. For both passenger-car and freight-car applications the ability of the flange to control and limit hunting oscillations is controlled by the axle load, with lightly loaded cars being significantly more susceptible to

hunting-induced derailment. The existence of coulomb friction in freight-car truck designs may tend to increase the critical speed on perfect tangent track. However, the presence of track irregularities sufficient to induce breakout of the friction device results in a sharp reduction in critical speed and creates the potential for sudden, violent hunting motions that result in derailment.

### Simple Flexibly Suspended Wheelset

The flexibly suspended wheelset shown in Fig. 1 contains the basic elements required to illustrate the high-speed hunting phenomenon of a conventional passenger car. For two-axle vehicles with soft secondary-suspension systems that effectively isolate the car body from the wheelsets at the high-speed hunting frequency, this model will accurately predict the critical hunting speed. In addition, the equations of motion of either a very flexible truck or an infinitely rigid truck are identical in form to the equations of motion of a single wheelset. For the model shown in Fig. 1, the equations of motion are

$$m(\ddot{y} + \ddot{y}_r) + 2f_L\left(\frac{\dot{y}}{V} - \psi\right) + K_y(y + y_r) + F_R(y) = 0 \quad (1)$$

$$C\ddot{\psi} + 2lf_T\left(\frac{l\dot{\psi}}{V} + \frac{r_1 - r_2}{2r_0}\right) + K_\psi\psi - M_R(y, \psi) = 0 \quad (2)$$

$$k_r y_r = F_R(y) + 2f_L\left(\frac{\dot{y}}{V} - \psi\right) \quad (3)$$

where

$r_0$  = rolling radius at centered position

$m$  = mass of wheelset

$C$  = moment of inertia

$y$  = wheelset lateral position relative to track center line

$l = \frac{1}{2}$  track gage

$y_r$  = track displacement

$\psi$  = wheelset yaw angle

$r_1$  = rolling radius of wheel 1

$r_2$  = rolling radius of wheel 2

$K_y$  = lateral suspension stiffness

$K_\psi$  = yaw suspension stiffness

$k_r$  = lateral track stiffness

$2f_L\left(\frac{\dot{y}}{V} - \psi\right)$  = lateral wheelset force due to creep

$2lf_T\left(\frac{l\dot{\psi}}{V} + \frac{r_1 - r_2}{2r_0}\right)$  = yaw moment resulting from tangential creep

forces

$F_R(y)$  = lateral force exerted by wheel/rail contact (flange forces)

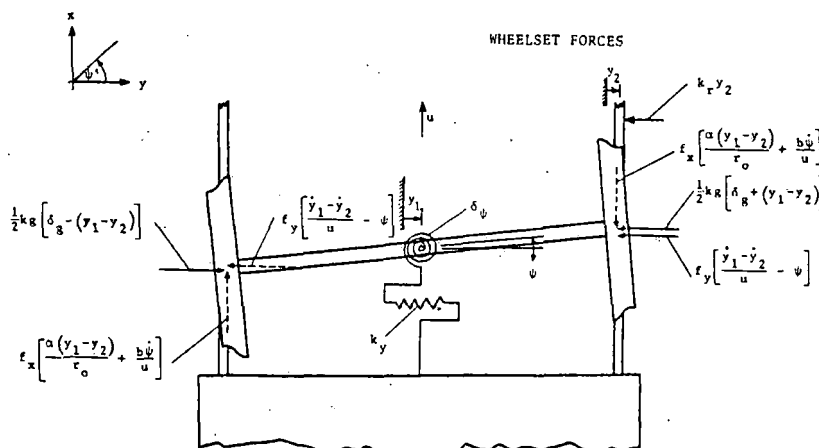


Fig. 1 Wheelset model

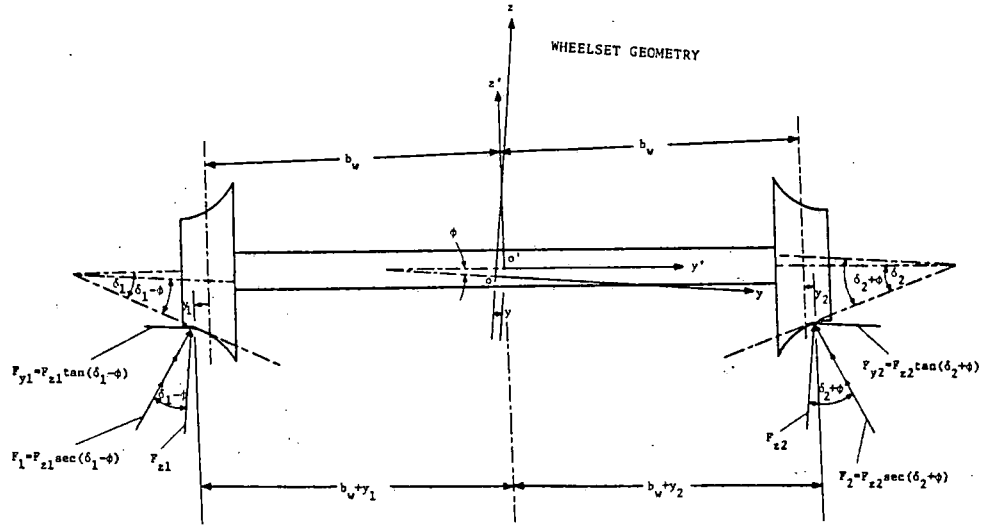


Fig. 2 Wheel contact forces resolved along xyz axes

$M_g(y, \psi)$  = yaw moment resulting from wheel/rail contact forces

In the describing-function approach the nonlinear elements in the equations of motion are replaced by stiffness or damping elements (which may be complex) that are functions of the amplitude of oscillation. The linear values are chosen to minimize the mean square error in force for the amplitude of displacement or velocity between the actual nonlinear force and the linearized approximation. The approach tends to work well for systems [8] where the variable operated on by the nonlinear elements is produced by operations that effectively act to integrate the force produced by the element. The describing-function values for the contact force (gravitational stiffness), contact force moment (yaw gravitational stiffness), and rolling radii difference (conicity) are defined by the minimization of the following mean square differences:

$$\epsilon_1^2 = \int_0^\infty [F_g(y) - K_g(Y)y]^2 dt \quad (4)$$

$$\epsilon_2^2 = \int_0^\infty [M_g(y, \psi) - K_a(Y)\psi]^2 dt \quad (5)$$

$$\epsilon_3^2 = \int_0^\infty \left[ \frac{r_1 - r_2}{z} - \alpha_e^*(Y)y \right]^2 dt \quad (6)$$

where

$K_g(Y)$  = gravitational stiffness

$K_a(Y)$  = yaw gravitational stiffness<sup>2</sup>

$\alpha_e^*(Y)$  = effective conicity

$Y$  = amplitude of lateral oscillation

The contact forces and moments are found from Fig. 2 as

$$F_g = \frac{W(l+y)}{2l} \tan(\delta_2 + \phi) - \frac{W(l-y)}{2l} \tan(\delta_1 - \phi) \quad (7)$$

$$M_g = \left[ \frac{W(l+y)}{2l} \tan(\delta_2 + \phi) - \frac{W(l-y)}{2l} \tan(\delta_1 - \phi) \right] l\psi = G(y)l\psi \quad (8)$$

where

$\phi$  = wheelset roll angle

$\delta_1$  = contact angle between wheel 1 and rail

$\delta_2$  = contact angle between wheel 2 and rail

The minimization for a sinusoidal input describing function yields

$$K_g = \frac{1}{\pi Y} \int_0^{2\pi} [F_g(y \sin \omega t)] \sin \omega t d(\omega t) \quad (9)$$

$$K_a = \frac{1}{\pi \psi_0} \int_0^{2\pi} M_g(y, \psi) \cos \omega t d(\omega t) = \frac{1}{\pi \psi_0} \int_0^{2\pi} [G(Y \sin \omega t)] l \psi_0 \cos \omega t d(\omega t) = \frac{1}{\pi} \int_0^{2\pi} [G(Y \sin \omega t)] l \cos \omega t d(\omega t) \quad (10)$$

assuming  $y$  and  $\psi$  are 90 deg out of phase, which is in agreement with the analysis results.

$$\alpha_e^* = \frac{1}{\pi Y} \int_0^{2\pi} \frac{(r_1 - r_2)}{z} \sin \omega t d(\omega t) \quad (11)$$

Substituting the describing functions and assuming a linear creep range, the equations of motion become

$$m(\ddot{y} + \ddot{y}_r) + 2f_L \left( \frac{\dot{y}}{V} - \dot{\psi} \right) + (K_y + K_g)y + K_y y_r = 0 \quad (12)$$

$$C\ddot{\psi} + 2f_T \left( \frac{l^2 \dot{\psi}}{V} + \frac{\alpha_e^* l y}{r_0} \right) + (K_\psi - K_a)\psi = 0 \quad (13)$$

$$k_r y_r = K_g y + 2f_L \left( \frac{\dot{y}}{V} - \dot{\psi} \right)$$

For the cases of interest here, the creep force is small compared to the contact force  $K_g y$ , and

$$y_r \approx \frac{K_g}{k_r} y$$

These substitutions permit equations (1) and (2) to be rewritten as

$$m\ddot{y} + 2f_L' \left( \frac{\dot{y}}{V} - \dot{\psi} \right) + (K_y + K_g^*)y = 0 \quad (14)$$

$$C\ddot{\psi} + 2f_T \left( \frac{l^2 \dot{\psi}}{V} + \frac{\alpha_e^* l y}{r_0} \right) + (K_\psi - K_a)\psi = 0 \quad (15)$$

<sup>2</sup> This is an approximate representation of the general multiple-input describing function. The approximation is good if  $\psi$  and  $y$  are 90 deg out of phase and the function  $M_g(y, \psi)l\psi$  has the property that  $G(y)$  is an even function.

where

$$K_g^* = \frac{Kg}{1 + Kg/k_r}, \quad f_L' = \frac{f_L}{1 + Kg/k_r}$$

For this system of equations the stability boundaries of the system are given by the Routh-Hurwitz criterion as

$$\omega_k^2 = \frac{\omega_\psi^2 + \left(\frac{\omega_T^2}{\omega_L^2}\right) \omega_y^2}{1 + \left(\frac{\omega_T^2}{\omega_L^2}\right) \left[1 - \left(\frac{\omega_\psi^2 - \omega_y^2}{\omega_L^2 + \omega_T^2}\right)^2\right]} \quad (16)$$

$$V_c = \omega_k \beta_k \quad (17)$$

$$\beta_k = \frac{r_0 l}{\alpha_e^*} \text{ (effective kinematic wavelength)}$$

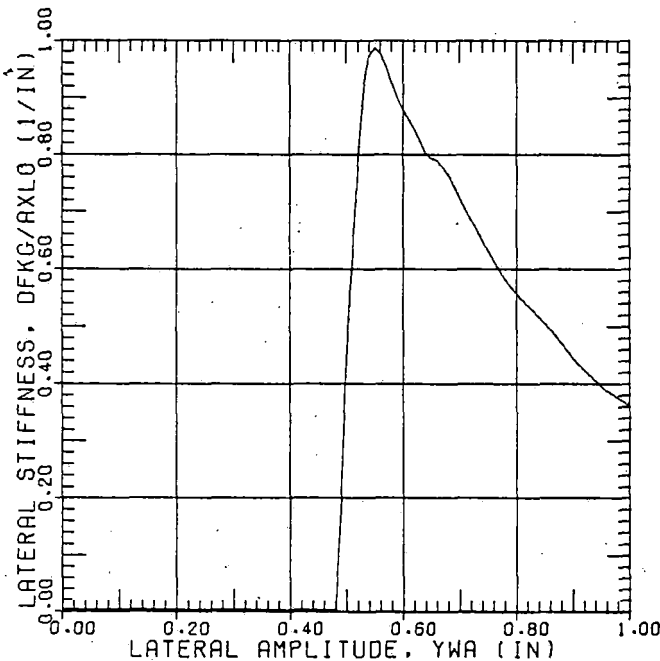
$$\omega_\psi^2 = \frac{(K_\psi - K_a)}{C}$$

$$\omega_T^2 = \frac{2f_T l^2}{C \beta_k}$$

$$\omega_L^2 = \frac{2f_L'}{m \beta_k}$$

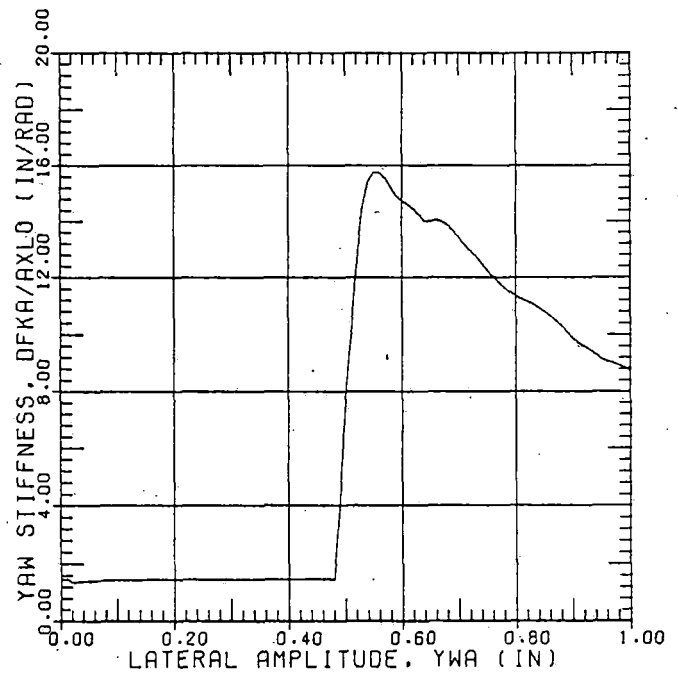
$$\omega_y^2 = \frac{K_y + K_g^*}{m}$$

A table of describing functions for the effective conicity and gravitational stiffnesses was prepared making use of the computer program for calculating rolling radii and contact angles developed under contract DOT-OS-40018 described in reference [9] and numerical integration of equations (9)-(11) for both a standard AAR contour and for the General Motors unipoint wheel contour interacting with new 140-lb rail. The describing functions for gravitational stiffness and effective conicity are shown in Figs. 3-8 for the two wheel contours



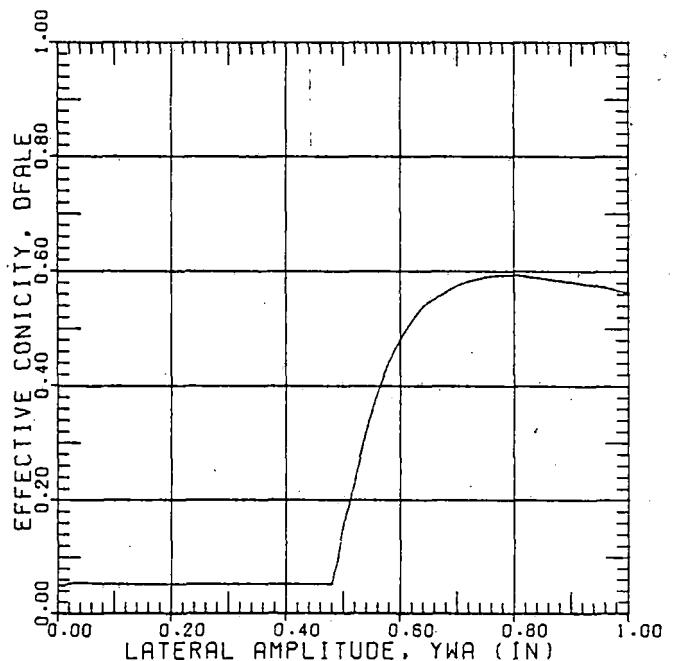
DATA A76A02.Q30  
DFKO: DESCRIBING FUNCTION FOR LATERAL GRAVITATIONAL STIFFNESS  
AXLO: AXLE LOAD  
AAR NEW TREAD AND FLANGE CONTOURS FOR ALL STEEL-TIRED WHEELS STANDARD  
NEW RAIL HEAD CONTOUR OF AREA 140RE STANDARD RAIL  
WHEEL GAUGE, 53.00 (IN)  
RAIL GAUGE, 56.50 (IN)  
RAIL CANT, 0.025 (RAD)

Fig. 3 Describing function for lateral gravitational stiffness



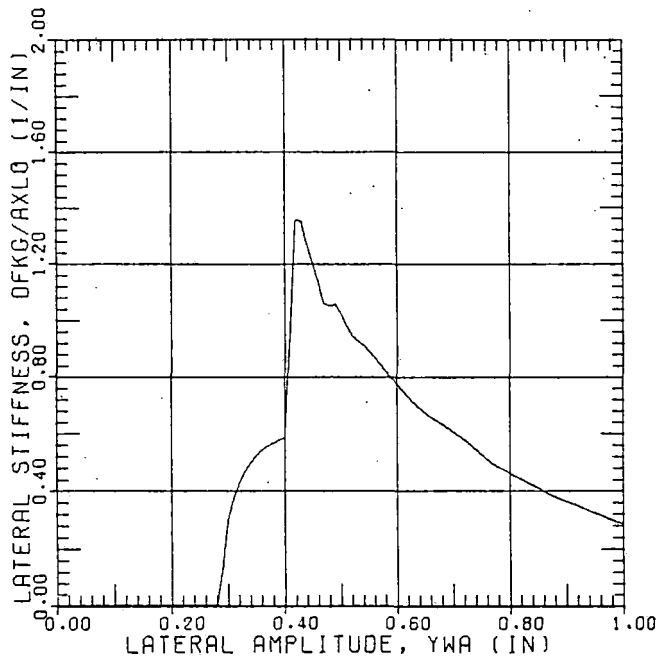
DATA A76A02.Q30  
DFKA: DESCRIBING FUNCTION FOR YAW GRAVITATIONAL STIFFNESS  
AXLO: AXLE LOAD  
AAR NEW TREAD AND FLANGE CONTOURS FOR ALL STEEL-TIRED WHEELS STANDARD  
NEW RAIL HEAD CONTOUR OF AREA 140RE STANDARD RAIL  
WHEEL GAUGE, 53.00 (IN)  
RAIL GAUGE, 56.50 (IN)  
RAIL CANT, 0.025 (RAD)

Fig. 4 Describing function for yaw gravitational stiffness



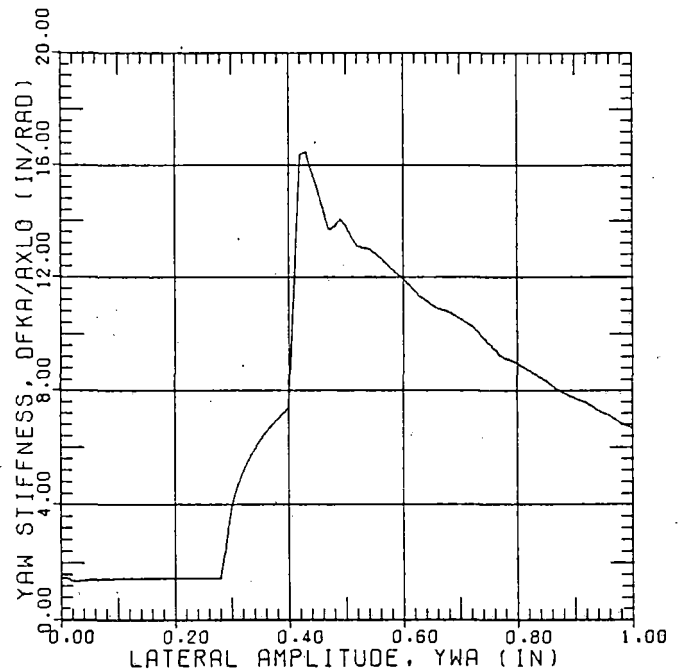
DATA A76A02.Q30  
AAR NEW TREAD AND FLANGE CONTOURS FOR ALL STEEL-TIRED WHEELS STANDARD  
NEW RAIL HEAD CONTOUR OF AREA 140RE STANDARD RAIL  
WHEEL GAUGE, 53.00 (IN)  
RAIL GAUGE, 56.50 (IN)  
RAIL CANT, 0.025 (RAD)

Fig. 5 Describing function for effective conicity



DATA A76R02.R30  
 DFKG: DESCRIBING FUNCTION FOR LATERAL GRAVITATIONAL STIFFNESS  
 AXLO: AXLE LOAD  
 GM UNI-POINT WIDE FLANGE NEW WHEEL CONTOUR  
 NEW RAIL HEAD CONTOUR OF AREA 140RE STANDARD RAIL  
 WHEEL GAUGE, 53.00 (IN)  
 RAIL GAUGE, 56.50 (IN)  
 RAIL CANT, 0.025 (RAD)

Fig. 6 Describing function for lateral gravitational stiffness



DATA A76R02.R30  
 DFKR: DESCRIBING FUNCTION FOR YAW GRAVITATIONAL STIFFNESS  
 AXLO: AXLE LOAD  
 GM UNI-POINT WIDE FLANGE NEW WHEEL CONTOUR  
 NEW RAIL HEAD CONTOUR OF AREA 140RE STANDARD RAIL  
 WHEEL GAUGE, 53.00 (IN)  
 RAIL GAUGE, 56.50 (IN)  
 RAIL CANT, 0.025 (RAD)

Fig. 7 Describing function for yaw gravitational stiffness

for a 56.5-in. rail gage. The calculation of the nonlinear hunting-oscillation stability boundaries was performed by selecting an amplitude, calculating the necessary describing functions, and substituting the result in equation (16) to find the critical velocity corresponding to this oscillation amplitude.

Fig. 9 shows the type of graph produced from hunting-stability calculations. If the vehicle is traveling at speed  $V_1$ , and as a result of some transient (e.g., a track irregularity) the wheelset is offset from the track centerline by a distance  $a$ , the wheelset will return to the track centerline with a decaying oscillation. However, if the wheelset is offset by an amplitude  $b$ , the solution is unstable and results in a growing oscillation and possible derailment. When the vehicle is traveling at speed  $V_2$  the wheelset will be in a limit-cycle condition with stable oscillations of amplitude  $d$ . An initial condition of amplitude  $c$  will result in a growing oscillation, until it is limited by the flange action to the limit-cycle amplitude  $d$ . If as a result of a transient the amplitude  $e$  has been achieved, the oscillation will decay until the limit-cycle amplitude  $d$  has been achieved. If the vehicle attempts to achieve a velocity greater than  $V_3$ , the wheelset will go into unbounded hunting oscillations and derail. The results of calculations of stability boundaries for a new AAR standard profile on new 140-lb rail for varying rail gage are shown in Fig. 10. The results indicate that the speed at which limit-cycle hunting oscillations occur and the maximum possible operating speed are relatively insensitive to track gage. However, the amplitude of the limit-cycle oscillation is directly proportional to flange clearance. Since the rms lateral force is approximately proportional to lateral oscillation amplitude, with the peak forces increasing much more rapidly, increases in track gage result in more severe wheel/rail forces. In order to reduce wheel/rail forces during high-speed operations where limit-cycle hunting may occur, some transit properties (e.g., New York City) and some railroad properties (e.g., Metroliner routes) have adopted the practice of tightening gage by  $\frac{1}{4}$  in. on tangent track.

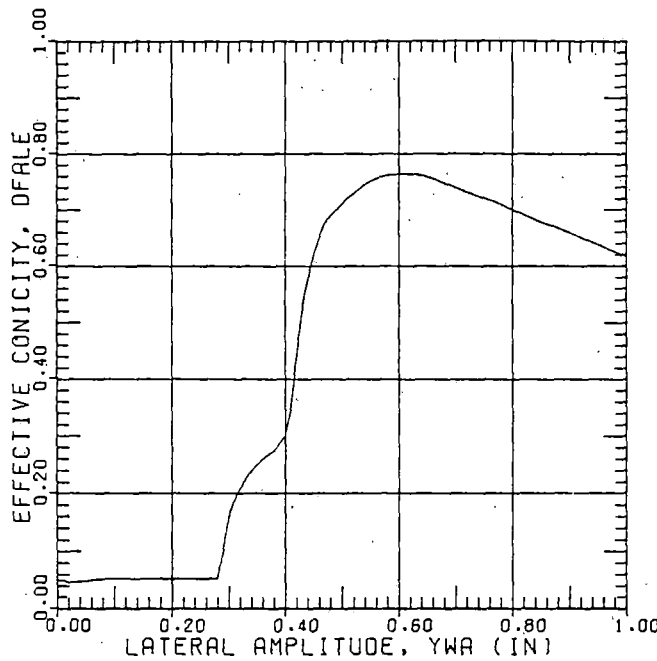
Fig. 11 shows the stability boundaries for a wheelset having the General Motors Unipoint profile for various track gages; the Unipoint profile is intended to reduce and control wheel wear by approximating a worn-wheel contour. The effectively wider flange of the Unipoint profile acts to reduce the effective flange clearance if the same wheel gage is used as with the AAR profile. As shown in Fig. 11, the Unipoint profile has about the same speed of the onset of limit-cycle hunting oscillations. However, the more gradual flange contour reduces the ability of the flange to resist wheel climbing motions and causes a reduction in the maximum speed that can be achieved prior to derailment. The Unipoint profile with the effectively tighter flange clearance results in increased sensitivity of the wheelset to hunting induced by track irregularities. A discontinuity in lateral alignment can more readily bring the wheelset to the derailment condition represented by point  $b$  of Fig. 9.

Figs. 12 and 13 show the influence of axle load on the boundaries for the standard AAR contour and for the Unipoint profile at standard track gage. It is seen that the speed at which limit-cycle oscillations begin is insensitive to axle load for this model; however, the maximum speed that can be achieved prior to derailment is strongly related to axle load.

The ability of the flange to limit high-speed hunting oscillations by maintaining stable limit cycles is directly dependent on axle load.

### Freight-Car Truck Wheelset Model

The simplified wheelset model described above assumes a linear suspension system that does not include the key nonlinear elements that have a strong influence on the behavior of the freight-car truck. In the freight-car truck, lateral motion of the axles is resisted by the truck warp stiffness in combination with the coulomb (dry) friction between the bolster and sideframe and the journal box and sideframe and at the centerplate and side bearings. Yaw motion is resisted by



DATA A76A02.R30

GM UNI-POINT WIDE FLANGE NEW WHEEL CONTOUR

NEW RAIL HEAD CONTOUR OF AREA 140RE STANDARD RAIL

WHEEL GAUGE, 53.00 (IN)  
RAIL GAUGE, 56.50 (IN)  
RAIL CANT, 0.025 (RAD)

Fig. 8 Describing function for effective conicity

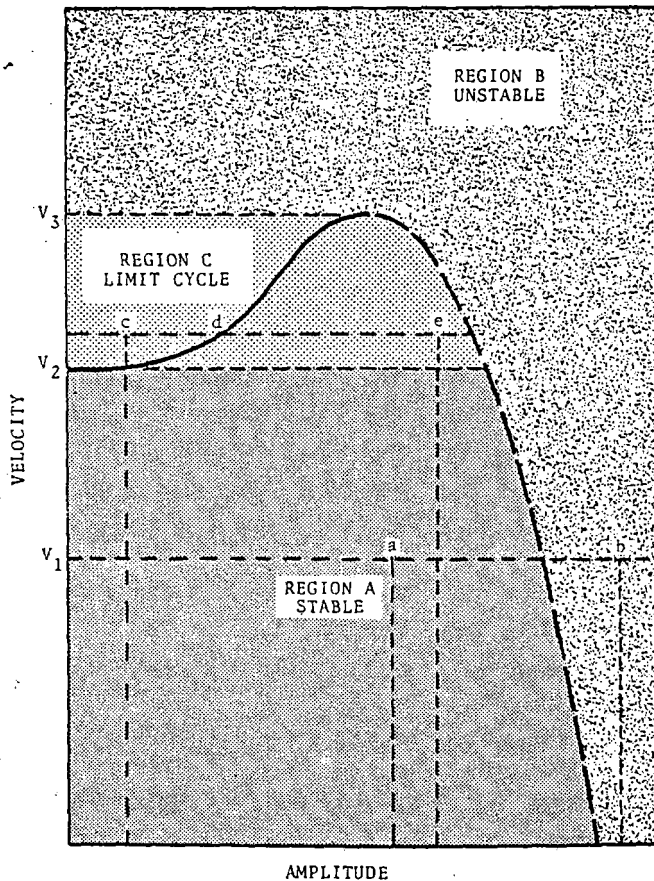
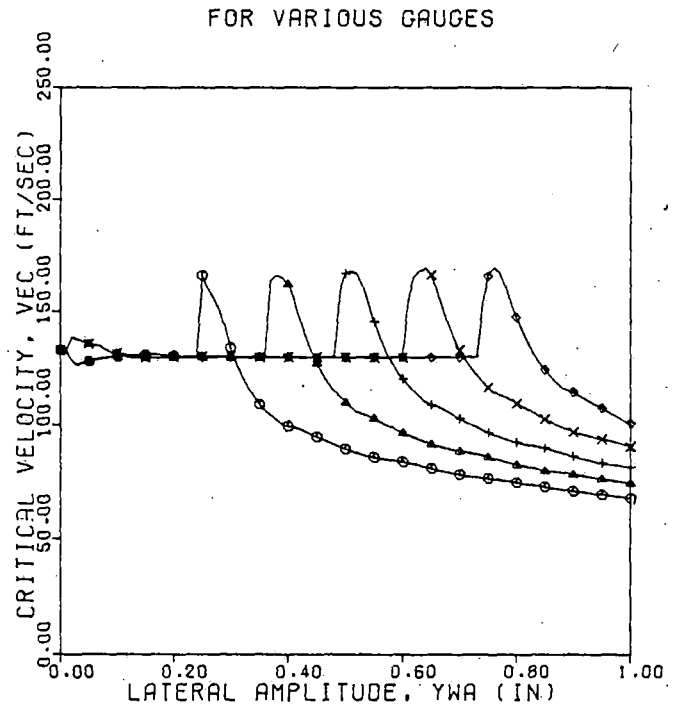


Fig. 9 Typical plot of wheelset critical speed versus limit-cycle amplitude



ARR NEW TREAD AND FLANGE CONTOURS FOR ALL STEEL-TIRED WHEELS STANDARD

NEW RAIL HEAD CONTOUR OF AREA 140RE STANDARD RAIL

WHEEL GAUGE, 53.00 (IN)  
RAIL CANT, 0.025 (RAD)  
AXLE LOAD, 6.00E+04 (LB)  
WHEELSET MASS, 15.00 (LB-SEC\*\*2/IN)  
WHEELSET YAW MOMENT OF INERTIA, 1.00E+04 (LB-IN-SEC\*\*2)  
LATERAL SUSPENSION STIFFNESS, 1.00E+03 (LB/IN)  
YAW SUSPENSION STIFFNESS, 4.00E+08 (LB-IN/RAD)  
RAIL LATERAL STIFFNESS, 1.00E+05 (LB/IN)  
LATERAL CREEP COEFFICIENT, 9.00E+06 (LB)  
TANGENTIAL CREEP COEFFICIENT, 9.00E+06 (LB)

SYMBOL	DATA	RAIL GAUGE (IN)
○	A76C01.L30	56.00
▲	A76C01.M30	56.25
△	A76C01.M50	56.50
×	A76C01.O30	56.75
◆	A76C01.P30	57.00

Fig. 10 Wheelset critical hunting speed versus limit-cycle amplitude for various gauges

the stiffness of the truck and by coulomb friction at the centerplate. To account for the suspension nonlinearities associated with real freight-car trucks, and to illustrate the approach for more complex systems, the simplified model discussed before is extended to a lateral suspension consisting of a spring and friction damper acting in parallel and a yaw suspension element with the spring and friction element in series. The force-deflection characteristics of these elements are shown in Fig. 14. With the nonlinear suspension elements, and neglecting rail compliance, equations (1) and (2) are rewritten as

$$m\ddot{y} + 2f_L \left( \frac{\dot{y}}{V} - \psi \right) + F_y(y, \dot{y}) + F_g(y) = 0 \quad (18)$$

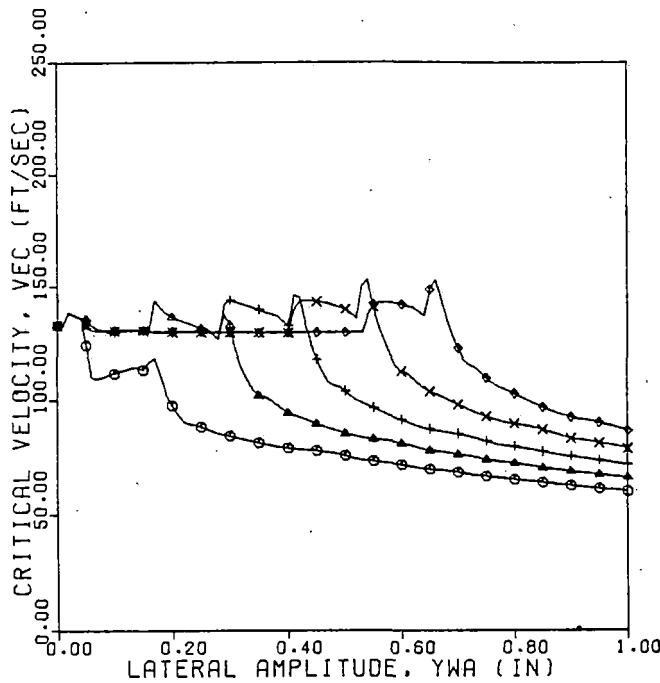
$$C\ddot{\psi} + 2lf_T \left( \frac{l\dot{\psi}}{V} + \frac{r_1 - r_2}{r_1 + r_2} \right) + M_\psi(\psi, \dot{\psi}) - M_y(y, \dot{\psi}) = 0 \quad (19)$$

where  $F_y(y, \dot{y})$  and  $M_\psi(\psi, \dot{\psi})$  represent the forces produced by the nonlinear suspension elements. The describing functions for these elements are given in standard texts [8] as

$$K_y^*(Y) = K_y + \frac{4F_0}{\pi Y} j \quad (20)$$

$$K_\psi^*(\Psi_0) = \frac{K_\psi}{2} [1 + f(-\beta)] + \frac{K_\psi}{\pi} (1 - \beta^2) j \quad (21)$$

where



OH UNI-POINT WIDE FLANGE NEW WHEEL CONTOUR

NEW RAIL HEAD CONTOUR OF AREA 140RE STANDARD RAIL

WHEEL GAUGE, 53.00 (IN)  
RAIL CANT, 0.025 (RAD)  
AXLE LOAD, 8.00E+04 (LB)  
WHEELSET MASS, 15.00 (LB-SEC\*\*2/IN)  
WHEELSET YAW MOMENT OF INERTIA, 1.00E+04 (LB-IN-SEC\*\*2)  
LATERAL SUSPENSION STIFFNESS, 1.00E+03 (LB/IN)  
YAW SUSPENSION STIFFNESS, 4.00E+06 (LB-IN/RAD)  
RAIL LATERAL STIFFNESS, 1.00E+06 (LB/IN)  
LATERAL CREEP COEFFICIENT, 9.00E+06 (LB)  
TANGENTIAL CREEP COEFFICIENT, 9.00E+06 (LB)

SYMBOL	DATA	RAIL GAUGE (IN)
○	A76C02-L30	56.00
△	A76C02-N30	56.25
+	A76C02-N30	56.50
×	A76C02-N30	56.75
◇	A76C02-P30	57.00

Fig. 11 Wheelset critical hunting speed versus limit-cycle amplitude for various gages

$j = \sqrt{-1}$  complex variable

$$\beta = \frac{\Psi_0 - 2\Psi_b}{\Psi_0}$$

$$f(\beta) \triangleq \begin{cases} -1 & \text{for } \beta < 1 \\ 2/\pi (\sin^{-1}\beta + \beta\sqrt{1-\beta^2}) & \text{for } |\beta| \leq 1 \\ +1 & \text{for } \beta > 1 \end{cases}$$

$F_0$  = lateral-suspension coulomb-force level

$\Psi_b$  = breakout yaw angle of yaw suspension element

$K_y$  = lateral suspension stiffness

$K_\psi$  = yaw-moment suspension stiffness

$\Psi_0$  = yaw amplitude

$Y$  = lateral amplitude

The quasi-linearized versions of equations (18) and (19) are

$$m\ddot{y} + \frac{2f_L}{V}\dot{y} + [K_y(Y) + K^*(Y)]y - 2f_L\psi = 0 \quad (22)$$

$$c\ddot{\psi} + \frac{2f_T l^2}{V}\dot{\psi} + [K_\psi^* - K_a]\psi + \frac{2f_T l}{r_0}\alpha_e^*(Y)y = 0 \quad (23)$$

The conditions for existence of a limit-cycle or stability boundary are again given by equation (16). However, the describing functions

are now functions of both the amplitudes  $Y$  and  $\Psi_0$ , and the procedure of simply selecting a value of  $Y$  and  $\Psi_0$  and finding the critical speed does not assume that equations (22) and (23) are satisfied.

Furthermore, for higher-order systems the Routh-Hurwitz criterion does not reduce to a single equation, and it represents a multitude of conditions. Accordingly, a computational algorithm was developed at M.I.T. to determine the stability of hunting oscillations and amplitudes of limit cycles; it is capable of handling higher-order systems and frequency-dependent describing functions. The following paragraphs illustrate the approach.

Equations (22) and (23) are placed in *state variable form* with  $x_1 = y$ ,  $x_2 = \dot{y}$ ,  $x_3 = \psi$ ,  $x_4 = \dot{\psi}$ . The matrix representation of the quasi-linearized equations is

$$\dot{\mathbf{X}} = \mathbf{N}\mathbf{X} \quad (24)$$

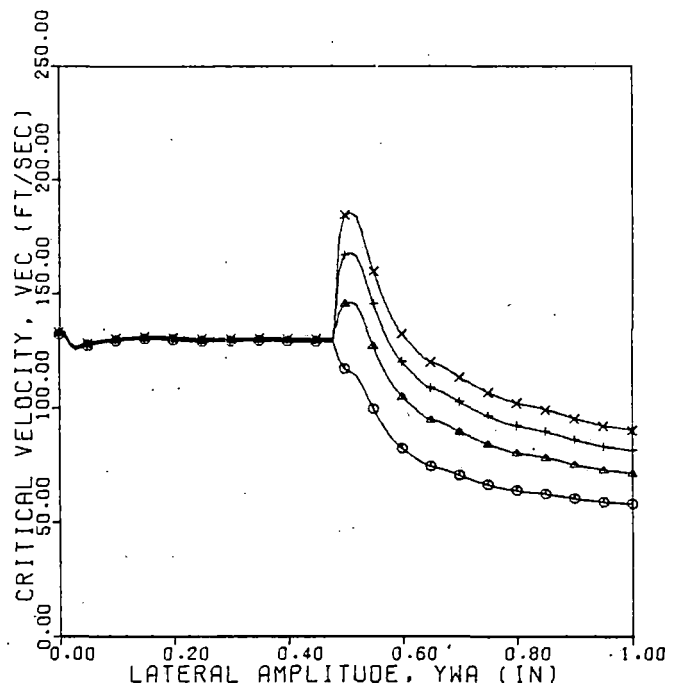
where  $\mathbf{X}$  is the  $4 \times 1$  state vector and  $\mathbf{N}$  is a  $4 \times 4$  matrix composed of linear and describing-function elements. If the wheelset is in a condition of self-sustained oscillation, each of the states undergoes an approximately sinusoidal oscillation, and the state vector  $\mathbf{X}$  can be expressed as

$$\mathbf{X}(t) = \bar{\mathbf{X}}e^{j\omega t} \quad (25)$$

Substituting equation (25) into (24) yields

$$[j\omega\mathbf{I} - \mathbf{N}](\bar{\mathbf{X}}) = 0 \quad (26)$$

Equation (26) is the necessary condition for hunting to occur; note



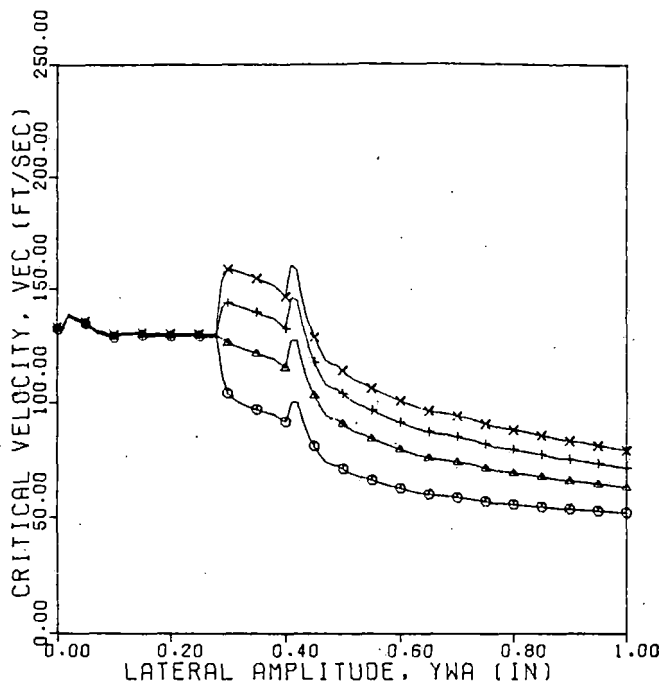
RAIL NEW TREAD AND FLANGE CONTOURS FOR ALL STEEL-TIRED WHEELS STANDARD

NEW RAIL HEAD CONTOUR OF AREA 140RE STANDARD RAIL

RAIL GAUGE, 56.50 (IN)  
WHEEL GAUGE, 53.00 (IN)  
RAIL CANT, 0.025 (RAD)  
WHEELSET MASS, 15.00 (LB-SEC\*\*2/IN)  
WHEELSET YAW MOMENT OF INERTIA, 1.00E+04 (LB-IN-SEC\*\*2)  
LATERAL SUSPENSION STIFFNESS, 1.00E+03 (LB/IN)  
YAW SUSPENSION STIFFNESS, 4.00E+06 (LB-IN/RAD)  
RAIL LATERAL STIFFNESS, 1.00E+06 (LB/IN)

SYMBOL	DATA	AXLE LOAD (LB)	LATERAL CREEP COEFFICIENT (LB)	TANGENTIAL CREEP COEFFICIENT (LB)
○	A76C01-N10	2.00E+04	3.00E+06	3.00E+06
△	A76C01-N20	4.00E+04	6.00E+06	6.00E+06
+	A76C01-N30	6.00E+04	9.00E+06	9.00E+06
×	A76C01-N40	8.00E+04	1.20E+07	1.20E+07

Fig. 12 Wheelset critical hunting speed versus limit-cycle amplitude for various axle loads



ON UNI-POINT WIDE FLANGE-NEW WHEEL CONTOUR

NEW RAIL HEAD CONTOUR OF AREA 140RE STANDARD RAIL

RAIL GRADE, 56.50 (IN)  
WHEEL GAUGE, 53.00 (IN)  
RAIL CANT, 0.025 (RAD)  
WHEELSET MASS, 15.00 (LB-SEC\*\*2/IN)  
WHEELSET YAW MOMENT OF INERTIA, 1.00E+04 (LB-IN-SEC\*\*2)  
LATERAL SUSPENSION STIFFNESS, 1.00E+03 (LB/IN)  
YAW SUSPENSION STIFFNESS, 4.00E+06 (LB-IN/RAD)  
RAIL LATERAL STIFFNESS, 1.00E+05 (LB/IN)

SYMBOL	DATA	AXLE LOAD (LB)	LATERAL CREEP COEFFICIENT (LB)	TANGENTIAL CREEP COEFFICIENT (LB)
○	R76C02.N10	2.00E+04	3.00E+06	3.00E+06
△	R76C02.N20	4.00E+04	6.00E+06	6.00E+06
+	R76C02.N30	6.00E+04	9.00E+06	9.00E+06
x	R76C02.N40	8.00E+04	1.20E+07	1.20E+07

Fig. 13 Wheelset critical hunting speed versus limit-cycle amplitude for various axle loads

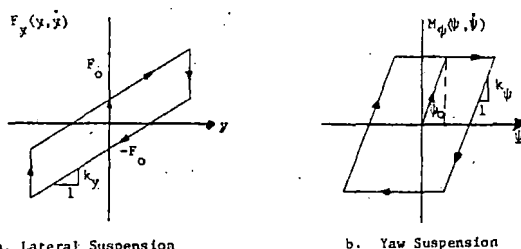


Fig. 14 Wheelset suspension nonlinearities

that this is precisely the condition required for a linear system to have an undamped oscillation, the only difference being that the elements of the  $N$  matrix are functions of the amplitudes  $Y$  and  $\Psi_0$  as well as the hunting frequency  $\omega$ . In order for a nontrivial solution of equation (26) to exist, the following condition must hold:

$$[j\omega I - N(Y, \Psi_0, \omega, V)] = 0 \quad (27)$$

Equation (27) represents two scalar equations (real and complex parts = 0).

The program developed [10] uses a parameter-optimization algorithm [11] to select a  $Y$ ,  $\Psi_0$ , and  $\omega$  for a given speed  $V$  that satisfies equation (27). Since there is a possibility that roots of equation (27) may not satisfy equation (26), the program developed finds a solution

to equation (27) and then checks equation (26). If equation (26) is not satisfied, a new initial point is generated. For higher-order systems it may prove more efficient to combine equations (26) and (27) into a single algorithm.

The values of  $Y$ ,  $\Psi_0$ , and  $\omega$  that satisfy equations (26) and (27) may correspond to either stability boundaries or to stable limit cycles. Stable limit cycles (hunting) are observable oscillations, while the other solutions represent stability boundaries. A perturbation technique was used to check for stability. The values of  $Y$ ,  $\Psi_0$ , and  $\omega$  that satisfy equations (26) and (27) guarantee that a pair of eigenvalues of the  $N$  matrix are on the imaginary axis. If the system is perturbed by a sudden change in  $Y$ , say  $\Delta Y$ , the stability of the solution is determined by whether the oscillation grows or returns to the original amplitude. By observing the migration of the eigenvalues on the imaginary axis caused by an amplitude perturbation, system stability is determined.

### Effects of Model Sophistication

Fig. 15 illustrates the general type of results obtained as well as the effect of model sophistication. The vertical line labeled 1 is the result of a purely linear model; it predicts a single critical speed, independent of amplitude, below which all perturbations decay and above which the system is unstable. Curve 2 represents the stability and limit-cycle boundaries of a wheelset model that includes a stiff deadband rail spring (to model flange contact) and suspension nonlinearities. The limit-cycle boundary (solid curve) is due to the stiff rail spring that provides whatever restoring force is required to keep the oscillation bounded. The dashed curve represents a stability boundary, i.e., disturbances below this curve will decay, while disturbances above it will grow until the solid limit-cycle boundary is reached. The low-amplitude part of the curve is determined by the parallel friction in the lateral suspension; higher values of lateral coulomb friction cause the stability boundary to approach the horizontal axis more slowly [7]. At intermediate amplitudes the stability boundary is determined primarily by the yaw-suspension breakout level ( $\Psi_b$ ); smaller values of  $\Psi_b$  cause the stability boundary to move to the left, thus indicating a lower critical speed. The linear model has really assumed an equivalent damping based on one amplitude and thus is valid for one point on Fig. 15; the difference between curves 1 and 2 illustrates the importance of using amplitude-dependent stiffness and damping in computing critical speeds.

Curve 3 represents the model given by equations (22) and (23), i.e., nonlinear wheel-profile geometry and nonlinear suspension elements. For low amplitudes this model yields identical results to curve 2, since the models are identical until the flange contacts the rail. The difference at higher amplitudes is due to the fact that the stiff rail spring always provides a stabilizing restoring force, while the realistic wheel-profile describing functions reach a point during wheel climb where they can no longer provide a stabilizing reaction force. Thus at speeds over 160 fps an initial displacement above the dashed line would lead to a derailment.

The result obtained here, that friction damping may act to inhibit hunting behavior at high speed, has been partially validated by the experimental results reported by Love [12]. Love describes field tests that indicate that constant-contact side bearings, which have the effect of increasing the frictional resistance to yaw motions of the truck relative to the car, act to reduce the hunting tendency of freight cars. Since at small amplitudes the describing functions for the lateral-suspension characteristic approach infinity, the assumptions on which the isolated wheelset analysis is based are not valid for small oscillations, and a full-car model is necessary.

Preliminary results evaluating the effects of coulomb friction on hunting behavior for a 9-degree-of-freedom model of a full freight car are reported in a companion paper [13]. This model, for the car and truck parameters used, predicts that the suspension friction will act to reduce the speed at which hunting-induced limit cycles will occur. This result may be due to the use of a perfectly rigid car body and the assumption of no series compliance with the friction elements in the model. It may also be true that the ability of friction damping to inhibit (or induce) limit-cycle hunting oscillations may be a strong

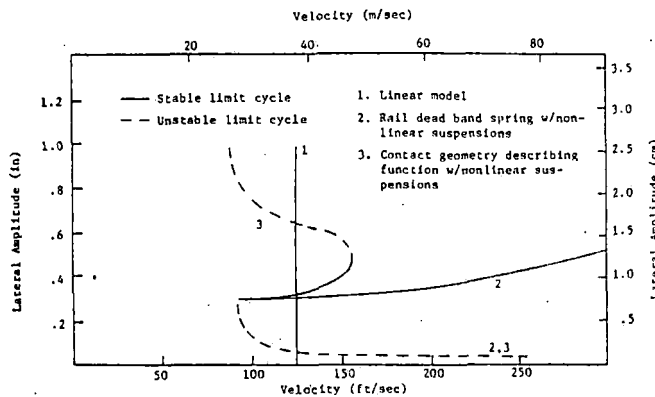


Fig. 15 Model sophistication effects

function of the parameters of a specific freight-car design. The question of whether coulomb friction acts to inhibit or induce limit-cycle hunting behavior is important and will be the subject of future studies.

### Parametric Studies

The influence of axle load, track gage, and wheel profile on freight-car wheelset hunting was investigated by using the computational algorithm developed and the model defined by equations (22) and (23). The parameter values used for the parameter studies are given in the Appendix, and the influence of axle load on the suspension parameters and creep forces was included, as shown in Table A1 in the Appendix.

The parametric studies were made for several values of axle loading (15,000, 35,000, and 70,000 lb) and track gage (56 in. or tight, 56.5 in. or standard, and 57.5 in. or wide), as well as for three different wheel profiles (new AAR, slightly worn AAR, and Heumann). A sample of results from the parametric studies is shown in Fig. 16.

Because of the high coulomb friction levels in the lateral suspension  $F_0$  used for the model, all of the curves shown in Fig. 16 are stability boundaries rather than hunting oscillations. Thus it can be interpreted that disturbances below the curves decay, while those above grow.

It is seen in Fig. 16(a) that increasing track gage increases the stable regime to the left of the curves. This implies that at a given velocity larger track irregularities can be tolerated on wide gage than on tight gage. This effect is directly related to flange contact occurring sooner at tighter gages.

Figure 16(b) indicates that for a given gage and wheel profile, increasing axle load has a definite stabilizing effect, especially at the higher amplitudes; i.e., for a given velocity, increasing axle load permits larger track irregularities to be encountered before the onset of instability. Also, the velocity range for guaranteed stable response is improved by increasing axle load. Axle load is found in the gravitational stiffness term, thus explaining this stabilizing influence. Note that for these plots the results with various axle loads are similar at low amplitudes. This trend is attributed to the wheelset being influenced primarily by the suspension elements (rather than by the conicity or gravitational stiffness terms) at low amplitudes.

Figure 16(c) examines the stability differences between wheel profiles for fixed combinations of axle load and gage. For a given speed at low amplitudes the worn wheel provides a slightly more stable response than the new wheel. For these amplitudes the effective conicities of the worn wheel are generally a bit larger than those of the new, but its gravitational stiffness contributions are considerably greater. Thus the gravitational stiffness counteracts the effective conicity, at least in the new-wheel/worn-wheel comparison for low amplitudes. The Heumann profile clearly exhibits poorer stability at low amplitudes, an effect caused by its high conicities in this range.

At higher amplitudes the new wheel clearly allows the highest

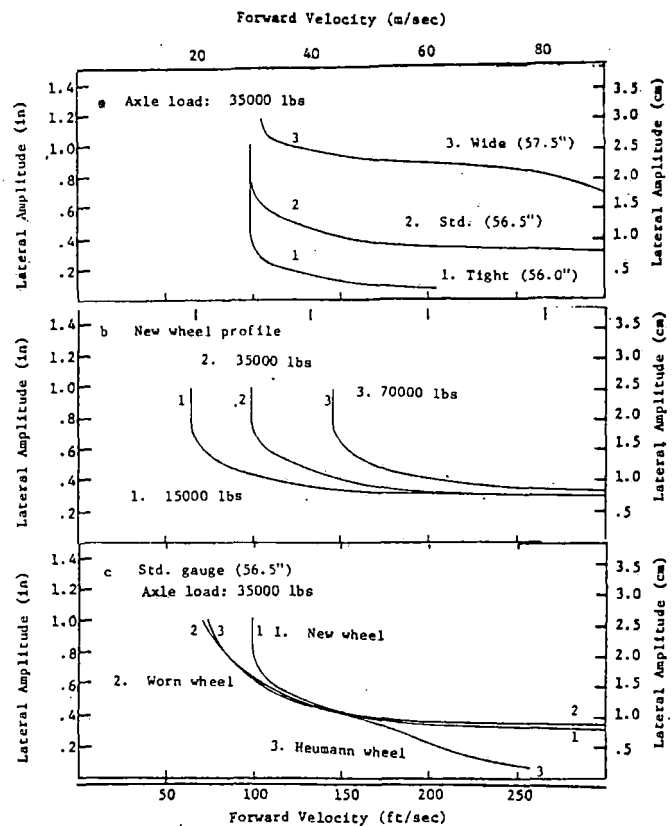


Fig. 16 Parametric study

speeds to be attained. Also, at these higher amplitudes the Heumann wheel exhibits slightly better stability than does the worn wheel. However, the real benefit from Heumann wheels is their tendency to wear more evenly and thus maintain their original stability locus. In contrast, the geometry of the standard AAR profile may change unpredictably with wear, making it difficult to design for long-term use.

It can be seen that Fig. 16 does not show characteristics similar to the plots of lateral amplitude versus velocity of Fig. 15. In Fig. 15, stable limit cycles were encountered at flange contact, whereas these plots do not show these trends. The describing functions are not that much different for the comparable new-wheel/worn-rail standard-gauge cases of this section. However, the suspension elements have much different constants for the two models examined. The much higher yaw-suspension stiffness and lateral-suspension coulomb force act as stabilizing terms in the new model. Thus the loci are located at very high velocities for some of the amplitude range. As a result the describing-function terms are overshadowed by the suspension terms in the amplitude ranges where the geometry changes considerably with displacement. When these suspension constants were returned to values similar to those found in the earlier models, plots similar to Fig. 15 were obtained:

### Wheelset-Model Validity

A question that arises is whether the results computed from the wheelset model accurately model how a real freight car would behave. Two areas of Fig. 16 are immediately suspect: (1) Large-amplitude ( $>0.7$  in.) results: the freight-car wheelset model assumed rigid rails; at these large amplitudes the track compliance should be included. (2) Low-amplitude, high-speed ( $<0.2$  in.) results: the dry-friction model used yields very large friction forces at small amplitudes; in practice dither and/or car-body motion would limit these forces; hence a full-car-body model should be used.

The intermediate-level amplitude results were compared with the



critical speeds computed using a full-car-body model, and excellent agreement was obtained.

## Conclusions

A procedure has been outlined that incorporates important wheel/rail profile and suspension nonlinearities into analytic hunting investigations. The computational algorithm outlined has been applied to a simple wheelset model to investigate the general trends produced by axle-load, suspension, and wheel-profile variations.

## Acknowledgment

The work described here was conducted in support of the Office of Rail Safety Research of the Federal Railroad Administration through in-house efforts at the DOT Transportation Systems Center and complementary efforts conducted at M.I.T. The M.I.T. work was conducted as part of contract DOT-TSC-902 with Clemson University.

## References

- 1 Wickens, A. H., "The Dynamic Stability of Railway Vehicle Wheelsets and Bogies Having Profiled Wheels," *International Journal of Solids and Structures*, Vol. 1, 1965, pp. 319-341.
- 2 Law, E. H., and Cooperrider, N. K., "A Survey of Rail Vehicle Dynamics Research," *Journal of Dynamic Systems, Measurement, and Control*, TRANS. ASME, Series G, Vol. 96, No. 2, June 1974, pp. 132-146.
- 3 Cooperrider, N. K., "High-Speed Dynamics of Conventional Railway Trucks," PhD thesis, Department of Mechanical Engineering, Stanford University, Stanford, Calif., 1968.
- 4 DePater, A. D., "The Approximate Determination of the Hunting Movement of a Railway Vehicle by Aid of the Method of Krylov and Bogoliubov," *Applied Scientific Research*, Section A, Vol. 10, 1961, pp. 205-228.
- 5 Law, E. H., and Brand, R. S., "Analysis of the Nonlinear Dynamics of a Railway Vehicle Wheelset," *Journal of Dynamic Systems, Measurement, and Control*, TRANS. ASME, Series G, Vol. 95, No. 1, March 1973, pp. 28-35.
- 6 Garg, D. P., "Describing Function Techniques for the Nonlinear Analysis of the Dynamics of a Rail Vehicle Wheelset," Final Report, U. S. Department of Transportation (FRA), July 1975.
- 7 Cooperrider, N. K., Hedrick, J. K., Law, E. H., and Malstrom, C., "The Application of Quasilinearization Techniques to the Prediction of Nonlinear Railway Vehicle Response," *Vehicle System Dynamics*, Vol. 4, No. 2-3, July 1975, pp. 141-148.
- 8 Gelb, A., and Vander Velde, W. E., *Multiple-Input Describing Functions and Nonlinear System Design*, McGraw-Hill, New York, 1968.
- 9 Cooperrider, N. K., Law, E. H., Hull, R., Kadala, P. S., Tuten, J. M., "Analytical and Experimental Investigation of Wheel-Rail Constraint Relationships," U. S. DOT Report No. FRA-OR&D, Dec. 1975.
- 10 Hannebrink, D. N., "The Application of Describing Functions to the Nonlinear Stability Analysis of a Railcar Wheelset," MS thesis, Massachusetts Institute of Technology, Cambridge, Mass., May 1976.
- 11 Hooke, R., and Jeeves, T. A., "Direct Search Solution of Numerical and Statistical Problems," *Journal of the Association for Computing Machinery*, Vol. 8, No. 2, Apr. 1961, pp. 212-229.
- 12 Love, R. B., "Improved Suspension for 100-Ton Cars on Rough Track: Effect of Heavy Axle Loads on Track," presented at the 12th Annual Railroad Engineering Conference, Pueblo, Colo., Oct. 1975, sponsored by Federal Railroad Administration, U. S. Department of Transportation.
- 13 Hull, R., and Cooperrider, N. K., "Influence of Nonlinear Wheel/Rail Contact Geometry on Stability of Rail Vehicles," ASME Paper No. 76-WA/RT-2.

## APPENDIX

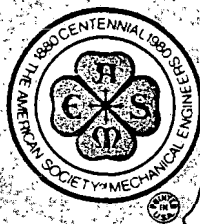
The freight-car wheelset model parameters (70-ton) are as follows:

$$\begin{aligned} m &= 76.6 \text{ slugs} \\ C &= 448 \text{ slug-ft}^2 \\ r_0 &= 1.375 \text{ ft} \\ F_0 &= 5200 \text{ lb} \end{aligned}$$

The values of  $f_t$ ,  $f_T$ ,  $K_y$ ,  $K_\psi$ , and  $\Psi_b$  vary with axle loading and gage and are given in Table A1.

Table 1 Model parameter changes as a function of axle load

AXLE LOAD	GAUGE	$f_t$ 10 <sup>6</sup> lbs/wheel	$f_T$ 10 <sup>6</sup> lbs/wheel	$K_y$ 10 <sup>4</sup> lbs/ft	$K_\psi$ 10 <sup>6</sup> ft-lbs/rad	$\Psi_b$ (rad)
15000 lbs	56.0"	1.361	1.471	1.379	1.916	.00122
	56.5"	1.361	1.471	1.379	1.916	.00122
	57.5"	1.361	1.471	1.379	1.916	.00122
35000 lbs	56.0"	2.394	2.587	3.490	2.108	.00248
	56.5"	2.394	2.587	3.490	2.108	.00248
	57.5"	2.394	2.587	3.490	2.108	.00248
70000 lbs	56.0"	3.801	4.107	7.187	2.444	.00463
	56.5"	3.801	4.107	7.187	2.444	.00463
	57.5"	3.801	4.107	7.187	2.444	.00463
NEW WHEEL CONSTANTS						
35000 lbs	56.0"	2.257	2.277	3.490	2.108	.00248
	56.5"	2.222	2.217	3.490	2.108	.00248
	57.5"	2.636	3.182	3.490	2.108	.00248
WORN WHEEL CONSTANTS						
35000 lbs	56.0"	2.146	2.060	3.490	2.108	.00248
	56.5"	2.193	2.164	3.490	2.108	.00248
	57.5"	2.325	2.460	3.490	2.108	.00248
HEUMANN WHEEL CONSTANTS						



An ASME PUBLICATION  
\$4.00 per copy \$2.00 to ASME Members

# ASME

81-WA/DSC-8

THE AMERICAN SOCIETY OF MECHANICAL ENGINEERS  
345 E 47 St., New York, N.Y. 10017

The Society shall not be responsible for statements or opinions advanced in papers or in discussion at meetings of the Society or of its Divisions or Sections, or printed in its publications. Discussion is printed only if the paper is published in an ASME Journal or Proceedings. Released for general publication upon presentation. Full credit should be given to ASME, the Technical Division, and the author(s).

REFERENCE 100

## Nonlinear Stability and Tracking of Rail Passenger Trucks

**D. Horak**

Member of Technical Staff,  
Bendix Advanced Technology Center,  
Columbia, MD

**D. N. Wormley**

Professor,  
Department of Mechanical Engineering,  
Massachusetts Institute of Technology,  
Cambridge, MA

*An analysis of a rail passenger truck which includes nonlinear wheel/rail geometry and creep forces is formulated for determining truck stability and response to rail alignment irregularities. Digital simulation studies using the analysis have illustrated the large amplitude flange to flange response which occurs in operation of a truck below critical speed on a track with significant alignment irregularity, of a truck near critical speed and excited by irregularities and of a truck operated above critical speed. The variations in temporal waveform, probability density and power spectral density of vehicle motions for these conditions are described. The influence of vehicle suspension parameters and wheel/rail geometry on truck stability and tracking ability is discussed and related to operating conditions.*

### NOMENCLATURE

A	track roughness constant
a	half of wheelset contact distance
$a_1$	wheelset roll coefficient
b	half of wheelbase
$C_{px}$	primary longitudinal damping (4 per truck)
$C_{py}$	primary lateral damping (4 per truck)
$C_{sy}$	secondary lateral damping (2 per truck)
$d_p$	half of the spacing of primary longitudinal springs
$d_s$	half of the spacing of secondary longitudinal springs
$f_{11}$	lateral creep force coefficient
$f_{12}$	lateral spin creep force coefficient
$f_{22}$	spin creep force coefficient
$f_{33}$	longitudinal creep force coefficient
F	creep force
$F_{susp}$	suspension force
$I_{tz}$	yaw moment of inertia of truck frame
$I_{wy}$	pitch moment of inertia of wheelset
$I_{wz}$	yaw moment of inertia of wheelset
$k_a$	track roughness scaling constant
$K_b$	bending stiffness of a truck
$K_{px}$	primary longitudinal stiffness (4 per truck)

$K_{py}$	primary lateral stiffness (4 per truck)
$K_{sy}$	secondary lateral stiffness (2 per truck)
$K_{s\psi}$	secondary yaw stiffness (1 per truck)
M	creep moment
$M_t$	mass of truck frame
$M_w$	mass of wheelset
N	wheel/rail normal force
$N_o$	static wheelset load
$r_o$	centered wheel rolling radius
V	vehicle speed
x	longitudinal coordinate
y	lateral coordinate
$y_{fc}$	flange clearance
z	vertical coordinate
$\alpha$	creep force saturation constant
$\delta$	contact angle
$\delta_o$	centered wheelset contact angle
$\lambda$	wheel conicity
$\mu$	wheel/rail friction coefficient
$\xi$	creepage
$\phi$	roll angle
$\psi$	yaw angle
$\Omega$	spatial frequency
$\Omega_w$	wheelset angular velocity

Contributed by the Dynamic Systems & Control Division of THE AMERICAN SOCIETY OF MECHANICAL ENGINEERS for presentation at the Winter Annual Meeting, November 15-20, 1981, Washington, D.C. Manuscript received at ASME Headquarters July 9, 1981.

Copies will be available until August 1, 1982.

## INTRODUCTION

Rail vehicles commonly employ profiled wheels to provide forces which restore the wheelset to the center of the track when the wheelset is displaced laterally. Studies of rail vehicles (1-15) have shown that below a critical speed the restoring forces stabilize the vehicle while above a critical speed, a form of instability in which the wheelsets move in a continuous sinusoidal type of motion from flange to flange occurs, called hunting. Recent field tests on a freight car (16) have shown that as speed is increased, from 0-20 m/s no hunting occurs, from 20 m/s to 25 m/s intermittent hunting occurs and above 25 m/s continuous hunting occurs. A primary rail vehicle design requirement is to achieve a critical speed at which hunting develops which is above the vehicle operating speed, since hunting results in high wheel/rail forces, frequent flange contact, poor ride quality and can increase the propensity for derailment.

Many analytical studies of rail vehicle stability have been conducted including studies (2-9) based upon purely linear models in which critical speed is defined as the lowest speed at which the system characteristic equation has an unstable root. Linear stability analysis neglects the effects of rail irregularities and wheel/rail nonlinearities on vehicle motion. A number of studies have employed various forms of equivalent linearization of wheel/rail nonlinearities in the study of single wheelsets and rigid trucks (10-13) and of more complete vehicles (14). A review of the various methods including sinusoidal describing functions and statistical linearization which allows inclusion of track irregularities is included in the study by Hedrick et al. (15). While the quasilinear studies cited have included varying degrees of wheel/rail nonlinearity, none have included creep force saturation. In field tests of passenger vehicles Gilchrist et al. (1) have described hunting in terms of a limit cycle which is essentially independent of rail inputs while Matsudaira (4) has observed that hunting depends on the level of rail alignment irregularities.

In the present study a nonlinear analysis is formulated for a rail passenger truck which includes wheel/rail nonlinearities resulting from normal force variation, geometry and creep force saturation. The model is used to determine truck response to rail alignment irregularities and in particular to determine the motions resulting from flange-rail contact at speeds approaching and above the speed at which hunting develops. The role of creep force saturation in the truck dynamic motion near this speed is evaluated.

## ANALYTICAL FORMULATION

A model for a passenger truck operating on track with alignment irregularities is formulated with six degrees of freedom as shown in Figure 1 - lateral and yaw motions of the truck frame and each wheelset. The truck frame has lateral and yaw secondary suspension elements connected to a carbody which is represented as traveling at constant velocity  $V$  in an inertial reference frame. The model is developed primarily to evaluate the influence of rail irregularities and wheel/rail nonlinearities on truck stability, thus a single truck model is used.

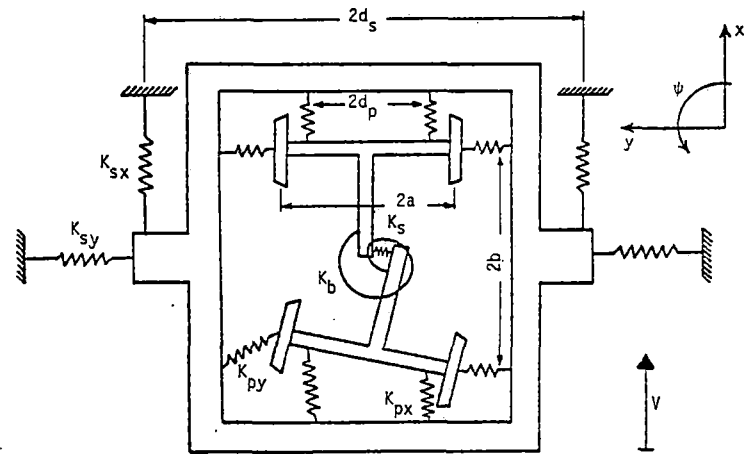


Fig. 1 Six degrees of freedom truck model  
(Each suspension element represents a spring and a damper in parallel)

## Truck Frame Equations

The truck frame equations of motion<sup>1</sup> are expressed in terms of the truck and each wheelset lateral motions  $y_t$ ,  $y_1$ ,  $y_2$  and yaw angles  $\psi_t$ ,  $\psi_1$  and  $\psi_2$ :

$$M_t \ddot{y}_t = 2K_{py} y_1 + 2C_{py} \dot{y}_1 + 2K_{py} y_2 + 2C_{py} \dot{y}_2 - [4K_{py} + 2K_{sy}] y_t - [4C_{py} + 2C_{sy}] \dot{y}_t \quad (1)$$

$$I_{tz} \ddot{\psi}_t = 2bK_{py} y_1 + 2bC_{py} \dot{y}_1 + 2d_p^2 K_{px} \psi_1 + 2d_p^2 C_{px} \dot{\psi}_1 - 2bK_{py} y_2 - 2bC_{py} \dot{y}_2 + 2d_p^2 K_{px} \psi_2 + 2d_p^2 C_{px} \dot{\psi}_2 - [4b^2 K_{py} + 4d_p^2 K_{px} + K_{sy}] \psi_t - [4b^2 C_{py} + 4d_p^2 C_{px}] \dot{\psi}_t \quad (2)$$

The primary suspension coupling the wheelset and the truck frame may be described as:

$$F_{susp_{y1}} = 2K_{py} (y_t + b\psi_t - y_1) + 2C_{py} (\dot{y}_t + b\dot{\psi}_t - \dot{y}_1) \quad (3)$$

$$F_{susp_{y2}} = 2K_{py} (y_t - b\psi_t - y_2) + 2C_{py} (\dot{y}_t - b\dot{\psi}_t - \dot{y}_2) \quad (4)$$

$$M_{susp_{zi}} = 2d_p^2 K_{px} (\psi_t - \psi_i) + 2d_p^2 C_{px} (\dot{\psi}_t - \dot{\psi}_i) \quad (5)$$

## Wheelset Equations

The wheelset equations<sup>2</sup> are derived using the free body diagram in Figure 2 following the development in (17). The external forces and moments acting on the wheelset are:

<sup>1</sup>Parameters are defined in the nomenclature.

<sup>2</sup>The equations presented here omit the radial suspension terms included in the model. These terms are listed in (8).

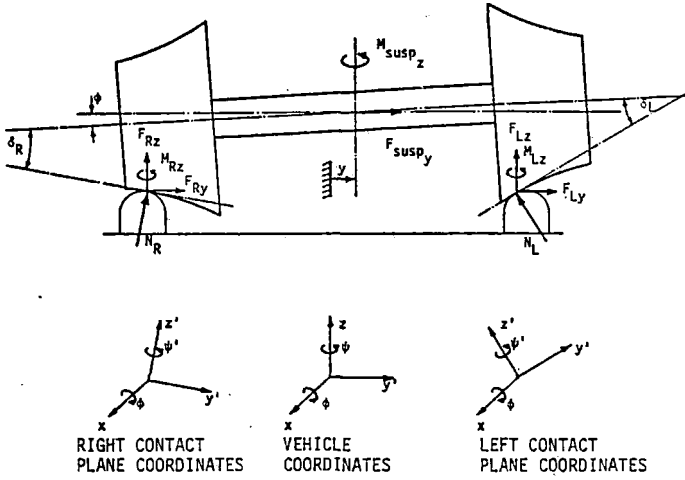


Fig. 2 Free Body Diagram of a Wheelset

$F_{susp_{y_i}}, M_{susp_{z_i}}$  - primary suspension force and moment

$F_{Rz}, M_{Rz}, F_{Ry}, F_{Lz}, M_{Lz}, F_{Ly}$  - creep forces and moments

$N_R, N_L$  - normal wheel/rail forces ('gravitational forces')

The wheelset equations may be derived as:

$$M_{w_i} \ddot{y}_i = F_{Ry} + F_{Ly} + F_{susp_{y_i}} + N_R \sin(\delta_R - \phi) - N_L \sin(\delta_L + \phi) \quad (6)$$

$$I_{wz_i} \ddot{\psi}_i = -I_{wy} \frac{V}{r_o} \dot{\phi} + (F_{Ry} - F_{Ly}) a \psi + (F_{Rx} - F_{Lx}) a + [N_R \sin(\delta_R - \phi) + N_L \sin(\delta_L + \phi)] a \psi$$

$$+ M_{Lz} + M_{Rz} + M_{susp_{z_i}} \quad (7)$$

The equations apply to both wheelsets, with the corresponding values of forces, moments and angles, and include large contact angle geometric nonlinearities as well as variable normal forces.

The normal reactions are computed by

$$N_{R_i} = \frac{[a - r_o \tan(\delta_L + \phi)] F_z^* - M_\phi^*}{[2a - r_o [\tan(\delta_L + \phi) + \tan(\delta_R - \phi)]] \cos(\delta_R - \phi)} \quad (8)$$

$$N_{L_i} = \frac{[a - r_o \tan(\delta_R - \phi)] F_z^* + M_\phi^*}{[2a - r_o [\tan(\delta_L + \phi) + \tan(\delta_R - \phi)]] \cos(\delta_L + \phi)} \quad (9)$$

where  $F_z^* = N_o - (F_{Rz} + F_{Lz})$

$$M_\phi^* = -I_{wy} \frac{V}{r_o} \dot{\psi} - (F_{Ry} + F_{Ly}) r_o + (F_{Rz} - F_{Lz}) a$$

The longitudinal, lateral and spin creepages in the contact planes are given following the development in (17) as:

Left Wheel:

$$\xi_{xL} = \frac{1}{V} [V(1 - \frac{r_L}{r_o}) - a \dot{\psi}]$$

$$\xi_{y'L} = \frac{1}{V} (\dot{y} + r_L \dot{\phi} - V \psi) \cos(\delta_L + \phi) + \frac{1}{V} (\dot{z} + a \dot{\phi}) \sin(\delta_L + \phi)$$

$$\xi_{spL} = \frac{1}{V} [\dot{\psi} \cos(\delta_L + \phi) - \Omega_w \sin \delta_L] \quad (10)$$

Right Wheel:

$$\xi_{xR} = \frac{1}{V} [V(1 - \frac{r_R}{r_o}) + a \dot{\psi}]$$

$$\xi_{y'R} = \frac{1}{V} (\dot{y} + r_R \dot{\phi} - V \psi) \cos(\delta_R - \phi) - \frac{1}{V} (\dot{z} - a \dot{\phi}) \sin(\delta_R - \phi)$$

$$\xi_{spR} = \frac{1}{V} [\dot{\psi} \cos(\delta_R - \phi) + \Omega_w \sin \delta_R] \quad (11)$$

A heuristic nonlinear creep model which combines Kalker's linear creep theory (18) with a creep force saturation representation is used for creep force computation. The creep forces at each wheel are given by

$$F_x = \alpha F_{x_{lin}}; \quad F_{y'} = \alpha F_{y'_{lin}} \quad (12)$$

where  $F_{x_{lin}}, F_{y'_{lin}}$  are the values computed with Kalker's linear creep coefficients, as follows:

$$F_{x_{lin}} = -f_{33} \xi_x \quad (13)$$

$$F_{y'_{lin}} = -f_{11} \xi_{y'} - f_{12} \xi_{sp}$$

the saturation constant,  $\alpha$ , is given by

$$\alpha = \begin{cases} \frac{1}{\beta} [\beta - \frac{\beta^2}{3} + \frac{\beta^3}{27}] & \text{for } \beta \leq 3 \\ \frac{1}{\beta} & \text{for } \beta > 3 \end{cases} \quad (14)$$

where

$$\beta = \frac{\sqrt{F_{x_{lin}}^2 + F_{y'_{lin}}^2}}{\mu N}$$

The creep spin moment is given by

$$M_z' = f_{12} \xi_{y'} - f_{22} \xi_{sp} \quad (15)$$

The values of the creep coefficients are a function of the normal loads  $N_R$ ,  $N_L$ , as follows:

$$\begin{aligned} f_{11} &= \left( \frac{N_i}{N_w} \right)^{2/3} f_{11N} ; f_{22} = \left( \frac{N_i}{N_w} \right)^{4/3} f_{22N} \\ f_{12} &= \left( \frac{N_i}{N_w} \right)^{2/3} f_{12N} ; f_{33} = \left( \frac{N_i}{N_w} \right)^{2/3} f_{33N} \end{aligned} \quad (16)$$

where  $f_{jk}$  are the nominal values computed with the static wheel load  $N_w = \frac{N_o}{2}$ , and  $N_i$  is the actual value of  $N_R$  or  $N_L$ . The contact plane creep forces and moments are then transformed to the truck coordinates by

Left Wheel

$$\begin{aligned} F_{Ly} &= F_{Ly'} \cos(\delta_L + \phi) \\ F_{Lz} &= F_{Ly'} \sin(\delta_L + \phi) \\ M_{Lz} &= M_{Lz'} \cos(\delta_L + \phi) \end{aligned} \quad (17)$$

Right Wheel

$$\begin{aligned} F_{Ry} &= F_{Ry'} \cos(\delta_R - \phi) \\ F_{Rz} &= -F_{Ry'} \sin(\delta_R - \phi) \\ M_{Rz} &= M_{Rz'} \cos(\delta_R - \phi) \end{aligned} \quad (18)$$

In the analysis the rolling radii  $r_L$  and  $r_R$ , the contact angles  $\delta_L$  and  $\delta_R$ , the wheelset vertical motion  $z$  and its roll angle  $\phi$  are taken from tables as functions of the excursions. The values of  $z$  and  $\phi$  are computed using data from tables and the time derivative of the excursion. The normal wheel/rail forces  $N_L$  and  $N_R$  are computed considering the nonlinear wheel/rail geometry, the creep forces, and the static loads. The track inputs enter the equations of motion through the nonlinear wheel/rail geometry terms,  $r_L$ ,  $r_R$ ,  $\delta_L$ ,  $\delta_R$  and  $\phi$  which are functions of the wheelset excursion ( $y - y_r$ ) and are tabulated in the computer code. These terms affect both the normal and the creep wheel/rail forces.

#### Linearized Wheelset Equations

A linearized model of the wheel/rail interaction forces is obtained from the nonlinear model if conical wheels, constant wheel/rail loads and a linear creep law are used (17). The following assumptions with respect to wheel/rail geometry are employed:

$$\frac{(r_L - r_R)}{2a} = \frac{\lambda}{a} \Delta y ; \quad \frac{(\delta_L - \delta_R)}{2} \approx 0$$

$$\phi \approx \frac{a_1}{a} \Delta y ; \quad a_1 = \lambda \quad (19)$$

$$\frac{(r_L + r_R)}{2} \approx r_o ; \quad \frac{(\delta_L + \delta_R)}{2} \approx \delta_o$$

The linear wheelset equations then become:

Lateral Equation:

$$\begin{aligned} M_w \ddot{y} &= \frac{-2f_{11}}{V} [\dot{y} + \frac{a_1 r_o}{a} \dot{y} - V\psi] - \frac{2f_{12}}{V} \dot{\psi} \\ &\quad - \frac{N_o}{a} a_1 y + F_{susp_y} + u_L(t) \end{aligned} \quad (20)$$

Yaw Equation:

$$\begin{aligned} I_{wz} \ddot{\psi} &= -I_{wy} \frac{a_1 V}{a r_o} \dot{y} - \frac{2af_{33}\lambda}{r_o} y \\ &\quad + \frac{2f_{12}}{V} [\dot{y} + \frac{a_1 r_o}{a} \dot{y} - V\psi] - \frac{2a^2 f_{33}}{V} \dot{\psi} - \frac{2f_{22}}{V} \dot{\psi} \\ &\quad + N_o a \delta_o \psi + M_{susp_z} + u_\psi(t) \end{aligned} \quad (21)$$

The linear alignment input terms in the equations are

$$\begin{aligned} u_L(t) &= \frac{2f_{11} a_1 r_o}{aV} y_r + N_o \frac{a_1}{a} y_r \\ u_\psi(t) &= \left( \frac{I_{wy} a_1 V}{a r_o} - \frac{2f_{12} a_1 r_o}{aV} \right) \dot{y}_r + \frac{2af_{33}\lambda}{r_o} y_r \end{aligned} \quad (22)$$

where  $y_r$  and  $\dot{y}_r$  are the alignment irregularity and its derivative at the wheel. If the inputs are referred to the leading wheelset,  $y_r = y_r(t)$  for the leading wheelset and  $y_r = y_r(t - 2b/V)$  for the trailing wheelset.

#### Rail Input Profile

A rail alignment input profile was generated by passing Gaussian white noise through a linear digital filter to generate a random Gaussian rail alignment time history. The spectral density of the alignment profile is:

$$S_a = \frac{2\pi A \Omega_c^2 k_a^2}{(\Omega^2 + \Omega_a^2)(\Omega^2 + \Omega_c^2)} ; \quad [\text{mm}^2/(\text{cycle/m})] \quad (23)$$

where the numerical values of the parameters in Equation (23) are given in Table 1 and where the parameter  $k_a$  is varied to represent various classes of track, with  $k_a = 0.5$ , corresponding approximately to data measured on class 6 track (19). Field studies of track geometry indicate that alignment track power spectral densities are best represented with  $\Omega_a = 0$  in Equation 23. In this study the value of  $\Omega_a = 0.05$  rad/m is introduced to achieve a finite mean square value of the alignment input, which is necessary

Table 1 Values of baseline vehicle parameters

a	0.716 m
a <sub>1</sub>	0.1
b <sub>1</sub>	1.295 m
C	17513 N-s/m
d <sup>sy</sup>	0.610 m
f <sub>11</sub>	9430000 N
f <sub>33</sub>	10230000 N
I <sub>t</sub>	3371 kg-m <sup>2</sup>
I <sub>t</sub>	761 kg-m <sup>2</sup>
K <sub>w</sub>	0.0 N-m/rad
K <sub>o</sub>	9120000 N/m
K <sub>px</sub>	5840000 N/m
K <sub>py</sub>	0.0 N/m
K <sub>s</sub>	350260 N/m
K <sub>sy</sub>	1356000 N-m/rad
K <sub>sψ</sub> = 2d <sub>s</sub> <sup>2</sup> K <sub>sx</sub>	3649 kg
M <sub>ψ</sub>	1751 kg
M <sub>w</sub>	133000 N
N <sub>o</sub>	0.457 m
r <sub>o</sub>	8.9 mm
y <sub>fc</sub>	0.1
λ	0.1
μ	0.2
A	3.37 mm <sup>2</sup> /(m/rad)
Ω <sub>c</sub>	0.824 rad/m
Ω <sub>a</sub>	0.05 rad/m

for digital simulation. For this value only wavelengths of 100 m/cycle or more are significantly distorted. The rms value of the alignment input with  $k_a = 1.0$  is 10.0 mm.

#### Baseline Parameters

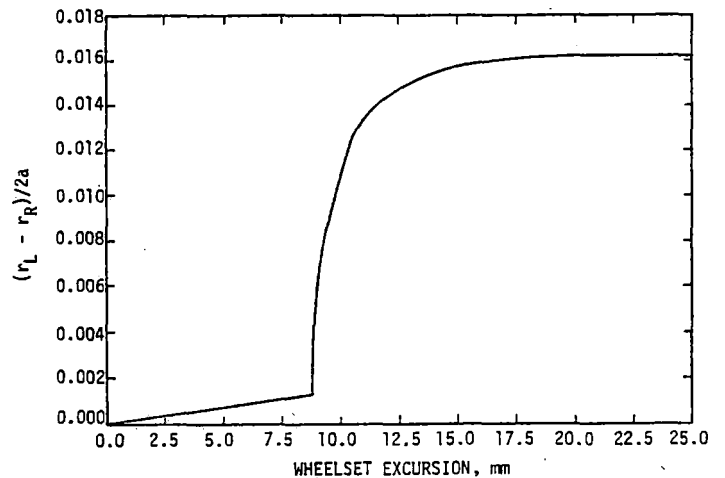
A set of baseline truck parameters which correspond to a conventional passenger truck are summarized in Table 1. The general wheel profile used in the study is conical in the tread region with a fixed constant conicity and has the standard AAR flange geometry; for a conicity of 0.07 the profile is the standard AAR profile. Both the flange clearance, and the tread region conicity may be varied parametrically in the analytical wheel profile. The rolling radii and contact angle differences for the profile with conicity of 0.1 are shown in Figure 3. In the digital simulation the wheel profile is stored in tables.

#### CRITICAL SPEED AND WHEELSET EXCURSION DATA

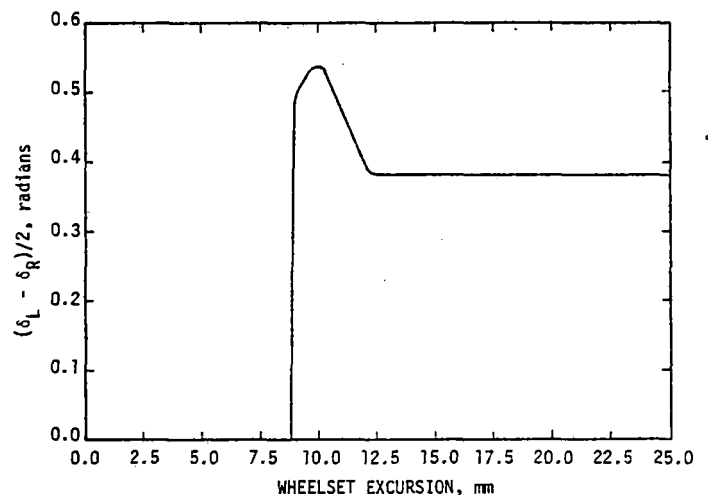
The critical speed of the baseline truck computed using the linear model is plotted in Figure 4 as a function of conicity for two sets of values of creep coefficients. The critical speed is a relatively weak function of creep coefficients and varies inversely with the square root of conicity,  $v_{cr} \approx 1/\sqrt{\lambda}$ . For the baseline vehicle the critical speed is 73 m/s at  $\lambda = 0.1$ .

The rms truck front wheelset excursion computed with the linear model is plotted in Figure 5 as a function of speed and conicity for the baseline vehicle operating with a track roughness coefficient  $k_a = 1.0$ . The rms excursion increases with speed at speeds far below the critical, because of the increased value of high frequency inputs. At speeds near the critical the excursion increases rapidly, because linear instability is approached.

Two operating points are identified in the figure, for which nonlinear digital simulations are conducted. Point A which is at a velocity about half the critical speed and Point B which is 85% of the critical speed. At Point A the rms excursion is 0.58 standard deviations of the flange clearance of 8.9 mm



(a) ROLLING RADII DIFFERENCE



(b) CONTACT ANGLE DIFFERENCE

Fig. 3 General wheel/rail geometry ( $\lambda=0.1$ ;  $y_{fc}=8.9\text{mm}$ )

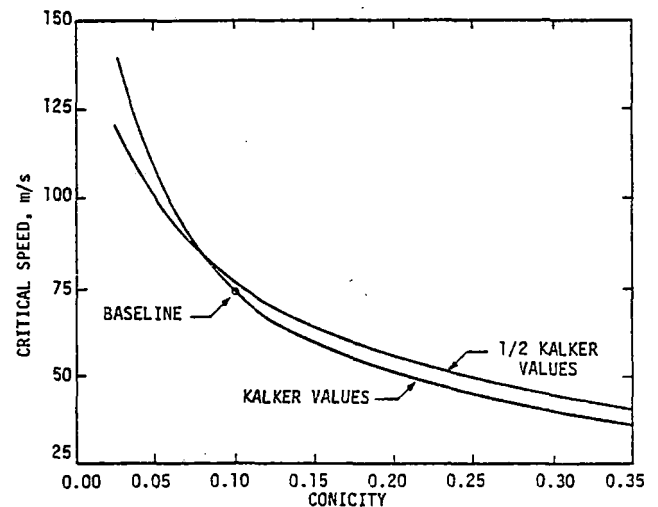


Fig. 4 Effect of conicity and creep coefficients on truck linear critical speed

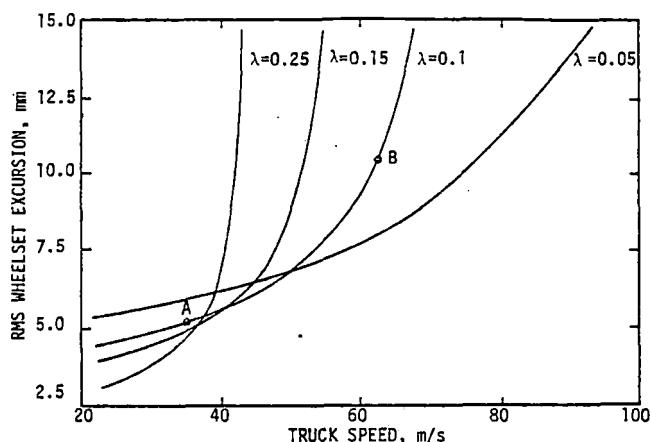


Fig. 5 Effect of speed and conicity on wheelset excursion ( $k_a=1.0$ )

indicating on a linear basis that the wheel excursion would exceed the flange clearance 8.7% of the time. If the track roughness spectral density level were reduced by a factor of four the rms excursion is reduced by a factor of two and is 0.29 standard deviations of the flange clearance. The corresponding time fraction for which the excursion exceeds the flange clearance is less than 0.06%.

Point B corresponds to an rms excursion which is 1.16 times the flange clearance, thus flange contact occurs almost with every cycle of kinematic motion. If the alignment spectral density were reduced by factor of four, the rms excursion would be 0.58 times the flange clearance and the excursion would exceed the flange clearance 8.7% of the time.

#### NONLINEAR SIMULATION

A set of five nonlinear simulations of the base-line truck running with a conicity of 0.1 at 36 m/s, 63 m/s and 76 m/s were performed. The excursion time history of the leading wheelset for each case is shown in Figure 6. Cases 1 and 2 represent vehicles operated at one half the critical speed with case 1 on smooth track,  $k_a=0.5$ , and case 2 on rougher track,  $k_a=1.0$ . In case 1 the vehicle rarely has flange contact and the excursion probability density shown in Figure 7a is almost Gaussian. In case 2 the wheelset flanges frequently and one of the wheels is in flange contact 1.4% of the time. This value is less than the linear estimate of 8.7%, because of the large forces developed on flanges. The excursion probability density is shown in Figure 7b and is no longer Gaussian.<sup>3</sup> During the simulation the maximum penetration into the flange is 0.46 mm. Case 2 illustrates a truck running with a large critical speed margin but in which frequent flanging occurs because of alignment irregularities. Even though penetration of the flange region is small, the excursion probability density function is modified significantly from a Gaussian density<sup>3</sup> and a linear analysis is inadequate to predict wheelset motions and forces.

Case 3 represents the truck running at 85% of its critical speed on a smooth track,  $k_a=0.35$ . In this case, intermittent hunting occurs at the kinematic frequency which is excited by track roughness.

<sup>3</sup>The probability density may be accurately represented by a  $\beta^*$  density function (20).

Because the truck is run below the critical speed, it is stable and the large excursions decay after several cycles.

In the fourth case the truck is run above the linear critical speed on a smooth track,  $k_a=0.1$ . Frequent flanging occurs and the response has a strong component at the kinematic (hunting) frequency. The probability density function for this case is shown in Figure 7c and illustrates the frequent excursion into the flange.

In the fifth case the truck is run above the critical speed on a moderately rough track,  $k_a=0.5$ . The time history is similar to that of the smooth track and is dominated by the kinematic response frequency. For the rough track case the maximum flange penetration of 2.8 mm indicates wheel climb which is significantly greater than the flange penetration of 0.38 mm in the smooth track case.

In cases where the truck operates far below its linear critical speed the kinematic mode damping ratio is high and the rms linear wheelset excursion is less than the rms alignment input, as at Point A in Figure 5. Cases 1 and 2 are in this category. The excursion spectral density for case 2 is shown in Figure 8a, and most of the mean squared value is in a relatively wide frequency band centered at the kinematic frequency at 2 Hz. In cases where the truck operates close to, or above its linear critical speed the linearly computed excursion is larger than the rail alignment excursion, as at point B in Figure 5. Cases 3, 4 and 5 are in this category. The excursion spectral density for case 4 is shown in Figure 8b. Most of the mean squared value is in a very narrow frequency band at the kinematic frequency at 5 Hz.

In cases 1, 2 and 3 the truck is stable in the tread region, and flange contact occurs due to rail irregularities. In cases 4 and 5 the motion generated in the tread region is unstable and grows each cycle until flange contact occurs. In all cases the net effect of the flange contact is stabilizing, and it forces the wheelset back to the centerline, preventing derailment.

When flange contact develops the wheel/rail geometry changes abruptly, as shown in Figure 3. The rolling radius of the flanging wheel increases significantly, resulting in a large longitudinal creepage, as shown by Equations (10) and (11). If the creepage-creep force relationship were linear, large moments due to longitudinal creep forces would develop and lead to the development of a yaw angle  $\psi$  in the direction away from the flange. The yaw angle would cause a large lateral velocity away from the flange, through lateral creep forces. Since this sequence of events would be associated with the very high conicities developed on flange, it would result in instability as in the linear model with high conicity, as shown in Figure 4. However, since the maximum creep force at each wheel is limited to the friction limit  $\mu N$ , the destabilizing effect of high conicity on flanges is significantly reduced. The primary effect during flange contact is the gravitational stiffness, which is a direct result of the large contact angle ( $\sim 60^\circ$ ) of the flanging wheel. The large normal force developed between the rail and the flange limits the penetration into the wheel flange region to the low values illustrated in the digital simulations. When the coefficient of friction between the wheels and the rails is increased, higher creep forces develop and the destabilizing effect of the high conicity on flange becomes more significant. The truck of case 2 with the nominal value  $\mu = 0.2$  develops maximum flange penetration of 0.46 mm, and the wheels are in flange contact 1.4% of the time. With  $\mu = 0.5$ , the maximum

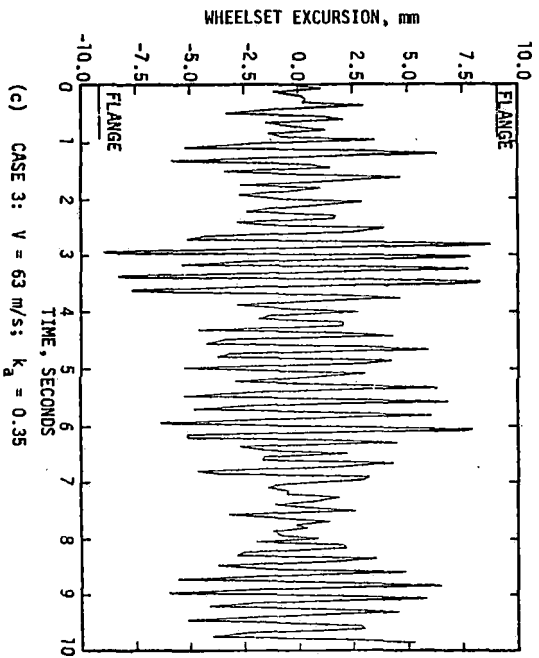
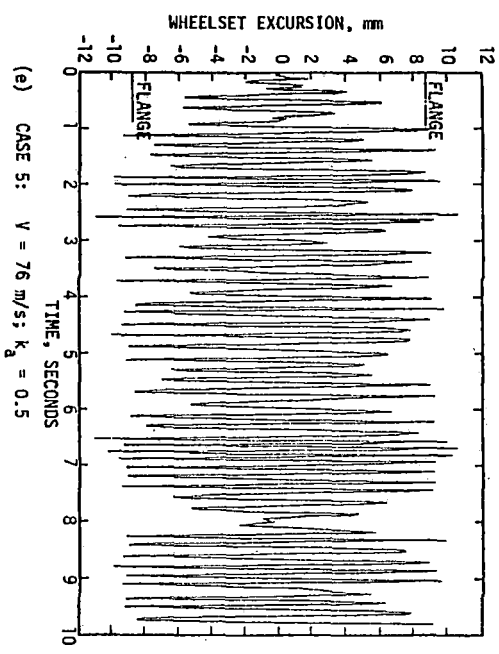
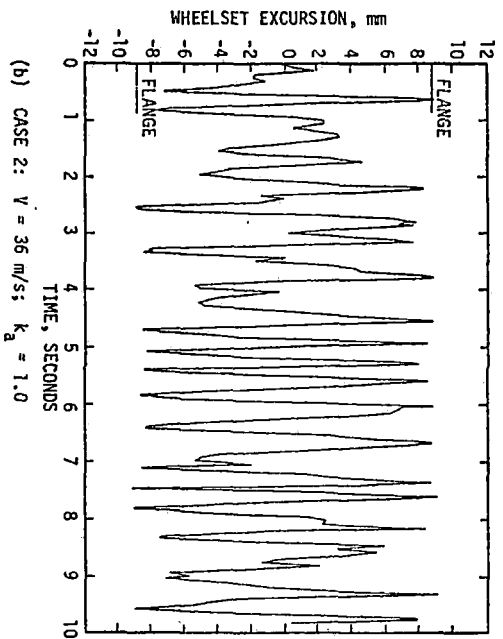
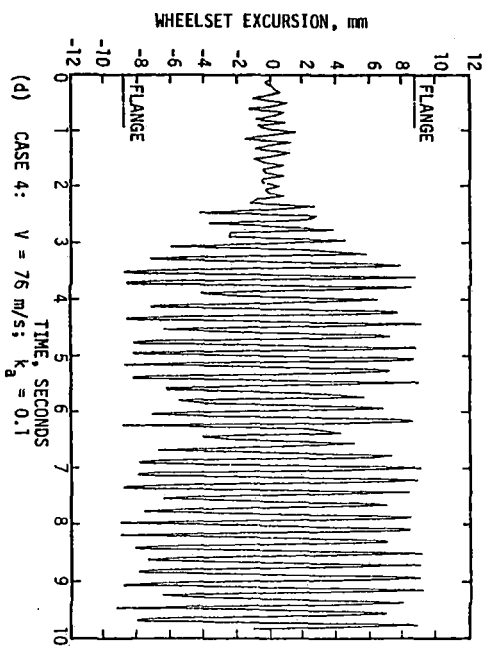
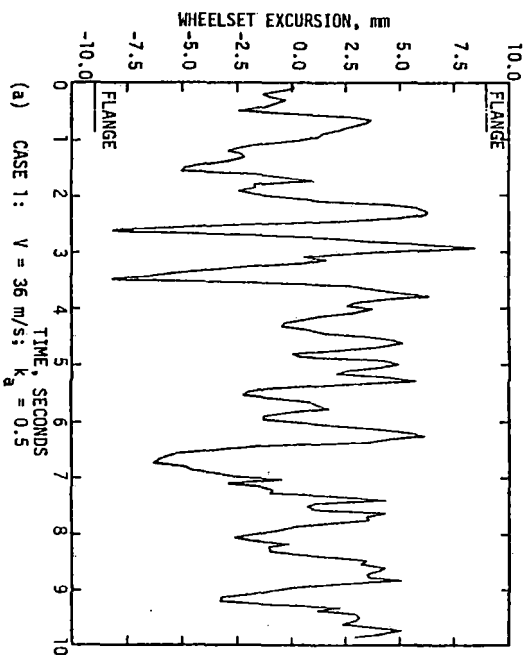
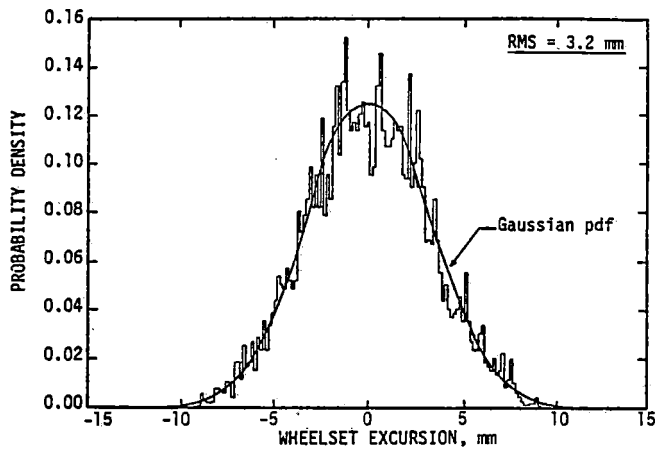
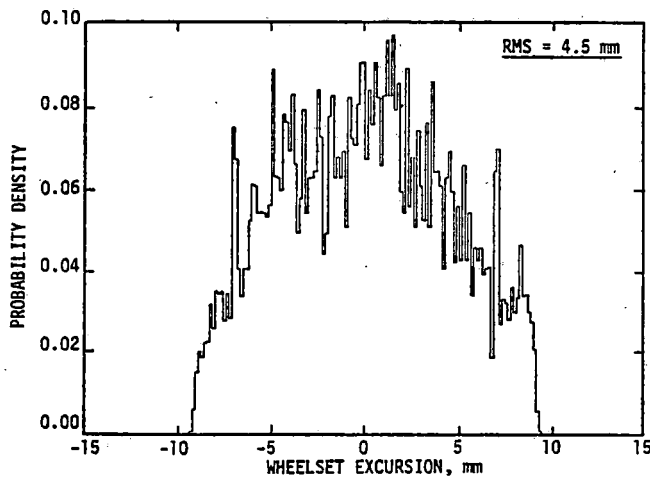


Fig. 6 Leading wheelset excursion

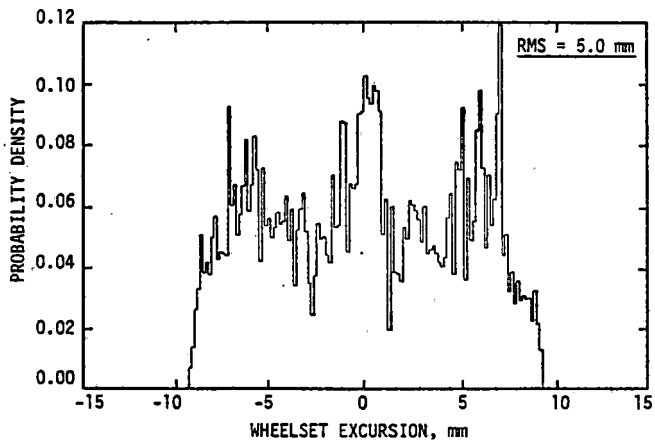




(a) CASE 1:  $V = 36 \text{ m/s}$ ;  $k_a = 0.5$

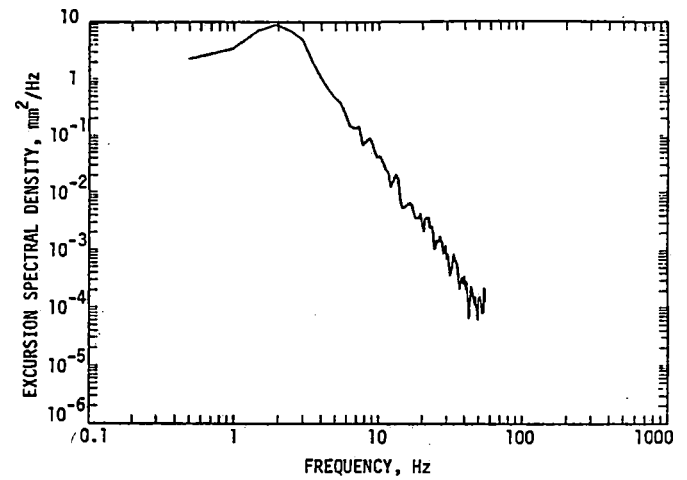


(b) CASE 2:  $V = 36 \text{ m/s}$ ;  $k_a = 1.0$

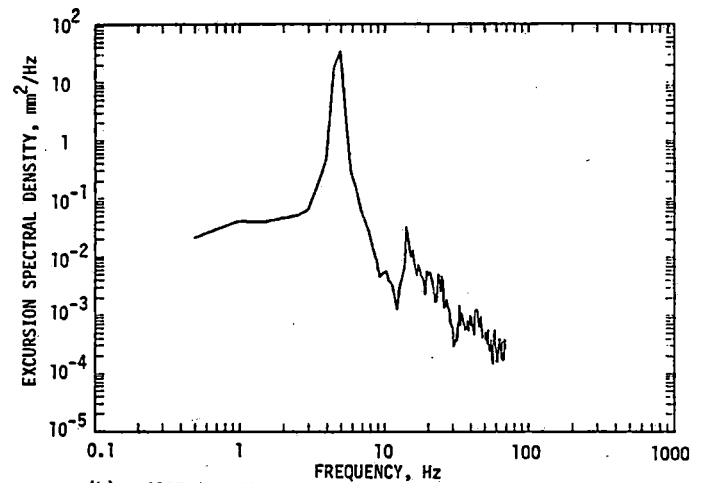


(c) CASE 4:  $V = 76 \text{ m/s}$ ;  $k_a = 0.1$

Fig. 7 Leading wheelset excursion probability density function



(a) CASE 2:  $V = 36 \text{ m/s}$ ;  $k_a = 1.0$



(b) CASE 4:  $V = 76 \text{ m/s}$ ;  $k_a = 0.1$

Fig. 8 Leading wheelset excursion spectral density

penetration increases to 0.59 mm and the wheels are in flange contact 2.3% of the time. A similar increase in severity of flanging is observed in the linearly unstable truck of case 4, when the coefficient of friction is increased. Thus the saturation level of the creep force is an important factor in response of flanging (hunting) rail vehicles, and the use of linear creep laws overestimates the severity of wheel climb.

#### PROTOTYPE TRUCK RESPONSE

A set of six truck designs in which primary suspension stiffnesses have been selected to yield critical speed for a conicity of 0.1 varying from 58 m/s to 88 m/s are summarized in Table 2. Two of the trucks

Table 2 Parameters of six truck designs

No.	$d^2 K_{p \text{ px}}$	$K_{p \text{ py}}$	$K_s$	$V_{cr} (\lambda=0.1)$	$R (\lambda=0.1)$
	N-m/rad	N/m	N/m	m/s	m
C1	2170000	2920000	0.0	58	830
C2	2170000	14600000	0.0	63	870
C3*	3390000	5840000	0.0	73	1250
C4	4340000	7300000	0.0	84	1580
R1	1080000	1460000	58400000	56	970
R2	2170000	2920000	58400000	88	1160

\* C3 is the baseline truck.

represent radial designs with finite shear stiffness,  $K_s$ , due to interaxle connections. For the trucks the minimum radius curve which can be negotiated in steady-state curving is also tabulated for a conicity of 0.1. For the conventional and radial truck designs as the critical speed is increased by altering suspension design, the degree of curve negotiation is decreased. The rms wheelset excursions computed with the linear model for the six trucks at 49 m/s are plotted in Figure 9 as a function of conicity. The excursions in Figure 9 also include contributions due to cross-level track inputs, which account for about 5% of the total rms values (20).

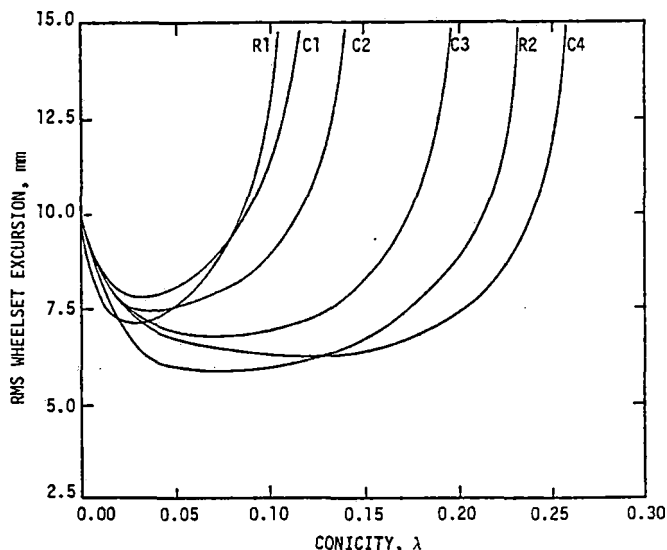


Fig. 9 Response of six truck designs  
( $V = 49$  m/s;  $k_a = 1.0$ )

For each truck design in Figure 9 the excursions at zero conicity are identical since the truck does

not track. As the conicity is increased the excursions are reduced since the truck is able to follow the track alignment longer wavelength irregularities and reduce the relative excursion. As the conicity is increased further a point is reached at which wheelset excursions increase as conicity is increased, because the stability margin of the truck is decreasing as the linear critical speed reduces with increased conicity. In truck design it is desirable to keep the truck from frequently flanging, thus for any truck design a conicity should be selected which provides a minimum excursion. For conventional designs 1 and 2, a conicity between 0.02 and 0.05 is desired since the trucks have a relatively low critical speed while for conventional design 3 and radial design 2 conicities between 0.03 and 0.11 are desirable providing an increased range of conicities for which excursions are kept to a minimum. For radial truck design 1 a conicity close to 0.025 is required while for conventional design 4 conicities between 0.05 and 0.017 are desirable providing an increased range of desirable conicities.

For the truck designs operating on a track with  $k_a=0.5$  the ratio of rms wheelset excursion to flange clearance at the optimum conicities is between one third and one half indicating infrequent flange contact occurs. This case corresponds to class 6 track.

The design criteria for truck stability can be initially considered in terms of wheelset excursions with desirable designs providing rms excursions which are a fraction of flange clearance at design operating speeds and which have a relatively broad capability for providing performance over a range of wheel conicities. The lower limit on conicity is determined to prevent large excursion due to poor tracking. The higher limit is determined to avoid large excursions as linear instability is approached.

The flanging frequency and severity of linearly stable trucks can be reduced by increasing the flange clearance, thus allowing the wheelsets to stop their lateral motion without flange contact. However, if linear instability is possible because of profile or suspension element wear, the flange clearance should be low so that the flange contact occurs before the wheelset lateral velocity diverges to large values due to instability and increases the propensity for wheel climb.

#### SUMMARY

A nonlinear analysis for rail passenger truck stability and response to track alignment irregularities has been developed. The analysis has been used to illustrate the influence of track roughness, wheel profile parameters and creep on wheelset flanging and truck stability.

For the passenger truck, linear analysis is capable of indicating when frequent flanging is likely and the linear critical speed provides a good indication of stability limits. At truck operating speeds below the linear critical speed, flanging occurs primarily due to the track alignment irregularities. As the ratio of rms excursion to flange clearance exceeds 0.4, the excursion probability density deviates significantly from a Gaussian distribution and nonlinear wheel/rail forces are significant.

The nonlinear simulations of cases in which frequent flanging occurs either due to track irregularities or due to lack of stability have indicated that the saturation level of creep forces is important and that the geometric restoring forces are the primary stabilizing forces during flanging.

# ACKNOWLEDGEMENTS

Support for the research reported in this paper was provided by the Office of University Research, U.S. D.O.T., under contract No. DOT-OS-70052 and by the Federal Railroad Administration and the Transportation Systems Center under contract DOT-TSC-1471.

## REFERENCES

- 1 Gilchrist, A.O. et al., "The Riding of Two Particular Designs of Four-Wheeled Railway Vehicle", Proceedings of the Institution of Mechanical Engineers, Interaction Between Vehicle and Track, Vol. 180, Part 3F, 1966, pp. 99-113.
- 2 Wickens, A.H., "The Dynamic Stability of Railway Vehicle Wheelsets and Bogies Having Profiled Wheels", Int. J. Solid Structures, Vol. 1, 1965, pp. 319-341.
- 3 Wickens, A.H., "Steering and Dynamic Stability of Railway Vehicles", Vehicle System Dynamics, 5(1975/1976), pp. 15-46.
- 4 Matsudaira, T., "Hunting Problem of High Speed Railway Vehicles with Special Reference to Bogie Design for the New Tokaido Line", Proceedings of Institute of Mechanical Engineers, Vol. 180, 1965, p. 58.
- 5 Scheffel, H., "The Hunting Stability and Curving Ability of Railway Vehicles", Rail International, February 1974, pp. 154-176.
- 6 Scheffel, H., "The Influence of the Suspension on the Hunting Stability of Railway Vehicles", Rail International, August 1979, pp. 662-696.
- 7 Cooperrider, N.K., "The Lateral Stability of Conventional Railway Passenger Trucks", Proceedings of the First International Conference on Vehicle Mechanics, 1968, pp. 37-54.
- 8 Bell, C.E., Horak, D. and Hedrick, J.K., "Stability and Curving Mechanics of Rail Vehicles", Presented at the 1980 ASME Winter Annual Meeting, Chicago, December 1980 (ASME paper 80-WA/DSC-15).
- 9 Horak, D., Bell, C.E. and Hedrick, J.K., "A Comparison of the Stability and Curving Performance of Radial and Conventional Rail Vehicle Trucks", presented at the 1979 ASME Winter Annual Meeting, New York, December 1979.
- 10 DePater, A.D., "The Approximate Determination of the Hunting Movement of a Railway Vehicle by Aid of the Method of Krylov and Bogoliubov", Paper delivered at the Xth International Congress of Applied Mechanics at Stressa, 1960.
- 11 Stassen, H.G., "Random Lateral Motions of Railway Vehicles", WTHD. No. 49, Laboratory for Measurement and Control, Delft University of Technology, the Netherlands, 1973.
- 12 Cooperrider, N.K., Hedrick, J.K., Law, E.H. and Malstrom, C., "The Application of Quasi-Linearization Techniques to the Prediction of Non-linear Railway Vehicle Response", Vehicle System Dynamics, Vol. 6, No. 2-3, July 1975, pp. 141-148.
- 13 Hannebrink, D.N., Lee, H., Weinstock, H., and Hedrick, J.K., "Influence of Axle Load, Track Gage, and Wheel Profile on Rail Vehicle Hunting", Journal of Engineering for Industry, Trans. ASME, Vol. 99, No. 1, February 1977, pp. 186-195.
- 14 Hull, R. and Cooperrider, N.K., "Influence of Nonlinear Wheel/Rail Contact Geometry on Stability of Rail Vehicles", Journal of Engineering for Industry, Trans. ASME, Vol. 99, No. 1, February 1977, pp. 172-185.
- 15 Hedrick, J.K., Cooperrider, N.K. and Law, E.H., "The Application of Quasi-Linearization Techniques to Rail Vehicle Dynamic Analyses", Technical Report prepared under U.S. Department of Transportation Contract DOT-TSC-FRA-78-6, November 1978.
- 16 Fries, R.H., Cooperrider, N.K. and Law, E.H., "Railway Freight Car Field Tests". Presented at the 1980 Winter Annual Meeting, November 1980, Chicago (ASME Paper 80-WA/DSC-7).
- 17 Arslan, A.V., "The Application of Statistical Linearization to Nonlinear Rail Vehicle Dynamics", Ph.D. thesis, Dept. of Mechanical Engineering, M.I.T., 1980.
- 18 Kalker, J.J., "On the Rolling Contact of Two Elastic Bodies in the Presence of Dry Friction", Doctoral Dissertation, Technische Hogeschool, Delft, Netherlands, 1967.
- 19 Corbin, J.C., "Statistical Representation of Track Geometry", Technical Report prepared under U.S. Department of Transportation Contract DOT-TSC-1211, April 1979.
- 20 Horak, D., "Passenger Rail Vehicle Dynamics", Ph.D. thesis, Dept. of Mechanical Engineering, M.I.T., 1981.

Section 5 points out that simple models will be used in the various performance regimes to complement the use of more sophisticated models being validated and applied. A set of such models which has thus far been identified as being useful is here documented. These models, however, are not necessarily a complete set. As the program continues, additional simple models may be required as new insights and behavior quirks are found in exercising and validating the sophisticated models, and in interpreting test data. The simple models include kinematic models, steady state models, and simple spring/mass models.

### KINEMATIC MODELS

The simplest kinematic model is that of a free wheelset. Numerous references giving an explanation of the motion of a free wheelset may be found in the literature, the earliest being Klingel (1) and Carter (2). For such motion it has been established that the wavelength of the laterally oscillating wheelset is

$$S = 2\pi \sqrt{\frac{ar}{\lambda}}$$

and the frequency is

$$f = \frac{V}{2\pi} \sqrt{\frac{\lambda}{ar}}$$

Where:

- a - half-rail gauge
- r - nominal rolling radius
- $\lambda$  - conicity or wheel taper ratio

These fundamental kinematic wavelength and frequency relationships provide a means of checking the more sophisticated lateral stability models especially at low speed where inertial effects are not significant.

The simple kinematic model can be extended to include the effects of the primary suspension stiffness, wheel/rail geometry, creep, and inertia in a 2 dof model in which coupled wheelset lateral and yaw displacements are represented (3). With this representation it is found that there is a critical speed above which any wheelset disturbance will grow with time. The critical speed is given by

$$V_c^2 = \frac{2 \left[ k_{py} d_1^2 \bar{F} + a^2 (k_{px} + k_g) \right] \lambda}{a^2 m_w + \bar{F} I_{wy}} \frac{\lambda}{ar}$$

(1) Klingel, "On the Performance of Railway Vehicles on a Straight Track," *Organ Fortschr. Eisenb. Wes.*, Vol. 38, 1883, pp. 113-123.

(2) Carter, F.W., "On the Stability of Running of Locomotives," *Proceedings of the Royal Society, Series A*, Vol. 121, 1928, pp. 585-611.

(3) Wickens, A.H., "The Dynamic Stability of Railway Vehicle Wheelsets and Bogies Having Profiled Wheels," *International Journal of Solids and Structures*, Vol. 1, No. 3, 1965, pp. 385-406.

Where:

- $k_{px}, k_{py}$  - lateral and longitudinal primary stiffnesses per bearing respectively
- $k_g$  - gravitational stiffness determined by the axle loading and wheel/rail geometry
- $d_1$  - distance from truck centerline to the axle bearing
- $m_w$  - mass of a wheelset
- $I_{wy}$  - yaw moment of inertia of a wheelset
- $\bar{F}$  - ratio of lateral to longitudinal creep forces

The kinematic wave length is unchanged, hence the frequency at the critical speed is

$$f_c = \frac{V_c}{2\pi} \sqrt{\frac{\lambda}{ar}}$$

A second 2 dof representation is also used by several researchers (4,5) to find the critical speed for a rigid two-axle truck. For that representation the secondary suspension is taken into account along with truck inertial effects. Assuming nearly equal lateral and longitudinal creep the critical speed for a symmetric rigid truck is given by Law and Cooperrider (6) as:

$$V_c^2 = \frac{\left[ k_r + 2\ell^2 k_g + 2(\ell^2 + a^2)(k_{sx} + k_g) \right] \frac{ra}{\lambda} (\ell^2 + a^2)}{I_{ty} + m_t (\ell^2 + a^2) \frac{ra}{\lambda} \frac{(\ell^2 + a^2)}{a^2}}$$

Where:

- $k_r$  - rotational centerplate stiffness per truck
- $k_{sx}$  - lateral secondary stiffness per side frame
- $\ell$  - the truck wheelbase
- $I_{ty}$  - total truck yaw moment of inertia
- $m_t$  - total truck mass

The kinematic frequency for a rigid truck is

$$f = \frac{V}{2\pi} \sqrt{\frac{\lambda}{ar} \left( \frac{a^2}{\ell^2 + a^2} \right)}$$

(4) Cooperrider, N.K., "The Lateral Stability of Conventional Railway Passenger Trucks," *Proceedings of the First International Conference on Vehicle Mechanics*, Wayne State University, Detroit, Michigan, July 1968.

(5) Tuten, J.M., Law, E.H., and Cooperrider, N.K., "Lateral Stability of Freight Cars with Axles Having Different Wheel Profiles and Asymmetric Loading," *ASME Paper No. 78-RT-3*, April 1978.

(6) Ibid.

Thus the effect of the truck wheelbase is to reduce the kinematic frequency of a truck below that of a simple wheelset. As in the case of a sprung wheelset the critical frequency for a rigid truck is governed by the kinematic frequency relationship:

$$f_c = \frac{V_c}{2\pi} \sqrt{\frac{\lambda}{ar} \left( \frac{a^2}{\ell^2 + a^2} \right)}$$

### TRUCK/WHEELSET MOTIONS.

Certain of the more sophisticated models to be assessed in the TDOP Phase II effort include degrees of freedom for which simple models can be used to explain high frequency behavior.

For example, it has been found that a 1 dof spring/mass model can explain the high frequency lateral oscillations of the two wheelsets with respect to the side frames. The model consists of one lumped mass for the two side frames, one lumped mass for the two wheelsets, and a spring representing the lateral primary suspension. The natural frequency for such a system is given by

$$f = \frac{1}{2\pi} \sqrt{\frac{2(m_w + m_s)k_{px}}{m_w m_s}}$$

Where:

$m_s$  - mass of side frame

The simple model is accurate provided the primary suspension stiffness  $k_{px}$  is large relative to the gravitational stiffness and  $k_{px}$  the secondary lateral stiffness. Another 1 dof model explains high frequency wheelset/truck warp motions. The model consists of two rotational inertias, one representing that of the wheelsets yawing in phase, the second representing the rotational inertia of the side frames and bolster as the truck warps. The two rotational inertias are connected by the primary suspension stiffnesses. For this system the natural frequency is

$$f = \sqrt{\frac{(k_w + 4k_{py}d_1^2)(2I_{wy} + 2m_s d_1^2 + I_{by})}{(2m_{sd_1^2} + I_{by})(2I_{wy})}}$$

Where:

$k_w$  - warp stiffness per truck (typically small compared to  $4k_{py}d_1^2$ )

$I_{by}$  - yaw moment of inertia of the bolster

This model is accurate for large values of primary longitudinal stiffness  $k_{py}$ .

A third 1 dof model can be used to predict another wheel set/truck natural frequency in which the wheelsets move laterally 180 degrees out of phase and the truck warps in phase with one of the two wheelsets, 180 degrees out of phase with the other. For small motions the wheelsets can be considered to be rotating about the center of the truck. The 1 dof model is then one rotational inertia representing the wheelset "rotation," a rotational inertia for the truck, and the lumped stiffness of the primary suspension. The frequency is given by

$$f = \frac{1}{2\pi} \sqrt{\frac{2k_{px}\ell^2(m_w\ell^2 + I_{sy})}{(m_w\ell^2)(I_{sy})}}$$

Where:

$I_{sy}$  - yaw moment of inertia of the side frame

Again the above analysis applies when  $k_{px}$  is large.

### CARBODY NATURAL FREQUENCIES

A great deal of insight can be obtained by comparing test data and model results with calculated natural frequencies for the fundamental carbody motions. These include:

- sway (pure lateral)
- bounce
- roll
- pitch
- yaw

Bounce, pitch, and yaw can generally be treated to a first order degree of accuracy as not being coupled to other motions. In the case of sway and roll, however, there is often significant coupling giving rise to the so called lower center roll and upper center roll motions. For those motions a 2 dof model with coupled carbody lateral and roll motions is required. The frequencies for the uncoupled motions are given below.

$$f_{\text{sway}} = \frac{1}{2\pi} \sqrt{\frac{4k_{sx}}{m_c}}$$

Where:

$m_c$  - carbody mass

$$f_{\text{bounce}} = \frac{1}{2\pi} \sqrt{\frac{4k_{sz}}{m_c}}$$

Where:

$k_{sz}$  - secondary suspension vertical stiffness per side frame

$$f_{\text{roll}} = \frac{1}{2\pi} \sqrt{\frac{4k_{sz}d_1^2}{I_{cr}}}$$

Where:

$I_{cr}$  - carbody roll moment of inertia about the center of gravity

$$f_{\text{pitch}} = \frac{1}{2\pi} \sqrt{\frac{2k_{sz}(\ell_f^2 + \ell_r^2)}{I_{cp}}}$$

Where:

$\ell_f$  - distance from front truck center to the carbody center of gravity

$\ell_r$  - distance from rear truck center to the carbody center of gravity

$I_{cp}$  - carbody pitch moment of inertia about the center of gravity

$$f_{\text{yaw}} = \frac{1}{2\pi} \sqrt{\frac{2k_{sx}(\ell_f^2 + \ell_r^2)}{I_{cy}}}$$

Where:

$I_{cy}$  - carbody yaw moment of inertia about the center of gravity

For the coupled roll and lateral motions the lower and upper center roll natural frequencies are given by:

$$f_{\text{l.c. roll}} = \frac{1}{2\pi} \sqrt{A - \sqrt{A^2 - B}}$$

$$f_{\text{u.c. roll}} = \frac{1}{2\pi} \sqrt{A + \sqrt{A^2 - B}}$$

Where:

$$A = \frac{2k_{sx}(I_{cr} + m_c h^2) + 2m_c k_{sz}d_1^2}{m_c I_{cr}}$$

$$B = \frac{16k_{sx}k_{sz}d_1^2}{m_c I_{cr}}$$

$h$  = distance from carbody center of gravity to center plate

Note that when  $h = 0$  the lower and upper center roll frequencies will be identical to the uncoupled frequencies.

## STEADY STATE VERTICAL DYNAMICS

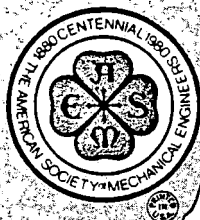
A simple model can be used to represent the steady state dynamics of a load moving over a continuous beam supported by an elastic foundation. While the analysis is more complex than can be treated here, the solution is well documented by Kenney (7) and Meisenholder. (8) In the latter, nondimensional beam deflection and stress are plotted as a function of nondimensional speed with various other parameter variations including foundation damping and load distribution.

## OTHER SIMPLE MODELS

Simple spring mass models are also likely to be used to obtain insight and check more sophisticated models in the steady state curving, trackability, and ride quality areas. These models are not sufficiently defined at the present time to document in this report.

(7) Kenney, J.T., "Steady State Vibrations of Beam on Elastic Foundation for Moving Load," *Journal of Applied Mechanics*, Trans. ASME, Vol. 21, No. 4, December 1954, pp. 359-364.

(8) Meisenholder, S.G., "Dynamic Interaction Aspects of Cable-Stayed Guideways for High Speed Ground Transportation," *Journal of Dynamic Systems, Measurement, and Control*, Trans. ASME, Special Issue on Ground Transportation, June 1974, pp. 180-192.



AN ASME PUBLICATION  
\$4.00 per copy \$2.00 to ASME Members

# ASME

THE AMERICAN SOCIETY OF MECHANICAL ENGINEERS  
345 E 47 St., New York, N.Y. 10017

The Society shall not be responsible for statements or opinions advanced in papers or in discussion at meetings of the Society or of its Divisions or Sections, or printed in its publications. Discussion is printed only if the paper is published in an ASME Journal or Proceedings. Released for general publication upon presentation. Full credit should be given to ASME, the Technical Division, and the author(s).

REFERENCE 132

**P. V. RamaChandran**

Manager  
Transportation Engineering  
Mem. ASME

**M. M. ElMadany**

Senior Research Engineer  
Assoc. Mem. ASME

Wyle Laboratories,  
Colorado Springs, CO

**N. T. Tsai**

Research Manager,  
Mechanical Systems,  
Federal Railroad Admin.,  
Washington, DC

## Performance Characteristics of Conventional Freight Vehicle Systems

*As part of TDOP/Phase II, experimental and analytic studies have been conducted to define the performance capabilities of the current freight car truck configurations. The results of these studies are used in arriving at quantitative characterization of performance of the standard, three-piece freight car truck under revenue service conditions. Field test data generated during TDOP/Phase I were supplemented with additional data gathered from field tests conducted during Phase II. Overall truck performance has been classified into four distinct and non-overlapping regimes, namely lateral stability, ride quality, steady state curve negotiation and trackability. Performance indices have been defined and quantified through the use of field test data. Correlating the quantified performance indices within each regime with representative operating conditions such as speed, lading, and track quality, ranges of quantified performance levels have arrived at as being characteristic of truck performance.*

### INTRODUCTION

The performance capabilities of current freight car truck configurations have been characterized through experimental and analytical studies conducted during the Federal Railroad Administration (FRA) - sponsored Truck Design Optimization Project (TDOP). The experimental studies were, to a large extent, undertaken during Phase I of the project, (1)\*. During Phase II, the performance data base generated during Phase I was evaluated with a view to apply the results, in consultation with industry, to the development of guideline performance characterizations of Type I truck configurations, (2).

Using a systematic methodology for the evaluation of freight car trucks, performance test data were reduced and analyzed; mathematical models were validated by comparative studies with respect to reduced test data; validated models were utilized in the simulation of additional performance data to aid in the interpretation of reduced test data; and a series of performance indices were quantified. By means of physical reasoning, the quantified performance indices were studied in relation to specific sets of operating conditions, such as speed, track quality, and lading conditions, to provide reasonable guidelines of performance that may be expected of Type I freight car trucks.

With the objective of arriving at quantified characterizations of freight car truck performance, four major performance regimes have been identified. These performance regimes are:

- o Lateral stability
- o Ride quality
- o Steady state curve negotiation
- o Trackability (harmonic roll, bounce, track twist and curve entry/exit)

Each of these regimes is primarily defined as a set of conditions with predominant features which distinguish one from another. Measurable quantities of truck performance, defined as performance indices, are identified within each regime. The overall characterization of truck performance consists of a range of quantified indices in each performance regime representative of truck performance under specified operating conditions. Performance data generated by means of field tests form the basis for quantification of the performance indices within each regime. The characteristics of car bodies and trucks tested during TDOP Phase I as well as the test matrix for high speed jointed track used in quantifying the performance characteristics of Type I trucks are given Appendix B.

This paper outlines the methodology used in the characterization of performance of Type I trucks in the various performance regimes, while describing and discussing the performance indices and the relationship of the developed characterizations of performance to specific operating conditions.

### LATERAL STABILITY REGIME - QUANTIFICATION OF TRUCK PERFORMANCE

The phenomenon of interest in this regime is hunting, which is a self-excited lateral, yaw and roll oscillation of the truck and carbody occurring above a certain 'critical' speed. Wheel tread and rail contours, surface condition of the rail, design features of the truck, characteristics of the suspension system, and the mass and mass distribution of the carbody are all parameters which influence the range of the critical speed.

The performance indices identified in the lateral stability performance regime are:

- o Critical speed

This performance index is identified through the use of the root mean square (rms) lateral acceleration levels.

\*Numbers in parenthesis designate References at end of paper.

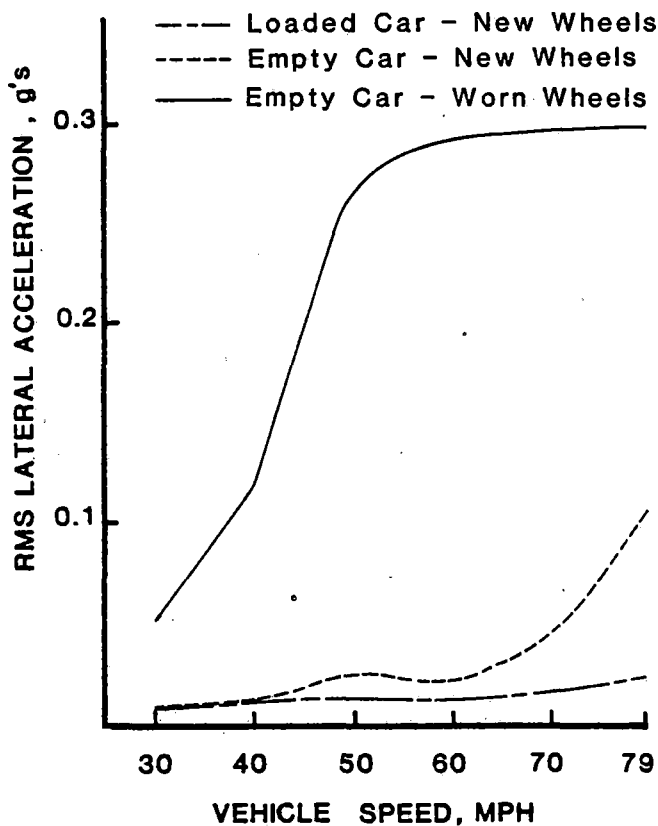


Fig. 1 RMS lateral acceleration versus speed - 70-ton trucks with flat cars

The rms value is calculated for unit (1 Hz) bandwidth around the characteristic frequency of hunting.

o Peak value of lateral acceleration (zero-to-peak). The peak lateral acceleration is defined as the absolute peak value (zero-to-peak). It is determined from an examination of the time history of the response data at the sill level of the carbody or the truck wheelsets.

#### Quantification of Performance Indices

Performance test data on Type I trucks operating in combination with different carbodies on jointed rail under various speeds and lading conditions were reduced and analyzed to quantify the performance indices in this regime (see Appendix B for the characteristics of carbodies and trucks tested as well as the test matrix). The process of quantification of performance indices consisted of (a) examination of time history data on the vehicle lateral motions at different locations on the carbody and the truck; (b) analysis of power spectral density functions on selected segments of data chosen on the basis of the time history data; (c) calculation of levels of lateral acceleration, evaluated for limited bandwidth; (d) extraction of peak values of lateral acceleration from the time history.

Characteristic performance levels in the regime of lateral stability are given in terms of rms lateral accelerations and peak lateral accelerations. Characteristic levels of performance, under the appropriately identified set of operating conditions, shall be limited by the upper bound of the bands of performance shown in the characterization charts given in Figs. 1 through 7. Lower bounds of per-

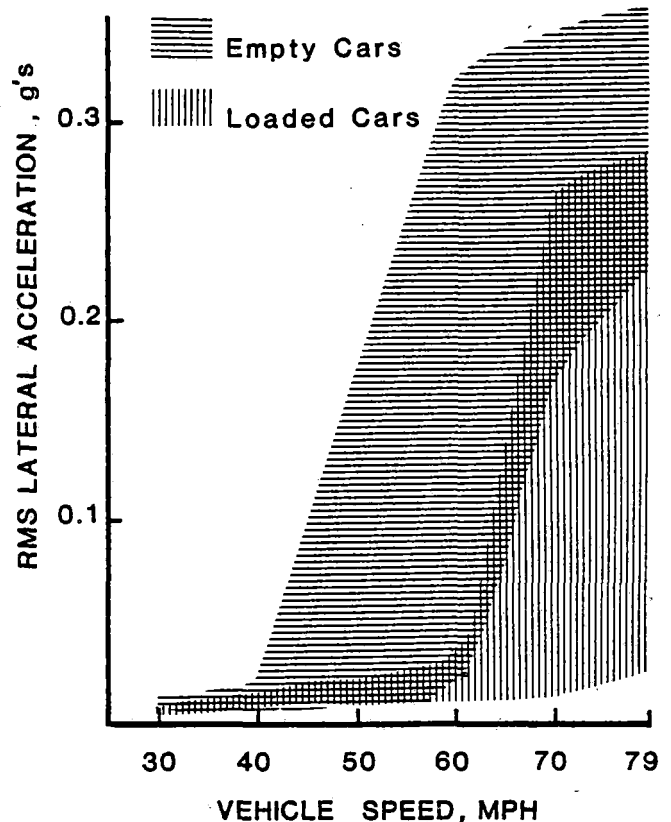


Fig. 2 RMS lateral acceleration versus speed - 70-ton trucks with box type cars, new wheels

mance, provided wherever possible, are shown for reference, indicating optimistic levels of performance that may be expected under the specified conditions.

A summary of the findings derived from the quantification of performance indices in the lateral stability regime using test data is given in Table 1.

A brief discussion of the test results for 70-ton and 100-ton trucks follows, (the reader is referred to Reference (2) for more details).

**70-Ton Trucks.** The empty flat car using worn wheels shows the earliest evidence of instability, at a speed range between 30 and 40 mph. The maximum acceleration level for this case increases sharply to 0.55 g at 40 mph, and to 1.1 g at 79 mph. No data are available on the same configuration in the loaded condition.

Analysis of test data for the flat cars with new wheels reveals no evidence of hunting associated with the case of loaded cars and the vehicle remains stable through the entire range of operating speeds up to 79 mph. However, in the empty condition with new wheels, hunting is evidenced in the speed range between 70 and 79 mph. In general, for

#### Conversion Factors for SI Units

1 in.	= 25.4 mm	1 ton (short 2000 lb) = 907.185 kg
1 ft	= 304.8 mm	1 lb = 4.448 N
1 mph	= 1.61 km/h	1 lb/in. = 175.1268 N/m



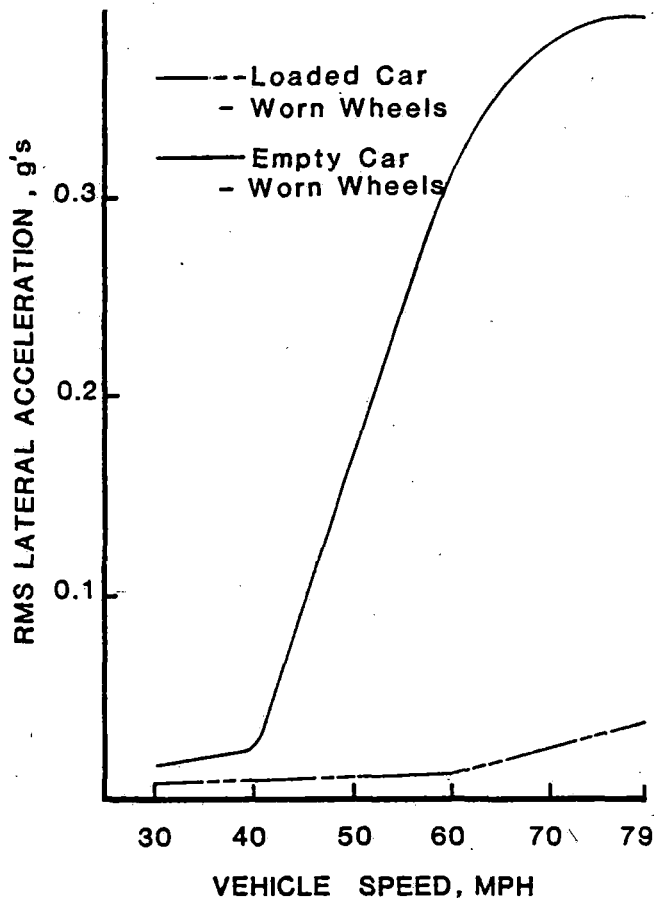


Fig. 3 RMS lateral acceleration versus speed - 70-ton trucks with box type cars, worn wheels

this configuration, the critical speed varies depending on the operating conditions, and, even more markedly so on the wheel profiles, with the predominant frequency of hunting in the range of 2.5 to 2.9 Hz.

The behavior of the mechanical refrigerator car and the box car can be placed into one category since the findings drawn from the performance test data indicate general conformity. Therefore, they will be grouped together and referred to as 'box type' cars. In the case of the empty box type cars with new wheels, hunting begins at a speed between 40 and 50 mph. In the case of the loaded box type cars, there is an indication of 'nosing,' i.e., hunting restricted to the leading end of the carbody only, initiated in the speed range between 60 and 70 mph, and continuing until 79 mph. To generalize, in this set of configurations, the critical speed increases with increasing loads; with regard to the effect of wheel profiles, the empty cars hunt at a lower frequency with worn wheels than with new wheels. While the empty box type cars hunt at a frequency slightly above 3 Hz with new wheels, those with worn wheels hunt at about 2.5 Hz. For the empty box type cars, the peak acceleration levels range from 0.66 g at 50 mph to 1.25 g at 79 mph.

**100-Ton Trucks.** The test data available consist of a 100-ton box car and a 100-ton covered hopper car, equipped with new wheels. Analysis of reduced data indicates that empty cars on new wheels exhibit hunting in the speed range between 70 and 79 mph. Further, the leading end of the carbody undergoes more pronounced motion than the trailing

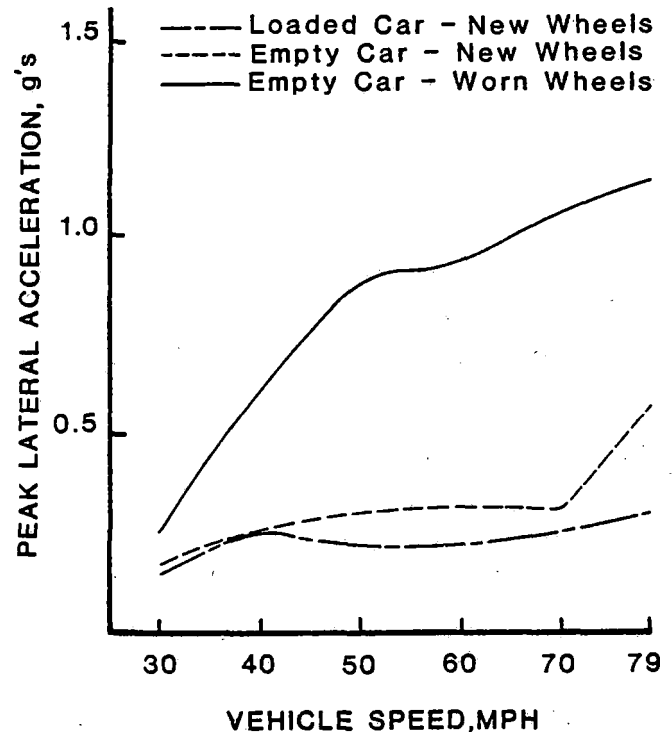


Fig. 4 Peak lateral acceleration versus speed - 70-ton trucks with flat cars

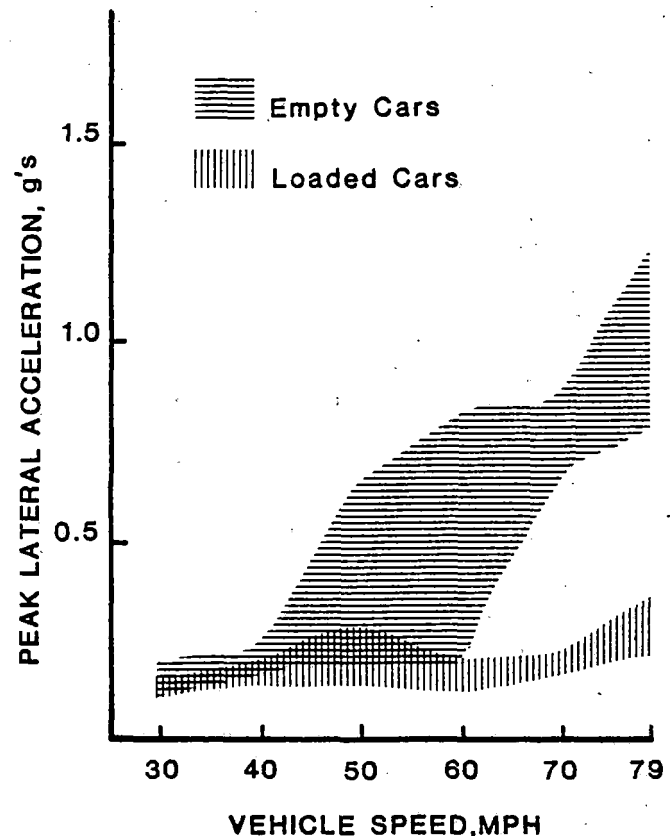


Fig. 5 Peak lateral acceleration versus speed - 70-ton trucks with box type cars, new wheels

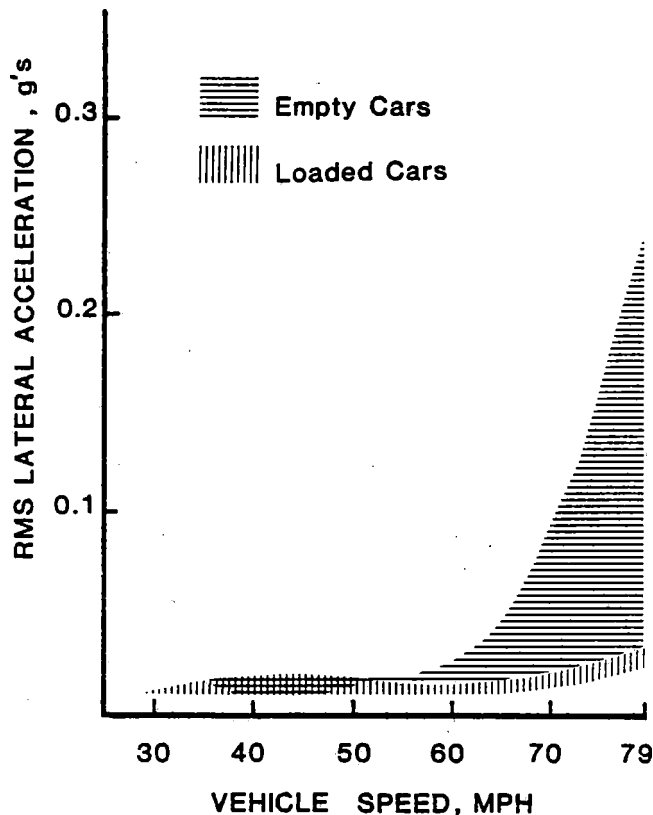


Fig. 6 RMS lateral acceleration versus speed - 100-ton truck with box type cars, new wheels

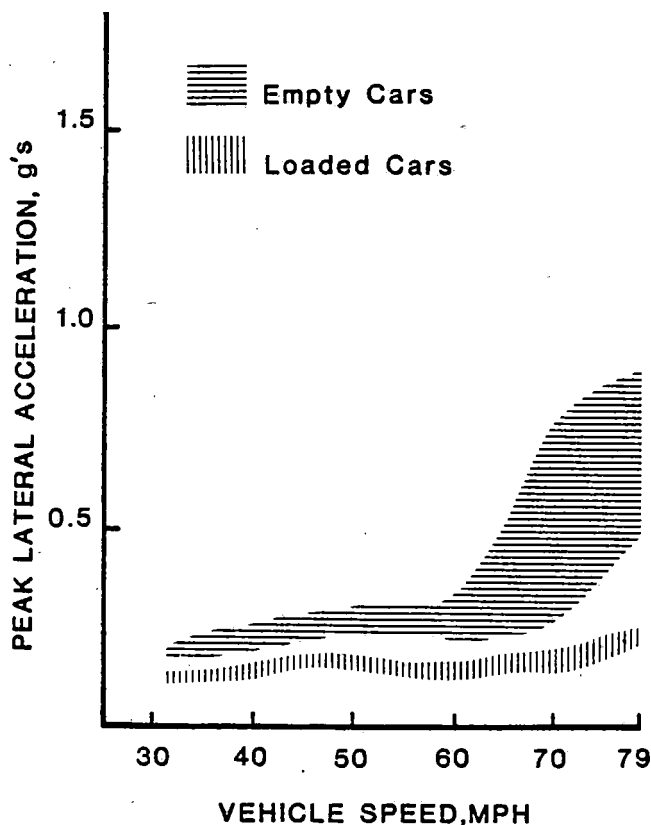


Fig. 7 Peak lateral acceleration versus speed - 100-ton trucks with box type cars, new wheels

end in the speed range between 60 and 70 mph. The peak lateral acceleration level experienced is about 0.8 g in the 70 to 79 mph speed range. In contrast, the loaded car configuration remains stable through the entire range of operating speeds up to 79 mph.

#### RIDE QUALITY REGIME - QUANTIFICATION OF TRUCK PERFORMANCE

Ride quality as a performance regime refers to the acceleration environment in the carbody and is meant to encompass the capability of the truck to attenuate the excitation arising from track irregularities. The characteristic of a truck to function as a mechanical filter in isolating the carbody from the disturbances induced by the track is of primary interest in this performance regime.

The performance index identified in this regime is:

##### o Transmissibility

Transmissibility, as presented here, is identified as the ratio of the rms value calculated from the response power spectral density within a specified frequency bandwidth to the rms value calculated from the track input power spectral density over a corresponding frequency bandwidth.

Transmissibility has been quantified for both the vertical and roll motions. Vertical acceleration response at the sill level and roll acceleration response at either end of the carbody in the frequency bandwidths of 0 to 4 and 4 to 10 Hz have been considered. The corresponding input consisted of power spectral densities of track profile in respect to vertical response, and track cross level in respect to roll response in the same frequency bandwidths.

Root mean square response over the wide band spectrum has been identified as a supplementary index. The rms values of the response power spectral densities for both the vertical and the roll accelerations were computed over the frequency range of 0-20 Hz.

#### Quantification of Performance Indices

The characterization of interest in this regime is the capability of the truck to attenuate track-induced vibrations. Extreme performance phenomena, such as resonance and other unstable conditions, are excluded from consideration in this regime since they have been accounted for within the other identified performance regimes. Performance test data from TDOP Phase I have been examined, reduced, and analyzed to quantify the performance indices selected for this regime. The quantification on the basis of test data followed the sequence outlined: (a) examination of time history data on the vehicle vertical and roll motions at different locations on the carbody and truck; (b) selection of data to be analyzed, excluding resonant and unstable phenomena from consideration; (c) analysis of power spectral density functions on selected data; (d) calculation of rms levels of vertical and roll accelerations, evaluated for selected bandwidths; and (e) calculation of transmissibility in both the vertical and roll directions, relating carbody response to track input as obtained from track geometry data, i.e., profile and cross level power spectral densities, respectively.

#### Data Analysis Methodology

The methodology of interpreting and analyzing the test data results is based on the general knowledge of the vehicle/track dynamic interaction. This dynamic interaction depends on:

i. System Transfer Function, which is a function of the vehicle structural characteristics, vehicle vibration-isolation system, and lading conditions.

These parameters determine the vehicle natural frequencies, and the corresponding mode shapes. In the vertical plane, the vibration of the freight cars is a function of

Table 1 Summary of results from analysis of test data in the lateral stability performance regime

Vehicle Configuration	Hunting* Yes/No	Critical** Speed Range mph	Hunting** Frequency Hz	RMS Lateral** Acceleration g	Peak Lateral** Acceleration g	Remarks
70-ton Trucks with Box Type Cars						
1. New Wheels/Empty	Yes	40-50	2.5-3.1	0.16-0.36	0.58-1.24	Initiation of nosing at 40-50 mph; fully developed hunting at 60-70 mph.
2. New Wheels/Loaded	No					Nosing initiated in the 60-70 mph speed range with an associated frequency range of 3.3 to 3.5 Hz, RMS acceleration of 0.27 to 0.29 g, and peak acceleration levels of 0.67 to 0.77 g. Nosing continued through the speed range up to 79 mph, the terminal speed for the test runs.
3. Worn Wheels/Empty	Yes	40-50	2.5	0.18-0.40	0.66-1.12	Leading end nosing & trailing end intermittent hunting at 40-50 mph. Both ends hunting with increasing speed.
4. Worn Wheel/Loaded	No	—	—	—	—	No evidence of hunting.
70-ton Trucks with Flat Cars						
1. New Wheels/Empty	Yes	70-79	2.8	0.11	0.59	Fully developed hunting at 70-79 mph.
2. New Wheels/Loaded	No	—	—	—	—	No evidence of hunting.
3. Worn Wheels/Empty	Yes	30-40	2.2-2.9	0.12-0.30	0.55-1.10	Fully developed hunting at 30-40 mph.
4. Worn Wheels/Loaded	—	—	—	—	—	No data available.
100-ton Trucks with Box Type Cars						
1. New Wheels/Empty	Yes	70-79	2.7	0.10-0.25	0.73-0.83	Fully developed hunting.
2. New Wheels/Loaded	No	—	—	—	—	No evidence of hunting.
3. Worn Wheels/Empty	—	—	—	—	—	No data available.
4. Worn Wheels/Loaded	—	—	—	—	—	No data available.

\*\*Hunting\* denotes full-body hunting as differentiated from nosing.

\*\*Includes nosing and full body hunting.

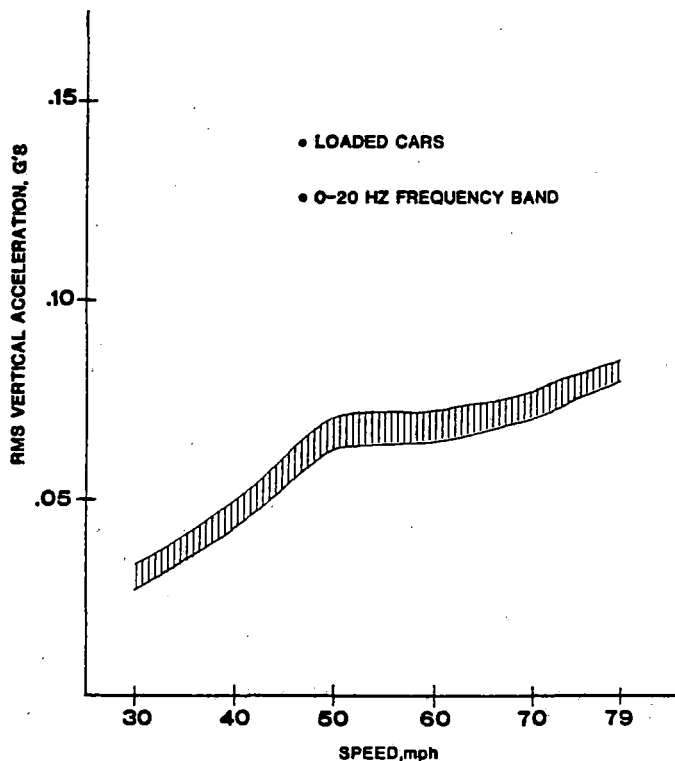


Fig. 8. RMS vertical acceleration at sill level versus speed - 70-ton trucks with flat cars

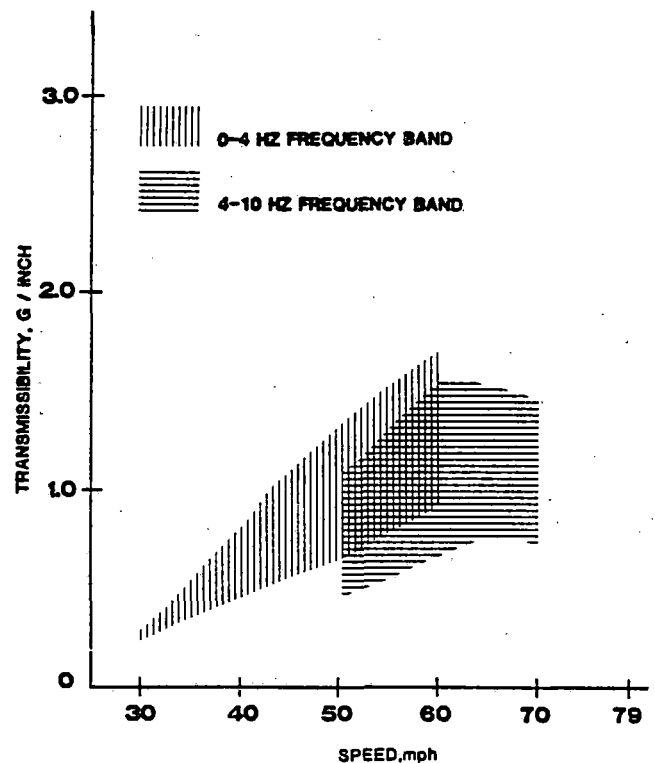


Fig. 9. Ratio of rms vertical acceleration at sill level to rms track profile versus speed - 70-ton trucks with box type cars

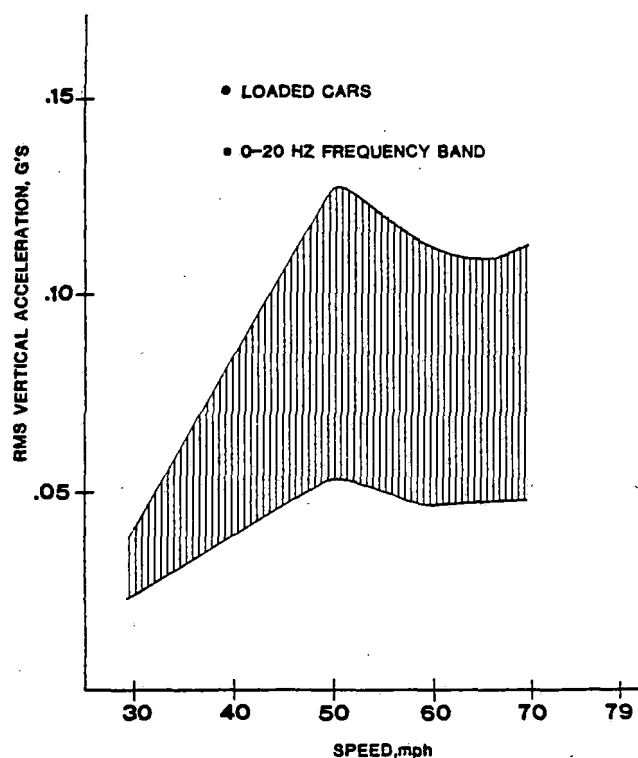


Fig. 10 RMS vertical acceleration at sill level versus speed -70-ton trucks with box type cars

the rigid body modes (bounce and pitch) as well as the flexural modes. These modes of vibration may interact with each other and result in several types of motions, such as bounce-flexure, and pitch-flexure. The corresponding frequencies may be higher or lower than the natural frequencies of the principal modes of vibration depending on whether these modes are in phase or out of phase with each other. Also, the roll motion depends on the lateral, roll and torsional modes of vibration as well as their interaction (for example, lower and upper center roll). The resulting coupled modes of vibration may lead to building up of higher amplitude response. Therefore, the freight car may exhibit resonance at several different critical speeds for any given loading condition.

Some form of mechanical vibration isolation system is provided at each truck to ensure smoother riding. In the standard Type I trucks, the dry friction damping is used as means to isolate the carbody from track excitations. It should be noted here that the dry friction is irrational in nature, and it excites the higher frequencies in the carbody than does the viscous damping. Also, the friction raises the natural frequencies of the system. In addition, this type of damping may lead to coupling the vertical and lateral motions of the freight car. It should also be pointed out that while friction damping might be effective in suppressing some of the resonances resulting from the rigid body modes, it is inadequate in the flexural and the coupled modes.

ii. Geometric Transfer Function, which is a function of number of axles, axle spacing, truck center distance, and vehicle speed.

The vehicle speed, combined with the track center distance, and the wheel base of the trucks, form a geometric transfer function which acts as a filter for the multiple inputs freight car system. This transfer function is characterized by several cancellation frequencies (frequencies at which the magnitude of the transfer function is zero)

depending on vehicle speed and wheel spacing. These cancellation frequencies cause notches or dropouts in the freight car response power spectra. Such notches may markedly attenuate system response, and mask the system resonances.

iii. Track Irregularities - Track irregularities are random in nature with some dominant periodic components arising from the rail joints. The harmonics of the rail joint may be strong enough to force the freight car system to vibrate at their frequencies, and to allow the mode shapes predicted by the eigenvalues of the system not to be developed. However, if these harmonics coincide with one of the principal modes or one of the submodes of vibration, the amplitude spectra will peak and this may lead to resonance.

Some of the analyzed data are shown in Figs. 8-13. The results obtained from the reduction and analysis of the test data have been summarized for 70-ton and 100-ton trucks.

**70-Ton Trucks.** In general, loaded box type cars on 70-ton trucks indicate increasing rms values of vertical acceleration with increasing speed and a tendency to resonate in the vertical plane at about 50 mph. In the case of empty

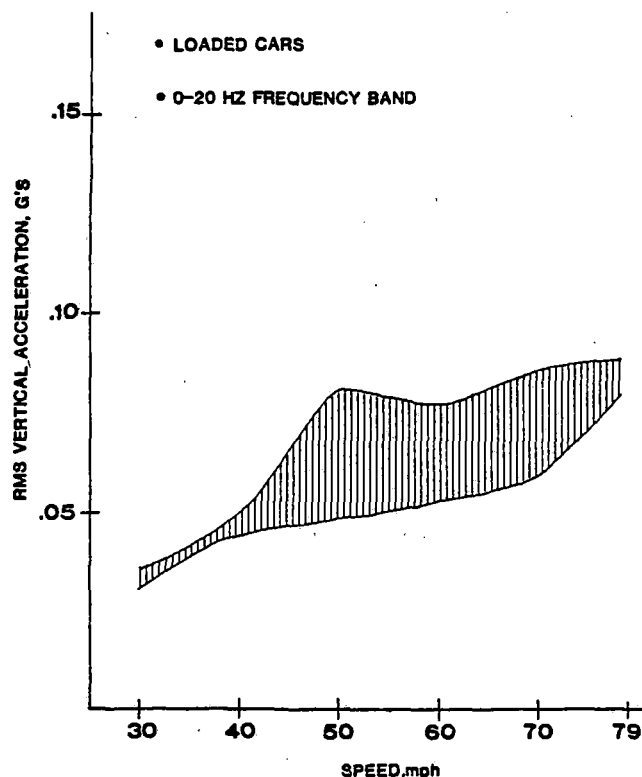


Fig. 11 RMS vertical acceleration at sill level versus speed -100-ton trucks with box type cars

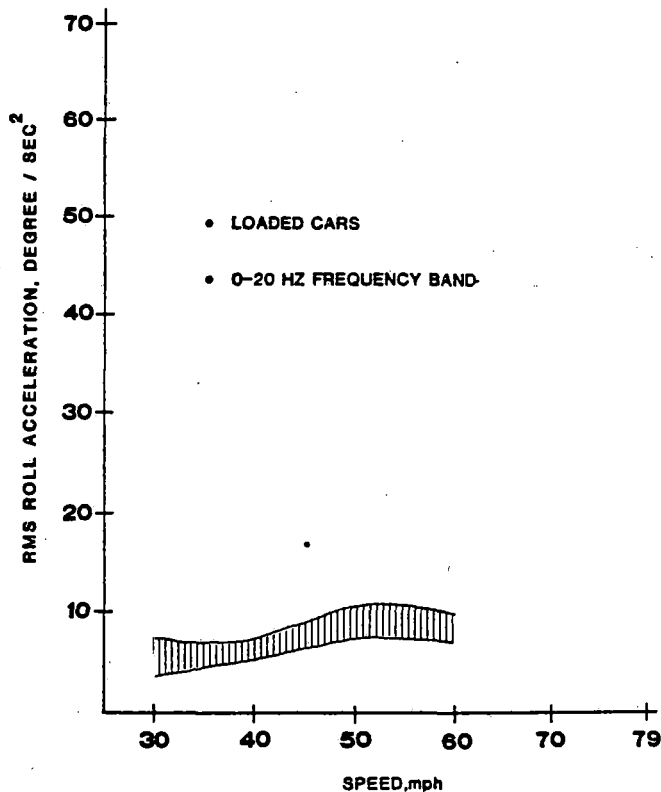


Fig. 12 RMS roll acceleration at either end of carbody versus speed - 70-ton trucks with box type cars

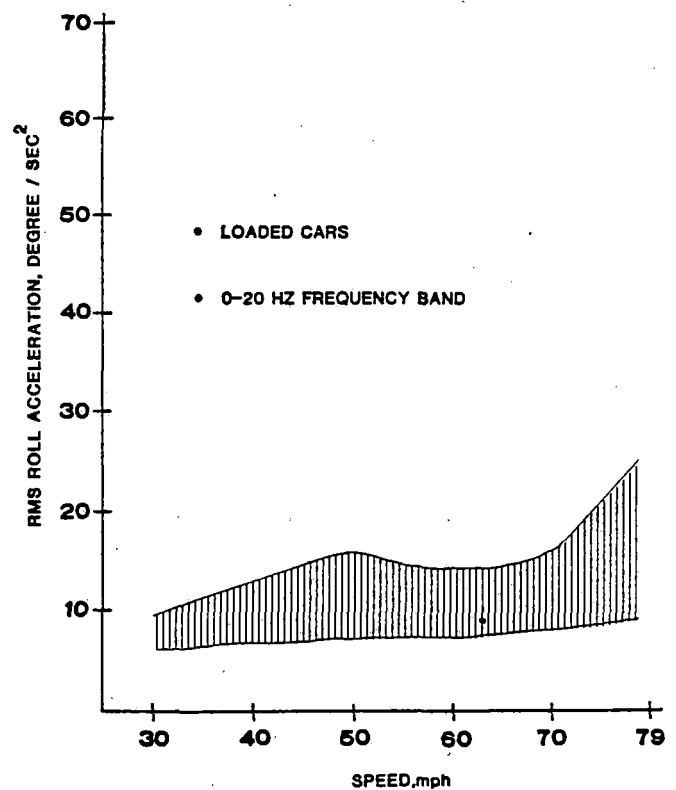


Fig. 13 RMS roll acceleration at either end of carbody - 100-ton trucks with box type cars

box type cars, the levels of vertical acceleration response are higher as compared to the response of the loaded cars, the implication being that loaded cars obtain better ride quality than empty ones. However, in one case the loaded box car indicated higher levels of vertical acceleration above 40 mph as compared to those of the empty car. This case is considered the exception rather than the rule, and one possible explanation for this phenomenon is the coincidence of the natural frequencies of the carbody with those of the excitations from the jointed track, as well as the coincidence of the truck center spacing with the spacing of rail joints.

In the case of the flat cars, only the loaded configuration has been analyzed since the empty configuration was extensively covered by the lateral stability regime by virtue of indications of hunting. The flexural modes of vibration of the car are believed to be significant contributors to the car response.

In the roll mode, the amplitude response of the loaded box type cars is lower than that of the empty cars. Analysis of data on the loaded flat car indicates that the contribution from the torsional mode of vibration is significant. At about 40 mph the response peaks, with the leading end undergoing higher amplitude response than the trailing end.

**100-Ton Trucks.** Once again, the loaded box type cars on the 100-ton trucks exhibit better vertical ride quality

characteristics as compared to those of the empty cars. The difference in the responses between the empty and the loaded cases is attributable, at least in part, to the higher natural frequencies of the empty cars and the effect of friction snubbing.

Among the box type cars in the roll mode, the hopper cars indicate lower levels of amplitude response as compared with those of the box cars. The trailing end of the carbody undergoes higher levels of roll acceleration than the leading end.

#### STEADY STATE CURVE NEGOTIATION REGIME - QUANTIFICATION OF TRUCK PERFORMANCE

In steady-state curve negotiation, horizontal forces between the wheels and rails act to rotate the truck about the center of the curve, even when there is no relative rotation between the truck and carbody. For standard freight car trucks, the lateral force that turns the truck in the curve is predominantly the flange force at the outer leading wheel, and is likely to contribute to the resistance of the truck to forward motion. It is believed that this flange force is responsible for much of the wear that leads to condemnation of wheels for "thin flange."

There are several factors that affect the performance of the vehicle during curve negotiation. These factors include vehicle characteristics (wheel profile, vehicle

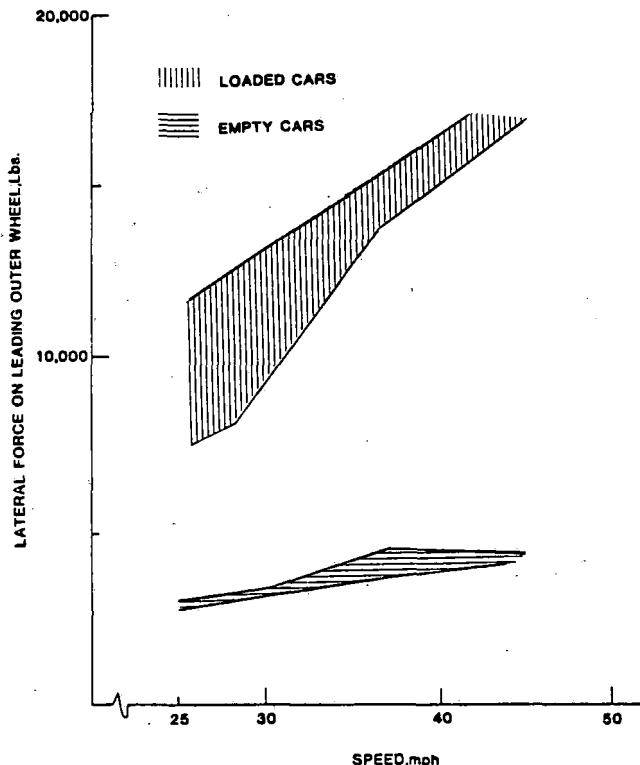


Fig. 14 Lateral force on leading outer wheel versus speed - 100-ton trucks with open hopper cars,  $6.0^{\circ}$  to  $6.2^{\circ}$  curved track

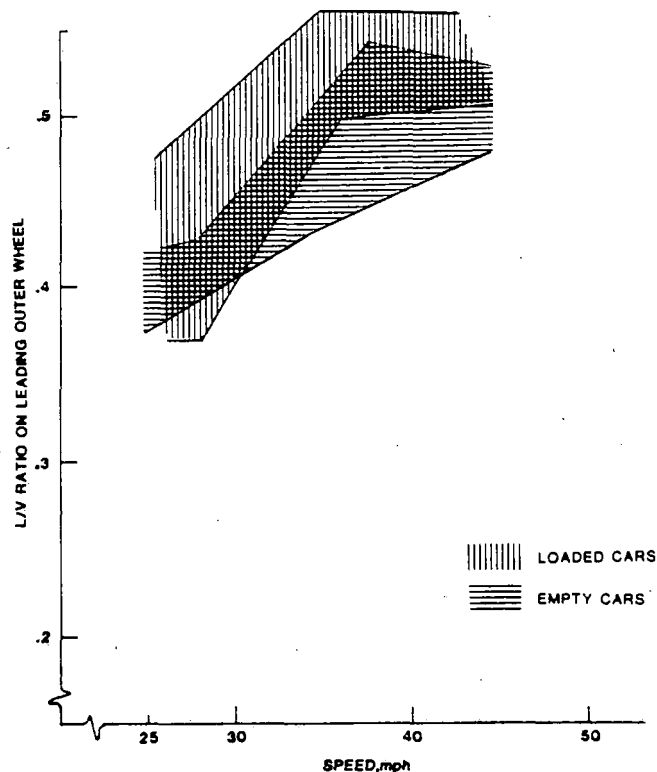


Fig. 15 L/V ratio on leading outer wheel versus speed - 100-ton trucks with open hopper cars,  $6.0^{\circ}$  to  $6.2^{\circ}$  curved track

weight and inertial properties, vehicle physical characteristics, etc.), track characteristics (degree of curvature, track geometry properties, grade, length of curve and spiral, etc.), and operating conditions (speed, lading, etc.). The performance indices identified in the steady state curve negotiation regime are:

- o Average lateral force on leading outer wheel
- o Average ratio of lateral to vertical forces (L/V ratio) on leading outer wheel
- o Average Angle of attack

#### Quantification of Performance Indices

The data used have been gathered from tests on track consisting of both left- and right-hand curves ranging from  $1.1^{\circ}$  to  $6.2^{\circ}$ , see Appendix B for curve profiles. The test vehicle configuration consisted of a 100-ton truck in combination with loaded and empty 100-ton open hopper cars, and AAR standard, 1/20 taper wheel profiles in the new condition. Test speeds were at balance, below balance, and above balance; a run at balance speed in the reverse direction was also conducted. The technique for measuring the forces at the wheel/rail interface is the "axle bending" technique (3). The axle bending technique makes use of the data gathered from strain gaging the axle for measuring axle bending and from the bearing adapters for measuring vertical forces. Data covering the track segments of constant curvature were used in quantifying performance in the steady state curve negotiation regime. In quantifying the lateral forces and L/V ratios on the leading outer wheel, the algebraic average and the standard deviation were computed from the test data.

Quantitative performance levels in steady state curve negotiation for 100-ton Type I trucks equipped with new wheels, AAR standard 1/20 taper, are shown in Figs. 14 through 17 in both the loaded and empty conditions. Figs. 14 and 15 show performance levels in terms of lateral forces and L/V ratios on the leading outer wheel as a function of speed; Figs. 16 and 17 show performance levels in terms of lateral forces and L/V ratios on the leading outer wheel as a function of the degree of track curvature near balance speed.

The results of the reduced data show that the lateral forces and L/V ratios are increasing with increasing degree of curvature and they tend to have the same characteristics. For the moderate curves of  $2.5^{\circ}$  and  $3^{\circ}$ , the lateral forces on the leading outer wheel of the loaded car are comparable. However, these lateral forces show substantial increase in magnitude as the degree of curvature increases reaching an approximate value of 14,000 lb on a  $6.2^{\circ}$  curve. The ratio of the dynamic lateral forces to the steady state lateral forces are lower for higher degrees of curvature. The values of the lateral forces and L/V ratios resulting from test runs in both the forward and reverse directions are comparable.

The following observations stem from a comparison of the results for the loaded and empty cars:

- a. During curve negotiation, the L/V ratios are more critical for the loaded cars than for the empty cars. This conclusion is based on mean values of L/V ratios at balance speed without considering the associated time duration.
- b. The rate of increase of the lateral forces and L/V

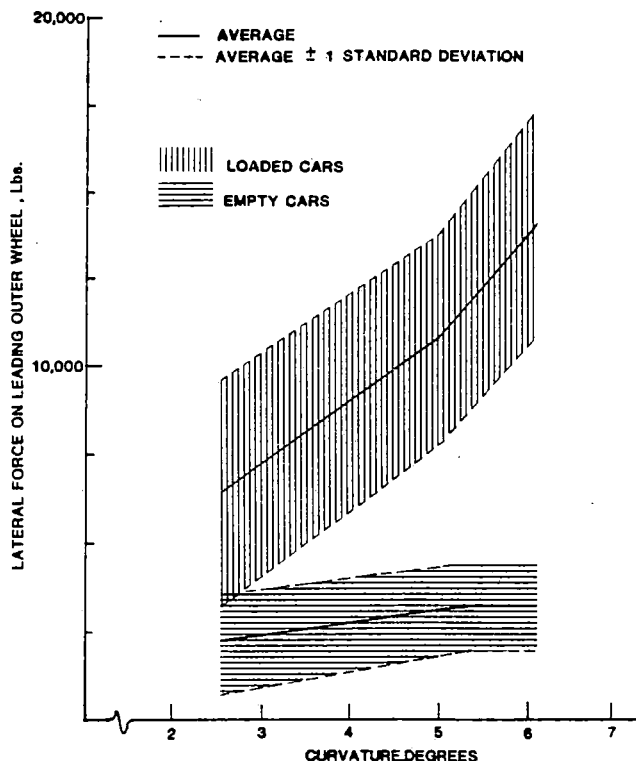


Fig. 16 Lateral force on leading outer wheel versus degree of curvature near balance speed -100-ton trucks with open hopper cars

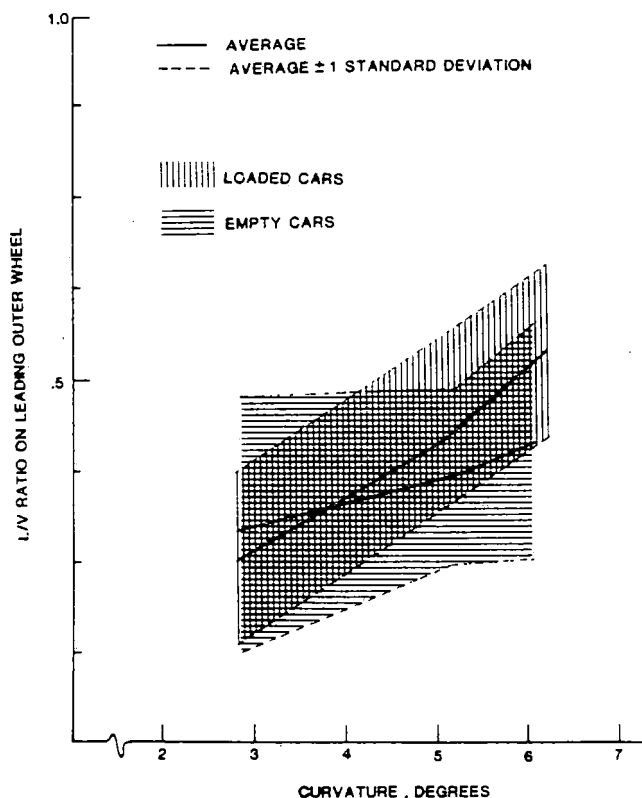


Fig. 17 L/V ratio on leading outer wheel versus degree of curvature near balance speed - 100-ton trucks with open hopper cars

ratios on the leading outer wheel with increasing degree of curvature is higher for the loaded cars than for the empty cars.

c. The ratio of the dynamic components of the lateral forces and L/V ratios to the steady state components are higher for the empty cars than for the loaded cars. This indicates that the dynamic effect of both curve entry and track irregularities is much higher for empty cars than for loaded cars.

Angle of attack measurements and results are given in Appendix A.

## TRACKABILITY REGIME - QUANTIFICATION OF TRUCK PERFORMANCE

The ability of a truck to maintain a safe range of vertical load distribution on all four wheels under a range of track conditions is of interest in this performance regime. Load equalization, periodic vertical rail irregularities, foundation modulus changes, as well as curve entry and exit are all conditions associated with this performance regime. Subclasses of the trackability performance regime and their associated performance indices are given below:

Performance Subregimes	Performance Indices
a. Harmonic roll	o Critical speed o Peak roll angle (zero-to-peak)
b. Bounce	o Critical speed o Peak vertical acceleration (zero-to-peak)
c. Track twist	o Wheel unloading index (peak value)
d. Curve entry/exit	o Wheel unloading index (peak value)

The wheel unloading index (WUI) is identified as follows:

$$WUI = 1 - W_L / (W_H / 3),$$

where,

$W_L$  = vertical force on most lightly loaded wheel

$W_H$  = sum of vertical forces on three most heavily loaded wheels

This definition of the wheel unloading index, in practical terms, implies that the higher the value of the index, the worse the condition of load equalization.

## Quantification of Performance Indices

**Harmonic Roll.** Data from shimmed track tests were reduced and analyzed with a view to quantify performance in the harmonic roll subregime. The shimmed track consisted of twenty 39-ft rail lengths with joints uniformly staggered at approximately 19 ft, 6 inches. The rail opposite each joint in the test zone was shimmed upward to yield a cross level variation of 0.75 inches. Test data on a 70-ton mechanical refrigerator car and a 100-ton box car have been analyzed. The two test cars were loaded and equipped with cylindrical wheels. The height of the center of gravity of the 70-ton refrigerator car is 88 inches above the rail, and the truck center distance is 45 ft, 8 5/8 inches. The corresponding values for the 100-ton box car are 94 inches and 46 ft, 3 inches, respectively.

Fig. 18 represents the quantified characterization in the harmonic roll subregime for 70-ton and 100-ton box type cars.

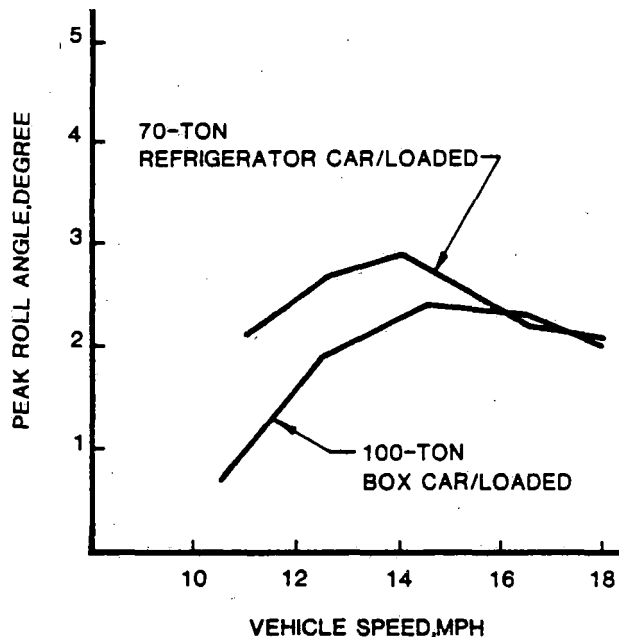


Fig. 18 Peak roll angle (carbody to side frame) versus speed, cylindrical wheels

Results of the reduction and analysis of the test data on the shimmed track showed that the loaded refrigerator car has the ability to extract energy from track input excitations, and the carbody reaches a state in which the rocking car exceeds its capability to absorb or dampen rolling motion. The peak roll angle at the leading end of the carbody is  $2.9^{\circ}$  for the refrigerator car at about 14 mph. The peak roll angle at the leading end of the carbody for the 100-ton box car is  $2.4^{\circ}$  at about 14.5 mph. The results also (not presented here) showed that the data are quite non-linear, and contain higher frequency components, particularly when acceleration responses are considered. The carbody is rolling about the lower center; in other words, the mode excited is the lower center roll.

**Track Twist.** Data from TDOP/Phase II yard tests (4) were reduced and analyzed to quantify truck performance in the track twist subregime. The truck tested was a 100-ton capacity Type I truck with a 100-ton open hopper car in both loaded and empty conditions. The yard track consisted of two curves. The degrees of curvature were  $16^{\circ}$  (left-hand curve) and  $15.75^{\circ}$  (right-hand curve), and the corresponding superelevations were -0.26 inches and -0.3 inches, respectively. The speed limit was 10 mph.

Characterization of performance in the load equalization subregime is provided by means of the wheel unloading index (WUI), which is the zero-to-peak value extracted from the time history.

Results of the reduction and analysis of test data indicate that the dynamic components of the lateral forces and L/V ratios are high. The wheel unloading index for the loaded car has a mean value of 0.138 and a standard deviation of 0.065 on the  $16^{\circ}$  curve. The corresponding values for the  $15.75^{\circ}$  curve are 0.208 and 0.108, respectively. The mean values of the wheel unloading index for the empty car (not shown here) are 0.409 and 0.264 for the  $16^{\circ}$  curve and  $15.75^{\circ}$  curve, respectively, with standard deviations of 0.083 and 0.73, respectively. It is noted that the wheel unloading index is substantially higher for the unloaded car than that for the loaded car. This is mainly due to the friction snubber in the suspension which permits little motion between the truck components for the empty car. It may be noted, however, that the field test data considered here included only trucks with constant friction snubbing.

**Curve Entry/Exit.** For the curve entry/exit subregime, TDOP/Phase II field test data were used. A 100-ton capacity Type I truck with an open hopper car in both loaded and empty conditions were tested. Tests were made at the balance speed for track curvature ranging from  $2.5^{\circ}$  to  $6.2^{\circ}$ . Test runs were repeated at below the balance speed and above the balance speed. The "axle bending" technique, (4), was used to determine the vertical and lateral forces at the wheel/rail interface. Characterization of performance in the curve entry/exit subregime is provided by means of wheel unloading index. These characteristics are presented in Figs. 19 and 20.

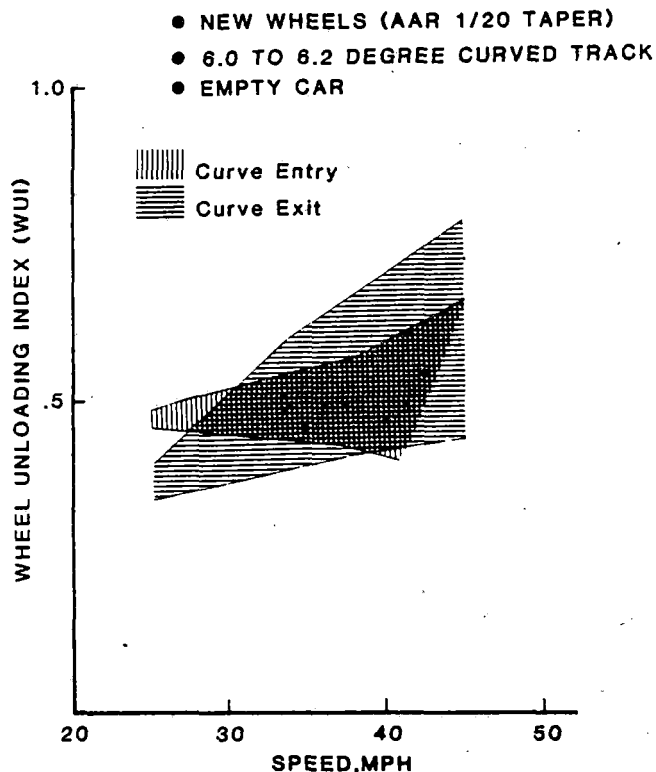


Fig. 19 Peak value of wheel unloading index versus speed - 100-ton trucks with empty open hopper cars,  $6.0^{\circ}$  to  $6.2^{\circ}$  curved track



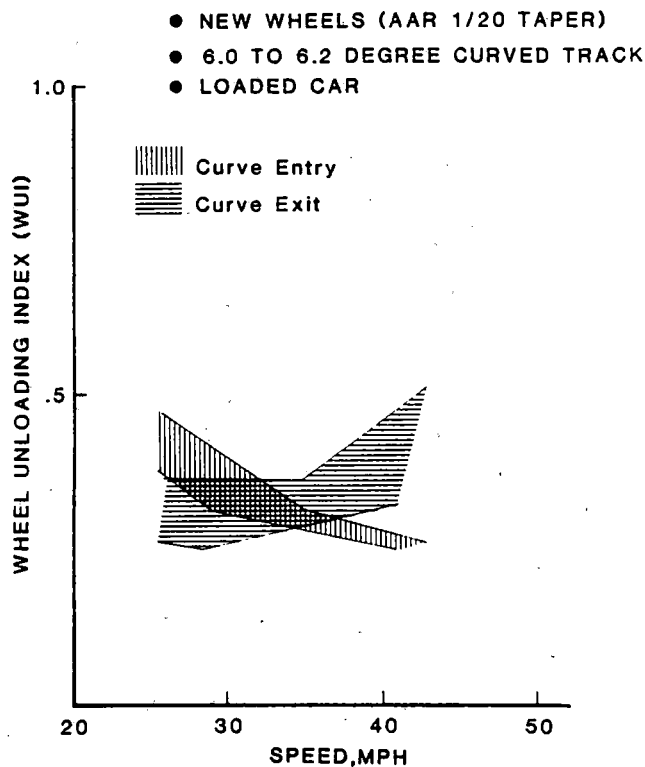


Fig. 20 Peak value of wheel unloading index versus speed - 100-ton trucks with loaded open hopper cars, 6.0° to 6.2° curved track

Analysis of the data indicates that, in general, the peak value of the wheel unloading index is increasing with increasing degree of curvature. The effect of speed on this index is not clear (i.e., does not have a discernable pattern) from the results. This might be due, in part, to the lack of definition of the statistical significances of this index. Rail contamination and vehicle nonlinearities may also lead to this phenomenon. However, it has been noticed that the empty cars experience a higher wheel unloading index than the loaded cars on all curves tested.

## CONCLUDING REMARKS

### Lateral Stability

Wheel profiles and lading conditions are the two significant parameters which influence performance in this regime. While the test data are generally considered adequate to investigate the effects of lading conditions on lateral stability performance, the data available for configurations using worn wheels are insufficient to examine in depth the effect of wheel profiles on hunting performance. Analysis of test data in this regime indicates that (a) loaded cars have less tendency to hunt; (b) amplitudes of motion for the 100-ton configurations are much lower than those for the 70-ton configurations; and (c) the effect of wheel profiles on configurations with empty box type cars seems to be more significant than on those with loaded box type cars.

### Ride Quality

The role of train speed on the ride quality response of the carbody is clearly discernible; as the train speed is increased, track excitation is more readily transferred to the car, resulting in higher amplitude response. Rail joint frequencies and the location of peaks in the power spectra are strongly related, indicating that the input excitation to the car arises mainly from the periodic rail joint spacing, with smaller contributions from the stochastic excitation from the random track irregularities. In general, response consists of rigid body modes and flexural modes; it is seen that the flexural modes of vibration of the carbody play a major role in the dynamic response of the freight cars. Lading conditions affect the ride quality in both the vertical and the roll modes, with the empty cars having higher amplitude response as compared to the loaded cars. In the roll mode, for loaded cars, 70-ton vehicles exhibit more desirable dynamic characteristics than the 100-ton vehicular combinations. In the vertical mode, the 100-ton trucks are more effective in attenuating the track excitations transmitted to the carbody than the 70-ton trucks.

### Steady-State Curve Negotiation

On sharp curves (5° - 6.2°), due to the fact that the lateral forces required to guide the truck through the curve are larger than the primary guidance achieved by the tangential forces at the wheel treads, the wheel flanges come into action. In other words, the wheel flanges perform the primary role in curve negotiability in curves of small radii. The leading outer wheel, which is the main guiding wheel when entering a curve, experiences and maintains larger lateral forces and L/V ratios above balance speed than does any other wheel. Above balance speed, the leading outer wheel also seems to be more sensitive to track curvature. Below balance speed, the trailing axle of the truck runs closer to the low rail of the curve, causing flange contact of the trailing inner wheel on sharp curves, and consequently experiences the highest forces. Below and at balance speed, the trailing axle carries the greater part of the net lateral forces for all curves considered. Past history of the truck (the initial configuration of the truck as it enters the curve) seems to have an influence on the level of the steady state lateral forces.

### Trackability

Accommodation of vertical track irregularities is an acknowledged advantage with the standard three-piece freight car truck featuring loose construction at the bolster-side frame and adapter-pedestal connections. This is reflected in the results indicating good vertical load distribution of the four wheels of the Type I truck, i.e., the trucks are able to maintain adequate vertical loads on all four wheels, especially with respect to the track twist and curve entry/exit subregimes of performance. The independent rotation of the side frames in the Type I truck may be credited with these good performance levels.

## ACKNOWLEDGEMENT

The work reported herein was sponsored by the Federal Railroad Administration (FRA). The authors would like to thank Mr. Phil Olekszyk and Mr. Arne Bang of the Federal Railroad Administration for their support during this project. Thanks are due to our colleagues and staff at Wyle Laboratories for their invaluable support and cooperation, and for the continued contribution and guidance of the members of the industry who participated in the TDOP Consultant Group.

## REFERENCES

- 1 Southern Pacific Transportation Company, "Freight Car Truck Design Optimization -Vol. II, Phase I Final Report," FRA Report No. FRA/ORD-78/12.II, February 1978.
- 2 RamaChandran, P.V., and ElMadany, M.M., "Truck Design Optimization Project (TDOP) Phase II -Performance Characterization of Type I Freight Car Trucks", FRA Report No. FRA/ORD - 81/10, January 1981.
- 3 Bakken, G.B., Peacock, R.A., and Gibson, D.W., "Wheel/Rail Measurements From Concept to Utilization", International Conference on Wheel/Rail Load and Displacement Measurement Techniques, Transportation Systems Center, Cambridge, Massachusetts, January 19-20, 1981.
- 4 Gibson, D.W., "Type I Truck Test Procedure", Wyle Laboratories Report No. C-901-0009-A, June 1980.

## APPENDIX A

### Angle of Attack Measurement

Measurement of the wheel/rail angle of attack was made through a vehicle-borne angle of attack measurement system, believed to be the first of its kind to be used in an extensive field test program. However, the field test data acquired through this instrumentation package exhibited considerable scatter and it was difficult to discern characteristic trends of truck performance from the data. Although simplifications and theoretical assumptions can be used in the interpretation of the data, it is not considered desirable to use theoretical reasoning as the sole basis in arriving at "characterization" of truck performance. Therefore, the results from the test data are presented without extensive interpretation in the hope of furthering future work in this area.

**Instrumentation System.** Angle of attack data are provided by noncontacting position sensors mounted on the right side of each axle of the leading truck. Two sensors measure the relative sideframe to wheel displacement, and two others measure the relative sideframe to rail displacement. The difference between the two sensors gives the relative angle; the difference between the sideframe to wheel and the sideframe to rail angles result in the angle of attack (see Figs. 21 and 22). The sensors are of the eddy current type, which result in a signal based on the average distance from the sensor to a surface.

**Field Implementation.** Irregularities of the surface make it difficult to obtain a consistent reference. Also, the car must be stopped to make the measurement; this could set the truck up in unnatural operating positions.

Examination of the angle of attack data on several segments of track shows that it generally does not vary by more than  $\pm 4$  minutes on tangent track. Even though a particular truck can take a set on tangent track, it is believed that the average angle of attack on tangent track provides a better zero reference than the static calibration. Therefore, angle of attack data are referenced to tangent track. Although not providing an absolute reference, this method does have the advantage of removing the bias of a particular truck. The sensitivity calibration is believed to be more accurate than the zero calibration.

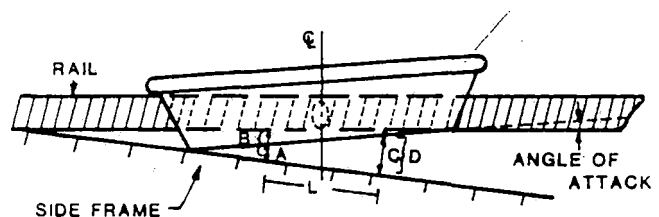


Fig. 21 Wheel/rail position measurement

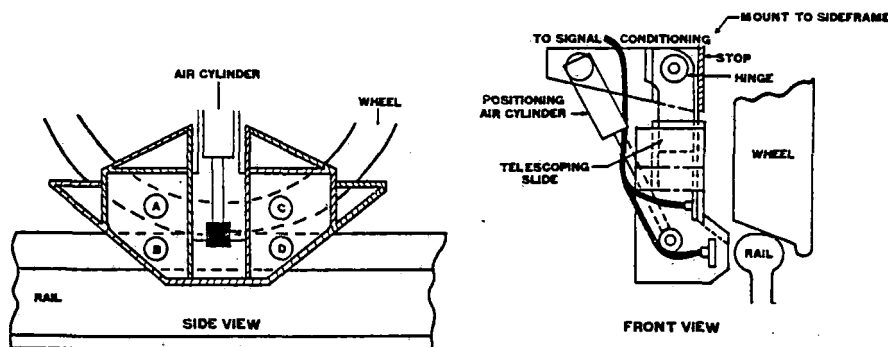


Fig. 22 Wheel/rail measurement system

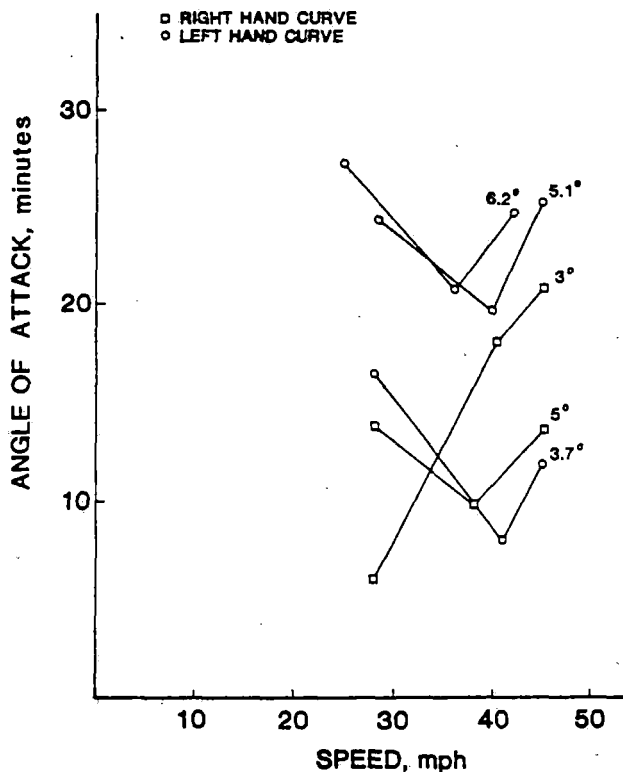


Fig. 23 Angle of attack versus speed - 100-ton trucks with loaded open hopper cars

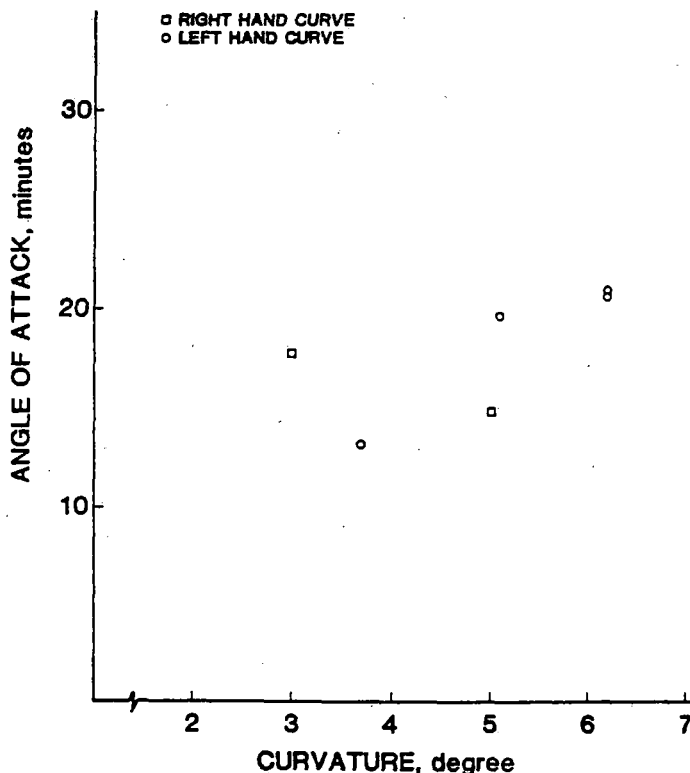


Fig. 24 Angle of attack versus degree of curvature near balance speed - 100-ton trucks with loaded open hopper cars

**Field Test Data.** The angle of attack data were analyzed using time history and statistical measurements (average and standard deviation of the signal). Fig. 23 shows the absolute average of the angle of attack as a function of speed, while Fig. 24 shows the absolute average angle of attack versus the degree of curvature near balance speed. After examining the time domain and the statistical properties of the angle of attack, the following remarks can be made:

- Considerable scatter in the results has been noted, and no clear-cut trends can be established. This is true both spatially, in the sense that there is considerable variation along a fixed radius curve, and in terms of the average between curves of the same radius. This scatter may be due to one or more reasons, namely, local variations in the track curvature; differences in truck set; large dependence on the truck history (i.e., direction and preceding curve); and errors in the collected data.
- The empty car data (not shown here) tend to have more scatter than the loaded car data.
- There is apparent difference between left-hand and right-hand curves. This difference may be caused by nonlinearity of the eddy current transducers due to overranging.

## APPENDIX B

Phase I of the Truck Design Optimization Project consisted of tests on five different types of cars equipped with different combinations of truck types and wheels. The characteristics of these car bodies and trucks are given in Tables 2 and 3, respectively.

The test matrix for high speed jointed track used during Phase II in quantifying the performance characteristics of Type I trucks in the performance regimes of lateral stability and ride quality is given in Table 4.

Test runs for the generation of performance test data relating to curve negotiation performance regime, as well as the curve entry/exit subregime of trackability, were conducted over a test zone comprised of mainline jointed track. Profiles and other related information for the different curves included in the test zone are given in Fig. 25.

Table 2 Carbody characteristics

	70-Ton Capacity Mechanical Refrigerator Car	70-Ton Capacity General Service Boxcar	70-Ton Capacity Long Low-Level Flatcar	100-Ton Capacity Auto Parts Boxcar	100-Ton Capacity Covered Hopper Cars
Light Weight	89,100 lb	61,200 lb	56,300 lb	87,300 lb	64,500 lb
Capacity	130,900 lb	154,000 lb	122,000 lb	174,000 lb	197,500 lb
Length Over Pulling Face of Coupler	63' 8-3/8"	55' 4-1/2"	93' 8"	68' 3"	54' 3-1/2"
Truck Centers	45' 8-5/8"	40' 10"	64'	46' 3"	40' 10"
Car Wheel Base	51' 4-5/8"	46' 10"	69' 1"	52' 1"	46' 4"
Overhang	9'	7' 3-1/2"	14' 10"	11'	71' 3-1/2"
Center of Gravity- Loaded	88"	84-3/8"	86"	94"	84-3/8"
Center of Gravity- Empty	66.6"	55"	23.6"	62"	55"
Centerplate Diameter	14"	14"	14"	16"	15"

Table 3 Truck characteristics

	70-Ton ASF Ride Control Truck	70-Ton Barber S-2-C Truck	70-Ton ASF Low-Level Truck	100-Ton ASF Ride Control Truck	100-Ton Barber S-2-C Truck
Wheel Base	5' 8"	5' 8"	5' 1"	5' 10"	5' 10"
Wheel Diameter	33"	33"	28"	36"	36"
Bolster Centerplate Diameter	13-3/4"	14"	14"	15"	16"
Centerplate Height	25-3/4"	25-3/4"	20-1/8"	24-13/16"	25-3/4"
Weight, lb	9,080	9,100	7,600	10,540	10,560
Gross Rail Load, lb	220,000	220,000	179,000	263,000	263,000
Vertical Spring Rate (Per Car), lb/in	94,466	89,653	97,450	108,333	109,367
Lateral Spring Rate (Per Spring Nest), lb/in	4,665 (at 9.47")* 7,795 (at 7.56")*	3,470 (at 9.47") 9,080 (at 7.56")	4,755 (at 9.06") 12,015 (at 8.31")	3,655 (at 9.47") 9,560 (at 7.56")	2,705 (at 9.47") 10,285 (at 7.56")
Friction Snubber Column Load, lb	3,140	Variable (Load-Dependent)	3,110	4,510	Variable (Load-Dependent)

\*Spring Nest Height

Table 4 High-speed jointed track test matrix

TDOP PHASE I TEST MATRIX USED DURING PHASE II ANALYSIS				<input checked="" type="checkbox"/> TEST DATA AVAILABLE	<input type="checkbox"/> NO TEST CONDUCTED
Truck	Carbody	Empty		Loaded	
		Wheel Profile			
		New AAR 1/20	Worn	New AAR 1/20	Worn
70-Ton ASF Ride Control	Refrigerator Car	●	●	●	●
70-Ton Barber S-2-C	Refrigerator Car	●		●	
	70-Ton Boxcar	●		●	
70-Ton Low Level ASF Ride Control	89-ft Flatcar	●	●	●	
100-Ton Barber S-2-C	100-Ton Boxcar	●		●	
100-Ton ASF Ride Control	100-Ton Covered Hopper Car	●		●	

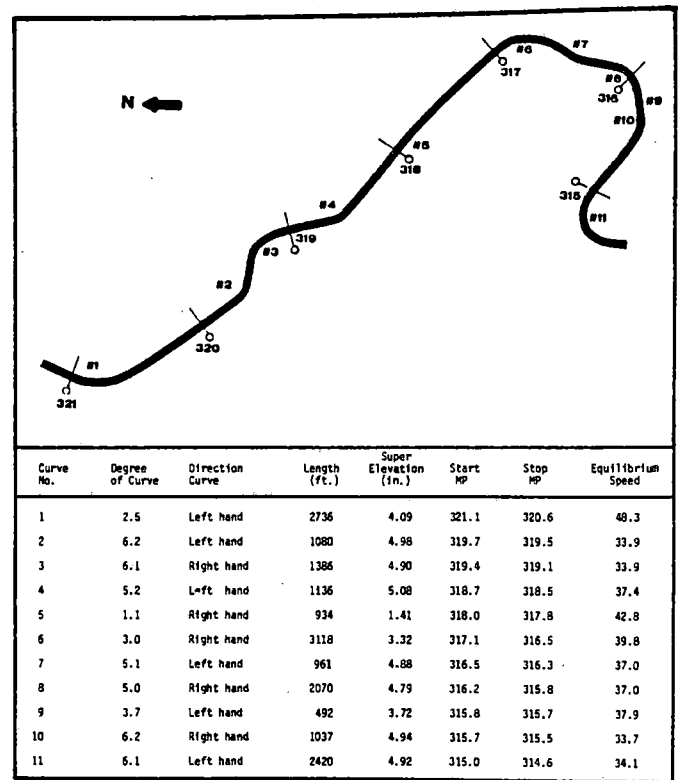
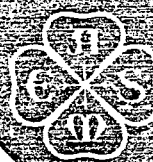


Fig. 25 Curve profiles - test zone



an ASME  
publication

\$3.00 PER COPY \$1.00 TO ASME MEMBERS

The Society shall not be responsible for statements or opinions advanced in papers or in discussion at meetings of the Society or of its Divisions or Sections, or printed in its publications.

REFERENCE 149

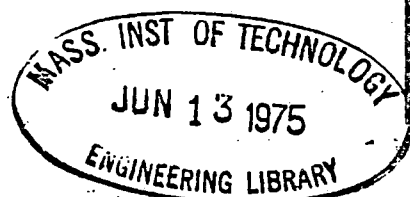
# The Lateral Dynamics of the Linear Induction Motor Test Vehicle

A. E. W. HOBBS

Head of Dynamics,  
British Rail Research and  
Development Division

T. G. PEARCE

Principal Scientific Officer,  
Dynamics Section, British Rail  
Division and Development Division



*The dynamic behavior of the LIM Test vehicle has been the subject of theoretical and experimental studies conducted for the U. S. Department of Transportation by British Rail's Research and Development Division. Key aspects of the studies of lateral stability, curving, and response to irregular track are described showing that an adequate stability margin exists for a conicity of 0.025. Satisfactory response characteristics are available for the anticipated roughness spectrum, but the linear curving regime does not encompass the higher range of operating speeds on the test track curve of 2.5 miles radius. To date (October, 1973) measured performance compares well with theory but change of conicity with tire wear is an unexpected difficulty due in part to the very high track quality. This tire wear is of peculiar form and not typical of the normal high speed railway.*

## Introduction

The United States Government High Speed Ground Transportation Act of 1965 authorized a number of research and development programs and demonstration projects one of which involved the manufacture and testing of a Linear Induction Motor propulsion system or LIM. This propulsion system was intended for the Tracked Air Cushion Vehicle, or TACV, now under test, but, in order to expedite its development and to decouple it from the first stages of the TACV program, the Department of Transportation made the decision to evaluate the LIM in a rail vehicle capable of 250 mph. The vehicle would be a conventional rail vehicle using existing steel wheel on steel rail technology and would run on a specially constructed track at the D.O.T. High Speed Ground Test Center at Pueblo, Colo. The design and manufacture of the test vehicle and linear motor were carried out by Garrett Airesearch with trucks supplied by the Budd Company. British Rail's Research and Development Division was awarded a contract to carry out a dynamic analysis of the test vehicle and provide support throughout manufacture and testing phases of the project. Initial work is reported fully in reference [1].<sup>1</sup>

The present paper describes that part of the dynamics studies which is concerned with lateral stability, guidance through the curved section of the track, and response to irregularities of the track, the last topic including a specification for track quality.

The paper also includes the results of vehicle testing available at the time of writing and, where possible, compares these with theoretical predictions.

## The LIM Test Vehicle

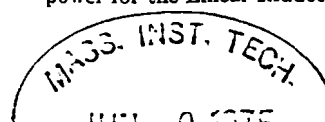
The LIM vehicle, Fig. 1, is of conventional railway vehicle configuration with car body carried on a pair of two-axle bogies (or trucks). It has steel railway wheels, each pair mounted on a common axle, and runs on standard gauge railway track. With few exceptions this arrangement has been the standard for railway vehicles for many years and it is in some parameter values only, particularly weight, that the LIM vehicle is exceptional. For example its total weight of 50,000 lb is little more than half the weight of typical European passenger vehicles and approximately a quarter that of some North American vehicles. The trucks are very light at 5800 lb each and bear a similar weight relationship to trailer bogies produced for normal railway use. The truck pivot spacing is small at 27 ft but the truck wheelbase of 8.5 ft is typical. A complete list of parameters is given in Table 1.

The vehicle structure is a tubular steel space frame clad with a low drag aluminum skin. The car body is carried on four Firestone 28 C "Airmount" air springs, augmented laterally by further air springs, which together provide both vertical and transverse flexibilities. Additional adjustable air volume is provided in the transverse structural member (or bolster) of the truck and fundamental frequencies within the range 0.6 Hz to 1.1 Hz transversely and 0.65 Hz to 1.8 Hz vertically can be achieved.

The car body houses a 3000 hp turbo-alternator set, providing power for the Linear Induction Motor itself, the auxiliary power

<sup>1</sup>Numbers in brackets designate References at end of paper.

Contributed by the Automatic Control Division for publication in the JOURNAL OF DYNAMIC SYSTEMS, MEASUREMENT, AND CONTROL. Manuscript received at ASME Headquarters, March 8, 1974. Paper No. 74-Aut-Q.



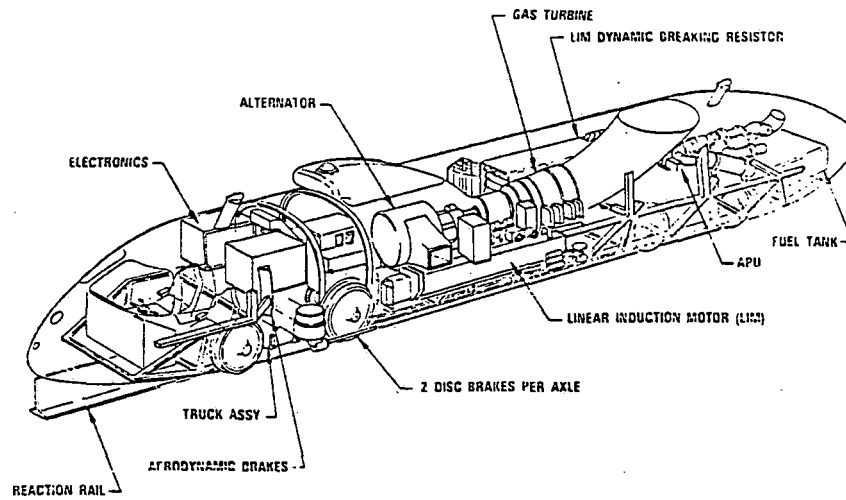


Fig. 1 The LIM test vehicle

unit, fuel tanks, driver's compartment, control systems, and telemetry equipment, (the vehicle is remotely driven for speeds above 100 mph). The LIM is suspended from the car body by four bearings giving transverse freedom; these allow the motor to be decoupled from transverse vehicle motions and guided by rubber-tired wheels which "pinch" the aluminum reaction rail. Traction links connect motor to body for propulsion and braking purposes with additional friction braking being provided by axle-mounted disks.

The trucks are based on the Budd Pioneer III design and have two-piece high strength alloy steel frames arranged to provide a relative pitch freedom between side frames. The lightweight wheelsets have hollow axles and inside axle bearings contained within specially designed rubber suspension elements whose stiffnesses can be varied to provide optimum dynamic characteristics. The truck frame pivots about a vertical axis with

frictional control with respect to the bolster which, in turn, is connected in yaw to the car body by rubber bushed traction rods.

## Equations of Lateral Motion

Inspection of the complete equations of motion of a railway vehicle of LIM vehicle configuration shows the existence of a longitudinal-vertical center-plane of symmetry. The vertical motions which are symmetric about this plane of symmetry are decoupled from the antisymmetric lateral motions, and will not be considered further in this paper. The lateral motions involve lateral translation, yaw, and roll coordinates for wheelsets, trucks, and car body, Fig. 2, and give rise to 17 second-order coupled differential equations. Fig. 3 shows the equations with truck roll eliminated which is a simplification justified by the

## Nomenclature

### Subscripts

$b$ = truck frame or secondary suspension	$F_y$ = lateral suspension force	$V_1 V_2 V_3$ = velocity of the contact ellipse on the wheel
$c$ = vehicle body	$G(f_i)$ = power spectral density of track roughness	$V'_1 V'_2 V'_3$ = velocity of the contact ellipse on the rail
$e$ = equilibrium condition on curved track	$G_\psi$ = yaw suspension couple	$W$ = axle load
$l$ = left wheel	$g$ = acceleration due to gravity	$y$ = lateral displacement
$0$ = perfectly aligned track with wheelset centrally placed	$k_y, k_\psi$ = lateral and yaw suspension stiffness	$Y, Y_B, Y_c$ = external lateral forces on wheelset, bogie frame, and body
$r$ = right wheel	$l_0$ = semispacing of wheel/rail contact points	$\gamma_1 \gamma_2$ = longitudinal and lateral creepages
$t$ = track coordinate	$M_s$ = yaw creep couple in contact plane axes	$\theta$ = roll displacement
$1, 2, 3, 4$ = wheelsets 1, 2, 3, 4	$M_w$ = yaw creep couple in wheelset axes	$\theta_c$ = external roll couple on vehicle body
$a, b$ = semimajor and semiminor axes of contact ellipse (e.g. in A.3)	$q$ = coefficient of wheel load increment/decrement due to cant deficiency	$\theta_d$ = cant deficiency angle
$a$ = truck semiwheelbase	$R_0$ = radius of curved track	$\lambda$ = effective conicity
$a_s$ = longitudinal semispacing of trucks	$r$ = wheel rolling radius	$\phi$ = pitch displacement
$C_{11} C_{22}$ } = creep parameters tabulated by Kalker	$s$ = differential operator $\frac{d}{dt}$	$\psi$ = yaw displacement
$C_y$ = lateral viscous damping	$T_1 T_2 T_3$ = creep forces in contact plane axes	$\psi, \psi_B, \psi_c$ = external yaw couple on wheelset, bogie, frame, and body
$E$ = Young's modulus (modulus of elasticity)	$T_x T_y T_z$ = creep forces in wheelset axes	$\omega_s$ = spin creepage
$f_{11} f_{22}$ } = longitudinal, lateral, lateral/spin, and direct spin creep coefficients	$V$ = forward speed of vehicle	$\Omega_s, \Omega'_s$ = angular velocities of spin of wheel and rail about an axis perpendicular to the contact plane

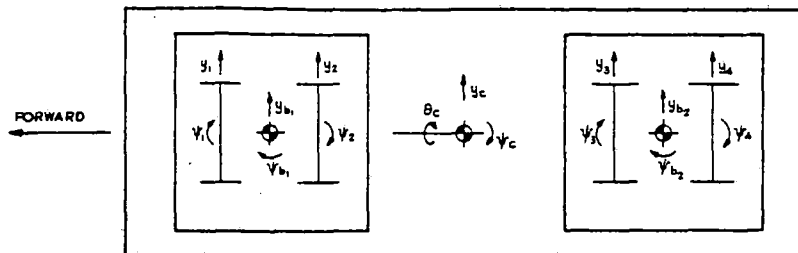


Fig. 2 Axis and coordinate systems

high primary roll stiffness. A further simplification is the neglect of the direct spin and lateral/spin creep terms involving  $f_{23}$ ,  $f_{32}$  which are very small for the LIM vehicle wheel/rail contact conditions. The derivation of these equations considers the forces and couples acting on the component parts of the vehicle through the inter-connecting springs and dampers and, in particular, the forces acting at the wheel-rail interface. This derivation is not given in this paper but the wheelset equations, being of special interest, are derived in detail in Appendix A.

## Dynamic Stability

The equations of lateral motion describe a non-conservative dynamic system with asymmetric terms, due to lateral creep and longitudinal creep with conicity, apparent in the stiffness matrix. There exists therefore the possibility of dynamic instability or hunting. For the LIM vehicle combinations of suspension parameters are possible which yield unstable and stable regions as a function of forward speed as indicated in Fig. 5. Two regions of instability are apparent which are characterized by different eigenvectors or mode shapes; these are bogie hunting, involving larger amplitudes of truck motion than car body motion, and body hunting, involving relatively larger motion of car body than trucks.

Table 1 Basic vehicle data

Basic vehicle data	
Wheelset mass	1,712 lb
Truck frame mass	2,393 lb
Wheelset radius of gyration in yaw	2 ft
Truck radius of gyration in yaw	2.63 ft
Axle load	9,600 lb
Longitudinal creep coefficient (Kalker's value)	$1.09 \times 10^6$ lb
Lateral creep coefficient (Kalker's value)	$1.0 \times 10^6$ lb
Truck wheelbase	8.5 ft
Wheel rolling radius	1.58 ft
Lateral semispacing of axleboxes	1.93 ft
Lateral semispacing of secondary yaw suspension	3.56 ft
Lateral semispacing of secondary roll suspension	3.56 ft
Body mass (excluding LIM)	21,500 lb
Body radius of gyration in roll	3.04 ft
Body radius of gyration in yaw	12.3 ft
Bogie pivot spacing	27 ft
Body height of c.g. above axle center	1.71 ft
LIM mass	5,300 lb
Body radius of gyration in pitch	12.3 ft
Bogie frame radius of gyration in pitch	2.6 ft
Preferred suspension stiffnesses	
Secondary longitudinal, per bogie	5,000 – 20,000 lb/in.
Secondary lateral, per bogie	600 – 2,800 lb/in.
Secondary vertical, per bogie	1,000 – 5,700 lb/in.
Primary longitudinal, per wheelset	86,000 lb/in.
Primary lateral, per wheelset	33,600 lb/in.

## Truck Hunting

The equations of motion in homogeneous form may be solved by analog or digital means to provide stability boundaries, or contours of zero damping. As a first stage of study, heuristic simplification suggests the consideration of a reduced mathematical model having six degrees of freedom involving the yaw and lateral translation coordinates of two wheelsets and truck frame. The truck is assumed to move at constant forward speed along the track center-line and has creep coefficients  $f_{11}$ ,  $f_{22}$ , appropriate to the axleload of the complete vehicle.

Fig. 4 shows the influence of primary lateral and yaw stiffnesses and secondary yaw stiffness upon the critical speed of truck hunting for two values of creep coefficient. The ratio of lateral to yaw stiffness of the primary (axlebox) bushes is maintained constant at a value appropriate to the cylindrical nature of the rubber elements (radial stiffness =  $2.5 \times$  axial stiffness). The value of effective conicity ( $\lambda = 0.025$ ) is obtained from the 1:40 taper of the wheel treads. Use of creep coefficients calculated according to Kalker's linear theory of creep (reference [2]) and a half of these values follows from the authors' experience of the applicability of this theory to both model and full-scale railway wheel situations. It will be noticed that the reduced creep coefficient case gives rise to an inadequate critical speed if secondary yaw restraint is not provided (i.e., of  $k_{y2} = 0$ ) and that the optimum critical speed is obtained with different values of primary stiffness according to creep coefficient. A compromise value has to be chosen and the stiffnesses recommended are those given in Table 1; these are at the low end of the available range. The tolerance of the truck to tire wear which usually produces an increased effective conicity can be seen in Fig. 5 where it is apparent that a conicity of up to  $\lambda = 0.1$  can be tolerated. Effective conicities in the range  $\lambda = 0.2$  to  $\lambda = 0.4$  are fairly common on most railway systems, where wheels are expected to have a reasonable life between overhauls (e.g., at least 100,000 miles), and therefore the LIM vehicle does require special attention to tire profiles.

## Body Hunting

Since the car body hunting tendency is little influenced by the values of primary stiffness within the range under discussion, the sensitivity of body hunting boundaries to secondary suspension parameters can be explored for the primary values given in Table 1. A range of secondary lateral stiffness is available by varying the air pressure in the lateral control springs and results for the two extreme values are presented; these stiffnesses are also given in Table 1. The secondary roll suspension, which is derived from the vertical suspension, is also considered for the two extremes of its available range.

The stability boundaries of Fig. 5 are obtained from the solution of the full 15 degrees of freedom lateral model. Eigenvectors show that the body hunting mode for low lateral damper rates is mainly lateral translation of the body with small amplitude



$$\begin{pmatrix}
 (m_s^2 + 2f_{zz}^2 + k_y) & -2f_{zz} & -k_y & -ak_y & 0 & 0 & 0 & 0 & 0 & 0 & 0 & 0 & 0 & 0 & 0 & 0 \\
 2\lambda f_{zy} f_{zy} & (I_z s^2 + 2f_{zy}^2 + k_y) & 0 & -k_y & 0 & 0 & 0 & 0 & 0 & 0 & 0 & 0 & 0 & 0 & 0 & 0 \\
 -k_y & 0 & (m_b s^2 + 2k_{yb} + c_{yb} s + k_{yb}) & -k_y & 0 & (-c_{yb} s - k_{yb}) & (-a_b c_{yb} s - a_b k_{yb}) & 0 & 0 & 0 & 0 & 0 & 0 & 0 & 0 & 0 \\
 -ak_y & -k_y & 0 & (I_z s^2 + 2a^2 k_y + 2k_{yb} + k_{yb}) & ak_y & -k_y & 0 & -k_{yb} & 0 & 0 & 0 & 0 & 0 & 0 & 0 & 0 \\
 0 & 0 & -k_y & ak_y & (m_s^2 + 2f_{zz}^2 + k_y) & -2f_{zz} & 0 & 0 & 0 & 0 & 0 & 0 & 0 & 0 & 0 & 0 \\
 0 & 0 & 0 & -k_y & 2\lambda f_{zy} f_{zy} & (I_z s^2 + 2f_{zy}^2 + k_y) & 0 & 0 & 0 & 0 & 0 & 0 & 0 & 0 & 0 & 0 \\
 0 & 0 & (-c_{yb} s - k_{yb}) & 0 & 0 & 0 & (m_s^2 - 2c_{yb} s + 2k_{yb}) & 0 & m_c h_c s^2 & 0 & 0 & (-c_{yb} s - k_{yb}) & 0 & 0 & 0 & 0 \\
 0 & 0 & (a_b c_{yb} s - a_b k_{yb}) & -k_{yb} & 0 & 0 & 0 & (I_z s^2 + 2a^2 k_y + 2k_{yb} + k_{yb}) & 0 & 0 & (a_b c_{yb} s - a_b k_{yb}) & -k_{yb} & 0 & 0 & 0 & 0 \\
 0 & 0 & 0 & 0 & 0 & 0 & m_c h_c s^2 & 0 & (-c_{yb} s - k_{yb}) & 0 & 0 & 0 & 0 & 0 & 0 & 0 \\
 0 & 0 & 0 & 0 & 0 & 0 & 0 & 0 & (m_s^2 + 2f_{zz}^2 + k_y) & -2f_{zz} & -k_y & -ak_y & 0 & 0 & 0 & 0 \\
 0 & 0 & 0 & 0 & 0 & 0 & 0 & 0 & 2\lambda f_{zy} f_{zy} & (I_z s^2 + 2f_{zy}^2 + k_y) & 0 & -k_y & 0 & 0 & 0 & 0 \\
 0 & 0 & 0 & 0 & 0 & 0 & (-c_{yb} s - k_{yb}) & (a_b c_{yb} s - a_b k_{yb}) & 0 & -k_y & 0 & (m_b s^2 + 2k_{yb} + c_{yb} s + k_{yb}) & 0 & -k_y & 0 & 0 \\
 0 & 0 & 0 & 0 & 0 & 0 & 0 & 0 & -k_{yb} & 0 & (I_z s^2 + 2a^2 k_y + 2k_{yb} + k_{yb}) & ak_y & -k_y & 0 & 0 & 0 \\
 0 & 0 & 0 & 0 & 0 & 0 & 0 & 0 & 0 & 0 & -k_y & ak_y & (m_s^2 + 2f_{zz}^2 + k_y) & -2f_{zz} & 0 & 0 \\
 0 & 0 & 0 & 0 & 0 & 0 & 0 & 0 & 0 & 0 & -k_y & 2\lambda f_{zy} f_{zy} & (I_z s^2 + 2f_{zy}^2 + k_y) & 0 & 0 & 0
 \end{pmatrix}
 \begin{Bmatrix}
 \dot{y}_1 \\
 \dot{y}_2 \\
 \dot{y}_3 \\
 \dot{y}_4 \\
 \dot{y}_5 \\
 \dot{y}_6 \\
 \dot{y}_7 \\
 \dot{y}_8 \\
 \dot{y}_9 \\
 \dot{y}_{10} \\
 \dot{y}_{11} \\
 \dot{y}_{12} \\
 \dot{y}_{13} \\
 \dot{y}_{14} \\
 \dot{y}_{15} \\
 \dot{y}_{16}
 \end{Bmatrix}
 =
 \begin{Bmatrix}
 0 \\
 0 \\
 0 \\
 0 \\
 0 \\
 0 \\
 0 \\
 0 \\
 0 \\
 0 \\
 0 \\
 0 \\
 0 \\
 0 \\
 0 \\
 0
 \end{Bmatrix}$$

Fig. 3 Equations of lateral motion

in-phase roll of the car body, giving a nodal centre some 26 ft below rail level. This mode is termed "lower sway." Body hunting in yaw also occurs although for "low" damper rates the unstable region is wholly contained within the lower sway boundary. Fig. 5 shows the stability boundaries for full and half creep coefficients for three values of conicity and for the "high" value of secondary lateral stiffness which has been adopted in practice. As in the case of truck hunting the influence of reduced creep coefficients is destabilizing and a substantial amount of lateral suspension damping ( $> 33$  percent of critical) in the "wheels-fixed" condition is necessary to stabilize car body hunting, the least stable mode in this case being body yaw. Fig. 6 gives the eigenvalues for the half creep coefficient case with 40 percent of critical damping in the "wheels-fixed" lateral translation coordinate. The least damped mode at the 250 mph maximum speed is body yaw with 8 percent of critical damping. The lower sway mode has 12 percent and the truck kinematic mode 21 percent. Relatively low damping of the body modes is not untypical of railway vehicles operating with low conicity and reduced creep coefficients and in the case of the LIM vehicle little improvement is possible. Further substantial increases of "wheels-fixed" lateral damping strengthen body-truck coupling and become de-stabilizing in themselves. It follows that the optimum lateral damping rate is best found experimentally in conditions of the actual track irregularity input

### Rotational Friction Between Bogie Frame and Bolster

The stability analysis of the complete vehicle makes the assumption that the secondary yaw restraint, necessary to provide adequate stability of the trucks, is purely elastic. In reality the rotational restraint consists of the bolster restraint arm rubber bushes, which are elastic and whose parameters have been used in the aforementioned studies, placed in series with rotational friction between bolster and truck frame. Thus relative yaw of the truck with respect to the bolster is permitted if the secondary yaw torque exceeds a prescribed value. The effectiveness of the secondary yaw stiffness depends upon the

presence of an adequate, but not excessive, rotational friction torque which is obtained in this case with the standard Pioneer III arrangement.

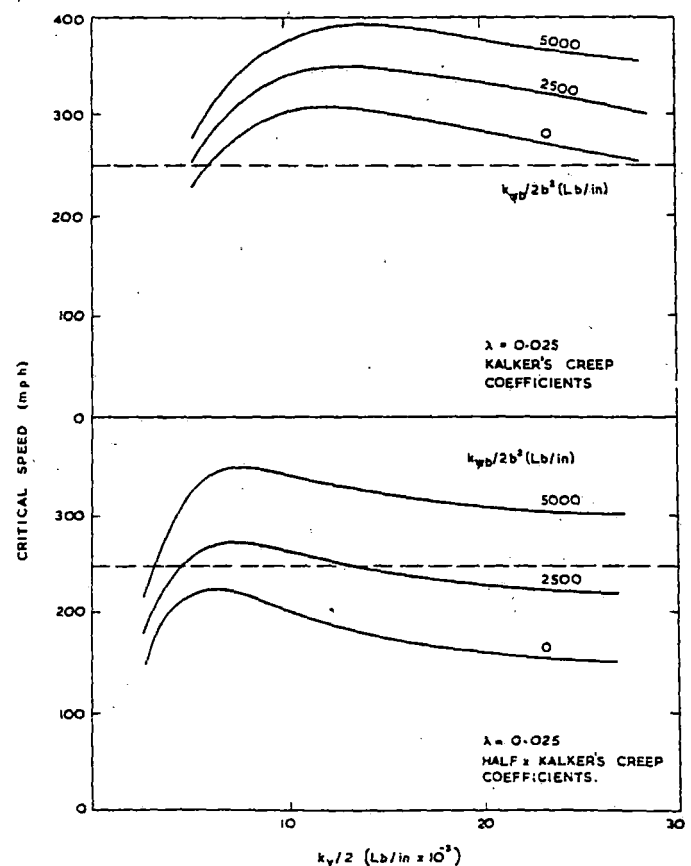


Fig. 4 Influence of plan-view stiffness on the critical speed of truck hunting

Table 2 Predicted acceleration counts on straight track at 250 mph

Lateral acceleration level (ft/sec <sup>2</sup> )	Exceedances per mile
+ 5.46	0.2
+ 3.64	2.3
+ 1.82	10.0
- 1.82	10.0
- 3.64	2.3
- 5.46	0.2

## Linear Curving Performance

Within certain limits of track radius and coefficient of friction a railway vehicle can be steered through circular curves by means of creep forces alone, with the tire flange playing no part in the guidance (reference [3]). The tread forces generated by track curvature and cant deficiency may be computed by applying the appropriate forcing functions to the lateral equations (Fig. 3) and omitting first and second derivative terms, to obtain the quasi-static linear solution. The forcing functions due to curvature and cant deficiency are derived in Appendix B. The effects of track irregularities will be super-imposed upon this solution which nevertheless represents the mean value of any dynamic response providing that linearity still obtains.

## Slip Boundaries

Having computed the tread forces, the curvatures and cant deficiencies where the resultant tread force exceeds the total friction force available are obtained. The graph of this limiting value as a function of curvature and cant deficiency is known as the "slip boundary" and is calculated for each wheelset of the vehicle. Fig. 7 is a typical result for the LIM vehicle with an assumed coefficient of friction of 0.2.

The slip boundaries for the various wheelsets overlap and it is evident that a linear solution of the static equations becomes invalid when any of the four wheelsets of the vehicle has slipped. Thus by superposition a region of no slip for any wheel is obtained within which the linear solution applies and outside of which

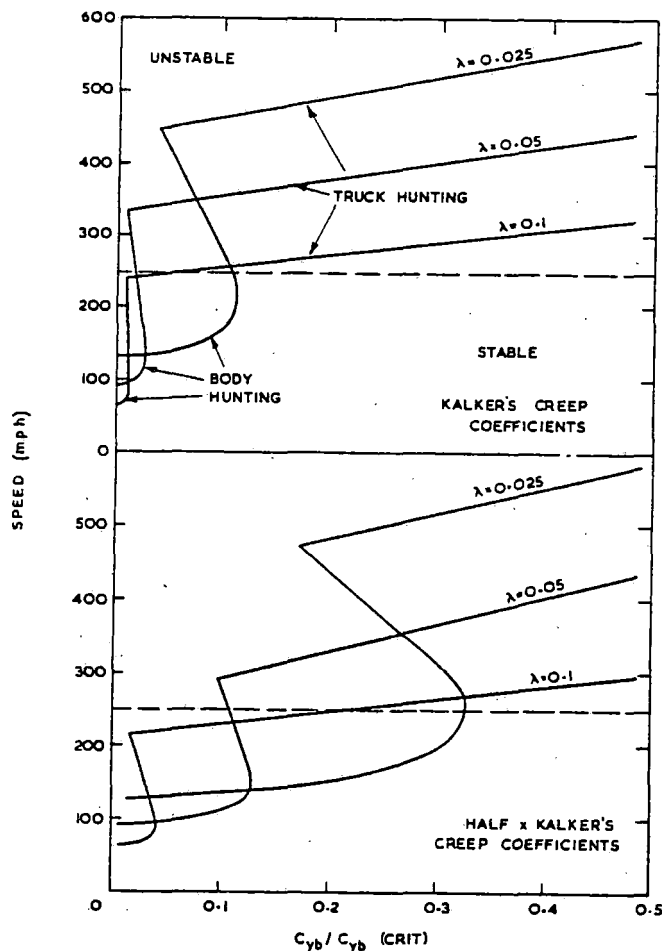


Fig. 5 Effect of conicity on body hunting boundaries

prediction of tread and flange forces becomes a non-linear, large creep problem. Reliable prediction of flange forces, with some

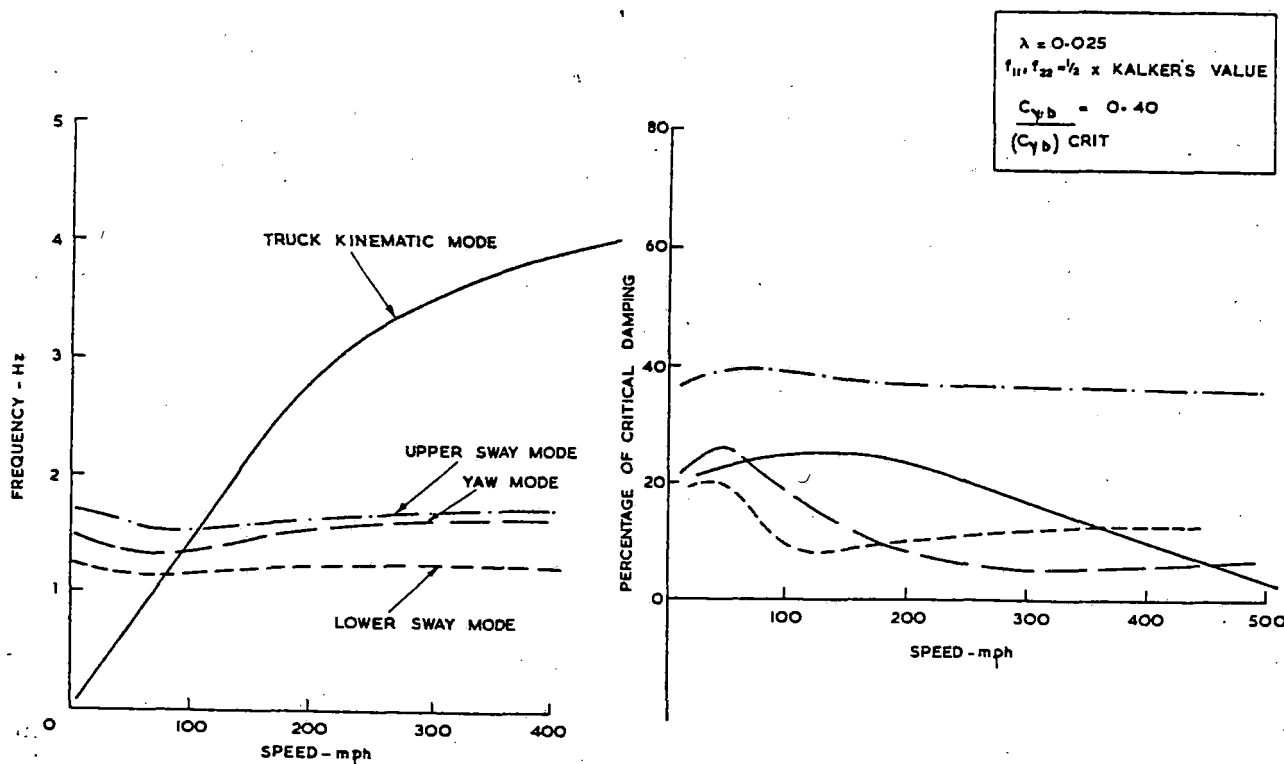


Fig. 6 Eigenvalues of LIM vehicle

treads in full slip and others not, is a technique which is not yet available and LIM vehicle operations within this regime must rely upon existing criteria for safety against derailment and track shifting (references [4, 5]).

## Flange Contact Boundaries

The wheelsets of a vehicle curving under linear, steady state conditions move away from the pure rolling line in order to generate the necessary creep torques to yaw wheelsets and trucks to an approximate radial alignment; these yaw torques oppose the yaw suspension torques which arise from the distorted plan-view vehicle geometry. The lateral motion is modified to some extent in the presence of unbalanced centrifugal forces, which, in the linear situation, are reacted by wheelsets yawing with respect to the radial line, and thereby generating lateral creep forces. The lateral shift is approximately proportional to the primary yaw stiffness and track curvature, and inversely proportional to the conicity and creep coefficient so it is apparent that a low conicity vehicle of LIM configuration can run into flange contact, having used up the available flangeway clearance, before tread forces exceed the total available friction force. (See Fig. 7). It is important to note that the flangeway clearance specified by British Railways was already unusually large in order to cater for this effect as far as possible. (Track gauge is 4 ft 8<sup>5</sup>/<sub>8</sub> in.).

## Curving Performance on the Pueblo Test Track

The track on which the LIM vehicle runs is a 6.03 mile section of the Department of Transportation's "high speed oval" having 2.65 miles of tangent track and 3 miles of circular curve of 2.5 miles radius. The circular curve section has 8 in. of superelevation of track cant. The vehicle is required to operate from zero speed to 250 mph on the curve and therefore experiences from 8 in. cant excess to 12 in. cant deficiency (at maximum speed). The equilibrium or balancing speed for the curve is 160 mph. Fig. 7 shows the predicted behavior of the LIM vehicle on curved track in general and the test curve in particular. It is evident that flange contact will always occur on the test track for the vehicle parameters given in Table 1, although a small increase in conicity or reduction in yaw stiffnesses will change this

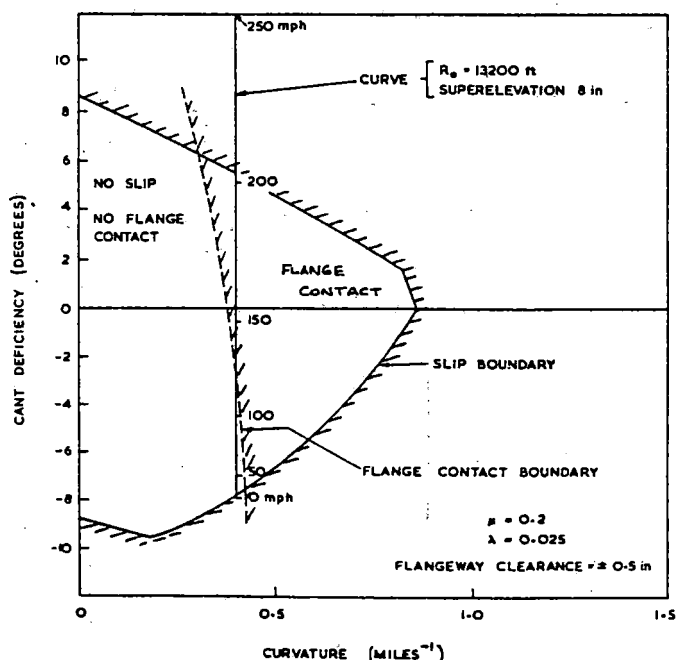


Fig. 7 Behavior of LIM vehicles on the curved sector of the Pueblo test track. Halved creep coefficients.

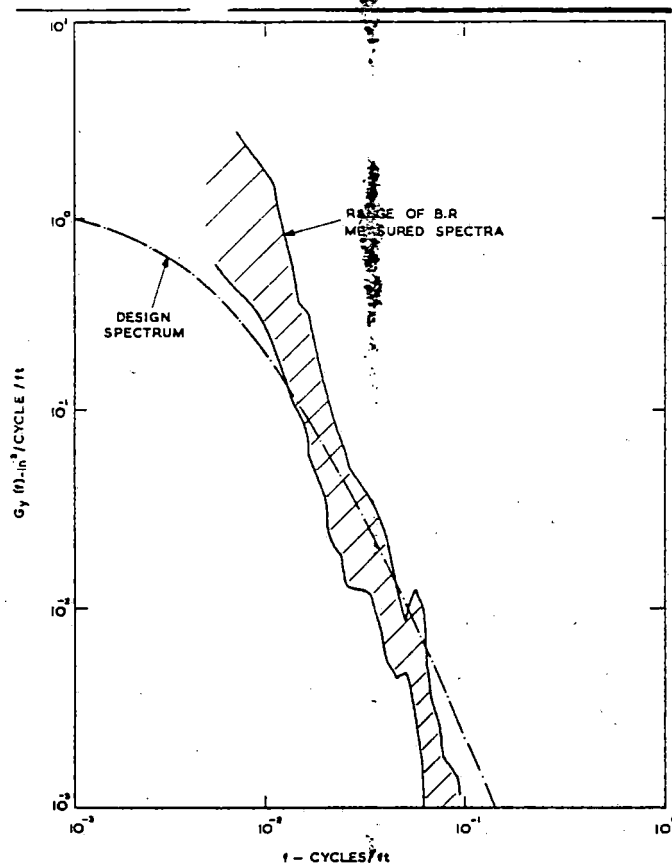


Fig. 8 Proposed lateral track spectrum

situation. Even so, at 250 mph, the curving behavior is substantially non-linear because of the very large cant deficiencies employed.

## Response to Irregular Track

The response of the LIM vehicle to the irregularities of its track is calculated with the assumption that it is a stationary random process, with both track input and vehicle response described by their Power Spectral Densities. For design purposes an algebraic expression was used to describe the track input spectrum and this was based on British Rail's experience. The expression has the form:

$$G(f_i) = \bar{G} \times W(f_i)$$

$$\text{where } W(f_i) = \frac{1}{2.5 \times 10^{-5} + f_i^2(1 + f_i^2)}$$

$$\bar{G} = 2.5 \times 10^{-5} \text{ in.}^2/\text{cycle/ft}$$

and  $f_i$  is the frequency of the track irregularities. This spectrum is shown in Fig. 8 where it is compared with a range of spectra from British Rail main line routes. Comparisons with spectra from other administrations is not made here but it should be noted that British Rail's spectra are typical of conventional railway track having sleepers and ballast. New track forms may well offer a substantial improvement in quality.

The response of the vehicle may be computed for each input coordinate separately and, as an example, the lateral track input spectrum is considered here. Nonlinear situations of curving or intermittent flange contact are excluded from the analysis which therefore provides only an assessment of vehicle performance. Matters of safety cannot be based upon the statistical approach described since even for the linear situation departure

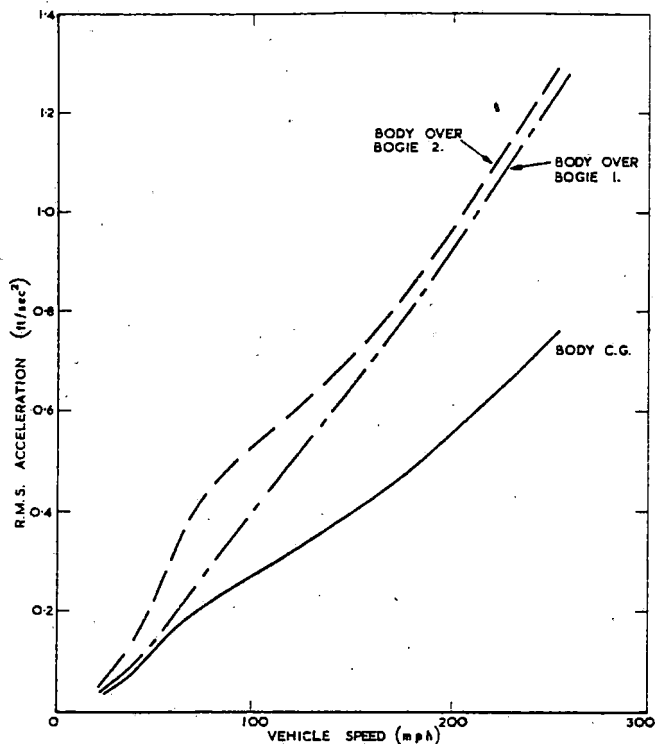


Fig. 9 Predicted body lateral acceleration as a function of speed

from a Gaussian distribution will make the prediction of extreme values very inaccurate.

Parameters of interest are car body acceleration, for ride prediction purposes, suspension forces and displacements for stressing and suspension travel, wheel/rail forces and relative motion for guidance assessment, and so on. Fig. 9, shows the variation of one of these parameters; the rms lateral acceleration of the car body, as a function of vehicle speed. Three positions are plotted, leading and trailing bogie locations, and vehicle centre of gravity and it can be seen that the outboard stations give rise to predicted accelerations which are typically 60 percent greater than the CG station. This is usual for a railway vehicle and follows from the superposition of response in the yaw and lower sway modes as well as the inherent filtering properties of the bogie vehicle itself. The predicted lateral accelerations at the design maximum speed would provide a satisfactory, but not exceptional, environment for a passenger vehicle and are to a large extent the result of the shape of the specified track spectrum at long wavelengths. With the assumption of normal distribution and including response to the cross-level input spectrum the predicted numbers of exceedences per mile of various

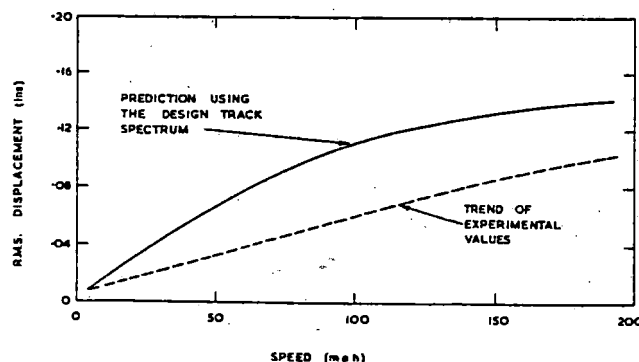


Fig. 10 Comparison of predicted rms suspension displacement with measured values. (Predictions based on "design" spectrum.)

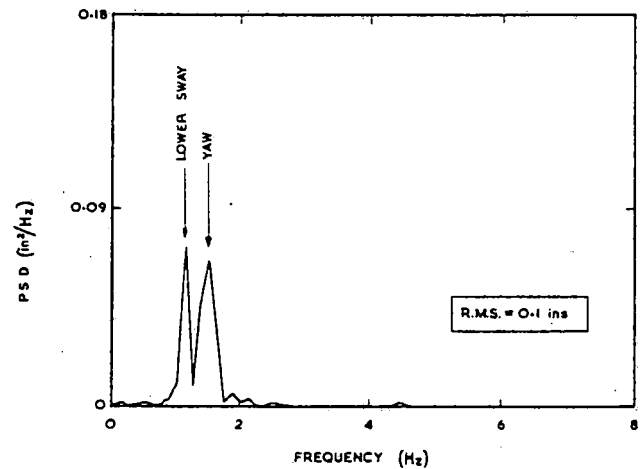


Fig. 11 Body/truck relative displacement P.S.D. at trailing truck. Speed 114.7 mph.

levels of body acceleration over the leading bogie are given in Table 2.

## Experimental Results to Date

Up to the time of writing maximum speeds in the region of 180–190 mph have been achieved with satisfactory dynamic behavior. However, an unforeseen problem has been that tire wear was more rapid than expected, although only on a small portion of the cross-sectional profile, leading to a substantially non-linear effective conicity. This point is discussed in detail later. Tires have since been reprofiled to the specified 1:40 cone in preparation for the final program of speed upgrading, commencing in November, 1973, leading to the target maximum of 250 mph. The restricted length of the test track has required the linear motor thrust to be augmented by jet thrust to achieve this speed and the overall weight of the vehicle has increased significantly. This has necessitated a small increase in the plan-view primary stiffnesses of the trailing truck due to the limited weight carrying capacity of the rubber bushes previously fitted, but it is not expected that the dynamic or curving performance will be significantly affected.

Operation at 250 mph will involve a cant deficiency of 12 deg and a consequent unbalanced centrepetal acceleration of 0.21 g which is outside the range of existing railway experience, other than during overspeeding incidents. The guidance in the test curve will be essentially non-linear if predictions prove correct and detailed monitoring for safety against flange-climbing derailment or the possibility of track shifting is necessary.

## Track Quality

After completion of the test track the power spectral densities of its irregularities in respect of gauge, cross-level, and lateral and vertical alignment were measured in 1971. The measuring system was fitted to a truck of one of the Department of Transportation's Test Cars and used the technique of offset measurement from a 14 ft chord, or beam, carried on the truck frame. Offsets were measured by capacitance probes. A chord length of 14 ft is insufficient for measurement of a high speed test track and reliable information at wavelengths greater than 50 ft is not yet available. This is an order less than required and the development of a new track measuring machine is awaited with interest. However, the inference from the available track measurements and from vehicle ride data is that the specified track quality has been achieved with a significant margin to spare. Fig. 10 shows the measured rms of trailing lateral suspension displacement as a function of forward speed compared with a

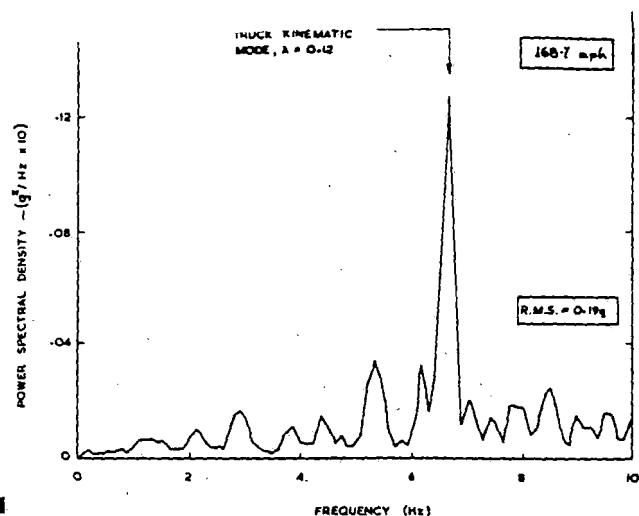


Fig. 12 Truck frame lateral acceleration P.S.D. Speed 168.76 mph

prediction using the specified track spectrum of Fig. 8.

### Vehicle Parameters

Some difficulty was experienced in producing the specified stiffness parameters at primary, or axlebox level. Stiffnesses proposed by British Rail's studies were at the very low extremity of those available with the LIM truck mechanical arrangements which also does not allow independent variation of lateral yaw and vertical parameters. For detailed dynamics experiments an alternative primary suspension arrangement would be preferable although it is appreciated that this might well increase truck weight, and is not available within the existing design.

Initial stiffness measurements, carried out on the rubber suspension elements by the Battelle Memorial Institute, indicated stiffnesses between five and twenty times stiffer than required in some cases and these were successfully corrected by attention to elastomer formulation and mechanical arrangement. Final checking was carried out by Garret Airesearch with the completed trucks.

### Vehicle Dynamics

The LIM test vehicle was moved from the Airesearch headquarters to the Department of Transportation's High Speed Test Centre at Pueblo in May 1971 in preparation for testing up to 100 mph, the first target maximum speed. Initial difficulties involved misaligned running of the trucks with all wheel flanges in contact with one rail. This was shown to be an "inverse curving" difficulty in which unequal wheelbases on a truck are equivalent to track curvature, and was corrected by adjustment of wheelbase on one side of the trucks until all axles were running centrally within the flangeway clearance on straight track. Correction was made easy by the very high quality of the test track so that misaligned running effects were not masked by low speed response to track irregularities. Since the trucks had been machined to less than 1/64 in. difference in wheelbase the error is attributed to asymmetries of the rubber suspension elements. Running speed was successfully increased to 90 mph on the 19th May.

The second phase of speed upgrading took place between 26th and 28th June 1972 when the maximum speed was increased from 90 mph to 155 mph. Predictions of dynamic behavior were generally confirmed with no instability being encountered and the main car body responses being in the lower sway mode at approximately 1.2 Hz and the yaw mode at 1.5 Hz as expected (see Fig. 6). These modes clearly dominate the measured lateral suspension displacement spectra of which Fig. 11 is a typical result from this testing session.

The period of the third phase of speed upgrading was between 31st July and 3rd August 1972 when a maximum speed of 188 mph was achieved. Car body motion was substantially similar in character to the lower speed behavior with suspension displacement increasing approximately linearly with speed, Fig. 10, but an unexpected feature of the truck lateral acceleration measurements became evident. It is typified by the truck frame lateral acceleration spectrum shown in Fig. 12 where a dominant energy peak occurs at approximately 6.7 Hz at 168.7 mph. The expected truck eigenvalue at this speed has a frequency of 2.5 Hz and further theoretical studies were undertaken to attempt to explain the observed behavior. Analysis of the truck acceleration spectra at all test speeds showed a clear kinematic root with frequency a linear function of speed (Fig. 13) for which the only available explanation is an effective conicity of  $\lambda = 0.12$  (c.f.  $\lambda = 0.025$  as originally fitted). The vehicle eigenvalues for this

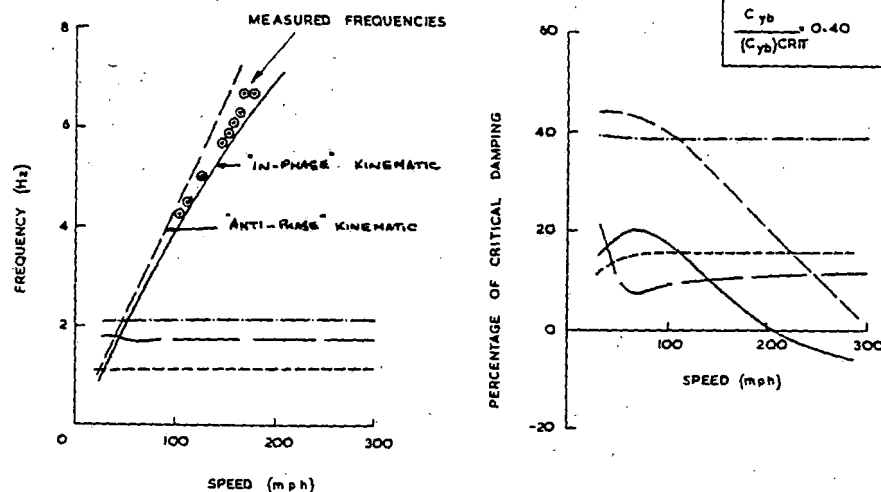


Fig. 13 Eigenvalues and measured frequencies

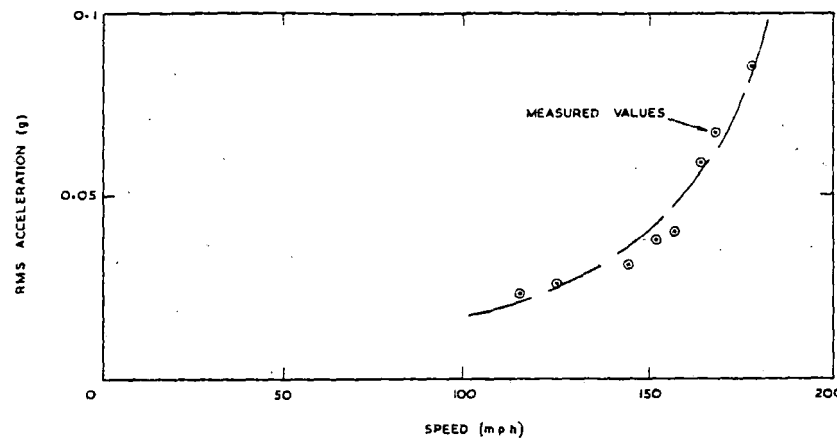


Fig. 14 RMS acceleration versus speed for area under kinematic peaks

case were calculated for comparison and also appear in Fig. 13. The eigenvalues for  $\lambda = 0.12$  predict a truck hunting speed of 200 mph and a plot of measured energy in the kinematic peaks of the truck acceleration spectra against speed confirms this (Fig. 14). Creep coefficients used were those according to Kalker [2].

It is the authors' view that the cause of the increased effective conicity is the narrow band of tread wear which was apparent on the wheels before reprofiling, the restricted nature of the wear resulting from the very high quality of track alignment and the good vehicle guidance. At Pueblo the contact position has so far rarely deviated from the wheel tread center-line since high speed running has been at or near the equilibrium speed for the curved section. The resulting small hollow, approximately 0.004 in. in depth, when matched to the rail cross-sectional profile, gives rise to the non-linear conicity characteristic with a value of  $\lambda = 0.12$  for the central portion only.

It is probable therefore that if 200 mph had been exceeded that a relatively small-amplitude limit cycle motion would have been evident, probably not of a catastrophic nature. It was decided, however, that, since the main purpose of the LIM vehicle was to check out the LIM itself up to 250 mph, the program did not at this stage allow sufficient time to investigate the phenomenon further. The wheels have therefore been reprofiled to a 1:40 cone for the phase four speed upgrading, and a careful check on tire wear will be maintained.

## Conclusions

The ability to operate a conventionally guided railway vehicle at speeds up to 250 mph under special conditions has been demonstrated by calculation. It must be stated, however, that a satisfactory compromise has not been found between the requirements of lateral stability and response on the one hand and curve negotiation under tread guidance conditions on the other. Substantial reliance will be placed upon flange guidance at the higher speeds with the curvature and track cant which exists. This is a special problem which need not apply so severely to very high speed railways in general. It has followed from the curvature restrictions imposed at Pueblo and demonstrates that the ruling curve radius for a 250 mph railway should be at least 5 miles.

Laying track to a standard which would give adequate passenger comfort at 250 mph has proved feasible and at the time of writing approximately 190 mph has been achieved satisfactorily.

An unexpected problem has been the relatively rapid change of shape of the tire profiles due to wear, this being concentrated

in the central portion of the tread because of the very high track quality.

## Acknowledgments

The authors are indebted to the British Railways Board for permission to publish this paper, and wish to acknowledge the encouragement and interest of the Chief of the Rail Systems Division of the United States Department of Transportation under whose Contract Number 3-0261 the work was carried out.

## References

- 1 Pearce, T. G., and May, B. J., "A Study of the Lateral Stability Curving and Dynamic Response of the Linear Induction Motor Test Vehicle," British Rail Research Department Technical Report under U. S. Dept., of Transportation Contract 3-0261 (PB 192718) Sept. 1969.
- 2 Kalker, J. J., "On the Rolling Contact of Two Elastic Bodies in the Presence of Dry Friction," 1967. Doctoral thesis presented to the University of Delft, 1917.
- 3 Boocock, D., "The Steady-State Motion of Railway Vehicles on Curved Track," *Journal of Mechanical Engineering Science*, Vol. 11, No. 6, 1969.
- 4 Newland, D. E., "Steering Characteristics of Bogies," *Railway Gazette*, 1968, Vol. 124, No. 19, p. 745.
- 5 Pfanz, P., "The Safety Problem in High Speed Traffic," *Glaser's Annalen*, Vol. 88, 1964, No. 5.
- 6 Amans, F., and Sauvage, R., "Railway Track Stability in Relation to Transverse Stresses Exerted by Rolling Stock. A Theoretical Study of Track Behaviour," *Monthly Bulletin of the I.R.C.A.*, Nov. 1969.

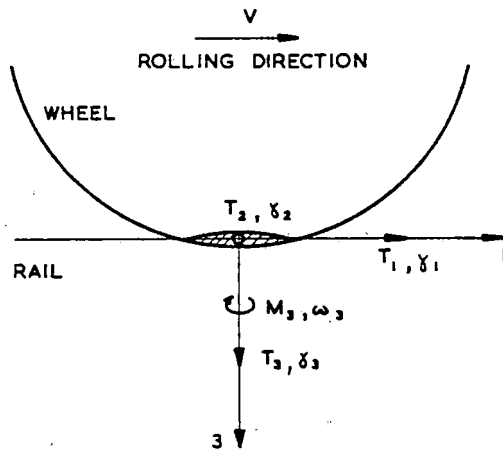
## APPENDIX A

### The Equation of Motion of a Coned Wheelset on Straight Track

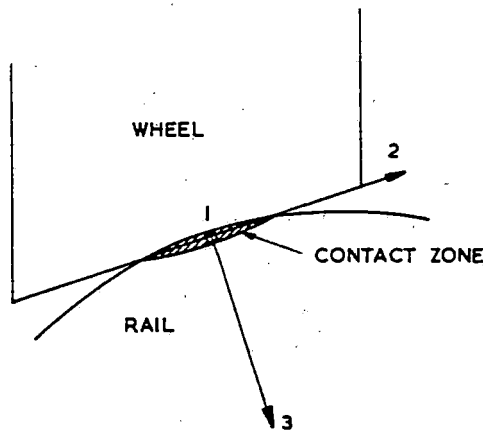
**Creep.** We define longitudinal, lateral, and spin creepages in terms of the rigid body velocities  $V'_1$ ,  $V'_2$ ,  $V'_3$  of the contact ellipse along the rail, and the rigid body velocities  $V_1$ ,  $V_2$ ,  $V_3$  of the contact ellipse around the wheel, referred to 0.1 2, 3 axes with their origin at the center of the contact zone (Fig. 15). We also define  $\Omega'_1$  and  $\Omega_1$  to be the angular velocities of spin of the rail and wheel about the 03 axis.

The longitudinal, lateral, and spin creepages are:

$$\left. \begin{aligned} \gamma_1 &= \frac{2(V'_1 - V_1)}{V'_1 + V_1} \\ \gamma_2 &= \frac{2(V'_2 - V_2)}{V'_1 + V_1} \\ \omega_3 &= \frac{2(\Omega'_1 - \Omega_1)}{V'_1 + V_1} \end{aligned} \right\} \quad (A.1)$$



a)



b)

Fig. 15 Contact zone axis system

The expression  $\frac{1}{2}(V'_1 + V_1)$  is the mean rolling velocity of the wheel along the rail. According to Kalker the forces and couple on the wheel will be:

$$\left. \begin{aligned} T_1 &= -f_{11}\gamma_1 \\ T_2 &= -f_{22}\gamma_2 - f_{23}\omega_3 \\ M_3 &= f_{32}\gamma_2 - f_{33}\omega_3 \end{aligned} \right\} \quad (A.2)$$

where  $f_{11} \dots f_{33}$  are the 'creep coefficients' defined by Kalker as follows:

$$\left. \begin{aligned} f_{11} \text{ (longitudinal)} &= E(ab)C_{11} \\ f_{22} \text{ (lateral)} &= E(ab)C_{22} \\ f_{23} \text{ (spin/lateral)} &= E(ab)^{3/2}C_{23} \\ f_{33} \text{ (spin)} &= E(ab)^2C_{33} \end{aligned} \right\} \quad (A.3)$$

$a$  and  $b$  are the semiaxes of the contact ellipse,  $E$  is Young's modulus, and  $C_{pq}$  are nondimensional coefficients which depend upon the ratio  $a/b$ , and Poisson's ratio.

### Creepages for the Railway Wheelset

Consider a wheelset with coned treads rolling freely along perfectly straight track with constant velocity  $V$  (Fig. 16). The cone angle,  $\lambda$ , is small, and the wheels have equal rolling radii,

$r_0$ , when the wheelset is centrally placed with respect to the lateral flange-rail clearance. The angular velocity of rotation of the wheelset about its axle is constant and equal to  $\dot{\phi} = -V/r_0$ .

The velocity components will be:

$$\left. \begin{aligned} V_{1r} &= \frac{Vr_r}{r_0} \\ V_{2r} &= -\dot{y} + V\psi \\ V_{3r} &= 0 \end{aligned} \right\} \quad (A.4)$$

for the right-hand wheel, and

$$\left. \begin{aligned} V'_{1r} &= V - l_0\dot{\psi} \\ V'_{2r} &= 0 \\ V'_{3r} &= 0 \end{aligned} \right\} \quad (A.5)$$

for the right-hand rail, with similar expressions for the left-hand wheel and rail.

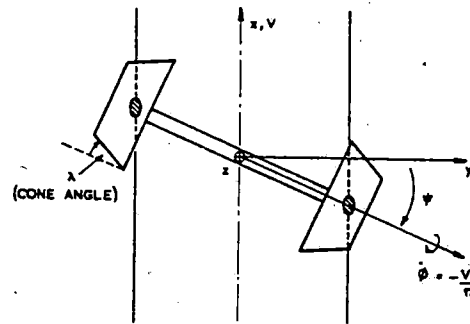
Angular velocities of spin for the right-hand wheel and rail are:

$$\left. \begin{aligned} \Omega_{3r} &= \dot{\phi}\lambda + \dot{\psi} \\ \Omega'_{3r} &= 0 \end{aligned} \right\} \quad (A.6)$$

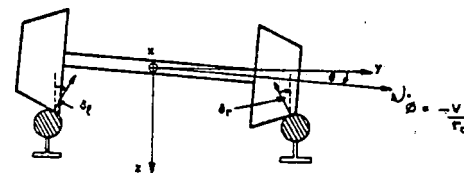
The expressions for the longitudinal, lateral, and spin creepages become, for the railway wheelset,

$$\left. \begin{aligned} \gamma_{1r} &= -\frac{l_0\dot{\psi}}{V} - \frac{\lambda y}{r_0} \\ \gamma_{2r} &= \frac{\dot{y}}{V} - \psi \\ \omega_{3r} &= -\frac{\lambda}{r_0} + \frac{\dot{\psi}}{V} \end{aligned} \right\} \quad (A.7)$$

with similar expressions for the creepages at the left-hand tread. Note that the effective conicity,  $\lambda$ , is defined as  $(r_r - r_l)/2y$ ,



a)



b)

Fig. 16 Wheelset axis system

which for the coned wheelset discussed here is exactly equal to the cone angle. For "profiled" wheels it is a function of the mutual geometry of wheel and rail and is a linearization of the change in rolling radius difference with lateral displacement,  $y$ .

### External Forces and Couple Acting on the Wheelset

Summing the creep forces and couples on the right and left-hand treads with respect to axes  $Ox, y, z$  through the wheelset center (Fig. 16), we have

$$\left. \begin{aligned} T_z &= 0 \\ T_y &= -2f_{22} \left\{ \frac{\dot{y}}{V} - \psi \right\} - 2f_{23} \frac{\dot{\psi}}{V} - \frac{W\lambda y}{l_0} \\ T_x &= -W \text{ (the axle load)} \\ M_x &= 2f_{22} \left\{ \frac{\dot{y}}{V} - \psi \right\} - 2f_{23} \frac{\dot{\psi}}{V} - \frac{2f_{11}l_0^2\dot{\psi}}{V} - \frac{2f_{11}l_0\lambda y}{r_0} \end{aligned} \right\} \quad (A.8)$$

For reasons of its extremely small size the yaw stiffness due to vehicle weight is omitted from the expression for  $M_x$ .

### Equations of Motion of a Free Wheelset

Adding the inertia terms to equations (A.8), the equations of motion of a free wheelset become, in matrix form with  $s$  the differential operator,

$$\left[ \begin{pmatrix} ms^2 + \frac{2f_{22}s}{V} + \frac{W\lambda}{l_0} & \left( \frac{2f_{22}s}{V} - 2f_{22} \right) \\ \left( -\frac{2f_{22}s}{V} + \frac{2f_{11}l_0\lambda}{r_0} \right) & \left( I_x s^2 + (2/V)(f_{11}l_0^2 + f_{33}) + 2f_{22} \right) \end{pmatrix} \right] \begin{bmatrix} y \\ \psi \end{bmatrix} = 0 \quad (A.9)$$

### Equations of Motion of a Two-Axle Vehicle

These can be written after calculating the suspension displacements and velocities and hence the forces acting between wheelsets and body. They are of the form

$$\left[ As^2 + \left\{ \frac{B}{V} + D \right\} s + C \right] (q) = 0 \quad (A.10)$$

having a velocity dependent damping matrix and an asymmetric stiffness matrix.

## APPENDIX B

### Forcing Functions Due to Curvature

**Equilibrium Rolling Line.** On curved track it is usual to define wheelset displacements,  $y$ , with respect to the "equilibrium rolling line" and wheelset yaw,  $\psi$ , with respect to the radial line of the curve. The equilibrium rolling line may be defined as the locus at rail level of the centre of the wheelset when its two rolling circles (left and right wheels) form cross-sections of a cone whose apex lies at the centre of curvature of the track. The difference in rolling radii of left and right wheels is then approximately given by:

$$r_r - r_l = -2r_0 l_0 / R_0 \quad (B.1)$$

Since the effective conicity,  $\lambda$ , of a wheelset is given by

$$\lambda = 1/2(r_r - r_l)/y \quad (B.2)$$

then the displacement of the equilibrium rolling line from the

geometrical center-line is given by

$$y_s = -r_0 l_0 / \lambda R_0 \quad (B.3)$$

### Quasi-Static Forces Acting on a Vehicle on Curved Track

The principal forces and couples acting are:

- (i) centrifugal forces.
- (ii) gravitational forces due to track cant.
- (iii) suspension forces due to track curvature.
- (iv) longitudinal and lateral creep forces at the treads.

Forces (i) and (ii) are balanced as far as possible, the net imbalance being termed the "cant deficiency." For small angles of cant this becomes:

$$\theta_d = (V^2/gR_0) - \theta, \quad (B.4)$$

Thus, for example, the unbalanced centrifugal force acting on a wheelset is  $(-mg\theta_d)$ .

The primary suspension exerts a lateral force and couple on the leading wheelset of magnitude

$$F_y = k_y(y_l - y_{b1} - a\psi_{b1}) \quad (B.5)$$

$$G_\psi = k_\psi \left( \frac{a}{R_0} + \psi_l - \psi_{b1} \right) \quad (B.6)$$

where  $2a$  is the bogie wheelbase. Similar expressions may be obtained for other wheelsets and for the secondary suspension forces and torques. Note that the only suspension force term due to curvature is that due to  $\frac{a}{R_0}$  in the yaw torque equation.

Expressions for the quasi-static creepages on curved track will differ from the tangent track situation and are, for the right hand wheel and rail in the terminology of Appendix A, and neglecting spin creep for simplicity:

$$\left. \begin{aligned} V_{1r} &= V(1 + \lambda(y + y_s)/r_0) + \dot{\phi}r_0 \\ V_{2r} &= V\psi \end{aligned} \right\} \quad (B.7)$$

$$\left. \begin{aligned} V'_{1r} &= V(1 - l_0/R_0) \\ V'_{2r} &= 0 \end{aligned} \right\} \quad (B.8)$$

The terms due to curvature are  $\dot{\phi}r_0$  and  $y_s$  in (B.7) where  $\dot{\phi}$  is the deviation of the wheelset angular rotation about its axle from the nominal  $\frac{V}{r_0}$  due to weight transfer under conditions of nonzero cant deficiency, and  $l_0/R_0$  in (B.8),  $\dot{\phi}$  is given by the following expression, which is derived from the assumption of torque balance in the wheelset rotation equation:

$$\dot{\phi} = 2q\theta_d V \lambda y / 3r_s^2 \quad (B.9)$$

Assuming linear force/creep relationships as in Appendix A, the total quasistatic lateral creep force and yaw torque on a wheelset in curved track are:

$$\left. \begin{aligned} T_y &= 2f_{22}\psi \\ M_x &= -2f_{11}^* \lambda l_0 y / r_0 \end{aligned} \right\} \quad (B.10)$$

Comparison with equations A.8 of Appendix A shows that both lateral force and yaw torque are substantially unchanged providing that wheelset displacement,  $y$ , is defined with respect to the equilibrium rolling line, and also that the longitudinal creep coefficient is modified to take account of weight transfer such that:

$$f_{11}^* = \left( 1 - \frac{4}{9} q^2 \theta_d^2 \right) f_{11} \quad (B.11)$$



**R. H. Fries**

Lecturer,  
Department of Mechanical Engineering,  
Arizona State University,  
Tempe, Ariz.

**N. K. Cooperrider**

Professor,  
Department of Mechanical Engineering,  
Arizona State University,  
Tempe, Ariz.  
Mem. ASME

**E. H. Law**

Professor,  
Department of Mechanical Engineering,  
Clemson University,  
Clemson, S.C.  
Mem. ASME

## Experimental Investigation of Freight Car Lateral Dynamics

*Field tests and accompanying data analysis to characterize the stable and hunting behavior of freight cars are discussed. These tests confirmed the fundamentally nonlinear nature of the conventional freight car. The hunting performance of an open hopper car is described by speed ranges in which intermittent hunting occurs. At speeds above the intermittent hunting speed ranges, hunting always occurs, and at speeds below these ranges, hunting does not occur. Results of evaluating the stability of the freight car in terms of the natural frequency and damping ratio of the least-damped vibration mode are presented. Anomalies in these results indicate that the damping ratio may not be an adequate stability measure for this nonlinear system. Root-mean-square values of significant vehicle motions are presented for the entire range of vehicle test speeds.*

### Introduction

An extensive series of tests to characterize the lateral dynamic behavior of rail freight cars was conducted by the Association of American Railroads (AAR) and the Union Pacific Railroad (UP). One of the objectives of this experimental work and subsequent data analysis was to provide data for comparison with results of theoretical analyses. These data were supplied to the authors' universities for use in their "Freight Car Dynamics" project.

This paper deals only with those portions of the field test devoted to vehicle lateral dynamics on tangent track. A companion paper is planned that will examine the comparisons between the test results reported here and the theoretical analyses. The theoretical developments that will form the basis for these comparisons are described elsewhere [1-4]. It is our hope that this paper, together with the field test report [5], will provide sufficient detail that the test data and results may prove useful to others.

The specific objective of this test program was to develop sufficient data to permit theoretical and experimental comparisons of the transient and random response of a rail freight car on tangent track. Thus, the tests involved several vehicle configurations run at speeds extending into the range where vehicle hunting occurs. Careful characterization of the vehicle and roadbed was required as well as extensive instrumentation of the test vehicle to measure component motions.

In the following sections, the test preparations and conduct, the results obtained from the test data, and the overall conclusions to be drawn from the work are discussed.

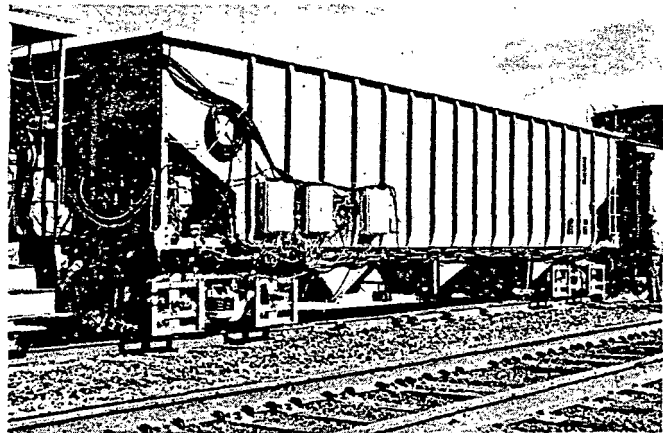


Fig. 1 L & N hopper test car

### Test Conduct

This experimental investigation involved laboratory testing to characterize the vehicle, on-site measurements of vehicle, rail and roadbed characteristics, vehicle instrumentation, test conduct, data reduction, and data analysis. Each of these activities is briefly described below.

**Vehicle Characterization.** The test vehicle was the 80-ton open hopper car on loan from the Louisville and Nashville Railroad shown in Fig. 1. The running gear consisted of a pair of ASF 70-ton A-3 Ride Control trucks.

The vehicle component inertia properties were compiled from a variety of sources. The wheelset mass and inertia properties were determined by laboratory tests at the Association of American Railroads (AAR) Research Center [6]. The sideframe and bolster inertia properties were determined as part of the truck characterization tests con-

Contributed by the Dynamic Systems and Control Division for publication in the JOURNAL OF DYNAMIC SYSTEMS, MEASUREMENT, AND CONTROL. Manuscript received by the Dynamic Systems and Control Division, May 29, 1980.

**Table 1 Test vehicle inertia properties. Conversion factors: 1 slug = 14.6 kg, 1 slug ft<sup>2</sup> = 1.36 kg m<sup>2</sup>**

	Wheelset	Sideframe	Bolster	Carbody
Mass (slugs)	76.6	24.0	36.1	1102 (light) 6282 (loaded)
Principal centroidal moment of inertia about lateral axis (slug ft <sup>2</sup> )	53.1	83.1	—	.227 × 10 <sup>6</sup> (light) 1.050 × 10 <sup>6</sup> (loaded)
Principal centroidal moment of inertia about vertical axis (slug ft <sup>2</sup> )	448.5	77.6	178.6	.234 × 10 <sup>4</sup> (light) 1.070 × 10 <sup>6</sup> (loaded)
Principal centroidal moment of inertia about longitudinal axis (slug ft <sup>2</sup> )	448.5	—	178.6	13,000 (light) 87,700 (loaded)

**Table 2 Suspension parameters. Conversion factors: 1 lb = 4.45N, 1 lb/ft = 14.6N/m**

TRANSLATIONAL suspension	Preload on centerplate, lb	K <sub>1</sub> , LB/FT	K <sub>2</sub> , LB/FT	K <sub>F</sub> , LB/FT	f, lb	δ, RAD
VERTICAL (two elements per truck)		2.5715 × 10 <sup>5</sup>		6 × 10 <sup>6</sup>	3500	
	*17742	6.1932 × 10 <sup>4</sup>		1.968 × 10 <sup>6</sup>	3669	
	20000	6.42 × 10 <sup>4</sup>		1.96 × 10 <sup>6</sup>	3650	
LATERAL (two elements per truck)	50000	9.24 × 10 <sup>4</sup>		2.1 × 10 <sup>6</sup>	3400	
	100000	1.662 × 10 <sup>5</sup>		2.52 × 10 <sup>6</sup>	3000	
	**101140	1.6784 × 10 <sup>5</sup>		2.6 × 10 <sup>4</sup>	2960	
ROTATIONAL suspension	Preload on centerplate, lb	K <sub>1</sub> , FT-LB/RAD	K <sub>2</sub> , FT-LB/RAD	K <sub>F</sub> , FT-LB/RAD	f, FT-LB	δ, RAD
	*17742	3.729 × 10 <sup>6</sup>	4.238 × 10 <sup>6</sup>	2.509 × 10 <sup>7</sup>	4687	2.18 × 10 <sup>-3</sup>
	20000	3.691 × 10 <sup>6</sup>	4.291 × 10 <sup>6</sup>	2.5 × 10 <sup>7</sup>	5000	
WARP (One element per truck)	50000	3.191 × 10 <sup>6</sup>	5.0 × 10 <sup>6</sup>	2.375 × 10 <sup>7</sup>	9166	
	100000	2.858 × 10 <sup>6</sup>	5.833 × 10 <sup>6</sup>	2.141 × 10 <sup>7</sup>	11666	
	**101140	2.48 × 10 <sup>6</sup>	5.84 × 10 <sup>6</sup>	2.10 × 10 <sup>7</sup>	11650	
YAW (one element per truck)	*17742				606	
	**101140				3450	

\*unloaded vehicle

\*\*loaded vehicle

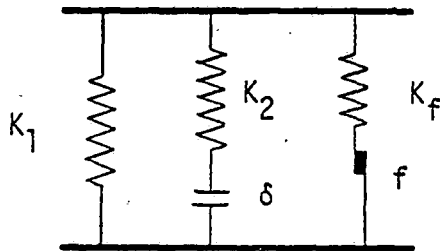


**Fig. 2 Generic suspension element**

ducted by American Steel Foundries (ASF) [7]. The carbody inertia properties were calculated by the AAR Research Center [6]. These inertia properties are summarized in Table 1.

The suspension characteristics of the test car were evaluated in tests conducted by the ASF [7, 8] and Martin Marietta [9]. The experimental results obtained for the four motions of the truck, namely lateral, vertical, warp, and yaw, led Martin Marietta to propose a generic suspension element as shown in Fig. 2. The characteristics of each suspension motion can be represented by a generic element of this type.

The generic element comprises a parallel combination of (a) a linear spring ( $K_1$ ); (b) a series combination of a linear spring ( $K_2$ ) and a deadband of clearance ( $\delta$ ); and, (c) a series

combination of a linear spring ( $K_f$ ) and a Coulomb friction element ( $f$ ). The characteristics of this element can represent very general force-deflection or torque-angular deflection test data.

The test data obtained by Martin Marietta together with the results obtained by ASF for the yaw breakout moment at the centerplate are presented in terms of the characteristics of the generic suspension element in Table 2. The tests were conducted for several values of preload on the centerplate corresponding to a range typical of light to loaded vehicles.

The parameters of the generic element vary with centerplate preload for the lateral, yaw, and warp motions while those for the vertical motion are unaffected by centerplate preload. The values for the nominally loaded and unloaded (or light) configurations are indicated in Table 2.

Even though considerable diligence and effort went into the collection of this data, it should still be used with some caution. Because only one of the two trucks was tested at Martin Marietta, we do not know the truck-to-truck variability. The other truck of the test vehicle may have had different characteristics. The centerplate friction data values are also somewhat uncertain. The only available values were those from the ASF tests of an entirely different bolster. Friction levels such as these are also subject to change with environmental conditions and wear.

The hopper car was tested in eight different configurations

**Table 3 Test configurations. Conversion factors: 1 lb = 4.45N, 1 T(English) = 0.907 T(metric)**

Configuration	Wheels	Load	Side-Bearings	Truck Stiffener	Centerplate
1	CN Profile A	0	0	None	Dry
2	CN Profile A	0	0	None	Lubricated
3	CN Profile A	0	2000 lb	None	Lubricated
4	CN Profile A	0	6000 lb	None	Lubricated
5	CN Profile A	0	0	ON	Lubricated
6	New	0	0	None	Lubricated
7	New	83.4 T	0	None	Lubricated
8	CN Profile A	83.4 T	0	None	Lubricated

to provide a variety of test conditions. The different configurations, shown in Table 3, were achieved by the use of different wheelsets, a truck stiffener, constant-contact sidebearings, unlubricated or lubricated centerplate, and the presence of a load in the vehicle.

Two wheel profiles were chosen for the test vehicle. One of these, the AAR Standard 1/20 tapered wheel profile, was selected to provide wheel-rail characteristics that would be well defined and insensitive to rail head characteristics. The second wheel profile, the CN Profile A, was developed by the Canadian National Railroad to approximate the worn wheel profiles found on that railroad.

In order to evaluate the effect of warp stiffness, the resistance of the frame formed by the sideframes and wheelsets to "parallelogramming" motion, a truck stiffening device was employed in one test series. This device consisted of structural steel members bolted transversely between ends of the side frames. Brackets welded to the side frames provided the attachment means for the cross members. The effect of the truck stiffener was to transform the truck to a very rigid box frame configuration.

The influence of variations in rotational resistance in yaw between the truck and car body bolsters was investigated by replacing the conventional side bearings with air bag units. These side bearings allowed adjustment of the bearing contact load. The friction characteristics of the side bearing devices were determined through tests conducted by the AAR [10]. Friction coefficients in the range of 0.33 to 0.42 were found for the side bearing surfaces under conditions approximating those in service. Three side bearing conditions were tested with the side bearing loads at 0, 2000 and 6000 lb per bag. Because the air bags unloaded the centerplate, the total frictional yaw resistance must account for the reduced centerplate frictional torque.

**Roadbed Characterization.** Tangent-track test runs were conducted on a section of the UP mainline near Barstow, California. Continuous welded-rail is in place in the test zone.

The roadbed characteristics were first measured in August, 1975, using the UP's Plasser-American EM-80 track evaluation car. This data was analyzed to determine the roadbed characteristics. Of the readily measurable roadbed characteristics, alignment and crosslevel are the most important forcing functions for the rail vehicle lateral dynamics. Power spectral densities (PSDs) of these parameters are shown in Figs. 3 and 4. Histograms of these parameters show essentially Gaussian amplitude distributions.

The two large peaks in the alignment PSD are introduced as a consequence of compensating for measurements made by the chordal offset method. These spurious peaks were excluded when the alignment PSD was integrated to obtain the standard deviation value shown in the figure. The peaks are not present in PSDs of the raw or uncompensated alignment data. Details of the compensation process can be found in [11].

The coherence between centerline alignment and crosslevel was computed and found to be fairly low, as shown in Fig. 5. This generally low value of coherence would justify an

assumption of independence between alignment and crosslevel. Peaks showing near 1 cyc/ft in Figs. 3, 4, and 5 are believed to be powerline contamination.

Rail head profiles were measured at many stations along the tangent track test zone. This measurement was done using a special profilometer loaned to us by the German Federal Railroads (DB).

**Instrumentation.** Displacement measurements provided the most useful data for investigating the lateral dynamic behavior. This instrumentation included 6 (sometimes 8) transducers on each truck to measure lateral and angular displacements of the wheelsets relative to the rails. One of these displacement transducers is shown in Fig. 6. The hardened steel shoe rides along the inside of the rail.

Each truck of the test vehicle was equipped with a hydraulic system that exerted a moment between the truck and the carbody with a pair of hydraulic cylinders on each truck. This system was used to provide an initial condition to the vehicle consisting of lateral and angular displacements of the trucks away from their equilibrium positions on the track. Pressure in one hydraulic cylinder was measured and recorded.

All data was recorded on board the AAR-100 Research Car, part of the test consist. The data was sampled at 100 Hz and recorded digitally on magnetic tape. In addition, selected channels were recorded on strip charts so they could be observed during or shortly after a particular test.

**Test Sequence.** The lateral vehicle dynamics investigation utilized results from the following two types of tests:

1. Random response tests were conducted at several speeds on tangent mainline track. No activation from the on-board hydraulic forcing system was used. Therefore, the primary disturbances acting on the test vehicle were those from the track irregularities.
2. Forced response tests were also conducted on tangent mainline, but for this series the on-board hydraulic forcer system was used to provide initial angular and lateral displacements of the test vehicle away from the equilibrium position. Upon rapid release of the imposed torques on both trucks, the response of the vehicle to the initial condition as well as track irregularities was recorded.

## Test Results

Test data was furnished by the AAR in the form of digital magnetic tapes. The data was analyzed in a number of ways to characterize both the hunting and stable response of the test vehicle on tangent track.

**Data Analysis Process.** The primary purpose of conducting the field tests described here was to provide real vehicle response data for comparison with predicted or calculated response data from several freight car mathematical models. Consequently, the first step in the data analysis process was to combine the signals recorded from individual transducers in a manner that constructs the variables of a 19-degree-of-freedom model of the test vehicle [5]. For example, the Truck A lateral displacement variable was constructed by summing

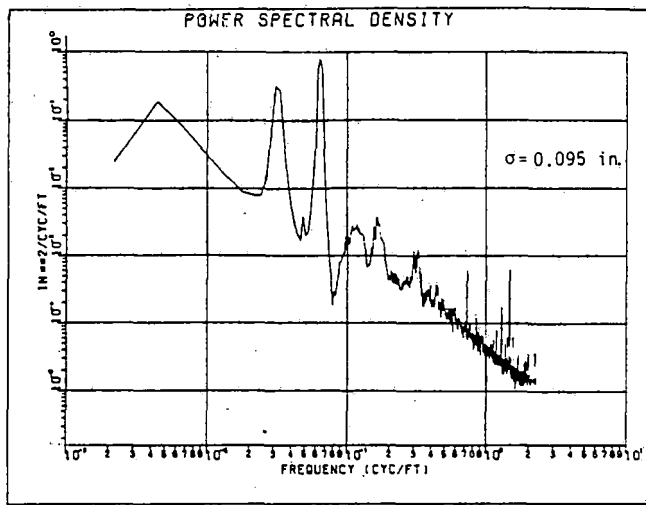


Fig. 3 PSD of centerline alignment. Conversion factors: 1 cyc/ft = 3.22 cyc/m, 1 in<sup>2</sup>/cyc/ft = 200 mm<sup>2</sup>/cyc/m, 1 in = 25.4 mm

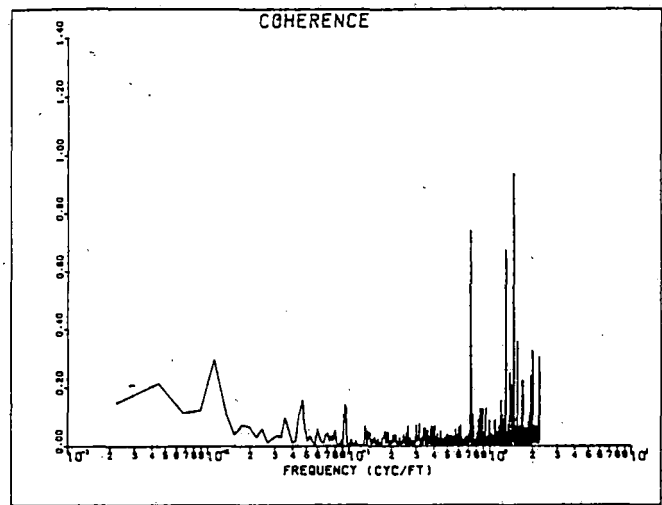


Fig. 5 Coherence between alignment and crosslevel. Conversion factor: 1 cyc/ft = 3.22 cyc/m

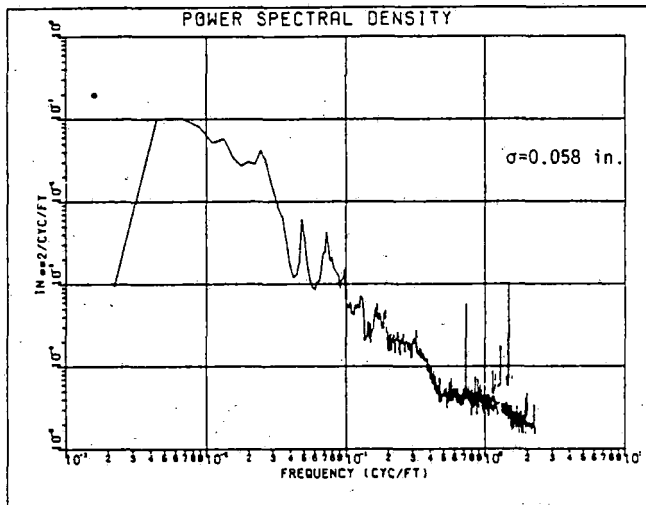


Fig. 4 PSD of crosslevel. Conversion factors: 1 cyc/ft = 3.22 cyc/m, 1 in<sup>2</sup>/cyc/ft = 200 mm<sup>2</sup>/cyc/m, 1 in = 25.4 mm

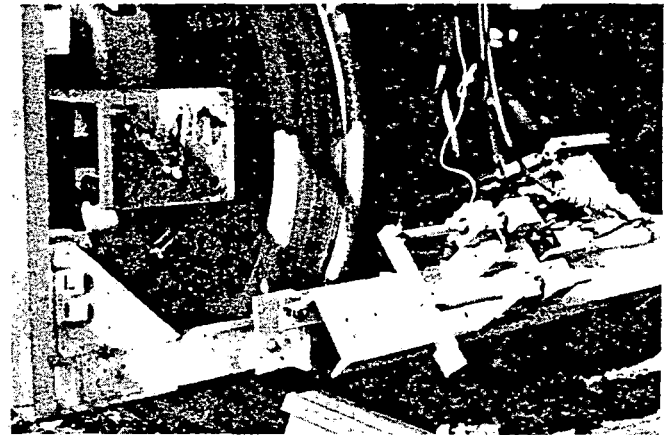


Fig. 6 Typical wheel-rail lateral displacement transducer

16 individual signals with appropriate weights. This summation increased the signal to noise ratio by averaging the noise from several transducers.

Time histories of all the signals to be analyzed were plotted and studied. Portions of test data from each configuration and speed of interest were selected for analysis. For most of the analysis, truck lateral displacements proved to be the most useful signals, although other variables were used as well.

The frequency and damping characteristics reported here for the unforced runs were obtained using the Random-Decrement technique [5, 12]. This process yields estimates of the natural frequency and damping ratio of the least-damped mode of the system. See Fig. 7 for a typical Random-Decrement signature.

Random-Decrement is a time-domain analysis procedure. For comparison purposes, damping ratios were also computed using a frequency-domain method based on determining the bandwidth of the resonant peak on a PSD plot. Similar results were obtained using both methods.

The final step in the damping ratio estimation process refines the initial damping ratio estimates. The least-damped mode for the hopper car is usually the kinematic mode. This mode has the characteristic that the natural frequency is very nearly proportional to vehicle speed. Thus when the speed varies over the duration of a data run, the dynamics of the process also vary. This variation results in a smearing of the

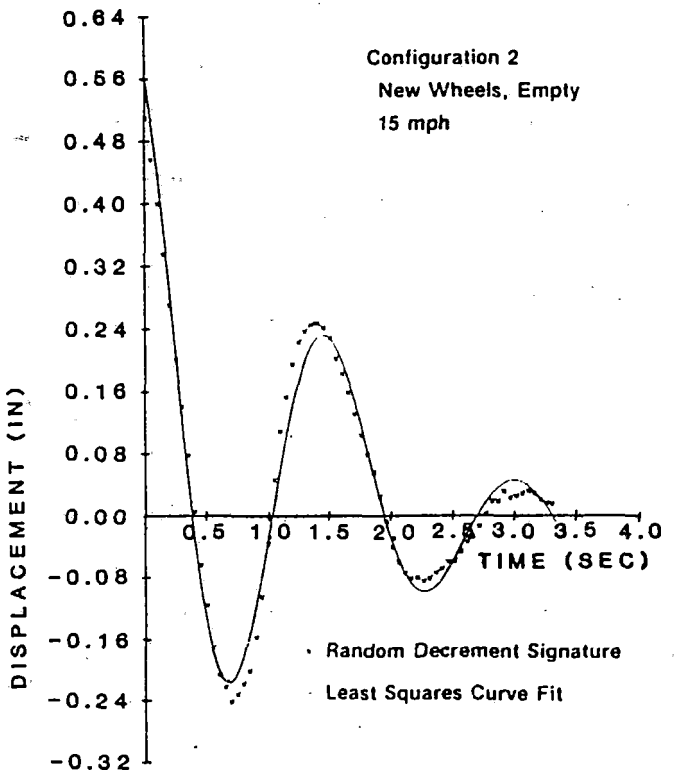


Fig. 7 Random-Decrement signature. Conversion factors: 1 in = 25.4 mm, 1 mph = 1.61 km/h

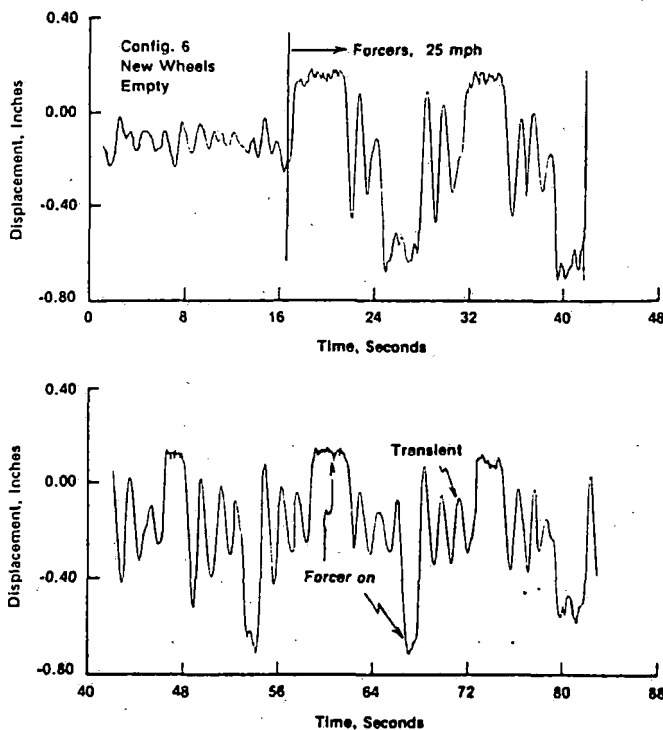


Fig. 8 Truck lateral displacement using hydraulic forcers. Conversion factor: 1 in = 25.4 mm

data in the frequency domain, and a broadening of the resonant peak associated with the least-damped mode. The broadening of the resonant peak represents an apparent increase in the damping ratio of the process. The net result is that damping ratio estimates are too high.

A computer program has been developed that refines the damping ratio estimates by accounting for the vehicle speed variations during a particular test run. The train speed channel is used in this program to determine the actual damping ratio that would have resulted in the observed damping ratio, given the known train speed variations. The assumptions are made that the vehicle dynamics are second order and lightly damped, and that natural frequency is proportional to train speed. This adjustment is negligible for large damping ratios, but can be substantial for damping ratios of the order of 0.1 and smaller.

Test vehicle response following application of the truck forcers was studied using the logarithmic decrement technique. The truck forcers apply a moment between the car body and the truck bolster, forcing the truck away from its equilibrium position near the center of the track. The vehicle dynamic behavior can be studied from the initial condition response that ensues when the forcers are released. Figure 8 shows a typical time history of the Truck A lateral displacement during a forced run. Time runs continuously between the two time segments shown. Damping ratio information is contained in the shape of the decay envelope, which is defined by the peaks in the response curve. Both positive and negative pairs of successive peaks were used to compute a large number of damping ratios for each speed. The damping ratios were then averaged to obtain a single damping ratio for each speed.

All three methods for computing modal damping ratios and frequencies can be applied to nonlinear as well as linear systems. The results, however, have questionable meaning for nonlinear systems.

Random response of the test vehicle was also analyzed using a spectral analysis computer program developed specifically for this test program [11]. Histograms, autocorrelation functions, PSDs and RMS values were computed for many variables.

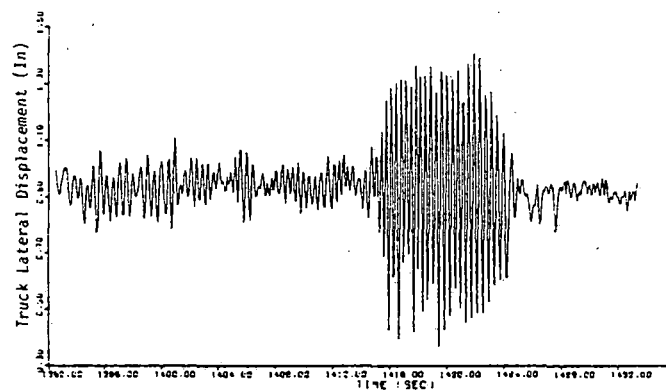


Fig. 9 Intermittent hunting. Conversion factor: 1 in = 25.4 mm

**Vehicle Hunting Characteristics.** An important result of the field tests is a characterization of the hunting performance of the test vehicle in its eight configurations. Discussions of hunting behavior based on linear system analysis are often conducted in terms of a unique hunting speed for the transition from stable to unstable running. These tests demonstrated that the hunting behavior of a freight vehicle can not be characterized by a single transition speed. There is actually a transition speed range in which intermittent hunting occurs. Below this range hunting never occurs, and above it sustained hunting always occurs. A typical burst of intermittent hunting, this one of about 12-s duration, is shown in Fig. 9. This data was recorded on a constant 48-mph test run of Configuration 2. This behavior is characteristic of a nonlinear system.

Figure 10 summarizes the hunting characteristics of the eight configurations during the random response test. The ordinate on these bar-type charts is percent of time the vehicle was hunting at a given speed. The data points used in constructing the graphs are shown. In every case a point is shown for zero-percent hunting. This point represents the speed at and below which no hunting was observed to occur. A point is also shown, when available, for 100-percent hunting, which is the speed at and above which sustained hunting was always observed to occur.

Most data points represent tape-recorded data. However, some data points come from written observations of the test crew. This is the case with the 100-percent hunting points for C3 Truck B, C5 Truck B and both trucks of C8. The 50-percent hunting on C6 Truck B at 82 mph is also from test crew observations, and was called "moderate hunting" and "marginal hunting" in the test log. It was somewhat arbitrarily set at 50-percent hunting.

The lines connecting the data points represent an estimate of the behavior at speeds between and beyond the test speeds. Since we have no information at intermediate speeds, the actual behavior may differ in these regions.

Some observations on each of the configurations are given below:

**C1.** No intermittent hunting was recorded for C1, the empty vehicle with CN wheels and unlubricated centerplates. The transition between no hunting and sustained hunting could be considerably more abrupt than shown.

**C2.** The C2 vehicle was the C1 vehicle with centerplates lubricated. The obvious effects were to lower the speed for hunting initiation and also to spread out the transition-speed range. The effect on the speed at which sustained hunting always occurred is not known, because no test runs were made for C2 at speeds exhibiting sustained hunting. C2 Truck B data show an unusual trend in which hunting occurred a lower

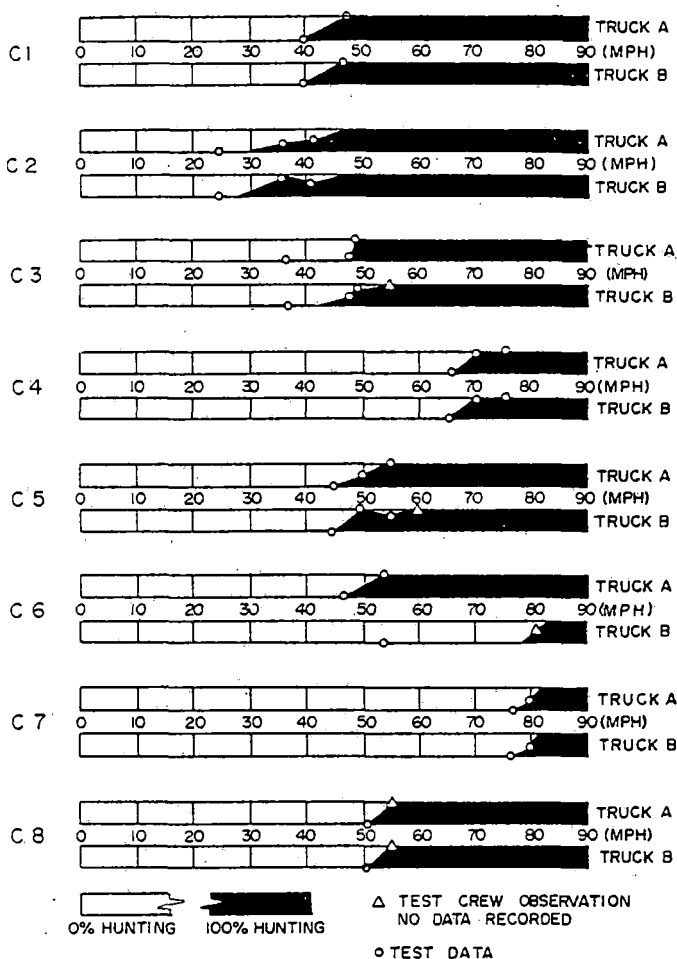


Fig. 10 Test vehicle hunting characteristics. Conversion factor: 1 mph = 1.61 km/h

percentage of time at 41.5 mph than it did at 35.7 mph. This also occurred on C5 Truck B test data.

C3. Addition of the constant-pressure sidebearing device to the C2 vehicle made the C3 vehicle. C3 exhibited an upward shift in the hunting-speed transition range.

C4. With a higher pressure in the side-bearing device in C4, the hunting speed transition range became even higher.

C5. The C5 vehicle was the C2 vehicle with addition of a warp stiffener. The hunting speed transition region was narrower and occurred at a higher speed than for C2.

C6. The C6 vehicle was the basic empty hopper car with lubricated centerplates and AAR straight-taper wheels. The Truck B wheels were quite new, exhibiting evidence of very little run-in, while the Truck A wheels had accumulated considerably more miles. It should be noted that the zero-percent hunting speed is shown as 46-mph for Truck A since no hunting occurred during the 46-mph unforced test run. However, on the 45-mph test run using truck forcers, sustained hunting occurred between application of truck forcers, and it ceased when the forcers were applied.

C7. The loaded C6 vehicle became C7. Hunting speeds for both trucks were about the same, the highest found during the test series.

C8. The C8 vehicle was the loaded hopper car with the CN wheels. Because no intermittent hunting was recorded, the nature of the transition is not known. The C8 vehicle had a higher hunting speed range than C2, the same vehicle empty.

**RMS Response.** The root mean square (RMS) value of any variable gives a good overall measure of the amplitude of motion occurring during a particular test run.

Figure 11 shows the RMS values of the model variables as a

function of speed for each of the configurations. For Configuration 6, we computed RMS values of all the model variables except one, carbody lateral bending, which was not available. In addition we computed the RMS values of two accelerations. For the other seven configurations we computed RMS values of the truck lateral displacements only.

Truck lateral displacement (measured relative to the actual track centerline) is an excellent indicator of hunting. In every case analyzed, when the RMS value of the truck relative lateral displacement exceeded 0.1 in., either sustained or intermittent hunting occurred. Likewise, when the RMS value was less than 0.1 in., no hunting occurred. A good hunting sensor for this field test series would have been a detector of truck relative lateral displacements exceeding 0.1 in. RMS.

The highest RMS value computed for relative truck lateral, 0.37 in., occurred on the Configuration 1 test at 36.7 mph for both Truck A and Truck B. Assuming a sinusoidal response, this value corresponds to a peak-to-peak amplitude of about 1 in., indicating continual flange contact. Because the actual response contains higher harmonics, the actual peak displacement is somewhat smaller.

**Frequency and Damping Characteristics.** Figures 12 through 15 show the estimates of natural frequency and damping ratio for Configurations 1, 2, 4, and 6. These estimates came from the Random-Decrement analysis of unforced tangent-track test runs.

In Fig. 12 the Configuration 1 damping-ratio plot shows a very uncharacteristic shape in that it has low damping ratios at the slowest speeds. A second estimate of the lowest speed (15 mph) damping ratios for both Trucks A and B from a different time segment yielded adjusted values of zero damping indicating unstable or nearly unstable behavior. These latter data points are not shown in the figure. Two separate portions of the 15-mph Configuration 1 test run were chosen for analysis because the time response appeared somewhat different in nature between the two. The portions yielding the zero damping-ratio estimates actually contained portions of low-amplitude oscillatory behavior. Observations of track data plots revealed no differences in track between the two test sections, so the reasons for the different behavior are not known.

In Fig. 13 the Configuration 2 damping-ratio estimates are plotted without the 35-mph Truck B data point because Truck B was hunting during this test run. For this case the frequency was higher, and the damping ratio lower on Truck B than on Truck A, which was not hunting. The high frequency, low damping behavior is characteristic of most of the hunting conditions we analyzed from the field tests.

The Configuration 4 data shown in Fig. 14 shows unusual behavior at both the 70- and 75-mph speeds. Two observations need to be made about these test speeds. First, because hunting occurred at both of these speeds, it is not unexpected that discontinuities would occur in the frequency and damping-ratio curves. However, on other configurations hunting was accompanied by increases in natural frequency above expected values, not decreases, as are shown here. The second observation is that the 70- and 75-mph runs were made on a different day than the lower speed runs introducing the possibility that conditions may have changed over time. One possibility is that the pressure in the air bags may have changed due to temperature changes, leakage or some other cause. The friction characteristics of the truck may also have changed. The actual reasons for the anomalous behavior at these two speeds are not known, however.

Figure 15 shows the Configuration 6 frequency and damping-ratio estimates. Most notable here are the very high damping ratios of Truck B. This is consistent with observations that Truck B hunting began at about 80 mph, substantially above the speed shown here. The 35-mph data

point is not plotted for Truck B because a very poor Random-Decrement signature was obtained for this speed. The time history of Truck B lateral displacement at this speed showed the presence of fairly high amplitude, short-duration (about one cycle) transients. These transients are believed to be spurious. They interfered with the Random-Decrement signature formation process sufficiently to render the frequency and damping-ratio estimates suspect for the 35-mph test run.

We also attempted analysis of the damping ratio and natural frequency for one of the loaded vehicle (Configuration 8) tests, but we had little success in obtaining a good Random-Decrement signature for these cases. This difficulty probably indicates the presence of two or more closely spaced dynamic modes for the loaded test vehicle.

The hydraulic forcer system described earlier provided a set of initial displacement and rotation conditions for the test vehicle. Upon release of the pressure in the hydraulic forcers, the test vehicle responded to the imposed initial conditions. The Configuration 6 Truck A forcer response was analyzed using the logarithmic decrement technique.

Figure 8 shows a typical response of the Truck A lateral displacement during a forced test run at 25 mph. Both positive and negative pairs of successive peaks were used to compute a large number of damping ratios for each test speed. Damping ratios were averaged to give the results shown in Fig. 16. The bands shown in the figure delineate the plus and minus one standard deviation levels. Figure 16 also shows the natural frequencies found during the forcer runs.

The mean damping ratios shown in Fig. 16 are about an

order of magnitude less than those found for Configuration 6 during the unforced runs. Two reasons may account for this difference.

First, the logarithmic-decrement technique is derived

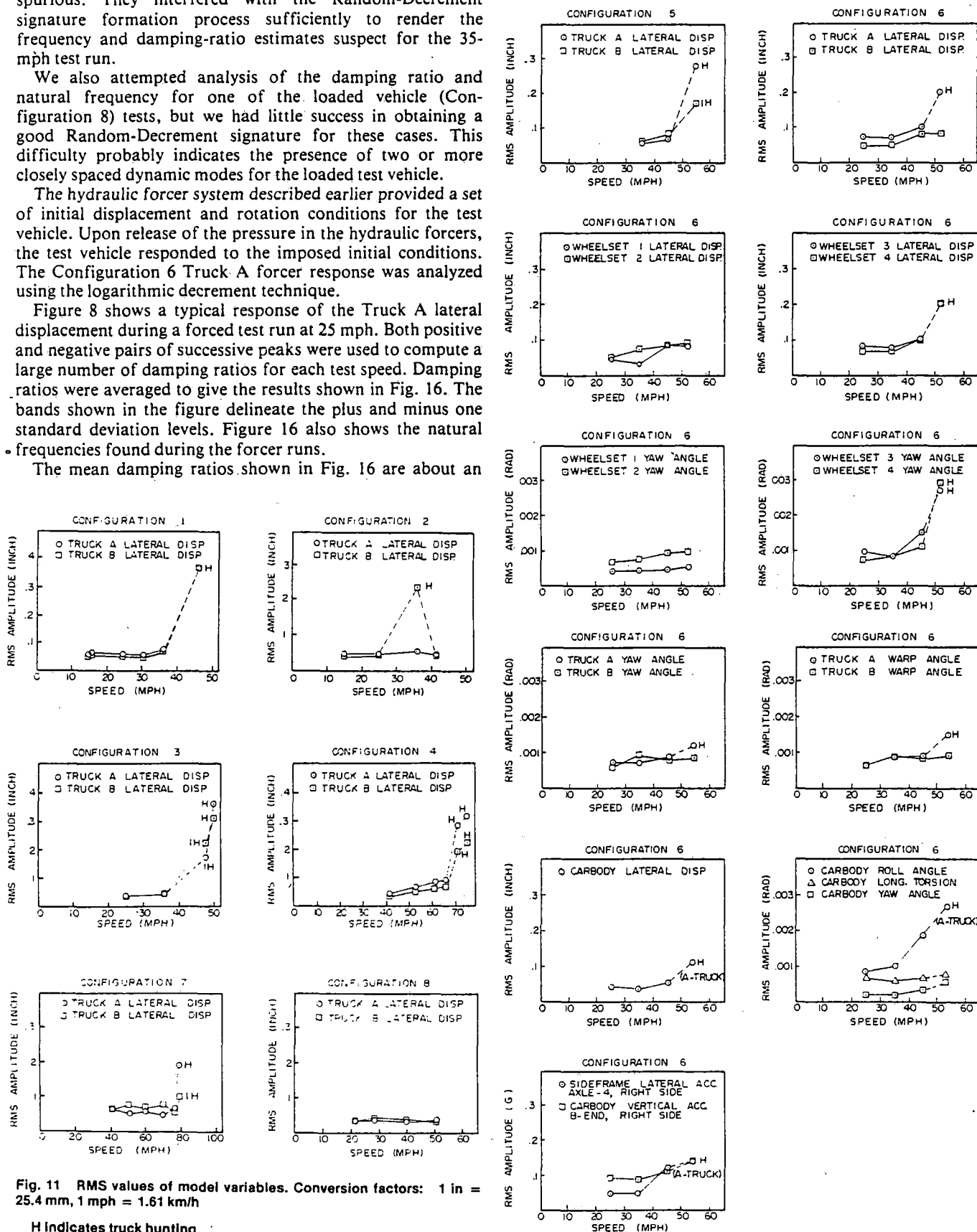


Fig. 11 RMS values of model variables. Conversion factors: 1 in = 25.4 mm, 1 mph = 1.61 km/h

H Indicates truck hunting  
IH Indicates intermittent hunting

Fig. 11 (continued)

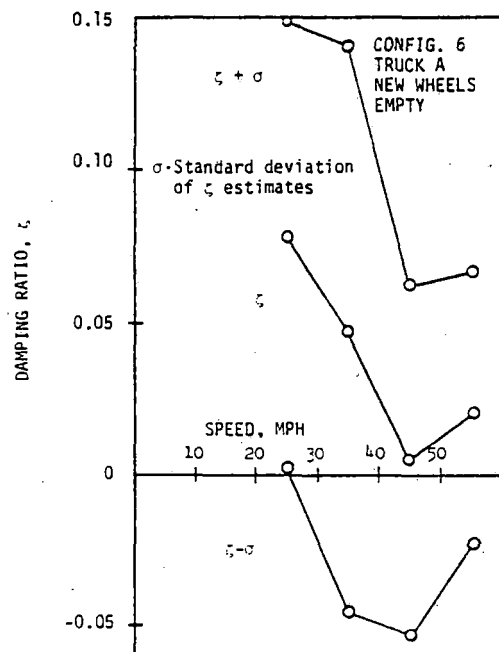
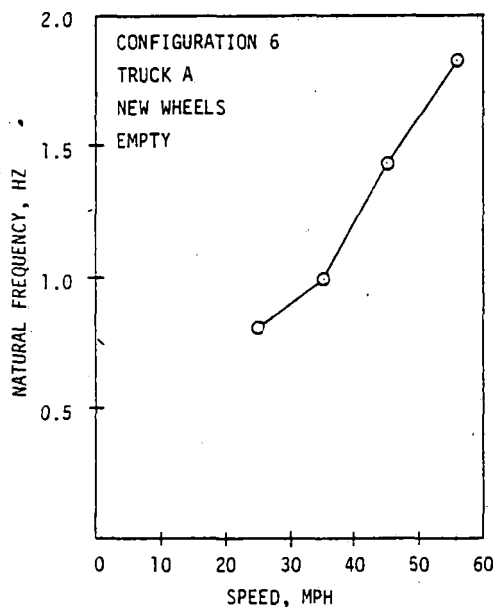
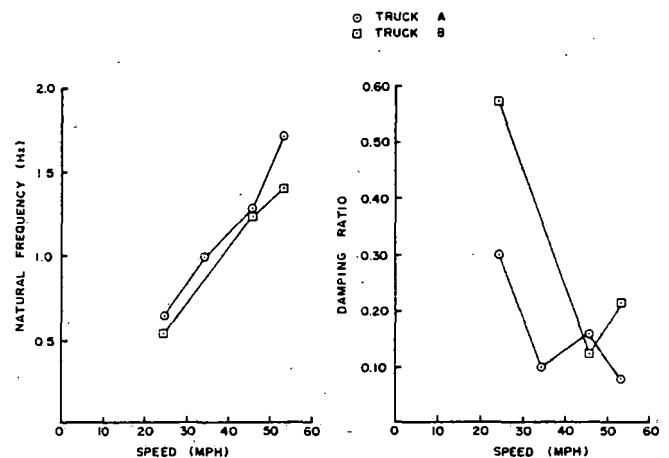
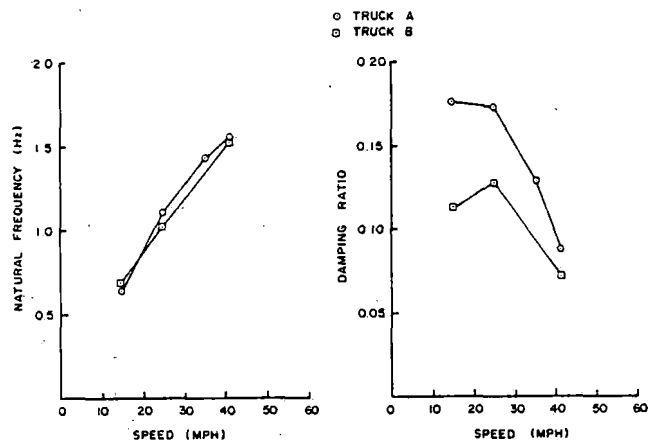
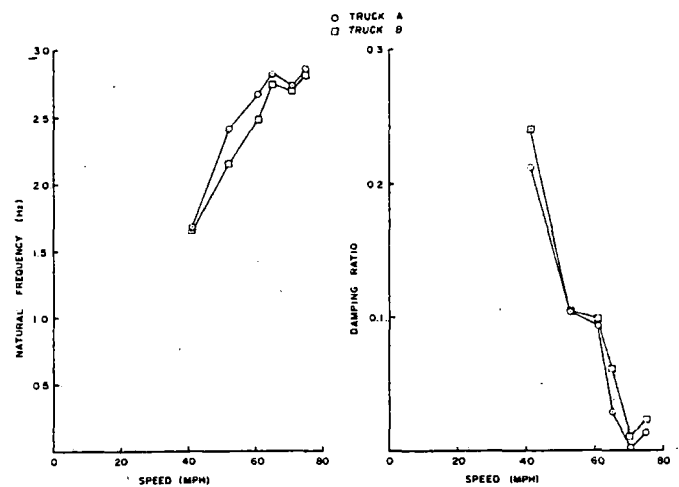
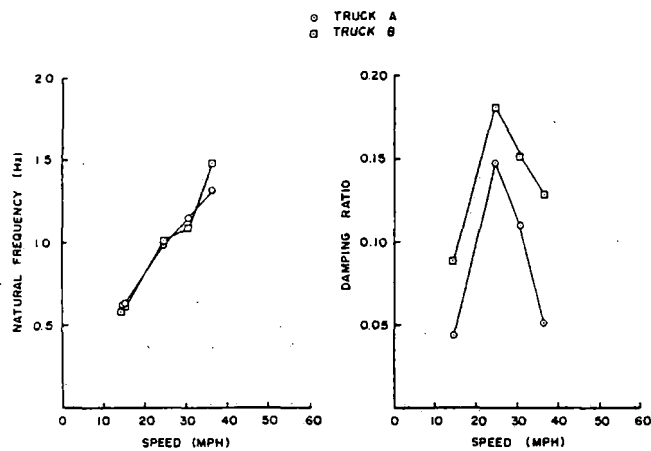


Fig. 16 Experimental damping ratio and natural frequency versus speed relationship from forced response data. Conversion factor: 1 mph = 1.61 km/h



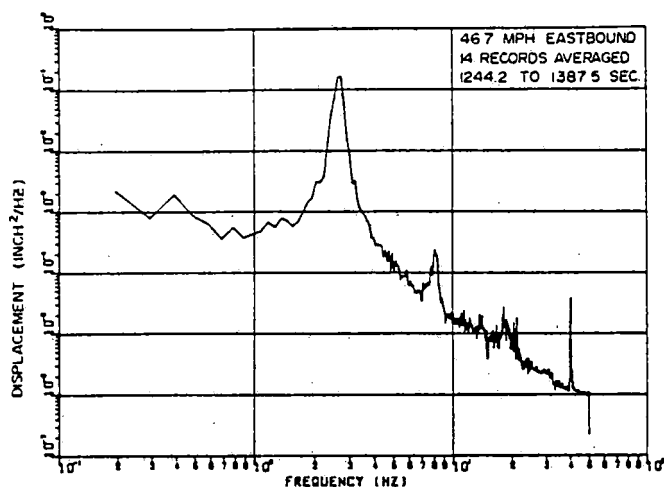


Fig. 17 Truck lateral displacement PSD - hunting. Conversion factors: 1 mph = 1.61 km/h, 1 in<sup>2</sup>/Hz = 645 mm<sup>2</sup>/Hz

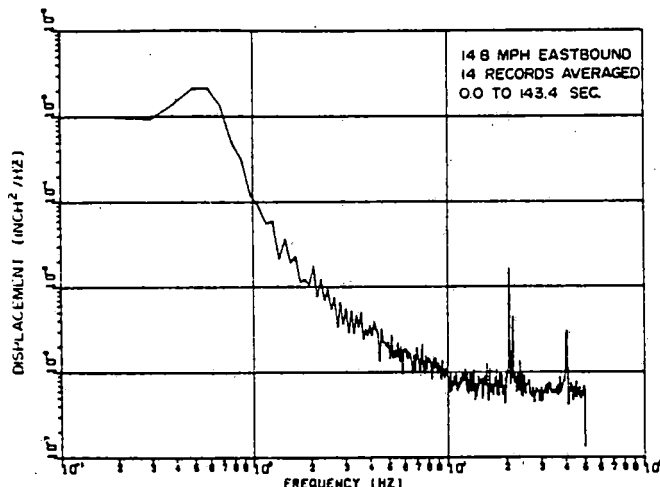


Fig. 18 Truck lateral displacement PSD - stable response. Conversion factors: 1 mph = 1.61 km/h, 1 in<sup>2</sup>/Hz = 645 mm<sup>2</sup>/Hz

assuming there are no forces on the system after release from the initial conditions. In this application the forces due to random rail irregularities are always present. The section of track on which these tests were run was selected because it was relatively good track. Nonetheless, the forcer-response data is contaminated by the random track forcing. It can be observed in Fig. 8 that there are several occasions when the displacement increased between successive peaks. These increases in peak value result from the rail forcing.

Nonlinearities such as Coulomb friction in the test vehicle also account for some of the differences between the damping-ratio estimates from the forced and unforced tests. For a nonlinear system with Coulomb friction the effective damping decreases with increased amplitudes of motion. Because the forced runs began with the flanges hard against the rails during the unloaded vehicle runs, the amplitudes were near maximum values. In contrast during unforced runs the amplitudes were smaller. As a result, smaller estimates of damping ratio would be expected for the forcer test runs.

The natural-frequency estimates shown in Fig. 16 are in every case somewhat higher than those from the unforced runs. This is probably due to the high amplitudes of motion occurring in the forced runs. The test results show a fairly consistent trend in which higher amplitudes of motion are associated with higher frequencies.

**Random Response.** Power spectral densities were computed for many of the measured vehicle motions. PSDs were obtained for both Truck A and Truck B lateral displacements for all configurations on tangent track at all test speeds. In addition, for the Configuration 6 runs PSDs were obtained for all available 19-DOF model variables. When viewing these PSD results it should be noted that only the positive half of a two-sided PSD spectrum is plotted. The values shown are therefore one-half the value of those corresponding to a single-sided spectrum.

Figures 17 and 18 show two typical PSD plots of truck lateral displacement. Of primary importance are the dominant peaks on these plots, which range in frequency from about 0.6 Hz for the 14.8-mph run to about 2.5 Hz for the 46.7-mph run. Each peak represents the energy associated with the least-damped system mode. The center frequencies of these peaks are the damped natural frequencies of the corresponding least-damped modes.

The shape of the predominant peak contains information about the damping ratio of the associated dynamic mode. The low-amplitude, wide peak shown in Fig. 18 represents fairly high damping, while the high-amplitude, narrow peak in Fig. 17 represents low damping. Truck A was actually hunting

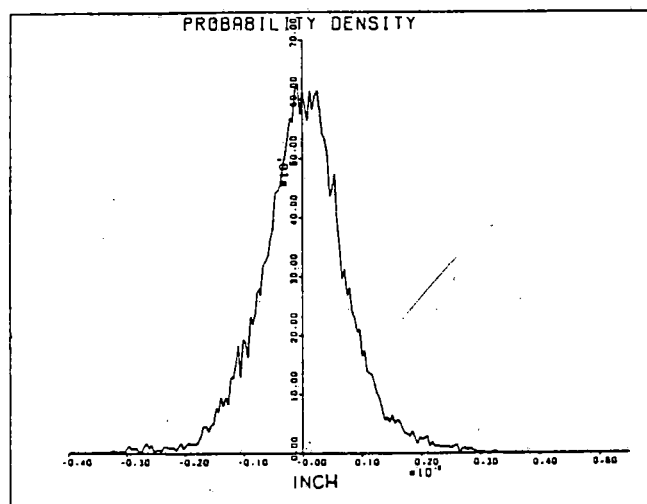


Fig. 19 Typical probability density function for stable behavior. Conversion factor: 1 in = 25.4 mm

during the 46.7-mph test run. The PSDs were used to estimate damping ratios, and results were consistent with those found from the Random-Decrement analysis.

The minor peak at about 8 Hz in Fig. 17 is associated with the wheel rotation rate. This peak is observable on many of the PSD plots. The noise spikes at 20 and 40 Hz have been associated with the motor-generator set on the AAR-100 Research Car. This noise in no way interfered with the analysis of the data since the frequency range was above the range of interest.

In conducting theoretical analysis of randomly forced dynamic systems in general, and of rail vehicles in particular, it is important to know the shape of the probability density functions of the random signals. We computed a sufficient number of probability density functions to conclude that for stable conditions, most of the variables had Gaussian-like density functions. Figure 19 shows an example of this from the Configuration 6 25-mph test run.

In contrast, for a hunting vehicle the probability density function exhibits a shape that is characteristic of the density function for a narrow-band random process. This may be seen in the Configuration 2 density function of Fig. 20.

We should note that our probability density functions are actually histograms that show the relative number of data points falling into uniformly spaced regions of the test variable. They must be normalized to obtain a true probability density function that integrates to a value of one.

## Summary and Conclusions

Several of our observations and conclusions concerning the test planning and conduct may be useful to others involved in similar tests. A very thorough effort was made to characterize the test vehicle. However, only one truck was characterized, and that effort was carried out many months prior to the test. Consequently, differences in suspension stiffness and friction between the two trucks, and the variations in suspension friction with environmental conditions remain unknown. In future tests, it would be desirable to identify the vehicle characteristics for both trucks at the time and place the tests are conducted.

The vehicle instrumentation and data recording system used in these tests were well thought out and performed well during the tests. The wheel-rail displacement probes, in particular, provided reliable and useful data. The greatest shortcoming of the tests, however, was the failure to obtain initial conditions for these devices. A simple procedure to zero these probes is needed.

We would have preferred, given the limitations of testing resources (and the benefit of hindsight), to have more test data for fewer vehicle configurations. Longer runs at the same speed, and runs at more speeds would have given enough data to analyze the anomolous behavior that often occurred. Holding speed more nearly constant during the test runs also would have made the data more useful.

One of the shortcomings of these tests was the lack of adequate roadbed geometry characterization. As explained earlier, alignment profile and gage data was gathered one year before and one year after the tests, but not during the tests. The actual roadbed condition during the tests was not known. In addition, we were unable to synchronize the vehicle test data with roadbed measurements. This proved to be particularly unfortunate, because we found that nonlinear friction in the vehicle suspension causes the vehicle behavior to depend strongly on the roadbed disturbances.

Considerable insight to the nature of the freight car lateral dynamic behavior was gained from the tests described here. Most significantly, the strongly nonlinear nature of the vehicle response was established. As a result of the strongly nonlinear characteristics of the vehicle suspension, no unique hunting speed exists for a given vehicle configuration. Instead, of hunting speed range exists. In the lower portion of this speed range hunting may be intermittent. Above some speed in this range sustained hunting always occurs. The differences seen between the random and forced response test results also provided evidence of the nonlinear behavior.

The use of modal frequency and damping ratios to characterize the relative stability of the freight car proved to be of questionable value for this nonlinear system. This matter has received further attention and will be discussed further in the companion paper that compares the test results with theoretical results.

Despite the nonlinear behavior, a dominant kinematic mode was evident in the test results. This kinematic mode exhibited a frequency nearly directly proportional to speed, a characteristic that is seen in the behavior of more nearly linear vehicles. The PSD analysis clearly shows the majority of energy to be associated with the kinematic mode. This mode is so strong that it can be observed directly in the time response of the vehicle.

The stability of the vehicle on tangent track is increased by adding rotational stiffness to the truck. This can be observed by noting that C5, which used truck stiffeners, had greater stability than C2 which was identical except for the stiffeners. The stability of the vehicle on tangent track is increased by adding rotational friction to the trucks. This can be observed by noting that C1, the vehicle with dry centerplates, had greater stability than C2. In addition C3 and C4, with the

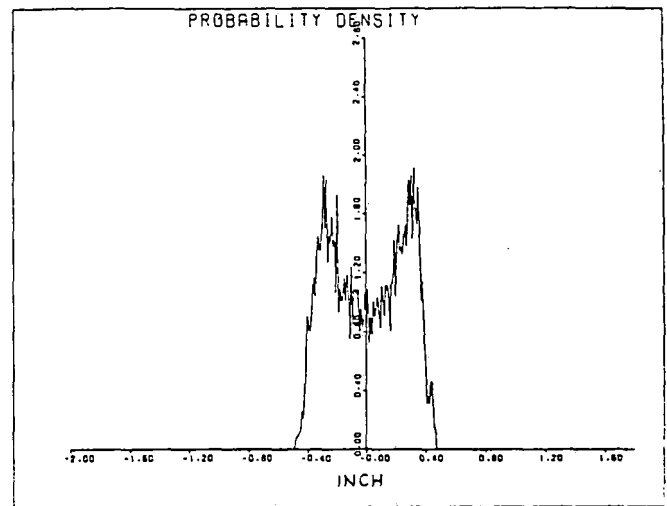


Fig. 20 Typical probability density function for hunting behavior. Conversion factor: 1 in = 25.4 mm

constant-contact sidebearing devices, showed greater stability than C2. The increased rotational friction of C1, C3, and C4 over that of C2 was achieved by means of increased Coulomb or sliding friction. It is important to recognize that when these friction elements are not sliding, that is, they are locked, the net effect is to add rotational stiffness.

## Acknowledgments

The effort described in this paper was supported by Contract DOT-OS-40018 with the Federal Railroad Administration. The cooperation of the Association of American Railroads and the Union Pacific Railroad in this project is also gratefully acknowledged.

The opinions expressed in this paper are those of the authors, and do not necessarily represent those of the FRA, AAR or UP.

## References

- 1 Cooperrider, N. K., Law, E. H., Fries, R. H., and Tsai, N. T., "Theoretical and Experimental Research on Freight Car Lateral Dynamics," *Proceedings of the Heavy Haul Railways Conference*, Perth, Western Australia, Sept. 1978.
- 2 Law, E. H., Hadden, J. A., and Cooperrider, N. K., "General Models for Lateral Stability Analyses of Railway Freight Vehicles," FRA-OR&D-77-36 (PB 272372), June 1977.
- 3 Hadden, J. A., and Law, E. H., "The Effects of Truck Design on Hunting Stability of Railway Vehicles," *ASME Journal of Engineering for Industry*, Vol. 99, No. 1, Feb. 1977, pp. 185-196.
- 4 Haque, I., Law, E. H., and Cooperrider, N. K., "Users' Manual for Lateral Stability Computer Programs for Railway Freight Car Models," Federal Railroad Administration Report No. FRA-OR&D-80/30, Apr. 1980.
- 5 Cooperrider, N. K., Law, E. H., and Fries, R. H., "Freight Car Dynamics: Field Test Results and Comparison with Theory," FRA-OR&D Report, May 1981.
- 6 Private communication from I. Gitlin, AAR Research Center.
- 7 Orr, D. G., ed., "70 Ton Truck Components Data, Physical Restraints, Mechanical Properties, Damping Characteristics," *Track-Train Dynamics Harmonic Roll Series*, Vol. 2, 1974.
- 8 McKeown, F. S., "Torsional Resistance at a Truck Bolster/Car Body Centerplate Interface," Test Report — Part IV, ASF Participation in AAR/RPI/FRA Track-Train Dynamics Program, American Steel Foundries, Test Engineering Department, Feb. 22, 1974.
- 9 Abbott, P., "Comparison of the Nonlinear Dynamic Characteristics of the Barber S-2 and ASF Ride Control Freight Trucks," Martin Denver Division Technical Report MCR-76-475, Contract NAS 8-29882, Sept. 1976.
- 10 Anon, "Truck Hunting Model Validation Lab Test to Find Friction Coefficient at Air Bag Side Bearing/Body Bolster Wear Plate," Association of American Railroads Research Center, Informal Report, Fall 1977.
- 11 Fallon, W. J., Cooperrider, N. K., and Law, E. H., "An Investigation of Techniques for Validation of Railcar Dynamic Analyses," Federal Railroad Administration Report FRA-OR&D-78/19 (PB 27996/AS), Mar. 1978.
- 12 Cole, H. A., Jr., "On-Line Failure Measurement and Detection of Aerospace Structures by Random Decrement Signatures," NASA-TND-4503, 1968.

REFERENCE 166



SOCIETY OF AUTOMOTIVE ENGINEERS, INC.  
400 Commonwealth Drive, Warrendale, Pa. 15096

## Track-Train Dynamics

**Peter W. Abbott and George Morosow**  
Martin-Marietta Corp.

**Jack Macpherson**  
Marshall Space Flight Center, NASA

SOCIETY OF AUTOMOTIVE ENGINEERS

National Aerospace Engineering  
and Manufacturing Meeting  
Culver City, Los Angeles  
November 17-20, 1975

751058

# Track-Train Dynamics

**Peter W. Abbott and George Morosow**

Martin-Marietta Corp.

**Jack Macpherson**

Marshall Space Flight Center, NASA

AMERICA'S RAILROADS TODAY have a fleet of more than 1.7 million freight cars traveling on approximately 200,000 miles of rail line. Before World War II, the railways were the dominant mode of land transportation. Despite a significant growth of other modes of transportation such as air and truck transportation industry during the last several decades, the railroad industry today accounts for almost 50 percent of all freight shipped. By 1980 the volume of freight traffic will be greater than one trillion ton miles annually. This represents approximately a one-third increase in today's traffic volume. Except for some specialized applications, the freight car today is basically the same as it was 50 years ago. Old designs have been perpetuated with only small changes. Although the design did not change, the train speed increased, and so did the size of the car and its payload weight. More demand is placed on design which was conceived a long time ago for conditions prevailing at that time.

The obsolete car design is not the only problem. Inadequate maintenance of rolling stock and of the rail and the road bed is another significant contributing factor in excessive equipment and rail wear resulting in numerous derailments.

As a result of an increasing number of accidents, the Association of American Railroads (AAR) in cooperation with the federal government and private railroad industry, embarked on an ambitious comprehensive ten-year program, Track-Train Dynamics, designed to pinpoint the problem areas, define the mechanics of the problem, propose the solution and finally help the railroads to implement the fixes.

Among numerous tasks and studies performed by industry, research institutions and government, a study was awarded to Martin Marietta Corporation, sponsored by the Federal Railroad Administration and administered by NASA through Technology Utilization office.

The intent of this paper is to focus the attention on one of the dynamic problems, namely the hunting phenomenon or instability of trucks and to outline an analytical-empirical approach to synthesizing a dynamic model suitable for investigation of hunting. The study is in progress but results obtained to date look promising enough to present a status report.

## PROBLEM DEFINITION

Until recently, not much attention has

---

## ABSTRACT

The purpose of this paper is to outline one of the serious dynamic problems involving railroad cars and to propose an orderly approach to the definition of a dynamic model through analysis and testing that can be used to investigate various fixes. The problem in question is the hunting phenomenon involving lateral instability of the car suspension (trucks). This phenomenon has been recognized as a major contributing factor in

a significant number of derailments causing millions of dollars in losses. This paper expounds on the mechanics and characteristics of hunting. The planned solution is outlined as a building block approach directed at formulating a test verified dynamic model of an open hopper freight car-truck assembly. Results obtained to date are presented together with conclusions related to the program.

been devoted to the mechanics of wheel-rail interaction and the associated dynamic behavior of car-truck systems. A system so defined contains the mechanism and a source of external energy required to produce instability or hunting which results in poor ride quality, excessive wear and ultimately may lead to derailment accidents. Only recently has a systematic approach to the problem definition and characterization been undertaken by both government and industry. Consequently, there is today an expanding bank of data and cadre of knowledge being compiled on track-train interaction problems.

Hunting is the dynamic instability of wheel sets or entire trucks as they roll down the track. It is produced by contact forces between the wheel tread and the rail. The fundamental motion consists of a lateral translation of the wheel set (along the axle) and a rotation about a vertical axis. This motion is further complicated by coupling with the truck degrees of freedom and finally with the car body.

The railroad truck is the essential part of this instability and merits, therefore, a closer look.

Figure 1 shows an overall view of a typical freight type truck assembly consisting of two side frames, two wheel sets and the bolster connecting the side frames. The centerplate located in the center of the bolster provides the bearing surface supporting the car body weight. The coil spring groups contained between the bolster and the side frames support and isolate the car. The

older trucks had journal bearings which permitted the wheel sets to slide freely along their axles. With the advent of tapered roller bearings, this free play was eliminated, and as it will be shown later, this change aggravated the hunting problem.

The wheel-rail interaction forces, called creep forces, are due to the microscopic sliding in the elliptical wheel-rail contact region (the wheel-rail interfaces). In this concept, the creep forces are linear functions of the axle displacements and velocities. Nonlinearities, mainly due to flange contact results in a limit cycle. The motion may be as large as  $3/4$  of an inch laterally. Typically, the hunting frequency is from 1.5 to 3 Hz, in the speed range from 40 mph and up.

Two most significant parameters which, for a given configuration, affect hunting speed are level of adhesion and wheel profile. Investigators conducting field hunting tests noticed that hunting did not occur when rails were wet from rain, suggesting a very low adhesion in this condition. The difficulty in deriving the actual creep coefficients is related to this in that other types of contamination (dust, oil, etc.) cause a similar reduction in adhesion.

The other significant parameter is the wheel profile. A new wheel starts as a cone, Figure 2. The angle is generally  $3^\circ$ . As the wheel wears, the profile of the tread becomes curved. This curvature causes hunting to occur at lower speeds through the additional terms generated in the equations

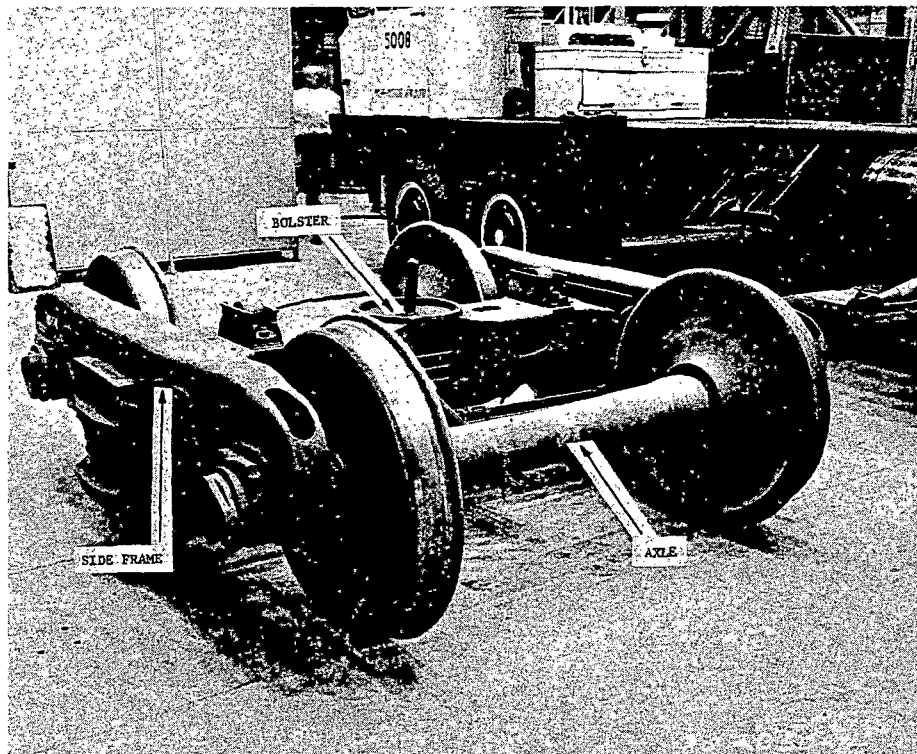


Figure 1-Typical freight truck

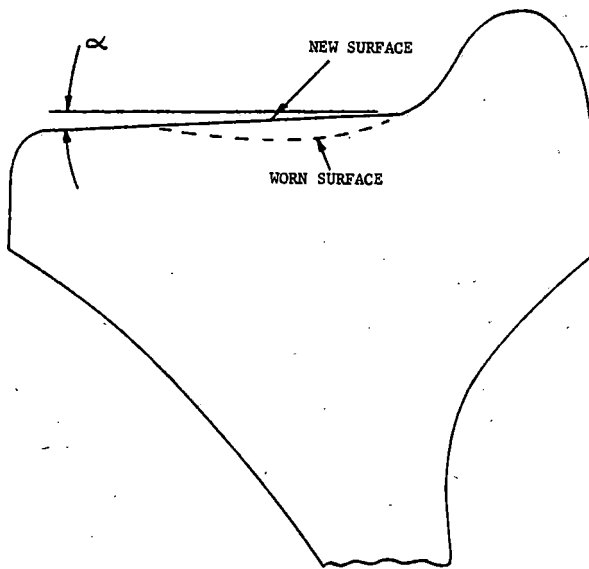


Figure 2-New and worn wheel profiles

of motion.

#### TECHNICAL APPROACH

The overall objective of this study was to synthesize a high fidelity mathematical model which has been verified by carefully controlled tests. A sequential, building block test approach was chosen to facilitate comparisons with appropriate analytical models starting with a simple subsystem and culminating with the complete nonlinear system. Figure 3 shows the flow of events leading to the final model. The natural physical separation of the car and truck lends itself nicely to the approach selected. Additionally, the physical differences between the car and truck, i.e., the linear nature of the car and nonlinear nature of the truck require different testing and analysis techniques. Finally, the combined system model requires an additional consideration for both test and analysis.

**TEST PROGRAM** - The intent of the entire test program was to obtain necessary data for comparison with the analytical model. To satisfy this goal and yet, to limit the test program to essential tests only, three distinct types of laboratory tests were decided upon. These were:

- (1) truck quasi-static test,
- (2) car modal survey,
- (3) system transfer functions.

The truck quasi-static test was designed to determine truck nonlinear joint properties (free play, hysteresis). The sequence of car body modal survey tests provided a configuration for linear modal model of that subsystem. Finally, the transfer function test introducing the forcing function at the wheel provided a check for the combined linear car body and nonlinear truck models.

**TRUCK QUASI-STATIC TEST** - Truck behavior

is the key to the system hunting. Experience indicates trucks with only subtle differences in their parameters display significant differences in hunting speeds. Therefore, a comprehensive test program was designed to define the significant characteristics of the truck. The truck consists of five very stiff members connected with nonlinear joints. There are two basic types of joints,

- (1) bolster-side frames,
- (2) axle-side frame.

The "Ride Control" truck tested contains, in addition to the previously mentioned spring groups, friction wedges preloaded with a separate spring parallel with the other springs. Figure 4 illustrates this concept. The axle-side frame joint consists of a bearing/bearing adapter which fits the roller bearing to the side frame. The side frame merely rests on top of the bearing adapter as shown in Figure 5. The play in this joint allows relative lateral, longitudinal and rotational motion with only friction to oppose the motion. The intent was to measure the truck characteristics in terms of "natural modes" which exercised these joints. In other words, the loading conditions were selected to approximate the operating conditions in a realistic and simple way. Out of a great number of test conditions, six deemed most significant were chosen:

- (1) vertical load on bolster,
- (2) lateral load on bolster,
- (3) longitudinal load on bolster,
- (4) moment about bolster longitudinal axis,
- (5) moment about bolster lateral axis,
- (6) truck warping (parallelogram).

The first load case was simply a vertical load applied to the bolster. All other load cases consisted of a vertical constant load on the bolster superimposed with the cyclic load at approximately .2 Hz. The constant load was adjustable between 20,000, 50,000 and 100,000 lbs. This range provides the typical variation of loading from empty to full. Figure 6 shows a typical test setup-condition 6, with the loading actuator acting on a diagonal. Reference 1 provided excellent correlation data for the bolster/side frame joint, by measuring friction and stiffness of individual spring groups.

This series of tests exercised all the joints in a way consistent with the constraints provided by the stiff structural elements. To measure the Coulomb friction in the joints accurately, the load was applied cyclically and ensuing displacement data (across the joints) recorded continuously. Loading rates of 2 seconds/cycle and 4 seconds/cycle were used to determine if there is any relation between the parameters measured and the velocity. Approximately 20 channels of deflection data were recorded.



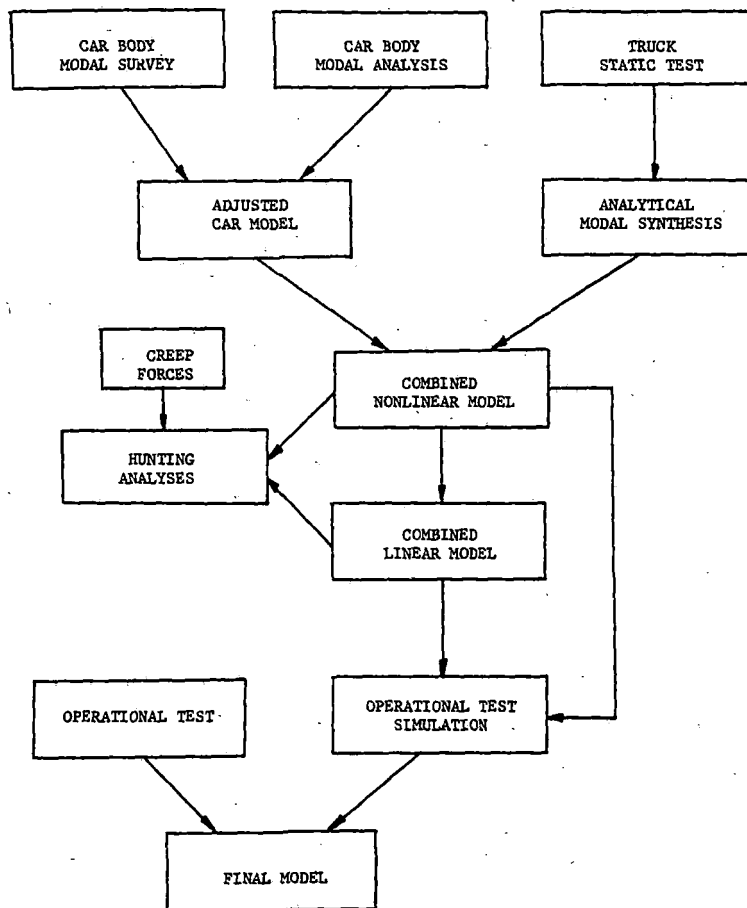


Figure 3-Test/analysis flow

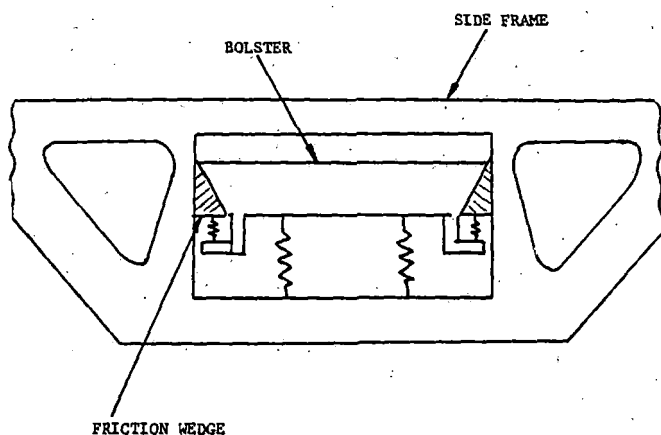


Figure 4-Bolster/side frame interface

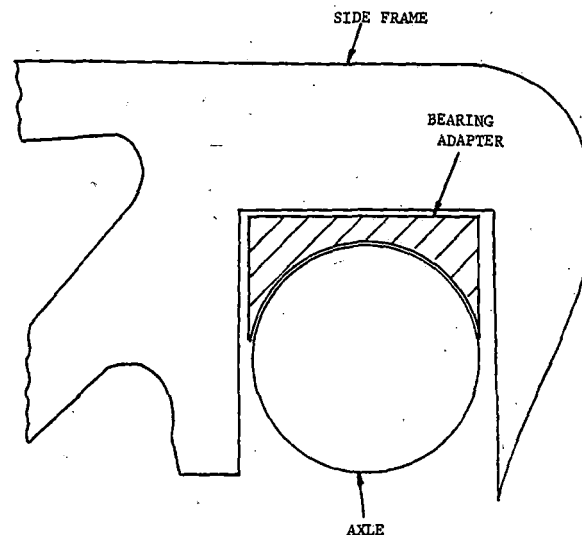


Figure 5-Side frame/axle interface

The Hybrid computer (EAI 8400) was used to cross-plot load-deflection data. Typical examples for several joints are shown in Figure 7. Figure 8 shows the location of the instrumentation. Only tests 1, 2 and 6 provided useful data. Other tests did not produce usable joint motions or duplicated data already obtained.

**MODAL SURVEY** - The purpose of this series of tests was to measure the modal parameters and more specifically, elastic characteristics of the car body. The car

empty test was performed supporting the test article on air springs and excited by six Unholtz Dickie electrodynamic shakers of 150 lb force each. Figure 9 illustrates the setup. Subsequently, the car was filled with 80 tons of industrial grade granulated and powdered coal and the test repeated. Because of excessive force requirements, simple mechanical force multipliers were

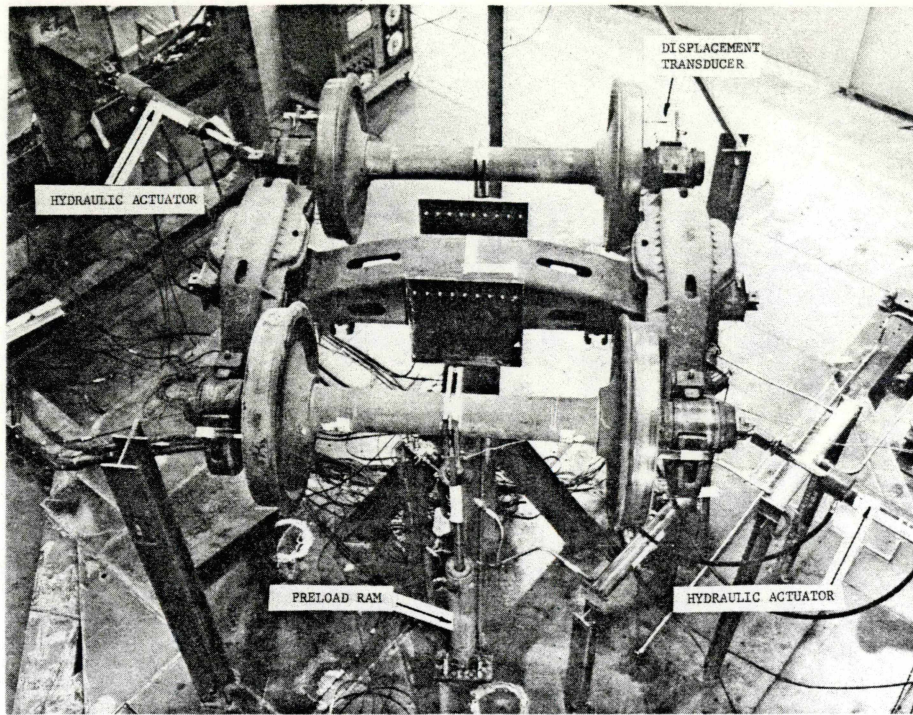


Figure 6-Typical static test-condition 6

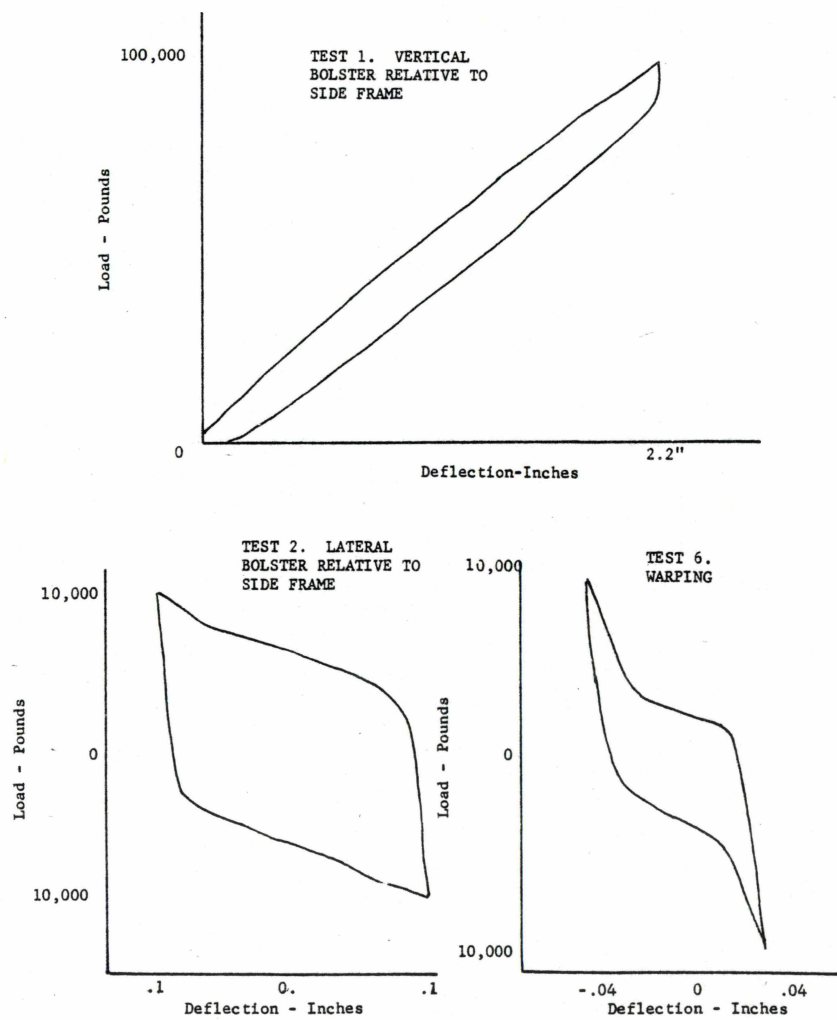


Figure 7-Typical hysteresis data



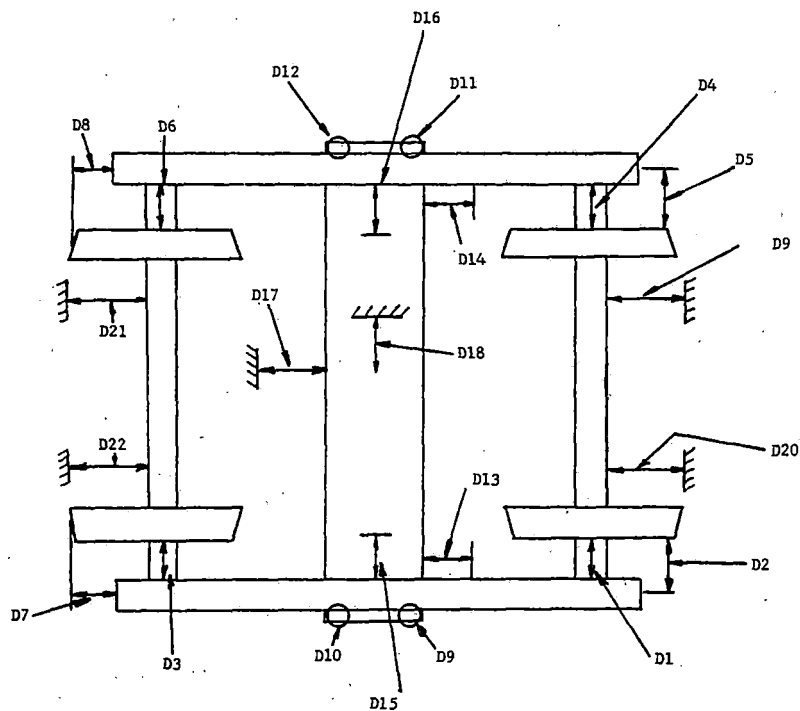


Figure 8-Static test instrumentation

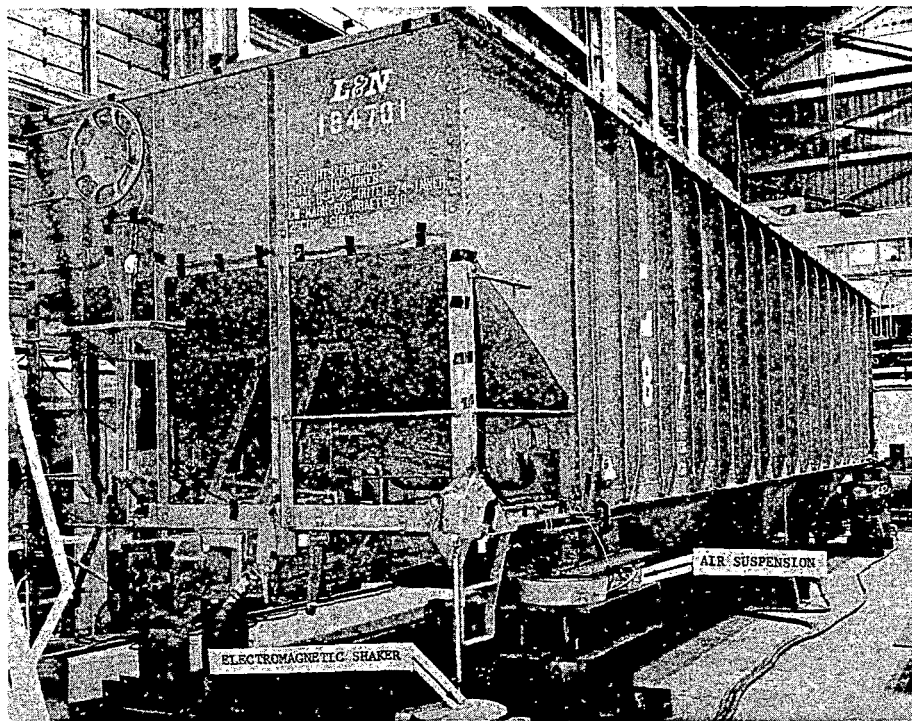


Figure 9-Modal survey set-up

installed as shown in Figure 10.

Instrumentation consisted of 40 channels of accelerometers and 6 channels of force gages.

The test technique consisted of running frequency sweeps with a fixed force vector designed to excite a particular mode shape. Key accelerometers were analyzed using the co-quad format to determine the location of resonant frequency of interest. A dwell and fine tuning of the particular mode was

conducted manually. Once the mode is properly tuned, the shape is taken using the quadrature values only. Figure 11 illustrates the instrumentation block diagram for this technique.

The lowest three natural modes were identified as torsion, lateral bending and vertical bending. Table I lists all significant results and comparisons with analysis. Figure 12 shows comparison of mode shapes. It is of interest that the original results

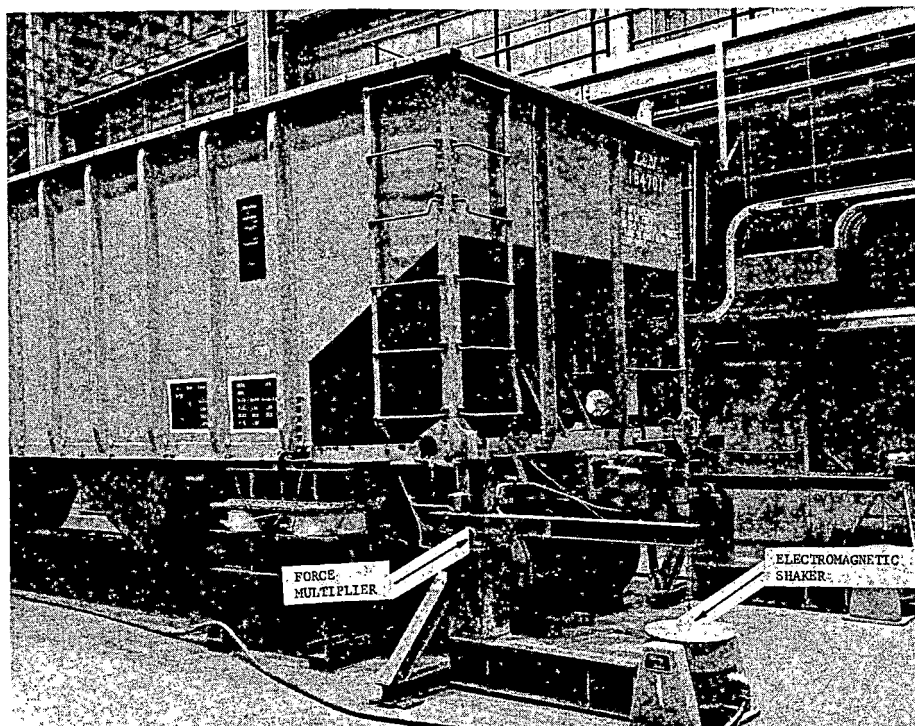


Figure 10-Mechanical force multipliers

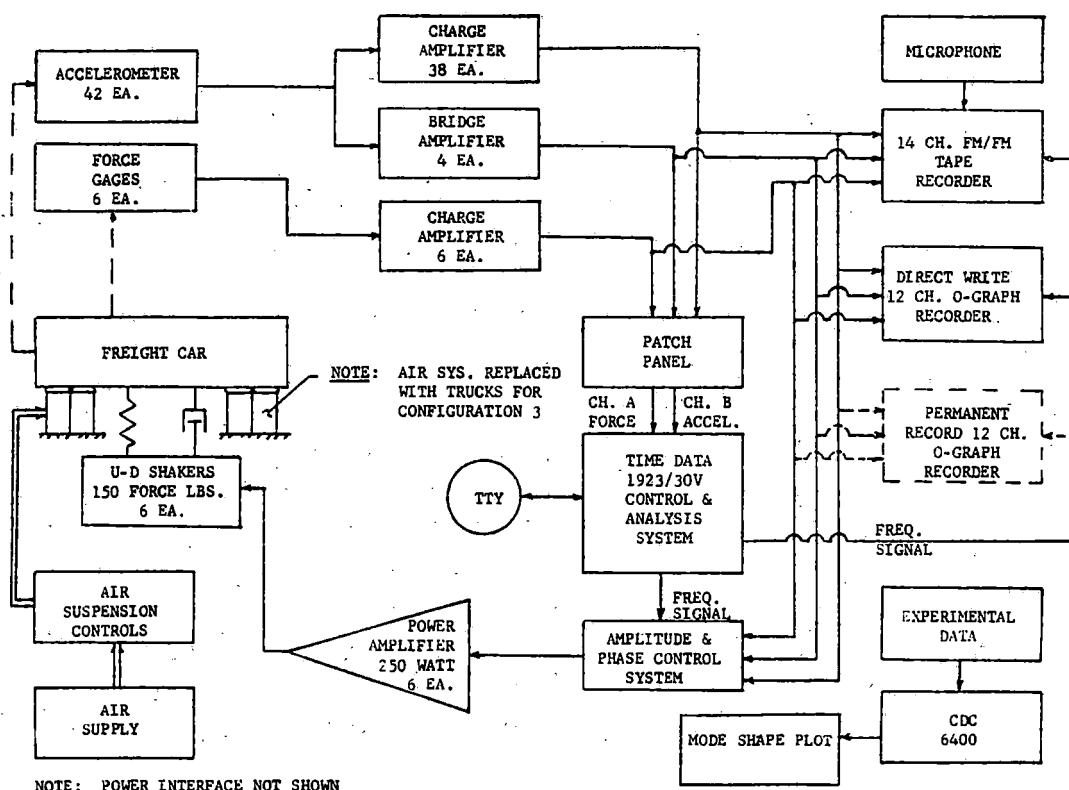


Figure 11-Modal survey block diagram

showed a considerable discrepancy compared to analysis. The discrepancy amounted to approximately 22% for all three modes. This is attributed, in general, to the manner in which the car was built compared to the drawings which were used as a basis for the finite element model. Two significant factors were noted: (1) lack of planarity of

the side walls of the car. The bow in the middle amounted to 2 in. The eccentricity was not accounted for in the analysis, (2) lack of continuous welds connecting the sill beam to the car. A continuous weld was assumed in analysis. Because, at this time, it is not known to what extent the car body dynamic characteristics influence the hunt-

Table I - Comparison of Analytical and Experimental Modal Frequencies

Mode	Empty Car		Full Car	
	Analysis	Experiment	Analysis	Experiment
Torsion	6.89 Hz	5.32	2.81	4.89
Lateral Bending	21.23	17.64	6.95	8.80
Vertical Bending	40.13	29.57	16.55	14.55

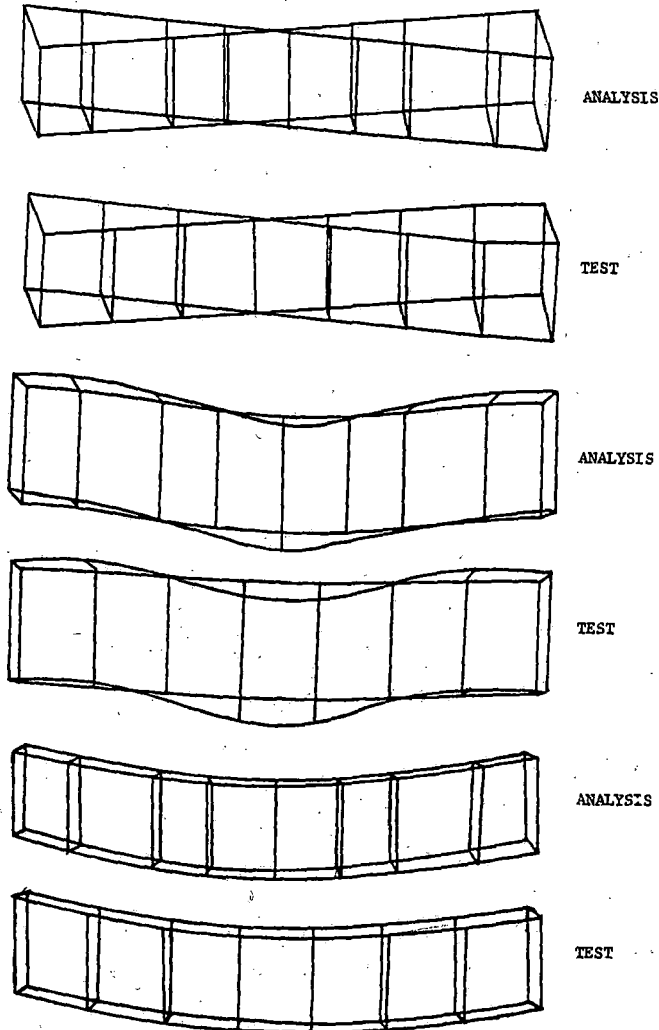


Figure 12-Comparison of analytical and experimental mode shapes-empty car

ing speed (probably a small effect); it was decided to postpone any further corrections to the analytical model until such time when it is determined that a 20% accuracy is inadequate. It should be noted that this particular open hopper car represents, probably, a limit in modeling difficulty because of its complex geometry. It is expected that other types of cars can be modeled considerably more accurately. A description of the finite element model will be provided at a later point.

**TRANSFER FUNCTION TEST** - The final leg of laboratory test-analytical model correlation is to subject the car-truck system to vibrational forces of the magnitude seen in actual service. The resulting motion is then compared to the analytical model motions. The dominant feature of correlation is the proper connection of the car and truck. The car-truck interface poses some problems. On the truck side of the interface is a flat surface approximately 14" in diameter with a lip extending upward approximately 1". The car side is also a flat surface slightly smaller in diameter and it fits down inside the lip. Therefore, vertical restraint is compression only. Lateral and longitudinal restraint is frictional until the car side contacts the lip on the truck. Rotational restraint about a vertical axis is frictional and the surfaces may rock about the other 2 axes. Rocking, incidentally, is normal operation. If the car rocks too much relative to the trucks, roll stops between the car and bolster, restrain any further relative motion.

The test setup is shown in Figure 13. Forces were applied to each axle of one truck or each wheel of one axle with the other truck fixed. The forced trucks wheels were on low friction slide plates, free to move in a horizontal plane. Force levels of 10,000 lbs were run from 2-30 Hz and responses measured. The instrumentations used were similar, but somewhat reduced, from the one used on previous tests.

**TRANSFER FUNCTION** - The data was analyzed using the Time Data 1923A computer. The algorithm used is FFT (Fast Fourier Transform) and plotted output is the ratio of response to input Fourier transforms. Since the system is nonlinear, the response is not always sinusoidal and our analysis technique acts as a very fine band pass filter. The correlation analysis results are in process but are not included in this paper.

**OPERATIONAL TEST** - Final verification of the analytical model will be made by observing the car-truck system in the actual operating environment. The car and truck

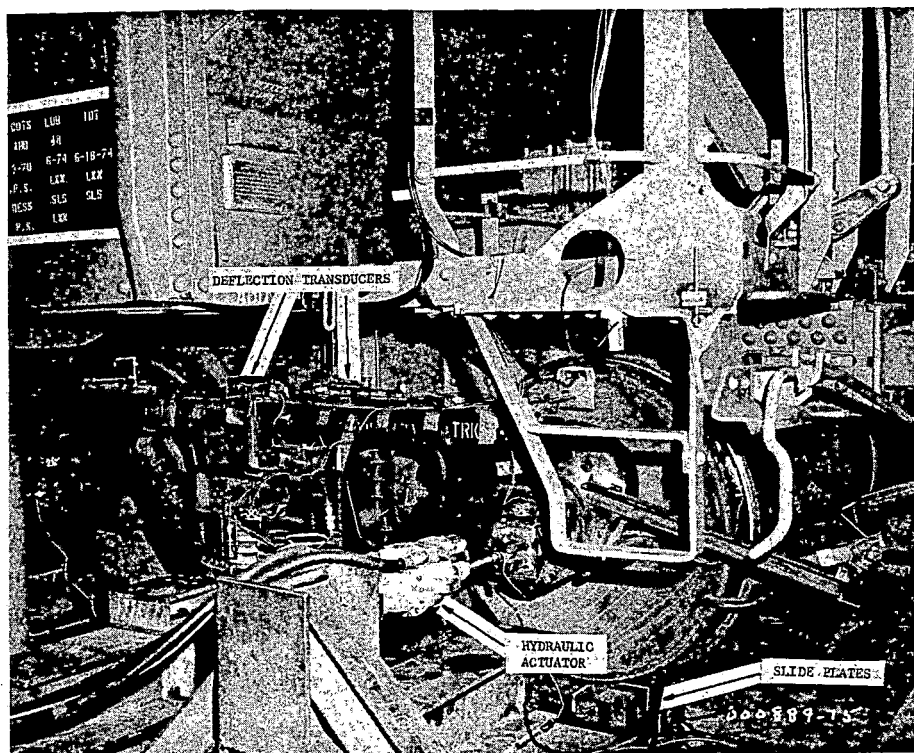


Figure 13-Transfer function set-up

will be completely instrumented and put in a consist with several instrumentation cars and buffer cars to obtain reasonable boundary conditions. Note that the hunting phenomenon is not thought to be sensitive to boundary conditions at the coupler.

This operational test is in conjunction with a study being conducted by Drs. Neil Cooperrider (ASU) and Harry Law (Clemson). They have developed both linear and nonlinear mathematical models to explain the hunting phenomenon and in addition are examining possible solutions to reduce the severity of hunting. Table II lists the various test conditions to be examined. The test will be conducted late 1975.

#### ANALYTICAL MODELS

**NONLINEAR TRUCK MODEL** - The analytical model was defined by estimating the joint parameters of stiffness, friction and free play (slop) based on the Reference 1 data and the test results. The model consists of 5 rigid bodies connected by the joint nonlinearities. Conceptually, a joint is modeled as shown in Figure 14. Each relative degree of freedom at a joint generates forces based on this joint model. The calculation of joint forces from this model is largely a matter of bookkeeping in order to satisfy the friction relationship  $F_f = -f V/|V|$  i.e., the Coulomb friction force is constant and opposite the relative motion. Table III gives the joint parameters used in the model.

In order to compare to the test results, the equations of motion were integrated numerically on a CDC 6500 digital computer. The equations of motion simplistically are

$$M \ddot{q} = T_1^T F_J + T_2^T F_A$$

These represent 30 equations where

$M$  = mass  
 $\ddot{q}$  = discrete accelerations  
 $F_J$  = joint forces  
 $F_A$  = applied forces  
 $T_1^T, T_2^T$  = transformations to obtain proper generalized force for discrete degrees of freedom

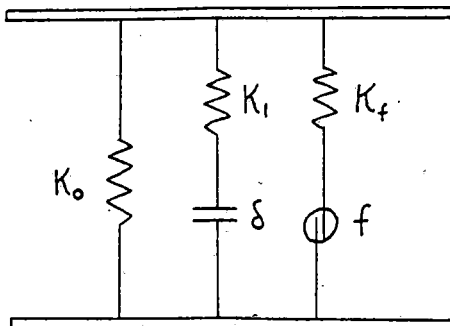
Figure 15 illustrates the results compared with measured data.

Obviously, the comparison is not exact. Asymmetries in the real structure and simplifying assumptions cause some deviations. However, the qualitative concept of relative energy stored and dissipated per cycle should provide a reasonable model for use in hunting evaluations.

**CAR LINEAR MODEL** - As previously mentioned, the car analyzed was on 80 ton open hopper coal car. The structural geometry is very complex, hence, a finite element model was appropriate in order to obtain the proper load paths for the fundamental structural modes. The original stiffness finite element model contained approximately 3000 degrees

Table II - Operational Freight Car Test Summary

Test No.	Basic Configuration	Modifications	Track Conditions
1	Full Car New Wheels	None	High Speed Tangent Track
2	Full Car Worn Wheels	None	High Speed Tangent Track
3	Empty Car Worn Wheels	None	High Speed Tangent Track
4	Empty Car New Wheels	None	High Speed Tangent Track
5	Empty Car Worn Wheels	Increase Truck Warping Stiffness	High Speed Tangent Track
6	Empty Car Worn Wheels	Supplemental Ride Control Device #1	High Speed Tangent Track
7	Empty Car Worn Wheels	Supplemental Ride Control Device #2	High Speed Tangent Track
8	Empty Car Worn Wheels	Remove #2 Pin Friction Wedges	High Speed Tangent Track
9	Empty Car Worn Wheels	Lubricate Center Plate	High Speed Tangent Track
10	Empty Car Worn Wheels	TBD	High Speed Tangent Track
11	Full Car New Wheels	TBD	High Speed Tangent Track
12-15	TBD	TBD	High Speed Tangent Track



- $K_0$  = initial stiffness  
 $K_1$  = hard stop  
 $\delta$  = free play  
 $K_f$  = friction stiffness  
 $f$  = Coulomb friction

Figure 14-Nonlinear joint model

of freedom as shown in Figure 16. The model was reduced in size to 98 degrees of freedom using static reduction. The structural mass matrix was formed using a coarse model of approximately 400 degrees of freedom and reduced to the 98 of the stiffness model.

The mass of the coal was added to the 98 degrees of freedom mass matrix using a least squares technique. The stiffness of the coal was ignored. In the least squares technique the coal is broken into several discrete lumps with 6 degrees of freedom each.

The center of mass motion of each lump is written in terms of the motion of the surrounding degrees of freedom.

$$q_S = T q_{cg}$$

$q_S$  = surrounding degrees of freedom  
 $q_{cg}$  = coal center of mass motion

Table III - Truck Joint Parameters

Degree of Freedom	Bolster/Side Frame				Side Frame/Axle			
	$K_0$	$K_1$	$f$	$\delta$	$K_0$	$K_1$	$f(\mu)$	$\delta$
X	$10^6$ #/in	$10^6$ #/in	-	0	0	$10^6$	.3	.1
Y	18600 #/in	$10^6$	3500 #	1. in	0	$10^6$	.3	.1
Z	22500 #/in	$10^6$	3500 #	3. in	$1 \times 10^6$	$10^6$	.1	0
$\theta_X$	871000. in#/rad	$10^6$	35000. in#	.2 rad	$10^6$	$10^6$	3.	.1
$\theta_Y$	986000. in#/rad	$10^6$	35000. in#	.03 rad	0	0	.03	.1
$\theta_Z$	10000. in#/rad	$5 \times 10^7$	15000. in#	.0025 rad	0	$10^6$	1.	.1

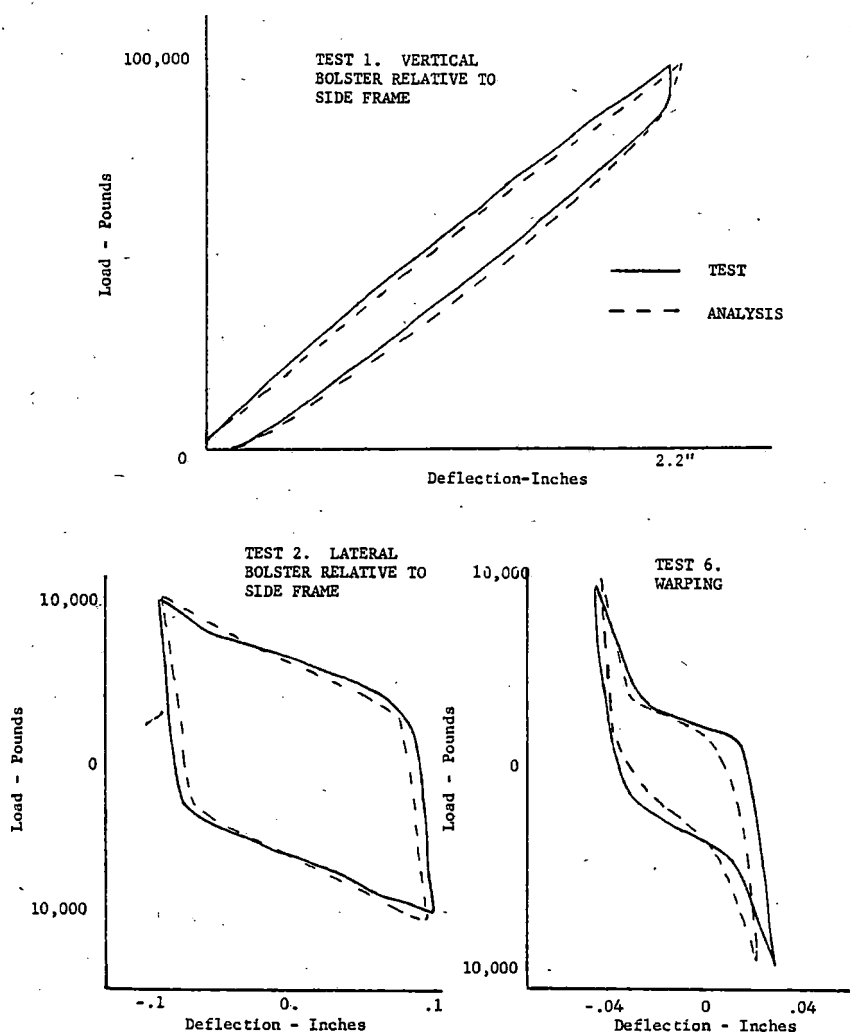


Figure 15-Comparison of analytical and experimental hysteresis results

$T$  = rigid body transformation

to solve for the inverse of the non-square matrix  $T$ , first multiply both sides of the equation by  $T^T$ . This yields

$$T^T q_S = T^T T q_{cg}$$

where the superscript  $T$  means transpose of a matrix.  $T^T T$  is now a  $6 \times 6$  matrix and can be inverted. Hence

$$q_{cg} = (T^T T)^{-1} T^T q_S$$

This is a least squares transformation

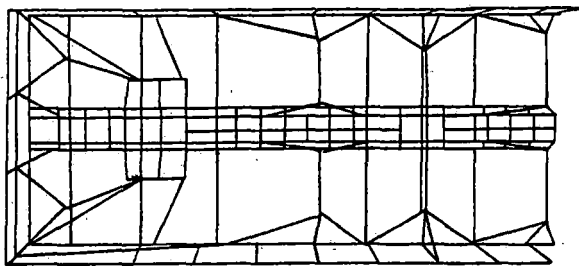


Figure 16-Half car finite element model

and essentially describes the motion of the coal cg as an "average" of the surrounding points. The mass of a coal segment is transformed to the surrounding points as

$$M_S = T_L^T M_{cg} T_L$$

where  $T_L = (T^T T)^{-1} T^T$

Results of this analysis were compared to test data as shown previously in Table I and Figure 12.

**HUNTING ANALYSIS** - The hunting analysis for this particular truck-car system is not complete. The wheel/rail interaction relationships are presented here for the sake of continuity.

Many authors (References 2 through 4) have conducted hunting analyses for single axles to full system with varying degrees of sophistication. The fundamental concept of wheel-rail interaction will be presented here without the confusion of the other parameters involved.

The wheel-rail forces depend upon a phenomenon called creep. Creep is defined as the ratio of the relative velocity of the wheel-rail interface divided by the forward velocity. It has been hypothesized that if the creep is small, the force is a linear function of creep. In this linear sense then, the degrees of freedom of an axle become coupled through the creep forces. The resulting stability of the system may be established by including these coupling terms in the equations of motion.

Many authors have approached the creep problem differently. Cooperrider, for example, (Reference 2), uses the relationships of Johnson, (Reference 3), which uses resultant creep, hence, is nonlinear in the creep variable. Law, on the other hand, (Reference 4), uses linear creep but adds spin creep and gyroscopic terms.

All authors agree, however, that theoretical creep values may differ by a significant amount from experimental values. This amount may be a factor of 3, the theoretical values being too high by this factor.

With this in mind, consider the wheel-

rail forces to be a linear function of the creep in each direction and ignore spin creep and its associated coupling with lateral motion. The typical axle is shown in Figure 17 with degrees of freedom noted.

The relative velocity at the contact point of wheels A and B in the longitudinal and lateral directions is given by

$$V_{AX} = V - a\dot{\theta}_z - \frac{V}{r_o} (r_o + \alpha y)$$

$$V_{BX} = V + a\dot{\theta}_z - \frac{V}{r_o} (r_o - \alpha y)$$

$$V_{AY} = -V\theta + \dot{y}$$

$$V_{BY} = -V\theta + \dot{y}$$

where  $V$  = forward velocity. If the creep coefficient is constant, the forces are given by

$$F_{AX} = \frac{V_{AX}}{V} f_c \quad \text{etc.}$$

An additional term called the gravitational stiffness is due to the slope of the wheel. Consider the Figure 18. If the axle displaces laterally, the angle of the normal force changes by an amount

$$\Delta\alpha = y \frac{\alpha}{a}$$

the force due to  $F = -\frac{2N\alpha}{a} y$

Therefore, the basic phenomena occurring are easily visualized even though they are indeed complex. The exact representation of creep seems unlikely since so many factors

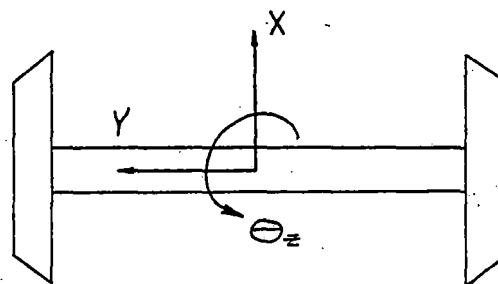


Figure 17-Axle degrees of freedom

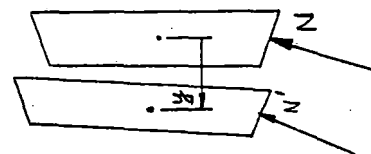


Figure 18-Gravitational stiffness

influence these forces.

It should be remembered that the purpose of this study is to establish a realistic hunting speed using relatively simple creep force representation so that parametric variations of the truck and car parameter can be made to determine the hunting speed sensitivity with respect to these parameters. The absolute hunting speed is of secondary importance.

#### CONCLUSIONS

As mentioned previously, the program is incomplete. Analyses are in progress but not far enough to make a definite conclusion regarding validity of the approach taken in this study. Suggested schedule of final verification runs using actual runs of the car on the revenue tract are presented in Table II. A test verified analytical model is in existence now. Its accuracy, in terms of hunting speed analysis, is yet to be verified by the operations test. The need to "fine tune" the model closer to test data will be determined by results of the hunting analyses. In retrospect, we feel that the truck static test was a very valid test. The car body modal test probably is not re-

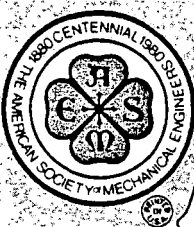
quired for most of the cars because their frequencies are too high for participation in the hunting phenomenon.

It is conceivable that the scope of investigations of other car-truck systems can be reduced without losing its validity.

#### REFERENCES

1. American Steel Foundries Participation in AAR/RPI/FRA Track Train Dynamics Program - Parts 1-7.
2. N. K. Cooperrider, "The Hunting Behavior of Conventional Railway Trucks," Presented at ASME, December 1970, New York Paper No. 70-WA/RR-2.
3. P. J. Vermeulen and K. L. Johnson, "Contact of Nonspherical Elastic Bodies Transmitting Tangential Forces," Journal of Applied Mechanics, Vol. 31, Trans. ASME Vol. 86, No. 2, June 1964, pp. 338-340.
4. E. H. Law, "Nonlinear Wheelset Dynamic Response to Random Lateral Rail Irregularities," Presented at ASME, November 1973, Detroit, Michigan, Paper No. 73-WA/RT-3.





AN ASME PUBLICATION  
\$4.00 per copy \$2.00 to ASME Members

# ASME

THE AMERICAN SOCIETY OF MECHANICAL ENGINEERS  
345 E 47 St., New York, N.Y. 10017

The Society shall not be responsible for statements or opinions advanced in papers or in discussion at meetings of the Society or of its Divisions or Sections, or printed in its publications. Discussion is printed only if the paper is published in an ASME Journal or Proceedings. Released for general publication upon presentation. Full credit should be given to ASME, the Technical Division, and the author(s).

REFERENCE 181

## Characterization and Analysis of the Wheel/Rail Load Environment at the Facility for Accelerated Service Testing (FAST)

**J. M. Tuten**

Research Scientist,  
Assoc. Mem. ASME

**D. R. Ahlbeck**

Principal Research Engineer

Battelle-Columbus Laboratories,  
Columbus, OH

*In 1979, a series of tests were conducted at the Transportation Test Center near Pueblo, Colorado to determine the vertical and lateral wheel/rail loads on the Facility for Accelerated Service Testing (FAST) track. During these tests the wheel/rail loads were measured at seven wayside locations in one of the curved track sections. The loads were measured for a variety of operating conditions and consist configurations. The data were indexed and a detailed statistical data base was constructed. Using this data base, the effects of speed, train direction, rail lubrication and vehicle component variations on the wheel/rail load environment were investigated. Statistics were generated and analyzed. This paper describes the wheel/rail loads test, the development of the data base, the types of statistical formats in which the data are represented, and a brief discussion of some of the test results.*

### INTRODUCTION

The Facility for Accelerated Service Testing (FAST) at the Transportation Test Center (TTC) near Pueblo, Colorado was created by the joint efforts of the Federal Railroad Administration (FRA), the Association of American Railroads (AAR), the Transportation Development Agency (TDA) of Canada, and by the railroads and the Railway Progress Institute (RPI). FAST provides simulated service testing of both track and vehicle components at rates of service much higher than possible under normal revenue traffic conditions.

The facility consists of a 4.8-mile (7.7-km) loop of track divided into sections which provide many variations in track construction. Experiments include both wood and concrete ties, a variety of rail fasteners, both bolted-joint and continuous-welded rail, different rail metallurgies and ballast conditions, on both tangent and curved track.

A test train of four locomotive units and about 75 cars (primarily loaded 100-ton-capacity cars) accumulates 100 to 125 laps around the track loop each night, five nights a week at a normal operating speed of 45 mi/h (72 km/h). At this rate, the test train subjected the track to over 150 million gross tons (MGT) of loading between September 1976 and December 1977. This is about seven times faster than possible on a revenue freight track. Numerous measurements of track and vehicle characteristics have been made at planned intervals to assess component performance and to establish rates of wear and degradation.

An important aspect of the FAST experiments is a statistical definition of the wheel/rail load

environment to which the track and vehicles are subjected. The load environment has been defined for typical revenue traffic in North America by several recent studies (1-3). However, the FAST train provides a unique, and in some respects, a more severe, load environment.

Instrumented wheelsets have been used to record wheel/rail loads under individual rail cars (4,5). To record loads under the complete train, wayside instrumentation was utilized in the "FAST Wheel/Rail Loads Test" conducted during the summer of 1979. After completion of these tests, a data base was generated to allow a statistical presentation of results. The wheel/rail loads data base developed during this effort is one of the most comprehensive developed to date. By combining a high degree of program flexibility with a very detailed indexing system, statistics were generated for a large number of individual test populations. This paper describes the wheel/rail load test, the development of the data base, the types of statistical formats in which the data are presented, and a brief discussion of some of the test results.

### TEST DESCRIPTION

The FAST Wheel/Rail Loads Test was the first comprehensive attempt to characterize the wheel/rail load environment at FAST. At the time the test was conducted, the FAST Facility had been in operation for almost three years and had accumulated just over 400 million gross tons of traffic. By conducting a specific series of tests to determine the wheel/rail load environment, test variables which might affect the load environment could be controlled. The overall objectives of the tests were:

- o Determine the lateral and vertical wheel/rail load versus speed relationship for the FAST consist on curved track;
- o Determine the effects of train operating characteristics (i.e., buff, draft and drift) on wheel/rail loads at specified speeds on curve track;

Contributed by the Rail Transportation Division of THE AMERICAN SOCIETY OF MECHANICAL ENGINEERS for presentation at the Winter Annual Meeting, November 15-20, 1981, Washington, D.C. Manuscript received at ASME Headquarters July 1, 1981.

- o Assess the dynamic performance of a 100-ton hopper car over various sections of the FAST Track, utilizing an instrumented wheelset;
- o Assess the effects of car component wear on vehicle dynamic performance;
- o Determine the differences in wheel/rail loads as a function of truck type;
- o Obtain load data to aid in establishing a correlation between FAST rail wear and predictive rail wear models being developed under the Track Train Dynamics Program; and
- o Develop correlation between wheelset vertical and lateral load data and wayside wheel/rail load data.

Runs in 59 distinct configurations were completed during the test program. Wayside data were recorded for 12 of these test configurations for a total of 101 train passes by the instrumented wayside site. Table 1 shows the run numbers and test parameters for each of the runs for which wayside data were recorded.

TABLE 1. FAST WAYSIDE DATA RUNS

Run No.	Number of Laps	Speed (mi/h) (km/h)	Train Direction	Test Date	Operating Conditions (Sect. 07)
5	6	30 (48)	CW	6/19	Draft
6	6	34 (54)	CW	6/19	Draft
7	6	34 (54)	CW	6/19	Buff
8	6	34 (54)	CW	6/19	Drift
9	20	45 (72)	CW	6/20	Draft
10	6	30 (48)	CCW	6/21	Draft
11	6	34 (54)	CCW	6/22	Draft
12	7	34 (59)	CCW	6/22	Buff
13	6	34 (54)	CCW	6/22	Drift
14	20	45 (72)	CCW	6/20	Draft
15	6	45 (72)	CCW	6/18	Draft un-lub*
16	6	45 (72)	CW	6/18	Draft un-lub

\*Curve lubricators inoperative.

#### Test Train Consist

The abbreviated train consist for the wheel/rail loads test was made up of cars from the FAST train. The consist was well documented and included from 54 to 56 cars pulled by three or four locomotives, depending on the particular test run. The majority of the test train consisted of loaded 100-ton hopper cars. Although the makeup of the consist was constant for each test run, it did vary slightly from test to test. The last twelve cars of the consist, however, were part of a test to determine the effect of car weight on the wheel/rail load environment, and maintained their position in the consist and in relation to each other for the duration of the test. This group was made up of 3 110-ton hopper cars, 3 100-ton hopper cars, 3 66-ton hopper cars, and 3 empty hopper cars, respectively. The different cars of the consist (excluding the weight test group) were equipped with various mechanical equipment and truck types to determine the effect such equipment would have on the wheel/rail load environment. Complete details of the results from this portion of the test are not presented in this paper. The data may be found in Reference 6 and will be reported in greater detail after further analysis has been completed.

#### Wayside Test Site Description

The wayside instrumentation was located in Section 7 of the FAST track, shown in Figure 1. This 1177-foot (359 m) CWR track section is a 5-degree (349 m radius) curve with 4-1/2 inches (11.4 cm) of superelevation and conventional wood tie construction. Seven irregularly-spaced locations were instrumented in this track section. Vertical and lateral strain gage load-measuring circuits were installed on both rails at each location by TTC personnel. The standard ORE "chevron" gage pattern on the rail web was used to measure vertical loads, while a Battelle-designed gage pattern on the rail base was used to measure lateral loads (7). The strain gage circuits were calibrated by applying known vertical and lateral loads through a special loading fixture and comparing the rail circuit response voltage with the known input loads. Values were thereby established in engineering units for step voltage changes from resistor shunt calibrations in each circuit. Four 14-channel signal-conditioning amplifier units utilizing frequency-division multiplexing were positioned at the trackside to minimize cable lengths to the strain gages. The multiplexed signals were recorded on analog tape at a central location for later processing.

#### Post-Test Data Reduction

Tape-recorded analog signals were converted to a digital format by a microprocessor-controlled field data reduction system. The multiplexed signals were first demodulated, then lowpass filtered at 300 Hz through 4-pole Bessel filters before analog-to-digital conversion. The microprocessor determined the peak value for each channel and each passing axle, converted the resulting voltage-related number to engineering units, and stored the peak value for printing and recording on digital cassette tape. The printer produced tables of peak values of lateral (L) and vertical (V) loads and L/V ratios for each axle passing each site.

Digital cassette tapes were then read into Battelle's CDC Cyber 74 computer system for further processing. Data were validated by comparing tabular values with oscillograph recordings to assure that signal quality was good on individual channels, that noise or tape drop-out problems were not encountered, and that axles of the train were not missed. Digital data were edited and corrected where necessary, and the validated data set was stored in an addressable file indexed by run number and multiplex number.

The next step in processing was to construct a file of indexed and sorted data values. A seven-digit index number was used to define the location (measurement site), car number, axle number, and run/lap number for each associated set of vertical and lateral load and L/V numbers. This keyed data base was then used as the basis for different statistical manipulations to produce both numerical and graphical formats.

#### Statistical Data Formats

In order to study the effects of various parameters, the data were organized into several statistical formats. These included numerical values of means and standard deviations, and plots of probability densities and cumulative probability distributions. By using the keyed data base, individual populations of data points could be examined if desired, such as the lateral loads at a specific crib number produced by Axle No. 1 of Car

# THE FAST TRACK

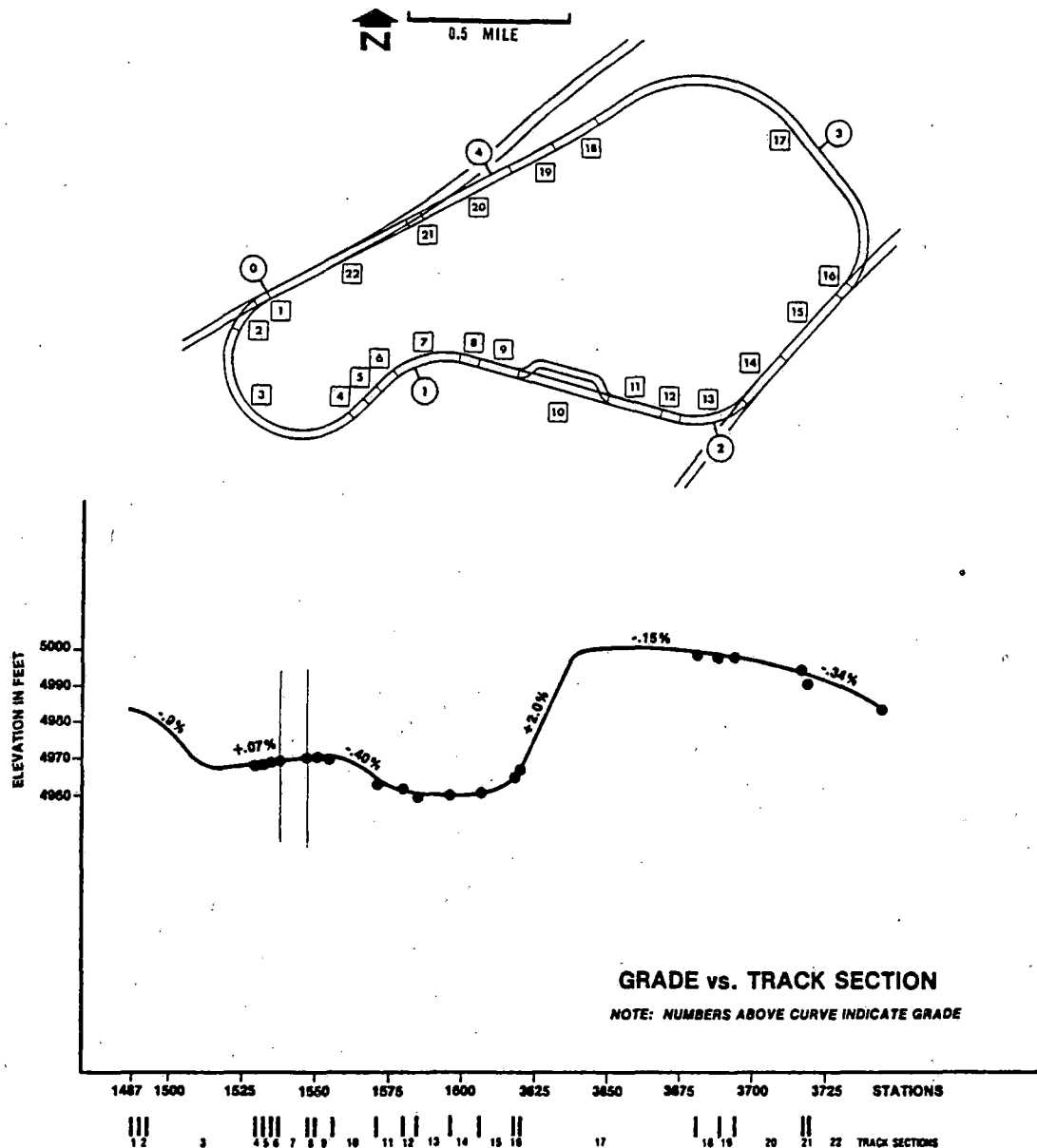


FIGURE 1. FAST TRACK LAYOUT

No. 013 on the high rail. Combinations of populations were used to provide a more substantial data base, such as lumping together the lateral loads of all lead-outer wheels (Axles 1 and 3) from all 7 measurement sites for all 100-ton hopper cars.

The statistical calculations were made by dividing the total expected data range into 200 equal intervals (bins) and summing the number of peak values under a specific key number (or combination of key numbers) occurring within this interval. Using the resulting "bin count" numbers, frequency-of-occurrence histograms (probability density) and frequency-of-exceedance plots (probability distribution) were generated through computer graphics routines.

An example of the frequency-of-occurrence histogram is shown in Figure 2. This plot shows the ratio of the number of peak loads within each of 50 1.2-kip (5.3 kN) load intervals which cover the expected vertical load range of 60 kips (267 kN).

By choice, the original 200 bins have been grouped by 4's. It is important to note that the quantitative results for the histogram depend on the selected load interval (bin size) and are therefore not unique. Increasing the load interval (reducing the number of bins) will increase the number of occurrences at a particular load level. This improves the averaging used for the estimate, but reduces the resolution.

Another useful format is the frequency-of-exceedance plot shown in Figure 3. This plot allows a quick determination of how many axles of the particular population will produce loads or L/V ratios greater than a given level. This format is of particular value in both fatigue and life cycle predictions. To produce this format, the number in each succeeding bin is subtracted from the total number over the range of the variable. The results are plotted on a normal probability graph so that a

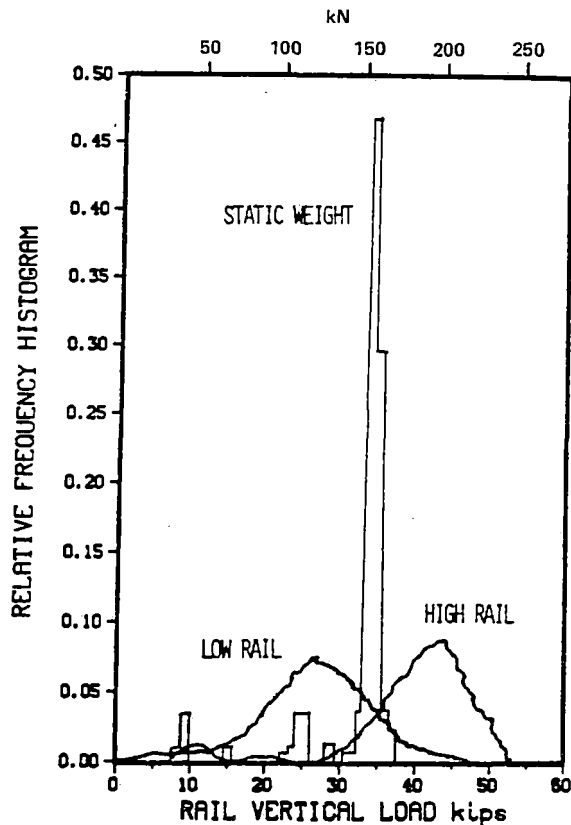


FIGURE 2. VERTICAL LOAD RELATIVE FREQUENCY HISTOGRAM

Gaussian distribution will appear as a straight line.

The interrelationship between lateral and vertical loads (not simply the L/V ratio) is of great interest, and is best characterized by frequency-of-exceedance of lateral load versus vertical load, as shown in Figure 4, or by the joint probability distribution of lateral and vertical loads, as shown in Figure 5. To calculate the joint frequency-of-exceedance, the load ranges of interest were first determined. A lateral load range of -10 to +28 kips<sup>1</sup> (-44 to +124 kN) and a vertical load range of 0 to 60 kips (267 kN) were chosen. These ranges were then divided into 20 equal intervals (bins) to give a 20 x 20 matrix of load pairs. The total number of loads occurring in each bin of the matrix was then tabulated. Using this frequency-of-occurrence matrix, the joint probability distribution of lateral load versus vertical load and the conditional distribution (probability of L for a given V) were calculated and used to generate the different plot formats of Figures 4 and 5. Figure 5 shows that two populations of cars are apparent: first the loaded cars centered near 40 kips (178 kN), and then the three empty cars at the end of the train, centered near 10 kips (44 kN) of vertical wheel load. As a further example of this format, results from the low rail are given in Figure 6. Here, the lateral loads from two distinct populations of axles--leading and trailing--under the loaded cars are evident.

<sup>1</sup> A positive lateral load is defined as spreading the rails.

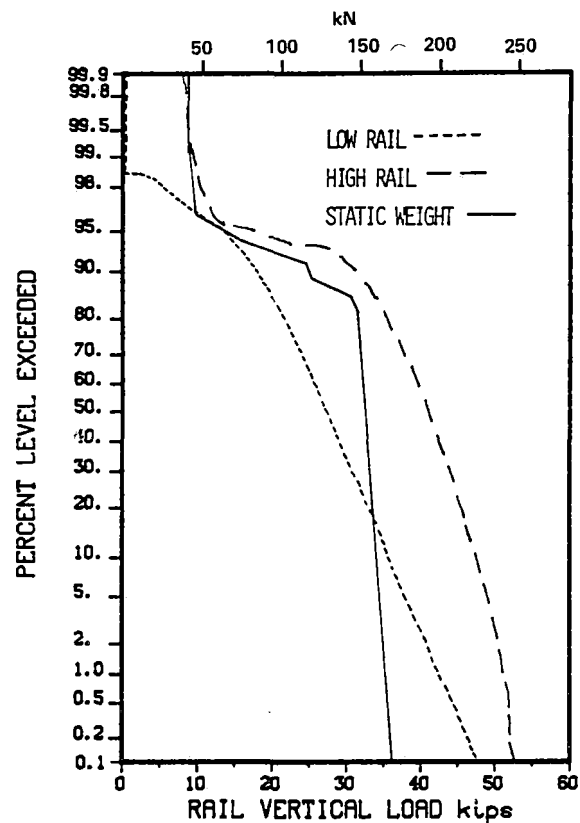


FIGURE 3. VERTICAL WHEEL LOAD EXCEEDANCE DISTRIBUTION FUNCTION.

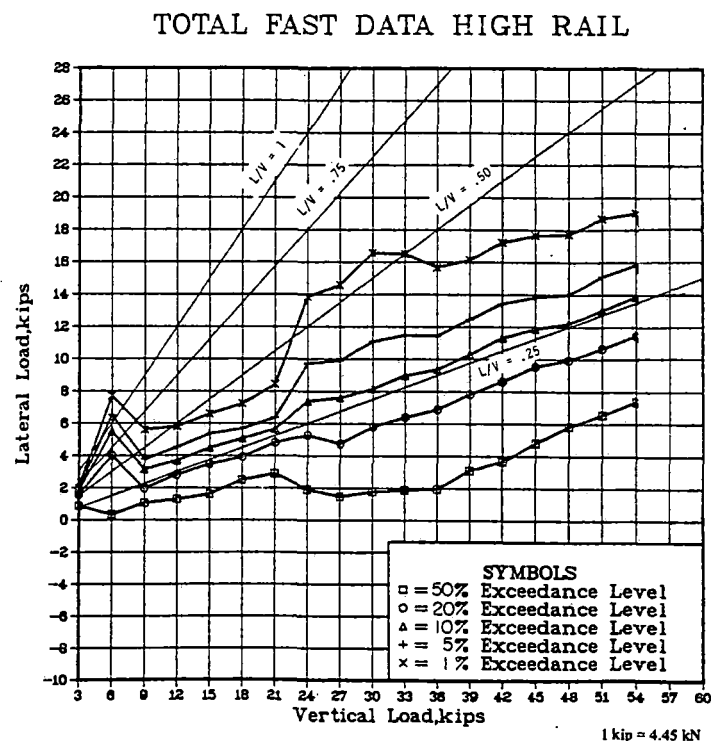


FIGURE 4. LATERAL LOAD EXCEEDANCE LEVELS FOR HIGH-RAIL FAST DATA

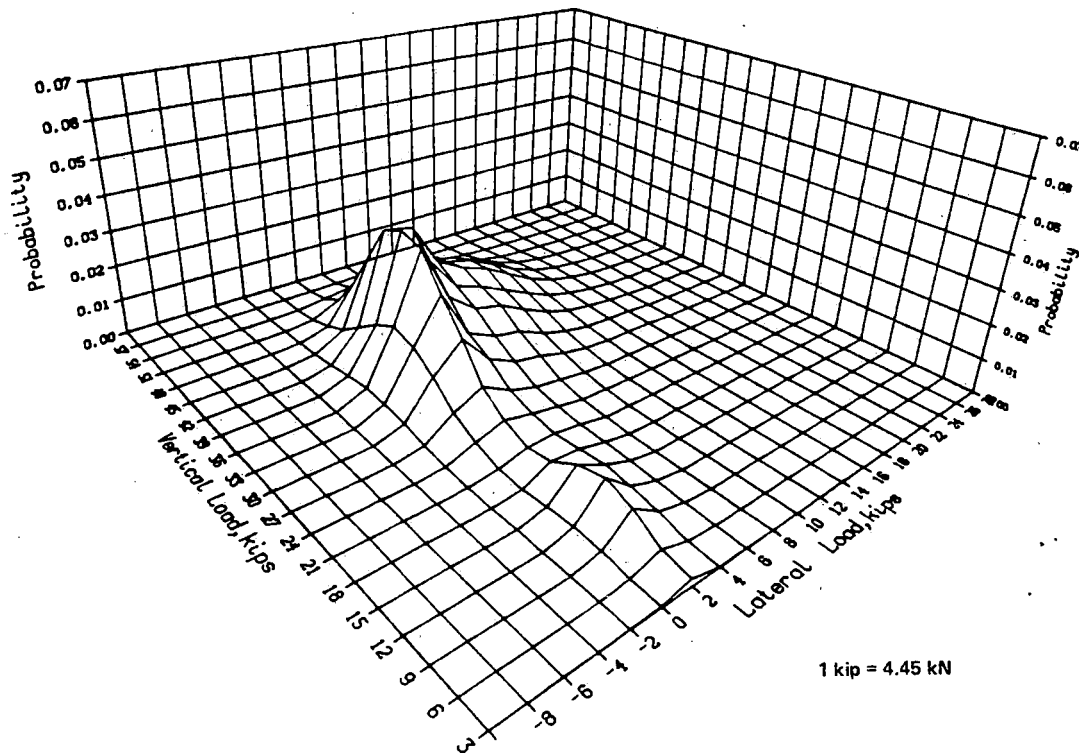


FIGURE 5. JOINT PROBABILITY DISTRIBUTION OF LATERAL AND VERTICAL LOAD FOR HIGH RAIL FAST DATA

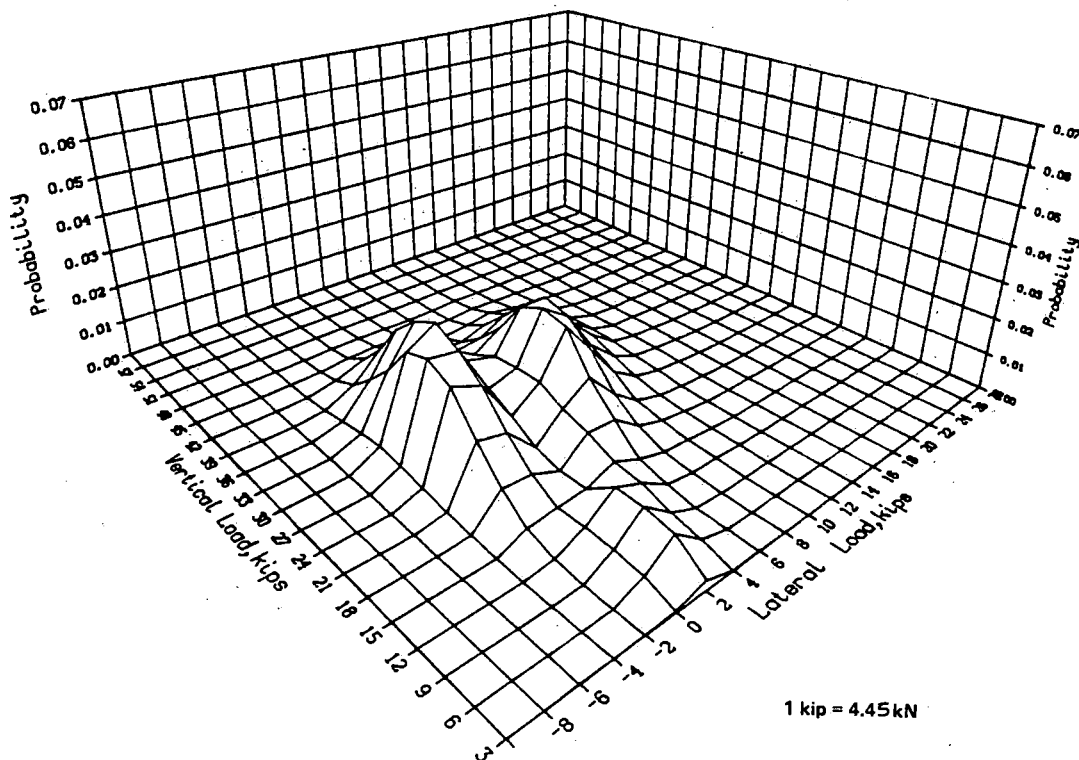


FIGURE 6. JOINT PROBABILITY DISTRIBUTION OF LATERAL AND VERTICAL LOAD FOR LOW RAIL FAST DATA

## EXPERIMENTAL RESULTS

Experimental wheel/rail load data can be understood best when compared with and used in conjunction with a predictive model. Figure 7 shows the lateral loads predicted for a 100-ton hopper car in steady-state curving. Loads for each of the four wheels of a standard "three-piece bogie" were calculated using Battelle's nonlinear computer code called SSCUR2, which is based on the wheelset curving equations of Newland (8). This program accounts for the nonrigid, lozenging behavior of the freight car truck, and includes the wheel adhesion limit, flange contact, rail lateral stiffness, and suspension stops (9). Mean values of lateral load from instrumented wheelset measurements made by IITRI are shown in Figure 7 to provide verification of these predictions.

In steady-state curving, the leading wheelset of a freight car truck will assume a positive angle of attack of approximately one-half degree, resulting in lateral creep forces on both rails directed toward the center of curvature. On a 5-degree (349 m radius) curve, the lead-outer wheel will assume flange contact with the high rail, resulting in a large oppositely-directed lateral force. This flange force may be 50 to 75 percent higher than the measured net lateral force, which is the vector sum of the flange and creep forces. As a result, the lead-outer wheel under a heavy freight car produces net lateral forces on both rails on the order of 10,000 lb (44 kN), tending to spread the rails apart.

The trailing wheelset assumes an almost neutral angle of attack, and consequently the lateral creep forces on this wheelset are substantially lower. At speeds above the "balance" speed (speed at which the

centrifugal and gravity force vectors cancel), the trailing-outer (high-rail) wheel may begin to assume flange contact, but the net lateral force on the rail is low compared with the leading-outer wheel.

In using the predictive model to explore the effects of wheelset and rail parameters, the adhesion limit (the maximum horizontal force vector as a percentage of the vertical, or normal, wheel load that can be sustained without slip) has the most noticeable effect of the steady-state lateral wheel loads. An adhesion limit of 0.25 and one-half the theoretical Kalker creep coefficients (10) were used in calculating the results presented in Figure 7.

### Comparing Wheelset and Wayside Loads

Wheel loads were recorded from an instrumented wheelset at the leading axle position under one of the 100-ton hopper cars at the rear of the FAST train consist (11). In addition to mean and standard deviation load values, continuous load-versus-distance plots were provided by IIT Research Institute for typical runs through the Section 7 curve. Pulses from wayside location detector targets provided identification of the instrumented wayside sites on these plots and allowed a direct comparison between the two transducer systems.

Two 45-mi/h (72 km/h) runs, one in the clockwise, the other in the counter-clockwise loop directions, were chosen to compare the wheelset and wayside values in Section 7. Pronounced oscillations in vertical loads and (particularly) high-rail lateral loads were noted in the instrumented wheelset load plots. Lateral high-rail wheel loads ranged up to 21,000 lb (93 kN) peak, and 14,000 lb (62 kN) peak-to-peak, on this leading wheelset with the primary oscillations on a 27 to 33 ft (8 to 10 m) wavelength. At this speed, these wavelengths correspond to a 2.0 to 2.4-Hz frequency, a combination of roll and yaw modes of car body motion (4,5). The lateral load peaks were in-phase with the vertical load peaks on the high rail. Low-rail lateral load oscillations, on the other hand, were less than 4,000 lb (18 kN) peak-to-peak in amplitude. The high-rail load oscillations were somewhat more pronounced in the clockwise direction of running.

In comparing simultaneous track and wheelset load measurements, the high-rail lateral load circuits appeared to read an average of 2,300 lb (10 kN) lower than the wheelset (between 15 and 25 percent of the mean load), with a standard deviation of over 2,700 lb (12 kN). However, if a spatial tolerance of 2 ft (1.2 m) is allowed on the location of wayside sites relative to the wheelset load trace, a much better comparison between the rapidly-varying wheelset load signals and the short load samples from the wayside transducers is found. This tolerance accounts for location detector system response time. Lateral loads then compare within 500 lb (2.2 kN) with a standard deviation of less than 1,000 lb (4.4 kN). This is illustrated in the wheelset time history shown in Figure 8 in which the wayside data has been superimposed.

A similar comparison between wayside and wheelset vertical loads was also made as shown in Figure 8. Good correlation between low-rail track and wheelset measurements was found, with a zero mean difference and a standard deviation of 3,700 lb (16.5 kN). Again, the scatter is most probably due to the spatial uncertainty in defining the exact location of the wayside site on the wheelset load

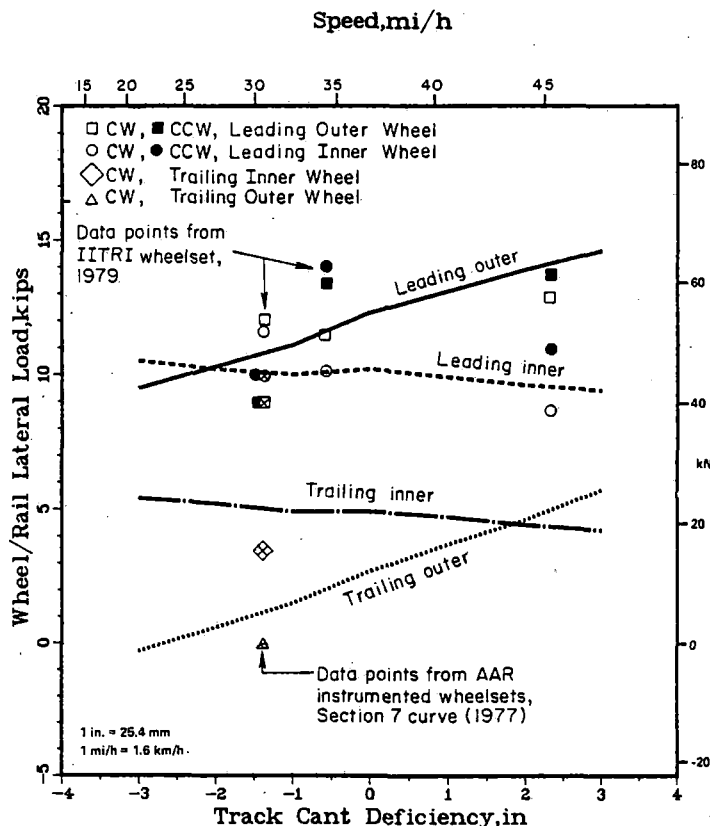


FIGURE 7. PREDICTED NET LATERAL WHEEL/RAIL LOADS UNDER 100-TON HOPPER CAR ON 5-DEGREE CURVE WITH 4-1/2-INCH SUPERELEVATION

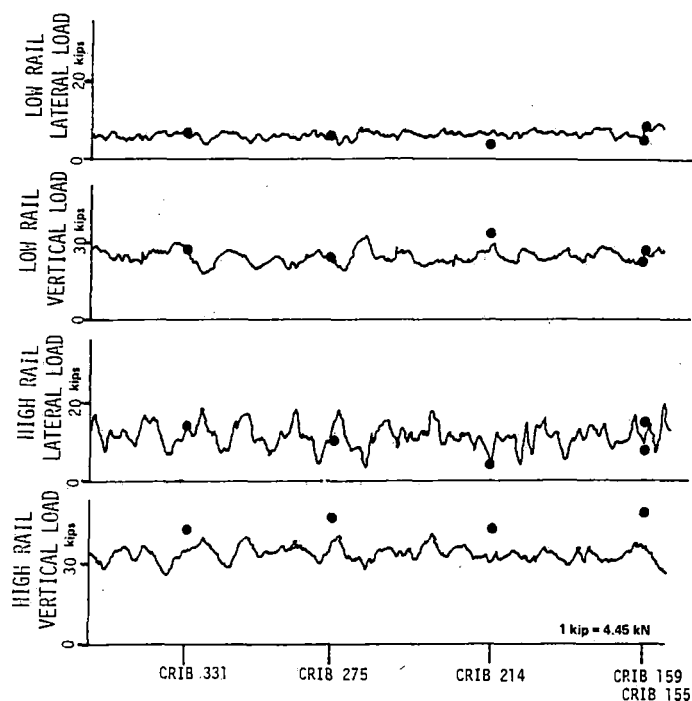


FIGURE 8. SAMPLE WHEELSET TIME HISTORY FROM RUN 9, LAP 14 WITH CORRESPONDING WHEELSET DATA

trace. High-rail vertical load measurements, however, showed the track transducers reading a consistently higher value, on the average 9,400 lb (42 kN). The track measurements showed the nearly-equal shift in load from low rail to high rail expected at this speed (roughly 4 inches, 102 mm of cant deficiency)<sup>1</sup>. While this difference is yet unresolved, it may indicate some nonlinearity or clipping in the higher range of wheelset load measurements.

A more important factor brought out by the load comparison, however, was the effect of wayside transducer spacing on the measured load spectra. Six of the seven wayside sites were located by TTC at a spacing ranging from 89 to 99 ft (27 to 30 m), the seventh being located one truck wheelbase from one of the center locations. The 27 to 33 ft (2.0 to 2.4 Hz) oscillation in high-rail lateral force at 45 mi/h therefore tends to "synchronize" with this wayside site spacing. In the clockwise direction, four of the high-rail wayside sites fell at the low portion of the wheelset load cycle, while the remaining three fell near the midpoint. In the counterclockwise direction, all but one high-rail site fell near the midpoint of the oscillation, and the remaining one fell near a load maximum. It is quite apparent that the average wayside lateral force on the high rail should be substantially lower than average wheelset lateral force in the 45 mi/h clockwise runs. This illustrates the need for randomly-chosen locations to define the wheel/rail load environment from wayside measurements with any statistical confidence (2).

While the design superelevation of the Section 7 curve is 4-1/2 inches (114 mm), the intersection of the high- and low-rail mean vertical loads occurs near 30 mi/h (48 km/h), indicating an actual superelevation of approximately 3 inches (76 mm). Recent geometry measurements show a variation between 3 and 4 inches.

#### Test Population Statistics

The high- and low-rail vertical load statistics for a combination of data from all test runs were shown in Figures 2 and 3, along with comparative plots of the static (weighed) wheel loads. The average wheel load measured from load scales was 30,900 lb (137 kN) with a standard deviation of 6300 lb (28 kN) for the test consist, while the mean vertical load from the wayside transducers in Section 7 was 32,200 lb (143 kN) with a slightly higher standard deviation of 7,400 lb (33 kN) as a result of curving and car dynamics.

Similar plots for the lateral loads and L/V ratios are given in Figures 9 and 10. The lateral load distributions are made up of two distinct populations, leading and trailing wheelsets in a truck, as shown by the two straight-line portions of the exceedance distribution plots which blend rather smoothly into one another. The mean lateral load was  $4,700 \pm 4,400$  lb<sup>1</sup> ( $21 \pm 20$  kN) on the high rail, and  $3,000 \pm 4,700$  lb ( $13 \pm 21$  kN) on the low rail. These statistical descriptors do not reflect the basic phenomenon shown in Figure 7, that the leading wheels generate high lateral curving forces, and the trailing wheels low forces. For that reason, leading and trailing wheelsets in a curve should be handled as separate data populations. Corresponding L/V ratios were  $0.12 \pm 0.12$  on the high rail,  $0.11 \pm 0.18$  on the low rail.

The data presented represent the load environment under the modified FAST consist in Section 7, excluding the three 110-ton cars in the consist not normally part of the FAST train for which the data were not combined in the overall statistics. Speeds of 30, 34 and 45 mi/h (48, 55 and 72 km/h) are included in the data set, where the normal operating speed of the FAST train is 45 mi/h (72 km/h). As noted previously, data at 45 mi/h may be skewed because of speed effects with relationship to transducer spacing and the dynamic response of typical 100-ton hopper cars.

#### Site Variations

Load measurements were made at seven different locations on the test curve. The statistics for the different sites were combined for several of the parameter variations in order to increase the population size and the statistical confidence in the results. Therefore, it was desirable to know the variation in the load statistics from site to site.

In Figure 11, the high- and low-rail vertical load exceedance functions are plotted for each measurement site from Run 9, the clockwise, 45-mi/h (72 km/h) run. The standard deviation of the mean loads from seven sites was 4 percent of the average mean load for the high rail vertical load, and 10 percent of the average mean load for the low rail vertical load.

The exceedance functions for the high-rail lateral load at each site during Run 9 are shown in Figure 12. The standard deviation of the mean loads from seven sites was 23 percent of the average mean load for the high rail. Similar results were obtained for the low rail.

#### Directional Effects

One parameter investigated in this study was the effect of train direction on the wheel/rail loads. After a number of test runs around the FAST loop in the clockwise direction (in which Section 7

<sup>1</sup> mean  $\pm$  1 standard deviation

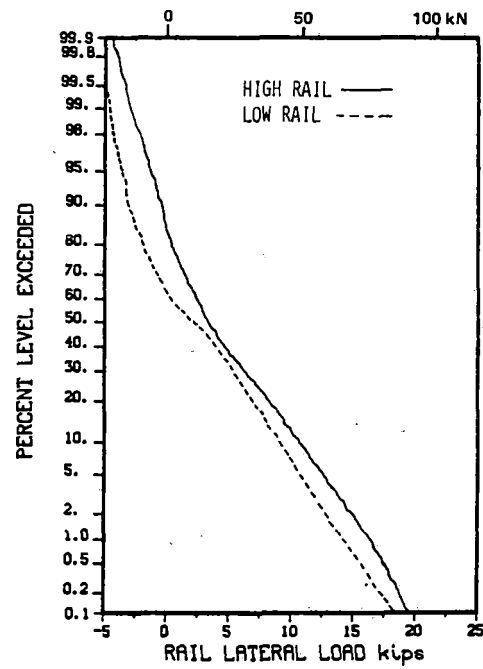
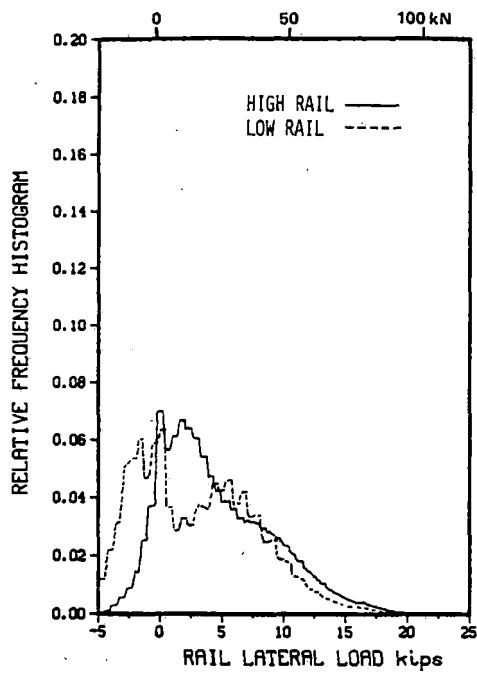


FIGURE 9. LATERAL LOAD STATISTICS FOR TOTAL FAST TEST

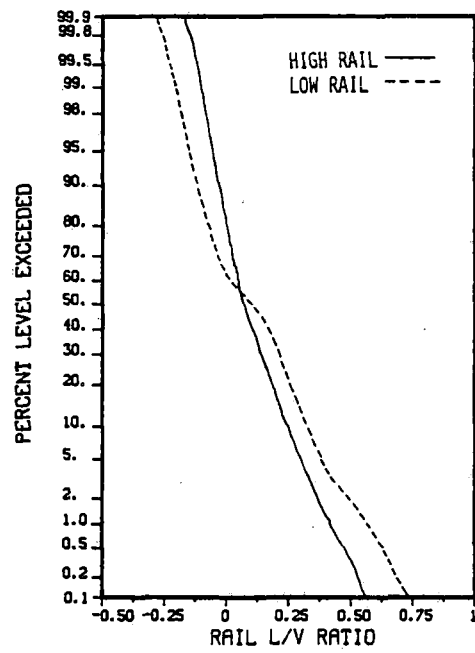
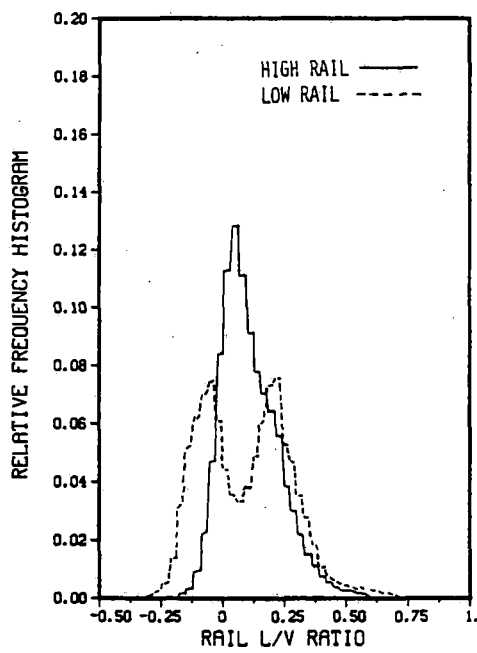


FIGURE 10. L/V RATIO STATISTICS FOR TOTAL FAST TEST



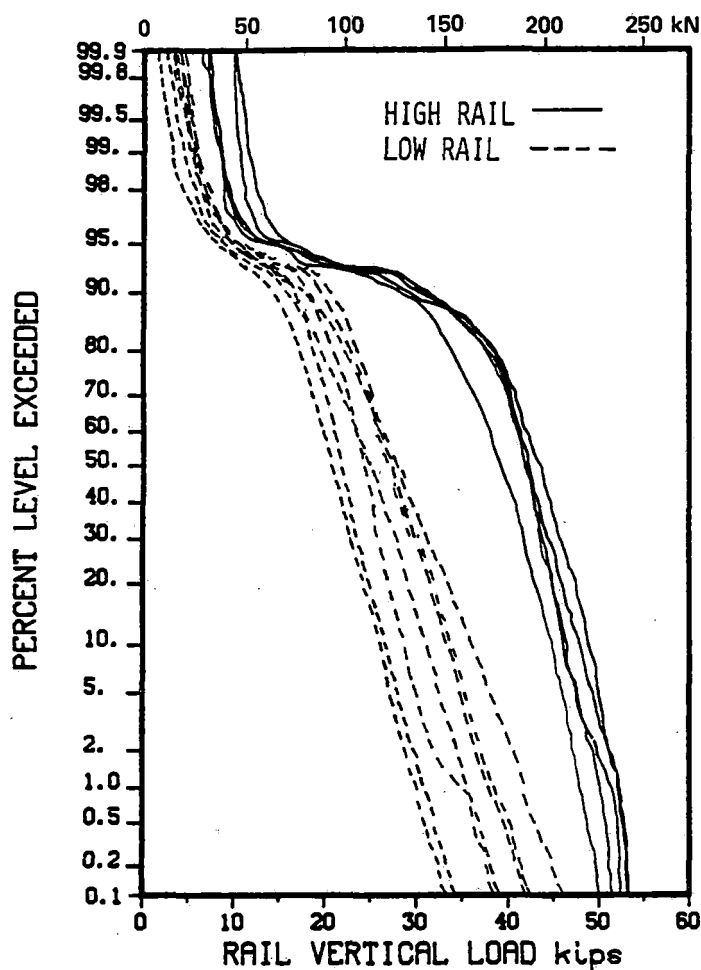


FIGURE 11. VERTICAL LOAD EXCEEDANCE DISTRIBUTION FUNCTIONS FOR EACH SITE (RUN 9 DATA)

is a left-hand curve), the test train was wye'd to run in the same orientation of cars, but in the opposite, counterclockwise direction. The effects of direction, as "seen" from the wayside transducers, is dramatically evident in Figure 13, which shows the lateral load exceedance plots for leading axles alone. As discussed previously, the major cause of this difference was the coincidence of hopper car dynamic oscillations at 45 mi/h (72 km/h) with the average spacing of the wayside measurement sites. This effect is less critical at other speeds and with a mixture of freight car types. Wheelset load measurements (11) showed a modest difference in average leading-axle lateral loads depending on the direction, with the counterclockwise runs up to 4,000 lb (18 kN) higher, about 30 percent, than the clockwise runs. In addition, there were several cars which exhibited a definite directional bias in their curving performance. The directional bias may be due to asymmetries in wheel profile and/or truck wear. These asymmetries were substantial enough to skew the truck into a "crabbing" orientation and produce a strong directional bias for the individual trucks, which in turn affected the overall load statistics.

No significant difference in vertical wheel load levels from runs in the two directions was noted in the wayside data.

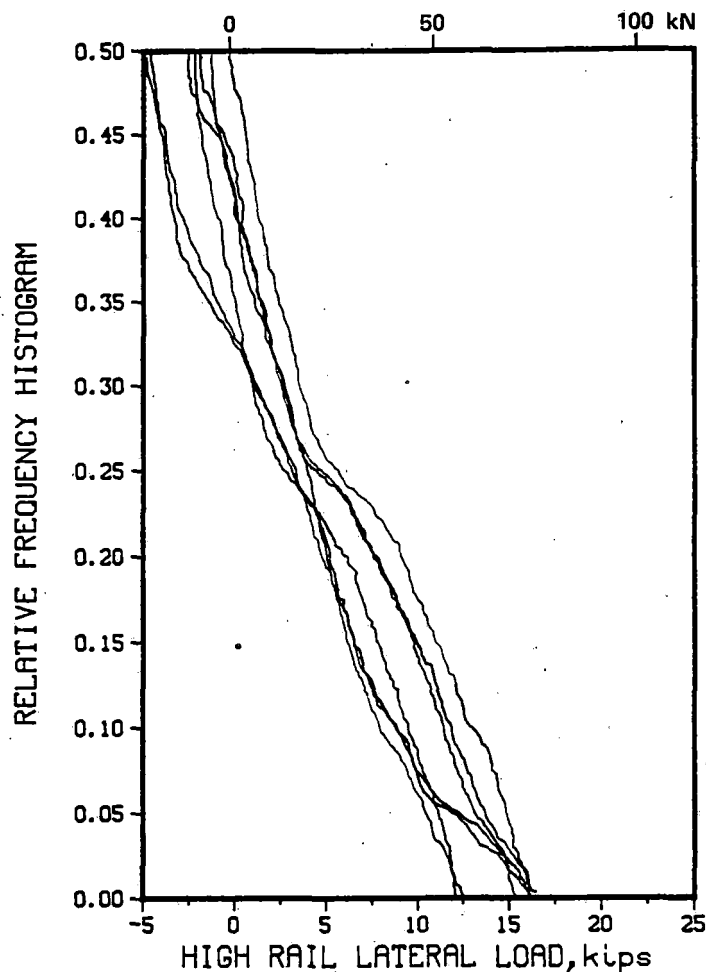


FIGURE 12. LATERAL LOAD EXCEEDANCE DISTRIBUTION FUNCTIONS FOR EACH SITE (RUN 9 DATA)

#### Speed Effects

Test runs were conducted at three different speeds, 30, 34 and 45 mi/h (48, 54 and 72 km/h), in order to determine the effects of train speed on the load environment. High and low rail vertical load statistics are shown in Figure 13 for the clockwise runs, and the weight shift to the outer rail due to increased speed can be seen. (The knee in the curve at the 92 percent level merely reflects the few empty cars in the train.)

The predicted shift in lateral loads to the high rail with increased train speed is shown in Figure 7. Both wheelset and wayside measurements of mean lateral force confirm this effect. It is interesting to note, however, that an apparent dynamic resonance occurs at 34 mi/h (54 km/h). Since both high- and low-rail forces on the leading axle are higher than predicted, this phenomenon may be associated with wheelset angle of attack and truck yaw angle in the counterclockwise direction, where the Section 7 right-hand curve immediately follows a left-hand curve. (In the clockwise direction, Section 7 is preceded by a tangent section.)

The exceedance plots of Figure 14 for all cars of the consist, which includes both leading and trailing wheels on the high rail, illustrate the expected shift in lateral load to the high rail with

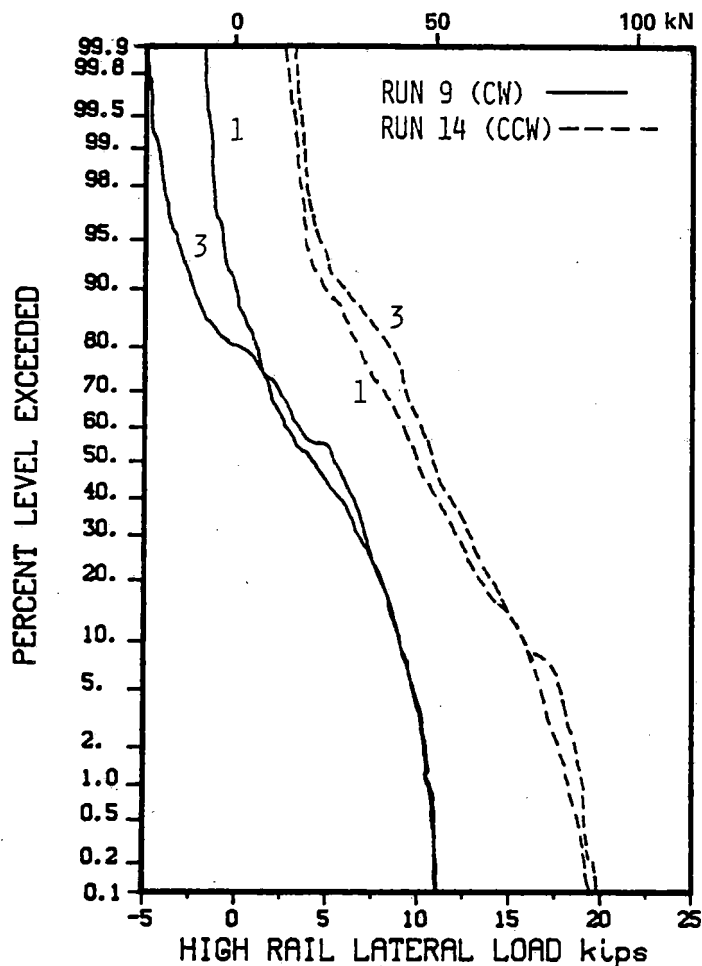


FIGURE 13. HIGH-RAIL LATERAL LOAD EXCEEDANCE DISTRIBUTION FUNCTION FOR EACH LEAD AXLE IN THE CW AND CCW DIRECTION

speed, with no evidence of higher loads at 34 mi/h. This is further evidence that leading wheelset angle of attack is the primary cause of higher lateral loads at this speed.

#### Other Test Variables

A number of other test variables were investigated during the FAST Wheel/Rail Loads Test. These included flange lubrication on the curve, train handling effects such as draft and buff loads, different car weights, truck parameters such as centerplate diameter, and radial truck performance. Results from these different parameter variations are under evaluation and will be reported in the near future.

#### CONCLUSIONS

The load environment at FAST, particularly the vertical loads, was more severe than anticipated. Train speed was found to have a strong influence on loads, due partly to the shift in loads to the high rail at higher cant deficiencies, and also due to car dynamic effects. Some directional differences in lateral loads were noted in the Section 7 curve, apparently as a result of different curve entry conditions—a tangent section from one direction, a reverse curve from the other direction.

One important conclusion from these tests is that randomized locations for wayside transducers

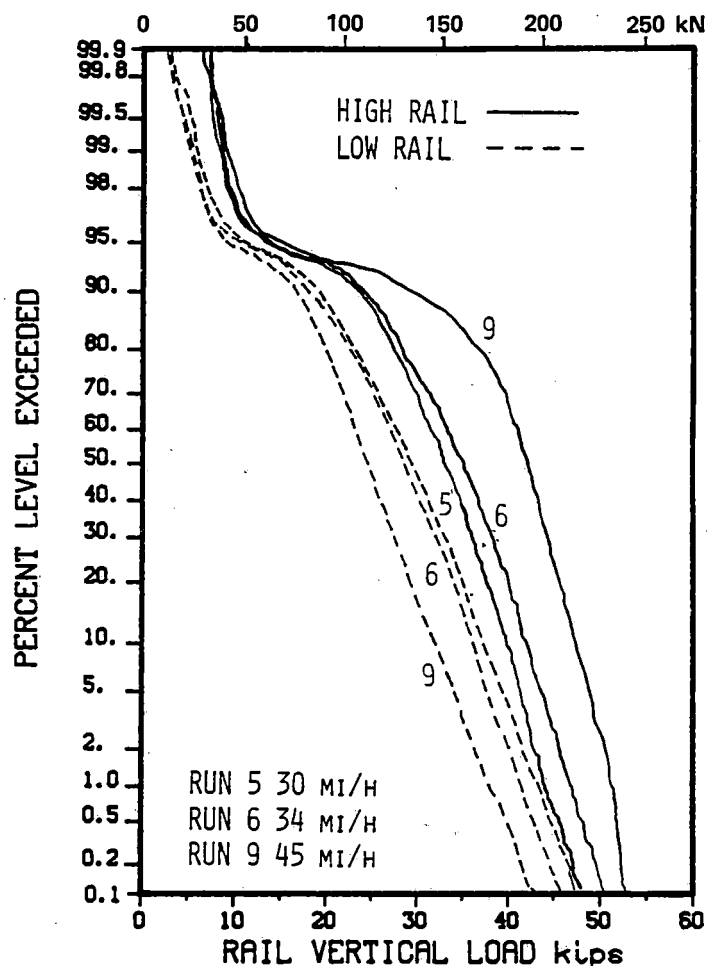


FIGURE 14. HIGH AND LOW RAIL VERTICAL LOAD EXCEEDANCE DISTRIBUTION FUNCTIONS AT DIFFERENT SPEEDS

are necessary to reduce a chance synchronization with the predominant vehicle load oscillations, which may result in skewed statistical results under certain conditions. To define the statistical aspects of the load environment, random placement of at least seven transducers within a homogeneous section of track is recommended for statistical confidence in results (2,3).

#### ACKNOWLEDGEMENTS

This paper is based on the authors' participation in the "FAST Wheel/Rail Loads Test" conducted during June-July, 1979, at the Transportation Test Center, Pueblo, Colorado. This initial work was funded by the Federal Railroad Administration under Contract DTFR53-80-C-0078 and by the Transportation Systems Center under Contract DOT-TSC-1595. During this test, the authors assisted the TTC staff during the installation and calibration of selected wayside sites on the FAST track and monitored the recording of wheel/rail load data during the tests.

Appreciation is expressed to Mr. Howard Moody of the Federal Railroad Administration and to Mr. Harold Harrison of Battelle for their assistance in completing this study, and to Dr. Milton Johnson of IITRI for providing comparative wheelset data.

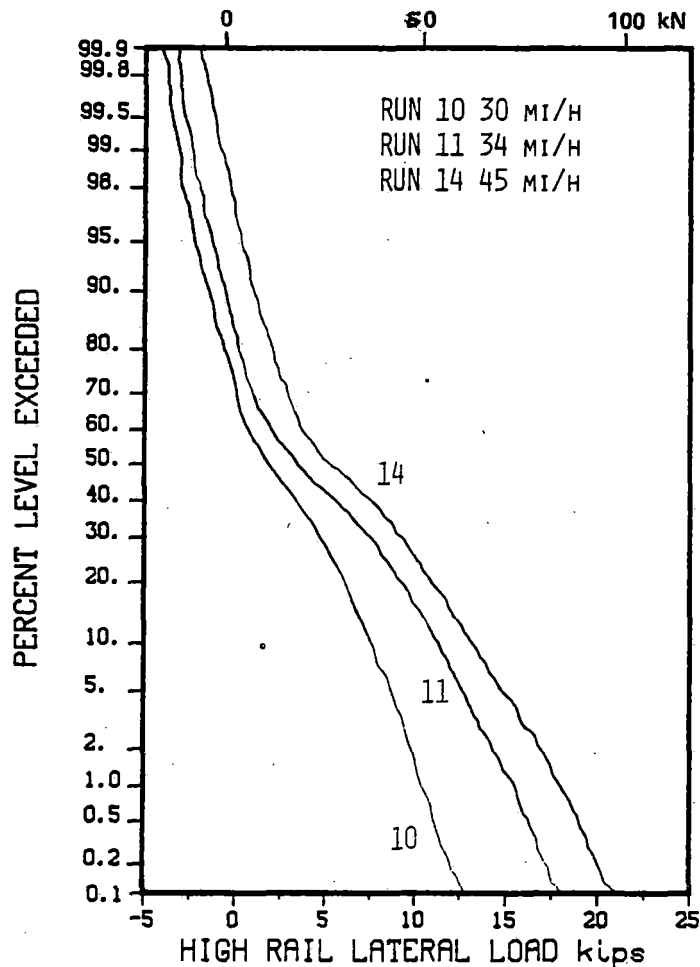
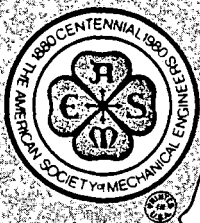


FIGURE 15. HIGH-RAIL LATERAL LOAD EXCEEDANCE DISTRIBUTION FUNCTIONS AT DIFFERENT SPEEDS

#### REFERENCES

1. Prause, R. H., et al, "An Analytical and Experimental Evaluation of Concrete Tie and Fastener Loads", Report No. FRA/ORD-77/71, December 1977.
2. Ahlbeck, D. R., Johnson, M. R., Harrison, H. D., and Tuten, J. M., "Measurements of Wheel/Rail Loads on Class 5 Track", Report No. FRA/ORD-80/19, February 1980.
3. Ahlbeck, D. R., "Predicting the Load Environment on Railroad Track", ASME Paper No. 80-RT-7, April 1980.
4. Kenworthy, M. and Jones, C. T., "Third Dynamic Hopper Car Test", Report No. FRA/TTC-80/01, March 1980.
5. Allen, R. A. and Peters, J., "Wheel/Rail Loads Test, Hopper Car Ride Data", Report No. FRA/TTC-80/07, August 1980.
6. Tuten, J. M. and Harrison, H. D., "FAST Wheel/Rail Loads Wayside Data Reduction", Final Report, Contract DTFR53-80-C-0078 (to be published).
7. Harrison, H. D. and Ahlbeck, D. R., "Development and Evaluation of Wayside Wheel/Rail Load Measurement Techniques", International Conference on Wheel/Rail Load and Displacement Measurement Techniques, DOT/TSC, January 19-20, 1980.
8. Newland, D. E., "Steering a Flexible Railway Truck on Curved Track", Trans. ASME, Journal of Eng'ring for Ind., August, 1969, pp. 908-918.
9. Ahlbeck, D. R., Dean, F. E., and Prause, R. H., "A Methodology for Characterization of the Wheel/Rail Load Environment-A Pilot Application", Final Report, Contract DOT-TSC-1051, June 1979.
10. Kalker, J. J., "On the Rolling Contact of Two Elastic Bodies in the Presence of Dry Friction", Doctoral Dissertation, Technische Hogeschool, Delft, Netherlands, 1967.
11. Johnson, M. R., Joyce, R. P., and Mancillas, C., "Use of an Instrumented Wheelset for Measurement of Wheel/Rail Forces at the Facility for Accelerated Service Testing (FAST)", Interim Report, Contract No. TTD 79-121-1 (AAR), August 1980.



AN ASME PUBLICATION  
\$3.00 per copy \$1.50 to ASME Members

# ASME

79-WA/RT-6

THE AMERICAN SOCIETY OF MECHANICAL ENGINEERS  
345 E 47 St., New York, N.Y. 10017

The Society shall not be responsible for statements or opinions advanced in papers or in discussion at meetings of the Society or of its Divisions or Sections, or printed in its publications. Discussion is printed only if the paper is published in an ASME Journal or Proceedings. Released for general publication upon presentation. Full credit should be given to ASME, the Technical Division, and the author(s).

REFERENCE 188

## A Methodology for Estimating the Derailment Probability of a Fleet of Railway Vehicles

**R. Brantman**

U.S. Department of Transportation,  
Transportation Systems Center,  
Cambridge, Mass.

**J.W. Griffin**

Dynamics Research Corp.,  
Wilmington, Mass.

**R.L. Jeffcoat**

The Analytic Sciences Corp.,  
Reading, Mass.  
Assoc. Mem. ASME

*Procedures for stochastic dynamic analysis are developed by which the probability of dynamically induced derailment of a fleet of rail vehicles can be estimated as a function of track quality and train operating conditions. Despite the wide variety of underlying causes, virtually any derailment can be classified as occurring in one of only a few fundamental modes; for each mode, candidate performance indices are defined to relate derailment potential to the dynamic state. A procedure is established to select and quantify those indices which are most highly correlated with the identified derailment modes. In order to treat large numbers of different vehicles, generic car families are defined on the basis of dynamic similarity. Each family is then characterized by statistical distributions of the physical parameters associated with its member.*

### ABSTRACT

Procedures for stochastic dynamic analysis are developed by which the probability of dynamically induced derailment of a fleet of rail vehicles can be estimated as a function of track quality and train operating conditions. Despite the wide variety of underlying causes, virtually any derailment can be classified as occurring in one of only a few fundamental modes; for each mode, candidate performance indices are defined to relate derailment potential to the dynamic state. A procedure is established to select and quantify those indices which are most highly correlated with the identified derailment modes. In order to treat large numbers of different vehicles, generic car families are defined on the basis of dynamic similarity. Each family is then characterized by statistical distributions of the physical parameters associated with its members. Efficient simulation of the response of an entire vehicle population to random and deterministic track inputs is accomplished using special nonlinear covariance propagation techniques. This methodology will be used in parametric studies to establish safe operating regimes, as a function of track quality, for individual vehicle families and for combined fleet populations.

### INTRODUCTION

A common goal of the railroad industry and the U.S. Department of Transportation is to provide a safe, cost-effective rail transportation system. One

of the major joint efforts under way is directed toward improving railway safety and economy through reduction of derailments resulting from the dynamics of train handling and track/train interaction.

Under the Improved Track Structures Program of the FRA's Office of Rail Safety Research, the Transportation Systems Center (TSC) has initiated research on reduction of derailments attributed to track-train interaction. Approximately 50% of all derailments are reported as being track-related. In 1975, these accounted for nearly 3000 derailments with a total economic loss (including direct damage and indirect railroad costs) estimated to be near 200 million dollars [1,2]. Of these derailments, over half were attributed to the dynamic interaction of the track and rail vehicle. It is this latter, very significant group of track geometry-induced derailments which defines the scope of the current work.

The specific objective of this activity is to establish relationships between derailment safety and track quality, vehicle characteristics, and train operating conditions which can be readily used by government and industry to:

- Establish safe operating regimes
- Assess the economics of maintenance and operations alternatives
- Recommend approaches for improved derailment safety.

This paper describes an analytical methodology developed to generate the required data, and illustrates some potential applications.

\*Numbers in square brackets refer to references at the end of the paper.

Contributed by the Rail Transportation Division of The American Society of Mechanical Engineers for presentation at the Winter Annual Meeting, New York, N.Y., December 2-7, 1979. Manuscript received at ASME Headquarters August 7, 1979.

Copies will be available until September 1, 1980.

## VIEW OF METHODOLOGY

Three elements are central to the methodology:

- Procedures for handling large numbers and varieties of vehicles and track conditions
- Track/vehicle interaction models and analysis tools that relate track geometry and train operating conditions to unsafe vehicle dynamic response characteristics
- A single measure of unsafe vehicle dynamic response that compares all vehicles under all track and train operating conditions.

We have chosen the probability of derailment threshold exceedance ( $P_d$  or "probability of derailment" for brevity) as this common safety measure. It represents that fraction of time during which a vehicle can be expected to be in a situation of impending derailment. It is a direct, complete, performance-based measure of track quality that absorbs dynamic effects, vehicle characteristics, and expected traffic.

Figure 1 illustrates the overall structure of the method. Analyses would be performed for a comprehensive matrix of combinations of track, train, and operating conditions; these are shown as input to the study. Probabilities of derailment for each group of vehicles would be produced as output. The system performance analysis involves the use of computer-based mathematical models of various rail vehicle dynamic processes to generate this output. Since we must deal with the entire fleet of U.S. rail vehicles and the entire spectrum of U.S. track, it is impractical to treat each on an individual basis. Therefore, the performance analysis makes use of statistical techniques to characterize these inputs.

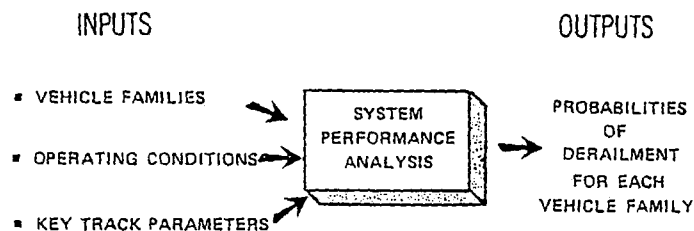


Figure 1 Input/Output Structure of Study

Table 1 lists five key technical issues which must be addressed in this multi-component dynamics problem, along with the solution approaches adopted. In the following sections, we discuss each issue in more detail.

### STUDY INPUTS

Input to the parametric study is of three kinds: vehicle characteristics, track characteristics, and operating conditions. Table 2 summarizes the way in which these inputs have been characterized.

#### Vehicle Families

The U.S. rail vehicle fleet consists of nearly two million vehicles, which may be categorized in

KEY ISSUE	SOLUTION APPROACH
Variety and Number of Vehicles	Classify Vehicles Into Dynamically Similar Groups Called "Families"
Random Inputs and Variable Parameters	Characterize Inputs and Parameters by Statistical Distributions
Complex Derailment Conditions	Develop Indirect Indicators of Derailment Validated by Experiment and Models
Complex Models	Develop Hierarchy of Validated, Simplified Models
Need for Compact Summary of Dynamic Characteristics	Summarize Results of Many Dynamic Analyses Into Figures of Merit That Relate Track Quality to Derailment Probability

Table 1 Key Technical Issues

VEHICLE TYPES	TRAIN OPERATING CONDITIONS	TRACK STRUCTURE	NOMINAL TRACK GEOMETRY	TRACK GEOMETRY VARIATIONS
STATISTICALLY CHARACTERIZED VEHICLE FAMILIES	<ul style="list-style-type: none"> <li>• SPEED</li> <li>• BRAKING FORCE</li> <li>• TRACTIVE EFFORT</li> <li>• TRAILING TONNAGE</li> </ul>	<ul style="list-style-type: none"> <li>• LATERAL COMPLIANCE</li> <li>• VERTICAL COMPLIANCE</li> <li>• STRUCTURAL LIMIT LOADS</li> </ul>	<ul style="list-style-type: none"> <li>• CURVATURE</li> <li>• GRADE</li> <li>• SUPERELEVATION</li> <li>• GAGE</li> </ul>	<ul style="list-style-type: none"> <li>• STATISTICALLY CHARACTERIZED TRACK CLASSES               <ul style="list-style-type: none"> <li>- ALIGNMENT</li> <li>- SURFACE</li> <li>- CROSSLLEVEL</li> <li>- GAGE</li> </ul> </li> <li>• DISCONTINUITIES               <ul style="list-style-type: none"> <li>- RAIL END MISMATCH</li> <li>- SWITCHES</li> <li>- FROGS</li> </ul> </li> </ul>

Table 2 Summary of Study Inputs

three broad classes: freight cars, passenger cars, and locomotives. Because of the breadth and diversity of these classes, it is advantageous to subdivide each into smaller vehicle families. A family is composed of vehicles which are similar to one another in those key configurational parameters which most significantly affect dynamic response. (As an example, a high-capacity box car and a covered twin hopper could fall into the same family if their lengths, weights, center-of-gravity heights, etc., were comparable. The dynamics of the two cars would, in this case, be expected to be similar.) Each family is then described by the statistical distributions of the physical parameters of all its members.

There are five reasons for subdividing classes into families. For ease of modeling, all members of a family should be describable by the same model structure; very flexible cars require separate treatment from very rigid ones, for example. Ease in statistical handling results when a large and diverse class is broken down into more homogeneous families. Ideally, families should be chosen so that the parameter distributions for each are clustered compactly about the mean, unimodal, and nearly normal. By the same token, changing fleet population and mixture are easily accommodated if the derailment probability has been separately determined for each constituent family. A very significant argument for a breakdown by dynamically similar families is the ability it gives one to identify problem vehicle types which are significantly more derailment-prone than average under certain operating conditions. Family-specific safety recommendations, whereby special operating restrictions are placed on such vehicles, would maintain safety without penalizing the majority of the fleet because of the poor behavior of a few.

Table 3 illustrates one possible method for freight car classification which embodies the requirements outlined above. Only four descriptors are needed to place a car in a family according to this simplified scheme: truck center spacing, gross weight, center-of-gravity height, and body flexibility. Because any combination of descriptor ranges defines a family, there are  $3 \times 3 \times 3 \times 5 = 135$  possible families based on Table 3. Some of these families, representing rare or unrealistic combinations of parameters, will be essentially empty, so the actual number of significant families may be much smaller. The classification given here is only illustrative, and is being improved as we obtain more data on the freight car fleet [3].

▪ TRUCK CENTER SPACING:	$\left\{ \begin{array}{l} < 35' \\ 35' - 48' \\ > 48' \end{array} \right.$
▪ GROSS WEIGHT:	$\left\{ \begin{array}{l} < 50 \text{ T} \\ 50 \text{ T} - 100 \text{ T} \\ > 100 \text{ T} \end{array} \right.$
▪ CENTER OF GRAVITY HEIGHT:	$\left\{ \begin{array}{l} < 45'' \\ 45'' - 70'' \\ > 70'' \end{array} \right.$
▪ BODY FLEXIBILITY:	$\left\{ \begin{array}{l} \text{RIGID} \\ \text{TORSION} \\ \text{TORSION AND BENDING} \\ \text{SHIFTING LOADS} \\ \text{SPRUNG LADING} \end{array} \right.$

ALL FOUR DESCRIPTORS ARE NEEDED TO DEFINE ANY ONE FAMILY.

Table 3

A Candidate Set of Freight Car Family Descriptors

Figure 2 shows an example of the family classification method, and illustrates two important points:

- A car's family can change depending on loading, because the load can affect weight, CG height, and flexibility.
- Any one family can contain cars of various mechanical types, provided only that they are similar in the four configurational descriptors.

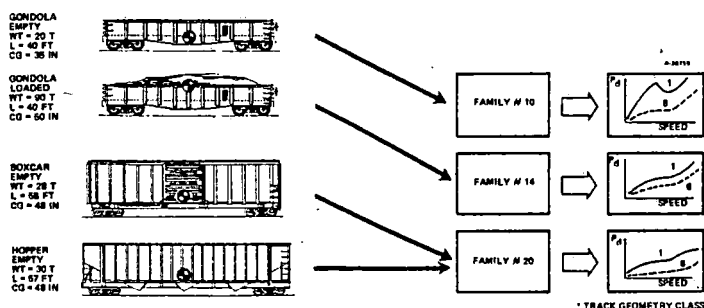


Figure 2 Example Illustrating Dynamic Classification of Freight Cars

## Train Operating Conditions

Train operating conditions also influence rail vehicle dynamic response and safety. The fundamental quantities which will be treated parametrically include train speed, braking force, tractive effort, and trailing tonnage. The effects of specific train makeup and train handling procedures will not be studied explicitly; however, the steady-state conditions that the train imposes on any individual vehicle can be specified in terms of vehicle speed, buff force, draft force, and coupler angles. By keeping these fundamental quantities as independent parameters of the study, we preserve considerable flexibility to apply the results to a wide variety of consists and operating procedures.

## Track Parameters

The track parameters necessary for the study can be categorized as track structure, nominal track geometry, and track geometry variations. Effects of the design and physical condition of the track and roadbed can be treated parametrically in terms of the basic track performance measures which they affect: lateral and vertical compliance, and structural limit loads. Accordingly, the underlying relationships between these parameters and the construction and condition of the track need not be known for our purposes, but are the subject of other current TSC and AAR studies [4,5].

The key variational track geometry parameters are alignment, surface, crosslevel, and gage variation, representing deviations from the nominal geometry parameters of curvature, grade, superelevation, and gage respectively. The analyses would be performed using values of these variations that conform to existing track class definitions. Because the latter refer to single-value maximum deviations, it is necessary to tie them to a statistical characterization of the actual track geometry which one obtains when such maxima are observed; this task requires both experimental measurement of track geometry and theoretical inference to determine the appropriate statistical measures. Each of the four geometry deviations has been found to have a periodic component (due primarily to joint spacing) and one or more stochastic components [6]. The shape and amplitude of the former and the spectral density of the latter are assumed to be correlated with the class to which the track is maintained [6], and to vary smoothly from one class to another. It is thus meaningful to speak of a continuum of track classes, with 3.5, for example, being midway between classes 3 and 4 with respect to all measures of geometry variation; Figure 3 illustrates these concepts for the simple case where only the stochastic process is present.

	MEASURED PSD	CORRESPONDING RMS	MAXIMUM ALLOWABLE
ALIGNMENT		CLASS 3: 0.438"	1 3/4"
		CLASS 3.5: 0.406"	1 5/8"
		CLASS 4: 0.375"	1 1/2"
CROSSLEVEL		CLASS 3: 0.5"	2"
		CLASS 3.5: 0.469"	1 7/8"
		CLASS 4: 0.438"	1 3/4"

Figure 3 Hypothetical Example of Generalized Track Class

When used in this fashion, track class becomes a convenient descriptor by which one can compactly refer to a collection of geometry parameters which are consistent with the spectrum of U.S. track. It should be emphasized, however, that even this generalized (continuum) class applies only to track which is built and maintained using conventional techniques. To accommodate other methods which might be developed in the future, and to allow for departures of track geometry from the assumed parametric relationships, the sensitivity of vehicle performance to the individual track geometry parameters can also be established.

## STUDY OUTPUTS

The ultimate output of the study outlined in this paper would be a collection of probabilities of derailment threshold exceedance, for each vehicle family, under all appropriate combinations of operating conditions and track parameters. Each one of these probabilities represents the net likelihood that a member of a particular vehicle family will derail in any of several possible modes (about which more will be said below). It includes the effects of parameter variability within the family. To determine the overall probability of derailment of an entire fleet of vehicles, it is a simple matter to construct a weighted sum of family probabilities, where the weighting factor is typically the mileage,  $M_i$ , accrued by the family:

$$P_d = \frac{\sum_{i=1}^N M_i P_{d_i}}{\sum_{i=1}^N M_i}$$

For each family, a table of derailment probabilities can be generated. Each element in the table represents a unique combination of conditions, and contains the corresponding probability of derailment. The hypothetical example of Figure 4 shows  $P_d$ , the probability of derailment, as ten to a negative power, a notation which accommodates a wide dynamic range. When all the families are collected into a fleet, their individual probabilities of derailment are weighted to give a single composite table of  $P_d$  such as Figure 5. These composite tables can be generated from the family-specific tables with very little effort, since the operation is purely algebraic. Thus, it is convenient to account for evolutionary changes in the fleet makeup.

FAMILY: # 1									
CONDITIONS: COASTING, RIGID TRACK, NOMINAL GAGE									
TRACK CLASS		1				2			
CURVATURE		0°	2°	4°	6°	0°	2°	4°	
SPEED	BUFF/DRAFT								
10 mph	100 T BUFF	10 <sup>-5.2</sup>	10 <sup>-5.1</sup>	10 <sup>-5.5</sup>	10 <sup>-5.1</sup>	10 <sup>-6.0</sup>	10 <sup>-5.9</sup>	10 <sup>-5.5</sup>	
	0	10 <sup>-6.0</sup>	10 <sup>-6.0</sup>	10 <sup>-5.7</sup>	10 <sup>-5.3</sup>	10 <sup>-6.5</sup>	10 <sup>-6.0</sup>	10 <sup>-5.8</sup>	
	100 T DRAFT	10 <sup>-5.5</sup>	10 <sup>-5.6</sup>	10 <sup>-5.9</sup>	10 <sup>-5.4</sup>	10 <sup>-6.6</sup>	10 <sup>-6.0</sup>	10 <sup>-5.9</sup>	
20 mph	100 T BUFF	10 <sup>-5.2</sup>	10 <sup>-5.1</sup>	10 <sup>-5.0</sup>	10 <sup>-4.8</sup>	10 <sup>-5.4</sup>	10 <sup>-5.4</sup>	10 <sup>-5.2</sup>	
	0	10 <sup>-5.7</sup>	10 <sup>-5.5</sup>	10 <sup>-5.2</sup>	10 <sup>-5.0</sup>	10 <sup>-5.9</sup>	10 <sup>-5.7</sup>	10 <sup>-5.6</sup>	
	100 T DRAFT	10 <sup>-5.2</sup>	10 <sup>-5.3</sup>	10 <sup>-5.3</sup>	10 <sup>-5.1</sup>	10 <sup>-6.0</sup>	10 <sup>-5.8</sup>	10 <sup>-5.6</sup>	

ENTRIES ARE PROBABILITIES OF DERAILMENT FOR A SINGLE VEHICLE FAMILY

Figure 4

Presentation of Derailment Probability (By Family)

FAMILY: COMPOSITE									
CONDITIONS: RIGID TRACK, NOMINAL GAGE									
TRACK CLASS		1				2			
CURVATURE		0°	2°	4°	6°	0°	2°	4°	
SPEED	BUFF/DRAFT								
10 mph	100 T BUFF	10 <sup>-5.8</sup>	10 <sup>-5.7</sup>	10 <sup>-5.5</sup>	10 <sup>-5.1</sup>	10 <sup>-6.0</sup>	10 <sup>-5.9</sup>	10 <sup>-5.5</sup>	
	0	10 <sup>-6.1</sup>	10 <sup>-6.0</sup>	10 <sup>-5.7</sup>	10 <sup>-5.3</sup>	10 <sup>-6.5</sup>	10 <sup>-6.0</sup>	10 <sup>-5.8</sup>	
	100 T DRAFT	10 <sup>-5.8</sup>	10 <sup>-5.9</sup>	10 <sup>-5.9</sup>	10 <sup>-5.4</sup>	10 <sup>-6.6</sup>	10 <sup>-6.0</sup>	10 <sup>-5.9</sup>	
20 mph	100 T BUFF	10 <sup>-5.2</sup>	10 <sup>-5.1</sup>	10 <sup>-5.0</sup>	10 <sup>-4.8</sup>	10 <sup>-5.4</sup>	10 <sup>-5.4</sup>	10 <sup>-5.2</sup>	
	0	10 <sup>-5.5</sup>	10 <sup>-5.1</sup>	10 <sup>-5.2</sup>	10 <sup>-5.0</sup>	10 <sup>-5.8</sup>	10 <sup>-5.7</sup>	10 <sup>-5.6</sup>	
	100 T DRAFT	10 <sup>-5.2</sup>	10 <sup>-5.3</sup>	10 <sup>-5.3</sup>	10 <sup>-5.1</sup>	10 <sup>-6.0</sup>	10 <sup>-5.8</sup>	10 <sup>-5.6</sup>	

ENTRIES ARE PROBABILITIES OF DERAILMENT FOR A CONSIST REPRESENTATIVE OF THE ENTIRE FLEET.

Figure 5

Presentation of Derailment Probability (Composite)

## DERAILMENT MODES, PROCESSES AND INDICATORS

In a systematic study of derailment, we find it useful to distinguish between a derailment mode, defined as the precise way in which the vehicle permanently leaves the track, and a derailment process, which is a characteristic pattern of dynamic response which can result in a derailment. As an illustration, "rock and roll" is a derailment process which may lead to derailment by the wheel lift mode.

Based upon an examination of the mechanics of the vehicle/track system, five fundamental derailment modes have been identified [7]:

- WHEEL LIFT - Flange moves vertically above the rail
- CAR-TRUCK SEPARATION - Carbody centerplate rises above center pin
- WHEEL CLIMB - Flange moves laterally beyond the rail
- RAIL DEFLECTION - Rail moves outward so that gage exceeds wheelset width
- SUDDEN COMPONENT FAILURE - Force or stress in critical vehicle or track component exceeds allowable level.

Wheel lift and car-truck separation are characterized by excessive displacements at low force. Wheel climb and rail deflection (e.g., rail rollover) involve excessive wheel-rail force at the time of derailment. Sudden component failure may arise from fatigue or shock loads. The fact that only five modes suffice to describe the whole spectrum of derailments underscores the central role of this concept in a derailment study.

The next question is how to decide whether a derailment will occur under a given set of dynamic conditions. For a derailment mode, the decision is not difficult: if a displacement or force exceeds a

The flowchart illustrates the Derailment Process, organized into four horizontal layers separated by dashed lines:

- DERAILMENT MODE:** Contains two boxes: "WHEEL CLIMB" and "WHEEL LIFT".
- DERAILMENT INDICATOR:** Contains two boxes:
  - Under "WHEEL CLIMB":  $Y_1 > Y_{1, \text{max}}$   
 $i = 1, N$
  - Under "WHEEL LIFT":  $Z_1 > Z_{1, \text{max}}$   
 $i = 1, N$
- DERAILMENT PROCESS:** Contains three boxes: "LATERAL RESPONSE", "STEADY CURVING", and "HUNTING".
- PERFORMANCE INDEX:** Contains one box:  $L/V$ ,  $\theta$ , and vertical dots.

**Flow:**

- Arrows point from "WHEEL CLIMB" and "WHEEL LIFT" to their respective indicator boxes.
- Arrows from the indicator boxes point to the "DERAILMENT PROCESS" layer.
- From the "DERAILMENT INDICATOR" for "WHEEL CLIMB", arrows point to "LATERAL RESPONSE", "STEADY CURVING", and "HUNTING".
- From the "DERAILMENT INDICATOR" for "WHEEL LIFT", an arrow points to "HUNTING".
- Arrows point from "LATERAL RESPONSE", "STEADY CURVING", and "HUNTING" to the "PERFORMANCE INDEX" box.

During the first phase of this study, a number of promising candidate performance indices were obtained from the literature and from independent analysis [7]. Table 4 lists those which are presently under investigation. Associated with each performance index is a critical threshold value which separates the safe and unsafe regions. Determination of these thresholds is equally important, and at least as difficult, as validation of the performance indices themselves. An original procedure has been developed to select and quantify those performance indices which are best predictors of derailment; this procedure is discussed in the next section.

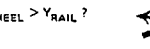
There are two basic components of a program of dynamic analysis: the system model, and the analytical procedure. These two aspects are, to a great extent, separable; but both must be given careful attention if the analysis is to yield results which are both reliable and economical.

The hierarchy of derailment predictors is reflected in the model hierarchy shown in Figure 7. This formulation is motivated by our need to analyze a large number of derailment situations in a cost-effective manner, while maintaining confidence in the validity of our results. Each level of predictor is associated with a model which is just elaborate enough to calculate that predictor accurately, but no more so. Each level model is developed from, and validated against, the next higher level. This validation has two essential parts: a check on the accuracy of the model, and a verification that the measure of safety can predict derailment adequately.

PERFORMANCE INDEX NUMBER	FUNCTIONAL FORM
1	$F_L/F_V$
2	$F_L/F_V - S$
3	$V_f^2 - (2 h_f - z_f F_V/M_w) \left( \left[ F_L \right]^{-1} u_e - \text{ctn} a_f / F_V \right) + \left[ 1 - u_e \text{ctn} a_f \right]$
4	$(F_L/F_V) \left( 1 - nS(i_w/G_w) \sqrt{N_w h_f / F_V} \right)$
5	$V_f^2 - 2gh_f$
6	$\frac{2M_w G V^2 a_e}{\pi r_o^3 \phi \left( \frac{N_A}{N_T} + \frac{N_B}{2} \right)} - S$
7	$\frac{2F_{CD}}{8 \left( \frac{N_A}{N_T} + \frac{N_B}{2} \right)} \left( \frac{z_c/R}{1 + (z_c/R)^2} \right) \frac{1}{\sqrt{1 - (z_c/R)^2}} - S$
8	$\frac{F_{CB}}{8 \left( \frac{N_A}{N_T} + \frac{N_B}{2} \right)} \left( \frac{z_c}{z_T} \right) - S$
9	$\left( \frac{z_w}{h_f} - \frac{z_c}{h_f} \right)$
10	$-F_{2w}$
11	$  \phi_B  $
12	$\frac{1}{2h_f} \left[ \frac{k_{rx} z_{rx}^2}{8 \left( \frac{N_A}{N_T} + \frac{N_B}{2} \right)} - v \left( \frac{N_A}{N_T} + \frac{N_B}{2} \right) \right]$
13	$F_L - F_L, \text{elim}$
14	$F_L - \Delta_V$ $F_V - \Delta_L$
15	$\left( F_V \frac{\psi_L}{\psi_S} \right) \left( \frac{F_L}{F_V} - \frac{\psi_L}{\psi_S} \left[ 1 + \beta \frac{\psi_S}{\psi_L} \left( 1 - \beta + 2\beta I \right) \right] \right) \left( 1 + 2\beta \left[ 1 - \frac{\beta}{1 - \frac{\beta}{2\beta}} \right] \right)^{-1} - F_{S, \text{elim}}$
16	$\Delta_{ch} - \Delta_{cl}$
17	$\Delta_{ch} - \Delta_{cl} + \psi_{cp} \left[ \phi_b - \phi_l \right]$
18	$-f_{ip}$
19	$\frac{1}{2h_{cp}} \left[ \frac{k_{cp} \Delta \Delta_{cp}^2}{\psi_B^2} - \psi_B \right]$
20	$i_{\text{max}} - i_{\text{elim}}$
21	$i_{\text{max}} - F_{\text{elim}}$
22	$\frac{F_L}{F_V} - \psi(t, \tau)$
23	$\Delta_{\text{ross}} - \Delta_{\text{ross}, \text{elim}}$
24	$F_L - F_{L, \text{elim}} (F_{AX}, F_V)$

```

    graph LR
      subgraph Accuracy_Simplicity
        direction TB
        A[↑ ACCURACY]
        S[↑ SIMPLICITY]
      end

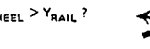
      R["REALITY -  
A CONTROLLED TEST"] --> D1["DERAILMENT -  
DID DERAILMENT OCCUR?"]
      D1 --> T["TRUTH MODEL -  
COMPLEX,  
NONLINEAR, COMPLETE  
DYNAMIC MODEL"]
      T --> D2["DERAILMENT INDICATOR -  
e.g.,  $Y_{WHEEL} > Y_{RAIL} ?$ "]
      D2 --> W["WORKING MODEL -  
SIMPLIFIED DYNAMIC MODEL"]
      W --> P["PERFORMANCE INDEX -  
e.g.,  $L/V > (L/V)_{CRIT} ?$ "]
      P --> F["FIGURE OF MERIT  
e.g., "]
      F --> FOM["FIGURE OF MERIT"]

      T --> TI["TRUTH INDICATOR  
▪ TRUTH MODEL  
▪ DERAILMENT INDICATORS"]
      W --> WI["WORKING INDICES  
▪ WORKING MODEL  
▪ PERFORMANCE INDICES"]
      FOM --> FM["FIGURE OF MERIT  
▪ FIGURE OF MERIT"]
  
```

The diagram illustrates the Validation Sequence, showing the progression from Reality to Figure of Merit, with increasing accuracy and simplicity.

**Accuracy and Simplicity:** Two large arrows on the left indicate increasing **ACCURACY** (upward) and increasing **SIMPLICITY** (downward).

**Validation Sequence:**

- REALITY** (A CONTROLLED TEST) leads to **DERAILMENT** (DID DERAILMENT OCCUR?).
- TRUTH MODEL** (COMPLEX, NONLINEAR, COMPLETE DYNAMIC MODEL) leads to **DERAILMENT INDICATOR** (e.g.,  $Y_{WHEEL} > Y_{RAIL} ?$ ).
- WORKING MODEL** (SIMPLIFIED DYNAMIC MODEL) leads to **PERFORMANCE INDEX** (e.g.,  $L/V > (L/V)_{CRIT} ?$ ).
- FIGURE OF MERIT** (e.g., ).

**Key Indicators and Metrics:**

- TRUTH INDICATOR:**
  - TRUTH MODEL
  - DERAILMENT INDICATORS
- WORKING INDICES:**
  - WORKING MODEL
  - PERFORMANCE INDICES
- FIGURE OF MERIT:**
  - FIGURE OF MERIT

The final arbiter of all models is reality, which consists of instrumented, controlled tests. These tests are used to validate analytical truth models, which are able to simulate the detailed conditions leading up to derailment. These are typically complex, high order, nonlinear models; however, the cost of repeated simulations, as required for a parametric study, would be prohibitive using such models. Instead, we introduce simplified dynamic working models which are tailored to specific derail-



ment processes and are practical for frequent use. Such models may or may not give an estimate of the derailment indicator, but they must provide the performance indices associated with the particular derailment modes and processes they are designed to simulate. Truth models are then used to validate the working models, and also to select the performance indices (and associated threshold values) which best correlate with derailment indicators. The selected performance indices become indirect, but quantified, measures of derailment for use with the working models.

Finally, the results of all parametric studies must be summarized in convenient input/output relationships for later use in evaluating the safety and economics of various types of train operation and track maintenance. The tables of derailment probability in Figures 4 and 5 typify the most basic form of system performance estimator; other formats (graphical or algebraic) can be obtained using multivariate interpolation or regression techniques. These relations can then be applied directly by the end users to develop overall figures of merit for any combination of track quality, fleet makeup, and train operating conditions.

#### Computational Procedure

Naturally, the success of an extensive parametric study hinges on the efficiency of the methods used to generate the individual values of  $P_d$  (the probability of derailment). Recall that  $P_d$  reflects the statistical distributions of several outputs of a complex, highly nonlinear model, with coefficients that are themselves distributions, subjected to stochastic track inputs and random initial conditions. Realistic models of vehicle dynamics contain many nonlinearities such as dual-rate springs, friction, concave wheel profiles, and other elements which contribute to dynamic response problems. Linear frequency-domain analysis will therefore not suffice for investigating many of the derailment phenomena. Furthermore, the fact that some vehicle parameters are themselves randomly distributed means that even linear equations take on a nonlinear form. Under these circumstances, one typically relies upon a direct time simulation of the system. One option would be to carry out a large number of simulations for each family, selecting a different set of parameters, initial conditions, and inputs for each trial until a statistically significant sample is accumulated. This "monte carlo" method can be very costly in computer time. A preferable alternative for our application is a technique for approximate covariance analysis of nonlinear dynamic systems [8]. It involves direct propagation of the statistics of the states, using multiple-input describing functions to treat nonlinearities [9]. A single such simulation thus approximates the results of many (tens or hundreds of) monte carlo runs, as shown in Figure 8. Reference 8 contains comparisons of the two methods applied to a variety of nonlinear systems.

This generalized covariance analysis method is the focal point of RVDCADET, a system of analysis tools tailored specifically to rail vehicle dynamic analysis. RVDCADET includes modules for:

- Deterministic Simulation
- Covariance Simulation (linear and nonlinear models)

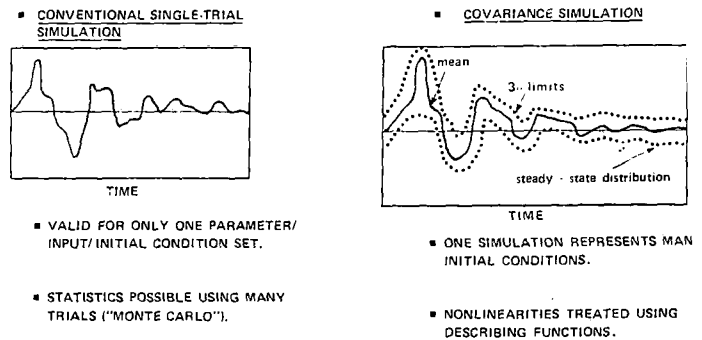


Figure 8 Covariance Simulation

- Eigenvalue - Eigenvector Analysis
- Limit Cycle Analysis
- Linear, Nonlinear, or Quasilinear Approach
- Steady-State Solution
- Transient, Periodic, or Stochastic Input.

RVDCADET is "executive" software, applicable to any qualifying model. The model characteristics are introduced in the form of structure modules and parameter values. The structure modules will correspond to vehicle models assembled largely from the Rail Vehicle Dynamics Library (RVDL), a comprehensive collection of computer analysis programs from various sources, including the Association of American Railroads, the Transportation Systems Center, the Federal Railroad Administration, and their contractors. The programs in the RVDL are a key resource in the analysis effort, embodying as they do the results of years of modeling, evaluation, and validation. Typically, because no single RVDL program is suited to direct use within RVDCADET, a structure module will be a composite of several RVDL models, plus additional modifications.

#### POTENTIAL APPLICATION OF STUDY RESULTS

Now let us consider ways in which the study output might be applied. Table 5 shows some of these. Determination of appropriate speed limits can be put on a firm footing using probability of derailment. Besides the conventional distinction between limits for passenger and freight service, the acceptable derailment risk level can be made a function of population density and of the degree of hazard associated with the lading. Many kinds of policy analysis become feasible when there is a predictive measure of derailment frequency available. The optimal track quality for various situations can be determined by trading off maintenance cost against the cost of derailments and of lost revenue due to reduced speed. The data can also be used to indicate directions for further safety improvements. Identification of problem vehicles, and the ability to assess new designs simply, should lead to safer rolling stock and locomotives. Track classes can be revised to provide a more consistent level of safety at all speeds, and a better understanding of the

SAFE OPERATING REGIMES	
•	Speed Limits (passenger/freight, normal/hazardous)
•	Track Quality Limits
ECONOMIC ASSESSMENT	
•	Maintenance Priorities
•	Optimum Operating Efficiency
•	Policy Analysis (cost, risk, viability)
RECOMMENDATIONS FOR IMPROVED SAFETY	
•	Identification of Problem Vehicles
•	Revised Track Classes
•	Improved Maintenance and Inspection

Table 5 Application of Study Results

relationship between track geometry and safety may lead to more cost-effective maintenance and inspection techniques.

Figure 9 shows how the tabulated  $P_d$  data can be graphed as curves of a safety index defined as  $-\log_{10}(P_d)$ , or the negative exponent of  $P_d$ . Note that a high value of the safety index denotes a low probability of derailment, and hence a high degree of safety. In this hypothetical example, the curves of safety index are plotted against speed for each of the six current track geometry classes, and for a particular set of operating conditions. If we assume that (by some policy decision)  $10^{-5.5}$  has been specified as an upper bound on allowable  $P_d$ , we can then determine the corresponding maximum safe speeds from the intersections of the safety index curves with the horizontal dashed line at the acceptable index of 5.5. No change in the definition of track class, as specified by maximum allowable track geometry deviations, is needed -- only a revision of speed limits. (It should be remarked that situations can arise in which the curves of safety index versus speed are much more tortuous than shown in Figure 9. In such

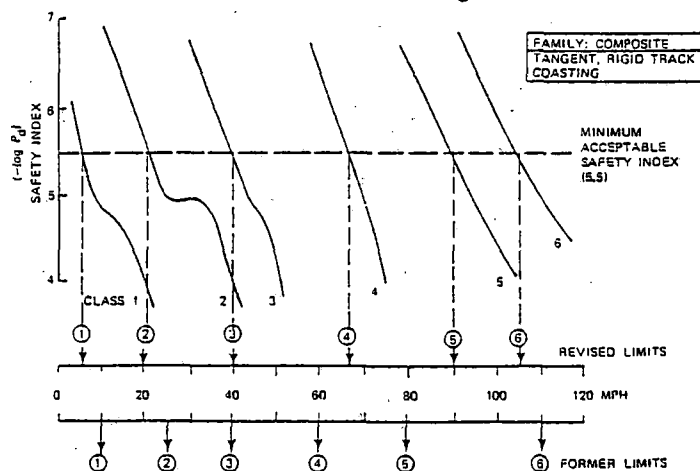


Figure 9 Hypothetical Example: Revised Speed Limits

cases the required reduction in speed limit may be so great that an alternative approach, such as those described below, is preferable.)

If, on the other hand, it is desired to maintain the current permissible speed limits, it may be necessary to redefine the geometric class definitions. The concept of a continuum of track classes makes this revision relatively simple. Figure 10 repeats the example above, but with unchanged speed limits. The dashed curves, which are readily calculated using the system performance estimators, correspond to fractional classes which just meet the safety index requirement at the desired maximum speeds. For example, to allow 25 mph operation, it would be necessary (in this hypothetical example) to upgrade Class 2 track to "Class 2.4" standards. This new Class 2' track would then have geometry limits that were proportionately scaled between the current Classes 2 and 3.

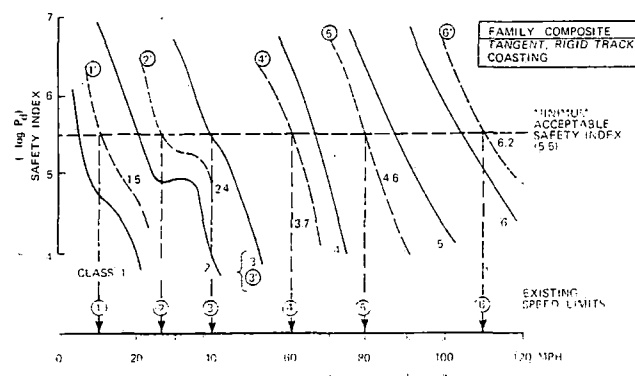


Figure 10 Hypothetical Example: Revised Track Classes

Track geometry need not be limited to the combinations which can be expressed in terms of a single class designation. An important aspect of this study is the development of sensitivity data, which measure the effect on safety of an independent change in each of the geometry parameters. In Figure 11, we see that current Class 4 track is (hypothetically!) better than necessary for the assigned 60 mph speed limit. This means that we can relax the geometry requirements and still meet the required safety index. The sensitivity data, along with economic information, may suggest that the greatest cost saving would result from relaxing just the standard for crosslevel while maintaining all other parameters at their Class 4 level. The dashed curve represents the modified standards for 60 mph track.

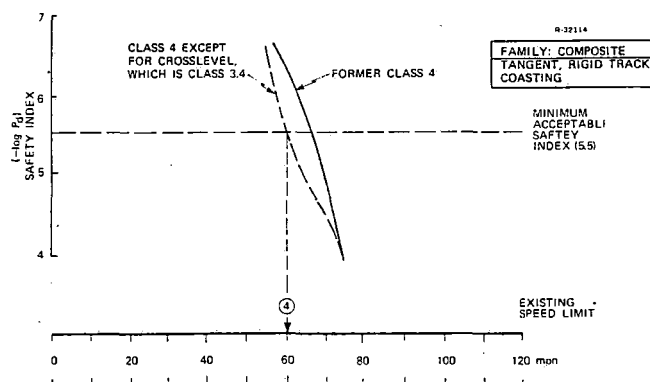


Figure 11 Hypothetical Example: Revised Limits on a Single Geometry Parameter

Notice that none of these example procedures requires further dynamic analysis or simulation, but only an algebraic manipulation of the data in the derailment probability tables. Numerous other applications suggest themselves. For example, one could define safe operating boundaries separately for each family or group of families; this would have the effect of putting special restrictions on problem cars, while giving added operational freedom to exceptionally good performers. There is also no necessity to fix a single permissible safety index for all speeds and all conditions. Since low speed derailments are generally less damaging than those at high speed, it may be economically justifiable to allow the required safety index to decrease at the lower speeds, rather than remaining constant as in the examples above. Similarly, the required safety index for general freight operation could be much lower than for hazardous loadings such as toxic gas or nuclear wastes. Determination of an acceptable derailment risk level is ultimately a policy decision which cannot be made on technical grounds alone. Nevertheless, the present study will furnish a quantitative means to predict the derailment probability for any class of operation -- an essential part of informed policy analysis.

#### CONCLUSION

In this paper, we have attempted to provide a concise summary of an approach to one aspect of railroad safety research: the relationship between track conditions and dynamically induced derailment. Because we must account for all the locomotives and cars which make up the U.S. fleet, and because the derailment process is a stochastic one, we have suggested a statistical approach. Use of the quasi-linear covariance analysis technique permits an efficient direct treatment of the statistics of nonlinear systems. The immediate results of this study would be probabilities of derailment for each vehicle family. These could be applied in diverse ways by the railroad industry and the government to improve safety, enhance productivity, and reduce costs.

Other analytical approaches to the reduction of geometry-caused derailment are also being pursued. For example, it is possible to designate important derailment "scenarios", comprising specific vehicles, operating conditions, and track geometry signatures, for which the response can be examined in detail. From a limited number of judiciously chosen scenarios, including both typical and worst-case conditions, boundaries on allowable limits for certain kinds of geometry variations can be established with some confidence. The methodology of this paper could then be applied to estimate the effect of these boundaries on the safety of the fleet as a whole. Whether the methodology is used to generate basic safety data or to evaluate recommendations developed by other means, it offers significant advantages in comprehensiveness and consistency.

#### ACKNOWLEDGEMENT

This work is supported under contract DOT-TSC-1302 by the U.S. Department of Transportation through the Federal Railroad Administration and the Transportation Systems Center, whose advice and assistance are gratefully acknowledged.

#### REFERENCES

1. "An Evaluation of Railroad Safety," Office of Technology Assessment, Report No. OTA-T-61, May 1978.
2. Accident Bulletin, Summary and Analysis of Accidents on Railroads in the United States, 1965 to 1975, U.S. Department of Transportation, Federal Railroad Administration, Office of Safety, Washington, 1974.
3. "Characterization of Railway Rolling Stock, Representative Loadings, and Wheel Profiles," Contract No. DOT-TSC-1362, Pullman-Standard Corporation.
4. Reiner, I., "Lateral Resistance of Railroad Track," D.O.T. Report No. FRA/ORD-77/41, August 1977.
5. Nessler, G.L., et al, "An Experimental Evaluation of Techniques for Measuring the Dynamic Compliance of Railroad Track," D.O.T. Report No. FRA/ORD-78/25.
6. Corbin, J., Cunney, E., and Sutermeister, R., "Statistical Representations of Track Geometry -- Final Report," Contract No. DOT-TSC-1211, Ensco, Inc., to be published.
7. Jeffcoat, R.L., and Griffin, J.W., "Performance Indices for Derailment Predication," The Analytic Sciences Corporation, Report No. TR-903-2, September 1978.
8. Taylor, J., "Handbook for the Direct Statistical Analysis of Missile Guidance Systems via CADET<sup>TM</sup>," The Analytic Sciences Corporation, Report No. TR-385-2, May 1975.
9. Gelb, A., and VanderVelde, W., Multiple-Input Describing Functions and Nonlinear System Design, McGraw-Hill, New York, 1969.

CADET is a trademark of the Analytic Sciences Corporation.

# Evaluation of Time-Duration Dependent Wheel Load Criteria for Wheelclimb Derailment

L. M. Sweet

Associate Professor and Associate Director  
Transportation Program.

A. Karmel

Graduate Research Assistant.

Department of Mechanical  
and Aerospace Engineering,  
Princeton University,  
Princeton, N.J. 08544

*The most widely accepted criterion for wheelclimb derailment defines an upper limit for safe operation on wheel/rail contact forces on the climbing wheel, with the limit varying with time duration of the forces. For dynamic wheelclimb processes with significant lateral velocities, lateral forces may be measured for short time durations that are larger than those that may be sustained without derailment in steady state. This paper shows, however, that the JNR and other time-duration dependent criteria based on wheel load measurements alone are unsuccessful in predicting derailment safety. For wheelclimb processes involving negligible lateral velocities, the derailment limit can be estimated from quasisteady analysis of wheel/rail forces. The evaluation of criteria is based on experiments with a single wheelset and a nonlinear theory for dynamic wheelclimb.*

## I. Introduction

The most widely accepted criterion for wheelclimb derailment defines an upper limit on wheel/rail contact forces on the climbing wheel, the limit varying with time duration of the forces. The reliability of this criterion in predicting derailment is of major importance, since it is used to evaluate the derailment safety of railroad vehicles, operating conditions, and track structures. This paper presents a detailed analytical and experimental evaluation of time-dependent wheel load derailment criteria for wheelclimb, and shows that this type of criterion alone is inadequate for derailment prediction.

There is a strong motivation for using wheel load measurements for derailment prediction. The mechanics of derailment for a complete truck are complex and highly nonlinear. At present no analytical model for complete trucks has been developed and validated that can relate measured variables other than wheel loads to derailment occurrence. The hope that wheel loads would be useful to derailment research has led to the development of instrumented wheelsets as major experimental research tools, which are also employed to study problems associated with failure, wear, and large deformation of wheels and track [1,2,3].

The need for accurate and reliable methods for derailment prediction has intensified recently as efforts increase to relate vehicle characteristics, train operation, and track maintenance standards to system safety. With increasing success, the relationships between vehicle and track descriptors and the resulting wheel/rail reaction forces have been quantified using analytical or empirical means [3-7]. The critical missing links are definitive specifications relating these forces to safety.

Contributed by the Dynamic Systems and Control Division of THE AMERICAN SOCIETY OF MECHANICAL ENGINEERS and presented at the Winter Annual Meeting, November 16-21, 1980, Chicago, Illinois. Manuscript received at ASME Headquarters July 12, 1980. Paper No. 80-WA/DSC-21.

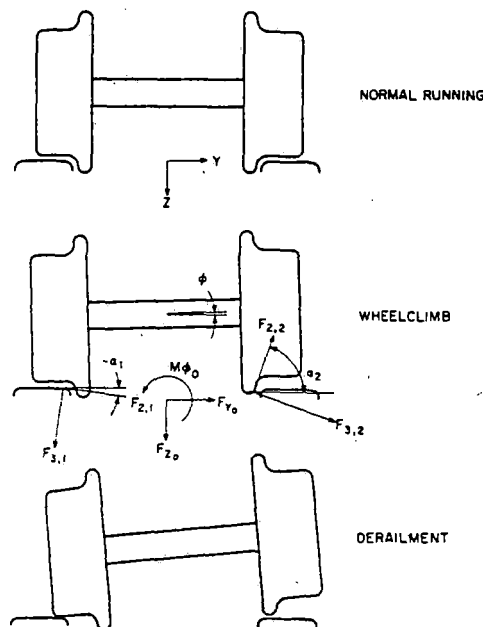


Fig. 1 Wheelset during wheelclimb derailment process, subject to externally applied and wheel/rail reaction forces

Derailment may occur as a result of several distinct processes, including wheelclimb, wheel lift, rail rollover, gage spreading, and component failure, each requiring specification of allowable wheel/rail forces or other measures [7]. This paper concerns the first of these processes, which is directly related to the dynamics of the vehicle on curved and tangent track, and to the track misalignments that excite the vehicle. Wheelclimb is a derailment process in which large lateral forces acting on the wheelset cause one wheel to climb

up and over the rail (see Fig. 1). When this wheel is in flange contact, large restoring forces resisting wheelclimb result from the large contact angle at the wheel/rail interface. Frictional effects, known as creep forces, aid or inhibit the process depending on the angle of attack of the wheel relative to the rail. The vector sum of the contact forces are measured by the instrumented wheelset and are distinct from the forces applied to the wheelset through its bearings.

Wheelclimb may occur at low forward and lateral velocities, with the resultant wheel/rail forces predicted using a quasisteady approach [8,11], and have been confirmed experimentally in [9,11,12]. Since the limit on lateral forces  $F_{v0}$  scales with vertical axle load  $F_{z0}$ , a derailment quotient, or  $L/V$  ratio, is often used. When significant lateral velocities occur during the wheelclimb process, lateral forces exceeding the quasisteady derailment limit generally occur, but only for relatively short time durations [3,4,5]. A criterion developed by the Japanese National Railways (JNR) attempts to account for the large contact forces by increasing the limit on allowed  $L/V$  ratios proportionally with  $1/t_1$ , where  $t_1$  is the duration of the force pulse when it is less than 0.05 s [13].

Three distinct wheelclimb derailment processes may be identified, which become the basis for detailed analysis:

(A) Quasisteady wheelclimb, in which lateral velocity is negligible and the yaw angle remains essentially constant. This process applies to derailment during steady state curving.

(B) Single degree-of-freedom wheelclimb, in which lateral velocity effects are important, but yaw angle remains essentially constant. This condition describes steady state curving plus train action, discrete changes in track geometry, or truck hunting with relatively stiff primary yaw suspensions for the wheelset.

(C) Two degree-of-freedom wheelclimb, which includes lateral velocity and changing yaw angle effects. This process describes dynamic curving, wheelset hunting, and truck hunting with relatively compliant yaw primary suspensions.

The objective of the analytical and experimental research summarized in this paper is the evaluation of the validity of

wheelclimb criteria based on wheel load measurements. Processes A and B are treated in detail, with Process C discussed qualitatively. A single wheelset is used to establish the fundamental mechanics of the wheelclimb process, preliminary to future study of more complex processes associated with complete trucks. In Section II, the experiments conducted to evaluate the derailment criteria are described. Section III presents the analytical development of criteria for quasisteady wheelclimb. The experimental data presented agrees well with the derived criterion. In Section IV, a nonlinear model for dynamic wheelclimb is developed; the model is validated for wheelset displacement responses to pulses in applied lateral forces. Simulations using the dynamic model indicate that the magnitude and duration of  $L/V$  ratios that would be measured during dynamic wheelclimb are not related in a functional way to derailment occurrence.

In Section V, time-duration dependent wheel load criteria for dynamic wheelclimb are evaluated. A variety of wheel load criteria, including the widely recognized JNR criterion, are applied to wheel load measurements taken from 112 derailment events, with none found to be successful in predicting derailment safety.

## II Description of Wheelclimb Experiments

The development of validated derailment criteria has been inhibited previously by practical limitations in obtaining a comprehensive set of experimental measurements of critical variables under a range of conditions. The apparatus used in this research is designed to provide detailed measurements of wheelset motions and loading during the evolution of derailment events. It is also designed to provide sufficient control of test conditions so that the reproducibility of results may be established and the complete spectrum of phenomena necessary for derailment prediction be explored.

The apparatus used to study wheelclimb derailment is a one-fifth scale model wheelset described in detail in [12]. The wheels and rails are machined to unworn profiles from a polycarbonate resin material, which assures proper scaling of

## Nomenclature

$b_v, b_z$ = wheelset lateral and vertical suspension mechanical damping	$L_1, L_2$ = horizontal distances from wheelset center to wheel/rail contact points	$\alpha_1, \alpha_2$ = contact angles, defined positive counterclockwise from horizontal
$f_{z,i}$ = nondimensional lateral creep force (contact plane coordinates, $i=1$ for left wheel in tread contact, $i=2$ for right wheel in flange contact)	$L/V$ = derailment quotient, ratio of lateral to vertical forces on axle or climbing wheel	$\beta$ = partial derivative of $z$ with respect to $y$
$F_{x,i}$ = normal force at contact point $i$	$m_1$ = wheelset mass	$\Gamma_1, \Gamma_2$ = wheel $L/V$ ratios on left and right wheels, respectively
$F_{z,d}$ = effective added vertical force due to wheelset dynamics	$m_2$ = truck frame mass	$\eta$ = nondimensional roll moment applied to wheelset
$F_{v0}, F_{z0}$ = lateral and vertical forces externally applied to wheelset	$M_{ext}$ = roll moment externally applied to wheelset	$\eta_d$ = nondimensional effective roll moment due to wheelset dynamics
$k_v, k_z$ = wheelset lateral and vertical suspension stiffness	$r_0$ = nominal wheel rolling radius	$\mu$ = coefficient of friction
$I_o$ = wheelset roll inertia	$t_1$ = duration of $L/V$ ratio pulse	$\phi$ = wheelset roll angle, defined positive counterclockwise from horizontal
	$V$ = forward velocity of wheelset	$\psi$ = wheelset yaw angle, defined positive when steered towards right rail (wheelclimb rail)
	$y$ = wheelset lateral displacement from track centerline	
	$z$ = wheelset vertical displacement from position when centered laterally	

the wheel/rail contact (creepage) forces in relation to the applied axle loading. The wheelset has lateral, vertical yaw, and roll degrees of freedom, and is attached to a force measuring system with vertical and lateral freedoms, the latter simulating a generalized truck mass. The track structure is tangent track, rigid in bending and torsion to eliminate interactions between wheelset and track deflections, and maintained to Class 6+ geometry.

The instrumentation used is shown in Fig. 2. The strain gage balance produces signals which are transformed into the total wheel/rail contact forces acting on the wheelset (axle  $L/V$  ratio). Comparisons with theory are made using the axle  $L/V$  ratio, since separate wheel force measurements were not made. Quasisteady derailment (Process A) is measured by progressive lateral loading of the model with a ballscrew drive motor, with vertical load, roll moment and forward velocity held constant. During the dynamic experiments (Processes B and C), a pneumatic servo actuated photoelectrically at specific locations along the 200m test track applies lateral forces to the wheelset model. The magnitude and duration of the applied lateral forces are varied during the series of experiments, as well as vertical axle load and forward velocity. To provide uniform initial conditions for the experiments, the wheelset is held against stops near the opposing rail prior to application of the lateral force. Responses are recorded on an FM tape recorder, and subsequently digitized for detailed analysis off-line.

Experiments on Process A were conducted at yaw angles over the range of  $-3$  to  $+3$  deg, for roll moments covering the range possible without wheel lift at either wheel. To simulate Process B, a series of experiments was conducted at constant yaw angles of  $3$  to  $-3$  deg by locking this degree of freedom. Experiments for Process C were conducted using a yaw spring suspension with low stiffness. Tests were conducted on the wheelset from below critical speed to beyond the onset of hunting. Lateral force pulse inputs were superimposed on the track inputs to simulate dynamic curving.

Experiments were performed to determine the reproducibility of the derailment events. This information is useful in determining the extent to which derailment processes may be described by differential equations in a deterministic manner, without including random variations in parameters or forcing functions. The results of these experiments were highly reproducible at specific track locations, but exhibited variation in results when the same forces were applied to the wheelset at different sites along the track. Since the rails were machined to a profile that is relatively uniform along the track and the rails cleaned with methyl alcohol prior to each test, the occurrence of derailment appears to be sensitive to minor local variations in friction coefficient and railhead profile.

### III Quasisteady Wheelclimb

**Analytical Development.** The quasisteady derailment limit (Process A) is derived by calculating the maximum applied lateral force that may be sustained for a given vertical force and roll moment applied to the wheelset. The net wheel/rail reaction forces and moments acting on the wheelset in steady state as shown in Fig. 1 are balanced by applied forces  $F_{y0}$ ,  $F_{z0}$ , and moment  $M_{\phi0}$  [10]:

Lateral force:

$$0 = F_{y0} + \sum_{i=1}^2 F_{3,i} (\mu f_{2,i} \cos \alpha_i + \sin \alpha_i) \quad (1)$$

Vertical force:

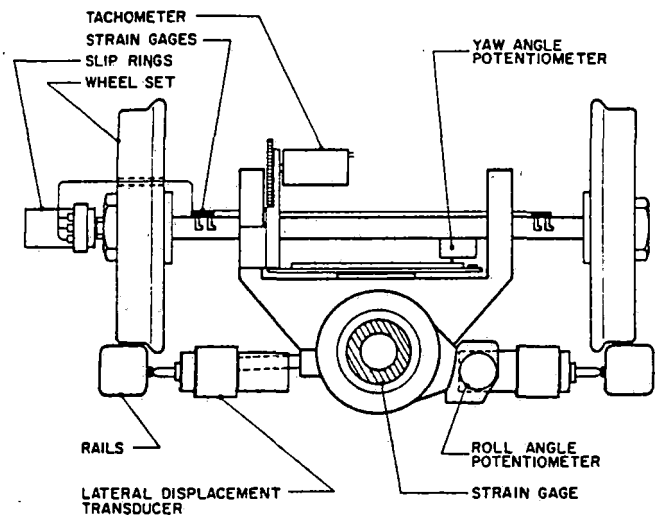


Fig. 2 Instrumentation for single wheelset wheelclimb experiments

$$0 = F_{z0} + \sum_{i=1}^2 F_{3,i} (-\mu f_{2,i} \sin \alpha_i + \cos \alpha_i) \quad (2)$$

Roll Moment:

$$0 = M_{\phi0} - \sum_{i=1}^2 (-1)^i L_i F_{3,i} (-\mu f_{2,i} \sin \alpha_i + \cos \alpha_i) \quad (3)$$

The normal forces  $F_{3,i}$  at the contact points may be eliminated to yield the vertical and lateral forces acting on each wheel. The wheel/rail reaction forces are then combined to give  $L/V$  ratios for the wheelset axle (both wheels) or for the climbing wheel only.

$$\left. \frac{L}{V} \right|_{\text{axle}} = [l_2 \Gamma_1 + l_1 \Gamma_2] + \frac{1}{2} \eta [-\Gamma_1 + \Gamma_2]$$

where

$$\Gamma_1 = \frac{\tan(\alpha_1 + \phi) + \mu f_{2,1}}{1 - \mu f_{2,1} \tan(\alpha_1 + \phi)}$$

$$\Gamma_2 = \frac{\tan(\alpha_2 + \phi) + \mu f_{2,2}}{1 - \mu f_{2,2} \tan(\alpha_2 + \phi)} \quad (4)$$

$$\eta = -\frac{2M_{\phi0}}{(L_1 + L_2)F_{z0}}$$

$$l_1 = \frac{L_1}{L_1 + L_2}$$

$$l_2 = \frac{L_2}{L_1 + L_2}$$

Parameters  $\Gamma_1$  and  $\Gamma_2$  are the individual wheel  $L/V$  ratios for the left and right wheels, respectively. Parameter  $\eta$  is the dimensionless roll moment, representing the degree of asymmetry in axle load between the extremes of wheel lift (with a practical range of  $\pm 1$ ). In the foregoing equations,  $f_{2,1}$  and  $f_{2,2}$  are the dimensionless lateral creep coefficients (including spin) on the left and right wheels,  $\phi$  the wheelset roll angle, and  $\alpha_1$  and  $\alpha_2$  the associated contact angles, defined to be positive counterclockwise. The nomenclature and coordinate system is developed in [8,10]. For the quasisteady process, parameters  $\Gamma_1$  and  $\Gamma_2$  are functions of lateral position  $y$  and yaw angle  $\psi$ ; for each value of  $\psi$ , a maximum for  $L/V$  exists, usually close to the value for  $y$  which yields the maximum contact angle on the climbing wheel.

The  $L/V$  ratio for the climbing wheel is often used itself as a

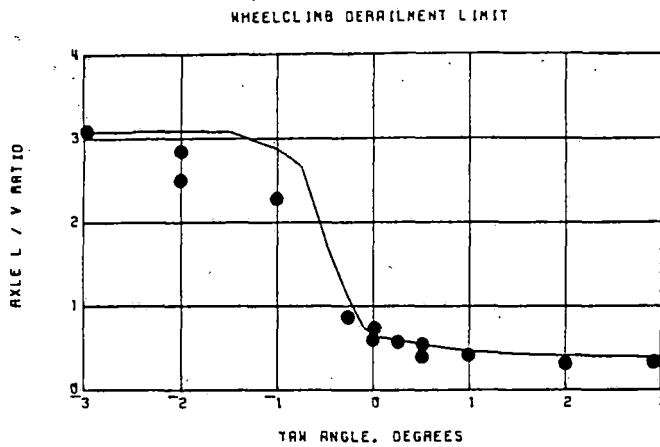


Fig. 3 Comparison of quasisteady theory and experiment for wheelclimb derailment limit with zero roll moment

derailment criteria, and is defined using the above parameters as<sup>1</sup>

$$\left. \frac{L}{V} \right|_{\text{climbing wheel}} = \Gamma_2 = \frac{\tan(\alpha_2 + \phi) + \mu f_{2,2}}{1 - \mu f_{2,2} \tan(\alpha_2 + \phi)} \quad (5)$$

For large yaw angles, equation (5) approaches the classical limit of Nadal [8], but for the range of conditions  $-3 \text{ deg} < \psi < +3 \text{ deg}$  the nondimensional creep  $f_{2,2}$  may vary considerably with wheelset loading, wheel/rail profiles, and yaw angle, over the range  $-1 < f_{2,2} < 1$ . Under quasisteady conditions, the creepages are functions only of the wheel and rail profiles, wheelset displacement, and yaw angle relative to the rail, so that equations (1)–(5) are independent of forward velocity  $V$ .

**Experimental Validation and Usefulness of Model.** The predicted and measured quasisteady axle  $L/V$  derailment limits are shown in Fig. 3 for zero applied roll moment. The agreement is very good for positive yaw angles, which constitute the lowest  $L/V$  ratio (most hazardous) regime. At negative yaw angles, derailment occurs at  $L/V$  ratios that are lower than predicted by quasisteady theory. Derailment limits for non-zero roll moments are shown in Fig. 4, exhibiting good agreement between measured and predicted values for positive yaw angles, but with the same discrepancy for negative yaw angles as for zero roll moment. The effect of roll moment for axle  $L/V$  (Fig. 4) is significant, in that it represents the change in derailment limit resulting from loading and unloading the derailing wheel. As discussed in [11], this effect is included in a single  $L/V$  ratio criterion when the wheel  $L/V$  ratio in equation (5) is used.

The results for quasisteady wheelclimb are consistent with roller rig data in [9], where the theory also overpredicts the derailment limit for negative yaw angles (but with a smaller error). The source of the discrepancy in the present tests has not been positively identified, but may be due either to the presence of the lateral track dynamic input (not accounted for in theory) or to local variation in friction coefficient or contact angle. Since the data presented are the only published results for tangent track experiments, conservative safety criteria should be based on the lower measured values rather than the theory for negative yaw angles.

#### IV Dynamic Wheelclimb

**Analytical Development.** Previously published models of wheelclimb derailment have been based on assumptions of constant friction coefficient and contact angle which greatly

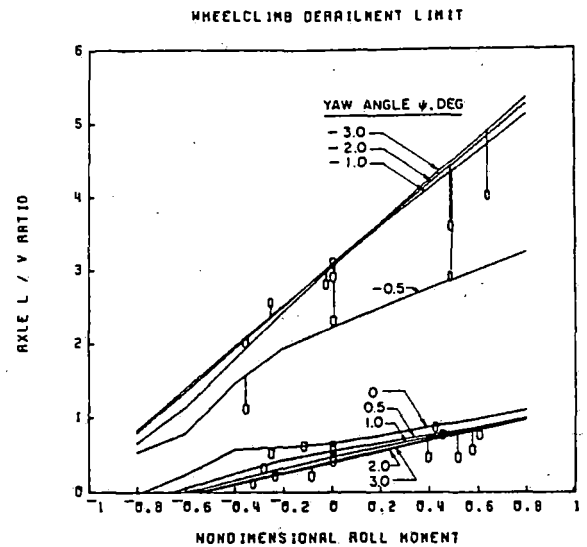


Fig. 4 Comparison of quasisteady theory and experiment for wheelclimb derailment limit for varying yaw angles and roll moments

simplify the analysis [7,9]. For the model to achieve predictive capability, nonlinear effects including creep forces, adhesion limits, variations in contact angles and contact zone geometry, kinematic constraints, and dynamic loading of the contact points should be considered. While the basic physics of these effects have been established in the literature, they have not been incorporated in an analysis yielding quantitative results for wheelclimb derailment. The goal of prediction of wheelclimb derailment, and comparison with experimental measurements, goes considerably beyond prior work.

In Process B, the yaw angle remains nearly constant during the derailment, but effects of lateral velocity  $\dot{y}$  are important both before and after flange contact. The yaw angle may remain constant due to a stiff primary suspension or kinematic constraints applied by the truck frames. The equations for lateral, vertical, and roll motions of the wheelset are,

**Motion in y-direction:**

$$(m_1 + m_2)\ddot{y} + b_y\dot{y} + k_y y = F_{y0} + \sum_{i=1}^2 [F_{3,i} (\mu f_{2,i} \cos \alpha_i + \sin \alpha_i)] \quad (6)$$

**Motion in z-direction:**

$$(m_1 + m_2)\ddot{z} + b_z\dot{z} + k_z z = F_{z0} + \sum_{i=1}^2 [F_{3,i} (-\mu f_{2,i} \sin \alpha_i + \cos \alpha_i)] \quad (7)$$

**Motion in  $\phi$ -direction:**

$$I_\phi \ddot{\phi} - m_1 r_0 \ddot{y} = M_{\phi 0} - \sum_{i=1}^2 [(-1)^i L_i F_{3,i} \cdot (-\mu f_{2,i} \sin \alpha_i + \cos \alpha_i)] \quad (8)$$

These equations result directly from summation of forces and moments in Fig. 1. The wheelset is assumed to have linear lateral and vertical suspensions, defined by  $b_y, k_y, b_z$  and  $k_z$ . Axle loads  $F_{y0}$ ,  $F_{z0}$ , and  $M_{\phi 0}$  are inputs to the system, while the normal forces  $F_{3,i}$  at the contact points are unknowns dependent on the wheelset motion.

If simultaneous single point contact is assumed for each wheel, kinematic constraints may be applied relating vertical

<sup>1</sup>For simplicity, assume right wheel is climbing.

displacement and roll to lateral displacement,

$$z = Z(y) = \beta(y) \cdot y \quad (9)$$

$$\phi = \Phi(y) = \frac{\beta(y)}{L} \cdot y \quad (10)$$

where  $\beta(y)$  is the partial derivative of  $z$  with respect to  $y$  and  $L = (L_1 + L_2)/2$ .

Using equations (7-10) to eliminate contact forces  $F_{3,i}$  and degrees of freedom  $z$  and  $\phi$  yields an equivalent single degree-of-freedom equation for lateral displacement  $y$  which is an extension of equation (4) to include dynamic effects,

$$(m_1 + m_2)\ddot{y} + b_y\dot{y} + k_y y = F_{y0} + \frac{1}{2}(\Gamma_1 + \Gamma_2)(-F_{z0} + F_{z_d}) + \frac{F_{z0}}{2}(\Gamma_1 - \Gamma_2)(\eta + \eta_d) \quad (11)$$

In equation (11), the nondimensional  $L/V$  ratios on the two wheels  $\Gamma_1$  and  $\Gamma_2$  have been generalized to include the effect of  $\dot{y}$ ,

$$\Gamma_1 = \Gamma_1(y, \dot{y}, \psi)$$

$$\Gamma_2 = \Gamma_2(y, \dot{y}, \psi) \quad (12)$$

The definitions for  $\Gamma_1$  and  $\Gamma_2$  given in equations (2) and (3) still apply, but the evaluation of creep coefficients  $f_{2,1}$  and  $f_{2,2}$  should now include the effect of lateral velocity. Parameters  $F_{z_d}$  and  $\eta_d$  reflect the changes in wheel/rail contact forces due to the wheelset dynamic loading,

$$F_{z_d} = (m_1 + m_2)\beta\ddot{y} + b_z\beta\dot{y} + k_z\beta y \quad (13)$$

$$\eta_d = \frac{2}{F_{z0}} \left( \frac{I_\phi}{L} - m_1 r_0 \right) \frac{\beta\ddot{y}}{L} \quad (14)$$

The dynamic vertical force  $F_{z_d}$  affects the left and right wheel contact force functions  $\Gamma_1$  and  $\Gamma_2$  symmetrically, while the dynamic roll moment  $\eta_d$  affects the two differentially. While the physical phenomena incorporated in the model have been identified previously in the literature, the present approach is new in the sense that the dynamic loading of the contact zones (equations (13-14)), nonlinear contact geometry (equations (9-10)), and nonlinear creep forces using the Kalker theory are included in the simulations to maintain model accuracy for the extreme conditions associated with derailment. The analysis is also unique in the manner by which it is formulated as a direct extension of the quasisteady theory.

Equation (11) is solved by numerical integration. Contact geometry functions including contact angles, contact ellipse geometry, and rolling radii are computed using the program in [14]; creep forces are computed using the Kalker method given in [15]. To speed computation, results from the foregoing are precomputed and stored for use in a table look-up procedure. In performing the simulations, the lateral velocity is assumed to be the same immediately before and after flange contact, which is equivalent to stating that impact effects are negligible. This is the case when the incident lateral velocities are less than the forward velocity, resulting in the initiation of flange contact being more like a "kiss" than a jolt. This assumption has been validated through our experiments, where velocity has been measured to be continuous at the initiation of flange contact, and large impulsive forces associated with an impact are absent in the wheel load measurements.

**Experimental Validation and Usefulness of Model.** Typical simulated responses of the wheelset to pulses in applied lateral force are shown in Figs. 5 and 6 for comparison with the measured signals. The parameters used in the simulations are summarized in Table 1, representing the scale model wheelset

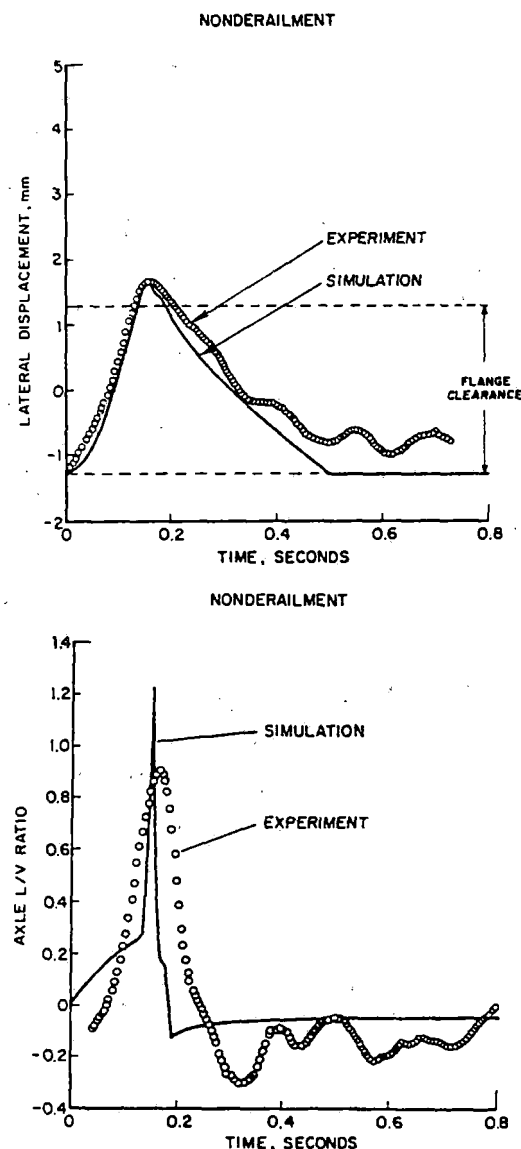


Fig. 5 Simulated and measured dynamic wheelset lateral displacement and axle  $L/V$  ratio responses to pulse lateral force input (nonderailing case)

Table 1 Parameters for one-fifth scale model wheelset experiment (Used in Simulations)

Parameter	Symbol	Value	Units
Wheelset mass	$m_1$	3.14	kg
Truck frame mass	$m_2$	8.91	kg
Lateral spring stiffness	$k_y$	1420.	n/m
Lateral damping	$b_y$	96.5	n-s/m
Vertical spring stiffness	$k_z$	0	n/m
Vertical damping	$b_z$	0	n-s/m
Applied vertical axle load	$F_{z0}$	67.0	n
Applied roll moment	$M_{\phi 0}$	0	n-m
Wheel rolling radius	$r_0$	84.1	mm
Distance between contact points	$L_1 + L_2$	287.	mm
Roll inertia	$I_\phi$	0.059	kg-m <sup>2</sup>
Friction coefficient	$\mu$	0.3	-

used in the experiment. The simulations include the dynamics of the pneumatic actuator used to apply the lateral force, which acts as a first order lag with 0.125 sec. time constant. The agreement between predicted and measured lateral displacements for nonderailing and derailing cases is good, although for the latter case the predicted derailment occurs more rapidly than that measured. While the time histories of



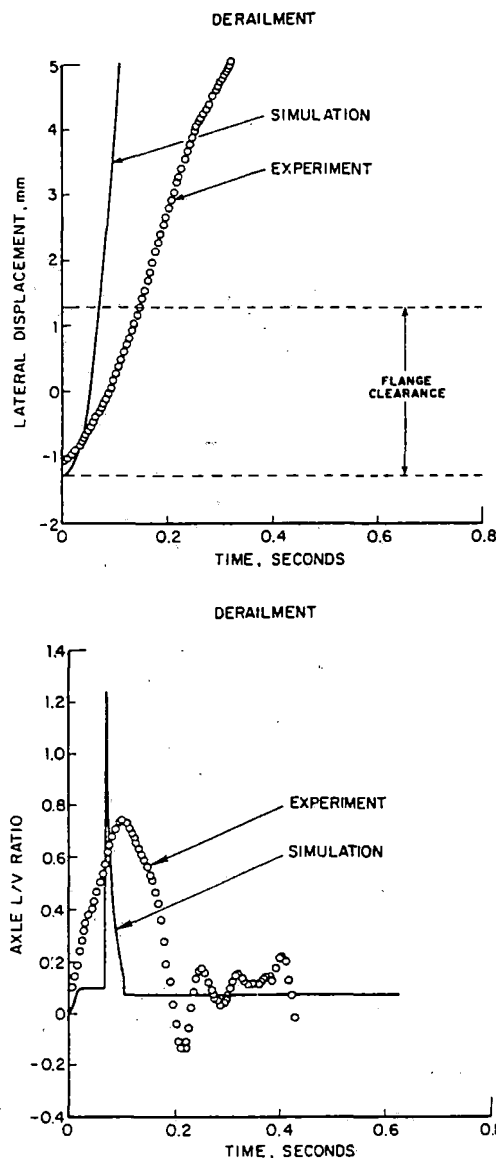


Fig. 6 Simulated and measured dynamic wheelclimb lateral displacement and axle  $L/V$  ratio responses to pulse lateral force input (derailing case)

displacements for these and other measured derailment events agree well with theory, refinement of the analytical model and measurement techniques is desirable to obtain more precise prediction of  $L/V$  ratios during dynamic wheelclimb. The measured  $L/V$  ratio pulse for the nonderailing case (Fig. 5) has a smaller maximum value and longer duration than predicted. Detailed examination of the simulation results shows that the  $L/V$  ratio response is very sensitive to friction coefficient, instantaneous contact geometry, and creepage, while the lateral displacement time history is not very sensitive. Since the  $L/V$  ratio pulse coincides in time with the initiation of large contact, the assumptions of (1) single point contact used to evaluate the contact geometry and (2) continuous contact to preserve well-behaved creep forces are critical. Further, the  $L/V$  measurement is derived from signals from the strain gage balance holding the wheelset axle instead of from strain gages mounted on the wheels; possible discrepancy between the actual wheel/rail contact forces and the  $L/V$  ratios measured under dynamic conditions by the balance may be resolved in future experiments using instrumented wheelsets. The discrepancy in duration of the  $L/V$  ratio peak measured in the derailing case (Fig. 6) is larger, due to the associated discrepancy in time required for the derailment to occur. The previously published theory for

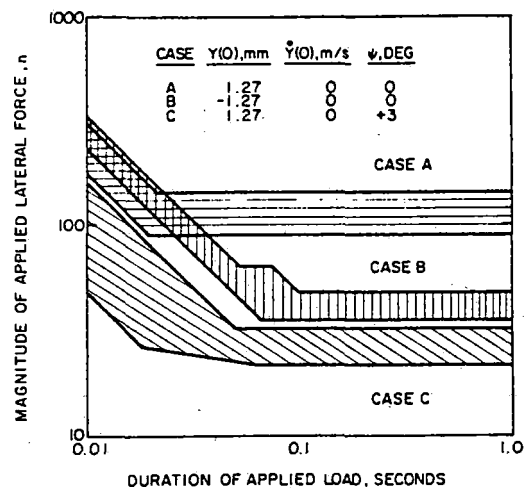


Fig. 7 Magnitude and duration of applied lateral forces resulting in simulated marginal derailments (shaded regions) for varying initial conditions and yaw angles. Nonderailments are below shaded regions, derailments are above.

dynamic wheelclimb does not attempt to predict time duration of the  $L/V$  ratio pulse, but instead *assumes* a duration of 0.01 s [9]. The measured durations are also generally higher than those predicted in the previous reference (up to 0.04 s).

The simulation model is useful in understanding the causes of dynamic wheelclimb derailment and the types of  $L/V$  ratio responses associated with different derailment events. For this discussion, derailment events are categorized on the basis of their maximum lateral displacements. For a wheelset with a 1.27 mm flange clearance (6.34 mm full scale), nonderailments have maximum lateral displacements (measured from the track centerline) of 1.9 mm in model scale (9.5 mm in full scale). A marginal derailment is defined for maximum excursions between 1.9 mm and 3.5 mm (9.5 mm and 17.5 mm full scale), with derailment defined to exceed 3.5 mm (17.5 mm full scale). In the marginal derailment case, the wheelset displacement exceeds the point of maximum contact angle, so that only a reversal in applied lateral force can prevent a complete derailment. At the onset of complete derailment, the contact angle reaches zero (i.e., the wheel is riding on its rim on top of the rail).

Using the simulation model, the amplitude and duration of the applied lateral force  $F_{y0}$  may be varied to yield a well-defined dynamic wheelclimb limit, as shown in Fig. 7 for given model parameters and initial conditions. Wheelclimb is inhibited by short duration of applied lateral force, either by limiting lateral displacement to less than the quasisteady limit or by reversing the direction of applied force to cause the wheelset to recover from a marginal derailment.

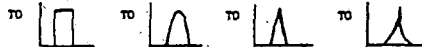
As shown in Fig. 7, the quasisteady limit (asymptotic value for large time duration) varies with yaw angle in Cases A and C, as would be expected from Process A, but also with initial conditions. Cases A and B differ only in that the wheelset starts from rest at different lateral displacements; Case B has a lower derailment limit because it reaches flange contact with significant momentum in the lateral direction that contributes to wheelclimb.

The results shown in Fig. 7 *should not be misinterpreted* to mean that derailment boundaries for  $L/V$  ratio amplitudes and time durations are similarly well-defined. The amplitude and duration of the  $L/V$  ratio pulse are dependent on the time histories of lateral displacement, velocity, and acceleration while in flange contact, which are not related in any simple functional way to the magnitude and duration of the applied force.

Table 2 Candidate wheelclimb derailment criteria

TYPE	ORDINATE	ABSCISSA	SENSITIVITY*
1	PEAK VALUE	TIME ABOVE ZERO (TAZ)	
2	INTEGRATED VALUE	TAZ	
3	INTEGRATED VALUE/TAZ	TAZ	
4	PEAK VALUE	TIME WITHIN N% OF PEAK (TNP)	
5	INTEGRATED VALUE	TNP	
6	THRESHOLD VALUE	TIME PULSE EXCEEDS THRESHOLD (TAT)	

\*SENSITIVITY TO PULSE AREA (A), SHAPE (S), AND DURATION ABOVE ZERO (D), EACH WITH OTHER PARAMETERS HELD CONSTANT. SHAPE VARIABLE S REPRESENTS TRANSITION THROUGH SHAPES



Examination of the simulation results in detail indicates that derailment criteria based on  $L/V$  ratio amplitude and duration alone are poor predictors of derailment. Once the wheelset displacement reaches the marginal derailment region, the contact angle on the climbing wheel falls off rapidly. The measured  $L/V$  ratios will also decrease rapidly, just at the most critical point in the derailment process. Therefore, meaningful interpretation of  $L/V$  ratio data is dependent on other variables, such as lateral displacement and velocity. This finding may indicate the direction for future research to be the synthesis of multivariable derailment criteria.

## V Evaluation of Derailment Criteria

**Commonly Used Criteria.** Although a larger set of variables are available from the experiments and simulations for use in synthesizing criteria for wheelclimb derailment, in this paper attention is restricted to those criteria which make use of the time histories of wheel loads only. The objective here is to evaluate the hypothesis that sufficient information exists in the wheel load measurements alone to predict derailment safety reliably.

The basic information available in these pulse-like signals may be distilled into the following quantities: peak value, integrated value, average value over pulse duration, shape of pulse, duration above threshold, etc. Table 2 is a summary of candidate criteria which are of the general form of a load amplitude versus time duration. To test the hypothesis, a wide selection of candidate criteria is explored. The widely used JNR Criterion is of Type 4 in the table; duration  $t_1$  is defined to be 1.5 times the period during which the pulse exceeds 50 percent of its peak value [13].

Criteria 1-5 yield a single data point for each event; Criteria 6 yields a locus of points as the threshold value is swept from

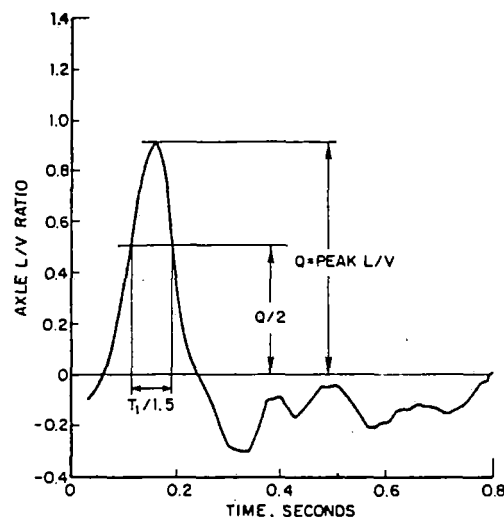


Fig. 8 Application of JNR criterion to typical measured  $L/V$  ratio pulse

zero to the pulse peak. All criteria may be applied to either  $L/V$  ratios or lateral forces alone. Criteria involving peak values may lack physical significance and are vulnerable to erroneous conclusions drawn from noisy instrumentation or wheel loads resulting from high frequency vibration. Integrated lateral force has units of change in momentum, although it does not represent the time change in momentum since only the wheel/rail reaction forces are being included. By dividing the integrated value by the time duration, the magnitude averaged over the pulse is obtained. Criteria 4 and 5 may be used to define pulse duration when the mean value of the signal before and after the pulse is above zero.

The sensitivity of each criterion to changes in pulse area, shape, and duration is shown in Table 2. In this context, sensitivity refers to the ability of a criterion to discriminate between pulses on the basis of area, duration, or shape by yielding a different  $(x,y)$  value or locus in the graph. For example, if a criterion sensitive to area were found to be a good derailment predictor, then derailment could be correlated with momentum. Many additional criteria can be proposed, but they generally will perform in a manner very similar to those in Table 2.

**Experimental Evaluation.** The recorded experimental wheel load and lateral displacement time histories were digitized and analyzed using computer subroutines which implemented the various criteria.

For Process B, 112 derailment events (occurrence of large  $L/V$  ratios or lateral displacements) were examined, distributed in the following test matrix. Cases were selected deliberately to be near the derailment limit, and do not reflect the distribution of their occurrence in the field.

Test Matrix	3 deg	Yaw Angle 0 deg	-3 deg
No derailment	10	19	1
Marginal derailment	9	13	17
Complete derailment	8	21	14

A special feature of these experiments is the large number of marginal and complete derailments which would not generally be available from full-scale field tests.

Figure 8 illustrates the application of the JNR criterion to a typical  $L/V$  ratio pulse, with the results of similar application

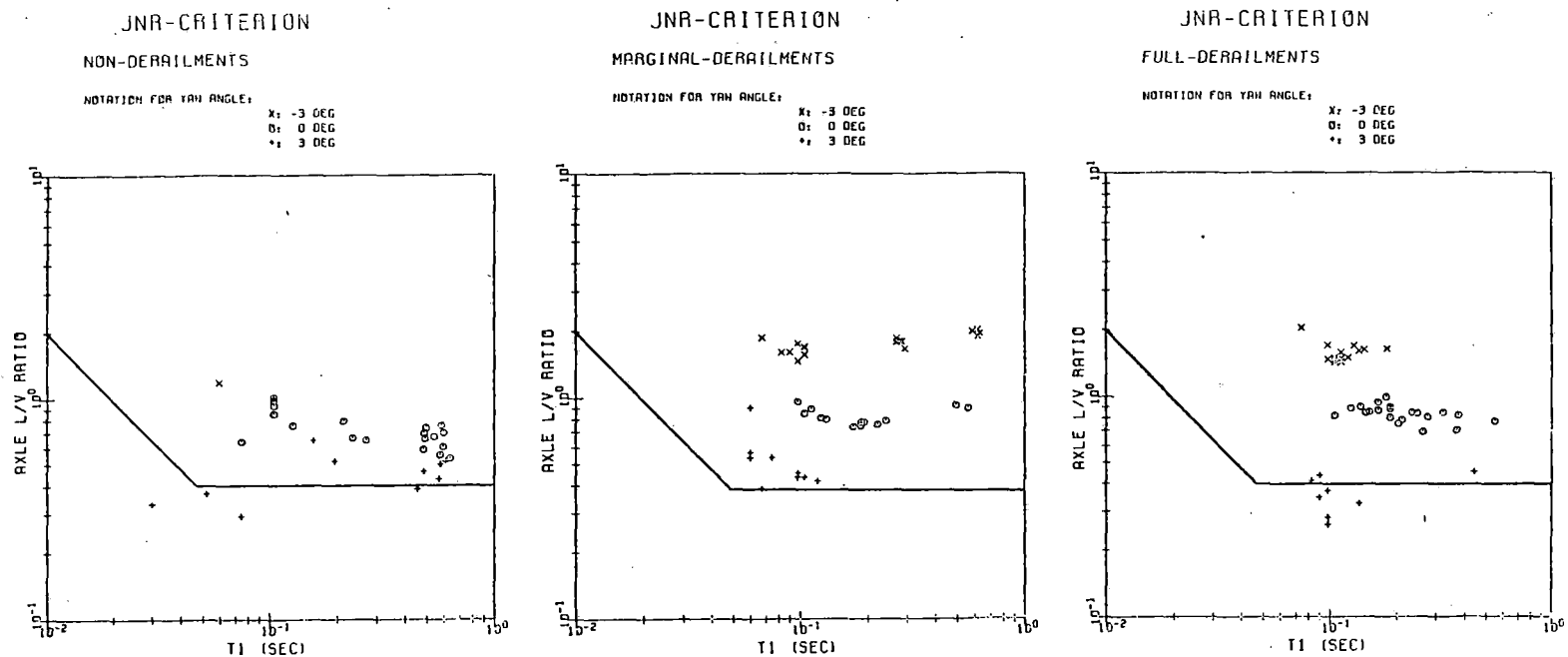


Fig. 9 Comparison of dynamic wheelclimb experimental data with JNR criterion

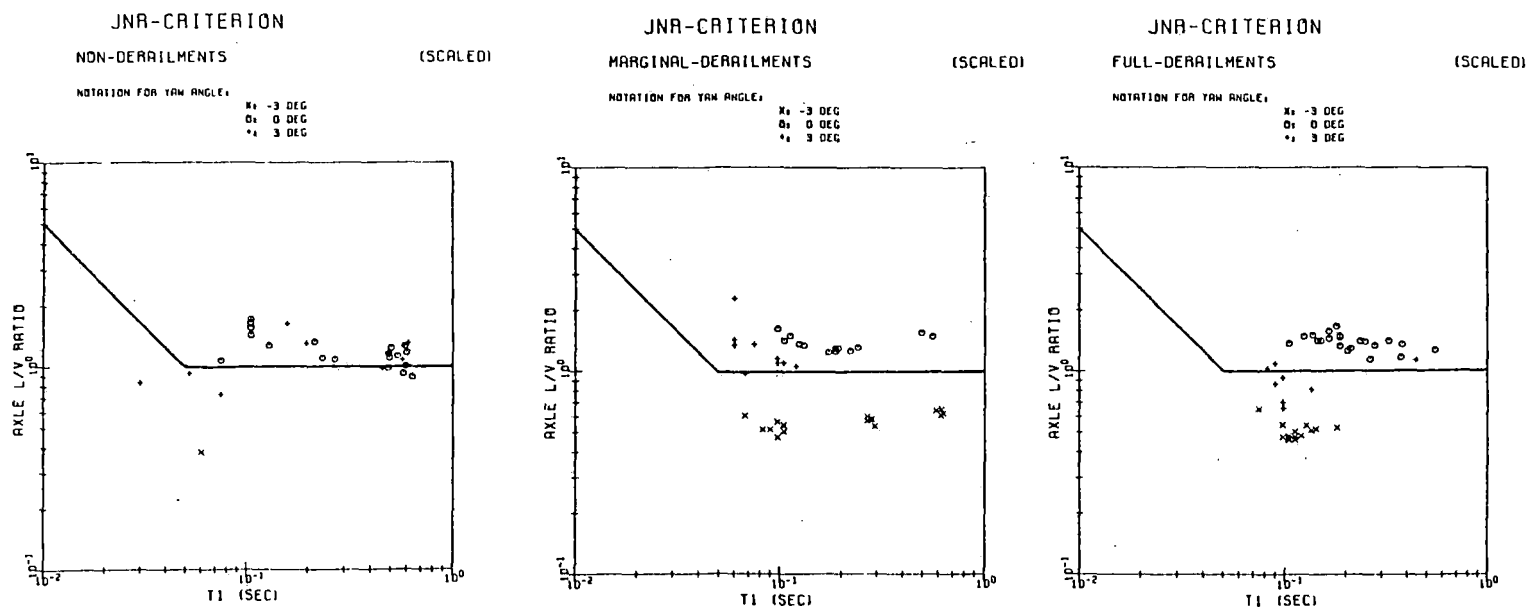


Fig. 10 Comparison of dynamic wheelclimb experimental data with JNR criterion rescaled with quasisteady limits at different yaw angles

to the events in the test matrix shown in Fig. 9. The JNR Criterion is modified using equations (4) and (5) to convert wheel  $L/V$  ratio to axle  $L/V$  ratio. It is clear from these results that not only does the JNR criterion not predict derailment, but that no criterion based solely on  $L/V$  ratio and time duration could separate the derailment, marginal derailment, and nond derailment regions. The data in Fig. 9 includes measurements at all yaw angles; from the quasisteady derailment results, strong influence of yaw angle could be expected. By rescaling the data and JNR Criterion by the quasisteady limits shown in Fig. 3 (0.4 at +3 deg, 0.6 at 0 deg, 3.1 at -3 deg), a normalized version of the JNR Criterion results, given in Fig. 10. The JNR Criterion is still an inadequate derailment predictor using this modification. The other candidate criteria in Table 2 were also found to be inadequate; details of the complete evaluation of criteria are given in [16].

Analysis of experimental results for Process C are more difficult to assess. From the measured responses, it was found that at flange contact the yaw moment resulting from longitudinal creep forces always steers the wheelset towards the track centerline (makes yaw angle more negative). Since the  $L/V$  ratios required for wheelclimb derailment increase with negative yaw angles, this steering action inhibits derailment. Dramatic differences in response to successive equal lateral force applications were observed to be due to the difference in yaw angle at initial flange contact, i.e., the derailment limit is dependent on the yaw angle at initial flange contact. Although a thorough analysis of data from the Process C experiments is beyond the scope of this paper, the limited evidence indicates that the predictive capability of  $L/V$  ratio indices alone would be poor, since the process is even more complex than Process B.

## V Conclusions

The experimental and analytical studies of wheelclimb derailment presented in this paper result in the following conclusions regarding derailment criteria:

1 Wheelclimb derailment criteria based on quasisteady theory are adequate for derailment prediction under conditions of negligible lateral incident velocity and constant positive yaw angle. At negative yaw angles, derailment occurs at  $L/V$  ratios somewhat below the predicted limits.

2 Application of the JNR and other time-duration dependent derailment criterion for nond derailment, marginal derailment, and complete derailment cases are each spread over an order of magnitude in  $L/V$  ratio amplitude and time duration. None of the criterion tested could distinguish between safe and unsafe conditions. Defining a safety criterion below the derailment data would be overly conservative, possibly excluding vehicles, operating conditions, and track and maintenance standards that could be demonstrated to be safe with a more discriminating criterion. Furthermore, the data provided do not necessarily establish a lower bound for derailment, since lower points possibly could be measured.

3 The analytical models presented in this paper aid in in-

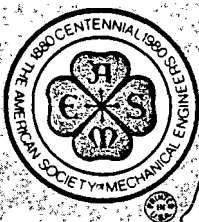
terpreting measurements resulting from dynamic wheelclimb processes, and offer the potential for development of implementable derailment criteria based on additional measurements that will augment information contained in the  $L/V$  ratio time histories. While they yield good agreement with measurements of wheelset displacement and derailment, exact prediction of the shape of the  $L/V$  response during wheelclimb requires more precise characterization of the local contact geometry and friction than present in the model.

## Acknowledgment

The authors acknowledge the assistance of E. Griffith and J. Grieb in design and fabrication of the apparatus and timely suggestions of Dr. R. Brantman of the U.S. Department of Transportation during the writing of this paper. The research was supported by the U.S. Department of Transportation, Transportation Systems Center, under Contract No. DOT-TSC-1603.

## References

- 1 Thompson, W. I., III, "Plate Instrumented Wheelsets for the Measurement for Wheel/Rail Forces," Report No. FRA/ORD-80-58, Federal Railroad Admin., Wash., D.C., Oct. 1980.
- 2 Prockington, A. R., and Allen, R. A., "Improved Data from Load Measuring Wheels," *I. Mech. E. Railway Engineer*, July/Aug. 1977.
- 3 Modrasky, J., Donnelly, W. J., Novak, S. P., and Smith, K. R., "Instrumented Locomotive Wheels for Continuous Measurements of Vertical and Lateral Loads," ASME Paper 79-RT-8, Feb. 1979.
- 4 Ikemori, M., "A Study of Track Maintenance for the Derailment Due to the Interaction Between Track and Vehicle," *JNR RTRI Quarterly Reports*, Vol. 19, No. 1, 1978.
- 5 Tong, P., Brantman, R., and Grief, R., "Analysis and Measurement of Locomotive Dynamic Characteristics," ASME Paper 79-WA/RT-10, Aug. 1979.
- 6 Dean, F. E., and Ahlbeck, D. R., "Criteria for High-Speed Curving of Rail Vehicles," ASME Paper 79-WA/RT-12, Aug. 1979.
- 7 Brantman, R., Griffin, J. W., and Jeffcoat, R. L., "A Methodology for Estimating the Derailment Probability of a Fleet of Railway Vehicles," ASME Paper 79-WA/RT-6, Aug. 1979.
- 8 Gilchrist, A. O., and Brickle, B. V., "A Re-Examination of the Proneness to Derailment of a Railway Wheelset," *J. Mech. Engr. Sci.*, Vol. 18, No. 3, 1976.
- 9 Arai, S., and Yokose, K., "Simulation of Lateral Motion of 2-Axle Railway Vehicle in Running," in *The Dynamics of Vehicles on Roads and Railway Tracks*, ed., Pacejka, H. B., Swets and Zeitlinger B.V., Amsterdam, 1976.
- 10 Sweet, L. M., and Sivak, J. A., "Nonlinear Wheelset Forces in Flange Contact - Part I: Steady State Analysis and Numerical Results," ASME JOURNAL OF DYNAMIC SYSTEMS, MEASUREMENT AND CONTROL, Vol. 101, No. 3, Sept. 1979.
- 11 Sweet, L. M., Karmel, A., and Moy, P., "Wheelclimb Derailment Criteria Under Steady Rolling and Dynamic Loading Conditions," in *The Dynamics of Vehicles on Roads and Railway Tracks*, ed., Willumeit, H.-P., Swets and Zeitlinger, B. V. Lisse, Aug. 1979.
- 12 Sweet, L. M., Sivak, J. A., and Putman, W. F., "Nonlinear Wheelset Forces in Flange Contact - Part II: Measurements Using Dynamically Scaled Models," ASME JOURNAL OF DYNAMIC SYSTEMS, MEASUREMENT AND CONTROL, Vol. 101, No. 3, Sept. 1979.
- 13 Matsudaira, T., "Dynamics of High Speed Rolling Stock," *JNR RTRI Quarterly Reports*, Special Issue, 1963.
- 14 Heller, R., and Cooperrider, N. K., "User's Manual for Asymmetric Wheel/Rail Contact Characterization Program," DOT Report FRA/ORD-78/05, Dec. 1977.
- 15 Goree, J. G., and Law, E. H., "User's Manual for Kalker's Simplified Nonlinear Creep Theory," DOT Report FRA/ORD-78/06, Dec. 1977.
- 16 Sweet, L. M., and Karmel, A., "Wheelclimb Derailment Processes and Derailment Criteria," Report on Contract DOT-TSC-1603, Princeton University, May 1981.



AN ASME PUBLICATION  
\$4.00 per copy \$2.00 to ASME Members

# ASME

THE AMERICAN SOCIETY OF MECHANICAL ENGINEERS  
345 E. 47 St., New York, N.Y. 10017

The Society shall not be responsible for statements or opinions advanced in papers or in discussion at meetings of the Society or of its Divisions or Sections, or printed in its publications. Discussion is printed only if the paper is published in an ASME Journal or Proceedings. Released for general publication upon presentation. Full credit should be given to ASME, the Technical Division, and the author(s).

REFERENCE 199

## A Quasi-Static Model to Rapidly Assess Lateral Train Stability

**R. Brantman**

Coordinator,  
Rail Dynamics Projects,  
Structures and Mechanics Branch,  
U. S. Department of Transportation,  
Transportation Systems Center,  
Cambridge, MA  
Mem. ASME

*The applications and capabilities of a computer-based quasi-static model for assessing lateral train stability are described. The model provides a rapid means of analyzing the ability of any consist to withstand quasi-static train buckling and stringlining forces as a function of track curvature. A significant feature of the model is its minimal core and CPU time requirements. It requires only 18K words of core, and can analyze a 100-car consist, in both buff and draft, at 17 individual degrees of curve in a total CPU time of 6 sec. As such, the model has potential for use not only by the researcher, but for direct on-line use by the yardmaster. Specifically, the model has been designed so that it can be used in real-time to evaluate and assist in train makeup, and to estimate the maximum safe locomotive dynamic brake and tractive effort force levels, at each degree of curve, for any given train consist.*

### 1. PROBLEM ADDRESSED

Railroad operations in North America have undergone many changes in recent years. During the last decade, for example, the use of larger and more specialized vehicles combined to reduce the average number of vehicles per freight train while increasing the net average freight train load by over 20 percent [1].\* This increase in average freight train load implies an increase in average longitudinal drawbar forces. Since lateral forces are created by the tensile (draft) or compressive (buff) drawbar forces in a train whenever the longitudinal centerlines of the vehicles are skewed relative to one another (such as in a curve), this increase in average drawbar force creates more opportunities for train action related accidents [2, 3]. According to the Federal Railroad Administration (FRA) accident statistics for 1979 [4], on average, there were two train handling derailments every day. The reported direct cost was close to 12 million dollars.

In light of this, the Transportation Systems Center (TSC) has sought to develop a Train Stability Analysis (TSA) computer model to assess the maximum allowable buff and draft force levels for safe curve negotiation of any given consist. This model can essentially be used in real-time to evaluate and assist in train makeup, and to establish maximum safe locomotive dynamic brake and tractive effort force levels.

\*Numbers in brackets refer to references listed at the end of the paper.

### 2. APPROACH

The model is that of a train rounding a uniform curve under steady-state buff or draft conditions, resulting from head-end dynamic braking or tractive effort. Under these conditions the train will assume some buckled or stringlined mode, constrained only by the trucks bearing hard up against the rails. This is illustrated in Figure 1, which shows the buckling mode to be a superposition of the nominal orientation of the cars on the track centerline, and some skewed position of the cars relative to the centerline, due to all the rail/wheelset/truck frame/carbody clearances being taken up under the lateral action of the coupler forces. The wheel/rail lateral forces produced, resulting from the steady-state curving forces and the lateral components of the coupler forces, can be very large.

The first general model to address this problem was developed by the Association of American Railroads (AAR) in conjunction with the Electro-Motive Division (EMD) of General Motors Corp., and is described in Reference [5]. This Quasi-Static Lateral Train Stability (QLS) model uses a numerical iteration scheme to obtain the quasi-static buckling or stringlining solution to a given set of operating and initial conditions. Since it is a simulation model, it provides a solution only to the specific input conditions. For a given train on a given curve, there would be many possible solutions, depending upon the specific operating and initial conditions just prior to braking or acceleration.

Contributed by the Dynamic Systems & Control Division of THE AMERICAN SOCIETY OF MECHANICAL ENGINEERS for presentation at the Winter Annual Meeting, November 15-20, 1981, Washington, D.C. Manuscript received at ASME Headquarters July 14, 1981.

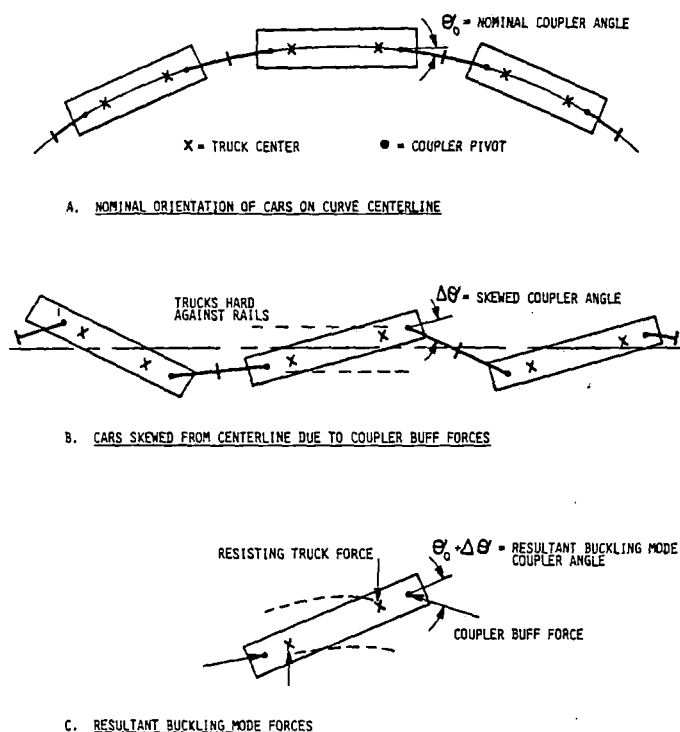


Fig. 1 Train Buckling When Rounding a Curve Under Buff

The Train Stability Analysis (TSA) model, developed at TSC, is an outgrowth of the QLS model. However, both its objective and computational approach are very different. The TSA model is not a simulation model; it does not attempt to simulate a specific set of given conditions, nor does it use numerical iteration. Rather, the TSA model formulates the problem analytically, using a set of nonholonomic constraints (corresponding to the possible buckling modes), and identifies the worst case, steady-state train buckling and stringlining conditions, for each degree of curve, for the given consist. The technical details of this approach are contained in Reference [6]. The end result is that the model not only automatically identifies what would be the worst case possible solution, but it operates about 100 times faster than QLS. In particular, the TSA computer model uses only 18K words of core, and can analyze a 100-car consist, in both buff and draft, at 17 individual degrees of curve in a total CPU time of 6 seconds.

Using the above approach, the TSA model identifies the maximum allowable dynamic braking and tractive effort force, at the head end, such that no car in the consist exceeds some specified critical L/V ratio. (Currently, a truckside L/V ratio of 0.6 is being used; however, the model can accept different criteria.) Since the model uses a quasi-static approach, and doesn't account for dynamic run-in/run-out conditions or track irregularities, it can only provide an indication of potentially unsafe conditions. However, if the analysis shows that the consist is only marginally safe under steady-state conditions, then it will certainly be unsafe dynamically.

### 3. VEHICLE PARAMETERS AFFECTING TRAIN STABILITY

The vehicle parameters that govern the lateral train stability problem, and which determine the induced truck forces, are shown in Figure 2. The general effect of these parameters upon the lateral stability of the vehicle (i.e., its ability to minimize the effect of train buckling or stringlining forces) is discussed below. These trends were developed from parametric studies that were conducted as described in Reference [7].

- o Overall Length (length over pulling faces). Vehicle length is a very significant parameter. As vehicle length increases, performance generally improves significantly under buff, but degrades substantially under draft. However, when a long car is coupled to a short car, the long car is adversely affected in both buff and draft, particularly as track curvature increases. One additional point that should be noted is that all cars have a much greater ability to tolerate draft than buff; so that even for a long car, its tolerance for draft could be twice that for buff.
- o A/B Ratio (the ratio of truck center spacing to coupler pivot spacing). This parameter, a measure of relative car overhang, contributes significantly to vehicle lateral stability. The larger the A/B ratio (i.e., the smaller the overhang), the more stable the car in both buff and draft. However, as with vehicle length, large mismatches in A/B ratio between adjacent cars can significantly impair stability.
- o Coupler Length. Increased coupler length can improve stability under all conditions.
- o Gross Weight. The stability of any vehicle increases proportionately with its weight.

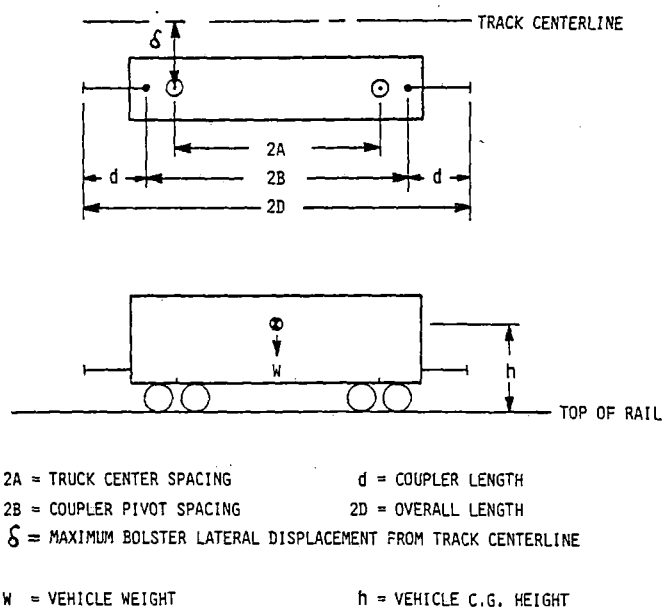


Fig. 2 Vehicle Parameters Affecting Lateral Train Stability

- o Center of Gravity (C.G.) Height. This parameter only has an effect during unbalanced curve negotiation. At the present time, the TSA model does not use this parameter since the model performs its stability analysis for balance speed conditions. A methodology for adjusting these results for cases of unbalanced curve negotiation is developed and discussed in Reference [7].
- o Maximum Bolster Lateral Displacement (maximum available body bolster displacement from track centerline, due to available clearances between the rail, wheelsets, truck frame, and carbody). This parameter governs the magnitude of the buckling mode, and as such, can substantially affect vehicle lateral stability. A nominal freight car value of 1.25 inches [5] is the standard default used by the TSA computer program.

#### 4. POTENTIAL APPLICATIONS

There are three major areas for potential application of the TSA computer program: (1) Operations Analyst, (2) Yardmaster, and (3) Locomotive Engineer.

(1) The Operations Analyst could use the TSA program in a variety of ways in the batch processing mode. First, there is the potential for optimization of train makeup based on considerations of train dynamics, as indicated in Reference [8]. Secondly, operating guidelines for safe curve negotiation, such as on usage of dynamic brake, could be formulated for any section of track. Lastly, the TSA program could be a useful tool in derailment investigations where train buckling or stringlining is suspected.

(2) The Yardmaster could use the TSA program in an interactive processing mode at the time that a train was being built in order to assess its safety. In this mode, the Yardmaster could obtain the following information about his train:

- o A summary table of maximum safe tractive effort and dynamic braking forces for each degree of curve,
- o Identification of the critical cars for that particular train, and
- o Analysis of alternative critical car placement, identifying the advantages that would be gained.

(3) Finally, the Locomotive Engineer, in a real-time processing mode, could use the summary table output from the TSA program in conjunction with a power force indicator and curvature measuring device, installed on the lead locomotive, to provide real-time advance warning of when his train was approaching unsafe buff or draft force levels. This application is illustrated in Figure 3, and is described in detail in Reference [7].

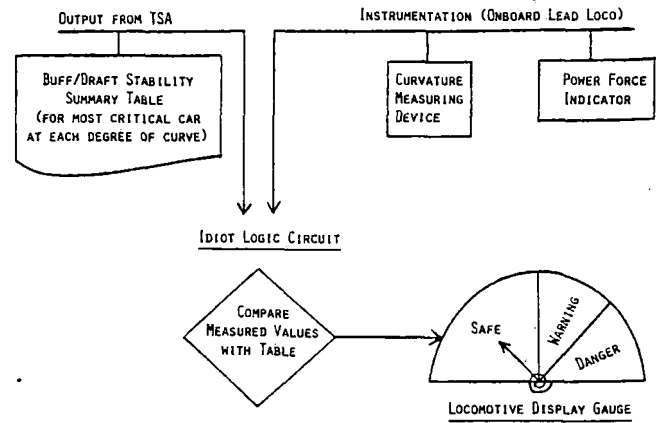


Fig. 3 Buff/Draft Derailment Warning Indicator (Provides Advance Warning of Unsafe Force Conditions)

#### 5. PROGRAM CAPABILITIES

The TSA computer program analyzes any given train consist and determines the maximum safe locomotive dynamic brake and tractive effort force levels for each car in the consist at varying degrees of track curvature. A consist data file provides the model with descriptive information about each car in the consist, while a user input file enables the user to select the analysis and output options he desires. Figure 4 illustrates the procedure.

Specifically, the user may specify the range of track curvatures to be considered, he may designate unit train blocks and destination blocks, and he may relocate individual cars or blocks of cars within the consist. Other input options enable the user to override defaults within the program.

As identified in Figure 4, output options include the following:

- (1) A consist listing displaying the data for the original consist and identifying any car relocations requested by the user.
- (2) A set of buff and draft analysis tables listing, for each destination block and each degree of curve, those cars having unacceptable dynamic braking or tractive effort force levels. These tables conclude with an overall worst case table identifying, for each degree of curve, the most critical car and, if cars have been relocated, the improvement in allowable dynamic braking and tractive effort force levels over the original consist configuration.
- (3) A set of buff and draft summary tables listing, for each degree of curve, the three most critical cars in the consist and the corresponding maximum safe dynamic braking and tractive effort force levels.
- (4) A set of detailed buff and draft stability tables displaying, for each car in the consist, its critical buckling and stringlining modes at each degree of track curvature, and its associated maximum buff and draft force capability.

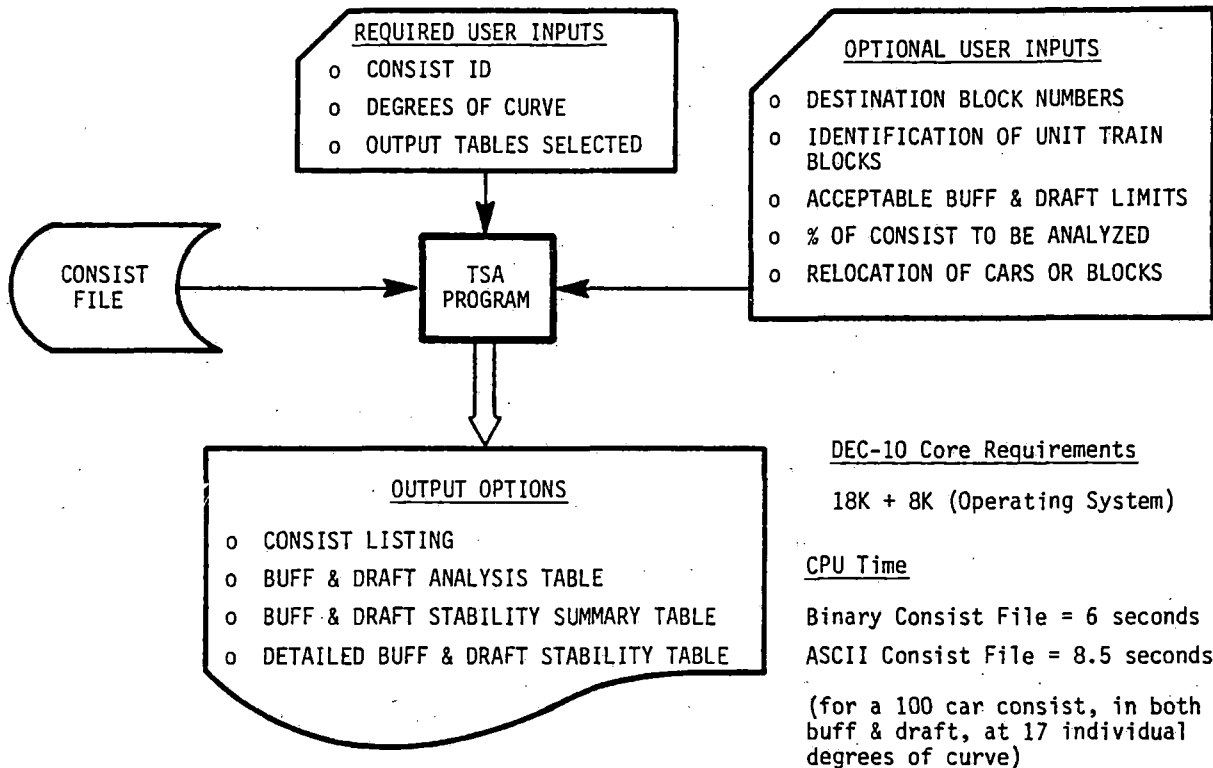


Fig. 4 TSA Input/Output Structure

The above output options are illustrated, respectively, for the case of buff, in Tables 1 to 4 at the end of this section. It should be noted that comparable tables would also be produced for draft. The comments output at the top of each table describe the information provided by that table. It is suggested that the reader become familiar with these tables before reading the next section, which describes an application example. Some additional points to note, in terms of buff, but equally applicable to draft, are as follows:

- o The maximum safe dynamic braking force at the head end is obtained by first computing the maximum safe buff force at the car, and then scaling by the proportion of trailing tonnage seen by the car.
- o All computed force values are cut off at a maximum value equal to the knuckle strength. The program default is 300 kips.
- o While DBF or Max Safe Force (Tables 2 and 3) represent the limiting safe head-end force levels, they say nothing about whether these force limits would be acceptable from a train operations requirements point of view.

- o The Buff Analysis Table (Table 2) represents an exception report, flagging all cars whose DBF falls below some acceptable value for train operations. The last column of Table 2 shows how much below the acceptable value the flagged car actually falls. The set of acceptable values as a function of track curvature (DBAV), can either be user supplied, or the program defaults can be used. The program defaults correspond to the maximum safe buff and draft force values obtained for an average performing, empty, DC-5 box car, under extreme mismatch conditions (see Reference [7]). As such, the default values represent a level of head-end performance that should be readily achievable, but which may not actually be adequate, particularly for a heavy train.
- o The Buff Stability Summary Table (Table 3) has been designed to provide information that could be useful to the locomotive engineer, giving him a feel for the overall capability of his train, and identifying where the critical cars are located.
- o The Detailed Buff Stability Table (Table 4) is intended for use by the researcher. It shows, for each car in the consist, as a function of track curvature, the worst case possible buckling mode, the corresponding maximum safe buff force at the car, and the resulting maximum safe dynamic braking force at the head end. The buckling mode ID numbers are explained in Reference [6]. The vehicle c.g. height, as explained earlier, is not used by the TSA computer model, but is accepted as a parameter for possible future use in extrapolating results to unbalanced curve negotiation.



CONSIST IDENTIFICATION =

SAMPLE TEST TRAIN

THE TRAIN IS A 100-CAR CONSIST WITH A TOTAL TRAILING TONNAGE OF 5160 TONS AND A TOTAL TRAIN LENGTH OF 6040 FEET (INCLUDING 3 LOCOMOTIVES TAKING UP 200 FEET).

\* COLUMN INDICATES CARS OR BLOCKS THAT HAVE BEEN RELOCATED WITHIN THE CONSIST.

"OLD" ALWAYS REFERS TO ORIGINAL CONSIST SEQUENCE, BEFORE ANY RELOCATIONS.

UT COLUMN INDICATES BLOCKS THAT HAVE BEEN IDENTIFIED AS UNIT TRAIN BLOCKS.

SEQUENCE #	CAR IDENTIFICATION	DESTINATION	OVERALL LENGTH (FT)	A/B RATIO	GROSS WEIGHT (TONS)	UT COL
NEW	OLD					
DESTINATION BLOCK # 1, 220 TONS, 10 CARS (AVERAGE CAR WT = 22 TONS)						
1	1	FLAT (BI-LEV)	BOSTON, MASS. /	92	.79	26
2	2	GON	BOSTON, MASS. /	32	.70	18
3	3	FLAT (BI-LEV)	BOSTON, MASS. /	92	.79	26
4	4	GON	BOSTON, MASS. /	32	.70	18
5	5	FLAT (BI-LEV)	BOSTON, MASS. /	92	.79	26
6	6	GON	BOSTON, MASS. /	32	.70	18
7	7	FLAT (BI-LEV)	BOSTON, MASS. /	92	.79	26
8	8	GON	BOSTON, MASS. /	32	.70	18
9	9	FLAT (BI-LEV)	BOSTON, MASS. /	92	.79	26
10	10	GON	BOSTON, MASS. /	32	.70	18
DESTINATION BLOCK # 2, 80 TONS, 5 CARS (AVERAGE CAR WT = 15 TONS)						
11	11	GON	PROVIDENCE, R.I.	32	.70	15 UT1
12	12	GON	PROVIDENCE, R.I.	32	.70	15 UT1
13	13	GON	PROVIDENCE, R.I.	32	.70	15 UT1
14	14	GON	PROVIDENCE, R.I.	32	.70	15 UT1
15	15	GON	PROVIDENCE, R.I.	32	.70	15 UT1
DESTINATION BLOCK # 3, 2600 TONS, 20 CARS (AVERAGE CAR WT = 130 TONS)						
16	16	AUTO PARTS	NEW LONDON, CONN /	95	.78	130 UT2
34	34	AUTO PARTS	NEW LONDON, CONN /	95	.78	130 UT2
35	35	AUTO PARTS	NEW LONDON, CONN /	95	.78	130 UT2
DESTINATION BLOCK # 4, 1020 TONS, 20 CARS (AVERAGE CAR WT = 51 TONS)						
36	36	BOX (INSUL)	NEW HAVEN, CONN /	55	.83	75
54	54	GON	NEW HAVEN, CONN /	45	.75	26
55	55	GON (DROP)	NEW HAVEN, CONN /	46	.79	30
DESTINATION BLOCK # 5, 790 TONS, 25 CARS (AVERAGE CAR WT = 31 TONS)						
56	56	GON	BRIDGEPORT, CONN /	56	.83	29
79	79	HOPPER	BRIDGEPORT, CONN /	36	.79	28
80	80	REEFER (MECH)	BRIDGEPORT, CONN /	56	.84	42
DESTINATION BLOCK # 6, 460 TONS, 20 CARS (AVERAGE CAR WT = 23 TONS)						
81	81	REEFER (MECH)	NEW YORK, N.Y. /	56	.84	42
82	82	REEFER (ICE)	NEW YORK, N.Y. /	45	.76	27
94	94	GON	NEW YORK, N.Y. /	32	.70	23 UT3
95	95	GON	NEW YORK, N.Y. /	32	.70	23 UT3
96	96	GON	NEW YORK, N.Y. /	32	.70	15 UT3
97	97	GON	NEW YORK, N.Y. /	32	.70	15 UT3
98	98	GON	NEW YORK, N.Y. /	32	.70	15 UT3
99	99	GON	NEW YORK, N.Y. /	32	.70	15 UT3
100	100	GON	NEW YORK, N.Y. /	32	.70	15 UT3

Table 1 Consist Listing

THE FOLLOWING IS A LIST OF ALL CARS FOR WHICH THE MAXIMUM ALLOWABLE DYNAMIC BRAKING FORCES ARE SMALLER THAN THE SPECIFIED ACCEPTABLE VALUES.

- \* THE CARS ARE LISTED BY DESTINATION BLOCK.
- \* WITHIN EACH BLOCK, THEY ARE LISTED IN ORDER OF DECREASING SEVERITY, FOR EACH DEGREE OF CURVE.
- \* FOLLOWING THE BLOCK LISTING IS AN OVERALL WORST CASE SUMMARY TABLE. THIS TABLE ALSO SHOWS THE IMPROVEMENT OVER THE WORST CASE OF THE ORIGINAL CONSIST CONFIGURATION IF CARS HAVE BEEN RELOCATED.

"DBAV" = THE SPECIFIED ACCEPTABLE VALUE ON DYNAMIC BRAKING FORCE LIMITS, FOR EACH DEGREE OF CURVE.

"DBF" = THE MAXIMUM ALLOWABLE DYNAMIC BRAKING FORCE FOR EACH CAR.

DESTINATION BLOCK # 1						DESTINATION BLOCK # 2					
DEGREE OF CURVE	DBAV (KIPS)	CAR SEQ #	CAR I.D.	DBF (KIPS)	DBF-DBAV (KIPS)	DEGREE OF CURVE	DBAV (KIPS)	CAR SEQ #	CAR I.D.	DBF (KIPS)	DBF-DBAV (KIPS)
( 0 )	(225)	10	GON	85	-140	( 0 )	(225)	11	GON	70	-155
		2	GON	120	-105			12	GON	70	-155
		4	GON	120	-105			13	GON	70	-155
		4	GON	120	-105			14	GON	70	-155
		8	GON	125	-100			15	GON	75	-150
( 2 )	(140)	10	GON	70	-90	( 2 )	(160)	11	GON	55	-105
		2	GON	110	-50			12	GON	55	-105
		4	GON	110	-50			13	GON	60	-100
		6	GON	110	-50			14	GON	60	-100
		8	GON	110	-50			15	GON	60	-100
		1	FLAT (BI)	130	-30	( 4 )	(120)	11	GON	50	-70
		3	FLAT (BI)	130	-30			12	GON	50	-70
		5	FLAT (BI)	135	-25			13	GON	50	-70
		7	FLAT (BI)	135	-25			14	GON	50	-70
		9	FLAT (BI)	135	-25			15	GON	50	-70
( 4 )	(120)	10	GON	60	-60	( 4 )	(120)	11	GON	50	-70
		1	FLAT (BI)	85	-35			12	GON	50	-70
		3	FLAT (BI)	105	-15			13	GON	50	-70
		5	FLAT (BI)	105	-15			14	GON	50	-70
		7	FLAT (BI)	105	-15			15	GON	50	-70
(16)	( 40 )	9	FLAT (BI)	105	-15	(16)	( 40 )	15	GON	35	-25
		1	FLAT (BI)	35	-25			11	GON	40	-20
		3	FLAT (BI)	35	-25			12	GON	40	-20
		5	FLAT (BI)	35	-25			13	GON	40	-20
		7	FLAT (BI)	35	-25			14	GON	40	-20
		9	FLAT (BI)	35	-25			15	GON	40	-20
		10	GON	40	-20						

OVERALL WORST CASE (BUFF)						
DEGREE OF CURVE	DBAV (KIPS)	CAR SEQ #	BLOCK #	NEW DBF-DBAV (KIPS)	ORIGINAL DBF-DBAV (KIPS)	IMPROVEMENT (KIPS)
( 0 )	(225)	11	2	(-155)	---	(---)
( 2 )	(160)	11	2	(-105)	---	(---)
( 4 )	(120)	11	2	( -70)	---	(---)
( 4 )	(105)	11	2	( -60)	---	(---)
( 8 )	( 75)	11	2	( -50)	---	(---)
(10)	( 65)	15	2	( -45)	---	(---)
(12)	( 75)	12	2	( -35)	---	(---)
(14)	( 70)	13	2	( -25)	---	(---)
(16)	( 40)	1	1	( -25)	---	(---)

Table 2 Buff Analysis Table

CONSIST IDENTIFICATION =

SAMPLE TEST TRAIN

THE TRAIN IS A 100-CAR CONSIST WITH A TOTAL TRAILING TONNAGE OF 5160 TONS AND A TOTAL TRAIN LENGTH OF 6040 FEET (INCLUDING 3 LOCOMOTIVES TAKING UP 200 FEET).

IT WAS ASSUMED THAT THE THREE MOST CRITICAL CARS IN THE CONSIST WOULD OCCUR WITHIN THE FIRST 100 CARS.

\*MAX SAFE FORCE\* = THE MAXIMUM ALLOWABLE DYNAMIC BRAKING FORCE, DEVELOPED AT THE DRAWBAR OF THE LOCOMOTIVE CONSIST, FOR SAFE CURVE NEGOTIATION OF EACH OF THE THREE MOST CRITICAL CARS.

\*DISTANCE FROM POINT\* = THE LOCATION OF THESE THREE CARS IN TERMS OF THEIR DISTANCE FROM THE POINT LOCOMOTIVE.

THE MAXIMUM SAFE FORCE LEVELS WERE BASED UPON BALANCE SPEED CONDITIONS. FOR BRAKING AT HIGH SPEED (4 INCHES UNDERBALANCE), THE MAXIMUM SAFE FORCE LEVELS COULD BE REDUCED BY UP TO 22 PERCENT. FOR BRAKING AT LOW SPEED (4 INCHES OVERBALANCE), NO REDUCTION WOULD BE EXPERIENCED BY A UNIT TRAIN, BUT UP TO A 16 PERCENT REDUCTION MIGHT BE EXPERIENCED BY MISMATCHED CARS.

DEGREE OF CURVE	MAX SAFE FORCE (KIPS)			DISTANCE FROM POINT (FEET)			CRITICAL CAR #		
	(1ST)	2ND	3RD	(1ST)	2ND	3RD	(1ST)	2ND	3RD
( 0 ) ... ( 70 )	70	70	...	( 825 )	850	875	....	( 11 )	12 13
( 2 ) ... ( 55 )	55	60	...	( 825 )	850	875	....	( 11 )	12 13
( 4 ) ... ( 50 )	50	50	...	( 825 )	850	875	....	( 11 )	12 13
( 6 ) ... ( 45 )	45	45	...	( 825 )	850	875	....	( 11 )	12 13
( 8 ) ... ( 45 )	45	45	...	( 825 )	850	875	....	( 11 )	12 13
(10) ... ( 40 )	45	45	...	( 950 )	825	850	....	( 15 )	11 12
(12) ... ( 40 )	40	40	...	( 825 )	850	875	....	( 11 )	12 13
(14) ... ( 35 )	40	40	...	( 950 )	200	325	....	( 15 )	1 3
(16) ... ( 35 )	35	35	...	( 200 )	325	450	....	( 1 )	3 5

Table 3 Buff Stability Summary Table: Maximum Allowable Dynamic Brake

CONSIST IDENTIFICATION =

SAMPLE TEST TRAIN

THE TRAIN IS A 100-CAR CONSIST WITH A TOTAL TRAILING TONNAGE OF 5160 TONS AND A TOTAL TRAIN LENGTH OF 6040 FEET (INCLUDING 3 LOCOMOTIVES TAKING UP 200 FEET).

THE FIRST 100 CARS WERE EXAMINED. THE TRACK CURVATURE RANGE IS FROM 0 TO 16 DEGREES IN 2 DEGREE INCREMENTS.

CAR SEQ #	CAR LOCATION POINTER	CAR I.D. --	C.G. HEIGHT (IN)	MAXIMUM SAFE LOCOMOTIVE DYNAMIC BRAKE AND CAR BUFF FORCE (KIPS) FOR EACH DEGREE OF CURVE									
				****									
				0	2	4	6	8	10	12	14	16	****
1	200	FLAT (BI	30	BUFF FORCE	235	129	85	73	59	50	43	38	34
				DYNAM BRAKE	(235)	(129)	(85)	(73)	(59)	(50)	(43)	(38)	(34)
				MODE	4	4	4	2	2	2	2	2	2
2	292	GON	30	BUFF FORCE	119	109	182	160	142	128	116	107	98
				DYNAM BRAKE	(119)	(109)	(183)	(160)	(143)	(128)	(117)	(107)	(99)
				MODE	4	4	1S	1S	1S	1S	1S	1S	1S
3	324	FLAT (BI	30	BUFF FORCE	231	130	103	79	64	53	46	40	36
				DYNAM BRAKE	(233)	(131)	(104)	(79)	(64)	(54)	(46)	(41)	(36)
				MODE	4	4	1L	1L	1L	1L	1L	1L	1L
4	416	GON	30	BUFF FORCE	119	109	182	160	142	128	116	107	98
				DYNAM BRAKE	(120)	(110)	(185)	(162)	(144)	(130)	(118)	(108)	(100)
				MODE	4	4	1S	1S	1S	1S	1S	1S	1S
5	448	FLAT (BI	30	BUFF FORCE	231	130	103	79	64	53	46	40	36
				DYNAM BRAKE	(235)	(133)	(105)	(80)	(65)	(54)	(47)	(41)	(37)
				MODE	4	4	1L	1L	1L	1L	1L	1L	1L
97	5907	GON	30	BUFF FORCE	66	55	47	45	43	41	39	38	36
				DYNAM BRAKE	(300)	(300)	(300)	(300)	(300)	(300)	(300)	(300)	(300)
				MODE	4	4	4	4	4	4	4	4	4
98	5939	GON	30	BUFF FORCE	66	55	47	45	43	41	39	38	36
				DYNAM BRAKE	(300)	(300)	(300)	(300)	(300)	(300)	(300)	(300)	(300)
				MODE	4	4	4	4	4	4	4	4	4
99	5971	GON	30	BUFF FORCE	66	55	47	45	43	41	39	38	36
				DYNAM BRAKE	(300)	(300)	(300)	(300)	(300)	(300)	(300)	(300)	(300)
				MODE	4	4	4	4	4	4	4	4	4

Table 4 Detailed Buff Stability Table

## 6. APPLICATION EXAMPLE

In this section an example is presented to show how the TSA computer model could be used in real-time to evaluate and assist in insuring adequate train makeup.

Suppose the yardmaster were to run the TSA program for the consist shown in the previous section. From Table 1, we see that the consist is a medium weight train of about 5000 tons, consisting of 100 cars, blocked in destination order, and pulled by 3 head-end locomotives. One might not normally expect such a train to provide any problems; except that there would be some concern about the empty long car/short car combinations at the head of the train. A person conversant with the information developed in References [7 and 8] might also be concerned about the very light block of short gons followed by the heavy block of auto parts cars. However, without quantitative information, and considering the imperatives of destination blocking, it becomes very hard to decide whether something should be done, and if so -- what?

Tables 2 and 3 (the analysis and summary tables) provide the needed information. Table 2 shows that blocks 1 and 2, as a whole, fail to meet the acceptable values, and are in fact, considerably below those values. Table 3 shows that the most critical car would be able to withstand less than 55 kips of head-end force above a 2 degree curve. It is clear, then, that the current consist configuration is, in fact, unacceptable. Additional information obtained from Table 2 is:

- o In the empty long car/short car combination, the short car is more critical at the low degrees of curve, with the long car becoming more critical once the curve is greater than a few degrees.
- o The light block of short gons is, in fact, more critical than the long car/short car block.
- o Only blocks 1 and 2 were flagged as unacceptable, but essentially every car within those blocks was flagged.

Based upon the above information, the most logical way of improving performance would be to move blocks 1 and 2 further back in the train. (Note: In evaluating the train's performance, one should also examine the corresponding draft analysis tables. Although not presented here, these tables indicated that the only unacceptable draft performers were the long cars in block 1. Accordingly, moving blocks 1 and 2 further back in the train should also correct the draft performance inadequacy.)

For our example, we will relocate blocks 1 and 2 behind block 4, which corresponds to about the middle of the train. In the TSA program, this is accomplished with only three data cards: one to indicate that this is a relocation run, and one to identify each block (or group of cars) that is being relocated. Tables 5 to 8, at the end of the paper, show the results.

Table 5 (the new consist listing) shows the new and old car sequence and block numbers. The \* column indicates those cars that were moved.

Tables 6 and 7 (buff and draft analysis) show that all cars now have acceptable head-end dynamic braking and tractive effort force values. Indeed, the new most critical cars all have force values that exceed the acceptable values in both buff and draft. This is indicated by the positive numbers in parentheses in the middle column of the worst case table. The improvement over the old worst case is shown in the last column. For both buff and draft, we see improvements that range between 100 and 200 kips. (Note that the zeroes in the draft table don't mean that there wasn't an improvement, but rather, that both the old and new values were cut off at the 300 kips knuckle strength limit.)

Table 8 shows a comparison of the buff stability summary tables produced before and after relocation. Comparing the maximum safe forces, we see the dramatic improvement from a consist that was limited to about 45 kips buff, to one that can now tolerate over 170 kips buff over most mainline curves. We note that this dramatic improvement was achieved simply by moving the two critical blocks to the middle of the train. More importantly, however, we note that the TSA computer model provided the user with the type of quantitative information that would enable intelligent assessment of a given train's safety, and of the advantages to be gained by alternative car placement.

## 7. PROGRAM AVAILABILITY

The TSA computer program is available in both IBM and DEC versions. The program, written in FORTRAN, is relatively machine independent, and is compatible with operating systems like TOPS. For further information, contact the author.

## ACKNOWLEDGMENTS

Development of the TSA computer program was sponsored by the Federal Railroad Administration's Office of Research and Development, Rail Vehicle Safety Research Division. The author would also like to express his appreciation for the excellent programming support provided by J.A. Tanne; and for the research and preparation support provided by W.I. Thompson, III and Barbara J. Coffey.

After Relocation

Blocks 1 and 2  
placed behind 4

CONSIST IDENTIFICATION =

SAMPLE TEST TRAIN

THE TRAIN IS A 100-CAR CONSIST WITH A TOTAL TRAILING TONNAGE OF 5160 TONS AND A TOTAL TRAIN LENGTH OF 6040 FEET (INCLUDING 3 LOCOMOTIVES TAKING UP 200 FEET).

\* COLUMN INDICATES CARS OR BLOCKS THAT HAVE BEEN RELOCATED WITHIN THE CONSIST.

"OLD" ALWAYS REFERS TO ORIGINAL CONSIST SEQUENCE, BEFORE ANY RELOCATIONS.

UT COLUMN INDICATES BLOCKS THAT HAVE BEEN IDENTIFIED AS UNIT TRAIN BLOCKS.

SEQUENCE #		CAR IDENTIFICATION	DESTINATION	OVERALL LENGTH (FT)	A/B RATIO	GROSS WEIGHT (TONS)	UT COL
NEW	OLD #						
DESTINATION BLOCK # 1, 2400 TONS, 20 CARS (AVERAGE CAR WT = 130 TONS) (OLD BLOCK # 3)							
1	16	AUTO PARTS	NEW LONDON,CONN/	95	.78	130	UT2
19	34	AUTO PARTS	NEW LONDON,CONN/	95	.78	130	UT2
20	35	AUTO PARTS	NEW LONDON,CONN/	95	.78	130	UT2
DESTINATION BLOCK # 2, 1020 TONS, 20 CARS (AVERAGE CAR WT = 51 TONS) (OLD BLOCK # 4)							
21	36	BOX (INSUL)	NEW HAVEN,CONN /	55	.83	75	
39	54	GON	NEW HAVEN,CONN /	45	.75	24	
40	55	GON (DROP)	NEW HAVEN,CONN /	46	.79	30	
DESTINATION BLOCK # 3, 220 TONS, 10 CARS (AVERAGE CAR WT = 22 TONS) (OLD BLOCK # 1)							
41	1 #	FLAT (BI-LEV)	BOSTON, MASS. /	92	.79	24	
42	2 #	GON	BOSTON, MASS. /	32	.70	18	
43	3 #	FLAT (BI-LEV)	BOSTON, MASS. /	92	.79	24	
44	4 #	GON	BOSTON, MASS. /	32	.70	18	
45	5 #	FLAT (BI-LEV)	BOSTON, MASS. /	92	.79	24	
46	6 #	GON	BOSTON, MASS. /	32	.70	18	
47	7 #	FLAT (BI-LEV)	BOSTON, MASS. /	92	.79	24	
48	8 #	GON	BOSTON, MASS. /	32	.70	18	
49	9 #	FLAT (BI-LEV)	BOSTON, MASS. /	92	.79	24	
50	10 #	GON	BOSTON, MASS. /	32	.70	18	
DESTINATION BLOCK # 4, 80 TONS, 5 CARS (AVERAGE CAR WT = 15 TONS) (OLD BLOCK # 2)							
51	11 #	GON	PROVIDENCE, R.I.	32	.70	15	UT1
52	12 #	GON	PROVIDENCE, R.I.	32	.70	15	UT1
53	13 #	GON	PROVIDENCE, R.I.	32	.70	15	UT1
54	14 #	GON	PROVIDENCE, R.I.	32	.70	15	UT1
55	15 #	GON	PROVIDENCE, R.I.	32	.70	15	UT1
DESTINATION BLOCK # 5, 790 TONS, 25 CARS (AVERAGE CAR WT = 31 TONS)							
56	56	GON	BRIDGEPORT,CONN/	56	.83	29	
79	79	HOPPER	BRIDGEPORT,CONN/	36	.79	28	
80	80	REEFER (MECH)	BRIDGEPORT,CONN/	56	.84	42	
DESTINATION BLOCK # 6, 460 TONS, 20 CARS (AVERAGE CAR WT = 23 TONS)							
81	81	REEFER (MECH)	NEW YORK, N.Y. /	56	.84	42	
82	82	REEFER (ICE)	NEW YORK, N.Y. /	45	.76	27	
94	94	GON	NEW YORK, N.Y. /	32	.70	23	UT3
95	95	GON	NEW YORK, N.Y. /	32	.70	23	UT3
96	96	GON	NEW YORK, N.Y. /	32	.70	15	UT3
97	97	GON	NEW YORK, N.Y. /	32	.70	15	UT3
98	98	GON	NEW YORK, N.Y. /	32	.70	15	UT3
99	99	GON	NEW YORK, N.Y. /	32	.70	15	UT3
100	100	GON	NEW YORK, N.Y. /	32	.70	15	UT3

Table 5 Consist Listing

## After Relocation (BUFF)

THE FOLLOWING IS A LIST OF ALL CARS FOR WHICH THE MAXIMUM ALLOWABLE DYNAMIC BRAKING FORCES ARE SMALLER THAN THE SPECIFIED ACCEPTABLE VALUES.

- \* THE CARS ARE LISTED BY DESTINATION BLOCK.
- \* WITHIN EACH BLOCK, THEY ARE LISTED IN ORDER OF DECREASING SEVERITY, FOR EACH DEGREE OF CURVE.
- \* FOLLOWING THE BLOCK LISTING IS AN OVERALL WORST CASE SUMMARY TABLE. THIS TABLE ALSO SHOWS THE IMPROVEMENT OVER THE WORST CASE OF THE ORIGINAL CONSIST CONFIGURATION IF CARS HAVE BEEN RELOCATED.

\*DBAV\* = THE SPECIFIED ACCEPTABLE VALUE ON DYNAMIC BRAKING FORCE LIMITS, FOR EACH DEGREE OF CURVE.

\*DBF\* = THE MAXIMUM ALLOWABLE DYNAMIC BRAKING FORCE FOR EACH CAR.

\*\*\*\* ALL CARS IN THE CONSIST HAVE ACCEPTABLE DBF VALUES \*\*\*\*

OVERALL WORST CASE (BUFF)						
DEGREE OF CURVE	DBAV (KIPS)	CAR SEQ #	BLOCK #	NEW DBF-DBAV (KIPS)	ORIGINAL DBF-DBAV (KIPS)	IMPROVEMENT (KIPS)
( 0 )	(225)	51	4	( 35 )	-155	( 190 )
( 2 )	(160)	51	4	( 55 )	-105	( 160 )
( 4 )	(120)	51	4	( 65 )	-70	( 135 )
( 6 )	(105)	51	4	( 70 )	-60	( 130 )
( 8 )	( 95 )	51	4	( 75 )	-50	( 125 )
(10)	( 85 )	51	4	( 75 )	-45	( 120 )
(12)	( 75 )	41	3	( 80 )	-35	( 115 )
(14)	( 70 )	41	3	( 65 )	-35	( 100 )
(16)	( 60 )	41	3	( 60 )	-25	( 85 )

Table 6 Buff Analysis Table

## After Relocation (DRAFT)

THE FOLLOWING IS A LIST OF ALL CARS FOR WHICH THE MAXIMUM ALLOWABLE TRACTIVE EFFORT FORCES ARE SMALLER THAN THE SPECIFIED ACCEPTABLE VALUES.

- \* THE CARS ARE LISTED BY DESTINATION BLOCK.
- \* WITHIN EACH BLOCK, THEY ARE LISTED IN ORDER OF DECREASING SEVERITY, FOR EACH DEGREE OF CURVE.
- \* FOLLOWING THE BLOCK LISTING IS AN OVERALL WORST CASE SUMMARY TABLE. THIS TABLE ALSO SHOWS THE IMPROVEMENT OVER THE WORST CASE OF THE ORIGINAL CONSIST CONFIGURATION IF CARS HAVE BEEN RELOCATED.

\*TEAV\* = THE SPECIFIED ACCEPTABLE VALUE ON TRACTIVE EFFORT FORCE LIMITS, FOR EACH DEGREE OF CURVE.

\*TEF\* = THE MAXIMUM ALLOWABLE TRACTIVE EFFORT FORCE FOR EACH CAR.

\*\*\*\* ALL CARS IN THE CONSIST HAVE ACCEPTABLE TEF VALUES \*\*\*\*

OVERALL WORST CASE (DRAFT)						
DEGREE OF CURVE	TEAV (KIPS)	CAR SEQ #	BLOCK #	NEW TEF-TEAV (KIPS)	ORIGINAL TEF-TEAV (KIPS)	IMPROVEMENT (KIPS)
( 0 )	(300)	1	1	( 0 )	0	( 0 )
( 2 )	(300)	1	1	( 0 )	0	( 0 )
( 4 )	(300)	1	1	( 0 )	-35	( 35 )
( 6 )	(300)	1	1	( 0 )	-125	( 125 )
( 8 )	(260)	1	1	( 40 )	-125	( 165 )
(10)	(210)	1	1	( 90 )	-110	( 200 )
(12)	(175)	41	3	( 110 )	-95	( 205 )
(14)	(150)	41	3	( 90 )	-80	( 170 )
(16)	(135)	41	3	( 70 )	-75	( 145 )

Table 7 Draft Analysis Table

## REFERENCES

1. "Yearbook of Railroad Facts," Association of American Railroads, Washington DC, (1981).
2. A.R. Pocklington, "Effects of Lateral Forces when Propelling Round Sharp Curves," Railway Gazette, (December 3, 1965), pp. 942-945.
3. A.R. Pocklington and T.P. Brown, "High Lateral Forces on Sharp Curves with Propelled Trains," Railway Gazette, (December 17, 1965), pp. 993-996.
4. "Accident/Incident Bulletin," No. 148, Federal Railroad Administration, Washington DC, (July 1980).
5. L.R. Thomas, R.D. MacMillan, and G.C. Martin, "Quasi-Static Lateral Train Stability Model - Technical Documentation," Report No. R-209, Association of American Railroads, Chicago IL, (April 1976).
6. R. Brantman, J.A. Tanne, and W.I. Thompson, III, "Train Stability Analysis Model (TSA): User/Analyst Manual," Report to be issued by U.S. DOT, Transportation Systems Center, Cambridge MA.
7. R. Brantman, "Maximum Allowable Buff and Draft Force Levels for Safe Curve Negotiation," Report to be issued by U.S. DOT, Transportation Systems Center, Cambridge MA.
8. "Track Train Dynamics to Improve Freight Train Performance," 2nd Edition, Report No. R-185, Association of American Railroads, Chicago IL.

CONSIST IDENTIFICATION =

SAMPLE TEST TRAIN

THE TRAIN IS A 100-CAR CONSIST WITH A TOTAL TRAILING TONNAGE OF 5160 TONS AND A TOTAL TRAIN LENGTH OF 6040 FEET (INCLUDING 3 LOCOMOTIVES TAKING UP 200 FEET).

IT WAS ASSUMED THAT THE THREE MOST CRITICAL CARS IN THE CONSIST WOULD OCCUR WITHIN THE FIRST 100 CARS.

"MAX SAFE FORCE" = THE MAXIMUM ALLOWABLE DYNAMIC BRAKING FORCE, DEVELOPED AT THE DRAWBAR OF THE LOCOMOTIVE CONSIST, FOR SAFE CURVE NEGOTIATION OF EACH OF THE THREE MOST CRITICAL CARS.

"DISTANCE FROM POINT" = THE LOCATION OF THESE THREE CARS IN TERMS OF THEIR DISTANCE FROM THE POINT LOCOMOTIVE.

THE MAXIMUM SAFE FORCE LEVELS WERE BASED UPON BALANCE SPEED CONDITIONS. FOR BRAKING AT HIGH SPEED (4 INCHES UNDERBALANCE), THE MAXIMUM SAFE FORCE LEVELS COULD BE REDUCED BY UP TO 22 PERCENT. FOR BRAKING AT LOW SPEED (4 INCHES OVERBALANCE), NO REDUCTION WOULD BE EXPERIENCED BY A UNIT TRAIN, BUT UP TO A 16 PERCENT REDUCTION MIGHT BE EXPERIENCED BY MISMATCHED CARS.

DEGREE OF CURVE	MAX SAFE FORCE (KIPS)			DISTANCE FROM POINT (FEET)			CRITICAL CAR #		
	(1ST)	2ND	3RD	(1ST)	2ND	3RD	(1ST)	2ND	3RD
( 0 ) ... (260)	265	265	...	(3900)	3925	3950	...	( 51)	52 53
( 2 ) ... (215)	215	220	...	(3900)	3925	3950	...	( 51)	52 53
( 4 ) ... (185)	185	190	...	(3900)	3925	3950	...	( 51)	52 53
( 6 ) ... (175)	175	180	...	(3900)	3925	3950	...	( 51)	52 53
( 8 ) ... (170)	170	170	...	(3900)	3925	3950	...	( 51)	52 53
(10) ... (160)	160	165	...	(3900)	3925	3950	...	( 51)	52 53
(12) ... (155)	155	155	...	(3275)	3900	3925	...	( 41)	51 52
(14) ... (135)	140	145	...	(3275)	3400	3525	...	( 41)	43 45
(16) ... (120)	125	130	...	(3275)	3400	3525	...	( 41)	43 45
<u>After Relocation</u>									
DEGREE OF CURVE	MAX SAFE FORCE (KIPS)			DISTANCE FROM POINT (FEET)			CRITICAL CAR #		
	(1ST)	2ND	3RD	(1ST)	2ND	3RD	(1ST)	2ND	3RD
( 0 ) ... ( 70)	70	70	...	( 825)	850	875	...	( 11)	12 13
( 2 ) ... ( 55)	55	60	...	( 825)	850	875	...	( 11)	12 13
( 4 ) ... ( 50)	50	50	...	( 825)	850	875	...	( 11)	12 13
( 6 ) ... ( 45)	45	45	...	( 825)	850	875	...	( 11)	12 13
( 8 ) ... ( 45)	45	45	...	( 825)	850	875	...	( 11)	12 13
(10) ... ( 40)	45	45	...	( 950)	825	850	...	( 15)	11 12
(12) ... ( 40)	40	40	...	( 825)	850	875	...	( 11)	12 13
(14) ... ( 35)	40	40	...	( 950)	200	325	...	( 15)	1 3
(16) ... ( 35)	35	35	...	( 200)	325	450	...	( 1)	3 5
<u>Before Relocation</u>									

Table 8 Buff Stability Summary Table: Maximum Allowable Dynamic Brake

781049

## Freightcar Vibration Test and Analysis Comparison – Validation of FRATE

G. Kachadourian

The MITRE Corp.

N.T. Tsai

Federal Railroad Administration

IN THE DEVELOPMENT OF any mathematical model it is advisable to demonstrate the degree of accuracy in duplicating real life phenomenon. Validation of models is usually accomplished through a parallel effort of analysis and experiment, with comparison of results to show the accuracy of the model. This paper presents the results of this type of validation effort. The vehicle modeled is a railroad flatcar loaded with two highway trailers generally referred to as a trailer on flatcar, or TOFC. Experimental data was acquired at the Federal Railroad Administration's Rail Dynamics Laboratory in Pueblo, Colorado.

The Federal Railroad Administration (FRA) and the Railroad Industry have been engaged in research and development activities related to the dynamics of trains and tracks. A main thrust of these activities has been to address those aspects where changes in dynamic characteristics would result in reduced maintenance costs, by virtue of reduced wear on track and railcar, and increased revenues by virtue

of being able to safely carry more fragile commodities. The part of these activities which are of interest to us was a series of vibration tests performed on a TOFC configuration using the Vertical Shaker System at the Rail Dynamics Laboratory. The objectives of this testing were to determine the vibration response characteristics of the TOFC configuration and to arrive at an optimum configuration, with respect to minimizing dynamic response, within the confines of practical parameter variations.

In conjunction with the TOFC vibration test the FRA contracted with Wyle Laboratories to develop a computer program for the dynamic analysis of freight cars. The program was to include a representation of the specific TOFC configuration and was also to have the capability, through simple modifications, to represent other railcar configurations. The resulting computer program has been given the acronym FRATE, for Freightcar Response Analysis and Test Evaluation. It uses a lumped parameter

---

### ABSTRACT

A nonlinear computer program for Freight Car Response Analysis and Test Evaluation (FRATE) has been developed under the sponsorship of the Federal Railroad Administration. The computer program incorporates a model of a Trailer on Flat Car (TOFC) configuration. Validation of the FRATE/TOFC program is being accomplished through comparison of analysis results to the results of vibration tests performed on a TOFC configuration at the Rail Dynamics Laboratory

in Pueblo, Colorado. Validation criteria include resonant frequency, deflection shape at resonance and amplification of input motions.

This paper presents a brief review of the FRATE/TOFC computer program, a summary of TOFC vibration test results and comparisons of test and analysis results. Procedures followed to achieve acceptable agreement between test and analysis are reviewed.



representation, includes certain nonlinear properties and is solved in the time domain by numerical approximation methods.

#### VALIDATION PROCEDURE

The validation process used for FRATE is one in which resonant conditions are first defined from the test data - frequencies, amplitudes and deflection shapes of the entire physical structure - and then the analysis is made to reproduce these resonant conditions as closely as the project constraints of budget and schedule allow. The process used depends on the skill and engineering judgment of the analyst since he makes the comparisons between test and analysis. If in his opinion parameter values (e.g., inertias, spring rates or damping values) need adjusting to produce a closer match between test and analysis he makes them on a sequential and/or parallel computer run basis. If in his opinion the model's topology (i.e., the equations of motion) requires modification he will do so in a manner similar to the parameter adjustment process. Throughout the validation process, the physical behavior of the model is constantly being monitored by the analyst who must repeatedly judge if the model is reasonable and consistent.

Prior to the start of the validation effort consideration was given to the possible use of some form of System Identification, Parameter Identification or Parameter Estimation Procedure. There were three overriding considerations which ruled out the use of any of these procedures. First, paramount importance was placed on maintaining clear visibility of physical/mathematical relationships of the simulation. Second, development of the FRATE computer program and performance of the TOFC vibration testing preceded any formal validation planning. Consequently it was a matter of using available data rather than tailoring the test to accommodate the validation effort. Third, automated identification/estimation procedures are invariably built around frequency domain solutions. It was felt that development of procedures for a time domain solution would require a major development effort with no assurance of ultimate success. (Reference 1).

#### MODEL DESCRIPTION

The freight car model of this report is a TOFC (Trailer on Flatcar) configuration evolved by Wyle Laboratories from work done by Healey (2) and Ahlbeck, et al, (3). It consists of the lumped mass simulation shown schematically in Figure 1. The railcar is represented by three rigid body masses: two trucks and the carbody. Carbody flexibility is included through application of a component normal mode technique using the first seven free-free normal modes. Each of the two highway trailers is represented by two rigid masses: one for the trailer body and one for the wheel/axle assembly.

#### NONLINEAR EFFECTS

The FRATE computer program was set up for solution in the time domain, using numerical integration methods, so that nonlinear effects could be included. Two types of nonlinear properties were included in the original FRATE: separation and large angle effects. The simulation permitted separation at the wheel-rail interfaces, at the truck spring-bolster interfaces and at the trailer tire - flatcar deck interfaces. Since large roll angles (up to  $\pm 5.0$  degrees) were to be analyzed there were no small angle assumptions made.

In the process of validation there were two additional types of nonlinear effects included: bilinear spring rates to simulate the change in roll stiffness with and without side bearings contact, and coulomb damping in the truck springs. These changes to FRATE are discussed below.

#### TRUCK MODEL

The simple, one mass, truck representation was adopted for two reasons: (1) the intended use of the model was for analysis of overall railcar dynamic response characteristics for which the one mass truck simulation is adequate (comparisons to experimental results shown in Reference 2 support this statement), and (2) the one mass truck simulation has computer cost advantages in that the size of the model is minimized and the higher frequencies and attendant small integration time step of a more complex truck model are avoided.

#### TRAILER MODELS

Each trailer is modeled by two lumped masses, one for the trailer body and the other for the wheel and axle assembly (i.e., the tandem). The trailer hitch is represented by three spring/dampers: vertical, lateral and angular in the roll direction. The tandem is made up of two vertical and one lateral spring/dampers representing the tires and a second set of two vertical and one lateral spring/dampers represent the springs.

#### CARBODY FLEXIBILITY

The flexibility of the carbody is included in the problem solution through the use of normal mode methods and the use of a superposition technique referred to by Levy, (4), as the Component Element method.

Developments and applications of the methods can be found in the literature, for example References 4, 5, and 6.

The vibration analysis was performed using ANSYS, a commercially available structural analysis program using finite element methods. The geometry of the flatcar was defined by a number of node points which described the endpoints of the structural elements making up the flatcar body. The section properties of these structural elements were calculated from flatcar structural member counterparts.

The carbody model was then reduced to an eleven mass, 26 degree of freedom (DOF) simulation using the Guyan Reduction method. The undamped natural frequencies and deflection shapes were obtained with ANSYS. Deflection

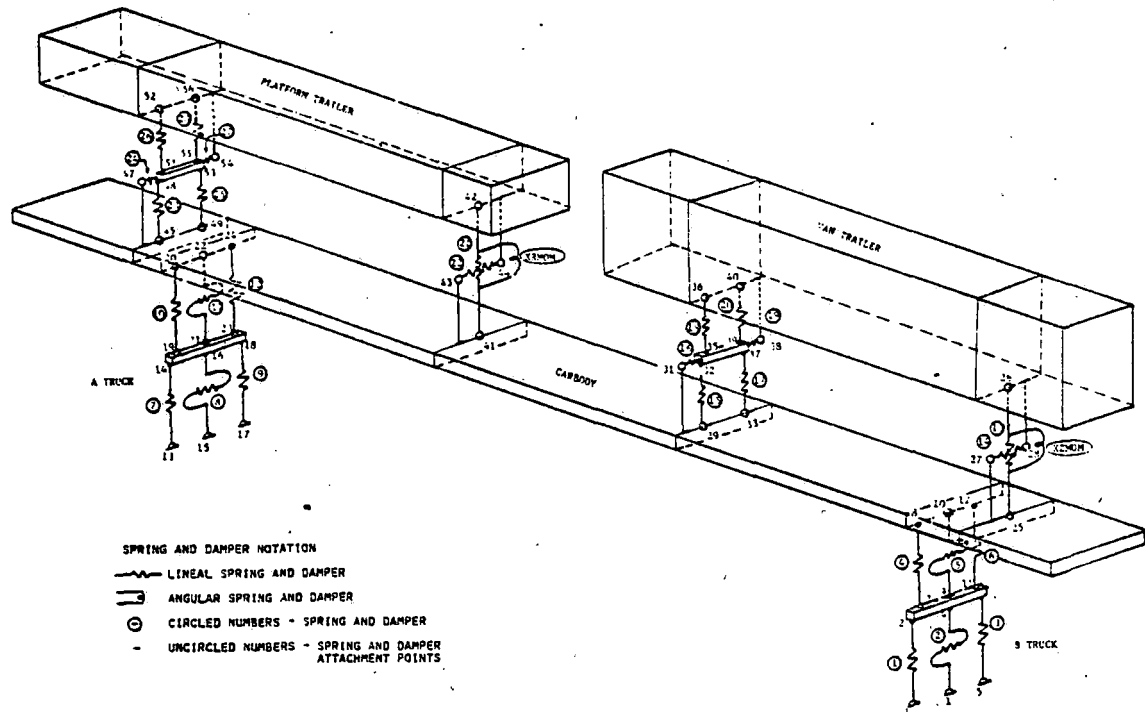


Fig. 1 - Schematic diagram of FRATE/TOFC math model showing spring/damper notations

shapes were normalized to obtain unity generalized mass. With this information the first seven "normal" modes were each included in the time domain problem as a separate equation of motion and treated as another lumped mass.

#### DESCRIPTION OF TOFC VIBRATION TEST

Trailer on a Flatcar optimization tests were performed using the Vertical Shaker System at the Rail Dynamics Laboratory (RDL), Pueblo, Colorado. The purpose of these tests was to determine the effect of TOFC system component variations on lading acceleration levels. Selected configurations of full-scale loaded and unloaded TOFC systems were tested by exciting all four wheels of one truck of a TTAX flatcar. Accelerometers and displacement transducers were mounted on the shakers, the flatcar, the two trailers located on the flatcar, and lading in the trailers. Analog-conditioned signals from these sensors were input to the VSS computer control system for digitization and data reduction.

The primary goal of this effort was to determine, under controlled laboratory conditions, the effect of TOFC configuration changes on lading acceleration levels. Acquisition of data for use in the validation of a math model was of lower priority. As a result the test data

available was less than desired for both the number of measurements and format of data recording.

Description of the testing presented in this report is brief and intended only to give an overview. A detailed reporting of the test can be found in References 7 and 8.

**TEST FACILITY** - The Vertical Shaker System (VSS) used for TOFC testing consisted of four 40,000 pound force, computer-controlled hydraulic shakers. As shown in Figure 2, the shakers were positioned under one end of the TTAX flatcar and operated to simulate pitch (all shakers in phase) and roll (left pair out of phase with the right pair). Instrumentation was located throughout the TOFC vehicle to permit determination of the frequencies and deflections at vibration resonance of the flatcar and trailers and the resulting effect on the lading in the trailers.

VSS computer programs were used to drive the shakers either in an incrementally swept sinusoidal frequency mode or in a constant sinusoidal frequency mode over a maximum frequency range of 0.2 Hz to 30.0 Hz. Initial TOFC pitch and roll sweep tests were performed using constant amplitude and constant acceleration excitation profiles; however, a number of these tests resulted in sufficiently large dynamic response to automatically terminate

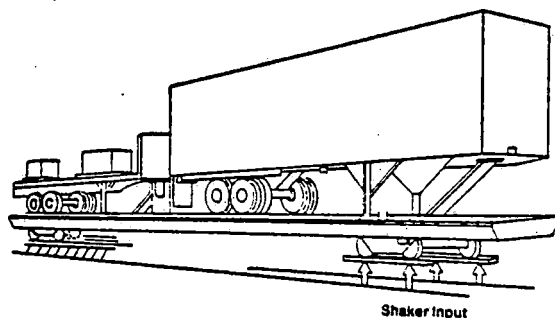


Fig. 2 - TOFC Test Configuration

the test due to VSS safety limit checks. This situation resulted in the establishment of sweep excitation profiles consisting of: a low-frequency constant displacement profile; a mid-frequency constant velocity profile; and a high-frequency constant acceleration profile. Constant frequency dwell tests were performed after observing TOFC peak response modes of interest from sweep test data. This type of shaker operation permitted close examination of TOFC system dynamics at predominant resonant frequencies.

**TEST CONFIGURATIONS** - A total of twenty TOFC configurations were tested using the VSS. The TTAX railcar, Serial #973295, utilized a suspension configuration consisting of ASF Ride Control trucks with D-5 spring groups, friction snubbing and standard side bearings. The trailers loaded on the TTAX railcars were a #ALLA Trailmobile van trailer, serial number L32820, and a #P41T Trailmobile flatbed trailer, serial number L32821. Additional suspension components tested on the TTAX flatcar included Stucki SV-6B horizontal stabilizers and Stucki resilient side bearings. Limited BarberS-2 truck testing was also performed.

The van trailer lading consisted of a 50,000 pound palletized load of canned goods and the flatbed trailer lading a 50,000 pound load of rail. Isle blocking and rear area cribbing were utilized to minimize movement of the palletized load in the van and strapping was used to contain the flatbed load.

**SUMMARY OF TEST RESULTS** - The summary of test results contained in Reference 7 was not in sufficient detail to feed a model validation effort. It was consequently necessary to request a new set of processed data from Wyle Laboratories in Colorado Springs, Colorado, who had the raw data stored on digital tape. The format of the data request was output/input amplitude ratio plotted against frequency (from sweep test runs) with a companion plot of output/input phase angles. A tabular data printout of all plotted data was also requested. An example plot of data is shown in Figure 3.

The quantity of TOFC vibration test data available on tape was far beyond practical limits of analysis. There were 116 sweep tests and 186 dwell and decay tests performed. There were between 80 and 100 response measurements made in each test or some 27,000 data plots potentially available for analysis. To obtain and use all of this data was out of the question.

Our primary objective was to validate the FRATE/TOFC model. Consequently the analysis of TOFC vibration data was planned to provide information needed for validation; specifically resonant frequencies, deflection shapes at resonance and damping estimates. Dwell and decay tests were eliminated. In doing this there was some sacrifice of information on the nonlinear characteristics of the vehicle. The plan limited the analysis of sweep test data to the three configurations of:

- a. empty undamped flatcar
- b. loaded undamped flatcar
- c. loaded, damped flatcar

Configuration (a) would permit validation of the flatcar in its simplest and most tractable condition. Configuration (b) would permit a validation of the model including the trailers. Condition (c) would validate the full up TOFC in its nominal configuration.

The data analysis procedure followed is outlined in Table I.

The phase angle data were used as an aid to identifying resonances since in a well behaved, linear, undamped system the  $90^\circ$  phase angle crossing can be used as a resonance identifier. However, because of the nature of our vehicle it was necessary to use the response amplitude ratio plots as the main tool for resonance identification. The procedure used was to first categorize measurement in five ways; measurements on the flatcar carbody structure, on the flatcar trucks, on the van trailer structure, on the lading within the van trailer and finally the platform trailer structure. The data was further divided into direction of measurement; vertical, lateral and longitudinal.

With the data thus divided superposition tracings were made of all accelerometer measurements on 15 plots, grouped three plots on each of 5 sheets of paper. A study of these superimposed plots, with referral to the original plots and tabular data as necessary, enabled the identification of resonant frequencies. Indications of what parts were the primary contributors of each resonance, the direction of predominant motions and a scaling of the relative importance or strength of each resonance were noted.

The next step after resonance identification was to obtain a tabulation of amplitude ratio and phase angle for each resonance identified using the computer tabulation. During this process a more precise frequency identi-

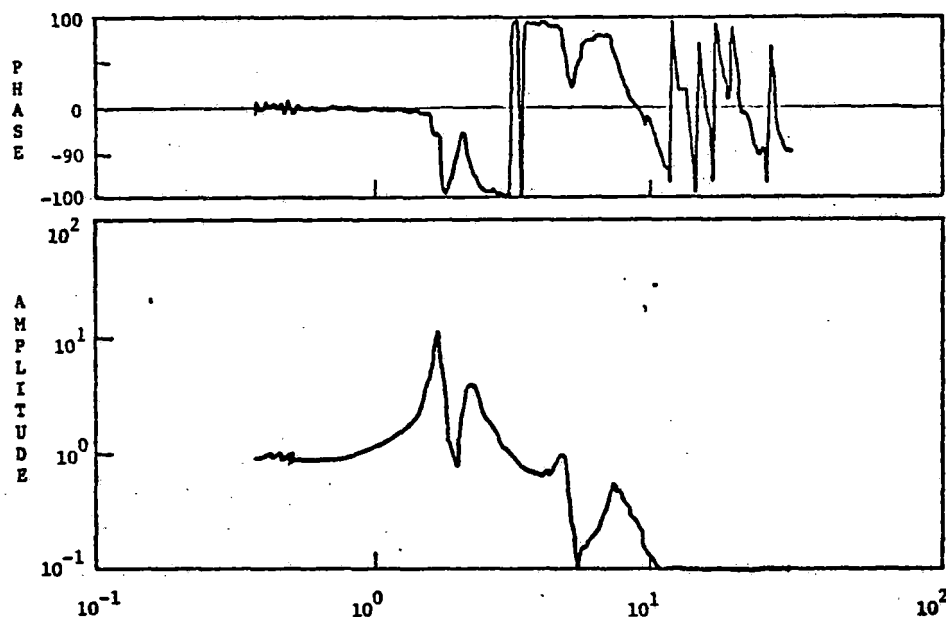


Fig. 3 - Example test data plot TOFC Optimization Test

cation was obtained by looking for maximum responses and  $90^\circ$  phase angle crossings.

It became apparent that we would not be able to obtain a deflection shape in its usual (normal mode) sense. There was an absence, in the phase angle data, of the in-phase or out-of-phase relationship associated with a normal mode deflection shape. It was necessary to study each deflection shape tabulation to find a predominant phase angle. This phase angle, called  $\phi_0$ , was used to adjust each amplitude by the following relationship:

$$A_1 = A_i \sin(\phi_i + 90 - \phi_0) \quad (1)$$

In order to facilitate the plotting of the test deflection shapes the plot subroutine SNAPSHOT, which had been developed in conjunction with FRATE, was modified to accept the test data. With computerized plotting of deflection shapes it was possible to obtain a sequence of deflection shapes through one cycle of motion. The "complex mode" nature of the resonances became quite obvious with the sequential pictures. Figure 4 presents a representative set of sequential deflection shapes for the fundamental vertical/pitch resonance. All of the

resonant frequencies identified in analysis of the test data are presented later.

#### ANALYSIS DESCRIPTION

The analysis procedure followed, using the FRATE computer program, was essentially the same as the test procedure. Excitation was applied to the B trucks; up and down sinusoidal frequency sweeps were performed to identify resonances; narrow band sweeps, dwells and decays were performed to characterize each resonance.

Analysis output was obtained in three forms: time histories, frequency spectra and deflection shapes. The frequency spectra were generated by performing frequency sweeps and plotting the results of response amplitude versus excitation frequency. The analysis process which evolved was to first identify fundamental resonance by the decaying vibrations. Then, frequency spectra were obtained for locating resonances above the fundamental. After all resonances had been thus identified, time history runs were made to more accurately locate the resonant frequency and to study the detail motions at resonance.

Table I - Outline Of Test Data Analysis Process

1. Request Data from Disc Storage
  - Format: Plotted/Tabulated
  - Which Runs Specified
  - Which Measurements Specified
2. Generate Superimposed Summary Plots
3. Identify Resonant Frequencies
  - Summary Plots
  - Single Plots
  - Print Data
4. Tabulate Amplitude and Phase Angle from Print Data for Each Resonance Identified
5. Identify Predominant Phase Angle
6. Store Data in Computer
7. Obtain Computer Plotted Deflection Measurements for Several Phase Angles
8. Draw Deflection Shapes

Resonance identification was made on the basis of maximum response and quadrature ( $\pi/2$ ) phase relationship between response and input motions. In some cases resonance identification was relatively clear. There were also resonances where the response vs. frequency curve was broad and muted and the phase angles were not at quadrature. In these cases resonance identification was based largely on the response curves and could not be done with the same degree of confidence.

Finally, deflection shape plots were made for each resonance identified. In most cases the deflection shapes were characteristic of complex modes rather than normal modes. That is, they had travelling rather than fixed node patterns. This effect is illustrated in the deflection shape plots shown in Figure 4. The complex mode effect is thought to be caused by application of excitation at one end and because of large damping in the system.

#### COMPARISON OF TEST/ANALYSIS RESULTS

The validation plan was to proceed sequentially from the empty, no snubber configuration to the fully loaded, no snubber and finally to the fully loaded, 100% snubber. The implied assumption in this plan was that differences between the empty and full configurations could be accounted for by mass and inertia differences. However, after a study of the resonant frequencies, summarized in Table II, it was concluded that

some spring rates in the rail car suspension system changed with the change in loading conditions. Consequently our approach was modified to comparing full and empty conditions simultaneously so that model changes could be picked which would result in improvements for both conditions.

For example, referring to Table II, the FRATE analysis frequencies are close to test frequencies for the fully loaded condition but high for the empty condition. The comparison is especially poor for the empty condition, first roll resonance where the analysis frequency is 1.2 times test. Model change objectives were consequently set to decrease stiffness for the empty condition and to find a change which would result in a change in roll stiffness but not in vertical stiffness.

A number of other observations were made from the comparisons of test and analysis results. These observations are summarized below.

**MISSING RESONANCES** in the FRATE results for the loaded conditions were noted and were hypothesized to be due to inadequate trailer models. This hypothesis was reinforced by the results of trailer vibration tests as reported in Reference 9. Reference 9 compared test results to the trailer model used in FRATE with the conclusions that trailer suspension should be softened and that trailer flexibility should be included.

**RESONANCES IDENTIFIED WITH CARBODY FLEXIBILITY** were noted to be high for the empty conditions. The comparisons appeared to be better for the full conditions but the missing resonances and the effects of the inadequate trailers models made it difficult to reach a clear conclusion.

**NONLINEAR EFFECTS** were most noticeable in the first roll resonance in the fully loaded condition. The apparent resonant frequency was sensitive to level of excitation and was found to vary between 0.5 Hertz for the highest level to 0.3 Hertz for the lowest level of excitation achieved in the test. This would indicate a nonlinear softening spring.

In support of this, the difference in response between up sweep and down sweep, as shown in Figure 5, is typical of a nonlinear softening spring. (Sweep rates in this frequency range were equivalent to about 10 minutes per octave which is slow enough to have no effect on response differences.)

**DEFLECTION SHAPES and EFFECTIVE SYSTEM DAMPING** were also compared. The comparison provided directions for changes in relative stiffness in the truck model springs to improve relative displacement comparisons and directions for changes to damping in general to improve response amplitude comparisons.

PHASE ANGLE, DEGREES

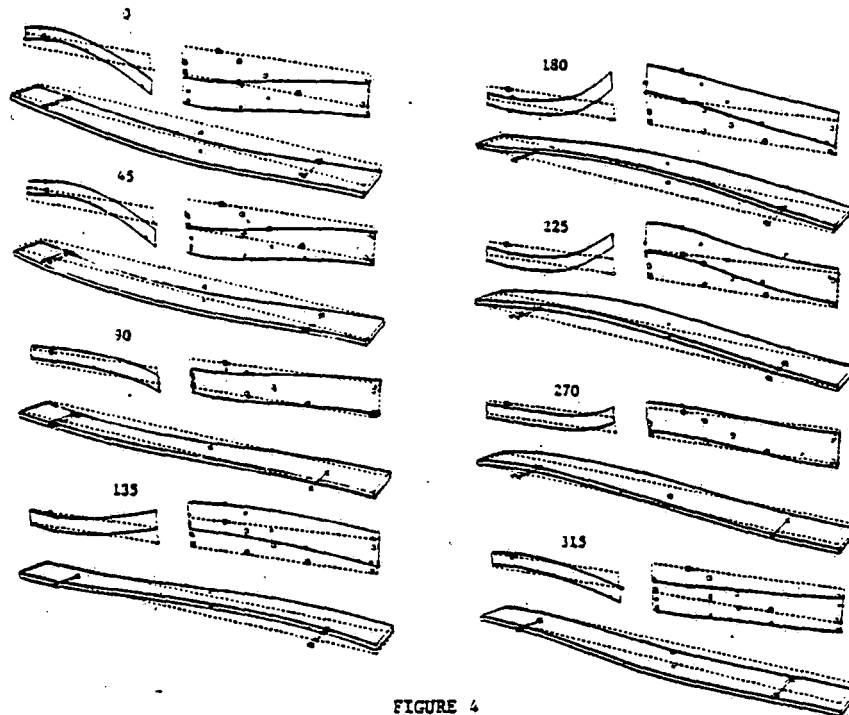


FIGURE 4  
TOFC TEST SEQUENCED SNAPSHOTS FOR THE FUNDAMENTAL VERTICAL/PITCH  
Frequency = 1.71 Hertz

#### MODIFICATIONS TO FRATE AND THE TOFC SIMULATION

There were many changes made to FRATE to achieve closer agreement between experimental and analytical results. A greater part of the changes were variations of spring and damper values. There were three mass term changes. There were changes to model topography requiring changes to certain of the basic equations of motion. The changes to the trailer models recommended in Reference 9 were incorporated with the exception that the trailers remained rigid bodies. Finally a coulomb damping representation was included.

The total modification procedure was too lengthy and involved to be described here. However there were certain changes made to the railcar trucks which are felt to be of general interest and are discussed. These changes have to do with a bilinear roll spring rate, a nonlinear transverse spring rate and a friction snubber.

#### TRILINEAR ROLL SPRING RATE OF TRUCKS -

With an examination of the truck configuration, sketched in Figure 6, one would conclude that the roll spring rate will have three different values; for when the center plate is seated, for when it is rocking and for when the side bearing is in contact. That is, for small amplitudes of roll motion where the center plate remains flat on its seat the major flexibility in roll is in the truck springs. At some amplitude of roll motion the transverse "g" forces will cause a moment at the center plate greater than the hold down movement afforded by the vertical "g" load of the carbody. At this point the center plate will start its rocking motion on its seat. As the roll amplitude is increased from this point the restoring moment, on the carbody, will decrease until side bearing contact is made. After side bearing contact is made the restoring moment is again dependent on the truck spring properties. For the range of amplitudes tested this would account for the nonlinear, softening spring effects.

Table II - Summary Comparison of Test &amp; Analysis Resonant Frequencies Using Prevalidation FRATE Model

## A. VERTICAL RESONANT FREQUENCIES (HERTZ)

## A.1 EMPTY FLATCAR

DESCRIPTION	TEST	ANALYSIS
VERTICAL TRANSLATION WITH BENDING	3.444	3.6
PITCH	4.213	6.7
CARBODY BENDING	5.185	8.1
CARBODY SECOND BENDING	10.805	13.0
CARBODY THIRD BENDING	17.640	-

## A.2 LOADED FLATCAR (TOFC)

DESCRIPTION	TEST	ANALYSIS
COUPLED TRAILER/ CARBODY PITCH/ BENDING	1.711	1.77
COUPLED TRAILER/ CARBODY PITCH/ BENDING	2.238	2.2
COUPLED TRAILER/ CARBODY PITCH/ BENDING	3.65	3.3
COUPLED TRAILER/ CARBODY PITCH/ BENDING	4.803	-
TRAILER SECOND BENDING	7.33	-
COUPLED CARBODY BENDING & VAN TRAILER BENDING	8.844	-
CARBODY SECOND BENDING	11.506	12.0

## B. ROLL RESONANT FREQUENCIES (HERTZ)

## B.1 EMPTY FLATCAR

DESCRIPTION	TEST	ANALYSIS
ROLL WITH LOW CENTER	1.184	3.8
ROLL WITH HIGH CENTER	2.000	5.5
CARBODY TORSION	10.114	13.3
CARBODY SECOND TORSION	16.209	-

## B.2 LOADED FLATCAR (TOFC)

DESCRIPTION	TEST	ANALYSIS
CARBODY ROLL WITH LOW CENTER	.50-.80	.87
CARBODY YAW	1.131	-
CARBODY ROLL WITH HIGH CENTER	2.330	-
PLATFORM TRAILER ROLL	2.681	-
COUPLED TRAILER & CARBODY ROLL	3.747	3.5
COUPLED TRAILER & CARBODY ROLL	6.222	-
COUPLED TRAILER & CARBODY ROLL	8.425	8.7
CARBODY TORSION	12.936	14.3

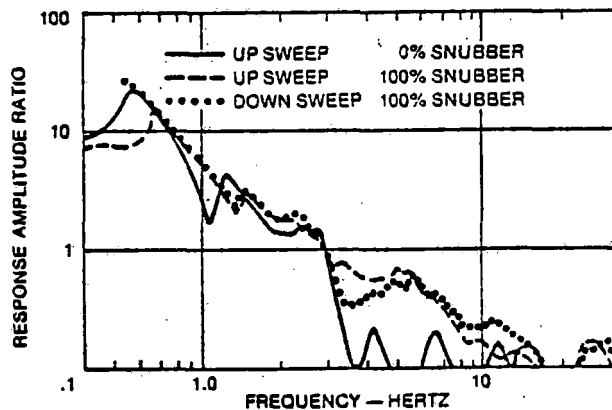


Fig. 5 - Comparison of response with up and down frequency sweep, TOFC Optimization Test: response location no. 48 (lading - top layer - center of trailer - lateral)

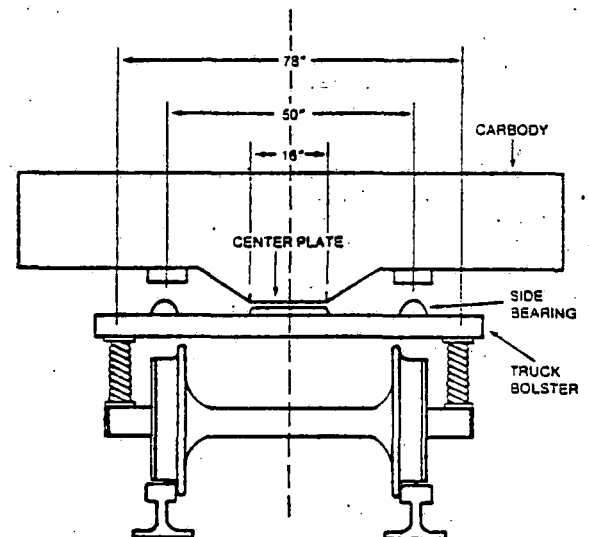


Fig. 6 - Sketch of freightcar end view showing center plate and side bearing

In order to be able to obtain a trilinear spring rate in roll without affecting the vertical characteristics the truck spring model configuration was modified as sketched in Figure 7. The new K(4) replaces the vertical properties of the old combined K(4) and K(6). The new K(6) replaces the roll properties of the old combined K(4) and K(6). The corresponding dampers were also modified in the same manner.

The next step would have been to program K(6), the truck roll spring, as trilinear to simulate the seated center plate, the rocking center plate and side bearing contact. However, we were unsuccessful in our attempts to simulate the kinematics of the rocking center plate with a one mass truck model. As a compromise K(6) was modeled as bilinear, the first section being made to represent roll motion before side bearing contact and the second section after contact.

With the bilinear truck roll spring it was recognized that the nonlinear, softening spring characteristics would not be achieved. However, it was concluded that the model could be considered valid if correlation of resonant frequencies was achieved and worst case (i.e. down sweep) resonance response was matched. The original and revised values of spring and damping rates are listed in Table III.

**TRUCK TRANSVERSE SPRING RATE** - The railcar suspension system contains two nests of coil springs in each truck, one nest on each side. Each nest contains 13 coil springs. The vertical, lateral and roll characteristics of the suspension system are determined by the vertical and lateral spring rates of the spring nests and their lateral spacing. Extensive testing has been performed and reported in Reference 10 on 70 ton truck components. The report shows the lateral spring rates for the spring nest of our configuration to be very nonlinear. For very light loads, corresponding to the empty conditions, this lateral spring rate was measured to be about 4000 lb./in. per spring nest, and 9000 lb./in. for the fully loaded condition.

Based on this information the truck lateral springs were varied separately for the empty and fully loaded cars to obtain agreement with test frequencies. The final values obtained were 1800 lb./in. empty and 3000 lb./in. full.

**COULOMB DAMPING** - Increasing and decreasing frequency sweeps were performed as a means of identifying resonant frequencies and detecting nonlinear characteristics. The frequency sweeps with roll motion input are also significant in that they actually represent the real life service condition of increasing or decreasing train speed on staggered, jointed rail. It was because of this fact that the response characteristics typified by Figure 5 was cause for concern. That is, the snubber can apparently cause a larger response than no snubber for a specific realizable condition. The inclusion of coulomb damping was consequently felt to be an important necessity for the study of modifications which will produce more effective snubbery.

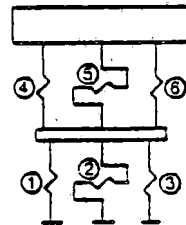
Table III- Revised Truck Spring/Damper Values.  
With Bilinear Roll Properties  
(For OK Snubber Condition)

ELEMENT	ORIGINAL VALUE	REVISED VALUES	
		Without side bearing contact	With side bearing contact
K(4), K(10)	22500 (1)	5000 (1)	5000 (1)
C(4), C(10)	70 (2)	140 (2)	140 (2)
K(6), K(12)	22500 (1)	.114E8 (3)	.0845E8 (3)
C(6), C(10)	70 (2)	.35E5 (4)	.21E6 (4)

units: (1.) pounds per inch  
(2.) pound seconds per inch  
(3.) inch pounds per radian  
(4.) inch pound seconds per radian

conversion factor: linear to angular: (78)<sup>2/2</sup>

ORIGINAL 8 TRUCK



MODIFIED 8 TRUCK

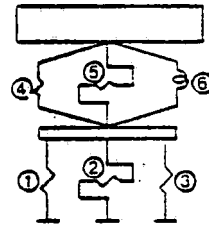


FIGURE 7  
TRUCK SPRING MODIFICATION FOR CENTER PLATE ROLL

Figure 8 is a truck side view which shows the snubber location. The snubbers are a pair of spring loaded friction shoes that move with the bolster and bear against friction plates on the side frame. Until the static friction forces in the snubbers are overcome, they provide a direct structural path from the bolster to the side frame, effectively locking out the spring nest. Once the static friction has been overcome the bolster moves relative to the side frame working against the spring nest and the snubber sliding friction.

Simulation of the snubber damper was incorporated into FRATE with the sliding point concept used in References 11 and 12. Figure 9 shows this change schematically. Again vertical motions and rolling motions are kept separate. KS4 and KS6 are springs which represent the relatively stiff structure of the bolster and side frame. The program logic was rewritten with the spring forces in K(4) and KS4 to be additive with the force in KS4 limited to the value MFS4 at which point the end of KS4 "slides". When the motion reverses KS4 will unload and load to -MFS4 at which point sliding again occurs. A load deflection path is pictured (not to scale) in Figure 10.

The roll counterparts K(6), KS6 and MFS6 were set up in a slightly different manner because the roll spring is tension and compression where the vertical spring will only transmit compression forces. A load deflection path for the roll springs is shown in Figure 11.



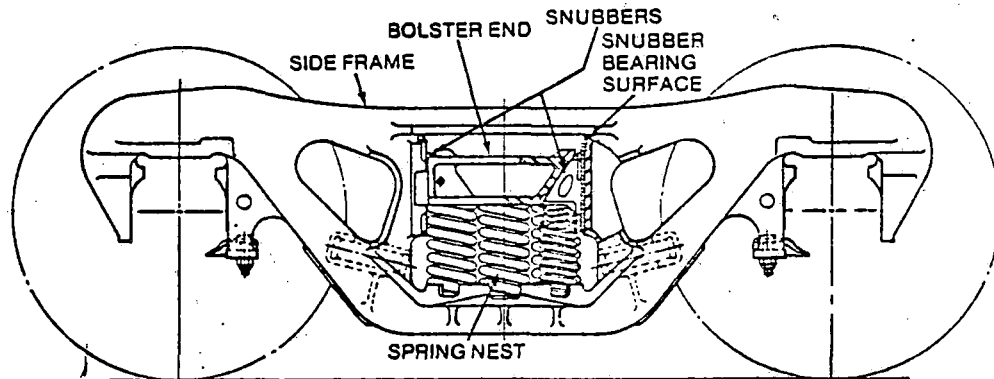
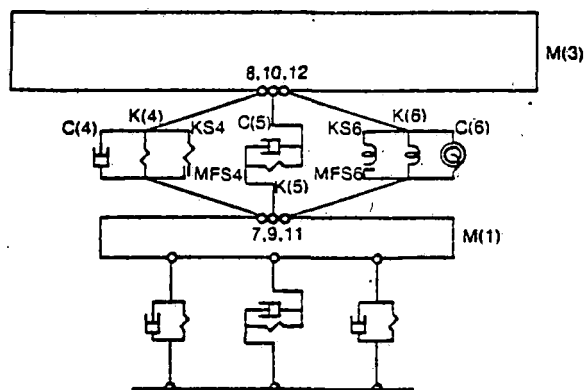


Fig. 8 - Side view of truck showing snubber location



- Legend:
- K(4) = total vertical spring rate for B truck
  - C(4) = viscous damper in parallel with K(4)
  - MFS4 = vertical friction damping force
  - KS4 = spring in series with MFS4
  - K(6) = total, bilinear, roll moment spring rate for B truck
  - C(6) = viscous damper in parallel with K(6)
  - MFS6 = angular friction damping moment
  - KS6 = roll moment spring constant in series with MFS6

Fig. 9 - Sliding coulomb damper representation of truck snubber

#### CORRELATION WITH MODIFIED MODEL

A summary of frequencies is shown in Table IV comparing resonances obtained from test data to resonances found with the revised FRATE/TOFC analysis. Frequency comparison is seen to be very good with the exception of the missing resonances in the analytical work which is attributed to the rigid trailer body assumption.

A qualitative comparison of deflection shape also shows good comparison again with the exception of trailer body flexing in the vertical resonances.

Up and down sweeps were also performed with the revised FRATE/TOFC analysis in order to check the accuracy of the sliding friction damper in reproducing the test nonlinear softening spring effects. Figure 12 presents the

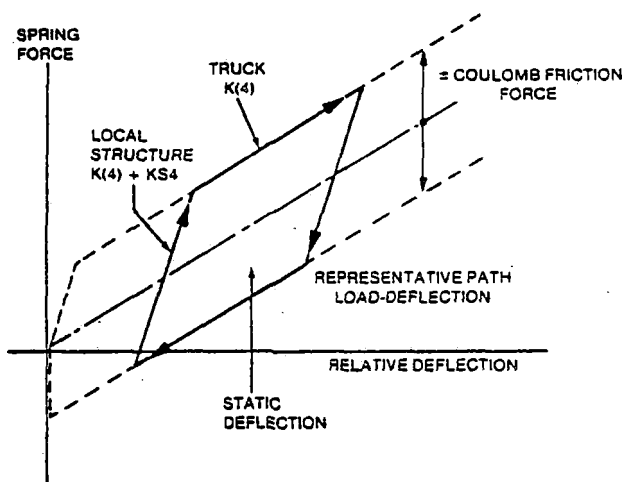


Fig. 10 - Load deflection curve for truck vertical spring with sliding friction force

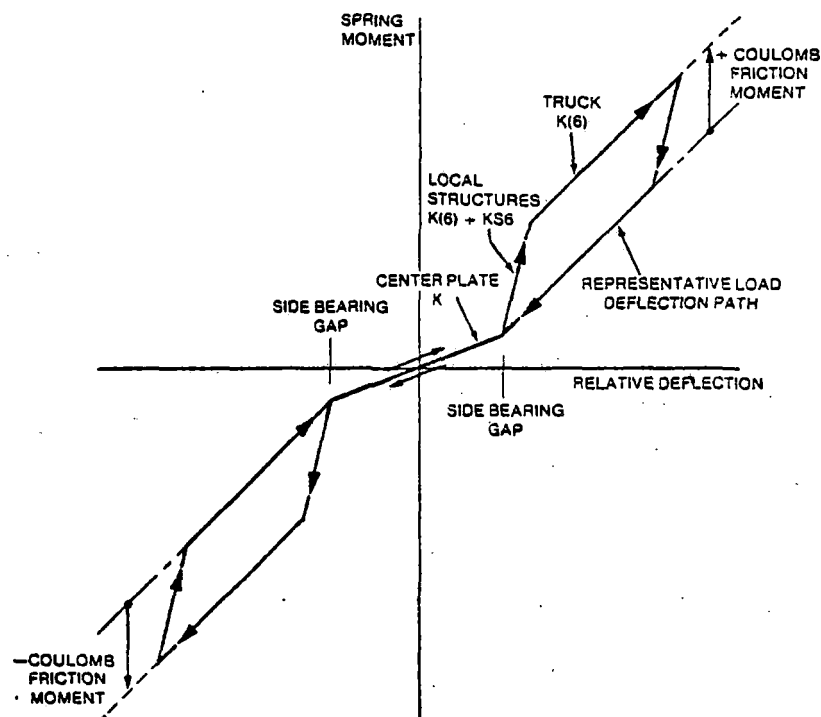


Fig. 11 - Load deflection curve for truck and center plate roll springs with sliding friction force

Table IV - Summary Comparison of Test Resonant Frequencies to Pre and Post Validated FRATE Results

## A. VERTICAL RESONANT FREQUENCIES (HERTZ)

## A.1 EMPTY FLATCAR

DESCRIPTION	TEST	ANALYSIS	
		①	②
VERTICAL TRANSLATION WITH BENDING	3.444	3.6	2.8
PITCH	4.213	6.7	4.6
CARBODY BENDING	5.185	8.1	6.2
CARBODY SECOND BENDING	10.805	13.0	9.9
CARBODY THIRD BENDING	17.640	-	-

## A.2 LOADED FLATCAR (TOFC)

DESCRIPTION	TEST	ANALYSIS	
		①	②
COUPLED TRAILER/CARBODY PITCH/BENDING	1.711	1.77	1.65
COUPLED TRAILER/CARBODY PITCH/BENDING	2.238	2.2	2.3
COUPLED TRAILER/CARBODY PITCH/BENDING	3.65	3.3	2.9
COUPLED TRAILER/CARBODY PITCH/BENDING	4.803	-	4.5
TRAILER SECOND BENDING	7.33	-	-
COUPLED CARBODY BENDING & VAN TRAILER BENDING	8.844	-	-
CARBODY SECOND BENDING	11.506	12.0	9.0

## B. ROLL RESONANT FREQUENCIES (HERTZ)

## B.1 EMPTY FLATCAR

DESCRIPTION	TEST	ANALYSIS	
		①	②
ROLL WITH LOW CENTER	1.184	3.8	1.16
ROLL WITH HIGH CENTER	2.000	5.5	2.22
CARBODY TORSION	10.114	13.3	10.0
CARBODY SECOND TORSION	16.209	-	-

## B.2 LOADED FLATCAR (TOFC)

DESCRIPTION	TEST	ANALYSIS	
		①	②
CARBODY ROLL WITH LOW CENTER	.50-.80	.87	.48-.7
CARBODY YAW	1.131	-	1.09
CARBODY ROLL WITH HIGH CENTER	2.330	-	1.9
PLATFORM TRAILER ROLL	2.681	-	2.1
COUPLED TRAILER & CARBODY ROLL	3.747	3.5	2.9
COUPLED TRAILER & CARBODY ROLL	6.222	-	6.1
COUPLED TRAILER & CARBODY ROLL	8.425	8.7	-
CARBODY TORSION	12.936	14.3	10.4

① Pre validation    ② Post validation

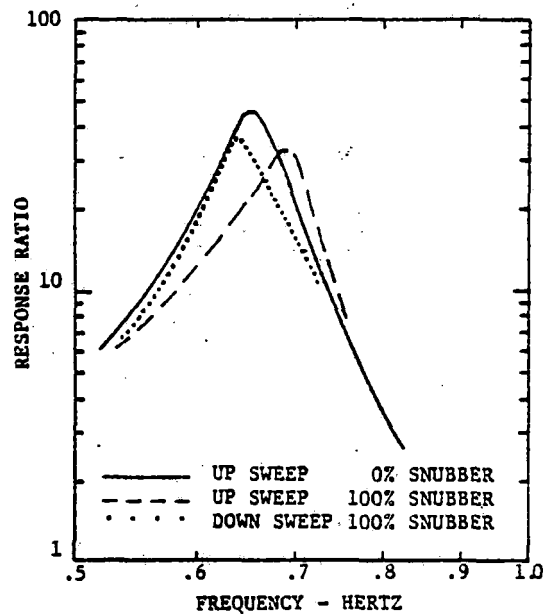


Fig. 12 - FRATE analysis results showing effect of coulomb damper on first roll resonance

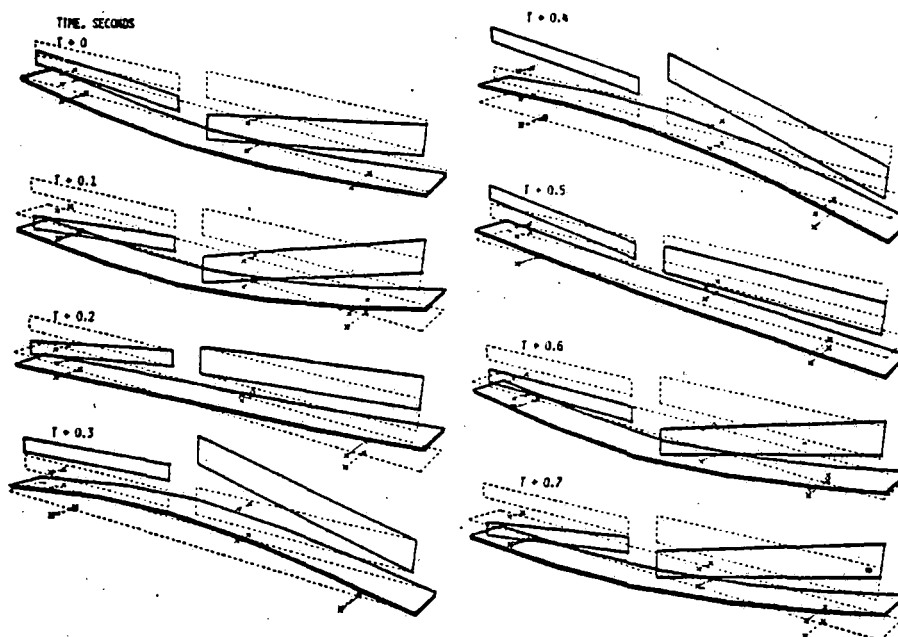


Fig. 13 - FRATE/TOFC sequenced snapshots, 1.65 Hz vertical resonance

response of a point in the model equivalent to the measured point shown in Figure 5. The comparison shows that we have not been able to reproduce the softening nonlinear spring characteristics.

Deflection shape comparisons were also made during the process of modifying the model as well as with the final configuration. Figures 13 and 14 are representative plots. Figure 13 is a sequence of deflection shapes through one cycle of motion and is directly comparable to the test sequence of deflection shapes shown in Figure 4. Excitation in the analysis was the same as test; i.e., at the B truck. Figure 14 compares a single picture from test and analysis.

#### CONCLUSIONS

Through a comparison of resonant frequencies and deflection shapes it has been shown that good comparison between test and analysis has been achieved. Model validation is claimed with limitations.

Because of the complex nature of the vehicle tested and the limited aspect of the experimental data, it was not possible to apply parameter estimation methods. The resulting model is possibly not as accurate as it might have been. On the other hand, because of the intuitive procedures followed, a better understanding of the physical/mathematical relation-

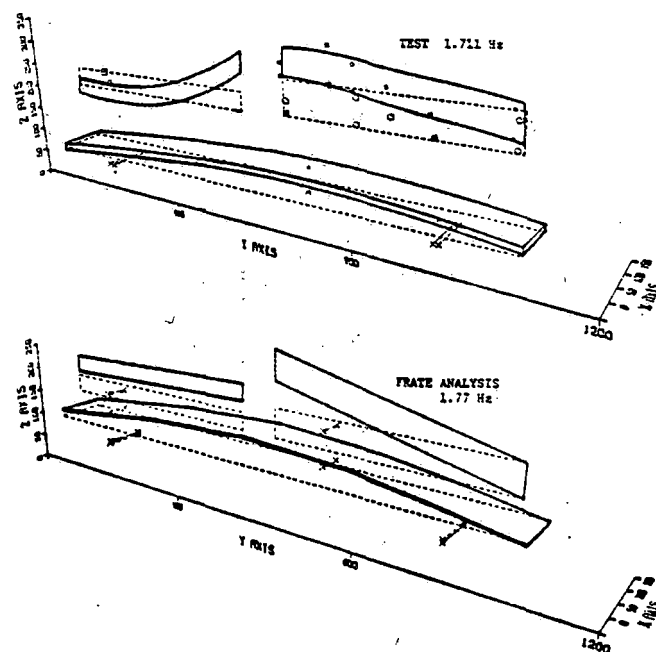


Fig. 14 - Analysis to test deflection shape comparison, TOFC configuration, first vertical resonance.

ship of the model has resulted. This is especially valuable since the applications of FRATE/TOFC will not be primarily for the test configuration against which validation was made. Applications will rather be in the study of how variations to the configuration will affect its dynamic response characteristics and in the study of other rail car configurations.

#### REFERENCES

1. Raymond Cohen, "Identification in Vibratory Systems, A Survey," R. W. Herrick Laboratories, Perdue, University, West Lafayette, Indiana, ASME No. 13320, Identification of Parameters in Distributed Systems.
2. M. J. Healey, "A Computer Method for Calculating Dynamic Responses of Nonlinear Flexible Rail Vehicles," ASME Paper No. 76-RT-5, 1976.
3. D. R. Ahlbeck, et al, "Comparative Analysis of Dynamics of Freight and Passenger Rail Vehicles," Battelle - Columbus, FRA-ORD&D, 74-39, March 1974.
4. Samuel Levy, and John P. D. Wilkinson, "The Component Element Method in Dynamics," McGraw-Hill Book Company, New York, New York, 1976.
5. L. C. Sutherland, "Sonic and Vibration Environments for Ground Facilities - A Design Manual," Wyle Laboratories Research Staff Report No. WR 68-2, March 1968, NASA Contract NAS8-11217.
6. W. C. Hurty, and Rubenstein, "Dynamics of Structures," Prentice-Hall June, 1964.
7. G. B. Bakken, and G. R. Fay, "Laboratory Techniques for Quantifying the Performance of Rail Vehicles Utilizing Servo-Controlled Hydraulic Vertical Actuators," ASME Publication No. 76-WA/RT-5 July 1976.
8. Carl Peterson, et. al., "Vertical Shaker System Laboratory Tests of Trailer on Flatcar (CR-124)", ENSCO, Inc., 20 South Quaker Lane, Alexandria, Virginia 22314.
9. George Kachadourian, "Results of MITRE Analysis of Data From Vibration Testing of a Van Trailer for the TOFC Program", MITRE Report No. WP 11799, August 1976.
10. Track-Train Dynamics, Harmonic Roll Series, Volume 2, "70 Ton Truck Component Data, Physical Restraints, Mechanical Properties, Damping Characteristics," 1974.
11. Peter W. Abbott, George Morosow and Jack MacPherson, "Track-Train Dynamics," SAE National Aerospace and Engineering and Manufacturing Meeting, Culver City, California. November 1975, SAE Paper No. 751058.
12. R. Heller, J. M. Tuten, P. S. Kadala and E. H. Law, "Analog and Digital Computer Simulation of Coulomb Friction," Report No. FRA/ORD-78-07, Interim Report, December 1977.



This paper is subject to revision. Statements and opinions advanced in papers or discussion are the author's and are his responsibility, not the Society's; however, the paper has been edited by SAE for uniform styling and format. Discussion will be printed with the paper if it is published

**Society of Automotive Engineers, Inc.**  
400 COMMONWEALTH DRIVE, WARRENDALE, PA. 15090

in SAE Transactions. For permission to publish this paper in full or in part, contact the SAE Publications Division.

Persons wishing to submit papers to be considered for presentation or publication through SAE should send the manuscript or a 300 word abstract of a proposed manuscript to: Secretary, Engineering Activities Board, SAE.

Anthology of Rail Dynamics Research,  
Volume II: References for Inclusion in Final  
Report , 1982  
Systems Control Technology, Inc

**PROPERTY OF FRA  
RESEARCH & DEVELOPMENT  
LIBRARY**